

Electronic Spectroscopy of Flavins in a Cryogenic 22 - Pole Ion Trap

vorgelegt von

M. Sc.

David Müller

an der Fakultät II – Mathematik und Naturwissenschaften

der Technischen Universität Berlin

zur Erlangung des akademischen Grades

Doktor der Naturwissenschaften

– Dr. rer. nat. –

genehmigte Dissertation

Promotionsausschuss:

Vorsitzender: Prof. Dr. Andreas Knorr

Gutachter: Prof. Dr. Otto Dopfer

Gutachter: Prof. Dr. Michael Schmitt

Tag der wissenschaftlichen Aussprache: 16. Juli 2021

Berlin 2021

Abstract

Flavins are of great biological relevance, but little information is known about the isolated flavins. This dissertation deals with the electronic photodissociation spectroscopy of cryogenically cooled flavins. The optical spectra are recorded with a tandem mass spectrometer coupled to a cryogenic 22 - pole ion trap and an electrospray ionization source. Here, the first high-resolution vibronic spectra of protonated and alkali metalated flavins isolated in the gas phase are reported. A joined approach of quantum chemistry and cryogenic ion spectroscopy is employed to reveal intrinsic information of the complexes including lumichrome, lumiflavin, and riboflavin. The systematic investigation provides accurate trends of the geometric, vibrational, and electronic properties. Precisely, all measured spectra are assigned to $S_1 \leftarrow S_0$ ($\pi\pi^*$) transitions. The experimentally extracted S_1 origin transitions are either blue- or red-shifted to those obtained for neutral flavins, which is connected to a decrease and increase in the intermolecular interaction strength upon $\pi\pi^*$ excitation, respectively. Importantly, the isomers are investigated in an isomer-selective fashion because the spectral absorption range is sensitive to the site of metalation and protonation. The intramolecular vibrational structure is similar for all investigated complexes, because the orbitals contributing to the electronic excitation do not cover the relevant functional group or the metal/proton. In contrast, the intermolecular structures is highly sensitive to the size and site of metalation, and the site of protonation. Finally, while the metals bind mostly electrostatic to the flavins, the smaller proton binds covalently to them.

Zusammenfassung

Flavine sind von großer biologischer Relevanz, aber nur wenige Informationen sind über die isolierten Flavine bekannt. Diese Dissertation beschäftigt sich mit der elektronischen Photodissoziationsspektroskopie von kryogenen Flavinen. Die optischen Spektren werden mittels eines Tandem-Massenspektrometers aufgenommen, welches mit einer kryogenen 22 - Pol Ionenfalle und einer Elektrospray-Ionisationsquelle ausgestattet ist. In dieser Arbeit werden die ersten hochau aufgelösten vibronischen Spektren von protonierten und alkali-metallierten Flavinen, die in der Gasphase isoliert wurden, präsentiert. Ein kombinierter Ansatz aus quantenchemischen Rechnungen und kryogener Ionenspektroskopie wird benutzt, um intrinsische Informationen von Lumichrom-, Lumiflavin- und Riboflavin-Komplexen aufzudecken. Die systematische Untersuchung liefert genaue Trends der geometrischen, vibrations und elektronischen Eigenschaften. Alle gemessenen Spektren werden den $S_1 \leftarrow S_0 (\pi\pi^*)$ Übergängen zugeordnet. Die experimentell extrahierten S_1 Bandenursprünge sind entweder blau- oder rotverschoben zu denen, die für neutrale Flavine gemessen wurden, was mit einer Abnahme bzw. Zunahme der intermolekularen Wechselwirkungsstärke bei $\pi\pi^*$ Anregung verbunden ist. Isomere können isomeraselektiv untersucht werden, da der spektrale Absorptionsbereich stark von der Position der Metallierung und Protonierung abhängt. Die intramolekulare Schwingungsstruktur ist für alle untersuchten Komplexe ähnlich, da die Orbitale, die zur elektronischen Anregung beitragen, weder die relevante funktionelle Gruppe noch das Metall/Proton beinhalten. Im Gegensatz dazu hängt die intermolekulare Struktur sehr stark von der Größe und der Position der Metallierung und der Position der Protonierung ab. Abschließend, die Metalle binden überwiegend elektrostatisch an die Flavine, währenddessen das kleinere Proton kovalent gebunden ist.

List of Publications

Effect of alkali ions on optical properties of flavins: vibronic spectra of cryogenic M⁺lumiflavin complexes (M=Li-Cs)

David Müller, Pablo Nieto, Mitsuhiro Miyazaki and Otto Dopfer

Faraday Discuss., 2019, **217**, 256

<https://doi.org/10.1039/C8FD00203G>

Optical spectroscopy of cryogenic metalated flavins: The O2(+) isomers of M⁺lumiflavin (M=Li-Cs)

David Müller and Otto Dopfer

J. Photochem. Photobiol., 2020, **3-4**, 100009

<https://doi.org/10.1016/j.jpap.2020.100009>

Vibronic optical spectroscopy of cryogenic flavin ions: the O2⁺ and N1 tautomers of protonated lumiflavin

David Müller and Otto Dopfer

Phys. Chem. Chem. Phys., 2020, **22**, 18328

<https://doi.org/10.1039/D0CP03650A>

Interaction of alkali ions with flavins: infrared and optical spectra of metal-riboflavin complexes

David Müller and Otto Dopfer

J. Phys. Chem. A, 2021, **125**, 3146

<https://doi.org/10.1021/acs.jpca.1c01846>

Optical spectroscopy of isolated flavins: photodissociation of protonated lumichrome

Alexander Sheldrick, David Müller, Alan Günther, Pablo Nieto and Otto Dopfer

Phys. Chem. Chem. Phys., 2018, **20**, 7407

<https://doi.org/10.1039/C8CP00590G>

Effect of alkali ions on optical properties of flavins: vibronic spectra of cryogenic M⁺lumichrome ions (M = Li-Cs) in the gas phase

Pablo Nieto, David Müller, Alexander Sheldrick, Alan Günther, Mitsuhiro Miyazaki and Otto Dopfer

Phys. Chem. Chem. Phys., 2018, **20**, 22148

<https://doi.org/10.1039/C8CP03950J>

Optical spectrum of the adamantane cation

Parker Brian Candrall, David Müller, Juliette Leroux, Marko Förstel and Otto Dopfer

Astrophys. J. Lett., 2020, **900**, 20

<https://doi.org/10.3847/2041-8213/abafbd>

BerlinTrap: A new cryogenic 22-pole ion trap mass spectrometer

Alan Günther, Pablo Nieto, David Müller, Alexander Sheldrick, Dieter Gerlich and Otto Dopfer

J. Mol. Spectrosc., 2017, **332**, 8

<https://doi.org/10.1016/j.jms.2016.08.017>

Eidesstattliche Erklärung

Hiermit versichere ich, dass ich die vorliegende Arbeit selbstständig verfasst und keine anderen als die angegebenen Quellen und Hilfsmittel benutzt habe. Alle Ausführungen, die anderen veröffentlichten oder nicht veröffentlichten Schriften wörtlich oder sinngemäß entnommen wurden, habe ich kenntlich gemacht.

Die Arbeit hat in gleicher oder ähnlicher Fassung noch keiner anderen Prüfungsbehörde vorgelegen.

Berlin, 31.05.2021

Ort, Datum

Unterschrift

Table of Contents

1. Introduction	1
1.1. Biomolecules	1
1.2. Flavins	1
1.3. Spectral and Photophysical Properties of Flavins.....	3
1.4. Gas-Phase Spectroscopy.....	4
1.5. IRMPD Spectroscopy of Flavins	6
1.6. Thesis Outline	6
2. Setup and Experimental Methods	9
2.1. Overview and Working Principle	9
2.2. Electrospray Ionization	10
2.3. Skimmer and MiniQP.....	11
2.4. Hexapole and QMS	12
2.5. Bender and Octupole.....	12
2.6. 22-Pole Ion Trap	12
2.7. ReTOF	13
2.8. Timing of BerlinTrap	13
2.9. Spectra and Laser Systems	15
2.10. Vacuum System	17
3. Theoretical Methods.....	19
3.1. Density Functional Theory	19
3.2. PBE0 and cc-pVDZ.....	20
3.3. Potential Energy Diagram	21
3.4. Franck-Condon Principle.....	22
3.5. PGOPHER and GAUSSIAN	23
3.6. Vibrational Cooling	24
3.7. Deexcitation Pathways	25
3.8. Natural Transition Orbitals	26
3.9. Natural Bond Orbitals	26
4. Publications	27
4.1. Effect of alkali ions on optical properties of flavins: vibronic spectra of cryogenic M ⁺ lumiflavin complexes (M=Li-Cs).....	27
4.2. Optical spectroscopy of cryogenic metalated flavins: The O2(+) isomers of M ⁺ lumiflavin (M=Li-Cs)	49
4.3. Vibronic optical spectroscopy of cryogenic flavin ions: the O2+ and N1 tautomers of protonated lumiflavin	63
4.4. Interaction of alkali ions with flavins: infrared and optical spectra of metal-riboflavin complexes	77

4.5.	Optical spectroscopy of isolated flavins: photodissociation of protonated lumichrome	93
4.6.	Effect of alkali ions on optical properties of flavins: vibronic spectra of cryogenic M ⁺ lumichrome ions (M = Li-Cs) in the gas phase	103
5.	Results and Discussion	117
5.1.	Assignment of VISPD Spectra	117
5.2.	Nature and Order of Electronic States	119
5.3.	Comparison S ₁ Adiabatic Excitation Energies	120
5.4.	Comparison of Experimental S ₁ Energies to Computed S ₁ Energies	124
5.5.	Introduction into Flavin Photophysics	125
5.6.	Analysis of VISPD Spectra	127
5.7.	Geometry Changes upon Electronic Excitation	132
6.	Conclusion and Outlook	133
	References	137
	Appendix	I
	Acknowledgements	II

1. Introduction

1.1. Biomolecules

Biomolecules are the building blocks of living organisms. Important biomolecules include for example DNA bases, amino acids, carbohydrates, and flavins.¹⁻³ The diverse functions of biomolecules are closely connected to their structure and also their environment. It is thus of particular interest to investigate the structure of biomolecules and to reveal the interplay between the biomolecule and its environment. Another major goal of research is the targeted manipulation of biomolecules to control their properties. The aim of this thesis is to investigate the intrinsic properties of an important class of biomolecules, i.e. protonated and metalated flavins, free from the influence of their environment.

1.2. Flavins

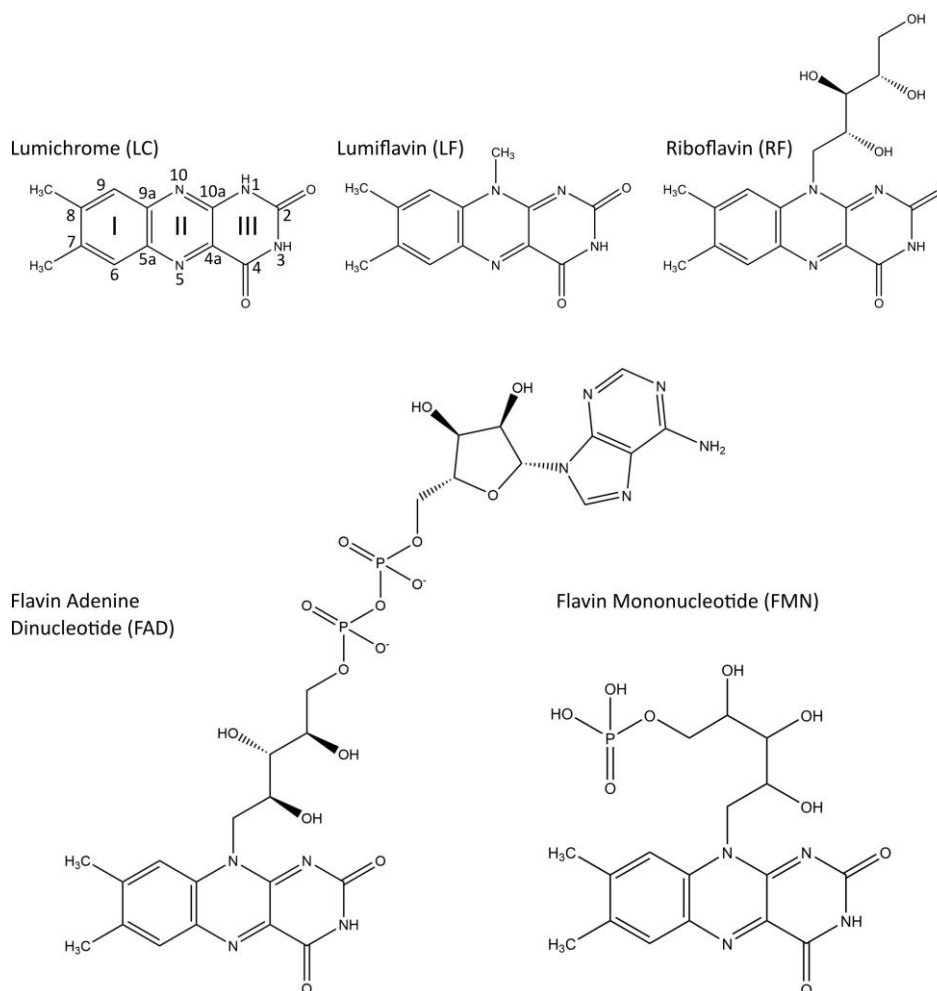


Figure 1. Chemical structures of lumichrome (LC), lumiflavin (LF), riboflavin (RF), flavin adenine dinucleotide (FAD), and flavin mononucleotide (FMN). The flavins differ by an alkyl substituent at the N10 position. The atom and ring numbering is according to IUPAC. The aromatic ring system comprises a benzene (I), pyrazine (II), and pyrimidine (III) ring.

The 1937 Nobel prize in chemistry was awarded to Paul Karrer for the synthesis and structural analysis of flavins.⁴ In general, flavins are yellow compounds (*flavus* is latin and means yellow) based on a heteroaromatic 7,8-dimethyl-10-alkyl-isoalloxazine structure (Figure 1). The aromatic ring system consists of a benzene (I), pyrazine (II), and pyrimidine (III) part. The various flavins (FI) differ by the functional group R at the nitrogen N10 position. The most important members of the flavin family include lumichrome (LC, 7,8-dimethyl-10-alkyl-alloxazine, R = H at N1 instead of at N10), lumiflavin (LF, R = CH₃), riboflavin (RF, R = ribityl), flavin adenine dinucleotide (FAD, R = ribophosphate + adenine), and flavin mononucleotide (FMN, R = ribophosphate). The chemical structure of these flavins is shown in Figure 1. The atom and ring numbering is assigned according to the IUPAC notation.

The most prominent member of the flavin family is RF, which is better known as vitamin B₂. Vitamins are either classified as fat soluble or water soluble. RF belongs to the water-soluble class of vitamins which can be absorbed through food. Foods that contain vitamin B₂ are milk, eggs, and green vegetable. The deficiency of any vitamin can cause a variety of diseases. The lack of vitamin B₂ for example can cause skin diseases. Due to its intense yellow colour, flavins are widely used as a dye for food and pharmaceuticals.^{2,5}

Flavins are used by Nature for a variety of biological processes.^{2,6–12} The majority of flavins do not occur in isolated form. For example, they occur as cofactors in flavoproteins, as FAD or FMN. Several flavoproteins have been reported so far, and every year new flavoproteins are discovered.² The reason why flavoproteins play a crucial role in many biological processes is that flavins are good electron acceptors and donors.¹² They can modulate parts of the molecule which do not directly absorb light.² One important process in which the flavin acts as a electron donor is for example is the repair of DNA.^{13,14} The DNA can be damaged for many different reasons (*e.g.* by ionizing radiation). One important DNA damage type is the generation of a cyclobutane pyrimidine dimer, where two nearby thymine molecules bind covalently to form a thymine dimer in the same DNA strand. Interestingly, photon radiation can not only cause lesions, but also trigger a possible DNA repair mechanism. For this process, the fully reduced FADH⁻ is involved in elementary steps of the DNA repair mechanism. Briefly, upon photon absorption FADH⁻ gets excited ($\text{FADH}^- + h\nu \rightarrow \text{FADH}^{*-}$) and an electron is transferred from the flavin to the thymine dimer. This electron transfer causes a bond-breaking process of the damaged part. Finally, the electron is transferred back to the flavin which closes the repair cycle.^{13,14} The elucidation of this DNA repair process was awarded with a Nobel prize in chemistry in 2015 to Lindahl, Modrich, and Sancar.¹⁴ Flavins are involved in quite a few more biological processes.^{7–9,12,14,15} For example, flavin-containing systems can act as blue-light sensors and as light-oxygen-voltage receptors in plants.^{15,16} Cryptochrome, a light-harvesting flavoprotein, is a potential magnetoreceptor for migrating animals employing the earth magnetic field,^{17,18} and flavins are also acting as electron donors and acceptors in the respiratory chain.⁸

1.3. Spectral and Photophysical Properties of Flavins

The spectroscopic and photophysical properties of flavins have been extensively studied in the past decades because of their crucial part in many photophysical processes. Flavins are thermostable, but highly photosensitive.^{2,7} For example, absorption of ultraviolet and visible light by FMN can result in several photofragments including LF and LC.¹⁹ The optically active flavin chromophore absorbs strongly in the UV-VIS range of the electromagnetic spectrum.⁷ A typical absorption spectrum of RF in aqueous solution exhibits four pronounced absorption bands at around 445, 375, 265, and 220 nm.⁷ The precise positions of these absorption bands are sensitive to external environmental factors (*e.g.*, pH, solvent, metal salt, and temperature). To understand these influences, the absorption properties of various flavins in different solvents have been studied as well as a function of the pH value.^{20–26} Depending on the pH, the flavin molecule is predominantly present in its neutral, cationic, or anionic form.^{24–26} Interestingly, for flavin in its cationic form (*e.g.*, LF at pH -1.08), the first two absorption bands which are characteristic and observed for the neutral flavin collapse to a broad, single absorption band.²⁵ The flavin chromophore is a strong photon absorber. Hence, according to the Einstein coefficients, neutral flavins are highly fluorescent.²⁷ In contrast, the anionic and cationic forms of flavins are non - fluorescent.²⁷ Furthermore, quenching of fluorescence has been described for metal-flavin complexes,^{28–30} and interactions of flavins with coordinating metal ions have been studied extensively.^{28–38}

Most of the experiments concerning flavins have been conducted in the condensed phase and at elevated temperature.^{24,39–47} A major goal is to investigate the bare, gas-phase flavins, free from any disturbing external factors to separate intrinsic properties from effects of environment. Hence, in the few past years, increasing effort has been made to investigate flavins in the gas phase.^{19,48–55} These experiments have been carried out for example for FAD mono- and dianions, alloxazine and LC anions, protonated alloxazine, and deprotonated RF.^{48–52} Unfortunately, most of these spectra are rather broad and unresolved because of spectral congestion arising from elevated temperature. Clearly, in order to obtain higher-resolution spectra containing more reliable information about geometric and electronic structure, cooling of the gas-phase ions to low temperatures is required.^{54,56–61}

Interpretation and understanding of the experimental data requires comparison to modern quantum chemistry calculations.^{21,62–79} This joined approach of quantum chemistry and experiments is a powerful tool to understand the physics underlying the photophysical properties not only of flavins. For example, by comparing computed absorption spectra to experimental absorption spectra one may be able to deduce the structure of the molecule. Here, density functional theory and time - dependent density functional theory coupled to multidimensional Franck-Condon simulations are used to analyse the experimental data.^{80,81} Calculations are often carried out for the isolated molecule, which neglects the effect of its environment. Both, the inclusion of solvent molecules,

vibronic effects, and temperature can improve the agreement between calculations and experiments.⁶⁷

1.4. Gas-Phase Spectroscopy

Spectroscopy is a powerful technique to gain information about molecules. It is of particular interest to remove the biomolecule from its natural environment to investigate its intrinsic properties.⁵⁷ Several experimental techniques to transfer molecules (neutral and ionic) into the gas phase have been proposed in the past. The simplest way to transfer neutral molecules into the gas phase is thermal heating. Unfortunately, this approach does not guarantee that the molecule of interest stays intact because many biomolecules are not thermostable. Another technique is laser desorption.⁸² This is often used for larger molecules. Here, the molecule of interest (*e.g.*, present as a rod or disk) is excited by a (pulsed) laser, and the desorbed molecule can then be transferred through a nozzle into the vacuum. The most widely used technique to softly transfer biomolecules into the gas phase is electrospray ionization.^{83–85} This powerful technique allows to transfer charged molecules (cations and anions) essentially without size limitations from solution into vacuum (given they are soluble).⁸³ The 2002 Nobel prize in chemistry was awarded to Fenn and Tanaka for their pioneering work on electrospray ionization and matrix-assisted laser desorption/ionization.^{83,86} The electrospray ionization technique is applied in this thesis to transfer flavin ions into the gas phase.^{87,88}

In contrast to the condensed phase, the number density of molecules in the gas phase is substantially smaller.⁸⁹ Charged molecules can be easily guided and trapped by electromagnetic fields. In the past years, many types of ion storage devices have been reported which allow trapping the molecules of interest. The most important devices include radio-frequency driven 3D Paul traps and linear traps.^{56,89–97} In 1989, Wolfgang Paul received the Nobel prize in physics for the development of the Paul trap.⁹⁸ Importantly, the traps can be coupled to a cryostat which allows cooling of the ions by means of a buffer gas, which reduces the internal energy of the ions.⁸⁹ Commercially available Paul traps have basically two drawbacks. First, these traps do not provide easy access for a laser. Second, the vibrational temperature is rather high and reaches above 40–50 K for a nominal trap temperature below 10 K.⁹²

Dieter Gerlich developed the first linear ion trap (22-pole) in 1992.⁸⁹ Since then, a variety of home-built traps with different numbers of poles ranging from 4–22 were designed.⁹⁹ In contrast to the Paul trap, linear traps are easily accessible for a laser beam, which is from the spectroscopy point of view highly beneficial. Furthermore, the ions can be cooled more efficiently. For example, a vibrational temperature in the order of 10 K has been reported.^{93,94} The radial confinement of ions in a 22-pole trap is highly sensitive to mechanical imperfections. In addition, the ion cloud density is minimal on the trap axis, which results in small overlap of the laser beam and the ion cloud.^{99–101} This drawback can be circumvented by lower-order ion traps, such as quadrupole and octupole traps.^{57,61,102,103} These

traps provide better radial confinement and a better overlap of the ion cloud with the laser beam can be achieved. A further development is the so-called 'wired' quadrupole trap.¹⁰⁴ This trap consists of four sets of thin rods which are arranged such that they reproduce a quadrupole field. This type of trap is less sensitive to mechanical imperfections, and the ion density is higher on the trap axis, which allows great overlap of the ions with a laser. This special design also allows easy access of a laser beam in both radial and axial direction. Here, a linear 22-pole trap is used for trapping and cooling of the ions.^{87,89} In addition, lower order multipoles (*e.g.*, quadrupole, hexapole, and octupole) are employed to guide and mass select the ions of interest.

In order to cool ions to temperatures below those achievable via buffer-gas cooling, the following approach can be used. A cell which is kept at room temperature contains the molecules of interest. A helium nanodroplet ($T = 0.4$ K) beam passes through this cell and picks up the molecules. Subsequently, a fraction of the He nanodroplets evaporates and cools itself and the contained molecule down to sub-Kelvins.^{105,106} This technique was successfully applied to many organic molecules, for example to neutral LF.⁵⁰ In general, cooling of the biomolecules within an ion trap is sufficient because the energy of the lowest vibrational energy levels is in the order of 20 cm^{-1} , and cooling the ions even further does not have a drastic impact.^{56,57}

Absorption measurements in the condensed phase rely on the direct absorption of photons according to the Lambert-Beer law. Due to the space-charge limit, the number density of ions which can be stored in an ion trap (*e.g.*, typically 10^6 ions cm^{-3}) is not high enough to perform direct absorption measurements.⁸⁹ Therefore, so-called action spectroscopy is employed to reveal information of the trapped molecules. Typically, biomolecules are polyatomic molecules with many chemical bonds.^{56,57} Upon excitation of the parent molecule with a laser, these bonds can break which can result in one or more charged fragments with different mass-to-charge ratios. This 'action' on the molecule can either be monitored as a depletion of the initial parent signal or as a generation of the laser induced fragment signal. The stronger the absorption, the higher is the intensity of the fragment signal or the depletion of the parent signal. The energy between different states of the molecule can be probed by tuning the wavelength of the laser.¹⁰⁷ The distribution of the generated fragments can be analysed by mass spectrometry. The most important mass analysers include quadrupole mass filter, time-of-flight mass spectrometer, and electromagnets.^{108,109} In our research group, different types of action-spectroscopy experiments have been carried out. The investigation of flavins by our group is divided in two steps. The first step includes infrared multiple photon dissociation (IRMPD) spectroscopy at room temperature, and the second step includes visible photodissociation (VISPD) spectroscopy of cryogenically cooled flavins (this thesis).¹¹⁰⁻¹¹⁸

1.5. IRMPD Spectroscopy of Flavins

In a first step our research group investigated mass-selected metalated and protonated flavins by means of infrared multiple-photon dissociation (IRMPD) spectroscopy and quantum chemical density functional theory calculations.^{110–112} The experiments were carried out at the free electron laser user facilities FELIX (Free Electron Laser for Infrared eXperiments)^{119,120} and CLIO (Centre Laser Infrarouge d'Orsay).¹²¹ All measurements were conducted at room temperature in the sensitive CO stretch range. The combined approach of IRMPD spectroscopy and quantum chemical calculations revealed the structure and preferred protonation and metalation (alkali and coinage) sites of LC, LF, RF, and FMN.^{110–112} As a result, these investigations demonstrate that the binding motif depends on both the type of flavin and the ligand. The flavin chromophore offers a variety of nucleophilic binding sites. The nomenclature of the most important binding sites relevant for this thesis is shown in Figure 2. The proton or metal cation benefits from the lone pairs of the heteroaromatic nitrogen and carbonyl oxygen atoms. For the O2+ and O4+ complexes, it was found that M^+ binds to both O and N atoms, and forms a chelate of the form N-M-O. For the O2 isomers, a nearly linear C-O2-M bond is formed. Due to the much smaller size of the proton, it can bind either to the nitrogen or oxygen atom as shown in Figure 2. This experimental and computational research leaves open the question of the electronic structure of these molecules which is the main target of this thesis.

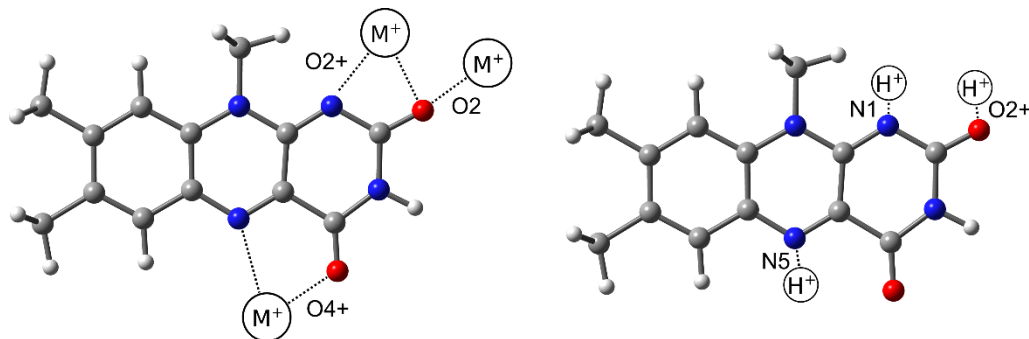


Figure 2. Nomenclature of various binding sites for M^+ (left) and H^+ (right) exemplary for lumiflavin (LF). Colour code: nitrogen (blue), oxygen (red), grey (carbon), hydrogen (white).

1.6. Thesis Outline

Due to the importance of flavins as photoactive molecules, it is of special interest to investigate their optical response. In this thesis, metalated (with alkali metals) and protonated flavins of different complexity are investigated by means of cryogenic ion spectroscopy. This thesis extends the first research phase in which IR spectra were measured to the optical domain to explore not only the geometric but also the electronic structure. The results presented here provide the first high-resolution optical spectra of any flavin isolated in the gas phase.

The recorded high-resolution spectra are analysed aided by quantum chemical calculations. In chapter 2, the experimental setup, a tandem mass spectrometer coupled to an electrospray ionization source, and a tuneable OPO/dye laser system is described. The mass-selected ions are trapped and cooled down in a cryogenic 22-pole ion trap. Optical spectra of the various flavin complexes are recorded by exciting the trapped ions with a pulsed laser and monitoring the laser induced fragments as function of the wavelength.^{87,88} The basic theoretical principles to understand the measured spectra are described in chapter 3. The publications obtained for this thesis are presented in chapter 4.^{113–118} The major findings are summarized and discussed in chapter 5 to describe the major general conclusions for the individual systems described in each paper. Finally, this thesis terminates with a conclusion and an outlook .

2. Setup and Experimental Methods

2.1. Overview and Working Principle

In this section, the setup and experimental methods are described. The data presented in this thesis are recorded employing the BerlinTrap apparatus, a schematic of which is shown in Figure 3.^{87,88} The BerlinTrap is a powerful setup to record VISPD spectra of mass-selected and cryogenically-cooled ions. The main parts of the experiment are described in the following section. Briefly, the setup comprises an electrospray ionization source (ESI) for ion generation, a quadrupole mass filter (QMS) for ion mass selection, a cryogenic 22-pole ion trap for storing and cooling the ions by means of He buffer gas, and a reflectron time-of-flight mass spectrometer (ReTOF) equipped with a microchannel plate (MCP) detector for ion detection. A more detailed description of the BerlinTrap can be found elsewhere.^{87,88} To record VISPD spectra, the BerlinTrap typically operates in a pulsed mode with a repetition rate of 10 Hz and is synchronized to a tuneable pulsed laser (OPO/dye).^{113–118} In the following section, the individual elements of the BerlinTrap are described in more detail.

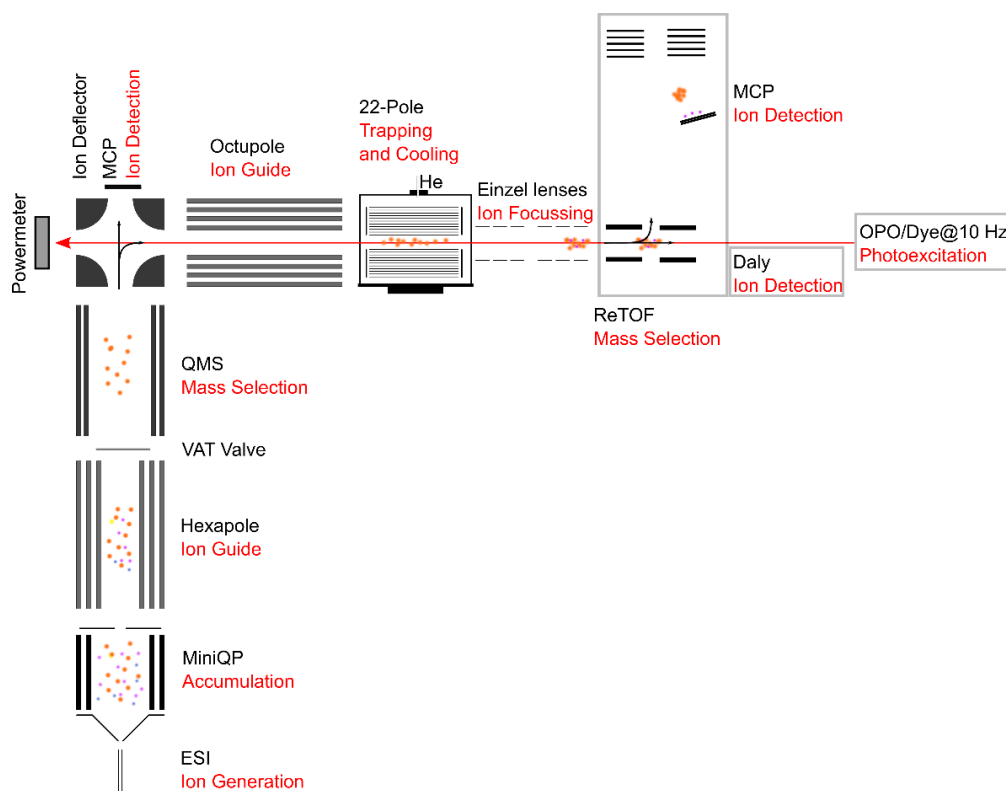


Figure 3. Schematic of the BerlinTrap setup; a tandem mass spectrometer is coupled to an electrospray ionization source and a temperature-controlled 22-pole ion trap. Ions with various m/z ratios are indicated as dots with different colour and size. The path of the laser beam is shown as a red arrow. Possible ion paths are shown as black arrows. A detailed description of the setup is given elsewhere.^{87,88} (ESI: electrospray ionization source, MiniQP: mini-quadrupole, QMS: quadrupole mass filter, MCP: microchannel plate detector, ReTOF: reflectron time-of-flight mass spectrometer, OPO: optical parametric oscillator).

2.2. Electrospray Ionization

The electrospray process is a gentle way to transfer large (bio-)molecules and also metal ions from solution into the gas phase. Importantly, the ESI process is a soft ionization technique. Thus, even biological macromolecules such as proteins can be transferred into the gas phase and ionized without destroying them.⁸³

A typical ESI experiment begins with a solution containing an analyte molecule being injected into the ESI needle through a capillary at atmospheric pressure. Between this capillary and a counter electrode, a high voltage potential (several kV) is applied and at high enough electrical fields, charged droplets are formed at the cone apex of the capillary. Two mechanisms have been proposed for ion generation, namely, charged residue and ion evaporation.^{85,122,123} In the former model, evaporation of the solvent results in an increase of charge density on the droplet surface until the Rayleigh limit is reached. At this limit, the droplet explodes into smaller parts due to Coulomb repulsion.¹²² The resulting droplets are again below the Rayleigh limit, and the process repeats until the bare gas-phase ions remain. In the second case, a single charged analyte molecule is desorbed from the droplet, which reduces the Coulomb repulsion within the droplet.^{85,123} Which effect is the dominant one can not be determined at this point.

The ESI source used here is commercially available from Agilent Technologies (1200 GC/MS and LC/MS/Varian). In a typical experiment conducted for this thesis (Figure 4), the solution is sprayed at a constant flow rate (typically 2 ml/h) at atmospheric pressure by a syringe pump through a small metal needle (0.1 mm inner diameter). The composition of the solutions to produce the various ionic flavin complexes is summarized in

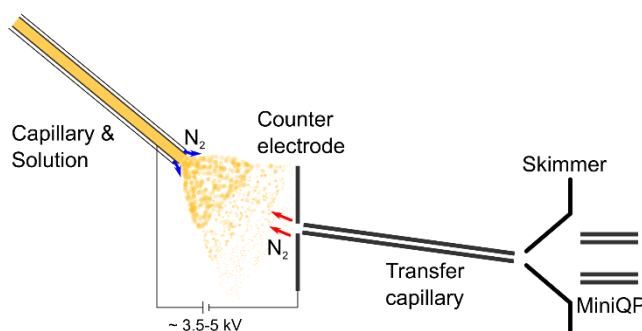


Figure 4. Schematic of the electrospray ionization source. A suitable solution is sprayed at a constant flow rate through a metal capillary. A high voltage potential is applied between the needle and the counter electrode. At the tip of the needle charged droplets are formed. The formation of droplets is supported by N₂ gas flow along the needle, as indicated by blue arrows. Heated N₂ gas flow against the droplets supports solvent evaporation, as indicated by red arrows. The transfer into the vacuum occurs at the end of the transfer capillary. The gas-phase ions are accumulated in the MiniQP before they are extracted and guided to the hexapole (not shown). Typical values for the ESI source are summarized in Table 2.

Table 1. A high voltage of 3.5 - 5.0 kV is applied between the needle and the counter electrode and the formation of droplets is further supported by N₂ nebulizing gas flowing along the needle. A transfer capillary (500 µm diameter, 15 cm length) is installed behind the counter electrode, at the end of which the solution is expanded into the vacuum. Solvent evaporation is supported by heated N₂ drying

gas (150 °C) flowing against the droplets, while the ESI source itself is heated to 30 °C to increase signal stability.

In the experiments discussed in this thesis, commercially available flavin powder (FI=LC, LF, or RF, purity >99 %) is used without further purification and dissolved in a mixture of methanol and water (Table 1). To generate M^+FI , an alkali metal chloride salt MCl is added to the solution. The ion production can be highly sensitive to the type of solvent. For example, to enhance protonation yield and to generate protonated H^+LF or H^+LC in sufficient abundance, formic acid is added to the solution containing methanol, water, and flavin powder.

Table 1. Composition of the solutions for creating ionic flavin complexes.

H⁺LC	H⁺LF	M⁺LC	M⁺LF	M⁺RF
2.5 mg LC	2-4 mg LF	2 mg LC	2 mg LF	1 mg RF
17 ml MeOH	19 ml MeOH	19 ml MeOH	20 ml MeOH	20 ml MeOH
2.5 ml HCOOH	2 ml HCOOH	1 ml H ₂ O	1 ml H ₂ O	1 ml H ₂ O
	1 ml H ₂ O	2-4 mg MCl	2-4 mg MCl	2 mg MCl

Table 2. Typical values for the elements of the electrospray source shown in Figure 4.

Instrument Parameters	
Flow rate	2 ml/h
Needle voltage	3.5-5 kV
Counter electrode	~100 V
Transfer capillary	80-200 V
Skimmer	10-20 V
MiniQP exit lens	5-20 V (Trapping) -(10-25 V) (Extraction)

2.3. Skimmer and MiniQP

The ions are skimmed behind the transfer capillary and trapped in a short mini-quadrupole (miniQP, $l=58$ mm). The miniQP is continuously filled with ions and trapping is ensured by collisions of the ions with background gas (usually N_2) at a pressure of $\sim 5 \times 10^{-3}$ mbar. This relatively high pressure ensures thermalization of the ions to ambient temperature. The thermalized ion ensemble is confined in axial direction by the potentials applied to the exit lens and the skimmer. The skimmer also acts as the entrance lens of the miniQP trap. In the radial direction, the ions are confined by an applied radiofrequency voltage ($f = 6.0$ MHz, Table 3). Furthermore, the skimmer allows to keep the rods of the miniQP clean, which is necessary to efficiently trap the ions. The exit lens potential can be pulsed to allow an extraction of the thermalized ions in bunches. The miniQP, skimmer, and transfer capillary are a single unit that can easily be dismounted for cleaning purposes.

2.4. Hexapole and QMS

After extraction of the ions out of the miniQP, the ions are guided via a home-built hexapole ion guide ($l=238$ mm, $f=6$ MHz) to a commercial QMS (Extrel, 150 QC). The hexapole chamber also serves as a differential pumping stage to ensure sufficiently low pressure ($\sim 10^{-8}$ mbar) for the following stages of the setup. In the QMS, the ions can be selected according to their mass-to-charge (m/z) ratio to exclusively transmit the desired parent ion. The mass range of the QMS covers up to m/z 1000, and the maximum mass resolving power of the QMS is on the order of $m/\Delta m \approx 1000$.

2.5. Bender and Octupole

After passing the QMS, the ions are guided to an electrostatic quadrupole deflector (bender) where they are either deflected by 90° for normal operation or transmitted linearly towards an “*on-axis*” MCP detector mounted behind the deflector for ion beam diagnostics. This diagnostics mode is highly beneficial to monitor and optimize the first part of the experiment (*e.g.*, ESI performance, miniQP trapping, QMS resolution), but will not play a role in the further discussion. Under normal operating conditions, the ions of interest are bent by the quadrupole deflector to an octupole ($l = 231$ mm, $f = 4$ MHz), that serves as an ion guide into the 22-pole ion trap.

2.6. 22-Pole Ion Trap

The linear 22-pole ion trap is the heart of the experimental setup.⁸⁹ An RF field applied to the rods in combination with pulsed entrance and exit lenses confine the ions both radially and axially in the trap. The 22-pole ($l = 36$ mm, $f = 7$ MHz) is mounted on a temperature-controlled cryostat (4-300 K, Sumitomo, SRDK-408D2, 1 W at 4.2 K), which is cooled to $T=6$ K for most of the experiments presented in this thesis. Cooling the ions is essential to avoid spectral congestion caused by hot bands.^{56,57} The mass-selected ions are trapped and cooled down by means of He buffer gas cooling. To this end, a single intense He pulse ($> 99.999\%$) is introduced through a pulsed piezo valve (repetition rate 10 Hz) directly into the 22-pole.⁸⁹ The 22-pole trap is covered by a copper shield in the shape of a box to ensure sufficient He density required for efficient trapping and cooling of the ions. The He gas itself is cooled by collisions with the rods, walls, and shield of the trap. The amount of He led into the trap can be controlled by the opening time of the piezo valve. The opening time is typically on the order of 1 ms, resulting in an average pressure of low 10^{-6} mbar. It must be kept in mind that the peak pressure is expected to be significantly higher. If the piezo valve is closed, the backing pressure in the 22-pole chamber reaches low 10^{-8} mbar.

The performance of the trap was characterized by several measurements. First, Cs^+ ions were trapped in the 22-pole for at least 15 min without any measurable loss of ions.⁸⁸ Second, the ions were cooled to an effective (ro-)vibrational temperature of around 20 K at a nominal trap temperature of 6 K. For example, the vibrational temperature of the protonated amino acid tyrosin H^+Tyr was

evaluated to be 18 ± 2 K by quantifying the hot band contributions of low-frequency modes.⁸⁸ The trap performance is in reasonable agreement with comparable traps reported in the literature.^{93,94} The cooling efficiency was also demonstrated through tagging experiments with He. For example, the complexation behaviour of hydronium ions with He ($\text{He}_n\text{H}_3\text{O}^+$, up to $n = 5$)⁸⁸ is similar to that reported with a comparable 22-pole ion trap.¹²⁴

Behind the trap, two modes of ion detection are available. First, along the linear 22-pole ion axis the ions are detected with a Daly detector. This configuration is suitable to monitor the performance of the 22-pole ion trap (*e.g.*, trapping efficiency) and the transmission through the Einzel lens systems, which are used to focus the ions as they exit the 22-pole trap. Similar to the “*on-axis*” MCP detector, the Daly detector is highly beneficial for alignment purposes, but it is not needed for recording the photodissociation spectra of the ions. Second, an orthogonal ReTOF mass spectrometer is used to record VISPD spectra.

Unfortunately, linear 22-pole traps have one drawback: the combination of the almost flat-bottom effective potential and the DC potentials on the entrance and exit lenses result in a minimum of the ion distribution on the trap axis.^{99–101} Hence, it is challenging to overlap a laser beam with the ion cloud within the trap. Here, we overlap the ions with the excitation laser behind the trap, after they are collimated using two Einzel lens stacks and before they are extracted into the orthogonal ReTOF.

2.7. ReTOF

The home-built ReTOF ($l = 1$ m, $m/\Delta m \approx 240$) is mounted orthogonally behind the 22-pole trap and is equipped with a MCP detector (Tectra, 2 MCP plates in chevron configuration, \varnothing 50 mm) for ion detection. For ion extraction into the ReTOF, high-voltage potentials (*e.g.*, 2900 and 3100 V) are applied by two fast switches (Behlke, GHTS 60) to the acceleration electrodes of the ReTOF. The orthogonal design makes it possible to monitor the ion masses simultaneously with high transmission (*e.g.*, parent ion and its photofragments).

Table 3. Parameters and properties for the various multipoles of the BerlinTrap. Reported are the diameter of the rods, the radius of the trap, the applied voltage, and the operating frequency.

	MiniQP	Hexapole	QMS	Octupole	22-pole
Driver	Home-built	CGC, RF-G50	Extrel, 150 QC	CGC, RF-G50	Home-built
\varnothing	3.2 mm	5.0 mm	19.0 mm	5.0 mm	1.0 mm
r_0	1.6 mm	5.0 mm	8.4 mm	7.5 mm	5.0 mm
U_0	250 V	350 V	variable	316 V	355 V
f	6 MHz	6 MHz	880 kHz	4 MHz	7 MHz

2.8. Timing of BerlinTrap

The BerlinTrap operates in a pulsed mode with a repetition rate of 10 Hz (Figure 5). At the beginning of a cycle, a He pulse is introduced into the 22-pole trap. The amount of He buffer gas is controlled by

the opening time (typically 1 ms) of the piezo valve. The ESI source produces ions continuously, which are trapped in the miniQP. At around 1.5 ms after the trigger for the piezo valve, the ions are extracted out of the miniQP and guided via several multipoles and Einzel lenses to the 22-pole. To achieve this, the potential of the exit lens of the miniQP is pulsed. The ions are trapped and cooled for around 90 ms in the 22-pole. After 99.5 ms the ions are extracted out of the 22-pole and guided via two Einzel lens stacks to the extraction region of the orthogonal ReTOF. To this end, both the potentials on the entrance and exit lenses of the 22-pole are pulsed. The delay between the 22-pole extraction and the ReTOF extraction depends on m/z because the path from the 22-pole to the ReTOF extraction region acts like a low-resolution time-of-flight. The laser operates at 10 Hz, too. It is tuned to achieve maximum temporal overlap with the ion cloud. This overlap is highest when the laser pulses are fired ca. 40 or 1 μ s before the extraction into the ReTOF.⁸⁷

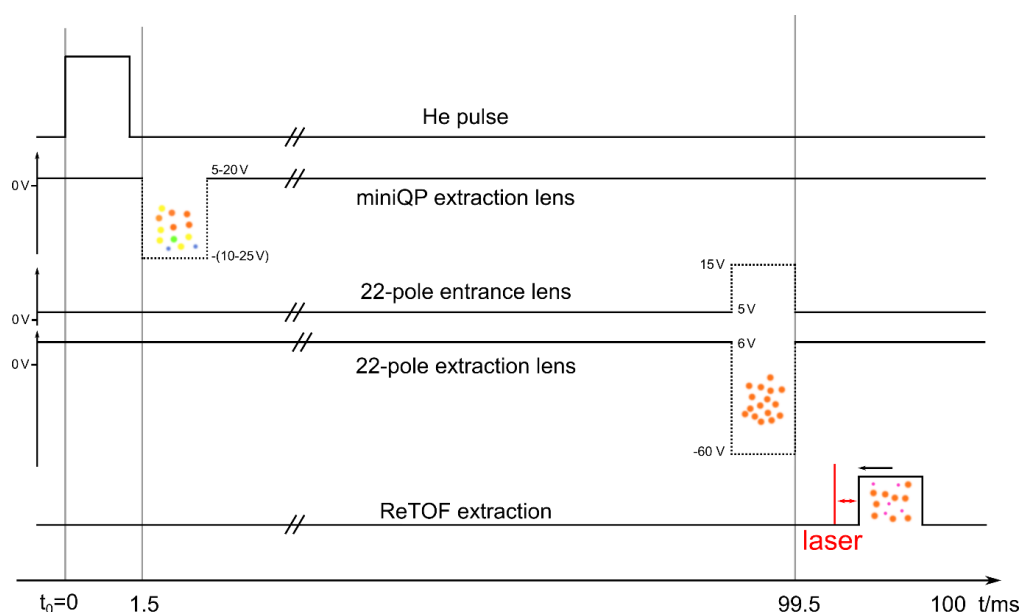


Figure 5. Typical timing schematic of a VISPD experiment. Both the ion cycle and the lasers are synchronized to 10 Hz. The ESI source (not shown) produces a continuous ion beam (not mass selected, indicated as coloured dots in the miniQP). At $t_0 = 0$ a He pulse with an opening time of typically 1 ms is introduced into the 22-pole ion trap. The delay between He pulse and miniQP extraction is set to maximize the ion intensity. Dashed lines indicate extractions out of the miniQP and the 22-pole. Otherwise, the trap is filled (miniQP) and the ions are trapped (22-pole, mass selected ions indicated as orange dots). Typical values for the potentials on the entrance and exit lenses are given in this figure. The zero volt value for the trap lenses is indicated. The timing of the extraction into the ReTOF is mass dependent. The laser pulse is tuned in time with respect to the ReTOF extraction (typically 1 or 40 μ s before extraction into the ReTOF) to achieve maximum temporal overlap with the ion cloud. Upon resonant photodissociation, both the parent and fragment molecules (indicated by orange and purple dots) are extracted simultaneously into the ReTOF. The timing for the He pulse and the ReTOF extraction are indicated by a trigger pulse. The schematic is not drawn to scale.

2.9. Spectra and Laser Systems

Electronic spectra are obtained by measuring the photo-induced dissociation yield of the selected molecules. To this end, two different light sources are available: an optical parametric oscillator (OPO) laser and a dye laser. Both lasers are pumped by the third harmonic of a nanosecond Q-switched Nd:YAG laser. Relevant specifications of the employed lasers are summarized in Table 4. The explored spectral range is substantially smaller compared to the possible tuning range of the OPO and dye lasers and covers mainly the UV/VIS range. Both employed OPO lasers (GWU, VersaScan and Continuum, Panther EX OPO) comprise a non-linear beta-barium borate crystal. Within this crystal, a pump photon is converted into a signal and idler photon. The higher-energy photon is referred to the signal, and the lower-energy photon is referred to the idler. The signal/idler wavelength is determined by phase - matching conditions in the OPO crystal. Therefore, by tuning the angle of the crystal, a wide range from UV to IR is accessible. In this thesis, only the signal wavelength of the OPO lasers has been used for spectroscopy. The idler wavelength has been filtered out. The dye laser (NarrowScan, Radiant Dyes) is pumped by the same Nd:YAG laser as the VersaScan OPO laser. A suitable dye (*e.g.*, Coumarin 120 and Stilbene 3) is dissolved in a mixture of water and ethanol. The dye acts as the active medium of the laser. Here, the dye laser is equipped with two dye cells to enhance the final laser power. Wavelength tuning is achieved via a diffraction grating with 1800 l/mm. Detailed information about which laser was used for which experiment/molecule can be found in the publications.^{113–118}

The bandwidth of a dye laser is substantially smaller compared to the bandwidth of an OPO laser. Hence, spectral broadening of transitions arising from the bandwidth of the lasers can be minimized with a dye laser. However, a disadvantage of dye lasers compared to OPO lasers is their small spectral tuning range for a given dye.

Table 4. Specifications of the employed laser systems. In this thesis, only a small part of the possible tuning range was used. The data for the pump lasers are typical for the conducted experiment. The pump lasers can also supply a beam with 1064 and 532 nm, which was not used for this thesis.

	VersaScan GWU	Panther EX OPO Continuum	NarrowScan Radiant Dyes
Type	OPO	OPO	Dye
Tuning range	206-2630 nm	205-2550 nm	370-900 nm
Explored range	420-570 nm	405-470 nm	428-439 nm
Bandwidth	~4 cm ⁻¹	~2 cm ⁻¹	~0.01 cm ⁻¹
Pump laser	Spitlight 1000 Innolas 355 nm 180 mJ/pulse	PowerLite DLS 9010 Continuum 355 nm 350 mJ/pulse	Spitlight 1000 Innolas 355 nm 100 mJ/pulse

To obtain a VISPD spectrum, the wavelength of the OPO/dye laser is scanned and the intensity of the parent and fragments is recorded at each wavelength. Typically, 50-100 mass spectra are averaged at each wavelength. The final VISPD spectrum is generated by linearly normalizing the fragment

intensity by the sum of the parent and fragment signals and the laser power. The laser wavelength is calibrated using a wavelength meter (Bristol 821) and the laser power is recorded by using a pyroelectric detector (OPHIR, Vega) at each wavelength.

As an example, a representative photodissociation mass spectrum of Cs^+LF recorded with *laser off* and *laser on* is presented in Figure 6.¹¹⁶ Herein, the laser wavelength is set to the S_1 origin (0^0) of the O4^+ isomer of Cs^+LF at around 19031 cm^{-1} (525.46 nm). Finally, a typical VISPD spectrum recorded at cryogenic temperatures ($T=6\text{ K}$) of $\text{Cs}^+\text{LF}(\text{O4}^+)$ is presented in Figure 7. The 0^0 transition is observed near 525 nm followed by a strong vibronic progression toward lower wavelengths. In the case of Cs^+LF , no fragmentation is observed below 525 nm.

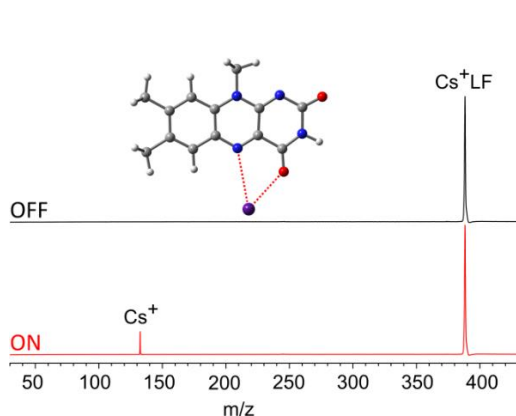


Figure 6. Mass spectra taken with the ReTOF-MS after mass-selecting Cs^+LF by the QMS and trapping in the cryogenic 22-pole ion trap ($T=6\text{ K}$). The *laser off* spectrum is shown in black and the *laser on* spectrum with the laser set to the S_10^0 origin transition at 19031 cm^{-1} of the O4^+ isomer is shown in red. It is seen that the parent molecule Cs^+LF fragments exclusively into $\text{Cs}^+ + \text{LF}$ upon photoexcitation. Typical fragmentation yield is on the order of a few percent.¹¹⁶

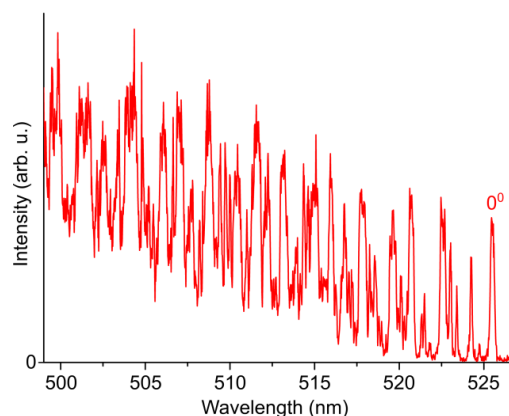


Figure 7. Representative VISPD spectrum of Cs^+LF recorded for a 22-pole ion trap temperature of 6 K . The origin of the electronic transition 0^0 is marked. The spectrum is recorded in the Cs^+ fragmentation channel, as indicated in Figure 6.¹¹⁶

For the sake of completeness, the resolution of the QMS is sufficient to exclusively transmit molecules with a single m/z value. However, $\text{M}^+\text{FI-He/N}_2$ ($\text{M}=\text{Li, Na}$) complexes can be formed within the trap, which can be observed in the mass spectra recorded in the ReTOF (shown for Li^+LF in Figure 8). Helium is available at high abundance as it is pulsed through the piezo valve into the trap for trapping and cooling, and N_2 arises from impurities in the He gas line. At lower temperatures ($T = 6\text{ K}$), no tagged N_2 complexes are observed because N_2 freezes onto the trap surface.

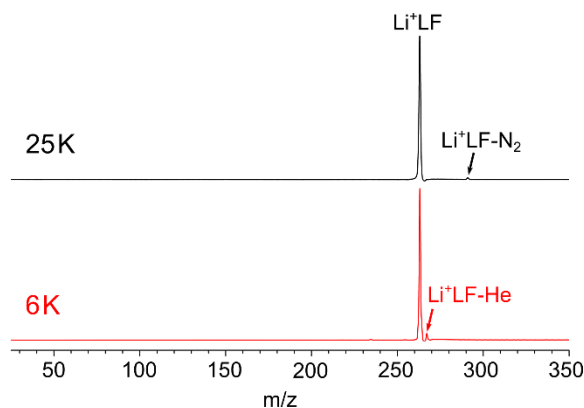


Figure 8. Mass spectra taken with the ReTOF-MS after mass-selection of Li^+LF by the QMS at 25 K (black) and 6 K (red). The tagged complexes are formed within the 22-pole ion trap. At $T=25$ K, $\text{Li}^+\text{LF-N}_2$ (1.3 %) is formed. At $T = 6$ K, $\text{Li}^+\text{LF-He}$ (2.8 %) is formed.^{113,116}

2.10. Vacuum System

Two vacuum conditions are required. First, in the miniQP chamber a sufficiently high pressure ($\sim 5 \cdot 10^{-3}$ mbar) is required for efficient trapping and accumulation of the ions. Second, ultra-high vacuum is needed in the 22-pole and ReTOF chamber. Pressures for the different stages of the experimental setup (achieved by differential pumping) are summarized in Table 5, and include pressures for the different chambers with the He buffer gas on and off. A vacuum gate valve (VAT) is installed behind the hexapole chamber which allows to clean the first stage of the experiment (*e.g.*, cleaning of transfer capillary, skimmer, and miniQP) without venting the stages behind the valve. The required vacuum conditions are achieved as follows. A combination of a roots blower (Leybold, RUVAC WA251, $304 \text{ m}^3\text{h}^{-1}$) and a rotary vane pump (Leybold, TRIVAC D65B, $65 \text{ m}^3\text{h}^{-1}$) is installed as a backing pump for the chambers before the VAT valve. For the stages behind the valve, a scroll pump (Edwards, xds35i, $35 \text{ m}^3\text{h}^{-1}$) is installed as a backing pump. High-vacuum conditions are achieved by several turbomolecular pumps (Pfeiffer, TMU/TPU, 240 ls^{-1}). The 22-pole chamber is pumped by a larger turbomolecular pump (Pfeiffer, Hi-Pace 700, 700 ls^{-1}).

Table 5. Pressures in the various chambers with the piezo valve closed and open (opening time 1 ms at a repetition rate of 10 Hz). The amount of He gas which is introduced into the 22-pole chamber can be controlled by the opening time of the piezo valve.

	Pressure in mbar Piezo valve closed	Pressure in mbar Piezo valve open
MiniQP	$5 \cdot 10^{-3}$	$5 \cdot 10^{-3}$
Hexapole	$5 \cdot 10^{-5}$	$5 \cdot 10^{-5}$
QMS	$2 \cdot 10^{-7}$	$4 \cdot 10^{-7}$
Octupole	$2 \cdot 10^{-8}$	$6 \cdot 10^{-7}$
22-pole	$2 \cdot 10^{-8}$	$1 \cdot 10^{-6}$
ReTOF	$5 \cdot 10^{-9}$	$8 \cdot 10^{-7}$

3. Theoretical Methods

In this thesis, a combined approach of quantum chemistry and VISPD spectroscopy is employed to unveil the information that is contained in the measured spectra. To this end, the basic principle of density functional theory (DFT), the Franck-Condon (FC) simulations and the underlying FC principle, the effects of cooling of the molecules and the possible relaxation mechanisms of the electronically excited state are described in this chapter.

3.1. Density Functional Theory

Here, static DFT and time-dependent DFT calculations (TD-DFT) are carried out.^{80,125,126} Unfortunately, the solution of the many-body Schrödinger equation is virtually impossible. The electronic wavefunction depends on the spin and on the three spatial coordinates for every single electron. DFT is a model in which the properties of the many-body system containing N electrons are fully described by the electron density $\rho(\vec{r})$. This reduction to a single quantity substantially reduces computational cost. The ground-state energy is a functional of the electron density, namely $E[\rho(\vec{r})]$. The one-particle Schrödinger equation

$$\left(-\frac{\hbar^2}{2m}\nabla^2 + V_{eff}\right)\psi_i(\vec{r}) = E_i\psi_i(\vec{r})$$

describes a system of non-interacting electrons. The first term of the Hamiltonian includes the kinetic energy operator. The second term describes an effective potential in which the non-interacting electrons are moving. The one-electron wavefunctions ψ_i ($i = 1, 2, \dots, N$) are the so-called Kohn-Sham orbitals. It must be kept in mind that the corresponding eigenenergies, E_i , have no physical meaning. The electron density can be described as the sum of the square of the Kohn-Sham orbitals:

$$\rho(\vec{r}) = \sum_i^N |\psi_i(\vec{r})|^2$$

The effective potential $V_{eff}(\vec{r})$

$$V_{eff}(\vec{r}) = V(\vec{r}) + \int \frac{\rho(\vec{r}')}{|\vec{r} - \vec{r}'|} d^3r' + V_{xc}[\rho(\vec{r})]$$

includes, in the order of appearance, the interaction of the nuclei and the electron $V(\vec{r})$, the Coulomb repulsion of the electrons, and the so-called exchange-correlation potential, which describes non-classical electron-electron interactions. This term is a functional of the electron density and its exact form is unknown. The Kohn-Sham equations must be solved self-consistently. First, an initial guess of the electron density is used to compute V_{xc} . This is used to generate an initial set of Kohn-Sham equations. Second, a new electron density is computed iteratively until a certain convergence criterion is met. In computational chemistry, the unknown one-electron Kohn-Sham orbitals can be written as a linear combination of known functions, *i.e.*, the so-called basis function/set¹²⁷

$$\psi_i = \sum_i^M c_i \phi_i$$

Many different types of basis functions are possible. The most widely used basis functions in quantum chemistry are of Gaussian-type ($\phi_G \sim e^{-\alpha r^2}$) or Slater-type ($\phi_S \sim e^{-\beta r}$). DFT calculations can be extended to TD-DFT calculations which allow to compute excited-state properties such as geometries of excited states and excitation energies. According to the Runge-Gross theorem, for a given initial wavefunction, a time-dependent density can be obtained from one external potential. In particular, the time-dependent potential is a functional of the time-dependent electron density. For example, the time-dependent electric field can be treated as a weak perturbation on the molecule, and by a linear response analysis, properties like the excitation energies can be computed.

3.2. PBE0 and cc-pVDZ

A typical DFT calculation requires a functional and a basis set. Both have to be chosen to be suitable for the system under investigation and available computational power and time. Whether or not a functional produces good results for a specific system can be tested by comparison to experiment. In this thesis, the PBE0 functional and the cc-pVDZ basis set have been employed for both DFT and TD - DFT. The PBE0 functional has been introduced by Perdew, Burke, and Ernzerhof.¹²⁸ It is a hybrid DFT functional that uses 25 % exact Hartree-Fock (HF) exchange and 75 % DFT exchange-correlation:

$$E_{xc} = E_{xc}^{GGA} + 0.25 (E_X^{HF} - E_C^{GGA})$$

The PBE0 functional employs the so-called generalized gradient approximation (GGA). The development of GGA functionals is based on experimental data and physical constraints.¹²⁸ Within the GGA, all parameters are fundamental constants. To increase the performance of the functional, E_{xc}^{GGA} is a function of both the electron density and its gradient. Even though the PBE0 functional is based exclusively on fundamental constants, it was shown to provide good agreement with experimental data.^{129,130}

The abbreviation cc-pVDZ stands for correlation-consistent polarized double zeta.¹³¹ Correlation-consistent polarized means that electron correlation and polarization functions are taken into account. Furthermore, two basis functions are included for each atomic orbital (double zeta). Both, the PBE0 functional and the cc-pVDZ basis set are used as implemented in the GAUSSIAN09/16 package.¹³² The medium-sized cc-pVDZ basis set is not suitable to properly treat heavier atoms. To this end, effective core potentials have been introduced for complexes including heavier atoms like potassium, rubidium, or caesium.¹³³ These core potentials account for relativistic corrections. The computational level used here is in good agreement to the experimental data in terms of vibrational and electronic energy.^{113–118} In addition, it yields similar results compared to higher level computational methods, which justifies the chosen computational approach.⁷⁹

3.3. Potential Energy Diagram

Figure 9 shows a schematic energy diagram (potential Energy surface, PES) of a molecule in its ground (S_0) and first electronically excited (S_1) state to help explain the concepts used in this thesis. S stands here for singlet ($S = 0$, $2S+1 = 1$). The geometry of the S_0 electronic ground state of the molecule of interest is optimized with respect to its total energy by means of DFT calculations. The geometry with lowest energy is represented by the minimum of the surface. Harmonic frequency calculations are carried out, and the zero-point corrected energy (ZPVE) of the system can also be calculated with it. Furthermore, these frequency calculations allow to distinguish between minima and first order saddle points (transition states) on the PES. Using TD-DFT calculations, the same can be done for the excited state that can have a different geometry than the ground state, represented here by a shift of the minima in the geometry coordinate.

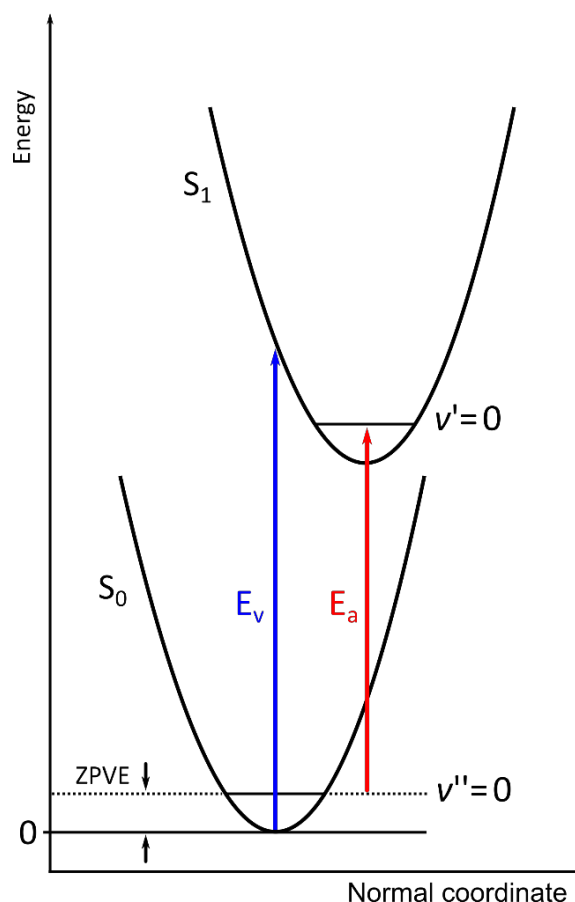


Figure 9. Schematic energy diagram showing the electronic ground state, S_0 , and the first excited state, S_1 . The vertical excitation energy is shown in blue and represents the energy difference between S_0 and an excited state at the minimum of the ground state geometry. The adiabatic excitation energy is shown in red and represents the energy difference between the optimized ground and excited state geometries. The dotted line represents the zero-point vibrational energy (ZPVE). For reasons of simplicity, a harmonic potential is drawn and only the first excited singlet state, S_1 , is shown.

Vertical excitation energies (E_v) correspond to the energy differences between the minimum of the optimized electronic ground state PES, S_0 , and the excited state PES at the ground state geometry. The energy difference between the zero-point corrected energies of S_0 and S_1 in Figure 9 and is called adiabatic excitation energy (E_a).

Typically, vertical excitation energies were computed for S_1 - S_n ($n=1,\dots,5$). For each transition into an excited state, the oscillator strength (f) was computed. The oscillator strength reported by GAUSSIAN is a dimensionless quantity that is a measure of the probability for an electronic excitation.

3.4. Franck-Condon Principle

In a first approximation, electronic spectra can be simulated by computing vertical excitation energies starting from the optimized ground state geometry. The resulting stick spectra can be further convoluted by Gaussian or Lorentzian functions with a certain width. However, this approach does not properly treat the profile of a real experimental spectrum, as it does, for example, not account for vibrational structure.

Another approach is to compare measured VISPD spectra to multidimensional FC simulations.^{81,134} A schematic overview of the FC principle is shown in Figure 10. The FC principle is suitable to predict intensities of transitions between two vibronic states (vibronic = electronic + vibrational). When a molecule absorbs a photon, it can undergo an electronic transition from its

initial state to an excited state. This transition usually occurs on a much faster timescale compared to the nuclear motion. Therefore, the positions of the nuclei remain unchanged during the transition, and the transition occurs vertically as indicated by a blue arrow in Figure 10. In general, within the dipole approximation the probability of a vibronic transition, P , is given by

$$P = \langle \psi' | \boldsymbol{\mu} | \psi'' \rangle$$

with the dipole operator, $\boldsymbol{\mu}$, and the wavefunctions of the initial and final state, ψ'' and ψ' , respectively. Within the framework of the Born-Oppenheimer approximation, the molecular wavefunction, ψ , can be written as a product of the electronic and nuclear wavefunctions (ψ_e and ψ_n , respectively),

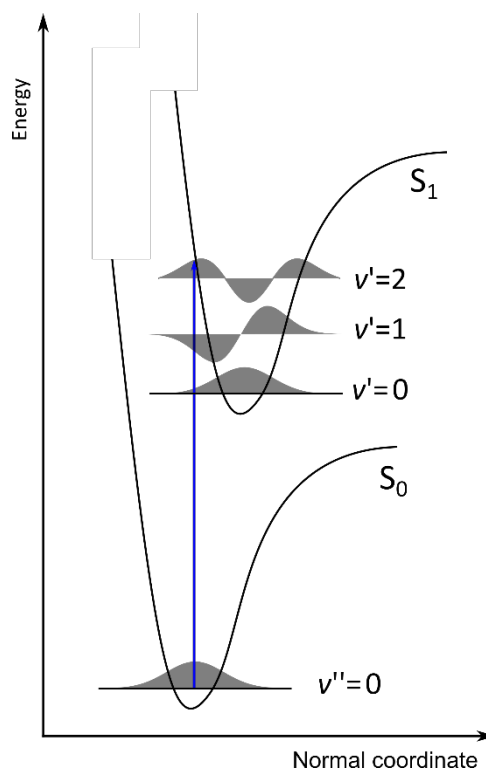


Figure 10. Illustration of the Franck-Condon principle. The electronic transition occurs vertically (blue arrow). In this example, the highest probability corresponds to the $0 \rightarrow 2$ transition, where the wavefunction overlap is highest. In this picture, only the vibrational electronic ground state is populated ($T = 0$ K).

$$\begin{aligned}
P &= \langle \psi' | \mu | \psi'' \rangle = \langle \psi'_e \psi'_n | \mu_e | \psi''_e \psi''_n \rangle + \underbrace{\langle \psi'_e \psi'_n | \mu_n | \psi''_e \psi''_n \rangle}_0 \\
&= \langle \psi'_e | \mu_e | \psi''_e \rangle \underbrace{\langle \psi'_n | \psi''_n \rangle}_{FC \text{ factor}}
\end{aligned}$$

The right-hand side of the sum is zero, because the electronic eigenfunctions of different electronic states are orthogonal ($\langle \psi'_e | \psi''_e \rangle = 0$). The left-hand side of the sum includes the electronic transition moment and the so-called FC factor. This overlap integral determines the relative intensity of a vibronic transition. In other words, the probability of a transition is highest where the overlap of the vibrational wavefunctions of the initial and final state is largest. If the nuclear arrangements of the initial and final electronic states are the same, the highest probability would be observed for $\Delta v = 0$. A change in geometry of the final state upon electronic excitation results in vibronic activity. For example, in Figure 10, the $v'' = 0 \rightarrow v' = 2$ transition is the most intense transition. Additionally, selection rules have to be applied to examine if a transition between two different vibronic states is allowed or not. First, electronic transitions are only allowed if the multiplicity of the initial and final states remain the same ($\Delta S = 0$). Hence, singlet-singlet transitions can be observed, whereas singlet-triplet transitions are practically weak. Second, symmetry selection rules can be applied to determine if a transition is allowed or not. In order for the transition matrix element to be non-zero, the direct product of the irreducible representation of the initial and final states and the transition moment operator must contain the totally symmetric representation of the point group of the molecule ($\Gamma(\psi') \otimes \Gamma(\mu) \otimes \Gamma(\psi'') \supset \Gamma_{TS}$).

3.5. PGOPHER and GAUSSIAN

In this thesis, the FC simulations are carried out using the programs PGOPHER and GAUSSIAN16.^{132,135} To this end, the geometries and normal modes of the initial and final states of interest are computed by means of DFT and TD-DFT. The computational cost for simulating FC spectra can be very high and easily exceed standard computational resources since, in principle, all vibrational levels of the excited state can be excited with a high number of quanta. Furthermore, vibrational levels of the electronic ground state are populated according to the Boltzmann distribution. Hence, with increasing temperature, the density of possible transitions increases substantially. Thus, some constraints have to be set for the FC simulation to reduce computational cost.

For FC simulations carried out with GAUSSIAN16, each vibrational mode in the excited state is excited with a maximum quantum number which is set manually (typically 3). Furthermore, an upper energetic bound for the computed spectrum is set. That value is referenced to the electronic origin transition and covers a spectral range of $\sim 600 \text{ cm}^{-1}$ above the origin. The choice of these two parameters makes it possible to perform the calculations in a practicable amount of time. For FC simulations carried out with PGOPHER, a maximum number of quanta is set for each individual mode. In contrast to GAUSSIAN16, PGOPHER is computationally less powerful and not all modes within a

desired spectral range can be populated. Therefore, the FC intensity is checked for each mode. Subsequently, all transitions with negligible intensity are excluded for the final FC simulation. The symmetry for each mode must be set manually for PGOPHER, whereas it is determined for GAUSSIAN16 automatically. Finally, all FC calculations are carried out for $T=0$ K. Hence, the molecule is in its electronic and vibrational ground state and the computed spectra do not contain any contribution from hot bands. This approach is justified because all VISPD experiments are conducted at cryogenic temperatures (typically <25 K), which sufficiently suppresses the contribution of hot bands.

3.6. Vibrational Cooling

The importance of cooling is briefly described here (Figure 11). Electronic spectra can be broad and unresolved for many reasons. For example, the thermal population of many vibrational states in the electronic ground state results in spectral congestion. A high density of transitions in an optical spectrum can also originate from several low-energy conformers. Furthermore, the excited-

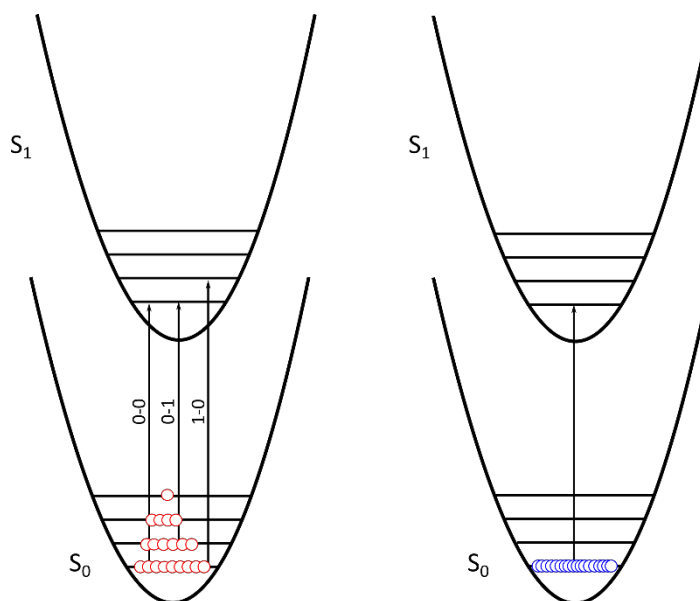


Figure 11. Schematic of cooling the ions, demonstrating the reduction of thermal spectral congestion. The vibrational levels are populated according to the Boltzmann distribution. At sufficiently low temperatures, the molecule is in the electronic and vibrational ground state. Hence, the spectrum does not contain any hot-band contribution.

state lifetime affects the spectral shape. According to the Heisenberg time-energy uncertainty relation, a short excited state lifetime results in a broad optical transition.

Importantly, the population of vibrationally excited states of the electronic ground state can be reduced by cooling, for example by means of buffer-gas cooling in an ion trap. The thermal population of the different vibrational levels follows the Boltzmann distribution assuming thermal equilibrium.

Hence, the vibrational temperature can be determined as

$$T = - \frac{\Delta E}{k_B \ln \left(\frac{I_{0-1}}{I_{1-0}} \right)}$$

with ΔE as the energy difference between the origin transition and the hot band, and I_{0-1} and I_{1-0} correspond to the intensity of a hot band and the fundamental of the considered normal mode, respectively. In this estimation, it is assumed that the FC factor is similar for both transitions. For example, to suppress the population a typical lowest vibrational mode of around 25 cm⁻¹ to 10 %, a vibrational temperature of 16 K is required.⁵⁷ The vibrational temperature can also be determined by direct comparison of the measured VISPD spectra to FC simulations which are carried out for $T > 0$ K.

3.7. Deexcitation Pathways

An electronically excited molecule generally does not remain in its excited state. Two possible deexcitation processes of an electronically excited state that are relevant in this thesis are schematically shown in Figure 12. These are called intersystem crossing (ISC) and internal conversion (IC). Both processes occur isoenergetically. For IC, the excited state relaxes via a state with the same multiplicity. For example, the electronically excited state couples to the electronic ground state, S_0 . For ISC, the relaxation occurs via the crossing of two potential energy surfaces of different multiplicity. Both

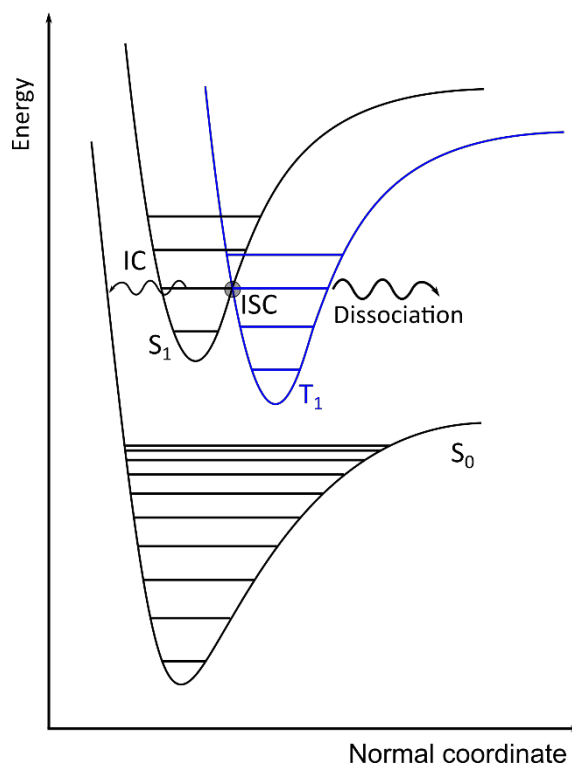


Figure 12. Schematic energy diagram to demonstrate possible photoreaction pathways upon optical excitation. From the excited state, S_1 , the molecule can relax via Internal Conversion (IC) or Intersystem Crossing (ISC).

processes result in vibrationally hot states. In the case of IC, the molecule can fragment via statistical dissociation on the electronic ground state if the energy is above the dissociation energy of S_0 . According to the Einstein coefficients, molecules which are strong photon absorbers are also strong photon emitters. Hence, the excited state can also relax via fluorescence to the electronic ground state.

3.8. Natural Transition Orbitals

The orbitals contributing to an electronic excitation are visualized by the Natural Transition Orbital approach using GAUSSIAN.^{132,136} In general, several orbitals can contribute to the electronic excitation which complicates the interpretation of the electronic excitation. To characterize the electronic transition, a new set of orbitals is introduced by an unitary orbital transformation. This simplifies the qualitative description of an electronic excitation, without changing the physically relevant transition density matrix.

3.9. Natural Bond Orbitals

The atomic charge distribution on the individual atoms is computed with the Natural Bond Orbital (NBO) analysis as implemented in GAUSSIAN.^{132,137} The charge on atom A is derived from the orthonormal natural atomic orbitals as

$$q(A) = Z(A) - \sum_k p_k(A)$$

with the nuclear charge on each atom, $Z(A)$, and the population $p_k(A)$.

4. Publications

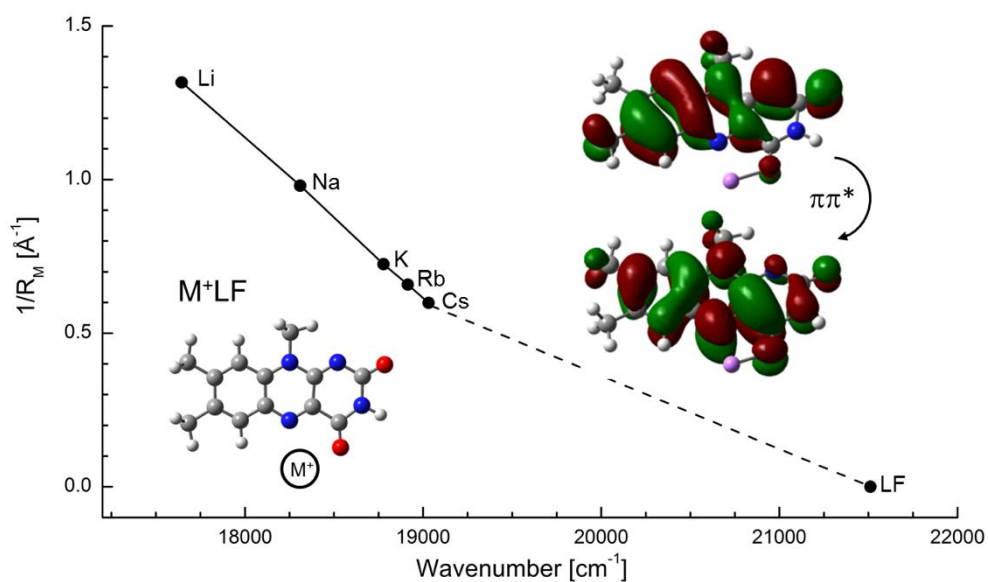
4.1. Effect of alkali ions on optical properties of flavins: vibronic spectra of cryogenic M⁺lumiflavin complexes (M=Li-Cs)

David Müller, Pablo Nieto, Mitsuhiro Miyazaki and Otto Dopfer

Faraday Discuss., 2019, **217**, 256

<https://doi.org/10.1039/C8FD00203G>

Reprinted with permission from The Royal Society of Chemistry





Declaration of Contribution

Experimental and computational data were acquired and analysed by David Müller. Preliminary computational data were acquired by Pablo Nieto and Mitsuhiro Miyazaki. The manuscript was written by David Müller, reviewed by all co-authors and finalized by Otto Dopfer. All work was supervised by Otto Dopfer.

PAPER

[View Article Online](#)
[View Journal](#) | [View Issue](#)

Effect of alkali ions on optical properties of flavins: vibronic spectra of cryogenic M^+ lumiflavin complexes ($M = \text{Li} - \text{Cs}$)†

David Müller,^a Pablo Nieto,^a Mitsuhiro Miyazaki ^{ab}
and Otto Dopfer ^{*ac}

Received 23rd November 2018, Accepted 7th January 2019

DOI: 10.1039/c8fd00203g

Flavin compounds are frequently used by nature in photochemical processes because of their unique optical properties which can be strongly modulated by the surrounding environment such as solvation or coordination with metal ions. Herein, we employ vibronic photodissociation spectroscopy of cryogenic M^+ LF complexes composed of lumiflavin (LF, $\text{C}_{13}\text{H}_{12}\text{N}_4\text{O}_2$), the parent molecule of the flavin family, and alkali ions ($M = \text{Li} - \text{Cs}$) to characterize the strong impact of metalation on the electronic properties of the LF chromophore. With the aid of time-dependent density functional theory calculations (PBE0/cc-pVDZ) coupled to multidimensional Franck–Condon simulations, the visible photodissociation (VISPD) spectra of M^+ LF ions recorded in the 500–570 nm range are assigned to the $S_1 \leftarrow S_0$ ($\pi\pi^*$) transitions into the first optically bright S_1 state of the lowest-energy M^+ LF(O4+) isomers. In this O4+ structure, M^+ binds in a bent chelate to the lone pairs of both the O4 and the N5 atom of LF. Charge reorganization induced by S_1 excitation strongly enhances the interaction between M^+ and LF at this binding site, leading to substantial red shifts in the S_1 absorption of the order of 10–20% (e.g., from 465 nm in LF to 567 nm in Li^+LF). This strong change in $M^+ \cdots \text{LF}$ interaction strength in M^+ LF(O4+) upon $\pi\pi^*$ excitation can be rationalized by the orbitals involved in the $S_1 \leftarrow S_0$ transition and causes strong vibrational activity. In particular, progressions in the intermolecular bending and stretching modes provide an accurate measure of the strength of the $M^+ \cdots \text{LF}$ bond. In contrast to the experimentally identified O4+ ions, the predicted S_1 origins of other low-energy M^+ LF isomers, O2+ and O2, are slightly blue-shifted from the S_1 of LF, demonstrating that the electronic properties of metalated LF not only drastically change with the size of the metal ion but also with its binding site.

^aInstitut für Optik und Atomare Physik, Technische Universität Berlin, Hardenbergstr. 36, 10623 Berlin, Germany. E-mail: dopfer@physik.tu-berlin.de; Fax: +49 30 314 23018

^bLaboratory for Chemistry and Life Science, Institute of Innovation Research, Tokyo Institute of Technology, 4259, Nagatsuta-cho, Midori-ku, Yokohama, Japan

^cTokyo Tech World Research Hub Initiative (WRHI), Institute of Innovation Research, Tokyo Institute of Technology, 4259, Nagatsuta-cho, Midori-ku, Yokohama, Japan

† Electronic supplementary information (ESI) available. See DOI: 10.1039/c8fd00203g

Introduction

In addition to amino acids, DNA bases, and carbohydrates, flavins are an important class of biomolecules. Flavins are yellow dye molecules (“flavus” means yellow in Latin) derived from the tricyclic heteroaromatic 7,8-dimethyl-10-alkyl-isoalloxazine chromophore and differ by the alkyl substituent R at the N10 position (Fig. 1). The most important members of the flavin family are lumiflavin (LF, R = CH₃, C₁₃H₁₂N₄O₂, 7,8-dimethyl-10-methyl-isoalloxazine), riboflavin (RF, R = ribityl) also known as vitamin B₂, the cofactor flavin mononucleotide (FMN, R = ribophosphate), and the co-enzyme flavin adenine dinucleotide (FAD, R = ribophosphate + adenine). The parent molecule, iso-lumichrome (iso-LC, R = H) is a metastable tautomer and occurs in the most stable structure as lumichrome (LC), in which the H atom of N10 is transferred to N1. For this reason, LF is often considered as the most simple stable flavin.

The isoalloxazine chromophore absorbs in a wide optical range, and the details of the optical spectrum and resulting photochemistry strongly depend on many intrinsic and environmental factors, including (1) the oxidation, protonation, and metalation states, (2) the substituent R, (3) solvation, and (4) coordination with counter ions. This strong modulation in the optical properties of flavins and flavoproteins is used by nature in various fundamental photochemical processes, in biocatalysis, and in redox reactions.^{1–5} For instance, they are involved in blue-light receptors (BLUF), in light-oxygen-voltage (LOV) sensing, in processes of the respiratory chain, in the enzymatic oxidation of glucose, and in the repair process of DNA. Two Nobel prizes in chemistry are strongly related to flavins. The first one was awarded in 1937 to Karrer for the synthesis and structural analysis of flavin compounds. The second one was awarded in 2015 to

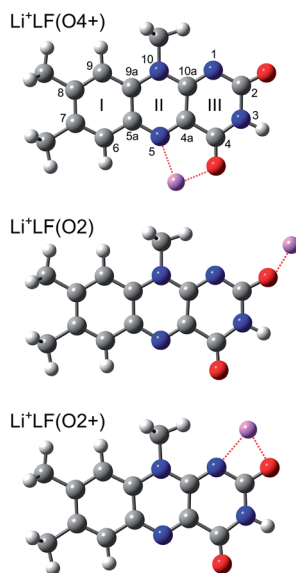


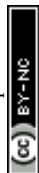
Fig. 1 Structures of relevant M⁺LF isomers calculated at the PBE0/cc-pVDZ level of theory illustrated for M = Li, along with atom and ring numbering. N/O atoms are indicated in blue/red colour.



Lindah, Modrich, and Sancar for unravelling the mechanism of DNA repair, which involves the fully reduced flavoprotein FADH^- . A number of biochemical processes of flavins are based on their strong interactions with coordinating metal ions.^{6–15}

Due to their importance, numerous studies have characterized the absorption properties of flavins by a variety of spectroscopies in the condensed phase (absorption, emission, time-resolved spectroscopy)^{16–19} and quantum chemical calculations.^{16,20–25} These studies reveal that the excited-state photochemistry and absorption of flavins from the ground electronic state (S_0) are controlled by optically bright $\pi\pi^*$ excitations of the aromatic π electron system and essentially dark $n\pi^*$ states involving the excitation of electrons from in-plane lone pairs of the various O and N heteroatoms. Some of these transitions are strongly affected by solvation and protonation. Concerning LF, the S_1 state observed near 450 nm is assigned to the first allowed $\pi\pi^*$ state, and calculations predict a large geometry change upon electronic excitation. As a result, there is a large difference between the vertical and adiabatic transition energies (of around 50 nm or 0.3 eV), implying that vibronic excitation and temperature have a substantial impact on the position, shape, and width of the S_1 absorption band.²⁵ Indeed, the absorption spectra observed in the condensed phase at room temperature are broad and unresolved, and thus do not provide reliable and precise information and understanding of the effects of the environment on the optical properties of flavins at the molecular level. Significantly, optical spectra of LF derivatives recorded at 4 K in an *n*-decane matrix (single crystals, Shpolskii method) show that low temperatures are required to obtain vibrationally resolved optical spectra with sharp rovibronic transitions.²⁶

Because of the strong dependence of the optical spectra on the environment, the intrinsic properties of the active flavin chromophore must be determined by the spectroscopy of molecules isolated in the gas phase. However, such studies are scarce, mainly because of the difficulties involved in generating cold flavin molecules and their ions and complexes in the gas phase. To this end, we recently started a research program to systematically characterize the geometric and electronic properties of flavin ions in their protonated, metalated, and micro-solvated states by infrared and optical photodissociation spectroscopy coupled to electrospray ionization (ESI) techniques for ion generation in the gas phase.^{27–32} Apart from our contributions to flavin spectroscopy summarized below, a few other studies on isolated flavins have appeared recently. The pioneering fluorescence spectrum of LF embedded in He droplets ($T = 0.4$ K) exhibits vibrational resolution and was assigned to the $S_1 \leftarrow S_0$ ($\pi\pi^*$) transition by comparison to quantum chemical calculations coupled to multidimensional Franck–Condon (FC) simulations.³³ The authors estimate that the S_1 origin observed at $21\,511\text{ cm}^{-1}$ (464.88 nm) is shifted by less than 1% upon the weak interaction with the He droplet. Optical spectra of room temperature cations and anions have recently been reported for FAD mono- and dianions,^{34–36} alloxazine and LC anions,³⁷ protonated alloxazine,³⁸ and a flavin derivative with a protonated amino side chain.³⁹ Significantly, all these latter studies report only optical spectra with very broad absorption bands because vibronic resolution cannot be obtained at elevated temperature ($T = 300$ K).³² As a consequence, the spectral information about shifts and (de-)protonation sites, *etc.* is quite limited, and the interpretation



relies heavily on quantum chemical calculations which may not always produce reliable quantitative predictions.

In the past few years, our group has applied infrared and optical photodissociation spectroscopy to mass-selected flavin ions, with the aim of characterizing the geometric, vibrational, and electronic structure of a number of protonated and metalated flavins ranging from LC to FMN in the electronic ground and first excited singlet states (S_0 , S_1).^{27–32} The flavin ions are generated by ESI in the gas phase and subsequently studied by (1) infrared multiple-photon dissociation (IRMPD) in an Fourier-transform ion cyclotron resonance mass spectrometer^{27–29} and (2) by electronic photodissociation in the visible range (VISPD) in a cryogenic ion trap coupled to a quadrupole/time-of-flight tandem mass spectrometer (BerlinTrap).^{30–32} Significantly, these studies report the first (and to date only) vibrationally-resolved spectra of flavins isolated in the gas phase, and thus provide for the first time reliable experimental information about protonation and metalation sites as well as their impact on the electronic properties. The IRMPD spectra recorded at room temperature display sufficient vibrational resolution to determine the preferred protonation and metalation sites of the flavins in the S_0 state by comparison to quantum chemical density functional theory (DFT) calculations.^{27–29} In contrast, vibronic resolution in electronic VISPD spectra of such ions can only be achieved at temperatures well below 100 K because only then can extensive spectral congestion from hot bands be avoided.^{30–32,40,41} In general, these studies reveal that the preferred protonation and metalation sites strongly depend on the substituent R of the flavin as well as the size and type of the metal ion, as illustrated for the alkali and coinage metal ions, $M = \text{Li–Cs}$ and Cu–Au .^{30–32} The most thoroughly studied so far are cations derived from LC and LF. IRMPD spectra demonstrate that protonation preferentially occurs at N5 in H^+LC and at O2 in H^+LF , in line with computational predictions at the B3LYP/cc-pVDZ level.²⁷ The two major metalation sites observed for M^+LC and M^+LF with alkali atoms $M = \text{Li–Cs}$ are the two CO groups, leading to the O4+ and O2(+) isomers shown in Fig. 1 for the case of Li^+LF .^{27–29} Their relative energies and bonding characteristics depend sensitively on the size of the alkali ion. The optical VISPD spectra of H^+LC and M^+LC with $M = \text{Li–Cs}$ observed in the 400–500 nm range are attributed to the lowest $\pi\pi^*$ excitation (S_1) of the N5 protomer of LC, $\text{H}^+\text{LC}(\text{N5})$, and the O4+ isomer of M^+LC , $\text{M}^+\text{LC}(\text{O4+})$.^{30–32} Significantly, massive red shifts ranging from ~ 2400 (Cs^+) to around $\sim 6000\text{ cm}^{-1}$ (H^+) observed for the adiabatic S_1 origins of the O4+ and N5 ions indicate the strong impact of metalation and protonation on the electronic structure of this prototypical flavin. On the other hand, calculations demonstrate that metalation/protonation at the O2(+) binding site has only a minor impact on the S_1 origin energies, illustrating that the binding site of M^+/H^+ is also an important parameter in tuning the electronic properties. Time-dependent DFT (TD-DFT) calculations at the PBE0/cc-pVDZ level provide accurate predictions for both the S_1 origin positions (to within 0.1 eV) and the vibrational analysis using FC simulations.^{30–32} As a result, the changes in the proton affinity of LC and the $\text{M}^+\cdots\text{LC}$ interaction strength are accurately probed by the corresponding electronic energy shifts and vibrational frequencies, demonstrating the high and reliable information content of the vibronic excitation spectra.

Herein, we continue our series of studies to VISPD spectroscopy of M^+LF ions to probe the impact of the alkali ions Li–Cs on the electronic structure of LF using the same experimental and computational approach as used for $\text{H}^+/\text{M}^+\text{LC}$.^{30–32} In



contrast to the previous IRMPD data on M^+LF ,²⁹ their VISPD spectra are highly isomer-selective, because the locations of the electronic transitions in the optical spectrum strongly depend on the M^+ binding site. The analysis by TD-DFT calculations reveals similarities and differences between M^+LF and M^+LC .

Experimental and computational details

Vibronic VISPD spectra of mass-selected M^+LF ions are obtained in a cryogenic ion trap tandem mass spectrometer (BerlinTrap) described in detail elsewhere.³⁰ The major components of this setup include (1) an ESI source for ion production, (2) a mini-quadrupole for ion accumulation, (3) a quadrupole mass spectrometer for filtering the M^+LF ions under investigation, (4) a cryogenic 22-pole ion trap for storing and cooling the ions employing He buffer gas, and (5) a reflectron time-of-flight mass spectrometer for the analysis of the fragment ions generated by photodissociation of parent ions. M^+LF ions ($M = Li-Cs$) are produced in the ESI source by spraying a suitable mixture at a constant flow rate of 2 ml h^{-1} . The solution is prepared by dissolving 1 mg LF (Sigma Aldrich, >99%) and 2–4 mg alkali metal chloride salt (MCl, Sigma Aldrich, >99%) in 20 ml methanol and 1 ml water. The resulting ions are accumulated for 90 ms in a short mini-quadrupole located after the skimmer. After passing through a hexapole, the desired M^+LF ions are selected by a tuneable quadrupole mass spectrometer and guided through an octupole into the cryogenic 22-pole trap mounted onto the coldhead of a cryostat held at 6 K. Here, the M^+LF ions are trapped for 90 ms and cooled down to a (ro)vibrational temperature of around 20 K by He buffer gas introduced into the trap by a pulsed piezo valve.³⁰ After extraction out of the 22-pole trap, the cold M^+LF ions are guided by a series of einzel lenses into the extraction region of an orthogonal reflectron time-of-flight mass spectrometer, where they are irradiated by visible photons emitted from a pulsed optical parametric oscillator (OPO) laser. The OPO laser (GWU, Versa-Scan) is pumped by the third harmonic of a nanosecond Q-switched Nd:YAG laser (Innolas, Spotlight 1000, 180 mJ per pulse at 355 nm) and delivers visible light pulses (beam diameter of 5 mm) with a bandwidth of around 4 cm^{-1} and an energy of up to 3 mJ in the spectral range 500–570 nm. The repetition rates of both the laser and BerlinTrap mass spectrometer are 10 Hz. Photodissociation occurs just before the extraction zone of the reflectron (*ca.* 10 μs before the ion extraction pulse). Hence, both parent and fragment ions can be detected with high transmission using a microchannel plate detector. The VISPD action signal is obtained by linearly normalizing the fragment ion signal by the parent ion signal and the laser intensity monitored simultaneously with the ion signals. Scans are taken in wavelength steps of 0.02 nm (corresponding to 0.8 cm^{-1} at 500 nm), and 50 mass spectra are averaged at each wavelength which is calibrated by a wavemeter. For all M^+LF ions, the only fragmentation process observed upon VISPD is dissociation into $M^+ + LF$ (Fig. S1 in ESI†). The photodissociation efficiency is of the order of a few % for strong transitions. The typical width of the transitions observed is in the range 5–10 cm^{-1} , and arises from the bandwidth of the laser ($\sim 4\text{ cm}^{-1}$), unresolved rotational substructure, overlapping vibronic transitions, and possibly lifetime broadening.

The experimental VISPD spectra of M^+LF are interpreted with the aid of quantum chemical calculations.⁴² To this end, DFT calculations at the PBE0/cc-



pVDZ level of theory are employed to optimize the electronic ground state (S_0) of LF and M^+LF . Subsequently, the vertical excitation energies of the first four excited singlet states (S_1 – S_4) are determined using TD-DFT at the same level of theory to roughly estimate their relative energies. Finally, the S_1 excited states are optimized using the corresponding S_0 structures as starting geometries. The efficient but reliable PBE0/cc-pVDZ level was previously employed for corresponding calculations of the related H^+LC and M^+LC ions and resulted in good agreement with experimental data for both vibrational and electronic energies.^{31,32} Test calculations with the larger cc-pVTZ basis set yield essentially the same results. Relativistic corrections for the heavier alkali metals (K–Cs) are included using the Stuttgart effective core potentials.⁴³ Harmonic frequency analysis is employed to ensure that the stationary points located on the potential are indeed minima. All reported binding energies (D_0) and relative energies (E_0) are corrected for the harmonic zero-point vibrational energy. Vibronic absorption stick spectra are obtained by multidimensional FC simulations ($T = 0$ K) using PGOPHER.⁴⁴ The orbitals contributing the most to each respective electronic excitation are determined using the natural transition orbital (NTO) approach.⁴⁵ The atomic charge distribution in the ground and excited electronic states is evaluated by employing natural bond orbital (NBO) analysis.⁴⁶ In both experiment and computation, only the monoisotopic species are considered.

Results and discussion

Overview VISPD spectra of the $S_1 \leftarrow S_0$ transition for all investigated M^+LF ions recorded in the M^+ fragment channel in the range 17 500–20 000 cm^{-1} (570–

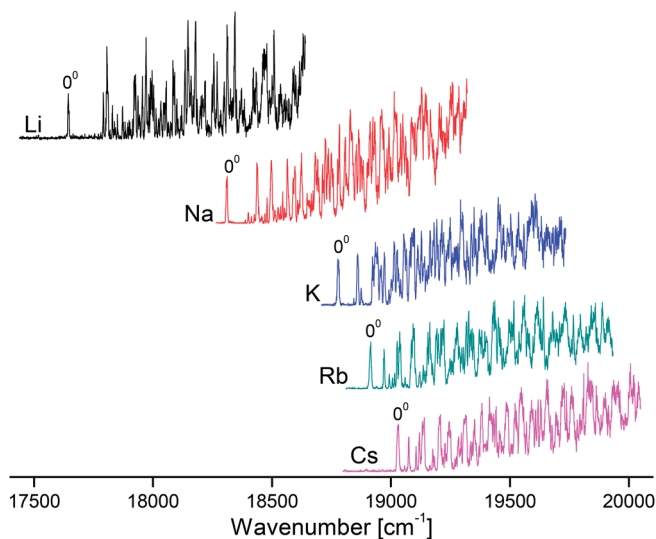
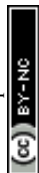


Fig. 2 Overview VISPD spectra recorded for M^+LF ($M = \text{Li} - \text{Cs}$) in the M^+ fragment channel at a trap temperature of $T = 6$ K. The origins (0^0) of the $S_1 \leftarrow S_0$ ($\pi\pi^*$) transitions assigned to the O4+ isomer are indicated.



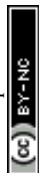
500 nm, 2.2–2.5 eV) are shown in Fig. 2. As can be seen, cooling the ions in the trap down to below 20 K is sufficient to efficiently suppress the appearance of hot bands and to achieve vibrational resolution even for such large biomolecules. The $S_1 \leftarrow S_0$ transitions exhibit sharp and intense S_1 origins (0^0) accompanied by long and intense vibrational progressions, indicative of substantial changes in the geometries upon electronic $\pi\pi^*$ excitation. The S_1 origin transitions of M^+LF observed at 17 645, 18 310, 18 778, 18 914, and 19 031 cm^{-1} for $M = \text{Li}-\text{Cs}$, respectively (Table 1) exhibit a strong dependence on the M^+ ion. In Fig. 3, these S_1 origins are plotted *versus* the inverse ionic radius of M^+ ($1/R_M$),^{29,47} and a nearly linear dependence is observed. This result is expected because the attractive interaction between M^+ and LF mainly arises from electrostatic forces, thus explaining the linear dependence of the S_1 origins on $1/R_M$ according to the Coulomb law.³² Unfortunately, the corresponding $S_1 \leftarrow S_0$ transition of bare LF has not been measured yet due to the difficulties involved in the production of cold LF molecules in the gas phase. However, the fluorescence spectrum of LF embedded in He droplets has been reported and its S_1 origin occurs at 21 511 cm^{-1} .³³ This value should be close to the S_1 origin of free LF because the interaction of a neutral molecule with the surrounding He droplet is small, leading to estimated shifts of less than 1% ($<250 \text{ cm}^{-1}$).³³ Indeed, the extrapolation of the measured S_1 origins of M^+LF to $1/R_M = 0$ (*i.e.*, $R_M \rightarrow \infty$, no metal) in Fig. 3 is consistent with this view. Hence, we use in the following the He droplet value for LF as the reference point for S_1 of bare LF to evaluate ΔS_1 shifts upon complexation with M^+ . Following this strategy, the ΔS_1 origin shifts amount to -2480 (Cs), -2597 (Rb), -2733 (K), -3201 (Na), and -3866 (Li) cm^{-1} , *i.e.* they strongly increase with the $M^+ \cdots LF$ interaction. These large red shifts are quite substantial (11.5, 12.1, 12.7, 14.9, 18.0%) and indicate that electronic excitation has a drastic impact on the strength of the $M^+ \cdots LF$ interaction, in line with the large FC activity in the $S_1 \leftarrow S_0$ transitions.

To identify the M^+LF isomers responsible for the VISPD spectra in Fig. 2, we first calculate the ground state geometries and adiabatic S_1 origins of low-energy M^+LF structures. LF offers a variety of attractive binding sites for M^+ cations, namely the lone pairs of the O and N atoms, as well as the aromatic π -electron

Table 1 Experimental adiabatic S_1 origin energies of M^+LF (in bold) and their ΔS_1 shifts (in cm^{-1}) upon metalation compared to values for various isomers calculated at the PBE0/cc-pVDZ level

Isomer	$S_1 \leftarrow S_0$	ΔS_1	Isomer	$S_1 \leftarrow S_0$	ΔS_1
LF(exp)	21 511^a	0	K⁺LF(exp)	18 778	-2733
LF	22 450	0	K ⁺ LF(O4+)	19 279	-3171
Li⁺LF(exp)	17 645	-3866	K ⁺ LF(O2+)	23 482	1032
Li ⁺ LF(O4+)	18 022	-4428	K ⁺ LF(O2)	23 208	758
Li ⁺ LF(O2+)	23 341	891	Rb⁺LF(exp)	18 914	-2597
Li ⁺ LF(O2)	23 137	687	Rb ⁺ LF(O4+)	19 451	-2999
Na⁺LF(exp)	18 310	-3201	Rb ⁺ LF(O2)	23 176	726
Na ⁺ LF(O4+)	18 784	-3666	Cs⁺LF(exp)	19 031	-2480
Na ⁺ LF(O2+)	23 498	1048	Cs ⁺ LF(O4+)	19 658	-2792
Na ⁺ LF(O2)	23 208	758	Cs ⁺ LF(O2)	23 160	710

^a Value of LF in He droplet (ref. 33).



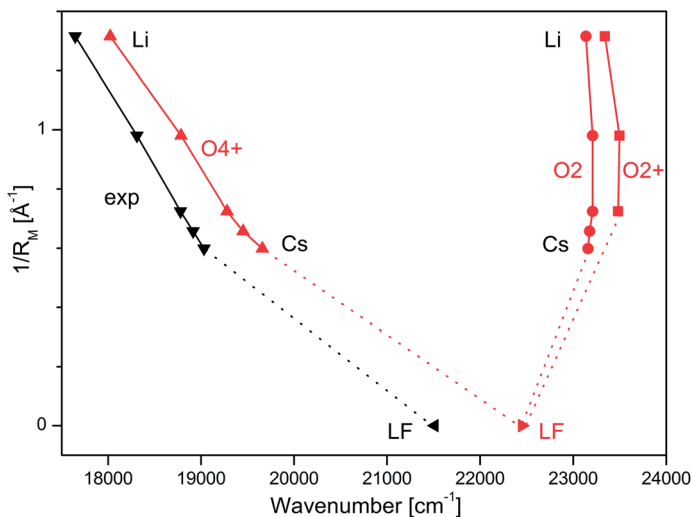


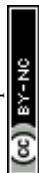
Fig. 3 Experimental S_1 origins extracted from the VISPD spectra of M^+LF compared to adiabatic S_1 origin energies of the O4+ and O2(+) isomers of M^+LF calculated at the PBE0/cc-pVDZ level plotted as a function of the inverse ionic radius of the metal ion ($1/R_M$). The M^+LF ions with $M = Rb$ and Cs do not have a stable O2+ structure. The experimental value for LF is taken from the He droplet spectrum.³³

system. In our previous IRMPD and computational study on M^+LF ions,²⁹ the most stable structures calculated at the B3LYP/cc-pVDZ level are the O4+, O2+, and O2 isomers shown in Fig. 1. In the O4+ and O2+ ions, M^+ forms strongly bent N–M–O chelates (N5–M–O4, N1–M–O2), which benefit from the interaction of M^+ with the lone pairs of both N and O. In contrast, in the O2 ions, the M^+ ions form a nearly linear bond to the C–O2 carbonyl group. In Table 2, the binding and

Table 2 Binding energies (D_0) and relative energies (E_0) of various isomers of M^+LF (in kJ mol^{-1}) calculated at the PBE0/cc-pVDZ and B3LYP/cc-pVDZ levels

Isomer	PBE0/cc-pVDZ		B3LYP/cc-pVDZ ^a	
	D_0	E_0	D_0	E_0
$Li^+LF(O4+)$	300.1	0.0	308.6	0.0
$Li^+LF(O2+)$	289.5	10.6	296.7	11.9
$Li^+LF(O2)$	279.7	20.4	288.6	20.0
$Na^+LF(O4+)$	219.7	0.0	226.1	0.0
$Na^+LF(O2+)$	214.2	5.5	218.9	7.2
$Na^+LF(O2)$	209.5	10.2	214.7	11.4
$K^+LF(O4+)$	176.0	0.0	180.2	0.5
$K^+LF(O2+)$	175.5	0.5	179.0	1.7
$K^+LF(O2)$	175.9	0.1	180.7	0.0
$Rb^+LF(O4+)$	157.9	1.0	159.4	2.1
$Rb^+LF(O2)$	158.9	0.0	161.5	0.0
$Cs^+LF(O4+)$	143.9	2.9	145.8	2.4
$Cs^+LF(O2)$	146.8	0.0	148.2	0.0

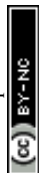
^a Ref. 29.



relative energies of these isomers obtained at the B3LYP/cc-pVDZ level²⁹ are compared to those derived here at the PBE0/cc-pVDZ level, and good agreement is observed. As expected, the binding energies strongly decrease with the size of the M^+ ion (*e.g.*, from 300 to 144 kJ mol⁻¹ for the O4+ isomer of Li and Cs, respectively). For M^+LF with $M = Li$ and Na , the O4+ isomer is the global minimum and the O2+ and O2 isomers are clearly less stable local minima with relative energies of $E_0 = 5\text{--}20$ kJ mol⁻¹. In contrast, for $M = K\text{--}Cs$, the energy spread of all the considered isomers is smaller (<3 kJ mol⁻¹), and the O2 isomer is either slightly more stable than, or isoenergetic with, the O4+ isomer. For the larger alkali ions Cs^+ and Rb^+ , the O2+ isomer is not stable, probably because of the repulsive interaction of the bulky M^+ ion with the CH_3 group at N10. This steric interaction between M^+ and the CH_3 groups implies that the O2+ isomers for the smaller alkali ions do not have C_s symmetry because the CH_3 group rotates out of the plane. In contrast, the geometries of the O4+ and O2 isomers have C_s symmetry. Details of the computed structures and vibrational frequencies in the S_0 state are discussed elsewhere.²⁹ Experimentally, the IRMPD spectra of M^+LF produced by ESI provide clear evidence for the presence of the O4+ and O2(+) isomers for $M = Li\text{--}K$, while for $M = Cs$ only the O2 isomer is clearly identified at room temperature.²⁹ No experimental information is available for Rb^+LF .

The first excited S_1 state of LF and M^+LF involved in the $S_1 \leftarrow S_0$ transition corresponds to an optically bright $\pi\pi^*$ excitation of a π electron from the HOMO to the LUMO. The adiabatic S_1 origins predicted for LF and the O4+ and O2(+) isomers of M^+LF are compared in Table 1 and Fig. 3 to the experimental values extracted from the He droplet spectrum (LF)³³ and the VISPD spectra (M^+LF). Clearly, the S_1 origins computed for the O4+ isomers fit the experimental values very well, with respect to both the absolute values and the dependence on $1/R_M$. The computed S_1 energies of M^+LF are systematically larger than the experimental ones by only 377–627 cm⁻¹ for Li–Cs, which corresponds to 2.1–3.3% of the transition energy. The maximum deviation of 0.08 eV is small for excited state transition energies, indicating that the employed computational level describes the electronic properties of LF well. Similar good performance of this functional has previously been observed for the electronic states of the related H^+LC and M^+LC ions.^{31,32} The difference for bare LF is somewhat larger (939 cm⁻¹), which may be due to the effect of the surrounding He droplet. In contrast to the O4+ ions, the S_1 energies calculated for the O2(+) isomers are much higher than the experimental ones (up to 5696 cm⁻¹, 0.71 eV, 32%) and do not depend much on $1/R_M$ (23 137–23 498 cm⁻¹). In addition, they are blue-shifted from the value for LF (by 687–1048 cm⁻¹). Hence, from comparison of the experimental and computational S_1 origin energies, the assignment of the experimental VISPD spectra in Fig. 2 can only be to the O4+ isomers. We can safely exclude the other low-energy O2(+) isomers, which are predicted to absorb near 23 000 cm⁻¹ (435 nm), *i.e.* at much higher energy than the O4+ isomers (17 600–20 000 cm⁻¹, 570–500 nm). Overall, the data in Fig. 3 demonstrate that the electronic properties of M^+LF depend drastically on the site of metalation and on the size of M^+ .

To analyse the vibrational structure in the $S_1 \leftarrow S_0$ transitions attributed to $M^+LF(O4+)$, they are plotted in Fig. 4 as a function of the S_1 internal energy. Similar to the corresponding spectra of $M^+LC(O4+)$,³² the spectra are dominated by progressions in low-frequency intermolecular $M^+\cdots LF$ in-plane bend and stretch modes (β and σ), which strongly vary with M^+ , and higher-frequency



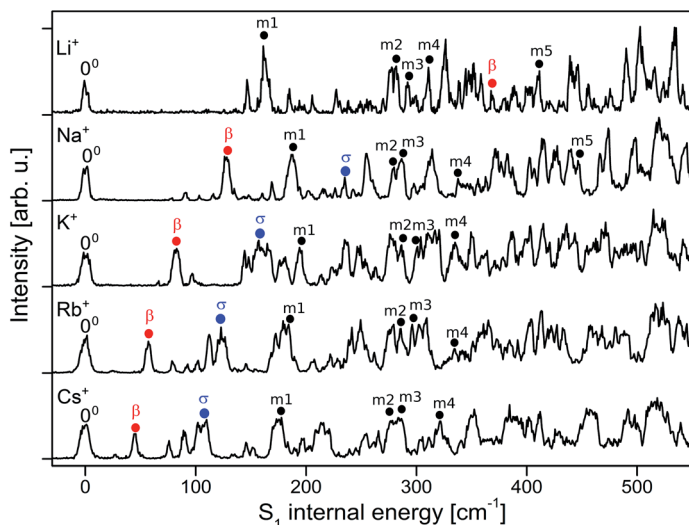


Fig. 4 Expanded view of the experimental VSPD spectra of M^+LF ($M = \text{Li–Cs}$) in the vicinity of the S_1 origin as a function of the S_1 internal energy, along with selected vibrational assignments of the O4+ isomers (Table S1 in ESI†).

intramolecular in-plane skeleton modes of the LF chromophore (denoted m_1 , m_2 , ...), which are relatively independent of M^+ . In an effort to assign the vibronic bands observed in the $S_1 \leftarrow S_0$ transitions attributed to $M^+LF(O4^+)$, we carried out FC simulations, with the major goal of extracting the informative β and σ frequencies. These FC simulations are compared in Fig. 5 to the VSPD spectra for the assigned O4+ isomers. The positions of major peaks observed in the VSPD spectra are listed in Table S1 in the ESI,† along with the assignment suggested by the FC simulations. Corresponding simulations for the O2(+) isomers are available in Fig. S2 in the ESI.† Clearly, the FC calculations strongly support the assignment of the VSPD spectra to the O4+ isomers. The FC simulations for O2(+) fit much worse, providing further evidence – in addition to the S_1 origin positions – that these isomers cannot be responsible for the measured VSPD spectra.

As expected from the C_s symmetry of the $M^+LF(O4^+)$ ions with the planar tricyclic aromatic ring, the FC simulations contain only progressions and combination bands of in-plane modes with a' symmetry. Overtones and even combination bands of out-of-plane a'' fundamentals have essentially no FC activity. Closer inspection of Fig. 5 and Table S1† reveals that indeed nearly all low-frequency a' modes have significant FC intensity and are assigned. In the following, we concentrate on the β and σ modes, because they probe the $M^+ \cdots LF$ interaction (Table 3). Similar to $M^+LC(O4^+)$, the progressions in σ are well reproduced by the FC calculations, while the intensities predicted for the progressions in β are substantially smaller than the observed ones (in particular for the heavy alkali ions, $M = \text{K–Cs}$). On the other hand, the computed (experimental) frequencies of $\beta = 45$ (44), 60 (57), 86 (82), 134 (128), and 375 (368) cm^{-1} and $\sigma = 111$ (108), 130 (124), 162 (157), 240 (234), and 626 (610) cm^{-1} for $M = \text{Cs–Li}$ match very well for all $M^+LF(O4^+)$ ions (Table 3). Similar to M^+LC ,³² the stretch frequencies are roughly twice the bend frequencies (*i.e.*, $\sigma \sim 2\beta$). The frequency



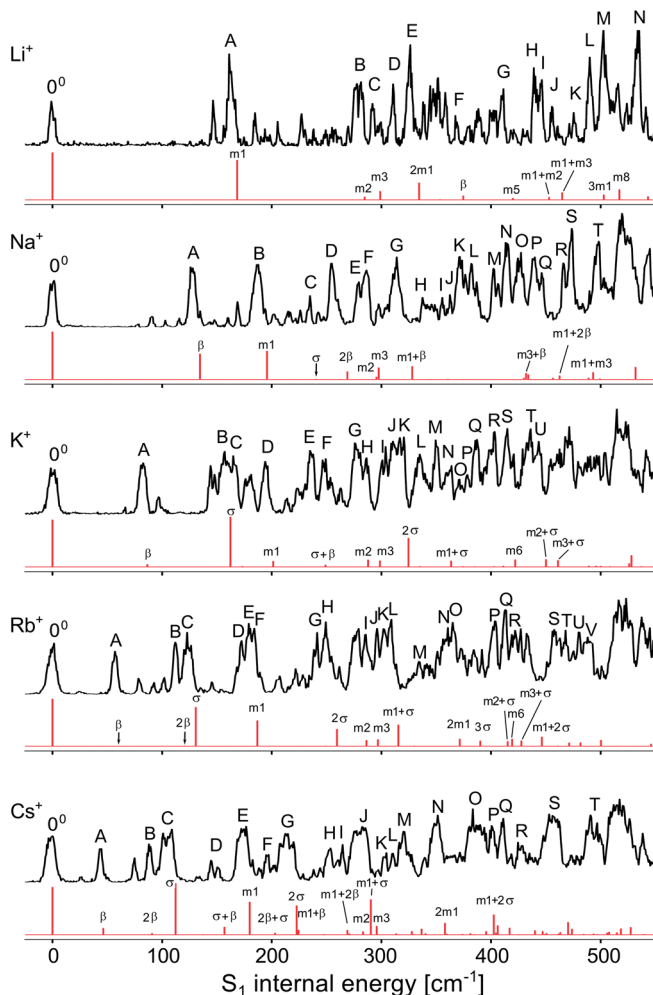
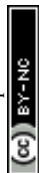


Fig. 5 Experimental VISPD spectra of M^+LF ($M = \text{Li–Cs}$) compared to FC simulations for the $M^+LF(\text{O4}^+)$ isomers as a function of the S_1 internal energy (Table S1 in ESI†).

increase for both types of modes along the series $\text{Cs} \rightarrow \text{Li}$ results from the increasing binding energy and angular anisotropy (*i.e.*, effective force constant) of the potential and the decreasing reduced mass. Applying a pseudodiatomic model, the measured σ frequencies yield force constants of $k = 149, 68, 49, 58$,

Table 3 In-plane intermolecular $M^+ \cdots LF$ bend and stretch frequencies (in cm^{-1}) of the S_0 and S_1 states of $M^+LF(\text{O4}^+)$ with $M = \text{Li–Cs}$ calculated at the PBE0/cc-pVDZ level compared to experimental values in S_1

	Li			Na			K			Rb			Cs		
	S ₀	S ₁	Exp.	S ₀	S ₁	Exp.	S ₀	S ₁	Exp.	S ₀	S ₁	Exp.	S ₀	S ₁	Exp.
β	320	375	368	121	134	128	71	86	82	48	60	57	36	45	44
σ	618	626	610	240	240	234	155	162	157	124	130	124	107	111	108



and 60 N m^{-1} for the $\text{M}^+\cdots\text{LF}$ bonds with $\text{M} = \text{Li-Cs}$. This rough approach works qualitatively for reproducing the drop in binding energy for Li-K. However, it fails for the larger alkali ions because the σ mode is not a bare pseudodiatom stretch but also involves a large LF in-plane bending component. Thus, the pseudodiatom force constant k of σ is not necessarily correlated to D_0 . As expected, the β and σ values computed for the S_1 excited state are systematically larger than those in the S_0 state, because the $\text{M}^+\cdots\text{LF}$ interaction becomes stronger upon $\pi\pi^*$ excitation (Table 3). In fact, the ΔS_1 red shift upon metalation directly reflects the increase in the binding energy upon S_1 excitation. Thus, S_1 excitation increases the binding energies of $\text{M}^+\cdots\text{LF}$ by 29.7, 31.1, 32.7, 38.2, and 46.2 kJ mol^{-1} for Cs-Li, which corresponds to 20.6, 19.7, 18.6, 17.4, and 15.4%, respectively, assuming the computed PBE0 binding energies for S_0 listed in Table 2.

As already observed for M^+LC ,³² the low-frequency intramolecular LF modes of M^+LF do not change much with M. This result is consistent with the view that the $\pi\pi^*$ excitation is located on the LF chromophore, with essentially no amplitude of the orbital wavefunctions on the M^+ ion. Computed frequencies are listed in Table S2 in the ESI† along with the suggested experimental assignments. The corresponding normal modes are quite similar to those of the related M^+LC ions discussed in detail elsewhere.³² A full set of the computed frequencies of LF and M^+LF in S_0 and S_1 is available in Table S3 in the ESI.† As expected from the similar orbitals, the intramolecular S_1 vibronic excitation of $\text{M}^+\text{LF}(\text{O}4+)$ is similar to the one observed for neutral LF in He droplets.³³ The latter spectrum is dominated by progressions in the lowest frequency mode of up to 3 quanta ($m_1 = 164 \text{ cm}^{-1}$), which also occurs in combination with other low-frequency intramolecular origins. Other low-frequency fundamentals are observed at 274, 403, 440, 513, and 593 cm^{-1} . These correspond well to our frequencies calculated for LF in the S_1 state of 165 (m_1), 276 (m_2), 409 (m_5), 444 (m_6), 521 (m_8), and $603 \text{ (}m_{10}) \text{ cm}^{-1}$. The lowest-frequency modes observed for Cs^+LF in S_1 (*i.e.*, the M^+LF complex with the weakest perturbation of LF by M^+) are quite similar, with 175 (m_1), 276 (m_2), 401 (m_5), and $410 \text{ (}m_6) \text{ cm}^{-1}$. These similarities in the vibronic activity in the excitation spectra of LF and $\text{M}^+\text{LF}(\text{O}4+)$ confirm that the same electronic state is excited and that the M^+ ion has only a weak impact on the electronic structure.

Interestingly, not all transitions observed in the VISPD spectra of M^+LF can be assigned by the FC simulations. For example, in the spectrum of Na^+LF , four weaker reproducible transitions appear at 78, 91, 103, and 116 cm^{-1} below the first FC active in-plane fundamental ($\beta = 128 \text{ cm}^{-1}$, band A). The origin of these transitions is presently less certain. (1) We may safely exclude an assignment to isomers other than $\text{M}^+\text{LF}(\text{O}4+)$, because they are predicted to absorb in a very different spectral range (Fig. 3). Hence, the transitions are linked to $\text{M}^+\text{LF}(\text{O}4+)$. (2) Thus, one option might be an assignment to $\text{S}_1 \leftarrow \text{S}_0$ transitions of tagged complexes of $\text{M}^+\text{LF}(\text{O}4+)$.³² Indeed, at low trap temperatures of $T = 6 \text{ K}$, $\text{M}^+\text{LF}(\text{O}4+)$ -He clusters are formed for the small alkali ions Li^+ and Na^+ , because they have large He binding affinities. $\text{M}^+\text{LF}(\text{O}4+)$ -He absorptions will also be detected in the M^+ fragment channel. To test this hypothesis, VISPD spectra of $\text{M}^+\text{LF}(\text{O}4+)$ are recorded at a higher trap temperature ($T = 13 \text{ K}$), at which no He-tagged clusters are formed (as verified by mass spectra, Fig. S3 in the ESI†). Significantly, the appearances of the VISPD spectra at 6 and 13 K are similar (Fig. S4 in the ESI†). In particular, the relative intensities of the transitions do not change. Hence, we may safely exclude contaminating signals from tagged ions. (3)



Additional transitions may also arise from slightly higher-energy singlet states of $M^+LF(O4^+)$. However, the next allowed and forbidden singlet states are predicted to be much higher in energy, as shown by the vertical transitions for the S_1 – S_4 states listed in Table 4. In particular, the S_2 and S_3 states are optically dark $n\pi^*$ states with zero oscillator strength. The next optically bright $\pi\pi^*$ state (S_4) has a similar oscillator strength to S_1 but is predicted to be far away ($\Delta\nu = 7000$ – 7300 cm^{-1}). Low-energy triplet states could be a further option but should be spin-forbidden and are not observed in the spectra of LF embedded in He droplets and the condensed phase. (4) Finally, the additional vibronic bands may arise from $S_1 \leftarrow S_0$ transitions of $M^+LF(O4^+)$ not included in the FC simulations. For example, FC forbidden transitions, such as out-of-plane LF fundamentals and combination bands of a'' symmetry, could gain intensity by vibronic coupling to other electronic states. Furthermore, the coupling of vibrational excitation to internal rotation of the CH_3 groups may also produce additional transitions (and could explain the observed unresolved doublets/multiplets of the S_1 origins).⁴⁸ Such transitions should not depend strongly on the M^+ ion, and indeed several of the low-frequency additional bands are visible in several of the M^+LF spectra at very similar frequencies. For example, most of the spectra have peaks at roughly 75, 93, 102, and 145 cm^{-1} . In addition, these transitions have a smaller width than the main bands, indicating an assignment to modes with different vibrational symmetry. Unfortunately, comparison of the predicted frequencies with the observed unexplained transitions does not yield a conclusive assignment because of the lack of reliable calculated intensities. Thus, a detailed assignment of these transitions has to await a more sophisticated theoretical treatment, which is beyond the scope of this work.

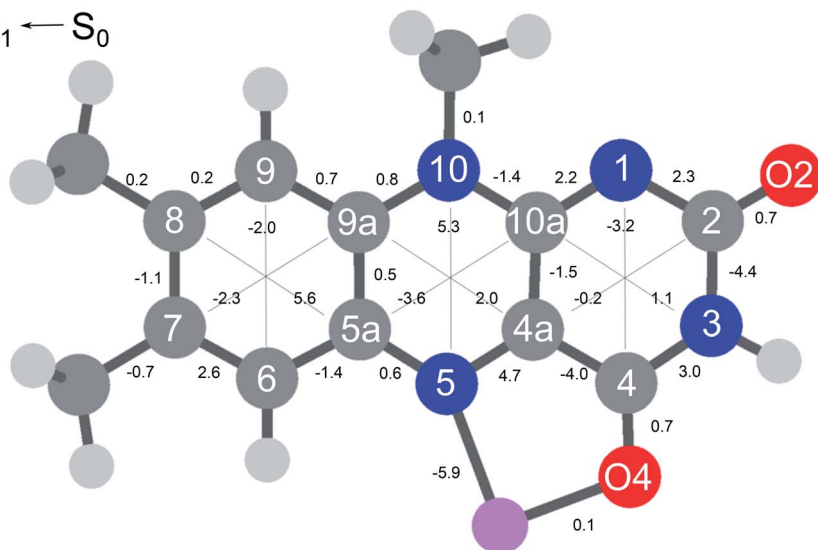
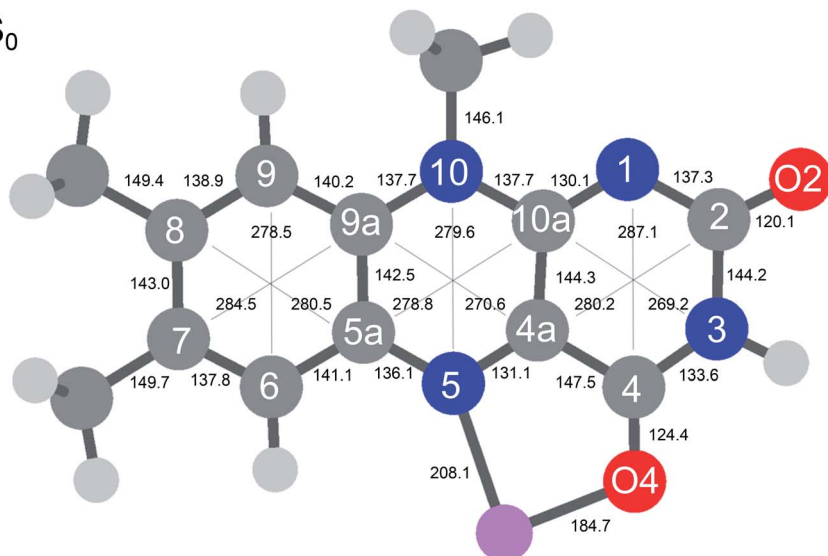
In Fig. 6 the geometry changes upon electronic excitation are visualized for the example of Li^+LF . Corresponding data for the other alkali metals Na–Cs are available in Fig. S5 in the ESI.[†] The strongest changes take place in rings I and II, because the HOMO and LUMO orbitals involved in the $S_1 \leftarrow S_0$ $\pi\pi^*$ transition are mostly located on these rings (Fig. 7). Ring I expands along the C5a–C8 axis (by 5.6 pm) accompanied by a moderate contraction of the C7–C9a and the C6–C9 axes (–2.3 and –2.0 pm, respectively). In ring II the maximum change is an elongation along the N5–N10 axis (5.3 pm). Only smaller geometry changes occur in ring III. Both CO bonds slightly elongate by 0.7 pm for all M^+LF

Table 4 Vertical transition energies (ν in cm^{-1} , λ in nm) and oscillator strength (f) for the first four excited singlet states of LF and $M^+LF(O4^+)$ with $M = Li$ – Cs calculated at the PBE0/cc-pVDZ level^a

	$S_1 (\pi\pi^*)$			$S_2 (n\pi^*)$			$S_3 (n\pi^*)$			$S_4 (\pi\pi^*)$		
	ν	λ	f	ν	λ	f	ν	λ	f	ν	λ	f
Li	20 595	485.56	0.141	25 463	392.72	0.0	27 581	362.57	0.0	27 622	362.03	0.187
Na	21 429	466.66	0.154	25 772	388.02	0.0	27 728	360.65	0.0	28 687	348.59	0.178
K	21 946	455.66	0.162	26 197	381.73	0.0	27 680	361.27	0.0	29 208	342.37	0.174
Rb	22 142	451.63	0.164	26 328	379.83	0.0	27 672	361.38	0.0	29 417	339.94	0.171
Cs	22 306	448.30	0.167	26 506	377.28	0.0	27 630	361.92	0.0	29 530	338.64	0.169
LF	25 236	396.26	0.213	26 121	382.84	0.0	27 585	362.51	0.0	32 250	310.08	0.136

^a Corresponding data for the $O2(+)$ isomers are available in Table S5 in ESI.





complexes. The relative structural changes of the LF chromophore upon electronic S_1 excitation are relatively independent of the metal ion, because the HOMO/LUMO orbitals are completely localized on the LF chromophore. As a result, the calculated oscillator strength is relatively independent of M (Table 4). However, charge reorganization upon S_1 excitation of LF has a substantial

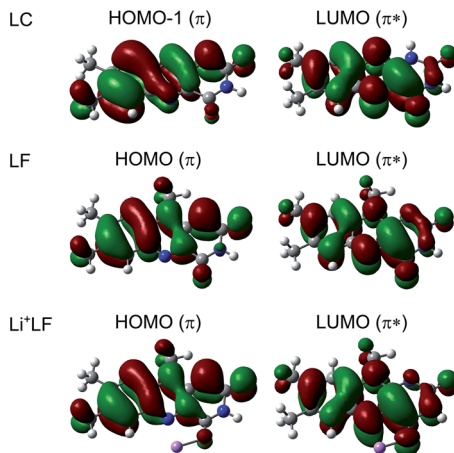


Fig. 7 Natural transition orbitals involved in the electronic $S_1 \leftarrow S_0$ ($\pi\pi^*$) transition (LUMO \leftarrow HOMO) of LF and Li^+LF computed at the PBE0/cc-pVDZ level. For comparison, the corresponding orbitals for LC are shown as well (for LC the $\pi\pi^*$ transition is S_2 and corresponds to LUMO \leftarrow HOMO-1).^{31,32}

impact on the strength of the $\text{M}^+ \cdots \text{LF}$ interaction. Fig. 8 details the NBO partial charges in both the S_0 and S_1 states of the LF chromophore. Significantly, the negative partial charge on N5 increases substantially from -0.376 to $-0.454e$ (by $0.078e$), while the corresponding increase in negative charge on O4 is smaller (from -0.577 to $-0.592e$, $\Delta q_{\text{O4}} = 0.015e$). As a result, the interaction of M^+ with N5 becomes much stronger in S_1 , while that of M^+ with O4 hardly changes. This view is consistent with the result that S_1 excitation leads to a drastic contraction of the M–N5 bond (by 5.9–16 pm for Li–Cs), while the M–O4 bond contraction is negligible (≤ 1.1 pm). The stronger $\text{M}^+ \cdots \text{LF}$ interaction in the S_1 excited state is compatible with the observed ΔS_1 red shifts. Finally, the strength of the $\text{M}^+ \cdots \text{LF}$ interaction scales with the magnitude of the small but noticeable charge transfer from M^+ to LF. While the positive partial charges on M^+ are 0.881, 0.922, 0.922, 0.928, and 0.917 e for Li $^+$ –Cs $^+$ in the S_0 state, they are systematically smaller in the corresponding S_1 state (0.860, 0.908, 0.909, 0.915, and 0.906 e). Clearly, the charge transfer in S_0 is largest from Li $^+$ to LF ($\Delta q = 0.12e$), because Li $^+ \cdots \text{LF}$ has the by far strongest bond. In addition, the enhancement of the charge transfer upon electronic excitation is also largest for this complex ($\Delta q = 0.021e$), because the increase in binding energy upon $\pi\pi^*$ excitation is most pronounced (Table S4 in the ESI †). In contrast to O4/N5, the negative charge density decreases at N1/O2 upon S_1 excitation which reduces the $\text{M}^+ \cdots \text{LF}$ interaction in the O2(+) isomers and explains their blue shifts in ΔS_1 .

To unravel more details about the VISPD process of $\text{M}^+\text{LF}(\text{O4}^+)$, the dependence of the M^+ fragment yield on the laser pulse energy is considered for excitation of the S_1 origin. For the heavy alkali ions Na–Cs, a linear dependence of the M^+ fragment ion yield is observed over a wide range (0–2.5 mJ), while for Li the dependence is nonlinear, indicating the VISPD process requires the absorption of a single photon for Na–Cs and two photons for Li (Fig. S6 in the ESI †). This result is consistent with the binding energies calculated for the S_0 state ($D_0 \sim 12\,030$,



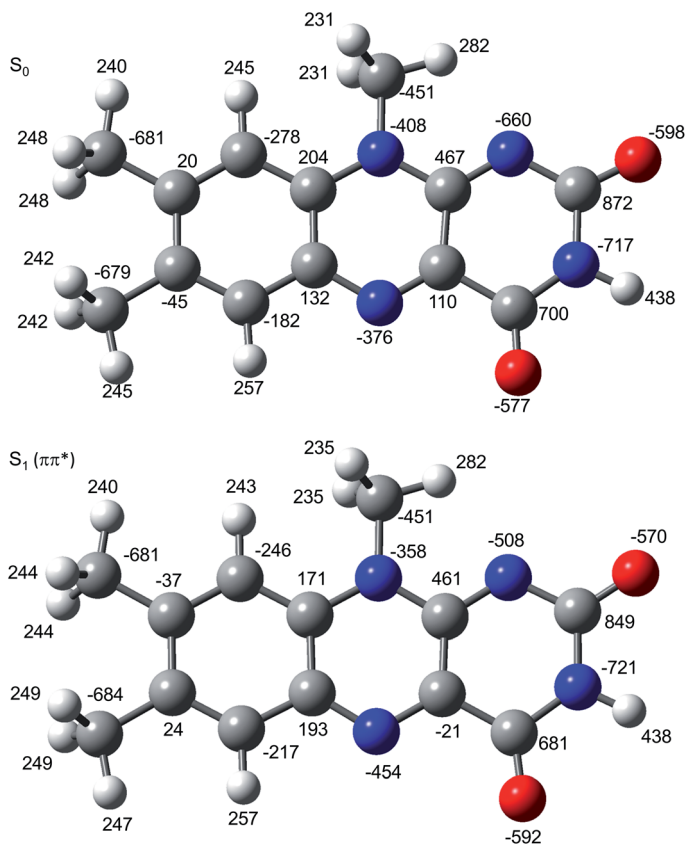


Fig. 8 Atomic charge distribution of LF (in $10^{-3}e$) in the S_0 and S_1 states using natural bond orbital analysis.

13 200, 14 710, 18 370, 25 090 cm^{-1} for Cs-Li), which are substantially lower than the measured S_1 origins for M^+LF with $M = \text{Cs-K}$ ($S_1 = 19\,031$, 18 914, 18 778 cm^{-1}), roughly the same for $M = \text{Na}$ ($S_1 = 18\,310$ cm^{-1}), and much larger for $M = \text{Li}$ ($S_1 = 17\,645$ cm^{-1}). Thus, according to these data, single-photon absorption should be sufficient for dissociation of M^+LF with $M = \text{Cs-Na}$, while at least two photons are required to dissociate Li^+LF . Although the photodissociation mechanism is not clear, we assume that the VISPD process occurs by internal conversion from the excited electronic state (S_1 for Na-Cs, $S_{n>1}$ for Li) to the S_0 state followed by statistical dissociation on the ground state.

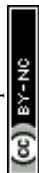
It is instructive to compare the optical properties of M^+LF with those determined recently for the related M^+LC complexes using the same experimental and computational approach.³² LF differs from LC such that LF has a CH_3 group at N10, while LC has a H atom at N1. The S_1 state of both flavins arises from $\pi\pi^*$ excitation and the involved orbitals are quite similar for both molecules (Fig. 7) and closely resemble those reported for 10-methyl-isoalloxazine.²³ As the LF orbitals are slightly more delocalized than those of LC, with a modest contribution on the additional CH_3 group at N10, the orbital energies and corresponding $\pi\pi^*$ transition energies are lower for LF. For example, the computed adiabatic S_1



origin of LF at $22\,450\text{ cm}^{-1}$ is strongly red shifted compared to the corresponding S_2 state of LC at $25\,899\text{ cm}^{-1}$ (by 3449 cm^{-1}), in agreement with experimental observations. We note that in LC, the first $\pi\pi^*$ state (S_2) lies slightly above the first $n\pi^*$ state (S_1), while the situation is reversed for LF. For both metalated flavins, the observed VISPD spectra are assigned to the O4+ isomers, forming N5–M–O4 chelates with similar binding energies of 139–296 and 144–300 kJ mol^{-1} for $M^+\text{LC}$ and $M^+\text{FL}$ with $M = \text{Cs–Li}$, respectively. Since the M^+ binding site is far away from the position of the relevant CH_3/H groups, and $\pi\pi^*$ excitation involves essentially the same orbitals, the large red shifts upon electronic excitation are similar for the O4+ isomers of both metalated flavins. For example, the $-\Delta S_1$ values computed for $M^+\text{LF}$ ($2792\text{--}4428\text{ cm}^{-1}$) are comparable to those of $M^+\text{LC}$ ($3182\text{--}5142\text{ cm}^{-1}$), again in good agreement with the experimental observations. Because of the similar bonding in $M^+\text{LC}(\text{O4+})$ and $M^+\text{LF}(\text{O4+})$ and the comparable mass of LC and LF ($m/z\,242$ versus 256), the intermolecular $M^+\cdots$ flavin frequencies β and σ are nearly the same, too. For example, $\beta = 45\text{--}350$ versus $45\text{--}368\text{ cm}^{-1}$ and $\sigma = 108\text{--}595$ versus $108\text{--}610\text{ cm}^{-1}$ are measured in the S_1 excited state. The main differences between LC and LF occur at the O2(+) binding site, because in the LC tautomer the H atom is bonded to N1, while in LF the free lone pair of N1 is available for bonding with M^+ (and H^+).^{28,31,32} Hence, $M^+\text{LC}$ can only form O2 but not O2+ isomers for steric reasons. In addition, while H^+LC prefers protonation at N5, for H^+LF the O2+ tautomer was observed.²⁷

Concluding remarks

In summary, the VISPD spectra of $M^+\text{LF}$ with $M = \text{Li–Cs}$ presented herein correspond to the first optical spectra of metalated LF complexes in the gas phase and provide a first impression of the effects of alkali metalation on the absorption properties of this simple flavin molecule. Significantly, cryogenic cooling of the ions is mandatory for achieving vibronic resolution in the excitation spectra and thus provides detailed experimental information about the changes in geometric, vibrational, and electronic structure upon electronic excitation, which cannot be obtained with room-temperature spectra. The analysis of the VISPD spectra with the aid of TD-DFT calculations coupled to multidimensional FC simulations allows for an unambiguous assignment of the spectra observed in the 500–570 nm range to transitions of the O4+ isomer into the optically bright first excited singlet state ($S_1 \leftarrow S_0$) which has $\pi\pi^*$ character. The good agreement between the observed adiabatic S_1 origins and those predicted at the PBE0/cc-pVDZ level ($<0.1\text{ eV}$) indicates that this economic DFT level reliably describes the electronic structure of flavin molecules. Because the other low-energy O2(+) isomers absorb in a rather different optical range, the recorded VISPD spectra of the O4+ ions are highly isomer-selective. This is in contrast to previous IRMPD spectra, in which absorptions of these isomers occur in the same spectral range and strongly overlap.²⁹ The intramolecular vibronic structure observed for $M^+\text{LF}$ is relatively independent of M^+ and similar to that of LF, because the molecular orbitals involved in the $S_1 \leftarrow S_0$ transition do not cover the M^+ ion. As a result, the large ΔS_1 red shifts upon M^+ complexation (up to $\sim 4000\text{ cm}^{-1}$ or $\sim 100\text{ nm}$) can be traced back to the increase in the intermolecular $M^+\cdots\text{LF}$ interaction upon S_1 excitation (up to $\sim 20\%$). This effect is specific to the O4+ metal binding site and



can be explained by the significant electron transfer to the N5 and O4 atoms upon $\pi\pi^*$ excitation, which increases the local electrostatic interaction of LF with the M^+ cation. Although the major vibronic structure in the VISPD spectra of $M^+LF(O4+)$ could be reproduced by simple FC simulations, the reliable explanation of minor absorptions tentatively attributed to vibronic coupling and/or internal CH_3 rotation requires a more sophisticated computational treatment. In many aspects, the photochemical properties of the O4+ isomers of M^+LF are similar to those of M^+LC ,³² because the molecular orbitals involved in the $S_1 \leftarrow S_0$ transition are only slightly affected by the structural differences of these two flavins.

In future work, this VISPD study on M^+LF can be extended along several directions. First, VISPD spectra recorded at shorter wavelengths are to be recorded to find and characterize higher excited singlet states of the O4+ isomers predicted in the 300–400 nm range (Table 4) and to search for the S_1 absorption of the O2(+) isomers, which were previously identified in the population of ESI-generated ions by IRMPD and have predicted S_1 origins in the 23 000–24 000 cm^{-1} (415–435 nm) range (Table 1). Second, M^+LF complexes with transition metal ions (*e.g.*, Cu^+-Au^+) and multiply charged ions (*e.g.*, Fe^{2+} , Mg^{2+}) are interesting targets²⁹ because of their biological relevance. Third, the optical spectrum of H^+LF is particularly interesting because the preferred protonation site of LF (O2+) is different from the metalation site observed here for M^+LF (O4+). Initial VISPD spectra for H^+LF reveal indeed absorptions near 23 100 cm^{-1} consistent with O2+ protonation. Forth, microhydrated clusters of M^+LF/H^+LF could provide detailed insight into the effects of stepwise solvation on the photochemical properties of these flavins, which according to solution experiments strongly depend on the considered excited state.

As a general conclusion, the combined approach of cryogenic ion spectroscopy coupled to TD-DFT calculations and FC simulations is a powerful tool to expand our knowledge of the photochemical and photophysical properties of flavins. Our initial promising studies on the smaller flavins LC and LF pave the way to larger and biologically more relevant flavins, such as RF, FMN, and FAD. Because these more complex molecules have flexible side chains, the detailed determination of their conformation-dependent photochemical properties is more challenging and requires the application of multiple-resonance laser schemes such as VIS/VIS or IR/VIS approaches.

Conflicts of interest

There are no conflicts to declare.

Acknowledgements

This work was supported by Deutsche Forschungsgemeinschaft (DFG, DO 729/6). M. M. is grateful for a senior research fellowship from the Alexander von Humboldt Foundation (2017–2019). O. D. acknowledges travel support from the World Research Hub Initiative (WRHI) of Tokyo Institute of Technology (Japan). Part of the computations was performed at the Research Center for Computational Science in Okazaki (Japan).

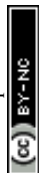


References

- 1 K. H. Dudley, P. Hemmerich, F. Müller and A. Ehrenberg, *Helv. Chim. Acta*, 1964, **47**, 1354–1383.
- 2 P. F. Heelis, *Chem. Soc. Rev.*, 1982, **11**, 15–39.
- 3 V. Massey, *Biochem. Soc. Trans.*, 2000, **28**, 283–296.
- 4 E. Silva and A. Edwards, *Flavins, Photochemistry, and Photobiology*, RSC Publishing, Cambridge, 2006.
- 5 W. Buckel and R. K. Thauer, *Chem. Rev.*, 2018, **118**, 3862–3886.
- 6 W. J. Rutter, *Acta Chem. Scand.*, 1958, **12**, 438–446.
- 7 I. F. Baarda and D. E. Metzler, *Biochim. Biophys. Acta*, 1961, **50**, 463–471.
- 8 P. Bamberg and P. Hemmerich, *Helv. Chim. Acta*, 1961, **44**, 1001–1011.
- 9 F. Müller, P. Hemmerich and A. Ehrenberg, *Eur. J. Biochem.*, 1968, **5**, 158–164.
- 10 A. W. Varnes, E. L. Wehry and R. B. Dodson, *J. Am. Chem. Soc.*, 1972, **94**, 946–950.
- 11 J. Lauterwein, P. Hemmerich and J. M. Lhoste, *Inorg. Chem.*, 1975, **14**, 2152–2161.
- 12 J. Lauterwein, P. Hemmerich and J. M. Lhoste, *Inorg. Chem.*, 1975, **14**, 2161–2168.
- 13 M. Benecky, T. Y. Yu, K. L. Watters and J. T. McFarland, *Biochim. Biophys. Acta*, 1980, **626**, 197–207.
- 14 S. Fukuzumi and T. Kojima, *J. Biol. Inorg. Chem.*, 2008, **13**, 321–333.
- 15 I. Ahmad, Z. Anwar, S. Ahmed, M. A. Sheraz and S. Khattak, *J. Photochem. Photobiol., B*, 2017, **173**, 231–239.
- 16 E. Sikorska, I. V. Khmelinskii, W. Prukała, S. L. Williams, M. Patel, D. R. Worrall, J. L. Bourdelande, J. Koput and M. Sikorski, *J. Phys. Chem. A*, 2004, **108**, 1501–1508.
- 17 W. Holzer, J. Shirdel, P. Zirak, A. Penzkofer, P. Hegemann, R. Deutzmann and E. Hochmuth, *Chem. Phys.*, 2005, **308**, 69–78.
- 18 A. Tyagi and A. Penzkofer, *J. Photochem. Photobiol., A*, 2010, **215**, 108–117.
- 19 A. Penzkofer, A. Tyagi and J. Kiermaier, *J. Photochem. Photobiol., A*, 2011, **217**, 369–375.
- 20 C. Neiss, P. Saalfrank, M. Parac and S. Grimme, *J. Phys. Chem. A*, 2003, **107**, 140–147.
- 21 J. Hasegawa, S. Bureekaew and H. Nakatsuji, *J. Photochem. Photobiol., A*, 2007, **189**, 205–210.
- 22 S. Salzmann and C. M. Marian, *Chem. Phys. Lett.*, 2008, **463**, 400–404.
- 23 S. Salzmann, J. Tatchen and C. M. Marian, *J. Photochem. Photobiol., A*, 2008, **198**, 221–231.
- 24 S. Salzmann and C. M. Marian, *Photochem. Photobiol. Sci.*, 2009, **8**, 1655–1666.
- 25 B. Klaumünzer, D. Kröner and P. Saalfrank, *J. Phys. Chem. B*, 2010, **114**, 10826–10834.
- 26 R. J. Platenkamp, H. D. Van Osnabrugge and A. J. W. G. Visser, *Chem. Phys. Lett.*, 1980, **72**, 104–111.
- 27 J. Langer, A. Günther, S. Seidenbecher, G. Berden, J. Oomens and O. Dopfer, *ChemPhysChem*, 2014, **15**, 2550–2562.
- 28 A. Günther, P. Nieto, G. Berden, J. Oomens and O. Dopfer, *Phys. Chem. Chem. Phys.*, 2014, **16**, 14161–14171.



- 29 P. Nieto, A. Günther, G. Berden, J. Oomens and O. Dopfer, *J. Phys. Chem. A*, 2016, **120**, 8297–8308.
- 30 A. Günther, P. Nieto, D. Müller, A. Sheldrick, D. Gerlich and O. Dopfer, *J. Mol. Spectrosc.*, 2017, **332**, 8–15.
- 31 A. Sheldrick, D. Müller, A. Günther, P. Nieto and O. Dopfer, *Phys. Chem. Chem. Phys.*, 2018, **20**, 7407–7414.
- 32 P. Nieto, D. Müller, A. Sheldrick, A. Günther, M. Miyazaki and O. Dopfer, *Phys. Chem. Chem. Phys.*, 2018, **20**, 22148–22158.
- 33 A. Vdovin, A. Slenczka and B. Dick, *Chem. Phys.*, 2013, **422**, 195–203.
- 34 M. H. Stockett, *Phys. Chem. Chem. Phys.*, 2017, **19**, 25829–25833.
- 35 L. Giacomozzi, C. Kjær, J. Langeland Knudsen, L. H. Andersen, S. Brøndsted Nielsen and M. H. Stockett, *J. Chem. Phys.*, 2018, **148**, 214309.
- 36 J. N. Bull, E. Carrascosa, L. Giacomozzi, E. J. Bieske and M. H. Stockett, *Phys. Chem. Chem. Phys.*, 2018, **20**, 19672–19681.
- 37 E. Matthews and C. E. H. Dessent, *J. Phys. Chem. Lett.*, 2018, **9**, 6124–6130.
- 38 E. Matthews, R. Cercola and C. E. H. Dessent, *Molecules*, 2018, **23**, 2036.
- 39 K. Lincke, J. L. Knudsen, A. Ø. Madsen, H. V. V. Kiefer, L. Skov, E. Gruber, K. V. Mikkelsen, L. H. H. Andersen and M. B. Nielsen, *Phys. Chem. Chem. Phys.*, 2018, **20**, 28678–28684.
- 40 T. R. Rizzo, J. A. Stearns and O. V. Boyarkin, *Int. Rev. Phys. Chem.*, 2009, **28**, 481–515.
- 41 N. S. Nagornova, T. R. Rizzo and O. V. Boyarkin, *Science*, 2012, **336**, 320–323.
- 42 M. J. Frisch, *et al.*, *GAUSSIAN09, Rev. D.01*, Gaussian, Inc., Wallingford CT, 2009.
- 43 I. S. Lim, P. Schwerdtfeger, B. Metz and H. Stoll, *J. Chem. Phys.*, 2005, **122**, 104103.
- 44 C. M. Western, *J. Quant. Spectrosc. Radiat. Transfer*, 2017, **186**, 221–242.
- 45 R. L. Martin, *J. Chem. Phys.*, 2003, **118**, 4775–4777.
- 46 E. D. Glendening, J. K. Badenhoop, A. E. Reed, J. E. Carpenter, J. A. Bohmann, C. M. Morales, C. R. Landis and F. Weinhold, *NBO 6.0, Theoretical Chemistry*, University of Wisconsin, Madison, 2013.
- 47 R. D. Shannon, *Acta Crystallogr., Sect. A: Cryst. Phys., Diffr., Theor. Gen. Crystallogr.*, 1976, **32**, 751–767.
- 48 P. J. Breen, J. A. Warren, E. R. Bernstein and J. I. Seeman, *J. Chem. Phys.*, 1987, **87**, 1917–1926.



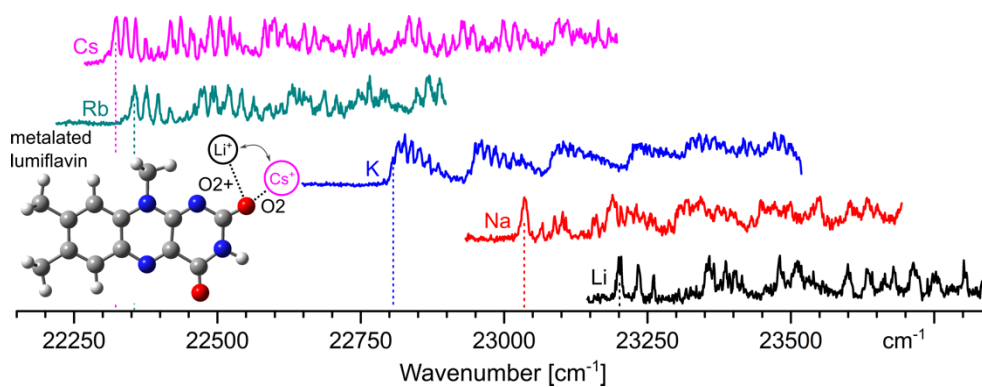
4.2. Optical spectroscopy of cryogenic metalated flavins: The O2(+) isomers of M⁺lumiflavin (M=Li-Cs)

David Müller and Otto Dopfer

J. Photochem. Photobiol., 2020, **3-4**, 100009

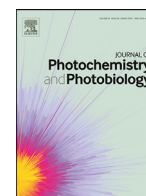
<https://doi.org/10.1016/j.jpap.2020.100009>

Reprinted with permission from Elsevier B.V.



Declaration of Contribution

Both experimental and computational analysis were carried out by David Müller. The manuscript of the article was written by David Müller and reviewed and finalized by Otto Dopfer. All work was supervised by Otto Dopfer.



Optical spectroscopy of cryogenic metalated flavins: The O2(+) isomers of M⁺lumiflavin (M=Li–Cs)

David Müller, Otto Dopfer*

Institut für Optik und Atomare Physik, Technische Universität Berlin, Hardenbergstr. 36, D-10623 Berlin, Germany



ARTICLE INFO

Keywords:

Flavins
Metalation
Cryogenic ions
Optical spectroscopy
Isomers
Excited states

ABSTRACT

Flavin complexes are used by nature in many photobiological processes, because their photochemical response in the visible range can be strongly modulated by their environment. Herein, we report optical spectra of mass-selected metal complexes of lumiflavin (LF) with alkali metal ions (M=Li–Cs) recorded in the visible range by photodissociation (VISPD) at cryogenic temperatures ($T < 20$ K). VISPD spectra are measured in a tandem mass spectrometer coupled to a cryogenic ion trap and an electrospray ionization source. The vibrationally-resolved VISPD spectra obtained in the 420–450 nm range are assigned to the $S_0 \leftarrow S_1$ ($\pi\pi^*$) transition of the O2(+) isomers of M⁺LF by comparison to time-dependent density functional theory calculations (PBE0/cc-pVDZ) coupled to multidimensional Franck–Condon (FC) simulations. The preferred binding motif and interaction strength strongly depend on the size of M⁺. The spectra of M⁺LF with the smaller M⁺ ions (M=Li and Na) are attributed to the most stable O2+ isomers characterized by a N1–M–O2 chelate binding motif in which M⁺ can interact with the lone pairs of both N1 and O2 of LF. Because of steric interaction with the CH₃ group at N10, the tricyclic aromatic ring is slightly bent and the VISPD spectra feature low-frequency out-of-plane bending modes of LF. Such an O2+ structure is sterically repulsive for the larger M⁺ ions (M=Rb and Cs), which instead form planar O2 minima with nearly linear C2–O2–M bonds. Their VISPD spectra are characterized by low-frequency in-plane bending modes (β) describing the M⁺...LF interaction. The VISPD spectrum of K⁺LF with the intermediate-size K⁺ ion is more complex and features very low-frequency modes resulting from a very shallow potential along the O2 \leftrightarrow O2+ isomerization coordinate, which cannot be described well by harmonic FC simulations. Electronic S₁ excitation slightly weakens the M⁺...LF interaction (6–9%), as deduced from the small ΔS_1 blueshifts upon metalation at the O2(+) binding site, consistent with the charge reorganization deduced from the molecular orbitals involved in $\pi\pi^*$ excitation. Overall, the effects of O2(+) complexation of LF are drastically different from those of the previously studied O4+ isomers, which are characterized by large ΔS_1 redshifts based on the strong increase in the M⁺...LF interaction (up to 20%) upon the same $\pi\pi^*$ excitation of the LF chromophore. The drastic site-specific variation in the photophysical response of the O2(+) and O4+ isomers arises mainly from the different effect of electronic excitation on the M⁺...LF bond strength rather than from the metal-induced change of the electronic structure and molecular orbitals of LF responsible for $\pi\pi^*$ excitation.

1. Introduction

Flavins are an important class of yellow dye molecules derived from the tricyclic heteroaromatic 7,8-dimethyl-10-alkyl-isoalloxazine chromophore, which is responsible for the photophysical properties of these biomolecules in the visible to ultraviolet spectral range. Prominent members of the flavin family include lumichrome (LC, substituent R = H at N1), lumiflavin (LF, R=CH₃ at N10, Fig. 1), riboflavin (RF, vitamin B₂, R=ribityl at N10), flavin mononucleotide (FMN, R=ribosephosphate at N10), and flavin adenine dinucleotide (FAD, R=ribosephosphate plus adenine at N10). Flavins are ubiquitous in nature, which uses their unique and largely variable photochemical properties in many biological pro-

cesses [1–7]. For example, they play a key role in blue-light receptors (BLUF), in light-oxygen-voltage (LOV) sensing, and in the DNA repair mechanism. In a number of biochemical processes, the strong interactions between flavins and metal cations play a crucial role [8–16]. For example, metal-ion complexation of RF quenches the fluorescence [11].

The optical response of flavins is rather diverse and can strongly be modulated by its environment, including the substituent R at N10, (de-)protonation, metalation, the oxidation state, and solvation (solvent polarity, pH value). Thus, flavins have extensively been studied in the condensed phase and by quantum chemical calculations [17–25]. The complicated excited-state manifold of the flavin chromophore comprises several low-lying electronic states with $\pi\pi^*$ (optically bright) and $n\pi^*$

* Corresponding author.

E-mail address: dopfer@physik.tu-berlin.de (O. Dopfer).

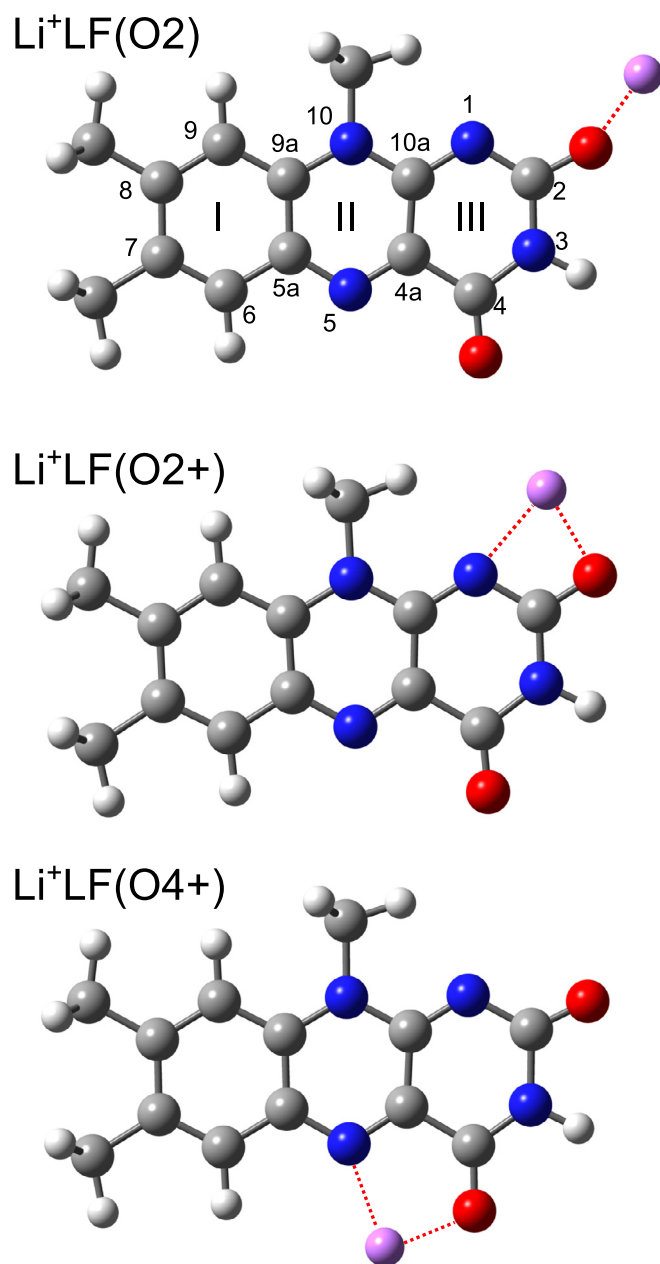


Fig. 1. Structures of Li⁺LF isomers calculated at the PBE0/cc-pVDZ level. Atom and ring numbering according to IUPAC notation is illustrated. The atomic color code is: O (red), N (blue), C (gray), H (white), Li (magenta).

(optically dark) character, arising from excitation of the aromatic π electrons and the lone pairs located at the N heteroatoms or the carbonyl O atoms. Their energetic position and mutual interaction can strongly be modulated by the flavin environment.

To separate external effects from the intrinsic properties of the flavin chromophore, gas-phase studies of the isolated flavin have to be performed. However, such spectroscopic studies are scarce and mostly conducted at room temperature [26–31]. Because of the resulting low-resolution spectra obtained, subtle effects such as small spectral shifts upon protonation and metalation cannot be measured at high precision. Thus, conclusions about the protonation and metalation site as well as the nature of the electronic states involved often remain unclear. Additionally, direct information about the interaction strength between flavins and the coordinating metal ions, for example derived from measuring the low-frequency intermolecular metal...flavin bend-

ing and stretching modes, can only be determined at vibronic resolution, which can only be achieved by cooling the ions down to cryogenic temperatures [32,33].

To this end, in recent years advanced research of flavins has focused on spectroscopy of cold molecules, which demonstrates the importance of cooling to reach vibronic resolution for large (bio)molecules [34]. The pioneering study of LF embedded in He droplets ($T = 0.4$ K), LF@He_N, clearly reveals vibronic resolution [35]. For example, the $S_1 \leftarrow S_0$ ($\pi\pi^*$) origin transition at 21,511 cm⁻¹ and its rich vibronic structure resulting from the large geometry change by S_1 excitation can readily be assigned by comparison to quantum chemical calculations.

In our group, we systematically characterize mass-selected flavin ions and their complexes in the gas phase by infrared and optical photodissociation spectroscopy combined with density functional theory (DFT) calculations [32,33,36–40]. In the first step of our strategy, we employ infrared multiple photon dissociation (IRMPD) spectroscopy at room temperature to determine the structure of protonated and metalated flavin ions in their ground electronic state (S_0), with particular focus on the preferred metalation and protonation sites [36–38]. For LF complexes with alkali ions (M^+LF , $M = \text{Li–Cs}$), the IRMPD spectra in the CO stretch range reveal the presence of the O4+ and O2(+) isomers for $M = \text{Li–K}$ (Fig. 1), whereas for Cs only the O2 isomer could be identified [38]. In the O4+ and O2+ isomers, the M^+ ion forms a bent N–M–O chelate (N1–M–O2 or N5–M–O4), in which the cation can benefit from interacting with the nucleophilic lone pairs of both O and N. In the O2 isomers, a more or less linear C–O2–M configuration is formed. DFT computations at the B3LYP/cc-pVDZ level show that the three M^+LF isomers are close in energy (within 20 kJ/mol, Table 1), whereby the energy differences and order of isomers somewhat depend on the size of M^+ . For $M = \text{Rb}$ and Cs, the large ionic radius of the alkali ion (R_M) prevents the formation of the O2+ isomer because of steric repulsion from the nearby CH₃ group of LF at N10. In the second step of our combined experimental and computational strategy, we employ electronic photodissociation spectroscopy of cryogenic ions in the visible range (VISPD) to probe the optical properties of these isomers [32,33,39–41]. To this end, we record VISPD spectra in a quadrupole/time-of-flight tandem mass spectrometer coupled to an electrospray ionization source and a cryogenic 22-pole ion trap (BerlinTrap) [41]. The S_1 origins of $M^+LF(\text{O4+})$ observed in the 464.9–525.5 nm range are strongly redshifted from those of bare LF (by 2480–3866 cm⁻¹ for Cs–Li), indicating that the $M^+ \dots LF$ interaction strongly increases upon S_1 excitation (by 15–20% for Li–Cs), in line with the HOMO/LUMO orbitals involved in this bright $\pi\pi^*$ state [32]. The rich vibronic structure arising from vibrational activity of the LF chromophore and the $M^+ \dots LF$ intermolecular modes has readily been assigned by comparison to time-dependent DFT (TD-DFT) calculations at the PBE0/cc-pVDZ level. These calculations predicted the $S_1 \leftarrow S_0$ ($\pi\pi^*$) transitions of the other low-energy O2(+) isomers near 430 nm, i.e. somewhat blueshifted from that of bare LF [32]. Thus, in the current work we apply the same spectroscopic and computational approach to search for the $S_1 \leftarrow S_0$ transition of the O2(+) isomers of M^+LF , which have already been identified previously by IRMPD spectroscopy [38]. Comparison with the $M^+LF(\text{O4+})$ isomers reveals the large impact of the metalation site on the optical properties of the LF chromophore. Further comparison with the recently studied H⁺LF ion, which protonates at the N1/O2+ sites, reveals the differences between attaching a proton or an alkali ion at this binding site of LF [40].

2. Experimental and computational details

Vibronic VISPD spectra of M^+LF ($M = \text{Li–Cs}$) complexes are recorded in the BerlinTrap tandem mass spectrometer setup [41], and previous applications of optical spectroscopy to cryogenic flavin ions have been reported elsewhere [32,33,39,40]. Briefly, the BerlinTrap consists of (i) an electrospray ionization (ESI) source for ion production, (ii) a short quadrupole ion trap for ion accumulation and thermalization (for 90 ms), (iii) a quadrupole mass filter (QMS) for ion selection, (iv) a 22-

Table 1

Binding energies (D_0) and relative energies (E_0 in parentheses) of various low-energy M^+LF isomers (Fig. 1) in the ground electronic state (S_0) calculated at the PBE0/cc-pVDZ level (in kJ/mol) [32].

	Li	Na	K	Rb	Cs
O2	279.7 (20.4)	209.5 (10.2)	175.9 (0.1)	158.9 (0.0)	148.2 (0.0)
O2+	289.5 (10.6)	214.2 (5.5)	175.5 (0.5)	–	–
O4+	300.1(0.0)	219.7 (0.0)	176.0 (0.0)	157.9 (1.0)	145.8 (2.9)

pole cryogenic ion trap for storing and cooling the ions via He buffer gas, and (v) an orthogonal reflectron time-of-flight mass spectrometer (ReTOF) for monitoring both parent and photofragment ions. M^+LF ions are generated by spraying a solution containing 20 ml methanol, 1 ml water, 1 mg LF (Sigma Aldrich, >99%), and 2–4 mg metal chloride salt (MCl, Sigma Aldrich, >99%) at a constant flow rate of 2 ml/h. The ions of interest are mass selected by the QMS and reach via an electrostatic quadrupole bender and octopole ion guide the cryogenic 22-pole ion trap ($T = 4\text{--}300\text{ K}$), which is typically kept at $T = 6\text{ K}$ using a He cryostat. In the 22-pole, the ions are trapped for around 90 ms and cooled down via an intense He buffer gas pulse to an effective (ro)vibrational temperature of typically 15–20 K. The cold ions are directed via Einzel lenses toward the ReTOF and excited by an optical parametric oscillator (OPO, GWU, VersaScan, bandwidth 4 cm^{-1}) pumped by the third harmonic of a nanosecond Q-switched Nd:YAG laser (Innolas, Spitlight, 355 nm, 180 mJ/pulse) shortly before they enter the extraction region of the ReTOF (ca. 10 μs before ion extraction). All M^+LF complexes fragment exclusively into M^+ and LF upon VISPD. The design and timing of the orthogonal ReTOF allows to simultaneously detect both the M^+ fragment and the remaining M^+LF parent complexes. The VISPD spectra are then generated by linearly normalizing the integrated M^+ fragment signal by the laser power (measured by a pyroelectric detector) and the parent ion signal. Typically, 50–100 mass spectra are averaged at each wavelength. To increase spectral resolution, the spectrum of K^+LF is additionally recorded at a step size of $\sim 0.3\text{ cm}^{-1}$ using a dye laser (Radiant Dyes, NarrowScan, Coumarin 120 dissolved in ethanol, bandwidth 0.014 cm^{-1}). Both laser systems are calibrated with a wavemeter. Both the laser pulses and the ion cycle are synchronized at 10 Hz repetition rate. Only monoisotopic complexes are considered for the experimental and computational analysis. The VISPD spectra are measured in the 22,220–23,850 cm^{-1} range (420–450 nm) at a step size of $\sim 1\text{ cm}^{-1}$. Additionally, the 450–500 nm range is recorded for Rb^+LF and K^+LF at an increased step size of 0.5 nm ($\sim 25\text{ cm}^{-1}$) to close the gap to the S_1 spectrum of the O4+ isomer. The dissociation efficiency strongly depends on the investigated complex. It is highest for the most weakly bonded Cs^+LF complex, for which it is in the order of a few percent. For the lightest complexes Li^+LF and Na^+LF , we observe small contributions of $Li^+LF\text{-He}$ and $Na^+LF\text{-He}$ at $T = 6\text{ K}$ in the corresponding mass spectra (Fig. S1 in the Supporting information (SI)), because the Li^+ and Na^+ ions have the largest He binding affinity due to their small ionic radii. However, their abundance is below 2% and thus the contamination of the VISPD spectra of M^+LF by these He adducts is negligible.

The experimental data are analyzed with the aid of quantum chemical calculation using GAUSSIAN16 [42]. First, DFT calculations at the PBE0/cc-pVDZ level are employed to optimize the electronic ground state (S_0) of M^+LF with $M=Li\text{--}Cs$ [43,44]. Second, time-dependent DFT (TD-DFT) calculations are carried out at the same level to determine adiabatic (S_1) and vertical ($S_1\text{--}S_4$) excitation energies originating from the optimized S_0 ground state. Cartesian coordinates of all optimized $S_{0/1}$ geometries are available in the SI. Multidimensional Franck–Condon (FC) simulations at $T = 0\text{ K}$ are performed using the routine implemented in GAUSSIAN16 to generate vibronic stick spectra [42,45]. The orbitals contributing to the electronic excitation are visualized using the natural transition orbital approach [46]. Transition state (TS) calculations are carried out using the QST2 approach. Binding energies are corrected for harmonic zero-point vibrational energy. For the heavier metals K–Cs,

relativistic corrections are accounted for using the Stuttgart effective core potential [47]. The atomic charge distribution in the ground and excited electronic states is evaluated by natural bond orbital (NBO) analysis [48]. The chosen computational PBE0/cc-pVDZ level has provided good agreement between experimental and predicted S_1 origin transitions (to within 0.1 eV) and the associated vibronic structures of the related H^+LC , M^+LC , and $M^+LF(O4+)$ ions [32,33,39,40]. In particular, this level correctly predicts the changes in the $M^+...LF/LC$ interaction strength upon $\pi\pi^*$ excitation.

3. Results and discussion

3.1. General analysis

LF offers several attractive binding sites for alkali metal cations, including (i) the nucleophilic N and O atoms of the heterocyclic ring and the two CO groups and (ii) the aromatic π electron system. Previous computations at the B3LYP/cc-pVDZ level reveal that the cation- π interaction is much weaker than the formation of σ complexes and that the O4+ and O2(+) isomers of M^+LF shown in Fig. 1 exemplary for $M=Li$ are most stable and thus identified by IRMPD spectroscopy [38]. Their binding energies (D_0) and relative energies (E_0) computed at the PBE0/cc-pVDZ level [32] for $M=Li\text{--}Cs$ in the ground electronic state (S_0) are similar to those at the B3LYP/cc-pVDZ level [38] and collected in Table 1. While in the O2 minima a more or less linear C2–O2–M bond is formed, the O4+ and O2+ isomers are characterized by bent O4–M–N5 and O2–M–N1 chelates, in which M^+ can interact with the lone pairs of both N and O. Steric repulsion between the CH_3 group at N10 and the heavy alkali ions Rb^+ and Cs^+ with their large ionic radii (R_M) prevents the formation of their O2+ isomers. The total binding energies and relative energetic order of the isomers depend on R_M . In general, the $M^+...LF$ interaction strength strongly decreases with increasing R_M , because the attractive potential is dominated by electrostatic interactions between the M^+ cation and the charge distribution of LF (e.g. charge-dipole forces), which decrease with increasing R_M . For example, $D_0=280\text{--}148\text{ kJ/mol}$ for O2 with Li–Cs, respectively. In addition, the energy differences between the various M^+LF isomers are rather small and decrease with increasing R_M from 20 to 3 kJ/mol for Li–Cs. Moreover, while O4+ is the global minimum for Li–K, the energetic order switches for Rb–Cs and O2 is computed to be slightly more stable at $T = 0\text{ K}$. The geometric structures of the O4+ and O2(+) isomers in the S_0 state and the effect of metalation on the LF chromophore and its IR spectrum have been discussed in detail elsewhere [38]. Briefly, all these M^+LF isomers have C_s symmetry in the S_0 state (with the exception of $Na^+LF(O2+)$), with M^+ lying in the plane of the tricyclic aromatic ring. With decreasing R_M , the $M...LF$ bonds become stronger and shorter, which is accompanied by increasing charge transfer from M^+ to LF. Experimentally, IRMPD spectra of M^+LF were recorded only for $M=Li\text{--}K$ and Cs, and for all these complexes at least two isomers were identified by their characteristic CO stretch bands for Li–Cs, namely O4+ and O2(+), whereby it was not possible to distinguish between O2 and O2+ [38]. (For Cs^+LF , only the O4+ isomer was assigned.) Consequently, we expect to observe both O4+ and O2(+) produced in the ESI source in significant abundance due to their small energy differences. Concerning the O2(+) isomers, from the binding energies reported in Table 1, we expect to detect predominantly the O2+ isomer for Li/Na and the O2

Table 2

Experimental adiabatic S_1 origin energies of LF and M^+LF (in bold) and their ΔS_1 shifts (in cm^{-1}) upon metalation (in parentheses) compared to values for various isomers calculated at the PBE0/cc-pVDZ level.

	Li	Na	K	Rb	Cs
O2(+) exp (ΔS_1)	21,511^a (0)	23,037^b (1526)	22,806^b (1295)	22,355^b (844)	22,323^b (812)
Calc (ΔS_1) ^c	22,448 (0)				
O2 calc (ΔS_1) ^c	23,133 (685)	23,205 (757)	23,181 (733)	23,172 (724)	23,157 (709)
O2+ calc (ΔS_1) ^c	23,335 (887)	23,495 (1047)	23,454 (1006)		
O4+ calc (ΔS_1) ^c	18,018 (–4430)	18,782 (–3664)	19,256 (–3192)	19,435 (–3013)	19,581 (–2867)
O4+ exp (ΔS_1)^c	17,645 (–3866)	18,310 (–3201)	18,778 (–2733)	18,914 (–2597)	19,031 (–2480)

^a Value of LF@He_N [Ref. 35].

^b O2+ for Li–K and O2 for Rb–Cs.

^c Ref. 32.

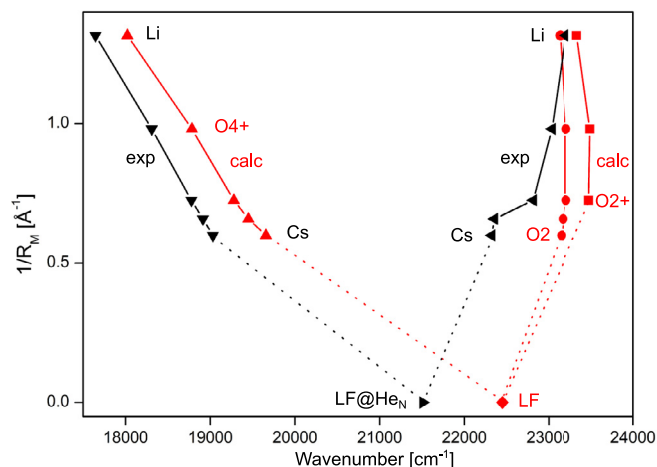


Fig. 2. Comparison of computed adiabatic S_1 origins of $M^+LF(O4+/O2/O2+)$ with $M=Li-Cs$ (PBE0/cc-pVDZ) to experimental band origins as a function of the inverse ionic radius of the alkali ion ($1/R_M$).

isomer for Rb/Cs, while for K no clear prediction is possible because of the nearly isoenergetic O2 and O2+ isomers. The geometries of all investigated O2(+) complexes are presented in Table S1 in the SI.

The adiabatic S_1 transition energies of the various M^+LF isomers are compared in Fig. 2 (Table 2) to that of bare LF as a function of the inverse ionic radius ($1/R_M$) [32]. Clearly, the binding site of M^+ has a large impact on the lowest $\pi\pi^*$ transition energy. For example, the computed S_1 origin shifts of the O4+ isomers are rather large and highly sensitive to R_M of the metal, with redshifts of $\Delta S_1=2867-4430\text{ cm}^{-1}$ for Cs–Li from the value of bare LF ($22,448\text{ cm}^{-1}$). The absolute transition energies and redshifts agree well with the measured values also included in Fig. 2 ($2480-3866\text{ cm}^{-1}$), whereby the latter are referenced to the S_1 energy of LF@He_N ($21,511\text{ cm}^{-1}$) [35]. In contrast to $M^+LF(O4+)$, the S_1 energies computed for the O2(+) isomers are much less affected by metalation and blueshifted with respect to that of LF by 887, 1047, and 1006 cm^{-1} for Li–K (O2+) and 685, 757, 733, 724, and 709 cm^{-1} for Li–Cs (O2), respectively. These shifts are relatively independent of M^+ with a maximum range of 160 (O2+) and 72 (O2) cm^{-1} . In addition, the S_1 origins of the O2 isomers are systematically lower in energy than those of the O2+ isomers, with an energy difference of $202-273\text{ cm}^{-1}$ for Li–K.

While our previous work has located the strongly redshifted S_1 transitions of $M^+LF(O4+)$ between $17,645$ and $19,031\text{ cm}^{-1}$ ($525-465\text{ nm}$), the current work focusses on the modestly blueshifted S_1 spectra of the O2(+) isomers with predicted S_1 origins between $23,133$ and $23,495\text{ cm}^{-1}$ ($425-432\text{ nm}$). To this end, we initially recorded an overview VISPD spectrum for Rb⁺LF to search for the S_1 origin of the O2 isomer predicted at 431.6 nm ($23,172\text{ cm}^{-1}$) by scanning from the S_1 origin of the O4+ isomer (at 528.7 nm , $18,914\text{ cm}^{-1}$) toward shorter wavelength (Fig. 3). A corresponding scan for K⁺LF is available in Fig.

S2 in the SI. In these overview scans, the $450-500\text{ nm}$ gap between the S_1 bands of O4+ and O2(+) is covered with the OPO laser at a larger step size of 0.5 nm . Subsequently, a high-resolution spectrum in the range below 450 nm is recorded. For M^+LF with Li, Na, and Cs only the higher resolution spectra are recorded, because the intermediate $450-500\text{ nm}$ range does not provide any structure for K and Rb (gray part of the spectrum in Figs. 3 and S2).

Using this strategy to search for the S_1 bands of $M^+LF(O2/O2+)$, we locate the vibronic VISPD spectra of M^+LF ($M=Li-Cs$) in the $22,220-23,850\text{ cm}^{-1}$ range presented in Fig. 4. The same spectra are plotted in Fig. S3 in the SI as a function of S_1 internal energy. As the VISPD spectra are measured at a trap temperature of $T=6\text{ K}$, vibronic structure is readily resolved and the appearance of hot bands is largely suppressed. Only for Rb⁺LF and Cs⁺LF, minor hot bands arising from the lowest-frequency mode in S_0 (17 and 15 cm^{-1}) are observed, confirming an effective vibrational temperature below 20 K . All VISPD spectra exhibit a distinct electronic 0^0 origin band accompanied by rich vibronic activity with extended progressions to higher energy, indicating a large geometry change upon electronic excitation. All measured spectra occur on some more or less constant background attributed to unresolved high-energy vibronic transitions resulting from the S_1 state of the O4+ isomer. In contrast, no VISPD signal is observed below the S_1 origin transition of the O4+ isomer, indicating that the $S_1 \leftarrow S_0$ ($\pi\pi^*$) origin of the O4+ isomer is the lowest-energy bright transition of all M^+LF isomers produced in the ESI source.

The electronic origins in the VISPD spectra of M^+LF in Fig. 4 occur at $23,202$, $23,037$, $22,806$, $22,355$, and $22,323\text{ cm}^{-1}$ for $M=Li-Cs$, respectively. They are included in Fig. 2 and compared in Table 2 to the adiabatic S_1 transitions computed for the O2(+) and O4+ isomers of M^+LF and the one computed and measured for bare LF. The latter value is obtained from laser-induced fluorescence measurements of LF@He_N [35], and serves as reference point for evaluating ΔS_1 shifts. The He environment is expected to have only a limited impact on the transition energy ($<1\%$, $<250\text{ cm}^{-1}$) [35]. The experimental 0^0 transitions of M^+LF are all blueshifted with respect to that of LF@He_N at $21,511\text{ cm}^{-1}$ by 1691 , 1526 , 1295 , 844 , and 812 cm^{-1} for Li–Cs, i.e., the shifts increase with decreasing R_M . These shifts are in good agreement with the predictions for the S_1 origins of the O2(+) isomers of M^+LF (Fig. 2, Table 2). We attribute the spectra of Rb⁺LF and Cs⁺LF to the O2 isomers because the computations do not predict any O2+ minimum, while the spectra of Li⁺LF and Na⁺LF are assigned to the O2 isomers, because of their larger binding energy in S_0 . This interpretation is fully supported by the quantitative agreement with the predicted absolute S_1 origins, their metal-induced ΔS_1 shifts, and the analysis of the vibronic structure discussed below. Assuming the computed binding energies in Table 1, these blueshifts indicate that the $M^+...LF$ interaction decreases by $3.8-7.9\%$ upon S_1 excitation. The isomer assignment of the K⁺LF complex is less certain (vide infra).

For completeness, we also compute the higher excited singlet states of the O2+ isomers up to S_4 (Table S2 and Fig. S4 in the SI). While the S_1 state has $\pi\pi^*$ character and is optically bright, the S_2 state has $n\pi^*$ character and is optically dark. The S_3/S_4 states are $n\pi^*/\pi\pi^*$ ex-

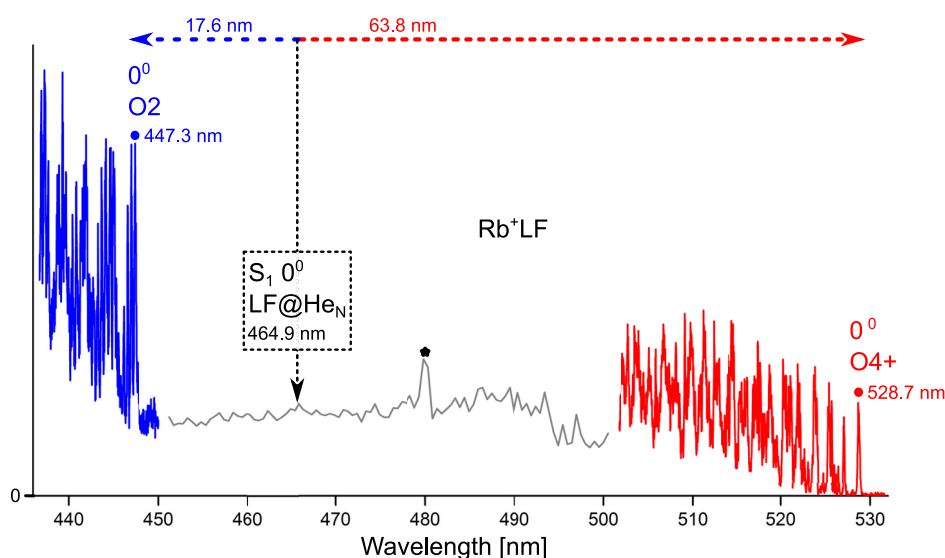


Fig. 3. Overview VISPD spectrum of Rb^+LF . The red part is attributed to the $S_1 \leftarrow S_0$ ($\pi\pi^*$) transition of the O4^+ isomer. The blue part is attributed to $S_1 \leftarrow S_0$ ($\pi\pi^*$) of the O2 isomer. The 0^0 origins of both isomers are marked. The value of the S_1 band origin of LF@He_N at 464.9 nm is marked with an arrow, along with shifts of the 0^0 transitions of the Rb^+LF complexes. The gray range is measured at an enlarged step size of 0.5 nm. The peak marked with an asterisk is an artefact and arises from a drop in laser intensity.

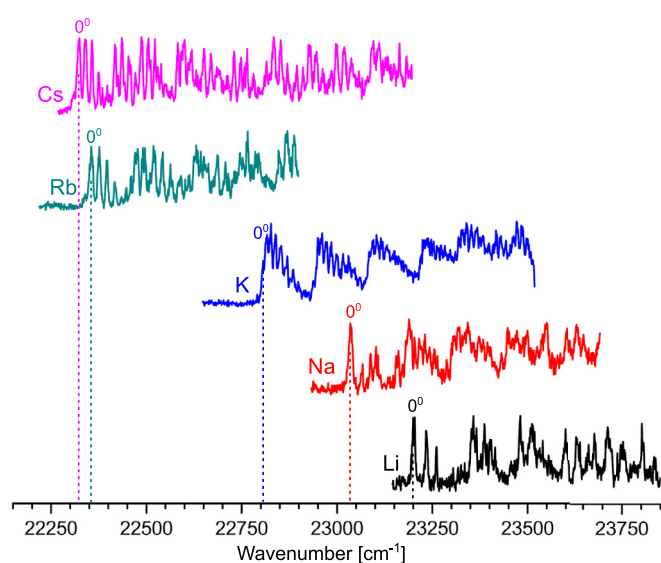


Fig. 4. VISPD spectra of the $S_1 \leftarrow S_0$ ($\pi\pi^*$) transition of the O2^+ isomers of M^+LF ($\text{M}=\text{Li}-\text{Cs}$) recorded with the OPO laser in the M^+ fragment channel at a trap temperature of $T = 6$ K.

citations, whereby their energetic order depends on the metal. In any case, the vertical excitation energy of the second optically bright $\pi\pi^*$ state lies at least 3016 cm^{-1} higher in energy than the S_1 ($\pi\pi^*$) state for all M^+ , and thus these states are outside the investigated spectral range. Similarly, the detection of the second optically bright S_4 ($\pi\pi^*$) state of the O4^+ isomer can safely be excluded, because its vertical excitation energy is again substantially higher in energy than the S_1 state of the O2^+ isomer ($1463\text{--}3880\text{ cm}^{-1}$) and thus outside the considered spectral range [32]. The $S_{2/3}$ states of the O4^+ isomer are optically dark $n\pi^*$ states with oscillator strength close to zero and thus difficult to detect experimentally. In the following sections, we separately discuss the Rb/Cs , Li/Na , and K cases.

3.2. Rb^+LF and Cs^+LF

In this section, we jointly discuss the results for M^+LF with the heavy alkali metals Rb and Cs , because their VISPD spectra in Fig. 4 are both attributed to their O2 isomer. For both M^+ ions, the O2^+ isomer is unstable because of steric repulsion arising from the nearby CH_3 group at

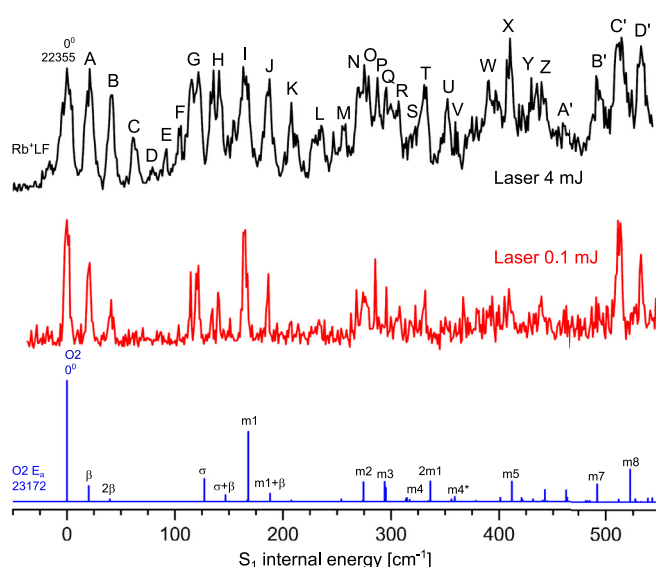


Fig. 5. VISPD spectra of Rb^+LF measured with the OPO laser at high (black) and low (red) laser energies as a function of S_1 internal energy compared to Franck-Condon simulations of the O2 isomer.

N10 . The overview VISPD spectrum of Rb^+LF covering the $531\text{--}437\text{ nm}$ range (Fig. 3) begins with the S_1 band attributed to the O4^+ isomer (in red, 0^0 at 528.7 nm) [32]. Toward higher energy, the vibronic density of this transition increases significantly resulting in a nearly constant unresolved background in the $500\text{--}450\text{ nm}$ range (gray part). Below 448 nm , a second vibrationally-resolved band appears on top of this background (in blue, 0^0 at 447.3 nm), which is assigned to the S_1 transition of the O2 isomer of Rb^+LF . While the S_1 origin of the O4^+ isomer is redshifted by 63.8 nm from that of bare LF@He_N (464.9 nm), the S_1 origin of the O2 isomer is blueshifted by 17.6 nm . The measured S_1 origins at $22,355$ (Rb) and $22,323$ (Cs) cm^{-1} deviate by only 3.7% (817 and 834 cm^{-1}) from the predicted adiabatic values, which is indicative for the reliability of the excited-state calculations. The observed ΔS_1 blueshifts of 844 and 812 cm^{-1} are also close to their predicted shifts (724 and 709 cm^{-1}).

In the next step, we analyze the vibrational structure observed in the VISPD spectra of Rb^+LF and Cs^+LF by FC simulations shown in Figs. 5 and 6, respectively. These spectra are plotted as a function of S_1 in-

Table 3

Frequencies of the intermolecular bend and stretch modes (β and σ) in the S_0 and S_1 states of $M^+LF(O_2)$ computed at the PBE0/cc-pVDZ level compared to experimental values (in cm^{-1}).

	Li			Na			K			Rb			Cs		
	S_0	S_1	exp	S_0	S_1	exp	S_0	S_1	exp	S_0	S_1	exp	S_0	S_1	exp
β	235	236	–	85	93	–	43	26	–	18	20	21	16	18	16
σ	585	585	–	264	260	–	215	216	–	127	127	118	104	103	95

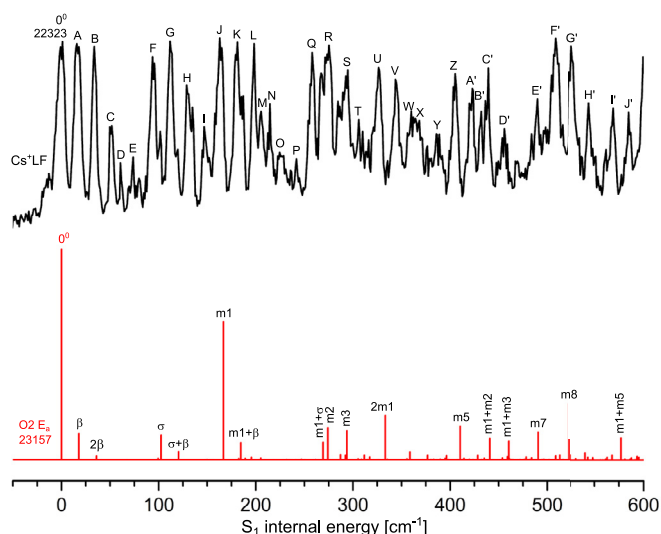


Fig. 6. Comparison between VISP spectrum of Cs^+LF (OPO, recorded at high laser power) and Franck-Condon simulations of the O_2 isomer as a function of S_1 internal energy.

ternal energy. For Rb^+LF , we report VISP spectra obtained with the midband OPO laser at full and reduced laser intensity (4 and 0.1 mJ). As a result, the low-power spectrum displays better spectral resolution and more reliable intensity distributions by avoiding power broadening. Thus, while the high-power spectra of M^+LF contain more spectral information, the low-power spectra provide more reliable intensity information and agree better with the predicted FC pattern. For example, the width of the 0^0 origin band of $\text{Rb}^+LF(O_2)$ decreases from 9.9 to 5.8 cm^{-1} when comparing the high- and low-power spectra. The latter width is close to the laser bandwidth of $\sim 4 \text{ cm}^{-1}$, whereby the difference of $\sim 2 \text{ cm}^{-1}$ may come from unresolved rotational substructure (and possibly lifetime broadening). Geometry optimization results for both complexes in structures with C_s symmetry in both S_0 and S_1 , implying that only vibrations with a' symmetry are FC active. These include predominantly fundamentals, overtones, and combination tones of in-plane modes and to a smaller extend even-quanta overtones or combination bands of out-of-plane modes. Indeed, the computed FC spectra show essentially only in-plane modes, while even quanta of a'' modes have negligible FC activity.

The observed vibrational modes can be divided into the a' intramolecular LF modes (denoted m1–m8) and the two low-frequency a' intermolecular $M^+ \dots LF$ bending and stretching modes (β and σ). A list of observed peaks and suggested assignments is available in Table S3 in the SI. A complete set of all vibrational modes of all considered $O_2(+)$ isomers of M^+LF is given in Table S4 in the SI. The β and σ modes directly probe the anisotropy and strength of the $M^+ \dots LF$ interaction (Table 3). Both Rb^+LF and Cs^+LF show an intense 0^0 origin, followed by short progressions up to three quanta in β (21 and 16 cm^{-1}) and one quantum in σ (118 and 95 cm^{-1}), which are well reproduced by the computations ($\beta=20$ and 18 cm^{-1} , $\sigma=127$ and 103 cm^{-1}), again confirming that the employed DFT level reliably describes the $M^+ \dots LF$ interaction. The β

and σ frequencies are lower for Cs^+LF because of its weaker $M^+ \dots LF$ bond and higher effective reduced mass.

The σ values computed for the S_1 state (126.9 and 102.6 cm^{-1} for Rb and Cs) are only slightly smaller than those for the S_0 state (127.4 and 104.9 cm^{-1}), illustrating that the strength of the $M^+ \dots LF$ bond is only slightly reduced by S_1 excitation of the O_2 isomer. This result is consistent with the small ΔS_1 blueshifts upon metalation, which directly reflect the decrease in the binding energy upon electronic excitation. On the basis of the computed binding energies for S_0 listed in Table 1, the ΔS_1 blueshifts of 10.1 and 9.7 kJ/mol for Rb and Cs result in a destabilization of the $M^+ \dots LF$ bond of 6.4 and 6.6%, respectively. This result is in stark contrast to the O_4+ isomers, for which a strong increase in the $M^+ \dots LF$ interaction strength by the same S_1 ($\pi\pi^*$) excitation is observed (up to 20% for Cs)[32], demonstrating that the metal binding site has a huge impact on the photochemical response of LF.

As observed previously for $M^+LC(O_4+)$ and $M^+LF(O_4+)$ [32,33], the intramolecular vibrational activity of the S_1 spectra of the $O_2(+)$ isomers of M^+LF is dominated by the low-frequency in-plane intramolecular modes of the LF skeleton (m1–m8). Such modes have also been observed in the laser-induced fluorescence spectrum of $LF@He_N$, because of the same S_1 ($\pi\pi^*$) excitation and the minor impact of M^+ on the nature of this electronic transition and thus the force field of these modes (Table 4). These normal modes are visualized in previous work [40]. For example, for $\text{Rb}^+LF(O_2)$ the measured LF modes at 164 (m1), 270 (m2), 294 (m3), 351 (m4*), 408 (m5), 492 (m7), and 510 cm^{-1} (m8) are very close to those of $LF@He_N$, with a maximum and mean deviation of 5 and 3 cm^{-1} , respectively. This result is further confirmed by the HOMO/LUMO orbitals contributing to the electronic S_1 ($\pi\pi^*$) excitation shown in Fig. 7, which are virtually the same for both LF and $M^+LF(O_2)$. These orbitals are delocalized over the planar tricyclic aromatic LF ring, with essentially no amplitude at the metal at O2. Also, the computed oscillator strengths are nearly identical (e.g., $f = 0.210$ and 0.213 for $S_1 \leftarrow S_0$ of $\text{Rb}^+LF(O_2)$ and LF, respectively). Only minor changes of the orbitals take place from HOMO to LUMO at the O2 and N1 atoms, whereas electron density shifts significantly to N5 and O4. This is consistent with the relatively small blueshift of the O_2 isomer, and the pronounced redshift of the O_4+ isomer (Fig. 2) [32].

3.3. Li^+LF and Na^+LF

In contrast to M^+LF with the heavy alkali ions Rb^+ and Cs^+ , for which the O_2 isomer is the single minimum at this binding site, the two minima O_2 and O_2+ are obtained for the smaller ions Li^+ – K^+ . This situation is similar to H^+LF with the even smaller proton for which also two minima (denoted N1 and O_2+) are predicted and indeed experimentally observed [40]. The O_2 and O_2+ minima have similar binding energies for Li–K (to within 3 kJ/mol), and these are separated by quite low isomerization barriers in both S_0 and S_1 , as shown in Fig. S5 in the SI. For Li and Na, the O_2+ isomer is 9.8 and 4.7 kJ/mol more stable than O_2 (including zero-point energy), i.e. the O_2+ structure is located in a distinct minimum in the S_0 state and thus should be populated in the ESI source. On the other hand, the barrier for $O_2 \rightarrow O_2+$ isomerization is rather low for both metals ($V_b=1.1$ and 0.6 kJ/mol), indicating that the O_2 population may be rather small because of the shallow potential well. Possibly, the zero-point level lies above the barrier and the O_2 isomer does not exist as stable isomer. Hence, for $M=\text{Li}$ and Na the computations predict mostly the O_2+ isomer. The energy difference between

Table 4

Low-energy intramolecular in-plane vibrational frequencies (m1–m8, in cm^{-1}) for the S_1 state of LF and $M^+LF(O2/O2^+)$ with $M=\text{Li–Cs}$ calculated at the PBE0/cc-pVDZ level compared to experimental data.

Mode	Li O2+		Na O2+		K O2+		Rb O2		Cs O2		LF	
	S_1	exp	S_1	exp	S_1	exp	S_1	exp	S_1	exp	S_1	exp ^a
m1	156	156	155	153	140	143	168	164	167	163	165	164
m2	275	278	278	271	274	274	274	270	274	272	276	274
m3	299	304	298	283	295	296	294	294	294	294	294	294
m4	326	325			325	316					322	
m4*							359	351	359	364	358	
m5	404	396	417	411	416	416	412	408	410	405	409	403
m6			468	462	456	457					444	440
m7	493	475	501	502			492	492	491	489	489	
m8	525	510	524	513	522	522	522	510	522	507	521	513

^a Values of LF@He_N [Ref. 35].

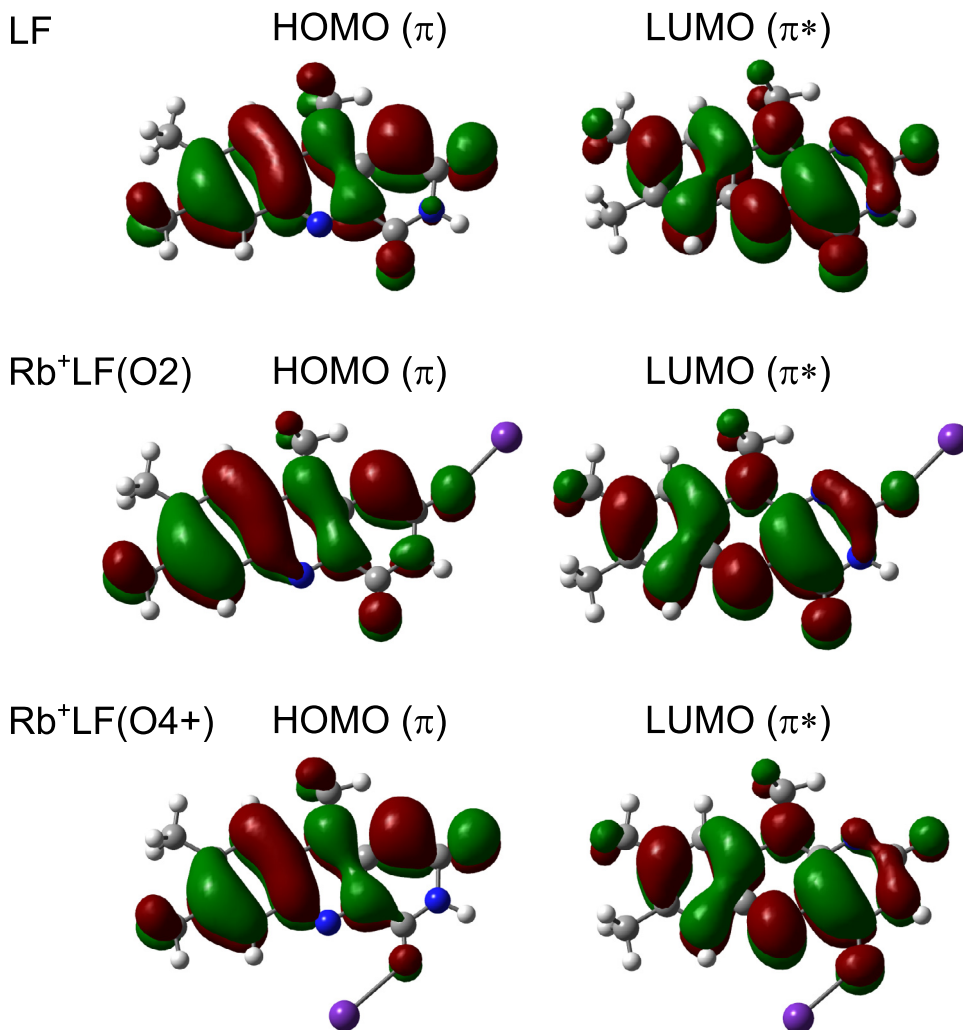


Fig. 7. Natural transition orbitals contributing to the $S_1 \leftarrow S_0$ ($\pi\pi^*$) transition of LF and the $\text{Rb}^+LF(O2/O4^+)$ isomers computed at the PBE0/cc-pVDZ level.

$O2^+$ and $O2$ is slightly smaller in the S_1 state but the $O2^+$ potential well is still significant (8.2 and 2.8 kJ/mol for Li and Na). Hence, we may expect a reasonably harmonic potential for the vibronic structure in their VISPD spectra, for which the FC simulation may produce reliable spectra. While the $O2$ isomers have C_s symmetric structures in S_0 and S_1 for both Li and Na, the $O2^+$ structures are nonplanar (C_1) in both S_0 and S_1 for Na and in S_1 for Li. In these nonplanar structures, the tricyclic ring becomes slightly bent along the N5–N10 axis, along with an out-of-plane rotation of the CH_3 group. Similar out-of-plane distortions are observed for the N1 protomer of H^+LF , while the $O2^+$ protomer keeps C_s symmetry in both the S_0 and S_1 state [40]. The reduced symmetry

of H^+LF is directly observed in the increased FC activity, particularly in the low-frequency out-of-plane modes, because in C_1 symmetry all these transitions become FC allowed [40].

The VISPD spectra of Li^+LF and Na^+LF , recorded with the OPO laser at high laser power (~ 4 mJ) to extract the maximum number of vibronic transitions, are compared in Figs. 8 and 9 to the spectra simulated for the $O2^+$ and $O2$ isomers. All spectra are again plotted as a function of S_1 internal energy. As already observed for Rb^+LF and Cs^+LF , the structured VISPD spectra are superimposed on a roughly constant background arising from unresolved high-energy vibronic transitions of the S_1 band of the respective $O4^+$ isomers. Clearly, the FC simulations for the $O2^+$ iso-

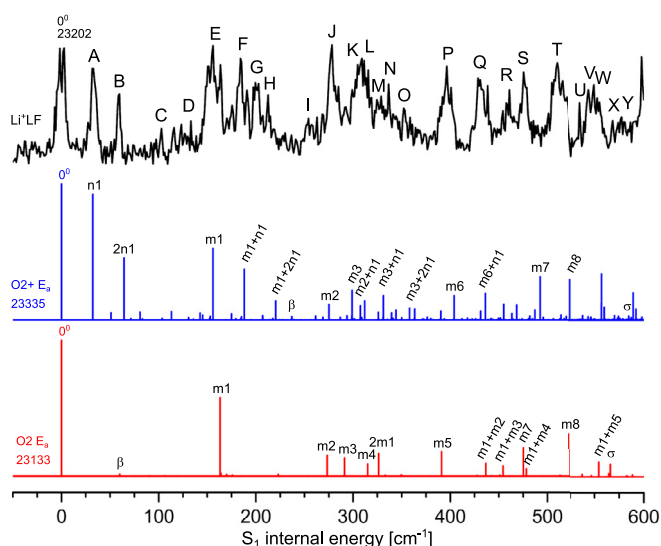


Fig. 8. Comparison between VISP spectrum of Li^+LF (OPO, recorded at high laser power) and Franck-Condon simulations of the $\text{O}_2(+)$ isomers as a function of S_1 internal energy.

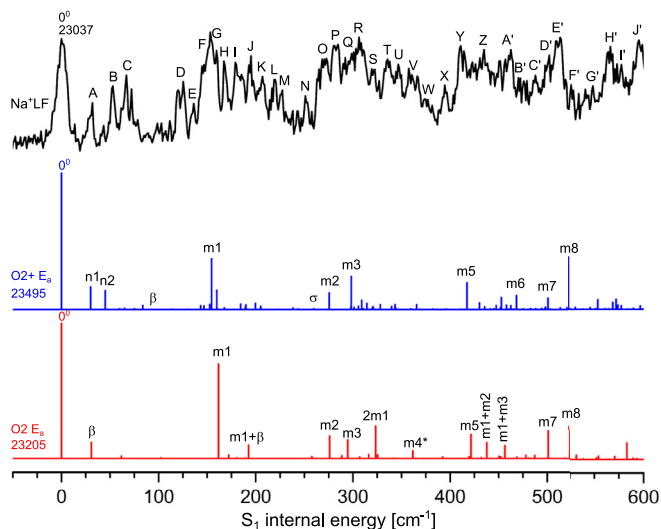


Fig. 9. Comparison between VISP spectrum of Na^+LF (OPO, recorded at high laser power) and Franck-Condon simulations of the $\text{O}_2(+)$ isomers as a function of S_1 internal energy.

mers fit the VISP spectra much better than those for the O_2 isomers, in particular in the low-energy part of the spectra. Thus, both the energetic and spectroscopic arguments clearly point to an assignment of the VISP spectra of Li^+LF and Na^+LF to their more stable O_2+ isomers. The observed S_1 origins at 23,202 and 23,037 cm^{-1} are blueshifted from that of LF@He_N by 1691 and 1526 cm^{-1} , which compares reasonably well to the predicted shifts of 887 and 1047 cm^{-1} (Fig. 2, Table 2). Again, this result is in contrast to the large ΔS_1 redshifts observed for the corresponding O_4+ isomers (3866 and 3201 cm^{-1}). Assuming the computed binding energies in Table 1 ($D_0=289.5$ and 214.2 kJ/mol), the observed ΔS_1 blueshifts of 20.2 and 18.3 kJ/mol for $\text{Li}^+\text{LF}(\text{O}_2+)$ and $\text{Na}^+\text{LF}(\text{O}_2+)$ imply a reduction in the $\text{M}^+\dots\text{LF}$ bond strength of 7.0 and 8.5% upon electronic excitation, respectively.

The vibrational modes of the O_2+ and O_2 isomers can again be divided into the a' intramolecular LF modes (m_1 – m_8) and the two low-frequency a' intermolecular $\text{M}^+\dots\text{LF}$ bending and stretching modes (β and σ). However, due to the reduced symmetry for O_2+ , also the low-

frequency a'' intramolecular LF modes (denoted n_1 – n_2) become FC active and are indeed observed in the VISP spectra of both Li^+LF and Na^+LF . A list of all observed peaks and assignments is given in Table S3 in the SI, and a complete set of all vibrational modes of all considered $\text{O}_2(+)$ isomers of M^+LF is given in Table S4 in the SI. The Li^+LF spectrum exhibits a short progression with two quanta in a mode with $\sim 32 \text{ cm}^{-1}$ resulting in bands A and B at 32 and 60 cm^{-1} above 0^0 with high relative intensity. This pattern is nicely reproduced by the FC simulations for the O_2+ isomer with respect to both frequency and intensity, with a butterfly-type out-of-plane mode n_1 at 32 cm^{-1} . A similar butterfly mode is observed for the N_1 isomer of H^+LF [40], and in line with the geometric deformation of the tricyclic ring described by a fold along the N_5 – N_{10} axis. There are a number of further low-intensity transitions with a a'' symmetry below $\sim 155 \text{ cm}^{-1}$ predicted in the FC simulations, which are however experimentally not resolved. Again, the S_1 spectrum contains a number of FC active “in-plane” modes (m_1 – m_8), which occur also in combination with the out-of-plane n_1 mode. An alternative assignment of the transitions in the VISP spectrum solely to the O_2 isomer appears impossible, because the computed S_1 spectrum of this C_s symmetric isomer lacks the low-frequency a'' modes observed experimentally. It is unclear whether the spectrum of this higher-energy isomer is hidden somewhere in the higher-energy part of the VISP spectrum. For example, the intense unexplained peak G might originate from $S_1 0^0$ of $\text{Li}^+\text{LF}(\text{O}_2)$. However, the S_1 origin of O_2 is predicted to appear on the red side of $S_1 0^0$ of $\text{Li}^+\text{LF}(\text{O}_2+)$ by 202 cm^{-1} and no such transition is observed. The absence of the O_2 isomer is in line with its lower stability and the extremely low isomerization barrier toward the more stable O_2+ global minimum. Interestingly, the intermolecular β and σ modes characteristic for the $\text{M}^+\dots\text{LF}$ bond do not show up as prominent bands in the VISP spectrum of $\text{Li}^+\text{LF}(\text{O}_2+)$ and its FC simulation. Their computed frequencies in the S_1 state are $\beta=237$ and 93 cm^{-1} and $\sigma=585$ and 260 cm^{-1} for $\text{M}=\text{Li}$ and Na , and thus they highly overlap with other vibronic intramolecular transitions preventing an unambiguous experimental assignment. In general, the VISP spectrum of Na^+LF in Fig. 9 shows in the low energy range also several transitions, which are indicative for the O_2+ isomer. However, a full spectral assignment is beyond the scope of this work and needs to await a more sophisticated theoretical approach for properly treating the anharmonic low-frequency modes. This is particularly relevant for the S_1 state, in which the computed barriers for $\text{O}_2\leftrightarrow\text{O}_2+$ isomerization (2.8 and 1.1 kJ/mol) are smaller than in the S_0 state.

As discussed already for the O_4+ isomer, tagged complexes are not responsible for any of the unassigned peaks [32]. Briefly, at an ion trap temperature of $T = 6 \text{ K}$, $\text{Li}^+\text{LF-He}$ and $\text{Na}^+\text{LF-He}$ clusters are formed by addition of He atoms to the mass-selected M^+LF ions in the ion trap (Fig. S1 in the SI). These clusters probably result in the same M^+ dissociation channel upon VISP and thus could produce additional peaks in the VISP spectra of M^+LF . To test this hypothesis, experiments are conducted at higher temperature to suppress He tagging. As shown in Fig. S1, for Na^+LF , increasing T from 6 to 15 K reduces the He tagging efficiency from 1.6% to below the detection limit. Moreover, the VISP spectra of Na^+LF recorded at 6 and 15 K are essentially the same (Fig. S6 in the SI), indicating that the Na^+LF spectra are completely free from contamination with signals from $\text{Na}^+\text{LF-He}$, as expected from the small abundance of the He-tagged complexes. For Li^+LF , the interaction of Li^+ with He and N_2 (arising from nitrogen impurities of the He gas line) is so strong that either $\text{Li}^+\text{LF-He}$ or $\text{Li}^+\text{LF-N}_2$ clusters are observed at any trap temperature (up to 300 K, Fig. S1 in the SI). Nonetheless, their abundance is also much lower than that of bare Li^+LF ($\leq 2\%$), suggesting that contamination of resonances from $\text{Li}^+\text{LF-He/N}_2$ in the VISP spectrum of Li^+LF are at most very minor. Other reasons for additional peaks not predicted by the FC simulations include vibronic coupling to the higher-lying dark $n\pi^*$ states (e.g. S_2) or hindered internal methyl rotation [49]. Indeed, the S_1 origin and also other peaks reveal unresolved substructure which may come from internal rotation states.

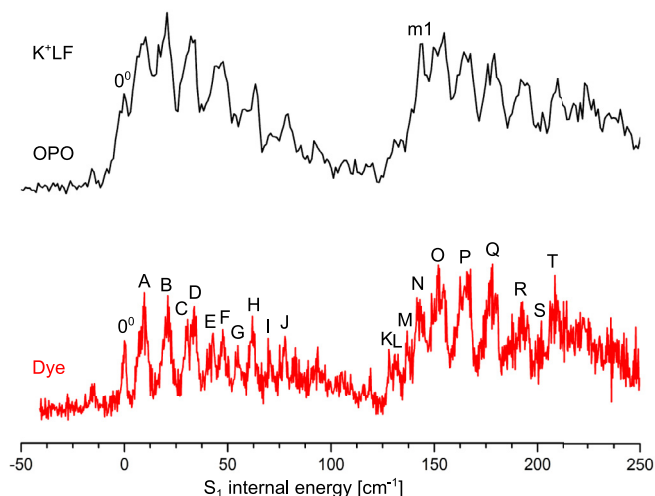


Fig. 10. VISPD spectra of K^+LF measured with the OPO (top) and dye (bottom) laser. The spectra (recorded at high laser power) are plotted as a function of S_1 internal energy.

3.4. K^+LF

With decreasing metal size, the M^+LF complex tends to form the $O2+$ isomer, as can be seen from the energy differences between $O2+$ and $O2$, with $\Delta E_0(O2-O2+)= -0.4 < 4.7 < 9.8$ kJ/mol for K–Li. For Rb and Cs, the $O2+$ isomer is not stable for steric reasons. Apparently, for $M=Rb$ and Cs only the $O2$ isomer is identified, while the $O2+$ isomer is strongly preferred for Li and Na. K is an interesting intermediate case, because the computations predict a very similar stability for $O2+$ and $O2$ (with 0.4 kJ/mol in favor of $O2$) and very low isomerization barriers between the two structures in both the S_0 and S_1 states ($V_b=1.7/2.3$ kJ/mol for $O2 \rightarrow O2+$ and $V_b=1.1/0.2$ kJ/mol for $O2 \leftarrow O2+$ in S_0/S_1), resulting in a rather shallow double minimum potential in both electronic states. Similar to the case of Li and Na, the computed S_1 transitions of the $O2(+)$ isomers of K^+LF are close in energy (to within 273 cm^{-1} , Table 2) because of the similar binding site. Hence, the exclusive consideration of binding energy and S_1 transition frequency is insufficient for a reliable prediction, which isomer is responsible for the measured VISPD spectra of K^+LF presented in Fig. 10.

The low-energy part of the K^+LF spectra (up to 250 cm^{-1} internal energy) recorded with the OPO and dye lasers are compared in Fig. 10, while a more extended part of the OPO laser spectrum (up to 600 cm^{-1}) is compared in Fig. 11 to the harmonic FC simulations for the $O2$ and $O2+$ minima. The VISPD spectrum of K^+LF differs in several ways from those measured for the other M^+LF complexes with $M=Li/Na$ and Rb/Cs (Fig. 4). The K^+LF spectrum is rather congested because of progressions with very low frequency of less than 10 cm^{-1} . Such low frequencies are not observed for the other M^+LF complexes. As a result, the OPO laser spectrum is poorly resolved and even the S_1 origin band cannot readily be extracted. The dye laser spectrum of K^+LF is much better resolved and allows to determine the S_1 origin band at $22,806$ cm^{-1} . The derived ΔS_1 blueshift from $LF@He_N$ of 1295 cm^{-1} is consistent with those of both the $O2$ and $O2+$ isomers (733 and 1006 cm^{-1}) and corresponds to a reduction in $K^+...LF$ bond strength by 15.5 kJ/mol (or 8.8%) upon S_1 excitation.

A list of observed vibrational peaks and suggested assignments of the K^+LF spectrum is given in Table S3 in the SI, and a complete set of all vibrational modes of all considered $O2(+)$ isomers is given in Table S4 in the SI. Bands A, B, and C at 8 , 20 , and 30 cm^{-1} suggest a vibrational progression in a mode with ~ 10 cm^{-1} . Peaks A and B are somewhat broader (~ 5 cm^{-1}) and more intense compared to the 0^0 origin band

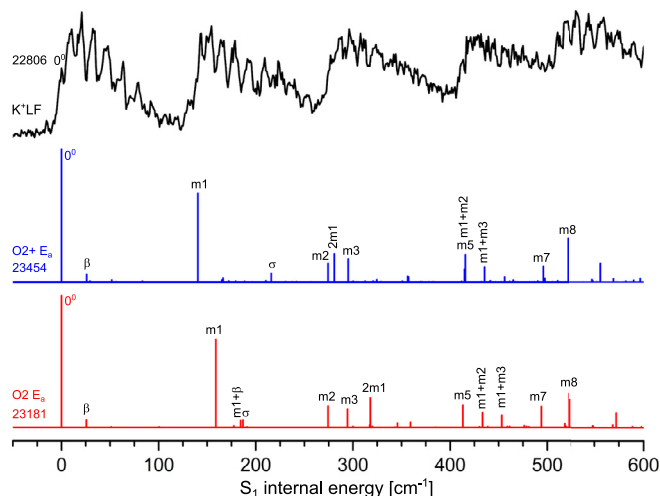


Fig. 11. Comparison between VISPD spectrum of K^+LF (OPO, recorded at high laser power) and Franck–Condon simulations of the $O2(+)$ isomers as a function of S_1 internal energy.

(1.7 cm^{-1}), which may indicate that they are composed of at least two individual modes with similar frequency, whose progressions get more and more separated into well resolved peaks C/D, E/F, and G/H for higher quanta. Due to the computed C_s symmetry of both isomers in the $S_{1/0}$ states, the simulated spectra are dominated by in-plane (a') normal modes, progressions, and combination bands, while even quanta of out-of-plane modes do only show very minor FC activity. The intermolecular bending mode in the S_1 state has the same frequency for both isomers ($\beta=26$ cm^{-1}) and shows only very little FC activity. This is quite different from the FC spectra simulated for the $O2$ isomers of Rb^+LF and Cs^+LF . Apparently, the harmonic FC simulations of both isomers are not able to reproduce the measured VISPD spectrum, again in contrast to the other M^+LF complexes. We attribute this result to the rather flat potential for $O2 \leftrightarrow O2+$ isomerization in both S_0 and S_1 , whose minimum energy path mostly proceeds along the β coordinate. The much wider potential well may explain the extended low-frequency progressions. Moreover, it comes as no surprise that the harmonic FC simulations fail to properly describe the vibrational structure of this rather anharmonic low-barrier double-minimum potential. Again, hindered internal CH_3 rotation and/or vibronic coupling to other electronic states may additionally complicate the VISPD spectrum.

Unfortunately, due to the large number of low-frequency transitions, the intermolecular β and σ modes cannot be extracted from the VISPD spectrum. However, the vibrational pattern observed with the 0^0 band is reproduced in combination with the intramolecular modes ($m1$ – $m8$). Interestingly, the $m1$ values computed for the $O2$ and $O2+$ isomers are quite different (159 and 140 cm^{-1}) and thus may allow to distinguish the two isomers. While the $O2$ isomers of Rb^+LF and Cs^+LF have a rather high predicted (168 and 167 cm^{-1}) and measured $m1$ frequency in the S_1 state (164 and 163 cm^{-1}), the corresponding frequencies of the $O2+$ isomers of Li^+LF and Na^+LF (computed as 156 and 155 cm^{-1} , measured as 156 and 153 cm^{-1}) are significantly lower. Analysis of the VISPD spectra of K^+LF suggests an assignment of band N at 143 cm^{-1} to $m1$, which is much closer to the value predicted for $O2+$ than for $O2$ (deviation of 3 versus 16 cm^{-1}). The σ mode computed as $\sigma=187$ and 216 cm^{-1} for $O2$ and $O2+$, respectively, can be safely excluded to be responsible for the intense peak N because of its high frequency and low FC activity. Consequently, based on the $m1$ frequency, we tentatively assign the observed spectrum to the $O2+$ isomer of K^+LF . The VISPD spectrum does not provide any evidence for the presence of a second isomer in the covered spectral range. Further support for an assignment to the $O2+$

isomer is provided by the plot of the S_1 origins as a function of $1/R_M$ in Fig. 2 (Table 2). The experimental S_1 origins show a pronounced jump between Rb and K, and this jump is reproduced by the computed S_1 origins for an assignment of Cs^+LF and Rb^+LF to the O2 isomer and a switch to the O2+ isomer for M^+LF with $\text{M} = \text{K-Li}$. The computed jump of 282 cm^{-1} between $\text{Rb}(\text{O2})$ and $\text{K}(\text{O2+})$ is in line with the observed one (451 cm^{-1}).

3.5. Further discussion

Electronic $\pi\pi^*$ excitation of M^+LF has a certain impact on the geometry of both LF and the $\text{M}^+\dots\text{LF}$ bond and the geometry changes upon S_1 excitation are summarized in Table S1 in the SI for the O2(+) isomers. As already noted for the O4+ isomer [32], the intramolecular geometry changes of the LF chromophore are relatively independent of the M^+ ion (and the M^+ binding site), because the HOMO/LUMO orbitals for $\pi\pi^*$ excitation are completely localized on the tricyclic LF ring without any contribution at the metal (Fig. 7). Hence, the intramolecular vibrational pattern is quite similar for M^+LF and LF@He_N [32,35,40]. For example, the geometry changes of the LF chromophore of $\text{Rb}^+\text{LF}(\text{O2})$ and $\text{Cs}^+\text{LF}(\text{O2})$ upon S_1 excitation are the same to within 1.0 pm.

In addition, the intermolecular $\text{M}^+\dots\text{LF}$ bonding does not change much by S_1 excitation. While for the O2 isomers of Rb and Cs, the M–O2 bond length is hardly affected (it contracts by 0.5 and 0.3 pm), the M–N1 bond elongates by 9.8 and 9.6 pm, respectively, thereby reducing the interaction with the N1 lone pair. As a result, the C2–O2–M angle increases significantly (by 7.1 and 6.4°) leading to a more linear C2–O2–M bond in the S_1 state, and this geometry change gives rise to the pronounced progression in the in-plane bending mode β predicted and observed for $\text{M}^+\text{LF}(\text{O2})$ with $\text{M} = \text{Rb}$ and Cs (Figs. 5 and 6). As a net result, the $\text{M}^+\dots\text{LF}$ bond becomes slightly weaker by S_1 excitation leading to the ΔS_1 blueshifts (Fig. 2). This geometry change may be rationalized by the NBO partial charge distribution of LF and M^+LF summarized in Table S5 and Fig. S7 in the SI. The partial charge at O2 and N1 of LF increases from S_0 to S_1 , and this change is more pronounced for N1 (from -0.660 to -0.508 e , $\Delta q_{\text{N1}} = 0.152\text{ e}$) than for O2 (from -0.598 to -0.570 , $\Delta q_{\text{O2}} = 0.028\text{ e}$). Consequently, the attractive $\text{M}^+\dots\text{N1}$ interaction is more reduced in the S_1 state compared to the $\text{M}^+\dots\text{O2}$ attraction, giving rise to the more linear but weaker C2–O2–M bond. For the $\text{M}^+\text{LF}(\text{O2+})$ isomers with $\text{M} = \text{Li}$ and Na , the M–N1 and M–O2 bonds of the N1–M–O2 chelate are hardly affected by S_1 excitation ($<1.4\text{ pm}$) resulting again in a minor destabilization of the $\text{M}^+\dots\text{LF}$ bond, as indicated by the small predicted and observed ΔS_1 blueshifts (Fig. 2). As the bending angle of the chelate does not change much by S_1 excitation, no progressions in β are predicted and observed in the S_1 spectra of $\text{M}^+\text{LF}(\text{O2+})$ with $\text{M} = \text{Li}$ and Na (Figs. 8 and 9). Instead, the LF chromophore changes the butterfly angle upon $\pi\pi^*$ excitation, giving rise to the excitation of the low-frequency intramolecular n1 mode. All VISPD spectra of M^+LF are compared in Fig. S8 in the SI to the FC simulations of the O2 and O2+ isomers to illustrate this geometry switch evidenced from the FC simulations. Considering the charge on the M^+ ion (Table S5), there is hardly any charge transfer from M^+ to LF for all alkali ions in both the S_0 and S_1 state at both the O2 and O2+ binding sites ($\Delta q_{\text{M}} < 0.06\text{ e}$). S_1 excitation does not have a big impact on charge transfer ($\leq 0.003\text{ e}$). Thus, the $\text{M}^+\dots\text{LF}$ bond is essentially electrostatic in nature and largely based on cation-dipole interactions supported by polarization and dispersion forces. As a result, the interaction increases monotonically with $1/R_M$, leading to larger binding energies and charge transfer for M^+ with a smaller R_M (Table 1).

To shed further light on the VISPD process, the photodissociation yield is measured at the S_1 origin bands of $\text{M}^+\text{LF}(\text{O2/O2+})$ as a function of the laser power in the range up to 3 mJ/pulse (Fig. S9 in the SI). Similar to the $\text{M}^+\text{LF}(\text{O4+})$ isomers [32], a linear power dependence is observed for the heavier alkali metals Na–Cs, indicative of a single-photon VISPD process for $\text{M}^+\text{LF}(\text{O2/O2+})$. On the other hand, a quadratic power dependence is found for Li, indicating that two photons

are required to drive the VISPD process for $\text{Li}^+\text{LF}(\text{O2+})$. We presume that the cold M^+LF ions are excited to S_1 , followed by rapid internal conversion to S_0 and subsequent dissociation on the ground electronic state. This picture is consistent with the computed binding energies of $\text{M}^+\text{LF}(\text{O2/O2+})$ with $\text{M} = \text{Na–Cs}$ ($D_0 \leq 214\text{ kJ/mol} \sim 17,900\text{ cm}^{-1}$ in S_0 , Table 1), which are substantially lower than the observed S_1 origin bands ($>22,000\text{ cm}^{-1}$, Table 2). In contrast, for $\text{Li}^+\text{LF}(\text{O2+})$, D_0 exceeds S_1 ($289\text{ kJ/mol} \sim 24,200\text{ cm}^{-1} > 23,202\text{ cm}^{-1}$), suggesting that one-photon absorption is not sufficient to drive VISPD. Hence, we suggest that excitation into higher S_n states by absorption of a second photon is required to detect VISPD of $\text{Li}^+\text{LF}(\text{O2+})$. The same effect was already observed for the $\text{M}^+\text{LF}(\text{O4+})$ isomers [32].

To estimate the effective vibrational temperature of the ions in the cryogenic trap, the intensity of the hot band transition originating from the β mode of $\text{Cs}^+\text{LF}(\text{O2})$ in S_0 (15 cm^{-1}) is analyzed in VISPD spectra recorded at various trap temperatures (Fig. S10 in the SI). The population analysis yields ion temperatures of $T = 26 \pm 11$ and $11 \pm 4\text{ K}$ for trap temperatures of $T = 25$ and 6 K , respectively. In particular the high intensity of the hot band observed in the 25 K spectrum (30% of the S_1^0 band) demonstrates the importance that cooling the ions down to well below 20 K is required for resolving vibronic spectra of such flavin complexes with low-frequency inter- and intramolecular modes. The estimated ion temperatures are in good agreement with previous experiments using this ion trap. For example, an effective temperature of $18 \pm 2\text{ K}$ was observed for protonated tyrosine at a trap temperature of 6 K [41].

It is instructive to compare the properties of the O2(+) isomers of M^+LF to those of the O4+ isomers studied previously [32], to unravel the effect of the metal binding site on the photophysics of the metalated flavin. Both isomers show certain similarities but also substantial differences. First, the binding energy resulting from the $\text{M}^+\dots\text{LF}$ interaction is relatively independent of the three binding sites because the electrostatic interactions between the metal cation and the nucleophilic lone pairs at N1/O2 are similar to those at N5/O4. However, the presence of the CH_3 group at N10 causes some steric hindrance at the N1/O2 site resulting in a double minimum potential at O2/O2+ for small alkali ions (Li–K), while for larger alkali ions the O2+ chelate is even unstable. No such steric effects exist at the N5/O4 site, and hence only a deep O4+ chelate minimum is computed while an O4 minimum is not found on the potential [38]. Thus, the vibrational structure is quite different for the O2(+) and O4+ isomers. The O4+ isomers are planar in both S_0 and S_1 , and thus the VISPD spectra are dominated by intermolecular in-plane bend and stretch modes (β , σ), along with the a' intramolecular LF modes (m1–m10). The VISPD spectra of the O2+ isomers with small M^+ ions are dominated by the low-frequency out-of-plane modes (n1–n2), resulting from the symmetry reduction from C_s to C_1 due to the steric hindrance with the CH_3 group at N10. Second, although S_1 excitation is completely localized on the LF chromophore and thus rather independent of the M^+ binding site (Fig. 7), its spectral response is substantially different because of the different charge reorganization of $\pi\pi^*$ excitation at the N5/O4 and N1/O2 atoms. The negative charge on N5/O4 is substantially increased upon S_1 excitation, leading to a drastically enhanced $\text{M}^+\dots\text{LF}$ interaction at the O4+ site (by up to 20%), which in turn produces the large ΔS_1 redshifts. On the other hand, the negative charge on N1/O2 is slightly reduced by S_1 excitation, leading to a slightly reduced $\text{M}^+\dots\text{LF}$ interaction at the O2(+) site (by 6–9%), which in turn results in small ΔS_1 blueshifts. Thus, the different photochemical response for metalation at the O4+ and O2(+) positions results from the change in the $\text{M}^+\dots\text{LF}$ interaction upon excitation and not from the change in the HOMO/LUMO orbitals involved in S_1 excitation by metalation.

Comparison between M^+LF and H^+LF also reveals certain similarities and differences. First, the proton is much smaller than the alkali ions and binds much stronger to LF via chemical rather than electrostatic bonding [40]. The two lowest energy isomers of H^+LF have the proton attached to O2+ or N1 and these two deep minima are separated by a quite high barrier from each other ($>156\text{ kJ/mol}$). While the O2+

global minimum of H^+LF is planar in both S_0 and S_1 , the slightly less stable N1 protomer is nonplanar because of the same steric repulsion from the CH_3 group at N10 as observed for the O2^+ isomers of M^+LF . Second, as the HOMO/LUMO orbitals are localized on the tricyclic aromatic ring, the S_1 transitions of both $\text{H}^+\text{LF}(\text{O2}^+)$ and $\text{H}^+\text{LF}(\text{N1})$ exhibit a small blueshift upon protonation, with $\Delta\text{S}_1=1617$ and 1691 cm^{-1} , pretty similar to those found herein for $\text{M}^+\text{LF}(\text{O2}/\text{O2}^+)$.

Comparison between M^+LF and M^+LC reveals the effects of substitution of functional groups on their photochemical response. Since LC has a H atom at the N1 position, O2^+ binding is not feasible [33,36]. Moreover, the $\text{M}^+\text{LC}(\text{O2})$ isomers have experimentally not been detected in the optical range yet, probably because they are substantially less stable than the O4^+ global minima (by $34\text{--}73\text{ kJ/mol}$ for Cs--Li). As $\text{M}^+\text{LC}(\text{O4}^+)$ and $\text{M}^+\text{LF}(\text{O4}^+)$ exhibit similar results in terms of bonding, ΔS_1 shifts upon $\pi\pi^*$ excitation, and vibronic activity, the results pointed out for $\text{M}^+\text{LF}(\text{O4}^+)$ can directly be transferred to those for $\text{M}^+\text{LC}(\text{O4}^+)$ [33].

4. Concluding remarks

In summary, we present herein high-resolution vibronic VISPD spectra of isolated metalated lumiflavin complexes (M^+LF , $\text{M}=\text{Li--Cs}$) measured at cryogenic temperatures in the blue part of the visible electromagnetic spectrum. The spectra are assigned with the aid of TD-DFT calculations (PBE0/cc-pVDZ) coupled with multidimensional FC simulations to the $\text{S}_1\leftarrow\text{S}_0$ ($\pi\pi^*$) transition of the $\text{O2}(+)$ isomers, which have been identified by previous IRMPD experiments and computational studies [38]. The present work extends our previous study of the O4^+ isomers, which absorb at longer wavelengths [32]. The S_1 spectra show rich vibrational structure in low-frequency inter- and intramolecular modes, which can only be resolved at cryogenic temperature. The assignment of this vibrational structure by multidimensional FC simulations is essential for isomer identification and emphasizes the importance of cryogenic cooling for structure determination and the evaluation of the $\text{M}^+\dots\text{LF}$ bond strength. In contrast to the large redshifts of the O4^+ isomers of $61\text{--}102\text{ nm}$ ($2480\text{--}3866\text{ cm}^{-1}$, $0.31\text{--}0.48\text{ eV}$), metalation at the $\text{O2}(+)$ site induces small ΔS_1 blueshifts of only $17\text{--}34\text{ nm}$ ($812\text{--}1691\text{ cm}^{-1}$, $0.10\text{--}0.21\text{ eV}$) with respect to S_1 of neutral LF embedded in He nanodroplets [35]. This result confirms that the photophysical response of LF can strongly be modulated by metalation at various ligand binding sites. In general, this modulation is not caused by the change of the molecular orbitals of the LF chromophore but rather by the change in the $\text{M}^+\dots\text{LF}$ interaction induced by electronic excitation. The HOMO/LUMO orbitals localized on the LF chromophore are rather insensitive to the metal binding site. However, the charge reorganization in LF upon S_1 excitation affects the intermolecular interaction with M^+ . While S_1 excitation strongly increases the $\text{M}^+\dots\text{LF}$ interaction strength of the O4^+ isomers (up to 20% for Cs) causing the massive ΔS_1 redshifts, it slightly reduces the interaction in the $\text{O2}(+)$ isomers ($\sim 6\text{--}9\%$) leading to the more modest ΔS_1 blueshifts upon M^+ complexation. In this way, the optical response for the $\text{O2}(+)$ isomers differ substantially from that of the O4^+ isomers, so that they can be studied in an isomer-selective fashion. This is rather different from IRMPD spectroscopy, where the IR spectra of both types of isomers strongly overlap. Interestingly, the binding motif and interaction strength of the $\text{O2}/\text{O2}^+$ isomers of M^+LF strongly vary with the size of M^+ . The large Rb and Cs ions form merely the O2 isomers with a nearly linear C2--O2--M bond. The O2^+ isomer with a N1--M--O2 chelate is unstable because of steric repulsion from the nearby CH_3 group at N10 . As a result, the VISPD spectrum is attributed to the O2 isomer and the rich vibronic structure in the low-frequency range of the S_1 band arises from the in-plane bending mode of the $\text{M}^+\dots\text{LF}$ bond, which is excited due to the geometry change in this coordinate by S_1 excitation. For the lighter and smaller M^+ ions, the O2^+ isomer becomes increasingly more stable than the O2 isomer, although the barriers for the $\text{O2}^+\leftrightarrow\text{O2}$ isomerization are small. Hence, for Li and Na the VISPD spectrum is attributed to the O2^+ global

minima, and the low-frequency vibronic structure in the S_1 band comes from out-of-plane intramolecular modes because S_1 excitation changes the butterfly bending angle of the O2^+ isomers having a slightly nonplanar aromatic ring due to steric interaction with the CH_3 group at N10 . Finally, the intermediate K case is complicated because O2 and O2^+ are essentially isoenergetic and the isomerization barrier between the two is low. As a result of the very flat potential along the bending coordinate, the VISPD spectrum of K^+LF is dominated by very low frequency modes, which cannot properly be reproduced by the harmonic FC simulations. As an outlook, future work using the same combined spectroscopic and computational approach will address biologically more relevant flavins, such as RF , FMN , and FAD along with (i) complexation with transition metal ions such as Cu^+ , Fe^{2+} , and Mg^{2+} and (ii) microhydration to follow step by step the impact of solvation.

Declaration of Competing Interest

None.

Acknowledgments

This work was supported by Deutsche Forschungsgemeinschaft (DFG, project [DO 729/6-2](#)).

Supplementary materials

Supplementary material associated with this article can be found, in the online version, at doi:[10.1016/j.jpap.2020.100009](#).

References

- [1] P.F. Heelis, The Photophysical and Photochemical Properties of Flavins (Isoalloxazines), *Chem. Soc. Rev.* 11 (1982) 15.
- [2] V. Massey, The Chemical and Biological Versatility of Riboflavin, *Biochem. Soc. Trans.* 28 (2000) 283.
- [3] A. Losi, Flavin-based Blue-Light photosensors: a photobiophysics update, *Photochem. Photobiol.* 83 (2007) 1283.
- [4] A. Sancar, Structure and Function of DNA Photolyase and Cryptochrome Blue-Light Photoreceptors, *Chem. Rev.* 103 (2003) 2203.
- [5] W. Buckel, R.K. Thauer, Flavin-Based Electron Bifurcation, A New Mechanism of Biological Energy Coupling, *Chem. Rev.* 118 (2018) 3862.
- [6] E. Romero, J.R. Gómez Castellanos, G. Gadda, M.W. Fraaije, A. Mattevi, Same Substrate, Many Reactions: Oxygen Activation in Flavoenzymes, *Chem. Rev.* 118 (2018) 1742.
- [7] E. Silva, A.M. Edwards, Flavins, Eduardo Silva, Ana M. Edwards (Eds.), RSC Publishing, Cambridge, 2006.
- [8] W.J. Rutter, K. Dalziel, H. Viervoll, M. Zackrisson, L. Ernster, E. Diczfalusy, The Interaction of Riboflavin, FMN, and FAD with Various Metal Ions: The Riboflavin Catalyzed Photochemical Reduction of Fe^{III} , and Photooxidation of Fe^{II} , *Acta Chem. Scand.* 12 (1958) 438.
- [9] I.F. Baarda, D.E. Metzler, Complexes of riboflavin with silver and other metal ions, *Biochim. Biophys. Acta* 50 (1961) 463.
- [10] P. Bamberg, P. Hemmerich, Farbe und Konstitution der Isoalloxazin-Silber-Komplexe. Zum Verhalten des Riboflavins gegen Metallionen II, *Helv. Chim. Acta* 44 (1961) 1001.
- [11] A.W. Varnes, R.B. Dodson, E.L. Wehry, Interactions of Transition-Metal Ions with Photoexcited States of Flavins. Fluorescence Quenching Studies, *J. Am. Chem. Soc.* 94 (1972) 946.
- [12] J. Lauterwein, P. Hemmerich, J.M. Lhoste, Flavonone-metal complexes. I. Structure and properties, *Inorg. Chem.* 14 (1975) 2152.
- [13] J. Lauterwein, P. Hemmerich, J.M. Lhoste, Flavonone-metal complexes. II. Paramagnetic interactions, *Inorg. Chem.* 14 (1975) 2161.
- [14] M. Benecky, T.-J. Yu, K.L. Watters, J.T. McFarland, Metal-flavin complexation. A resonance Raman investigation, *Biochim. Biophys. Acta – Protein Struct.* 626 (1980) 197.
- [15] S. Fukuzumi, T. Kojima, Control of redox reactivity of flavin and pterin coenzymes by metal ion coordination and hydrogen bonding, *J. Biol. Inorganic Chem.* 13 (2008) 321.
- [16] I. Ahmad, Z. Anwar, S. Ahmed, M.A. Sheraz, S.-U.-R. Khattak, Metal ion mediated photolysis reactions of riboflavin: A kinetic study, *J. Photochem. Photobiol. B: Biol.* 173 (2017) 231.
- [17] A. Tyagi, A. Penzkofer, pH dependence of the absorption and emission behaviour of lumiflavin in aqueous solution, *J. Photochem. Photobiol. A: Chem.* 215 (2010) 108.
- [18] A. Tyagi, A. Penzkofer, Absorption and Emission Spectroscopic Characterization of Lumichrome in Aqueous Solutions, *Photochem. Photobiol.* 87 (2011) 524.
- [19] E. Sikorska, I.V. Khmelinskii, W. Prukla, S.L. Williams, M. Patel, D.R. Worrall, J.L. Bourdelande, J. Koput, M. Sikorski, Spectroscopy and Photophysics of Lumiflavins and Lumichromes, *J. Phys. Chem. A* 108 (2004) 1501.

- [20] C. Neiss, P. Saalfrank, M. Parac, S. Grimme, Quantum Chemical Calculation of Excited States of Flavin-Related Molecules, *J. Phys. Chem. A* 107 (2003) 140.
- [21] J. ya Hasegawa, S. Bureekaew, H. Nakatsuji, SAC-CI theoretical study on the excited states of lumiflavin: Structure, excitation spectrum, and solvation effect, *J. Photochem. Photobiol. A: Chem.* 189 (2007) 205.
- [22] S. Salzmann, C.M. Marian, Effects of protonation and deprotonation on the excitation energies of lumiflavin, *Chem. Phys. Lett.* 463 (2008) 400.
- [23] S. Salzmann, V. Martinez-Junza, B. Zorn, S.E. Braslavsky, M. Mansurova, C.M. Marian, W. Gärtner, Photophysical Properties of Structurally and Electronically Modified Flavin Derivatives Determined by Spectroscopy and Theoretical Calculations, *J. Phys. Chem. A* 113 (2009) 9365.
- [24] S. Salzmann, J. Tatchen, C.M. Marian, The photophysics of flavins: What makes the difference between gas phase and aqueous solution? *J. Photochem. Photobiol. A: Chem.* 198 (2008) 221.
- [25] B. Klumünzer, D. Kröner, P. Saalfrank, (TD-)DFT Calculation of Vibrational and Vibronic Spectra of Riboflavin in Solution, *J. Phys. Chem. B* 114 (2010) 10826.
- [26] M.H. Stockett, Photo-induced proton-coupled electron transfer and dissociation of isolated flavin adenine dinucleotide mono-anions, *Phys. Chem. Chem. Phys.* 19 (2017) 25829.
- [27] L. Giacomozzi, C. Kjær, J. Langeland Knudsen, L.H. Andersen, S. Brøndsted Nielsen, M.H. Stockett, Absorption and luminescence spectroscopy of mass-selected flavin adenine dinucleotide mono-anions, *J. Chem. Phys.* 148 (2018) 214309.
- [28] J.N. Bull, E. Carrascosa, L. Giacomozzi, E.J. Bieske, M.H. Stockett, Ion mobility action spectroscopy of flavin dianions reveals deprotomer-dependent photochemistry, *Phys. Chem. Chem. Phys.* 20 (2018) 19672.
- [29] E. Matthews, R. Cercola, C.E.H. Dessent, Protomer-Dependent Electronic Spectroscopy and Photochemistry of the Model Flavin Chromophore Alloxazine, *Molecules* 23 (2018) 2036.
- [30] E. Matthews, C.E.H. Dessent, Observation of Near-Threshold Resonances in the Flavin Chromophore Anions Alloxazine and Lumichrome, *J. Phys. Chem. Lett.* 9 (2018) 6124.
- [31] K. Lincke, J. Langeland, A. Ø. Madsen, H.V. Kiefer, L. Skov, E. Gruber, K.V. Mikkelsen, L.H. Andersen, M.B. Nielsen, Elucidation of the intrinsic optical properties of hydrogen-bonded and protonated flavin chromophores by photodissociation action spectroscopy, *Phys. Chem. Chem. Phys.* 20 (2018) 28678.
- [32] D. Müller, P. Nieto, M. Miyazaki, O. Dopfer, Effect of alkali ions on optical properties of flavins: vibronic spectra of cryogenic M^+ lumiflavin complexes ($M = \text{Li-Cs}$), *Faraday Discuss.* 217 (2019) 256.
- [33] P. Nieto, D. Müller, A. Sheldrick, A. Günther, M. Miyazaki, O. Dopfer, Effect of alkali ions on optical properties of flavins: vibronic spectra of cryogenic M^+ lumichrome ions ($M = \text{Li-Cs}$) in the gas phase, *Phys. Chem. Chem. Phys.* 20 (2018) 22148.
- [34] R.J. Platenkamp, H.D. van Osnabrugge, A.J.W.G. Visser, High-resolution fluorescence and excitation spectroscopy of N3-undecylflavin in n-decane, *Chem. Phys. Lett.* 72 (1980) 104.
- [35] A. Vdovin, A. Slenczka, B. Dick, Electronic spectroscopy of lumiflavin in superfluid helium nanodroplets, *Chem. Phys.* 422 (2013) 195.
- [36] A. Günther, P. Nieto, G. Berden, J. Oomens, O. Dopfer, IRMPD spectroscopy of metalated flavins: structure and bonding of M^{q+} -lumichrome complexes ($M^{q+} = \text{Li}^+ \text{-Cs}^+, \text{Ag}^+, \text{Mg}^{2+}$), *Phys. Chem. Chem. Phys.* 16 (2014) 14161.
- [37] J. Langer, A. Günther, S. Seidenbecher, G. Berden, J. Oomens, O. Dopfer, Probing Protonation Sites of Isolated Flavins Using IR Spectroscopy: From Lumichrome to the Cofactor Flavin Mononucleotide, *ChemPhysChem* 15 (2014) 2550.
- [38] P. Nieto, A. Günther, G. Berden, J. Oomens, O. Dopfer, IRMPD Spectroscopy of Metalated Flavins: Structure and Bonding of Lumiflavin Complexes with Alkali and Coinage Metal Ions, *J. Phys. Chem. A* 120 (2016) 8297.
- [39] A. Sheldrick, D. Müller, A. Günther, P. Nieto, O. Dopfer, Optical spectroscopy of isolated flavins: photodissociation of protonated lumichrome, *Phys. Chem. Chem. Phys.* 20 (2018) 7407.
- [40] D. Müller, O. Dopfer, Vibronic Optical Spectroscopy of Cryogenic Flavin Ions: The O_2^+ and N_1 Tautomers of Protonated Lumiflavin, *Phys. Chem. Chem. Phys.* 22 (2020) 18328.
- [41] A. Günther, P. Nieto, D. Müller, A. Sheldrick, D. Gerlich, O. Dopfer, BerlinTrap: A new cryogenic 22-pole ion trap spectrometer, *J. Mol. Spectrosc.* 332 (2017) 8.
- [42] M.J. Frisch, et al., GAUSSIAN16, Rev. C.01, Wallingford, CT, 2016.
- [43] T.H. Dunning, Gaussian basis sets for use in correlated molecular calculations. I. The atoms boron through neon and hydrogen, *J. Chem. Phys.* 90 (1989) 1007.
- [44] C. Adamo, V. Barone, Toward reliable density functional methods without adjustable parameters: The PBE0 model, *J. Chem. Phys.* 110 (1999) 6158.
- [45] V. Barone, J. Bloino, M. Biczysko, F. Santoro, Fully Integrated Approach to Compute Vibrationally Resolved Optical Spectra: From Small Molecules to Macrosystems, *J. Chem. Theory Comput.* 5 (2009) 540.
- [46] R.L. Martin, Natural transition orbitals, *J. Chem. Phys.* 118 (2003) 4775.
- [47] I.S. Lim, P. Schwerdtfeger, B. Metz, H. Stoll, All-electron and relativistic pseudopotential studies for the group 1 element polarizabilities from K to element 119, *J. Chem. Phys.* 122 (2005) 104103.
- [48] J.P. Foster, F. Weinhold, Natural hybrid orbitals, *J. Am. Chem. Soc.* 102 (1980) 7211.
- [49] P.J. Breen, J.A. Warren, E.R. Bernstein, J.I. Seeman, A study of nonrigid aromatic molecules by supersonic molecular jet spectroscopy. I. Toluene and the xylenes, *Acc. Chem. Res.* 87 (1987) 1917.

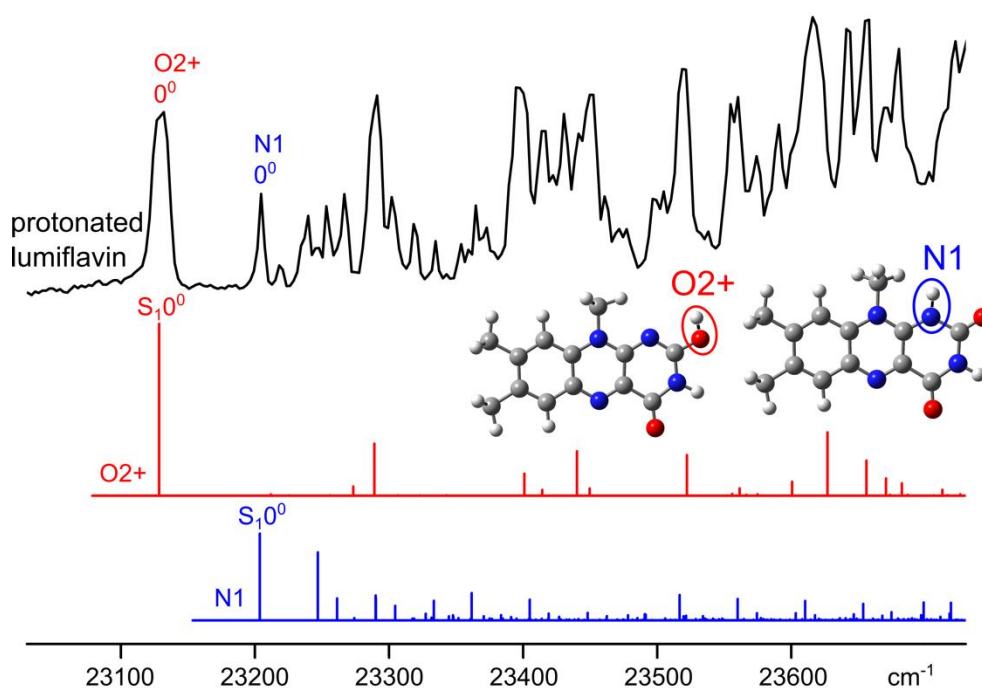
4.3. Vibronic optical spectroscopy of cryogenic flavin ions: the O2+ and N1 tautomers of protonated lumiflavin

David Müller and Otto Dopfer

Phys. Chem. Chem. Phys., 2020, **22**, 18328

<https://doi.org/10.1039/D0CP03650A>

Reproduced with permission of the PCCP Owner Societies



Declaration of Contribution

Both experimental and computational analysis were carried out by David Müller. The manuscript of the article was written by David Müller and reviewed and finalized by Otto Dopfer. All work was supervised by Otto Dopfer.



Cite this: *Phys. Chem. Chem. Phys.*,
2020, 22, 18328

Vibronic optical spectroscopy of cryogenic flavin ions: the O2+ and N1 tautomers of protonated lumiflavin†

David Müller and Otto Dopfer *

Flavins are key compounds in many photochemical and photophysical processes used by nature, because their optical properties strongly depend on the (de-)protonation site and solvation. Herein, we present the vibronic optical spectrum of protonated lumiflavin (H^+LF), the parent molecule of the flavin family, obtained by visible photodissociation (VISPD) spectroscopy in a cryogenic ion trap. By comparison to time-dependent density functional theory (TD-DFT) calculations at the PBE0/cc-pVDZ level coupled to multidimensional Franck–Condon simulations, the spectrum recorded in the 420–500 nm range is assigned to vibronic bands of the optically bright $\text{S}_1 \leftarrow \text{S}_0(\pi\pi^*)$ transition of the two most stable H^+LF tautomers protonated at the O2+ and N1 position. While the most stable O2+ protomer has been identified previously by infrared spectroscopy, the N1 protomer is identified here for the first time. The S_1 band origins of $\text{H}^+\text{LF}(\text{O2+})$ and $\text{H}^+\text{LF}(\text{N1})$ at 23128 and 23202 cm^{-1} are shifted by 1617 and 1691 cm^{-1} to the blue of that of bare LF measured in He droplets, indicating that the proton affinity of both tautomers is slightly reduced upon S_1 excitation. This view is consistent with the molecular orbitals involved in the assigned $\pi\pi^*$ transition. The spectrum of both protomers is rich in vibrational structure indicating substantial geometry changes by $\pi\pi^*$ excitation. Interestingly, while the O2+ protomer is planar in both electronic states, the N1 protomer is slightly nonplanar giving rise to large vibrational activity of low-frequency out-of-plane modes. Comparison with protonated lumichrome and metalated lumiflavin reveals the impact of functional groups and the type of the attached cation (proton or alkali ion) on the geometric and electronic structure of flavins.

Received 8th July 2020,
Accepted 4th August 2020

DOI: 10.1039/d0cp03650a

rsc.li/pccp

1. Introduction

Flavins are yellow dye molecules and represent a fundamental class of photochemically active biomolecules. They are derived from the tricyclic heteroaromatic 7,8-dimethyl-10-alkyl-isoalloxazine chromophore, which is responsible for their photophysical properties. The various flavins differ by their substituent R at the N10 position. Important members of the flavin family include iso-lumichrome (iso-LC, R = H), lumiflavin (LF, R = CH_3 , Fig. 1), riboflavin (RF, vitamin B₂, R = ribityl), flavin mononucleotide (FMN, R = ribophosphate), and flavin adenine dinucleotide (FAD, R = ribophosphate + adenine). Because iso-LC is less stable than LC (R = H at N1 instead of N10) and thus a metastable species, LF is often considered as the parent molecule of the flavin family. Flavins absorb light in a broad spectral range ranging from the visible to the ultraviolet, and

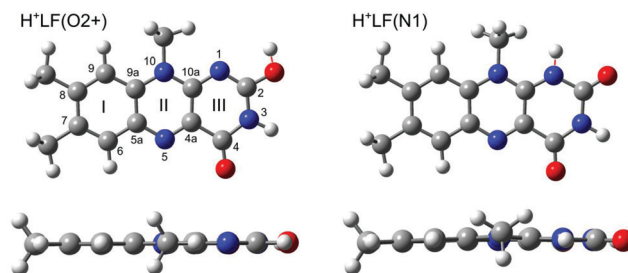


Fig. 1 Top and side views of the structures of the two most stable protomers of H^+LF (O2+ and N1) in the S_0 state obtained at the PBE0/cc-pVDZ level. The O2+ protomer has a planar ring system (C_s), whereas the N1 protomer is slightly bent along the N5–N10 axis (C_1). Atoms are labelled according to IUPAC nomenclature. The structures of further protomers (O2–, O4±, N5, OH±) are shown in Fig. S3 in the ESI.†

their photophysical properties are determined by the interplay between the optically bright $\pi\pi^*$ excitations of the aromatic π electrons and the optically dark $n\pi^*$ excitations originating from the lone pair electrons of the heterocyclic N atoms and the oxygen atoms of the CO groups in the tricyclic ring. This interplay can readily be modulated by the flavin environment,

Institut für Optik und Atomare Physik, Technische Universität Berlin,
Hardenbergstr. 36, D-10623 Berlin, Germany. E-mail: dopfer@physik.tu-berlin.de;
Fax: +49 30 314 23018

† Electronic supplementary information (ESI) available. See DOI: 10.1039/d0cp03650a



such as the substitution of functional groups, (de-)protonation, the oxidation state, metalation, and solvation. As a result, nature utilizes flavins for a plethora of photochemical processes, including light harvesting, DNA repair, and enzyme catalysis.^{1–7}

Flavins have extensively been investigated by spectroscopy in the condensed phase and quantum chemical calculations.^{8–18} Concerning LF, the first excited singlet state (S_1) observed near 445 nm is attributed to the first optically allowed $\pi\pi^*$ state. The large geometry changes upon S_1 excitation result in a substantial difference between the vertical and adiabatic excitation energies and thus a large Stokes shift of 90 nm in fluorescence.⁹ While the maximum of the S_1 band of LF occurs in a narrow spectral window (441–447 nm) and thus is relatively independent of the solvent, the second absorption band assigned to the next $\pi\pi^*$ state is highly sensitive to solvation (332–367 nm), because of its sensitivity to hydrogen bonding with the solvent.⁹ Protonation of LF has a drastic impact on its absorption spectrum and shifts its first absorption band in aqueous solution from 441 nm (neutral, pH 6–8) to 394 nm (protonated, pH \sim 1.1).^{8,11} Hydrogen bonding with the solvent leads to a redshift of the optically bright S_3 state and hence reduces the gap between S_1 and S_3 , resulting in the single broad absorption band at 394 nm observed experimentally.¹⁵ In the spectroscopic study,¹¹ protonation at N1 of LF was assumed although there was no evidence for the protonation site from the experimental data. Computational studies on the photo-physics of H^+LF consider only protonation at N1 and N5 in both gas phase and aqueous solution,¹⁵ although O2+ was computed to be the most stable protomer at the HF level.¹⁷ The former computation¹⁵ predicts the N1 protomer to be more stable than the N5 protomer in the S_0 state, while the energy order is reversed in the $S_1(\pi\pi^*)$ state. Significantly, all optical spectra of flavins recorded in the condensed phase at room temperature are broad and vibrationally unresolved. Consequently, details of individual environmental effects on the optical properties cannot be extracted. To this end, it is essential to cool the molecules down to cryogenic temperatures.^{19,20} Indeed, the recent optical laser-induced fluorescence (LIF) excitation spectrum of neutral LF doped into superfluid He nanodroplets ($T = 0.4$ K) was assigned to vibronic structure of the $S_1 \leftarrow S_0(\pi\pi^*)$ transition, with an adiabatic S_1 origin at $21\,511\text{ cm}^{-1}$ (464.87 nm).²⁰ It was argued that the He environment has typically only a minor impact on the transition energy ($< 1\%$, $\sim 250\text{ cm}^{-1}$). The low temperature in the He droplet allows to resolve the rich vibronic structure in the S_1 excited state of LF, which illustrates the large geometry change upon electronic $\pi\pi^*$ excitation.

To reveal the intrinsic optical properties of isolated flavins completely free from external perturbations, spectroscopic studies in the gas phase are required. However, such studies are scarce because of the difficulties involved in transferring such biomolecules in large abundance into the gas phase. This obstacle can be circumvented by electrospray ionization (ESI) techniques, which can be used to efficiently transfer flavin ions into the gas phase for interrogation with action spectroscopy. In recent years, this approach has been applied to a few cationic and anionic flavins of various complexity to study their

photophysical properties.^{21–26} However, all these experiments were conducted at room temperature, leading to broad and unresolved electronic spectra of similar appearance as in the condensed phase. As a result, the clear discrimination between environmental effects and intrinsic properties is challenging if not impossible. Concerning flavins, it is not even possible to reliably determine the (de-)protonation sites. To this end, cryogenic cooling is required to obtain high-resolution electronic spectra at the level of vibrational resolution, which then provides precise details about the isomeric structure of the flavin ion and the nature of the electronic states responsible for the absorption process.

To characterize the structure and intrinsic optical properties of flavins isolated in the gas phase, we have initiated a few years ago a research program to systematically investigate the effects of protonation, metalation, and solvation on flavins with increasing complexity, ranging from LC to FMN. In the first step of the research strategy, the geometric structure of protonated and metalated flavins is determined in the ground electronic state (S_0) by infrared multiple photon dissociation (IRMPD) of mass-selected ions generated by ESI. Although these experiments are conducted at room temperature, the IRMPD spectra recorded in the fingerprint range exhibit sufficient resolution to determine the preferred protonation and metalation sites by probing the highly structure-sensitive CO stretch vibrations.^{27–29} With the aid of density functional theory (DFT) calculations at the B3LYP/cc-pVDZ level, the IRMPD spectrum of protonated LF (H^+LF) has been assigned to the most stable O2+ protomer, while significant contributions of higher energy isomers have been excluded.²⁷ Significantly, these IRMPD studies present the first spectroscopic data of any flavin molecule in the gas phase. In a second step, we have extended our initial spectroscopic characterization of flavins in the ground electronic state to electronically excited states. For this purpose, we employ a recently commissioned cryogenic ion trap tandem mass spectrometer (BerlinTrap)³⁰ to record visible photodissociation (VISPD) spectra of mass-selected flavin ions generated by ESI and cooled to cryogenic temperatures ($T < 20$ K). Significantly, cooling of the ions enables us for the first time to obtain vibrationally resolved electronic spectra of isolated flavins. Analysis of these vibronic VISPD spectra with time-dependent DFT (TD-DFT) calculations coupled to multidimensional Franck-Condon (FC) simulations provides reliable and precise information about the protonation and metalation sites as well as the nature and adiabatic energy of the involved electronic excitation along with the resulting structural changes. The initial application to the $S_1 \leftarrow S_0(\pi\pi^*)$ transition of H^+LC confirms N5 as the preferred protonation site already inferred from its IRMPD spectrum.^{27,31} N5 protonation of LC causes a remarkably large S_1 redshift of $\sim 6000\text{ cm}^{-1}$, which can be rationalized by the molecular orbitals involved in this $\pi\pi^*$ excitation. Subsequent studies characterize the effects of metalation of LC and LF with alkali metal cations ($M = \text{Li-Cs}$) on their optical properties, illustrating that the $M^+ \cdots LF/LC$ interaction strength and thus the S_1 excitation energy shifts depend strongly on the metalation site.^{32,33} Herein, we extend these



VISPD studies to H^+LF . The major questions to be addressed are the observed protonation sites, the effects of protonation on the optical properties of LF, and the differences between H^+LF and $\text{H}^+\text{LC}/\text{M}^+\text{LF}$ studied previously by the same spectroscopic and computational approach.

2. Experimental and computational details

Vibronic VISPD spectra of H^+LF are measured in a cryogenic ion trap coupled to a tandem mass spectrometer (BerlinTrap) and an ESI source.³⁰ Briefly, ions are generated in the ESI source by spraying at a flow rate of 2 ml h^{-1} a solution of 2–4 mg LF (Sigma Aldrich, >99%) dissolved in 19 ml methanol, 1 ml water, and 2 ml formic acid to enhance protonation. The produced ions are skimmed, accumulated, and thermalized for 90 ms in a short quadrupole located directly behind the skimmer. After passing through a hexapole ion guide, the H^+LF ions are mass-selected by a quadrupole, deflected by a quadrupole bender, and guided through an octopole into a temperature-controlled cryogenic 22-pole ion trap ($T = 4\text{--}300 \text{ K}$) held at 6 K. In the trap, the ions are stored for around 90 ms and cooled down *via* He buffer gas cooling to vibrational temperatures below 20 K.³⁰ The cold ions extracted from the 22-pole are transferred *via* a series of electrostatic lenses toward the extraction region of an orthogonal reflectron time-of-flight mass spectrometer, where they are irradiated by a laser pulse around $40 \mu\text{s}$ before pulsed ion extraction. The generated photofragment ions are detected simultaneously with the remaining parent ions using a dual microchannel plate detector. Photons in the visible range are generated by an optical parametric oscillator (OPO, GWU, VersaScan, bandwidth of 4 cm^{-1}) pumped by the third harmonic of a nanosecond Q-switched Nd:YAG laser (Innolas, Spitlight 1000, 355 nm, 180 mJ per pulse) operating at a repetition rate of 10 Hz to be synchronized with the cycle of the tandem mass spectrometer setup. A selected part of the VISPD spectrum is also recorded at higher resolution using a dye laser (Radiant Dyes, NarrowScan, Coumarin 120 and Stilbene 3 dyes dissolved in ethanol, bandwidth of 0.014 cm^{-1}) pumped by the same type of Nd:YAG laser (355 nm, 100 mJ per pulse). The wavelength of the OPO and dye laser outputs is calibrated by a wavemeter. VISPD spectra measured between $23\,050$ and $23\,750 \text{ cm}^{-1}$ ($421\text{--}434 \text{ nm}$) are obtained by normalising the integrated signal of all fragment ions by the parent ions and the laser intensity measured at the exit of the instrument by a pyroelectric detector. The mass spectra of the ions extracted from the trap do not show any peaks arising from tagging of H^+LF with He or N_2 . At a trap temperature of 6 K, the N_2 impurity gas in the He buffer gas line freezes out at the cold walls of the trap. Tagging with He is not observed because the binding energy is too low for He attachment to H^+LF at an effective vibrational ion temperature of $T = 15\text{--}20 \text{ K}$.

The vibronic VISPD spectra are assigned by comparison to quantum chemical (TD-)DFT calculations at the PBE0/cc-pVDZ level using the GAUSSIAN16 package.^{34–36} To this end, the structures of all low-energy protomers are optimized in the

ground electronic state (S_0). All reported proton affinities (here taken as protonation energies at $T = 0 \text{ K}$) and relative energies (E_0) are corrected for harmonic vibrational zero-point energy. Vertical energies and oscillator strengths for electronic excitations are computed for both singlet (up to S_4) and triplet states (up to T_4). Adiabatic energies are obtained (up to S_2 and T_1) by optimizing the excited states using the converged ground state geometry as starting point. Cartesian coordinates and energies of all relevant structures are provided in the ESI.[†] Multidimensional Franck–Condon simulations at $T = 0 \text{ K}$ are carried out to generate vibronic excitation spectra.³⁷ In previous studies on related flavins (H^+LC , $\text{M}^+\text{LC}/\text{LF}$ with $\text{M} = \text{Li–Cs}$),^{31–33} the employed PBE0/cc-pVDZ level was shown to be a computationally efficient and reliable DFT approach for calculating vibronic spectra. Orbitals contributing to the observed transitions are determined using the natural transition orbital (NTO) approach.³⁸ Energy barriers at transition states (TS) between different protomers are calculated using the QST2 method and are not corrected for zero-point energy. Harmonic frequency analysis is employed to determine the nature of stationary points as minima or transition states. The atomic charge distribution of the ground and excited states is evaluated using the natural bond orbital analysis (NBO).

3. Results and discussion

Initial overview VISPD spectra of H^+LF are recorded at a larger step size of 0.5 nm starting from 500 nm ($20\,000 \text{ cm}^{-1}$) and scanning to the blue to search for structured resonant absorption. This spectral range is suggested by the adiabatic S_1 origin prediction at 443.75 nm ($22\,535 \text{ cm}^{-1}$) for the most stable $\text{O}2^+$ protomer, which was identified as the single H^+LF isomer present in the ESI source by our previous IRMPD experiments.²⁷ The first pronounced transition is indeed detected at 432.38 nm ($23\,128 \text{ cm}^{-1}$), and thus the VISPD spectrum is investigated in the vicinity of this peak at higher resolution using a smaller step size ($22\,700\text{--}23\,800 \text{ cm}^{-1}$). Resonant VISPD of the H^+LF parent ion (m/z 257) at $23\,128 \text{ cm}^{-1}$ results in a variety of fragment ions with m/z 145, 156, 159, 171, 186, 199, 214, and 242 appearing with different branching ratios (Fig. S1 and Table S1 in the ESI[†]). The H^+LF ions stored in the ion trap are cold and thus no fragmentation is observed without laser excitation. In particular, there are no fragments resulting from metastable decay and collision-induced dissociation (CID) upon extraction of the cold ions from the trap. Previous IRMPD spectra of H^+LF reveal the photodissociation products m/z 145, 159, 171, 186, and 214 in the ground electronic state.²⁷ Apart from m/z 145, these can be explained by formal loss of OCNH (isocyanic acid) and combinations of OCNH with CO. New mass peaks observed exclusively upon VISPD of H^+LF include m/z 242 and 199, which are rationalized by loss of CH_3 and $\text{CH}_3 + \text{OCNH}$. Hence, electronic excitation of H^+LF opens a new fragmentation channel not operating upon IRMPD occurring in the S_0 state. This new channel involves loss of CH_3 , probably the methyl group attached to N10. The VISPD fragmentation pattern of H^+LF is



much more complex than that observed for $S_1(\pi\pi^*)$ excitation of H^+LC , for which only two fragment channels are observed for both VISPD and CID, namely loss of $CO + NH_3$ (or $HCN + H_2O$) and loss of $OCNH + CO$. Consequently, the ring opening reaction upon VISPD is different for H^+LF and H^+LC , confirming that the photochemistry of H^+LC differs strongly from that of H^+LF .

The obtained vibronic action spectra of H^+LF generated for each individual fragment channel (Fig. S2 in the ESI†) are very similar with respect to the positions, widths, and relative intensities of all transitions observed. This result is in contrast to the corresponding IRMPD spectra of H^+LF , which are complicated by further resonant IR absorption of the some of the initial fragment ions.²⁷ The maximum fragmentation efficiency for VISPD of H^+LF is of the order of a few percent ($\sim 2.5\%$ for the most intense fragment channel), and the total VISPD spectrum generated by adding all action spectra of the individual fragments shown in Fig. 2 is used for further analysis. The total VISPD yield amounts to around 10% suggesting reasonable overlap between the ion and laser beams. Interestingly, although the VISPD spectrum observed for the m/z 242 ion (loss

of CH_3) and the related m/z 199 ion (loss of $CH_3 + OCNH$) also matches the other action spectra well in the range from 23 130 to 23 750 cm^{-1} , we detect substantial unstructured signal in these particular channels down to at least 20 000 cm^{-1} (500 nm) indicating that the process leading to these fragments is different from the others (as already indicated by their different behaviour in IRMPD and VISPD mass spectra). Similarly, also for the other mass channels there is slowly decaying and structureless background fragmentation signal to the red of the first absorption peak. In general, cooling of the ions to temperatures below 20 K is sufficient to completely suppress hot band transitions and to measure well-resolved vibronic VISPD spectra for such biomolecular ions. The VISPD spectrum of H^+LF exhibits rich vibrational structure indicating substantial geometry changes upon electronic excitation.

To assign the electronic VISPD spectrum by TD-DFT calculations, we first optimize various low-energy protomers in their ground electronic state (S_0) and compute their vertical and adiabatic singlet excitations and their corresponding vibronic spectra. The proton affinities (PA), computed here as protonation

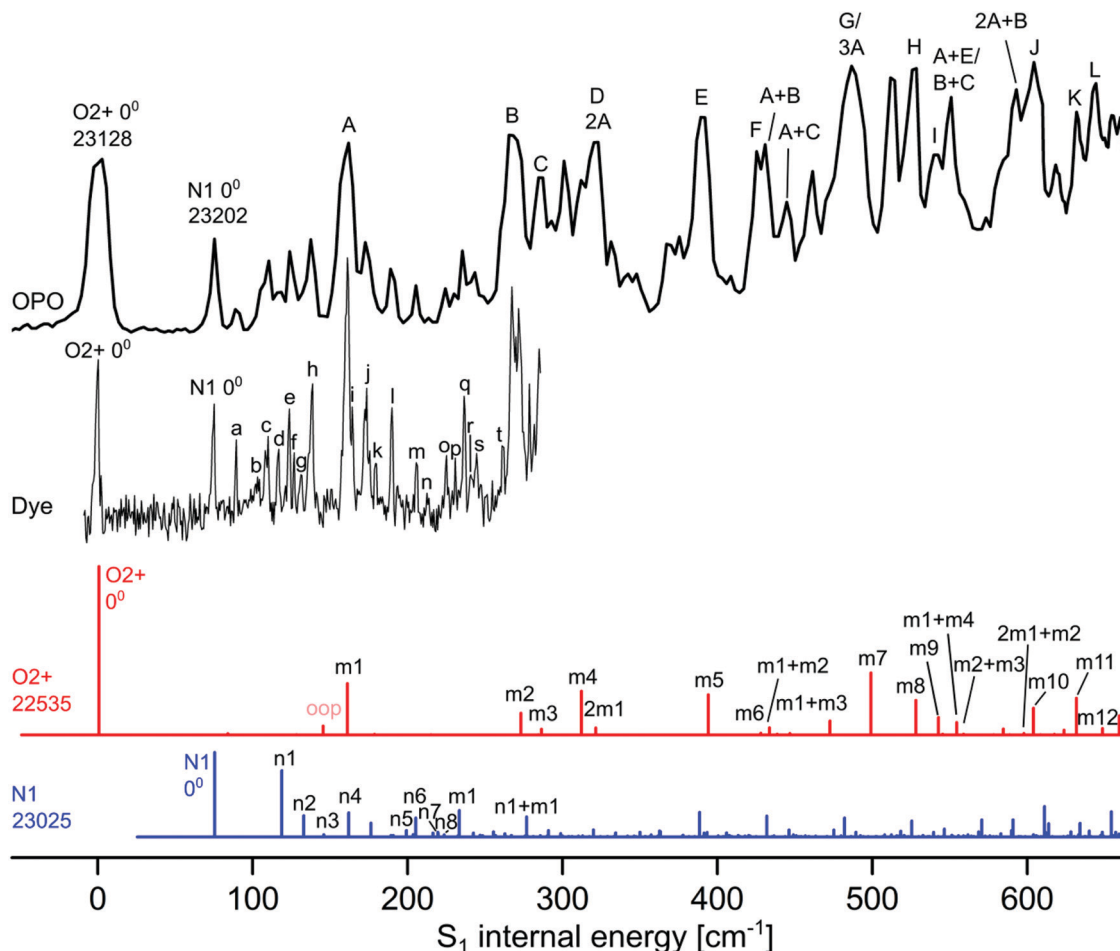


Fig. 2 Experimental VISPD spectrum of H^+LF recorded with the OPO and dye laser compared to Franck-Condon (FC) simulations of the two most stable protomers $O2^+$ (red) and $N1$ (blue). All spectra are referenced to the experimental S_1 internal energy of the $O2^+$ protomer. The absolute values of the origins are given in cm^{-1} . The calculated FC spectra are scaled vertically to match the associated intensity of the experimental S_1 origins. The calculated FC intensity of the $O2^+$ origin is one order of magnitude higher than that of the $N1$ protomer. Peak positions and suggested vibrational and isomer assignments are given in Tables 4 and 5.



Table 1 Proton affinities (PA) and relative energies (E_0) for the S_0 state of various protomers of H^+LF computed at the PBE0/cc-pVDZ level compared to data at the B3LYP/cc-pVDZ level (in kJ mol^{-1})

Protomer	PBE0/cc-pVDZ	B3LYP/cc-pVDZ
	PA (E_0)	PA (E_0)
O2+	971.7 (0)	974.0 (0)
N1	956.7 (15.0)	961.0 (13.0)
O2−	945.6 (26.1)	948.6 (25.4)
O4+	936.1 (35.6)	939.5 (34.5)
N5	919.8 (51.9)	924.6 (49.4)
OH++	944.6 (27.1)	945.4 (28.6)
OH+−	949.3 (22.4)	950.5 (23.5)
O4−	904.6 (67.1)	909.4 (64.6)

energies for $T = 0$ K, and the relative energies (E_0) in the S_0 ground state obtained for the most stable H^+LF protomers at the PBE0/cc-pVDZ level are listed in Table 1. The PBE0 values agree well with previously reported B3LYP data using the same basis set.²⁷ In the low-energy protomers shown in Fig. 1 and Fig. S3 in the ESI†, the proton is attached to one of the nucleophilic lone pairs of the N atoms (N1 and N5) or carbonyl O atoms (O2 and O4). For the O protonated tautomers, the \pm sign indicates the orientation of the OH proton with respect to the N3H group (+ away, − toward).²⁷ The most stable protomer is O2+ with PA = 972 kJ mol^{-1} , and the previous IRMPD spectrum was exclusively assigned to this H^+LF protomer.²⁷ The next protomer close in energy is N1 at $E_0 = 15$ kJ mol^{-1} , while all further protomers obtained by direct protonation of LF (O2−, N5, O4+, O4−) or protonation coupled to lactam–lactim tautomerization (OH+−, OH++), in which the N3H proton migrates to a CO group, are significantly higher in energy (> 22 kJ mol^{-1}). In the following, we focus mostly on the most stable O2+ and N1 tautomers, while corresponding results for higher energy protomers are given in the ESI†.

As a next step, we compute vertical excitation energies (E_v) and oscillator strengths (f) for the S_1 – S_4 states of the various H^+LF protomers (Table 2 and Fig. S4 in the ESI†). These excitations include optically bright $\pi\pi^*$ and optically dark $n\pi^*$ excitations of bonding aromatic π electrons and nonbonding lone pair electrons (n) of N and O into empty nonbonding π^* orbitals. Among the S_1 – S_4 states, there are two $\pi\pi^*$ and two $n\pi^*$ states. The oscillator strengths of the bright $\pi\pi^*$ states are

typically several orders of magnitude larger than those of the dark $n\pi^*$ states. Concerning the vertical transitions, the S_1 state is bright ($\pi\pi^*$), while the S_2 state is dark ($n\pi^*$) for all considered protomers, while the order of the second $\pi\pi^*$ and $n\pi^*$ states is switched for some of the tautomers. For O2+, the oscillator strength for $S_1(\pi\pi^*)$, $f = 0.063$, is two orders of magnitude higher than for S_2 ($f = 0.0007$), which is located 1951 cm^{-1} above S_1 . The second optically bright $S_3(\pi\pi^*)$ state lying 2850 cm^{-1} above S_1 has a substantially higher oscillator strength ($f = 0.34$) than S_1 , while $S_4(n\pi^*)$ at 4417 cm^{-1} above S_1 is again dark ($f = 0.0001$). The N1 tautomer has a similar electronic coarse structure as O2+. The bright $S_1(\pi\pi^*)$ state ($f = 0.025$) lies 435 cm^{-1} below the dark $S_2(n\pi^*)$ state ($f = 0.004$). The $S_3(\pi\pi^*)$ state is 2606 cm^{-1} above S_1 and again much brighter ($f = 0.39$). These results are in good accordance with quantum chemical calculations performed by other groups for related systems.^{9,13,15,39}

Direct comparison with the experimental vibronic spectra requires the computation of adiabatic excitation energies (E_a) and vibrational normal modes as input for the FC simulations. To this end, we optimized the S_1 and S_2 states for all considered protomers (Table 2 and Fig. S5 in the ESI†). The resulting S_1 origins are listed in Table 3, along with the protonation-induced shifts from S_1 of bare LF. The $S_1(\pi\pi^*)$ origin computed for LF as 22 448 cm^{-1} agrees well with the value measured in He droplets (21 511 cm^{-1}), which should be close to the origin of the bare molecule with an estimated error of less than 250 cm^{-1} .²⁰ The small difference between the experimental

Table 3 Comparison of adiabatic S_1 origin energies of LF and several H^+LF protomers (in cm^{-1}) along with their protonation-induced shifts (ΔS_1) calculated at the PBE0/cc-pVDZ level of theory compared to available experimental values

	S_1 calc.	ΔS_1 (calc.)	S_1 exp.	ΔS_1 (exp.)
LF	22 448	0	21 511 ^a	0
O2+	22 535	87	23 128	1617
N1	23 025	578	23 202	1691
O2−	22 341	−107		
O4+	17 682	−4766		
N5	15 622	−6826		
OH++	20 762	−1686		
OH+−	21 074	−1374		
O4−	18 046	−4402		

^a Value measured in He droplets (ref. 20).

Table 2 Vertical and adiabatic transition energies ($E_{v/a}$) of the first four excited singlet states of various protomers of H^+LF (in cm^{-1}), along with their oscillator strength (f) calculated at the PBE0/cc-pVDZ level

	$S_1(\pi\pi^*)$		$S_2(n\pi^*)$		$S_3(n\pi^*/\pi\pi^*)$		$S_4(n\pi^*/\pi\pi^*)$	
	E_v (E_a)	$f (\times 10^3)$	E_v (E_a)	$f (\times 10^3)$	E_v	$f (\times 10^3)$	E_v	$f (\times 10^3)$
LF	25 236 (22 448)	212.6	26 121 (21 620)	0.4	27 585	0.4	32 250	136.3
O2+	25 553 (22 535)	63.2	27 504 (23 703)	0.7	28 403	339.2	29 970	0.1
N1	26 388 (23 025)	25.4	26 823 (22 488)	3.6	28 994	385.3	30 227	1.8
O2−	25 295 (22 341)	67.7	27 453 (23 568)	0.8	28 322	334.7	30 491	0.0
O4+	20 229 (17 682)	95.4	26 568 (22 280)	0.2	26 724	239.3	28 613	0.0
N5	18 207 (15 622)	122.0	20 342 (14 731)	0.0	25 583	0.1	25 808	186.4
OH++	23 595 (20 762)	62.1	24 751 (20 828)	0.0	27 928 (26 389)	377.3	33 085	20.1
OH+−	23 987 (21 074)	51.4	25 125 (21 734)	0.2	28 305 (26 919)	404.2	34 001	1.0
O4−	20 683 (18 046)	87.5	25 701 (20 994)	0.4	26 948	263.0	29 828	0.0



and computed S_1 origins of $\sim 1000\text{ cm}^{-1}$ ($\sim 0.1\text{ eV}$) confirms that the chosen DFT level describes the electronic structure of this type of flavin well.^{31–33} In general, the protonation-induced ΔS_1 shifts depend strongly on the site of protonation and span a large range from -6826 to $+578\text{ cm}^{-1}$. Interestingly, for the N1 protomer the order of the excited S_1 and S_2 states changes, when going from vertical to adiabatic energies. Thus, for this protomer, the first dark $n\pi^*$ state is adiabatically located slightly lower than the first bright $\pi\pi^*$ state by 537 cm^{-1} (nonetheless, we keep herein the notation of the order of the states obtained from the vertical transitions). Significantly, only the S_1 origins of O2+ and N1 exhibit S_1 blueshifts upon protonation.

The total VISPD spectrum of H^+LF presented in Fig. 2 is referenced to the first peak at $23\,128\text{ cm}^{-1}$ (432.38 nm) observed in the range above $20\,000\text{ cm}^{-1}$ (below 500 nm), which is assigned to the origin band (0^0) of the observed electronic transition. This spectrum is recorded using the OPO laser with a spectral resolution of 4 cm^{-1} and maximal available intensity ($3\text{--}4\text{ mJ}$ per pulse at a beam diameter of 5 mm) at a step size of 2.5 cm^{-1} . The spectral range covers up to $\sim 600\text{ cm}^{-1}$ of S_1 internal energy. A higher-resolution spectrum covering the first $\sim 300\text{ cm}^{-1}$ is also recorded using the dye laser with a spectral resolution of 0.014 cm^{-1} and similar intensity (3 mJ per pulse at a beam diameter of 5 mm) at a step size of $\sim 0.5\text{ cm}^{-1}$ (Fig. 2). The peak positions and suggested vibrational and protomer assignments are given in Tables 4 and 5. The OPO spectrum shows a series of broader transitions ($\sim 10\text{ cm}^{-1}$) labelled with capital letters A–L built on the origin at 0 cm^{-1} internal energy, along with a series of significantly narrower transitions ($\sim 5\text{ cm}^{-1}$) starting from an origin at 75 cm^{-1} and labelled with lowercase letters (a–t). These two series are assigned to the $S_1 \leftarrow S_0(\pi\pi^*)$ electronic transitions of the two most stable O2+ and N1 protomers of H^+LF , respectively. Their derived S_1 origins of $23\,128$ and $23\,202\text{ cm}^{-1}$ agree well with the predicted values of $22\,535$ and $23\,025\text{ cm}^{-1}$, respectively. The experimental blueshifts with respect to LF of $\Delta S_1 = 1617$ and 1691 cm^{-1} are in accord with the computed shifts of $\Delta S_1 = 87$ and 578 cm^{-1} , when taking into account the error in both experiment (effect of the He droplet on

Table 5 Experimental frequencies (in cm^{-1}) in the S_1 state of $\text{H}^+\text{LF(N1)}$ compared to harmonic values computed at the PBE0/cc-pVDZ level

Band	ν (exp.)	ν (calc.)	Assignment
0^0	23 202	23 025	0^0
a	15		
b	29		
c	36	43	n1
d	42		
e	49	58	n2
f	52		
g	57		
h	63	70	n3
i	90		
j	98	87	n4
k	105		
l	115	124	n5
m	131	132	n6
n	139		
o	150	144	n7
p	156	148	n8
q	162	158	m1
r	166		
s	170		
t	187		

the S_1 origin of LF)²⁰ and computation. The previous VISPD study on the $S_1 \leftarrow S_0$ transitions of the related O4+ protomers of M^+LF ($\text{M} = \text{Li–Cs}$) using the same computational approach yields differences of less than 650 cm^{-1} between measured and computed adiabatic S_1 origins.³³ Additionally, deviations in the same order of magnitude have been reported for the S_1 transitions of $\text{H}^+\text{LC(N5)}$ (809 cm^{-1}) and $\text{M}^+\text{LC(O4+)}$ (up to 1154 cm^{-1}).^{31,32} Clearly, the S_1 origins predicted for the other H^+LF protomers fit less well. In particular, the computed S_1 origins of the N5 and O4± tautomers exhibit large redshifts of $\sim 4000\text{--}7000\text{ cm}^{-1}$, similar to those observed for O4+ of M^+LF .³³ The OH± tautomers also have substantial computed S_1 redshifts of $\sim 1500\text{ cm}^{-1}$. The only other protomer with a predicted nearby S_1 origin is O2– with $\Delta S_1 = -107\text{ cm}^{-1}$. As expected, the S_n energies of the O2± tautomers are similar (as are those of O4±) because their electronic structure is not much affected by the different orientation of the excess proton. However, we may exclude O2– at this stage from an assignment to any of the two identified S_1 origins, because of its significantly higher energy relative to O2+ ($\Delta E_0 = 26\text{ kJ mol}^{-1}$). For the N1 and O2± isomers, the second optically bright $S_3(\pi\pi^*)$ state is predicted to be substantially higher in energy than S_1 (by $\Delta E_v = 2606\text{--}3027\text{ cm}^{-1}$) so that we can also safely exclude this option. On the other hand, the S_3 states of the N5 and O4± are calculated to be nearby considering their vertical energies (Table 2). Unfortunately, all efforts to optimize these higher excited states have failed (because of running into conical intersections) so that we cannot predict the adiabatic transition energies. Thus, we may at this stage exclude this option just by their rather low stability ($E_0 > 35\text{ kJ mol}^{-1}$). In case of the other high-energy OH± protomers, the bright S_3 states have predicted adiabatic origins far away from the observed transitions ($> 3000\text{ cm}^{-1}$) so that an assignment of these isomers may safely been rejected. An assignment to a triplet state appears unlikely (Fig. S4 in the ESI†). In summary, by considering both

Table 4 Experimental frequencies (in cm^{-1}) in the S_1 state of $\text{H}^+\text{LF(O2+)}$ compared to harmonic values computed at the PBE0/cc-pVDZ level and corresponding data of LF

Band	ν (exp.)	ν (calc.)	Assignment	LF (exp.) ^a	LF (calc.)
0^0	23 128	22 535	0^0	21 511	22 448
A	160	160	m1	164	165
B	268	272	m2	274	276
C	285	286	m3		294
D	317	312	m4		322
E	389	393	m5	403	409
F	425	427	m6	440	444
G	486	498	m7		489
H	526	527	m8	513	521
I	539	542	m9		545
J	603	603	m10	593	603
K	633	631	m11		635
L	645	648	m12		669

^a Data measured in He droplets (ref. 20).



the predicted optically bright adiabatic and vertical S_1 and $S_{3/4}$ energies and the relative stabilization energies, the only assignment of the band origins observed at 23 128 and 23 202 cm^{-1} is to S_1 of the two most stable O2+ and N1 protomers and we adapt this scenario for the remaining analysis.

The magnitude and direction of the S_1 shifts upon protonation for the different H^+LF protomers can be rationalized by the molecular orbitals involved in the first $\pi\pi^*$ excitation and the resulting charge reorganisation. To this end, we consider in Fig. 3 the natural transition orbitals (HOMO and LUMO) for LF and the O2+ and N1 protomers of H^+LF and in Fig. S6 and Table S2 in the ESI† the NBO charge distribution in both electronic states of LF. S_1 excitation of LF decreases the negative charge on both N1 (by 0.152 e from -0.660 to -0.508 e) and O2 (by 0.028 e from -0.598 to -0.570 e). Thus, S_1 excitation reduces the attraction of the proton at these binding sites, leading to a reduced proton affinity in the S_1 state, which directly translates into the S_1 blueshifts for the two protomers N1 and O2+ (and also the small redshift for O2−). On the other hand, S_1 excitation increases the negative partial charge on N5 (by 0.078 e from -0.376 to -0.454 e) and O4 (by 0.015 e from -0.577 to -0.592 e), which increases the proton affinity and thus produces S_1 redshifts for N5 and O4+ (and also O4−). This view is confirmed by the molecular orbital wavefunctions in Fig. 3, which show large changes in the amplitudes near O4 and N5 but only small ones near O2 and N1, explaining the large S_1 redshifts for N5 and O4± and the small blueshifts (redshift) for N1 and O2+ (O2−) upon protonation.

In the next step, we assign the vibrational structure in the S_1 state of the O2+ protomer by comparison to FC simulations (Fig. 2). As already mentioned, the broader peaks in the OPO spectrum are attributed to this most stable protomer, and the FC simulations provide convincing evidence for this assignment

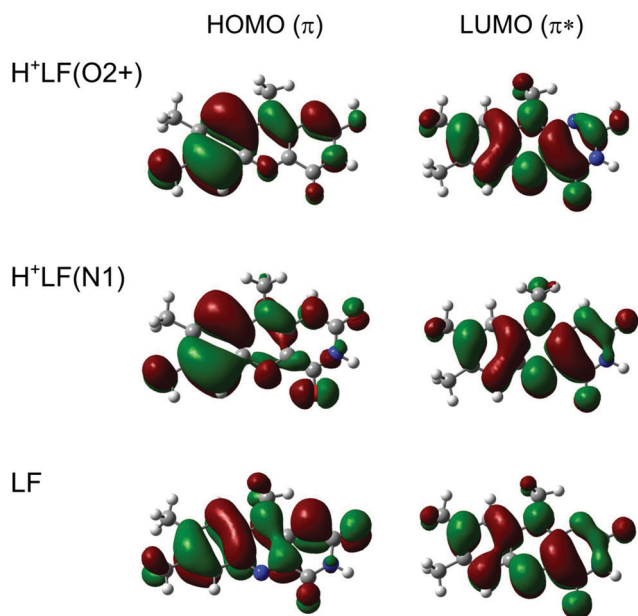


Fig. 3 Natural transition orbitals involved in the electronic $S_1 \leftarrow S_0(\pi\pi^*)$ transition of LF, $\text{H}^+\text{LF}(\text{O2+})$, and $\text{H}^+\text{LF}(\text{N1})$ calculated at the PBE0/cc-pVDZ level.

(Table 4). Apart from the three CH_3 groups, $\text{H}^+\text{LF}(\text{O2+})$ is planar in both the S_0 and S_1 states (C_s), so that only modes with a' symmetry are FC active. This includes all in-plane fundamentals, their combination bands and their overtones. Moreover, even quanta of out-of-plane modes (a'') are also FC allowed. Indeed, the O2+ protomer has 12 a' fundamentals below 650 cm^{-1} and all are observed in the VISPD spectrum (A–L, m1–m12, Table 4) with various intensities. A full set of calculated vibrational frequencies sorted by symmetry for the S_0 and S_1 states for both protomers (O2+ and N1) is available in the ESI† (Tables S3 and S4). The experimental frequencies of O2+ agree well with the computed values, with maximum and average deviations of 12 and 3 cm^{-1} , respectively. In addition, the relative intensities of fundamentals and overtone/combination bands predicted by the FC simulations reproduce satisfactorily the measured pattern. Some deviations in relative intensities may result from power broadening and saturation effects described below. The overall convincing agreement confirms the given isomer assignment and illustrates again the suitability of the computational approach. The normal modes denoted m1–m12 were described in some detail in our previous study on M^+LF clusters and are shown in Fig. S7 and S8 in the ESI† for LF and $\text{H}^+\text{LF}(\text{O2+})$.³³ The three modes associated with the excess proton are the in-plane OH stretch and bend modes, which are outside the investigated spectral range ($\sigma_{\text{OH}} = 3779$ cm^{-1} , $\beta_{\text{OH}} = 1208$ cm^{-1}), and the out-of-plane OH torsion, which is FC forbidden ($\tau_{\text{OH}} = 537$ cm^{-1}). The observed m1–m12 modes are essentially in-plane ring deformation modes of the LF moiety and only little affected by the excess proton at O2. Thus, their frequencies deviate only little from those of bare LF, with maximum and average differences of 21 and 9 cm^{-1} , respectively. Indeed, the vibrational structure of the LIF excitation spectrum of the S_1 state of LF in He droplets²⁰ is very similar to the VISPD spectrum of the $\text{H}^+\text{LF}(\text{O2+})$ protomer with respect to both the band positions and intensities (Fig. S9 in the ESI†), indicating that the same electronic $\pi\pi^*$ transition is observed in both molecules. This view is further confirmed by the molecular orbitals involved in this $S_1 \leftarrow S_0$ transition, which have essentially no amplitude at the excess proton. For example, the LIF spectrum of LF is dominated by progressions of mode m1 = 164 cm^{-1} with several other fundamentals,²⁰ and the corresponding progression for $\text{H}^+\text{LF}(\text{O2+})$ has a frequency of m1 = 160 cm^{-1} . The m1 mode is an in-plane bending motion of the outer aromatic rings I and III. Mode m2 describes a rocking motion of the methyl group at C8 coupled to a shear deformation of ring II. Mode m3 is similar to mode m2 but contains mainly a rocking motion of the methyl group at C7. For details of all detected in-plane normal modes m1–m12 the reader is referred to Fig. S8 in the ESI.† The FC simulations of the O2+ protomer predict a few low-intensity combination bands and overtones of out-of-plane (oop) modes with a'' symmetry, for example at 84 and 144 cm^{-1} (2×42 and 2×72 cm^{-1}). As expected for an electronic transition between two states with C_s symmetry, their FC activity is rather weak.

In addition to the broad transitions in the OPO spectrum labelled A–L, which are readily assigned to the O2+ protomer by the FC simulations, there are many sharper transitions starting from the band at 75 cm^{-1} internal energy. They are better



resolved in the spectrum recorded with the dye laser and some 20 transitions are detected below 300 cm^{-1} (Fig. 2). These rather intense transitions are not predicted by the FC simulations for the O2+ protomer. Most of them could, in principle, be explained by FC forbidden a'' modes of the O2+ protomer (and combinations thereof) and such an assignment is presented in Table S5 in the ESI†. The only explanation for such pronounced transitions is vibronic coupling of the $S_1(\pi\pi^*)$ state with a dark $n\pi^*$ state. For example, the $S_2(n\pi^*)$ state of O2+ is calculated to be only 1168 cm^{-1} above the $S_1(\pi\pi^*)$ state. Although, we cannot exclude such a scenario, it is not favoured here because it is difficult to rationalize such high-intensity FC forbidden transitions by vibronic coupling, while the FC approximation works well for the in-plane modes. Moreover, the rather different widths of the transitions point toward two different species or two different electronic states. Initially, the VISPD spectrum has been measured at the highest laser intensities available to detect as many transitions as possible. In the OPO spectrum measured with 4 mJ per pulse, the widths of the band origins at 0 and 75 cm^{-1} are 13.7 and 4.3 cm^{-1} , respectively. The latter value is close to the bandwidth of the laser ($\sim 4\text{ cm}^{-1}$). Other factors contributing to the large width of the origin at 0 cm^{-1} include lifetime broadening, unresolved rotational substructure, and power broadening. The widths of the two transitions in the spectrum taken with the dye laser decrease to 2.6 and 1.4 cm^{-1} at reduced laser power, indicating that most of the large width of the O2+ transitions in the OPO spectrum arises from power broadening rather than from a short lifetime. However, at any laser power tried (until the signal disappears at the achieved signal-to-noise ratio), the transition at 0 cm^{-1} is broader than that at 75 cm^{-1} .

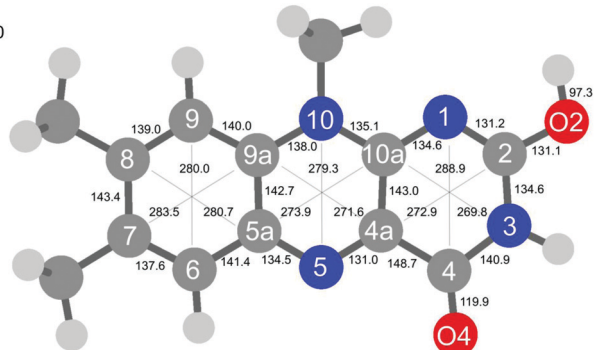
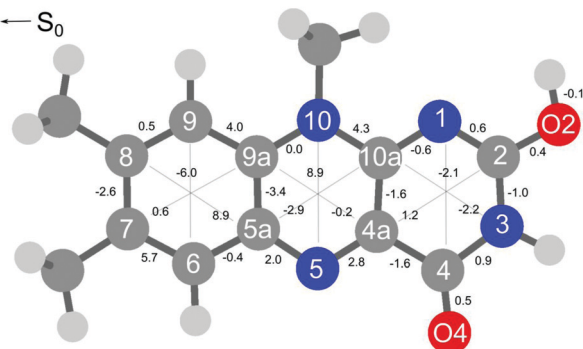
Our mass spectra do not show any evidence for cluster formation of mass-selected H^+LF ions stored in the cold trap during He buffer gas cooling. Thus, we can exclude any $\text{H}^+\text{LF}(\text{O2+})\text{-L}_n$ clusters (e.g., $\text{L} = \text{He}, \text{N}_2$, or H_2O) as carriers for the sharp bands in the OPO spectrum. Thus, as an alternative and here favoured interpretation, these transitions are attributed to another protomer of H^+LF , namely the second most stable N1 protomer, which is rather low in energy ($E_0 = 15\text{ kJ mol}^{-1}$). Interestingly, the N1 protomer is slightly nonplanar in both the S_0 and S_1 excited state, leading to a reduction in symmetry from C_s to C_1 upon protonation.¹⁵ The N1 protomer is slightly bent along the N5–N10 axis leading to a butterfly-type deformation, which is somewhat more pronounced in the S_1 state than in the S_0 state (7° versus 3°). Moreover, the CH_3 group at N10 rotates out of the plane (by $\sim 30^\circ$), probably because of steric hindrance between the H atom that is in the aromatic plane of neutral LF and the excess proton added at N1. The barrier to planarity is rather small, and amounts to $V_b = 1.6/0.4\text{ kJ mol}^{-1}$ at the transition state with C_s symmetry in the S_0/S_1 state with an imaginary frequency of $i113/i137\text{ cm}^{-1}$ for the concerted motion of CH_3 rotation and bending of the aromatic ring. The close proximity of the excess proton in O2+ and N1 leads to a double minimum potential for proton transfer. The barrier for this tautomerization process is very high in both the S_0 and S_1 states ($V_b = 156$ and 157 kJ mol^{-1} for $\text{O2+} \rightarrow \text{N1}$ in S_0 and S_1) so that these

isomers can be treated as two distinct protomers cooling down in their own deep potential wells.

The vibronic $S_1 \leftarrow S_0$ spectrum predicted for the N1 protomer by the FC simulations is compared in Fig. 2 to the VISPD spectrum of H^+LF . We reiterate that the order between the lowest bright $\pi\pi^*$ and dark $n\pi^*$ excited states changes for this protomer when going from vertical to adiabatic excitations, and that the bright $\pi\pi^*$ state is in fact the S_2 state. The origin of the computed spectrum is aligned with the peak at 75 cm^{-1} internal energy, requiring a redshift of merely 177 cm^{-1} for the origin calculated at $23\,025\text{ cm}^{-1}$. The calculated FC spectra are scaled vertically to match the associated intensity of the experimental S_1 origins. The calculated FC intensity of the O2+ origin is one order of magnitude higher than that of the N1 protomer, while the oscillator strengths differ by a factor of only 2.5 (0.063 versus 0.025). This difference may indicate a somewhat higher abundance of the more stable O2+ protomer, although it is rather difficult to estimate the abundance ratio of both protomers in a more quantitative fashion because of different FC pattern and possibly different photodissociation cross sections. Due to the loss of symmetry, all modes of the N1 protomer become FC allowed, and thus the density of predicted transitions is much greater than for the O2+ protomer. This is particularly noticeable in the vicinity of the S_1 origins, because the low-frequency out-of-plane fundamentals forbidden for O2+ become allowed and quite active for N1. The FC simulations for N1 clearly do not match the experimental spectrum with the same quality as the corresponding simulations for O2+ with respect to both frequency and relative intensities. A tentative assignment for the transitions a–t is suggested in Table 5. The first four modes (n1–n4) above the S_1 origin are predicted at $43, 58, 70$, and 87 cm^{-1} , with corresponding experimental frequencies of 36 (c), 49 (e), 63 (h), and 98 (j) cm^{-1} , respectively. Mode n1 is a butterfly motion describing the motion leading to nonplanarity of the molecular ion, while mode n2 describes shearing or twisting of the tricyclic ring around its long axis. Mode n3 corresponds to a hindered internal rotation of the CH_3 group at C7, while mode n4 is a rocking motion of the whole CH_3 group at N10 (see Fig. S10 in the ESI† for a graphical representation of the a'' normal modes). There are more peaks in the experimental spectrum than in the FC simulation, such as the low-frequency transition at 15 cm^{-1} (a). We find indeed several pronounced transitions with a spacing of $14\text{--}16\text{ cm}^{-1}$, which may indicate a very low-frequency out-of-plane mode not properly predicted by the harmonic calculations. Several reasons may cause the failure of the simple harmonic FC calculations of these low-frequency a'' modes. First, the barrier of the bent N1 structure to linearity is rather low in both S_0 and S_1 ($< 2\text{ kJ mol}^{-1}$), which may cause substantial errors in the harmonic force field and/or large anharmonic corrections for the butterfly motion (mode n1) and resulting FC intensities. Second, several low-frequency modes involve hindered internal methyl rotations,⁴⁰ which may not be described well by the harmonic approach. Third, out-of-plane modes may be affected by vibronic coupling to the dark $n\pi^*$ state lying just 537 cm^{-1} below the bright $\pi\pi^*$ state.



ORTEP diagram of the crystal structure of 1,2-bis(4-oxo-4H-chromen-3-yl)ethane. The diagram shows the molecular structure with thermal ellipsoids at the 50% probability level. Displacement ellipsoid axes are labeled S_0 , S_1 , and S_2 . Bond lengths (Å) and angles (°) are provided for the structure.

 S_0 
$$S_1 \leftarrow S_0$$


contraction of the C6–C9 axis of -6.0 and -5.8 pm. Ring II elongates along the N5–N10 axis by 8.9 (O2+) and 6.8 pm (N1). Ring III, where the excess proton is located in both protomers, experiences a smaller deformation. We find as a maximum change a contraction of the N3–C10a distance of 2.2 pm (O2+) and 3.1 pm (N1). The two C=O bonds elongate by 0.4 – 0.5 pm in O2+ and N1. As expected, the changes in the O–H and N–H bond lengths of the excess proton are negligible (≤ 0.1 pm) for both protomers. According to the FC principle, these structural changes upon electronic excitation translate directly into the excitation of the vibronic transitions. For example, the geometry changes of O2+ reflect closely the amplitudes of normal mode m1, giving rise to the progression observed in the electronic spectrum. Concerning the N1 protomer, the angles between the planes of ring I and III with a folding axis along N5–N10 decreases from 177° in S_0 to 173° in S_1 , thus inducing excitation of the butterfly mode c.

This journal is © the Owner Societies 2020

second C4–O4 bond slightly contracts (by 1.2 pm). On the other hand, N1 protonation hardly affects the C–O bond lengths, with a small contraction of 1.2 pm. As expected protonation at both N1 and O2+ has a large impact on the skeleton of ring III due to changes in the conjugation. Protonation at O2+ substantially contracts the C4a–C2 axis (by 9.5 pm) and to a smaller extent the N1–C4 axis (by 1.4 pm), while the N3–C10a axis slightly elongates (by 2.0 pm). Protonation at N1 deforms ring III in a different way. The N1–C4 distance contracts by 7.9 pm and the N3–C10a axis is stretched by 8.2 pm, while the third axis C4a–C2 is less affected (by +3.6 pm). In the earlier IRMPD study of H⁺LF, the CO stretching frequencies are used as a sensitive indicator for the proton binding sites.²⁷

The substitution of functional groups, protonation, and metalation has a large impact on the photophysical properties of flavins. To this end, it is instructive to compare the H⁺LF results obtained herein with those previously obtained for H⁺LC and M⁺LF.^{31,33} LC differs from LF such that LC has no functional group at N10 but a H atom at N1, while LF has a CH₃ group at N10 and no group at N1. Consequently, the N1 position is not available for protonation of LC. Instead, IRMPD and VISPD spectra of H⁺LC reveal preferred protonation at N5, in line with quantum chemical calculations, and only the most stable H⁺LC(N5) protomer has been detected so far. Thus, when going from LC to LF, the preferred protonation site changes from N5 to O2+/N1. This switch in protonation site has a drastic effect on the optical spectrum, and herein we consider specifically the behaviour of the lowest $\pi\pi^*$ state. While N5 protonation of LC induces a drastic redshift in the S₁ excitation energy (by around 6000 cm⁻¹ from ~25 000 to 19 962 cm⁻¹ or by 51 nm from ~400 to 501 nm), protonation of LF at O2+ and N1 causes a smaller blueshifts (of the order of ~1500 cm⁻¹ from ~21 500 to ~23 000 cm⁻¹ or by ~30 nm from ~465 to ~435 nm). Actually, the molecular orbitals involved in S₁ excitation of LC and LF do not differ much,³³ and thus the magnitude and direction of the shifts upon protonation at the same protonation site are not so different for LC and LF (Table S6 in the ESI[†]). For example, large ΔS_1 redshifts are also predicted herein for N5 and O4+ protonation of LF (6826 and 4766 cm⁻¹, Table 2), with predicted S₁ origins at 15 622 and 17 682 cm⁻¹ (640 and 565 nm), a spectral range not yet investigated. However, the H⁺LF(N5) and H⁺LF(O4+) protomers are relatively high in energy ($E_0 = 52$ and 36 kJ mol⁻¹) and were thus not been detected in the previous IRMPD study.²⁷ Similarly, the calculated S₁ energies of LC/LF(O2+) are quite similar (22 422/22 535 cm⁻¹) but again the H⁺LC(O2+) protomer has not been identified in its IRMPD spectrum because of its elevated relative energy ($E_0 = 70$ kJ mol⁻¹).^{27,31} As a result of the different protonation sites and position of the functional H/CH₃ groups, the fragmentation processes of H⁺LC(N5) and H⁺LF(O2+/N1) upon VISPD are rather different. While for H⁺LC only two main fragments are observed, namely loss of CO + NH₃ (or HCN + H₂O) and loss of OCNH + CO, the photodissociation mass spectrum of H⁺LF(O2+/N1) is much richer, with many more fragmentation channels, indicating that the ring opening process upon VISPD is quite different for both protonated flavins.

In recent IRMPD experiments for M⁺LF with M = Li–Cs, the O4+ and O2(+) isomers have been identified by their characteristic CO stretch frequencies.²⁸ In these metalated ions, which are isovalent to H⁺LF, the smaller alkali cations Li–K are large enough to simultaneously benefit from interacting with the nucleophilic lone pairs of the neighboring N and carbonyl O atoms by forming chelates of the type O4–M–N5 and O2–M–N1. Thus, there is only a single potential minimum between O2 and N1 and between O4 and N5. The ionic radius of the larger alkali ions Rb–Cs causes Pauli repulsion with the CH₃ group at N10, so that no O2–M–N1 chelate can be formed, and the resulting O2 isomers feature a linear C2–O2–M bond. In contrast, the proton is much smaller than all alkali ions, and thus double minimum potentials are developed for H⁺LF, with two deep minima separated by high barriers for the N1 and O2+ as well as the N5 and O4+ protomers. In general, the O4+ and O2(+) isomers of M⁺LF have quite similar stabilities to within $\Delta E_0 \leq 16$ kJ mol⁻¹. The VISPD spectra of M⁺LF(O4+) exhibit large metalation-induced S₁ redshifts of 2480–3866 cm⁻¹ for M = Cs–Li from the S₁ origin of bare LF, which increase in magnitude for decreasing ionic radii of M.³³ In line with this trend, the protonation-induced redshifts predicted for H⁺LF(O4+/N5) are even larger (4766/6826 cm⁻¹). For the O2(+) isomers of M⁺LF, much smaller ΔS_1 blueshifts of 710–1048 cm⁻¹ are calculated,³³ and preliminary unpublished VISPD spectra confirm this prediction. The calculated corresponding protonation-induced blueshifts are of similar magnitude (87 and 578 cm⁻¹ for O2+ and N1), in line with the experimentally estimated values (1617 and 1691 cm⁻¹). The fragmentation processes upon VISPD of the isovalent M⁺LF and H⁺LF are quite different. While M⁺LF fragments exclusively into M⁺ and LF by simply breaking the mostly electrostatic M⁺···LF bond (with binding energies of $D_0 = 150$ –300 kJ mol⁻¹), the proton affinities of the O2+ and N1 protomers of H⁺LF are much larger (PA = 957–972 kJ mol⁻¹), leading to a more complex fragmentation pattern involving ring opening processes. The detailed mechanism for VISPD of the H⁺LF protomers remains unclear. Measurements of the VISPD yield as a function of laser power indicate a linear dependence rather than a quadratic one (Fig. S14 in the ESI[†]). This result may be taken as evidence for single-photon dissociation, which for example may involve S₁ excitation followed by internal conversion to the S₀ state and statistical dissociation on this ground state. However, the VISPD mass spectra differ from those of the CID and IRMPD process, suggesting dissociation upon visible excitation occurs on an excited state potential. This may occur by electronic predissociation from S₁ to the continuum of S₀ (one-photon process) or by resonant two-photon or multiphoton excitation *via* S₁ to a higher excited S_n state followed by dissociation. While a quadratic or higher order dependence would be indicative of the latter process, the observed linear dependence is consistent with both scenarios.

In general, the absorption spectra of flavins and their derivatives recorded in the condensed and gas phase at room temperature are broad and without any vibrational structure. Thus, they do not provide reliable and precise information about the nature of the observed electronic states and the impact of the environment on their photophysical properties. In contrast, early work in cryogenic



matrices demonstrated that cryogenic cooling to low temperature is required to achieve vibronic spectra of the excited states.¹⁹ The only spectroscopic work on cryogenic flavins includes the LIF spectrum of LF recorded in He droplets²⁰ and our VISPD spectra on protonated and metalated flavin cations recorded in cryogenic ion traps.^{30–33} To illustrate the effect of isolating and cooling the flavin ion, the cryogenic VISPD spectrum of isolated H⁺LF measured herein is compared in Fig. S15 in the ESI† to the absorption spectrum of H⁺LF in aqueous solution at room temperature, in which the protonated flavin is generated at low pH.¹¹ Significantly, while the VISPD spectrum reveals numerous vibronic transitions in the spectral range 420–440 nm with the S₁ origins of the O2+ and N1 protomers at 432.38 and 431.00 nm, the solution phase spectrum exhibits a single broad transition peaking at 394 nm with a width of ~60 nm and no information about the protonation site (although the authors assume N1 protonation).¹¹ Our vertical transition energies computed for the O2+ and N1 protomers (E_v = 391 and 379 nm) are within 3 and 15 nm of the solution-phase spectrum, suggesting that hydration effects are probably not very substantial. It is however difficult to extract any reliable quantitative information about the solvation effects on the S₁ transition energy. To this end, future spectroscopic measurements of microhydrated H⁺LF-(H₂O)_n clusters under controlled solvation conditions are required.

4. Concluding remarks

Herein, we present the first optical spectrum of isolated protonated lumiflavin (H⁺LF), the simplest member of the photochemically important flavin family. The vibronic spectrum, measured by electronic photodissociation (VISPD) of cold ions in a tandem mass spectrometer coupled to an electrospray source and a cryogenic ion trap, exhibits rich vibrational structure arising from large geometry changes upon electronic excitation. The analysis of the measured VISPD spectrum by TD-DFT calculations coupled to multidimensional FC simulations suggests an assignment of the spectral features near 430 nm to the optically bright S₁ ← S₀($\pi\pi^*$) transition of the two most stable H⁺LF tautomers protonated at either the O2+ or the N1 position (E_0 = 0 and 15 kJ mol⁻¹), with band origins at 23 128 and 23 202 cm⁻¹, respectively. While the O2+ global minimum has been identified in previous IRMPD experiments, the less stable N1 local minimum separated by a large barrier of ~150 kJ mol⁻¹ is assigned herein for the first time. Although this discrepancy may be due to different ESI conditions in the two studies (IRMPD *versus* VISPD), we ascribe the detection of the less stable isomer by the much higher spectral resolution and sensitivity of cryogenic electronic spectroscopy compared to the room-temperature IRMPD approach. While the planar O2+ protomer has C_s symmetry with a regular FC pattern in totally symmetric in-plane modes, the N1 isomer is slightly bent giving rise to a much denser vibronic structure produced by low-frequency out-of-plane modes. The observed modest blue-shifts in the S₁ origins upon protonation are in line with the molecular orbitals involved in this $\pi\pi^*$ transition and the related atomic charge distributions of both electronic states,

which are indicative of a small reduction of the proton affinity in the excited electronic state of both protomers. In that sense, the O2+ and N1 tautomers of H⁺LF show a rather similar photochemical response. Their spectral behaviour is, however, very different from that of the related H⁺LC ion, which prefers protonation at N5 and thus has a drastically different optical spectrum, confirming that substitution of flavins with functional groups can indeed drastically change their photochemical properties. Future efforts of extending this work include (i) the confirmation of the detection of the two different H⁺LF tautomers by double resonance techniques (IR-VIS or VIS-VIS), (ii) the study of larger flavin ions with higher biochemical relevance such as FMN and FAD, and (iii) the investigation of microsolvated flavin ions with particular focus on hydration.

Conflicts of interest

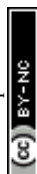
There are no conflicts to declare.

Acknowledgements

This study was supported by Deutsche Forschungsgemeinschaft (DFG, project DO 729/6-2). We thank Alkwin Slenczka for providing a digital version of the spectrum of LF.

References

- 1 V. Massey, *Biochem. Soc. Trans.*, 2000, **28**, 283.
- 2 P. F. Heelis, *Chem. Soc. Rev.*, 1982, **11**, 15.
- 3 A. Losi, *Photochem. Photobiol.*, 2007, **83**, 1283.
- 4 A. Losi and W. Gärtner, *Photochem. Photobiol.*, 2011, **87**, 491.
- 5 A. Sancar, *Chem. Rev.*, 2003, **103**, 2203.
- 6 W. Buckel and R. K. Thauer, *Chem. Rev.*, 2018, **118**, 3862.
- 7 E. Romero, J. R. Gómez Castellanos, G. Gadda, M. W. Fraaije and A. Mattevi, *Chem. Rev.*, 2018, **118**, 1742.
- 8 K. H. Dudley, A. Ehrenberg, P. Hemmerich and F. Müller, *Helv. Chim. Acta*, 1964, **47**, 1354.
- 9 E. Sikorska, I. V. Khmelinskii, W. Prukla, S. L. Williams, M. Patel, D. R. Worrall, J. L. Bourdelande, J. Koput and M. Sikorski, *J. Phys. Chem. A*, 2004, **108**, 1501.
- 10 W. Holzer, J. Shirdel, P. Zirak, A. Penzkofer, P. Hegemann, R. Deutzmann and E. Hochmuth, *Chem. Phys.*, 2005, **308**, 69.
- 11 A. Tyagi and A. Penzkofer, *J. Photochem. Photobiol., A*, 2010, **215**, 108.
- 12 A. Tyagi and A. Penzkofer, *Photochem. Photobiol.*, 2011, **87**, 524.
- 13 C. Neiss, P. Saalfrank, M. Parac and S. Grimme, *J. Phys. Chem. A*, 2003, **107**, 140.
- 14 J. Hasegawa, S. Bureekaew and H. Nakatsuji, *J. Photochem. Photobiol., A*, 2007, **189**, 205.
- 15 S. Salzmann and C. M. Marian, *Chem. Phys. Lett.*, 2008, **463**, 400.
- 16 S. Salzmann, J. Tatchen and C. M. Marian, *J. Photochem. Photobiol., A*, 2008, **198**, 221.
- 17 M. Meyer, H. Hartwig and D. Schomburg, *J. Mol. Struct.: THEOCHEM*, 1996, **364**, 139.



- 18 E. Sikorska, I. V. Khmelinskii, J. Koput, J. L. Bourdelande and M. Sikorski, *J. Mol. Struct.*, 2004, **697**, 137.
- 19 R. J. Platenkamp, H. D. van Osnabrugge and A. J. W. G. Visser, *Chem. Phys. Lett.*, 1980, **72**, 104.
- 20 A. Vdovin, A. Slenczka and B. Dick, *Chem. Phys.*, 2013, **422**, 195.
- 21 M. H. Stockett, *Phys. Chem. Chem. Phys.*, 2017, **19**, 25829.
- 22 E. Matthews, R. Cercola and C. E. H. Dessent, *Molecules*, 2018, **23**, 2036.
- 23 K. Lincke, J. Langeland, A. Ø. Madsen, H. V. Kiefer, L. Skov, E. Gruber, K. V. Mikkelsen, L. H. Andersen and M. B. Nielsen, *Phys. Chem. Chem. Phys.*, 2018, **20**, 28678.
- 24 J. N. Bull, E. Carrascosa, L. Giacomozzi, E. J. Bieske and M. H. Stockett, *Phys. Chem. Chem. Phys.*, 2018, **20**, 19672.
- 25 E. Matthews and C. E. H. Dessent, *J. Phys. Chem. Lett.*, 2018, **9**, 6124.
- 26 L. Giacomozzi, C. Kjær, J. L. Knudsen, L. H. Andersen, S. B. Nielsen and M. H. Stockett, *J. Chem. Phys.*, 2018, **148**, 214309.
- 27 J. Langer, A. Günther, S. Seidenbecher, G. Berden, J. Oomens and O. Dopfer, *ChemPhysChem*, 2014, **15**, 2550.
- 28 P. Nieto, A. Günther, G. Berden, J. Oomens and O. Dopfer, *J. Phys. Chem. A*, 2016, **120**, 8297.
- 29 A. Günther, P. Nieto, G. Berden, J. Oomens and O. Dopfer, *Phys. Chem. Chem. Phys.*, 2014, **16**, 14161.
- 30 A. Günther, P. Nieto, D. Müller, A. Sheldrick, D. Gerlich and O. Dopfer, *J. Mol. Spectrosc.*, 2017, **332**, 8.
- 31 A. Sheldrick, D. Müller, A. Günther, P. Nieto and O. Dopfer, *Phys. Chem. Chem. Phys.*, 2018, **20**, 7407.
- 32 P. Nieto, D. Müller, A. Sheldrick, A. Günther, M. Miyazaki and O. Dopfer, *Phys. Chem. Chem. Phys.*, 2018, **20**, 22148.
- 33 D. Müller, P. Nieto, M. Miyazaki and O. Dopfer, *Faraday Discuss.*, 2019, **217**, 256.
- 34 T. H. Dunning, *J. Chem. Phys.*, 1989, **90**, 1007.
- 35 M. J. Frisch, *et al.*, *Gaussian 16, Rev. C.01*, Wallingford, CT, 2016.
- 36 C. Adamo and V. Barone, *J. Chem. Phys.*, 1999, **110**, 6158.
- 37 V. Barone, J. Bloino, M. Biczysko and F. Santoro, *J. Chem. Theory Comput.*, 2009, **5**, 540.
- 38 R. L. Martin, *J. Chem. Phys.*, 2003, **118**, 4775.
- 39 S. Salzmann, V. Martinez-Junza, B. Zorn, S. E. Braslavsky, M. Mansurova, C. M. Marian and W. Gärtner, *J. Phys. Chem. A*, 2009, **113**, 9365.
- 40 P. J. Breen, J. A. Warren, E. R. Bernstein and J. I. Seeman, *Acc. Chem. Res.*, 1987, **87**, 1917.



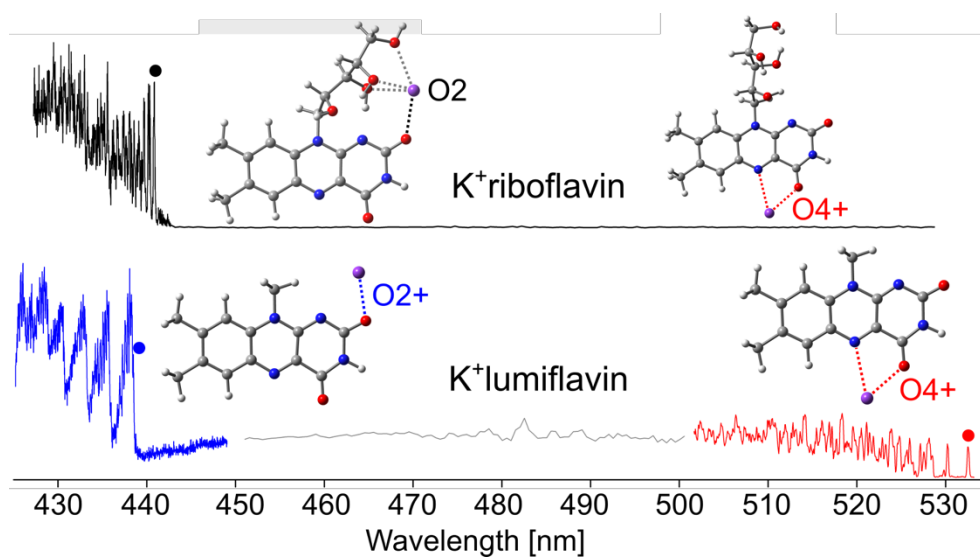
4.4. Interaction of alkali ions with flavins: infrared and optical spectra of metal-riboflavin complexes

David Müller and Otto Dopfer

J. Phys. Chem. A, 2021, **125**, 3146-3158

<https://doi.org/10.1021/acs.jpca.1c01846>

Reprinted with permission from the American Chemical Society



Declaration of Contribution

Both experimental and computational analysis were carried out by David Müller. The manuscript of the article was written by David Müller and reviewed and finalized by Otto Dopfer. All work was supervised by Otto Dopfer.

Interaction of Alkali Ions with Flavins: Infrared and Optical Spectra of Metal–Riboflavin Complexes

David Müller and Otto Dopfer*



Cite This: *J. Phys. Chem. A* 2021, 125, 3146–3158



Read Online

ACCESS |



Metrics & More

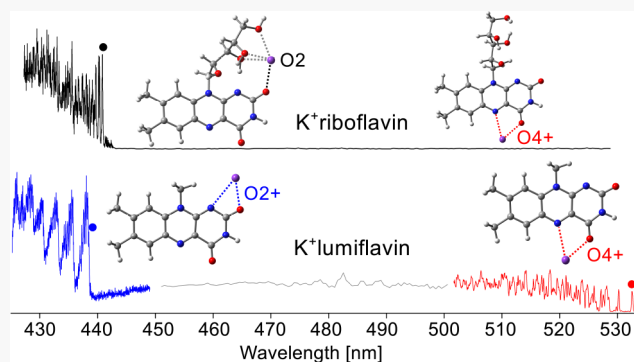


Article Recommendations



Supporting Information

ABSTRACT: Flavin compounds are of great interest in biochemistry because of their diverse functions in catalytic and photochemical processes. The intrinsic optical properties of flavins depend sensitively on their environment such as complexation with metal ions. Herein, we characterize the interaction of alkali metal ions (M^+) with riboflavin (RF, vitamin B₂). To this end, two different experimental spectroscopic approaches are employed to determine the structural, vibrational, energetic, and optical properties of M^+RF complexes by comparison with density functional theory (DFT) calculations at the PBE0/cc-pVDZ level. First, infrared multiple photon dissociation (IRMPD) spectra recorded at room temperature demonstrate that M^+ binds to one of the two available nucleophilic carbonyl groups (CO₂, CO₄) of RF, denoted O₂ and O₄₊ isomers, as revealed by characteristic shifts of the CO stretch modes upon metalation. Second, the optical spectrum of K^+RF is recorded between 428 and 529 nm in a cryogenic ion trap held at 6 K by visible photodissociation (VISPD). Analysis of the VISPD spectrum by time-dependent DFT calculations coupled to Franck–Condon simulations demonstrates that in fact only the O₂ isomer of M^+RF is formed by electrospray ionization, while the spectroscopic signatures of the O₄₊ isomer are absent. The VISPD spectrum is attributed to the $S_1 \leftarrow S_0$ ($\pi\pi^*$) transition of the O₂ isomer, which is calculated to be much more stable than the O₄₊ isomer because of additional multiple interactions of M^+ with the OH groups of the ribityl (sugar) side chain attached at N10 of RF. In contrast, there is no evidence for the presence of the O₄₊ isomer, in which M^+ forms a chelate complex, with M^+ binding to both O₄ and N5. A comparison between RF (ribityl at N10) and lumiflavin (LF and CH₃ at N10) reveals the drastic effects of the side chain on the structural, energetic, and optical properties of the flavin interaction with metal ions. While for M^+LF the O₂ and O₄₊ isomers are close in energy and both observed experimentally, for M^+RF the O₂ isomer is strongly favored due to the additional interaction with the side chain. Although the S_1 energies of $M^+RF(O_2)$ and $M^+LF(O_2)$ are quite similar, because the $\pi\pi^*$ transition is localized on the same isoalloxazine chromophore for both flavins, the vibrational structures are strongly different because the soft bending potential for the $M^+\cdots$ flavin interaction is strongly affected by the ribityl side chain at N10. In contrast to H^+RF , which prefers protonation at N1, steric repulsion of the larger M^+ ions with the ribityl side chain prevents metalation at N1, leading to the formation of the O₂ global minimum.



1. INTRODUCTION

Flavins are an important class of yellow dye molecules that play a crucial role in many biological systems due to their rich and strongly variable photochemical and photophysical properties, which can readily be modulated by several factors including (de)protonation, oxidation, solvation, metalation, and substitution of functional groups. The basic common structural unit of all flavins is the tricyclic heteroaromatic 7,8-dimethyl-10-alkylisoalloxazine chromophore with a flavin-specific alkyl substituent R at the N10 position (Figure 1). Prominent members of the flavin family are lumichrome (LC, R = H at N1 and not at N10), lumiflavin (LF, R = methyl = CH₃), riboflavin (RF, R = ribityl = CH₂(HCOH)₄H), flavin mononucleotide (FMN, R = ribophosphate), and flavin adenine dinucleotide (FAD, R = ribophosphate + adenine). Flavin-based molecules and complexes are of high biological

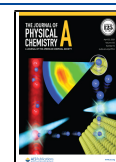
relevance and can act, for example, as blue-light sensors, light-oxygen-voltage (LOV) receptors, and coenzymes, and participate in the DNA-repair mechanism.^{1–7} In addition, the interaction of flavins with coordinating metal ions is of special interest.^{8–18} For example, the photoluminescence of RF strongly depends on the metal \cdots RF interaction.^{11,16,18}

Flavins show strong optical absorptions in the UV–VIS part of the electromagnetic spectrum. The rich photophysics

Received: March 1, 2021

Revised: March 29, 2021

Published: April 8, 2021



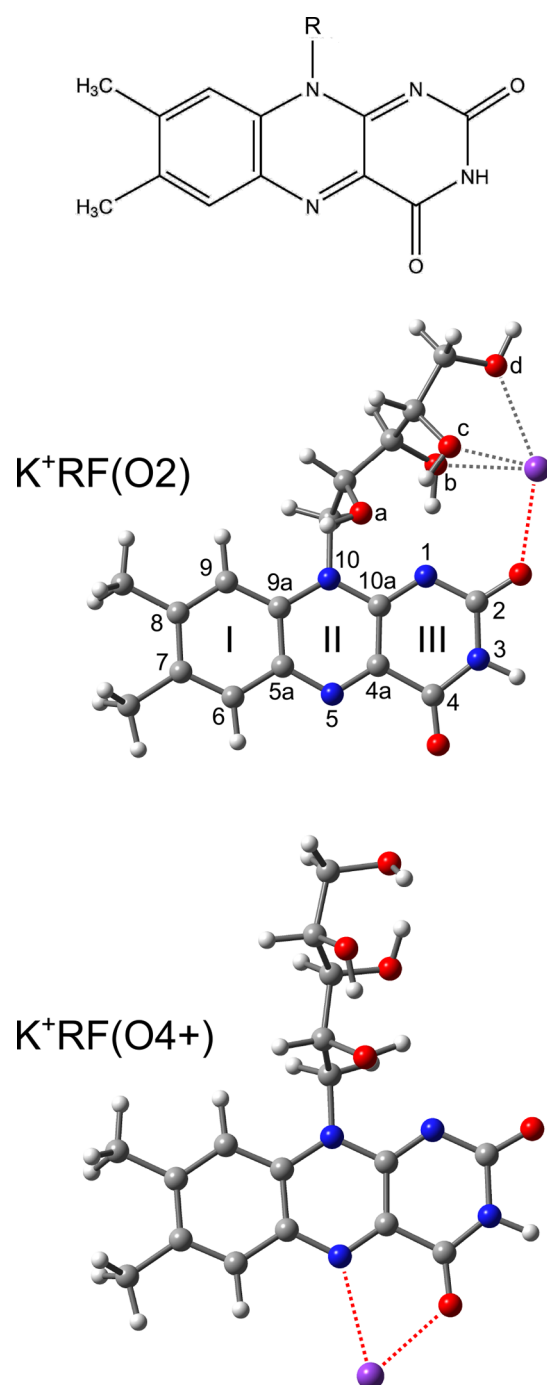


Figure 1. Scheme of the 7,8-dimethyl-10-alkylisoalloxazine chromophore of flavins ($R = \text{CH}_3$ for LF, $R = \text{ribityl}$ for RF), along with optimized ground-state structures of $\text{K}^+\text{RF}(\text{O2}/\text{O4+})$ computed at the PBE0/cc-pVDZ level. Ring and atom numbering according to IUPAC notation. The O atoms at the ribityl chain are labeled a–d. The atomic color code is O (red), N (blue), C (gray), H (white), and K (purple).

originates from a variety of low-lying bright $\pi\pi^*$ and dark $n\pi^*$ transitions arising from the extended aromatic π -electron system and the lone-pair orbitals of heterocyclic N and carbonyl O atoms. The energies and the mutual interactions of these states can be strongly modulated by the details of the flavin and its environment. To understand the intrinsic properties of flavins and the impact of their interaction with the surrounding environment at the molecular level, spectroscopy

of isolated flavins and their complexes is required, in addition to solution experiments. To this end, both experiments^{18–34} and quantum chemical calculations^{25,35–48} have been applied extensively to flavins in both condensed and gas phases. However, nearly all spectra have been recorded at room temperature and thus suffer from low spectral resolution arising from inhomogeneous spectral broadening by the solvent or the matrix (in condensed-phase experiments) and/or unresolved vibrational structure, which complicates the assignments of structural isomers (e.g., arising from different (de)protonation and metalation sites) and the nature of the electronic transitions. Hence, high-resolution optical spectroscopy of bare flavin molecules and their complexes in vacuo and under cryogenic conditions is highly advantageous in determining the details of their geometric and electronic structure. Unfortunately, such gas-phase data are rather scarce. For example, pioneering fluorescence excitation and emission spectra of the S_1 – S_0 ($\pi\pi^*$) transition of LF embedded in superfluid He nanodroplets demonstrate the importance of cooling for vibrational resolution and provide detailed insights into the geometric, vibrational, and electronic structure of this simple neutral flavin molecule.³² However, no such spectra are available for the more complex RF molecule studied in the present work.

In our group, cationic protonated or metalated complexes of flavins are investigated by two different experimental spectroscopic approaches combined with density functional theory (DFT) calculations. In both spectroscopic approaches, the flavin ions are produced by electrospray ionization (ESI). In a first step, infrared multiple-photon dissociation (IRMPD) spectroscopy of mass-selected ions at room temperature has been employed in the sensitive CO stretch range to determine the preferred protonation or metalation (coinage and alkali metals) sites of several flavins with increasing complexity, ranging from LC to FMN, in their ground electronic state (S_0).^{49–51} Concerning RF, IRMPD and DFT data reveal that protonation exclusively occurs at N1 and not at O2 (see Figure 1 for the atomic-numbering scheme).⁵⁰ In a second step, optical spectra of cryogenic metalated and protonated flavin ions are recorded in a tandem mass spectrometer coupled to a cryogenic ion trap (BerlinTrap) by means of visible photodissociation (VISPD) to probe their electronic structure by comparison to time-dependent DFT (TD-DFT) calculations.^{52–56} These data on H/M⁺LC and H/M⁺LF reveal that their photophysical properties drastically depend on the site of protonation/metalation and the size of the alkali metal ion. Herein, we extend the application of both spectroscopic approaches to M⁺RF complexes, with the major goal of exploring the effects of the long and flexible ribityl side chain at N10 on the geometric, vibrational, electronic, and energetic properties of the metal–flavin complexes.

Quantum chemical calculations for bare and microsolvated RF predict a bright $\pi\pi^*$ excitation for the $S_1 \leftarrow S_0$ transition. The orbitals contributing to this transition are mostly localized on the tricyclic aromatic ring. Hence, the photophysical properties are not expected to differ substantially when comparing LF with RF (i.e., when replacing methyl by ribityl at N10).^{25,31,34,35,41,44,45,47,57} Experimentally, the properties of RF have been extensively studied by static and time-resolved absorption and emission spectroscopy (IR, Raman, and optical) in the condensed phase.^{21,25,26,28,33,43,45} It was found that the absorption properties of RF depend on the solvation environment (solvent, pH, metal salt, and temperature). For

instance, the first $S_1 \leftarrow S_0$ ($\pi\pi^*$) absorption band of RF in ethanol recorded at 77 K is observed at 443 nm. However, even cooling the ions down to 77 K does not yield vibrationally resolved spectra (the electronic transition has a width of ~ 100 nm),⁴⁴ and the effect of solvation remains unclear, with shifts on the order of ~ 10 nm of the central band maximum of the $S_1 \leftarrow S_0$ band.^{26,35} Furthermore, metalated RF complexes have been investigated as well in the condensed phase.^{8,11,16–18} Interestingly, the fluorescence and absorption spectra of RF with various metal salts dissolved in water reveal that the shifts in the electronic transitions can strongly depend on the type of metal ion. For example, while the presence of Na^+ ions shifts the maximum of the S_1 absorption band by only 1 nm from 446 to 447 nm, Ag^+ ions cause a much larger red-shift of 24 nm to 470 nm.¹⁸ No explanation was given for this different behavior. Our recent studies on related M^+LF complexes suggest that it may result from different metal-binding sites.^{54,56}

2. EXPERIMENTAL AND COMPUTATIONAL DETAILS

IRMPD spectra of mass-selected M^+RF complexes are measured at room temperature (~ 300 K) in the fingerprint range ($1000\text{--}2000\text{ cm}^{-1}$) at the high-intensity IR free electron laser (IR-FEL) facilities CLIO (Centre Laser Infrarouge d'Orsay, $\text{M} = \text{Li}$ and Cs)⁵⁸ and FELIX (Free Electron Laser for Infrared eXperiments, $\text{M} = \text{Na}$)^{59,60} in Fourier transform ion cyclotron resonance (FT-ICR) mass spectrometers equipped with an ESI source. Details of the technique and experimental conditions are described in previous applications to ionic flavin complexes^{49–51} and other organic ions.^{61,62} Briefly, M^+RF ions are produced in an ESI source by spraying a solution of methanol and water (typical ratio 5:1) containing RF (Sigma-Aldrich, $>99\%$) and MCl salt. The ions are accumulated and thermalized in a hexapole and transferred into the ICR trap. Subsequently, M^+RF ions are mass-selected in the ICR and irradiated by the IR-FEL. Parent and fragment ions are monitored as a function of the laser frequency. The IRMPD efficiency is then calculated as $R = -\ln(I_{\text{parent}}/I_{\text{total}})$, in which I_{parent} is the parent ion intensity, I_{fragment} is the sum of the fragment intensities, and $I_{\text{total}} = I_{\text{parent}} + I_{\text{total}}$. The final IRMPD yields are linearly normalized for variations in the IR laser intensity.

VISPD spectra of K^+RF are recorded in a tandem mass spectrometer combined with a cryogenic ion trap (Berlin-Trap).⁶³ Briefly, the experimental setup comprises an ESI source to generate K^+RF ions, a short quadrupole to accumulate the ions (90 ms), a quadrupole mass spectrometer (QMS) to select the parent ions of interest, a cryogenic 22-pole trap ($T = 6$ K) to store and cool the ions via He buffer gas cooling (90 ms), and an orthogonal reflectron time-of-flight mass spectrometer (ReTOF) to detect both fragment and parent ions. A solution containing 1 mg of RF (Sigma-Aldrich, $>99\%$, 0.13 mM), 20 mL of methanol, 1 mL of water, and 2 mg of KCl (1.3 mM) salt is sprayed at a flow rate of 2 mL/h. The ions in the 22-pole trap cool down to an effective (ro-)vibrational temperature of ~ 20 K.^{52–56,63} Shortly before ion extraction into the ReTOF, the K^+RF ions are excited by a pulsed optical parametric oscillator (OPO, GWU, VersaScan, ~ 2 mJ/pulse, bandwidth 4 cm^{-1}) pumped by the third harmonic of a nanosecond Q-switched Nd:YAG laser (Innolas, Spitlight 1000, 355 nm, 180 mJ/pulse). Both parent and fragment ions are monitored simultaneously at a microchannel plate detector located at the end of the ReTOF. VISPD spectra

are generated by integrating the K^+ signal, which is the only fragment ion observed upon VISPD (Figure S1), at each wavelength in the range from 428 to 529 nm. The VISPD spectrum is linearly normalized by both laser power and parent ion signal. Both the OPO laser and the BerlinTrap are synchronized at a repetition rate of 10 Hz. The VISPD spectrum is recorded in the range 428–443 nm with a step size of 0.02 nm. Additionally, the OPO laser is scanned up to 529 nm with an increased step size of 0.5 nm to cover the same spectral range as for K^+LF .^{54,56} The widths of the transitions are in the order of $5\text{--}10\text{ cm}^{-1}$ and originate from the OPO bandwidth (4 cm^{-1}), unresolved rotational substructure, and possibly lifetime broadening.

The experimental data are analyzed with the aid of quantum chemical (TD-)DFT calculations at the PBE0/cc-pVDZ level,⁶⁴ which has proven to provide reliable vibrational and electronic spectra as well as interaction energies.^{48,52–56} First, the structure in the electronic ground state (S_0) of RF and M^+RF is optimized manually by using a large number of starting geometries. In general, the flexible ribityl chain at N10 increases the number of low-energy isomers significantly as compared to the LF case studied earlier.^{51,54,56} Subsequently, vertical excitation energies (E_v) are computed for the four first excited singlet states ($S_1\text{--}S_4$) originating from the optimized S_0 state of RF, the four most stable $\text{K}^+\text{RF}(\text{O}2)$ isomers, and one of the possible $\text{K}^+\text{RF}(\text{O}4+)$ isomers. Additionally, their S_1 states are optimized to compute adiabatic excitation energies (E_a). The chosen computational level has proven to properly account for the structural, vibrational, energetic, electronic, and optical properties of flavins and their protonated and metalated ions.^{52–56} All presented binding and relative energies (D_0 , E_0) are corrected for harmonic zero-point vibrational energy. Cartesian coordinates and energies of all relevant structures are available in the Supporting Information. In the simulated IR spectra, vibrational frequencies in the fingerprint range are scaled empirically with a factor of 0.941. The orbitals contributing most to the electronic excitation are visualized using the natural transition orbital approach.⁶⁴ Multidimensional Franck–Condon (FC) simulations are carried out to generate harmonic vibronic stick spectra, and vibrational frequencies remain unscaled.⁶⁴ Only the monoisotopic species are considered in both experiment and calculation. Relativistic corrections for the heavier M^+ ions ($\text{K}\text{--}\text{Cs}$) are considered by using the Stuttgart effective core potential.⁶⁵

3. RESULTS AND DISCUSSION

Flavins offer several attractive binding sites for metal cations, including the nucleophilic lone pairs of the heterocyclic N atoms (N1, N5) and the oxygen atoms of the two CO groups (O2, O4) as well as the aromatic π electrons of the tricyclic isoalloxazine ring. In the case of RF, the four OH groups of the $\text{CH}_2(\text{HCOH})_4\text{H}$ ribityl sugar side chain also offer attractive lone pairs. Previous calculations for M^+LC and M^+LF and corresponding IRMPD spectra have shown that out-of-plane π -bonding of alkali cations to the flavin chromophore (cation- π interaction) is substantially weaker than in-plane σ -bonding to the lone pairs and thus not considered further here.^{49,51} This procedure is further justified by the corresponding VISPD spectra.^{52,54,56} For M^+LF complexes,⁵¹ the lowest-energy isomers identified by DFT calculations and IRMPD spectra are the O2, O2+, and O4+ isomers, which are all within a narrow energy range of $\Delta E_0 = 20, 10, 0.5, 1,$ and 3 kJ mol^{-1} for $\text{Li}\text{--}\text{Cs}$ (Table 1). Because of their similar energies, the

Table 1. Binding and Relative Energies (D_0 , E_0 in Parentheses, kJ mol^{-1}) of the Most Stable O2+ Isomer and the O4+ Isomer of M^+LF Compared to Those of M^+RF

M	isomer	M^+RF	M^+LF^a
Li	O2	411.4 (0.0)	279.7 (20.4)
	O2+		289.5 (10.6)
	O4+	298.3 (113.1)	300.1 (0.0)
Na	O2	292.7 (0.0)	209.5 (10.2)
	O2+		214.2 (5.5)
	O4+	217.0 (75.7)	219.7 (0.0)
K	O2	254.3 (0.0)	175.9 (0.1)
	O2+		175.5 (0.5)
	O4+	173.2 (81.1)	176.0 (0.0)
Rb	O2	220.7 (0.0)	158.9 (0.0)
	O4+	154.7 (66.0)	157.9 (1.0)
Cs	O2	209.3 (0.0)	148.2 (0.0)
	O4+	141.8 (67.5)	145.8 (2.9)

^aRef 54.

energetic order of the M^+LF isomers changes with the size of M^+ . While O4+ is slightly more stable than O2+ for $\text{M} = \text{Li-K}$, O2 becomes the global minimum for the larger Rb and Cs ions. In the O2+ and O4+ isomers of M^+LF , M^+ binds in a bent O–M–N chelate to LF (O2–M–N1, O4–M–N5) because it can benefit from the interaction with the lone pairs of both O and N. For the larger alkali ions ($\text{M} = \text{Rb}$ and Cs), the steric repulsive interaction with the CH_3 group at N10 prevents the formation of the O2+ isomer. On the other hand, for all M^+ ions, the O2 isomer with a more linear C2–O2–M bond is stable and close in energy to the O2+ structure (for $\text{M} = \text{Li-K}$), and both isomers are separated by low O2 \leftrightarrow O2+ isomerization barriers ($\leq 11 \text{ kJ mol}^{-1}$). In general, the $\text{M}^+\cdots\text{LF}$ interaction is mostly electrostatic in nature and thus increases substantially with decreasing ionic radius of M^+ (e.g., $D_0 = 146\text{--}300 \text{ kJ mol}^{-1}$ for the O4+ isomers of Cs–Li, Table 1).⁵⁴

Concerning RF, no experimental information about the structure of the side chain is available. The most stable conformer computed in the present work has a more or less linear ribityl chain and no hydrogen bond between the ribityl chain and ring III of the isoalloxazine ring. Stable local minima with such a hydrogen bond have been predicted.^{28,48} Several isomers differing in the configuration of the ribityl chain are obtained here, and the three lowest-energy local minima with a bent chain, which are within 11.1 kJ mol^{-1} of the global minimum, are presented in Figure S2. In the following, we consider only the global minimum conformer of RF, which serves as a reference structure for evaluating the effects of metalation.

While the O2+ and O4+ isomers of M^+LF are nearly isoenergetic, the situation changes drastically for M^+RF because M^+ at the O2 binding site can have multiple additional and strong $\text{M}^+\cdots\text{OH}$ interactions with the nucleophilic OH lone pairs of the ribityl side chain. As this chain is quite flexible, it can readily rearrange upon metalation to optimize these $\text{M}^+\cdots\text{OH}$ bonds. These multiple additional interactions are not feasible when M^+ binds at the O4+ site. Hence, the energy gap between the O2 and O4+ isomers increases drastically in favor of O2 when methyl is substituted by ribityl (i.e., LF \rightarrow RF). As the side chain at N10 has little impact on the charge distribution at the O4+ site, the binding energies of the $\text{M}^+\text{RF}(\text{O4+})$ and $\text{M}^+\text{LF}(\text{O4+})$ isomers are essentially the same for the same M (to within 4.0 kJ mol^{-1} , Table 1). In general,

the D_0 values of $\text{M}^+\text{RF}(\text{O4+})$ are systematically lower by $1.8\text{--}4.0 \text{ kJ mol}^{-1}$ than those of $\text{M}^+\text{LF}(\text{O4+})$. In contrast to the O4+ structures, the binding energies of the O2 isomers increase drastically upon methyl \rightarrow ribityl substitution. For the most stable $\text{M}^+\text{RF}(\text{O2})$ isomers found in the present work, D_0 increases by 131.7, 83.2, 78.4, 61.8, and 61.1 kJ mol^{-1} for $\text{M} = \text{Li-Cs}$, which corresponds to 39–47% (Table 1). Again, the binding energies of the $\text{M}^+\text{RF}(\text{O2})$ isomers strongly decrease with increasing ionic radius of M^+ ($D_0 = 411.4, 292.7, 254.3, 220.7$, and $209.3 \text{ kJ mol}^{-1}$ for Li–Cs). As a result, the energy gap between O2 and O4+ increases drastically for M^+RF and amounts to $\Delta E_0 = 67.5\text{--}113.1 \text{ kJ mol}^{-1}$ for Cs–Li. From these computational thermochemical data, we may predict that under the current experimental conditions only the O2 isomer is populated. At this stage, we note that there are several O4+ and O2 isomers of M^+RF with comparable energies resulting from different configurations of the flexible ribityl side chain. For RF and $\text{M}^+\text{RF}(\text{O4+})$, we report only the data of the most stable isomer found in this work (which may not necessarily be the true global minima because we do not apply a systematic global optimization approach). For $\text{M}^+\text{RF}(\text{O2})$, we find several low-energy isomers denoted O2(*n*), which are lower in energy than the most stable O4+ isomer, and we discuss in the main text in detail only the most stable one identified (i.e., O2(1) = O2, Figures S3 and S4). In these O2(*n*) minima identified, M^+ binds to O2 with varying conformations of the ribityl chain at N10, whereby the chain tends to bend more toward the M^+ ion with decreasing ionic radius because of the increasing attractive $\text{M}^+\cdots\text{ribityl}$ interaction. However, because of their relatively high energy compared to O2(1), e.g., $\Delta E_0 \geq 32 \text{ kJ mol}^{-1}$ for $\text{M} = \text{Li}$, they are not considered further here but are included in Table S1. Because of the strong $\text{M}^+\cdots\text{ribityl}$ attraction and the potential formation of attractive OH \cdots N1 H bonds between the OH groups of ribityl and N1, the formation of the N1–M–O2 chelate is not favorable and no low-energy O2+ isomer is found for M^+RF . For similar steric reasons, metalation of RF at N1 is not feasible. This result is in contrast to protonated RF (H^+RF), for which the N1 isomer is the most stable global minimum, with a computed energy gap of 26 kJ mol^{-1} to the lowest-energy O2+ isomer.⁵⁰ This difference is readily explained by the large ionic radii of M^+ as compared to H^+ and the difference in chemical bonding (mostly electrostatic for M^+ and covalent for H^+).

The thermochemical data predict the predominant production of the $\text{M}^+\text{RF}(\text{O2})$ isomers in the ESI source. To test this hypothesis by experiment, we consider in a first step IRMPD spectra of a number of M^+RF complexes. These are recorded at room temperature for $\text{M} = \text{Li, Na, and Cs}$. Although due to limited FEL beam time not all alkali ions are investigated, we cover the small and large ionic radius regimes. The IRMPD spectra are recorded in the fingerprint range ($1000\text{--}2000 \text{ cm}^{-1}$) to include the CO stretch modes between 1600 and 1800 cm^{-1} , which are particularly sensitive for identifying the preferred M^+ binding sites in the S_0 state by comparison to DFT calculations.^{49–51}

The IRMPD spectra measured for Li^+RF (CLIO), Na^+RF (FELIX), and Cs^+RF (CLIO) are compared in Figure 2. The IRMPD spectrum of Na^+RF (m/z 399) recorded at FELIX is exclusively observed in the Na^+ channel (loss of RF). The IRMPD spectrum of Li^+RF (m/z 383) recorded at CLIO is observed in various mass channels with significant intensities. These are, with decreasing abundance (measured at the resonance at 1545 cm^{-1}), the fragment ions m/z 263 (48%,

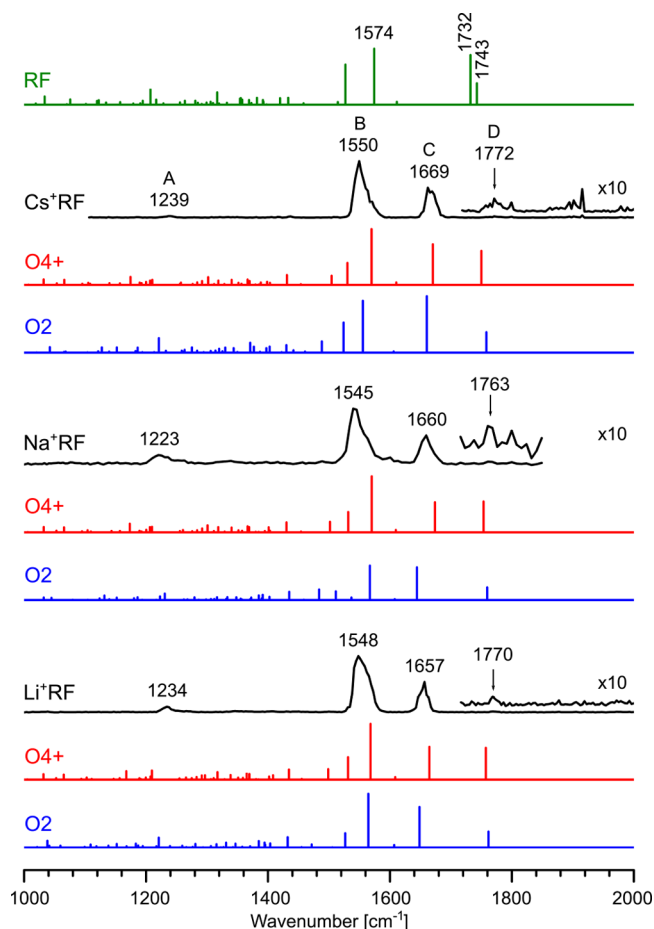


Figure 2. IRMPD spectra of M^+RF with $M = Cs, Na, \text{ and } Li$ (black) compared to linear IR absorption spectra of the most stable O2 isomer (blue) and the less stable O4+ isomer (red) computed at the PBE0/cc-pVDZ level. For comparison, the spectrum calculated for bare RF is included. Computed frequencies are scaled empirically by 0.941. To visualize the weak band D, this spectral range is vertically expanded by a factor of 10.

Li^+LF , loss of ribityl apart from CH_3), m/z 249 (30%, Li^+LC or Li^+ iso-LC, loss of ribityl), m/z 366 (13%, loss of OH), m/z 224 (6%), and m/z 340 (3%). The mass of Li^+ (m/z 7) is too low to be detected with the available FT-ICR. However, the binding energy of the small Li^+ cation to the isoalloxazine ring is so strong that Li^+ probably remains connected to the various organic fragments upon IRMPD. The IRMPD spectrum of Cs^+RF (m/z 509) recorded at CLIO is again observed in the Cs^+ fragment channel (m/z 133, >95%) due to the weak $Cs^+\cdots RF$ bond. Other very minor channels are m/z 375 ($RF-H^+$, deprotonated RF) and m/z 44 (CO_2^+ and/or $C_2OH_4^+$).

All three IRMPD spectra feature an intense peak B at ~ 1550 cm^{-1} (1548, 1545, and 1550 cm^{-1} for Li, Na, and Cs, respectively) and a second intense transition C at 1657, 1660, and 1669 cm^{-1} . A third weak feature A is observed at 1234, 1223, and 1239 cm^{-1} , while a fourth band D at 1770, 1763, and 1772 cm^{-1} also shows only very little intensity in all three spectra, probably because of the strongly decreasing FEL laser intensity toward the blue end of the spectra. From previous experience with metalated and protonated flavins,^{49–51} it is clear that the prominent free CO stretch bands occur near 1800 cm^{-1} while the metal-bonded CO stretch band is observed in the range 1600–1700 cm^{-1} . Thus, we can safely attribute band D to a free CO stretch, while band C corresponds to a metal-bonded CO stretch mode. This result already provides a first experimental indication that the M^+ ion in the observed M^+RF isomers is attached to either O2 or O4. In addition, band B around 1550 cm^{-1} is a typical signature of coupled ring stretch mode(s) of the C–C and C–N bonds in the isoalloxazine ring.^{49–51}

The experimental IRMPD spectra of M^+RF are compared in Figure 2 to linear IR absorption spectra of the O2 (blue) and O4+ (red) isomers, as well as the spectrum computed for bare RF. The frequencies of the two CO stretch and most intense ring modes of M^+RF ($M = Li-Cs$) and bare RF in their S_0 state are reported in Table 2. The computed linear IR spectra are empirically scaled by 0.941 for all M^+ ions to optimize the agreement of bands B–D with the computed frequencies (see Figure S5 for the computed spectra of all M^+RF). This required scaling factor is significantly smaller than those used previously for M^+LF (0.964/0.973 for Li–Na and K–Cs, respectively),⁵¹ probably because the binding energy is substantially higher for M^+RF due to the additional interaction of M^+ with the ribityl side chain (at least for the O2 isomers). As a result, the M^+RF ions need to absorb more IR photons to drive the IRMPD process, which typically causes a systematic red-shift of the IRMPD spectrum compared to the linear one-photon IR spectrum.⁶⁶ This result provides further evidence for the predominant detection of the O2 isomer because this isomer selectively has a particularly high binding energy (Table 1). For example, when taking the computed binding energies of 293 and 217 $kJ\ mol^{-1}$ for the O2 and O4+ isomers of Na^+RF , respectively, 14 and 10 photons with 1800 cm^{-1} are required for IRMPD into $Na^+ + RF$. Inspection of Figure 2 reveals that the IRMPD spectra simulated for the O2 and O4+ isomers are not too different, so that a clear-cut isomer assignment of the experimental spectrum appears difficult. Nonetheless, while band B is rather insensitive to the isomeric structure, the splitting of the bound and free CO stretch bands C and D as well as band A are better reproduced for O2 than for O4+, providing further support for the predominant presence of O2. The large splitting observed for bands C and

Table 2. Frequencies (in cm^{-1} , Scaled by 0.941) of Bound and Free CO2 and CO4 Stretch and Ring Vibration in the Electronic Ground State (S_0) of RF and the O2 and O4+ Isomers of M^+RF Computed at the PBE0/cc-pVDZ Level

	ν_{CO2}	ν_{CO4}	ν_{ring}		ν_{CO2}	ν_{CO4}	ν_{ring}
RF	1732	1743	1574	RF	1732	1743	1574
Li (O2)	1649	1762	1565	Li (O4+)	1757	1665	1568
Na (O2)	1644	1760	1567	Na (O4+)	1753	1674	1571
K (O2)	1657	1759	1563	K (O4+)	1751	1669	1570
Rb (O2)	1664	1758	1563	Rb (O4+)	1750	1673	1571
Cs (O2)	1661	1758	1555	Cs (O4+)	1750	1670	1750

D assigned to bound and free CO stretch modes is reproduced by the calculations for both O2 and O4+ and confirms the initial conclusion that M^+ binds to one of the CO groups of RF. This result becomes quite obvious by comparison to the IR spectrum computed for bare RF. In the case of M^+LF , the simultaneous presence of two bound CO stretch bands in the IRMPD spectra has been indicative for the presence of two distinct isomers, namely, O2+ and O4+. ⁵¹ For M^+RF , no such large splitting is resolved (but also not predicted), and thus, the IRMPD spectra in the CO stretch range are consistent with the presence of both O2 and O4+. Actually, comparison between the IRMPD spectra of M^+RF and M^+LF (see Figure S6 for $M = Li$) reveals similarities in the main transitions but richer structure in the M^+LF case. Interestingly, without calculations one would extrapolate from the assigned M^+LF spectrum in the bound CO stretch range that the much less stable O4+ isomer, and not the O2 global minimum isomer, is observed for M^+RF , which illustrates the importance of calculations and other spectroscopic signatures such as optical spectroscopy.

To decide about the presence of the O2 and/or O4+ isomers, optical spectroscopy of cryogenic ions is more suitable because the electronic transitions of both isomers occur at rather different spectral ranges, as previously shown for M^+LF , for which the $S_1 \leftarrow S_0 (\pi\pi^*)$ origin transitions are observed at 567–525 nm for the O4+ isomers and at 431–448 nm for the O2+ isomers (see Figure 3 for $M = K$). ^{54,56} To this end, we record as an example the VISPD spectrum of K^+RF in the BerlinTrap held at 6 K and analyze this spectrum by TD-DFT

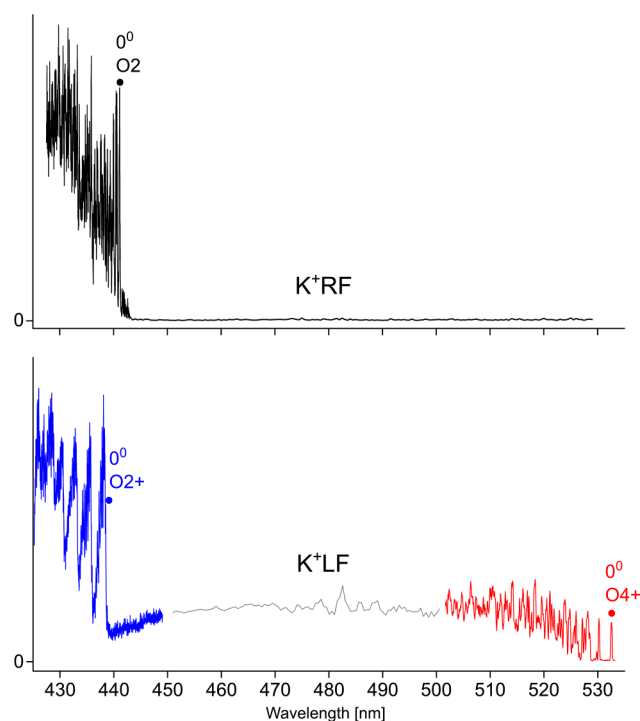


Figure 3. VISPD spectrum of K^+RF recorded at $T = 6$ K in the K^+ fragment channel (top) and assigned to the $S_1 \leftarrow S_0 (\pi\pi^*)$ transition of the O2 isomer. The range above 443 nm is recorded with an increased step size of 0.5 nm. VISPD spectrum of K^+LF covering the same spectral range (bottom). ^{54,56} The gray part of the spectrum is recorded with an increased step size of 0.5 nm. The red part is assigned to the S_1 band of the O4+ isomer, and the blue part is assigned to the S_1 band of the O2+ isomer.

calculations. The K^+ case is chosen because the VISPD spectrum of the $K^+LF(O2)$ is rather complex with a high density of low-frequency vibronic transitions upon S_1 excitation attributed to the soft potential for $O2 \leftrightarrow O2+$ isomerization. The introduction of the nearby ribityl side chain is expected to have a significant impact on this potential. The overview VISPD spectrum of K^+RF is compared in Figure 3 to the one of K^+LF in the range 425–535 nm, which covers the S_1 bands of the O4+ and O2+ isomers. Similar to K^+LF , the K^+RF parent ion dissociates solely into K^+ and neutral RF upon VISPD (Figure S1). This fragmentation pattern is consistent with that observed for IRMPD described earlier for medium-sized alkali ions complexed with RF. Clearly, cooling the ions down to $T < 30$ K suppresses hot band transitions and enables vibronic resolution of biomolecular complexes of this size. ^{67–72} The first absorption peak observed at 22 670 cm^{-1} (441.1 nm) is assigned to the origin band (0^0) of the optically bright $S_1 \leftarrow S_0 (\pi\pi^*)$ transition of the O2 isomer. The intense and well-resolved S_1 0^0 band origin is accompanied by intense vibronic activity arising from a large geometry change upon S_1 excitation. Assuming the computed binding energy of the most stable O2(1) isomer (21 258 cm^{-1} , 254.3 $kJ\ mol^{-1}$), single-photon absorption should be sufficient to dissociate K^+RF . Clearly, the parent molecule K^+RF does not fragment below the S_1 0^0 transition, and the VISPD signal is zero (apart from minor hot bands discussed later). This observation indicates that (i) no bright electronic transition of the O2 isomer and (ii) no other bright transition of any other isomer is detected in the energy range above 441 nm. This result is in stark contrast to the VISPD spectrum of K^+LF also shown in Figure 3 (and all other M^+LF complexes), ^{54,56} clearly illustrating the drastically different photophysical responses of K^+RF and K^+LF produced by ESI. In contrast to K^+RF , K^+LF exhibits strong VISPD in the full considered spectral range. The high-energy part of the K^+LF spectrum (blue) is assigned to the $S_1 \leftarrow S_0 (\pi\pi^*)$ transition of the O2+ isomer (with a band origin at 438.48 nm), while the low-energy part (red) is associated with the $S_1 \leftarrow S_0 (\pi\pi^*)$ transition of the O4+ isomer (with a band origin at 532.54 nm). ^{54,56} The intermediate part of the K^+LF spectrum (gray) never decays to zero and originates from the high density of unresolved vibronic $S_1 \leftarrow S_0$ transitions of the O4+ isomer. ^{54,56} The direct comparison of both spectra in Figure 3 immediately indicates the absence of any O4+ isomer for K^+RF (from the lack of any VISPD signal in the 500–540 nm range and the zero VISPD signal down to 441 nm), a conclusion strongly supported by the results of quantum chemical calculations concerning both the thermochemical data (Table 1) and the optical properties.

The DFT calculations predict several potential low-energy candidates of K^+RF , which may be responsible for the measured VISPD spectrum in Figure 3. The vertical and adiabatic excitation energies predicted for the four most stable O2(1–4) isomers and the single considered O4+ isomer are compared in Table 3 to the experimentally extracted S_1 origin transition at 22 670 cm^{-1} . Unfortunately, the $S_1 \leftarrow S_0$ spectrum of bare RF has not been reported yet, probably due to difficulties in the generation of sufficient abundance in the gas phase. Moreover, the transition measured in the condensed phase is rather broad and dependent on the solvent. ^{16,25,26,35,43,44} For example, the S_1 band of RF measured in methanol has its maximum at 444 nm with a width on the order of 100 nm (corresponding to $22\,500 \pm 2\,500\ cm^{-1}$). ³⁵ Hence, no accurate experimental reference point for extracting

Table 3. Experimental S_1 Origin Transition of K^+RF Compared to Vertical and Adiabatic Excitation Energies ($E_{v/a}$) of the First Excited Singlet State (S_1) Computed at the PBE0/cc-pVDZ Level^{a,b}

	S_1 exp	S_1 calc E_a (E_v)	Δ		S_1 exp	S_1 calc E_a (E_v)	Δ
RF	22500 \pm 2500 ^c	22320 (25193)	0	LF	21511 ^d	22448 (25236)	0
$K^+RF(O2)$	22670			$K^+LF(O2+)$	22806	23454 (26063)	1006
$K^+RF(O2(1))$		22393 (25981)	73				
$K^+RF(O2(2))$		22994 (25684)	674				
$K^+RF(O2(3))$		23318 (25926)	998				
$K^+RF(O2(4))$		23388 (25996)	1068				
$K^+RF(O4+)$		17025 (21241)	−5295	$K^+LF(O4+)$	18778	19256 (21946)	−3192

^aAll values are given in cm^{-1} . Relative shifts of E_a between RF and K^+RF are given as Δ . Global minimum structures of K^+RF and RF are presented in Figure S3. For comparison, corresponding data are given for K^+LF . ^b K^+LF data taken from refs 54 and 56. ^cMeasured in methanol (ref 35).

^dMeasured in He nanodroplets (ref 32).

Table 4. Vertical Excitation Energies (in cm^{-1}) and Oscillator Strengths (f) for RF, LF, and the Three Most Stable O2 Isomers (1–3) and the O4+ Isomer of K^+RF Computed at the PBE0/cc-pVDZ Level

	RF	f	LF	f	$K^+RF(O2(1))$	f	$K^+RF(O2(2))$	f	$K^+RF(O2(3))$	f	$K^+RF(O4+)$	f
S_1	25193	0.1607	25236	0.2126	25981	0.1778	25654	0.1389	25926	0.1652	21241	0.1254
S_2	26447	0.027	26121	0.0004	26841	0.0020	27001	0.0182	27283	0.0007	24162	0.0366
S_3	28445	0.0015	27585	0.0004	29308	0.0032	29413	0.1324	29470	0.0496	26054	0.0008
S_4	30960	0.0175	32250	0.1362	30149	0.2246	29555	0.1219	29936	0.1974	26223	0.0030

the effect of metalation of RF on its S_1 state is available in the gas phase. Thus, to examine the effect of the ribityl chain on the optical properties, the current results for K^+RF are compared herein to those of K^+LF published recently (Table 3 and Figure 3).^{54,56} For example, the experimental S_1 origins of $K^+RF(O2)$ and $K^+LF(O2+)$ at 22 670 and 22 806 cm^{-1} , respectively, differ by only 136 cm^{-1} , confirming that the K^+RF band arises indeed from S_1 of an O2-type isomer. This conclusion is supported by the vertical excitation energy predicted for O2(1) of K^+RF , which also differs only by a similarly small amount of 82 cm^{-1} from that of $K^+LF(O2+)$. The corresponding difference in the adiabatic S_1 energies is somewhat larger (1061 cm^{-1}), which may arise from a larger error in calculating the zero-point energy for the rather floppy complexes. Overall, there is good agreement between the computed adiabatic S_1 origins of the assigned O2(1)/O2+ isomers of K^+RF/K^+LF with the experimental data, with differences of only 277 and 648 cm^{-1} , respectively. These deviations are relatively small for excited-state calculations, indicating the reliability of the computational approach for this type of metal–organic complex. In addition, the other O2(n) isomers with $n = 2–4$ have similar computed adiabatic and vertical S_1 energies as the O2(1) isomer (to within 995 and 297 cm^{-1} , respectively), suggesting that the orientation of the ribityl side chain has only a minor impact on the S_1 energy of the O2 isomers of K^+RF . In contrast, the adiabatic S_1 energy predicted for the much less stable $K^+RF(O4+)$ isomer ($E_0 = 81$ kJ mol^{−1}, Table 1) is predicted at 17 025 cm^{-1} and, hence, significantly red-shifted from the values reported for the O2+ isomers of K^+RF/K^+LF (by 5 368 and 6 429 cm^{-1} , respectively), confirming that the O4+ isomer cannot be responsible for the K^+RF band near 23 000 cm^{-1} . In summary, from the comparison of the VISPD spectra of K^+RF and K^+LF and the TD-DFT calculations, the observed transition of K^+RF is clearly attributed to S_1 of an O2-type isomer. Methyl \rightarrow ribityl substitution at N10 has essentially no impact on the S_1 energy of this isomer. We cannot decide about the configuration of the ribityl side chain because it does not have a significant influence on the S_1 transition energy (Table

3). On the other hand, the presence of the O4+ isomer of K^+RF is clearly below the detection limit. Its absence is in contrast to the K^+LF case and clearly due to its much smaller binding energy as compared to the O2 isomer(s) because of the lack of the stabilizing interaction of K^+ with the ribityl chain. It is certainly not due to a reduced fragmentation (and thus detection) efficiency because the S_1 energy of the O4+ isomer is clearly above its computed dissociation energy (17 000 versus 15 000 cm^{-1}).

Typical for flavins, the excited-state manifolds of RF and K^+RF comprise several optically bright $\pi\pi^*$ states and optically dark $n\pi^*$ states. The vertical energies and oscillator strengths (f) computed for the lowest four singlet excited states are summarized in Table 4 for LF, RF, and the O2(1–3) and O4+ isomers of K^+RF . In all cases, the S_1 state corresponds to $\pi\pi^*$ excitation with high oscillator strengths ($f = 0.13–0.21$). On the other hand, the computed f values for the $n\pi^*$ states are close to zero and somewhat larger for RF when compared to LF (e.g., $f = 0.027$ and 0.004 for S_2 of RF and LF, respectively). For both RF and K^+RF , the $S_{2/3}$ states are optically dark $n\pi^*$ states, whereas the S_4 state is again an optically bright $\pi\pi^*$ excitation (for RF, it is S_3). Finally, the oscillator strengths are of comparable magnitude for RF and K^+RF , e.g., $f = 0.1607$ and 0.1778 for S_1 of RF and K^+RF , respectively. This view is in line with the natural transition orbitals contributing to the lowest electronic excitation (LUMO \leftarrow HOMO, $S_1 \leftarrow S_0 \pi\pi^*$) visualized in Figure 4 for the O2(1) isomer of K^+RF , RF, and LF. Clearly, in all three cases, the orbitals are mostly localized on the tricyclic aromatic isoalloxazine chromophore, with only modest contribution on the ribityl chain of K^+RF and the methyl group of LF at N10 and no amplitude on the M^+ ion. Hence, the vertical excitation energies (and oscillator strengths) are quite similar for LF, RF, K^+LF , and K^+RF . Similar to LF, significant electron density is shifted to N5/O4 upon S_1 excitation, while only modest changes occur for the atomic charges at O2 (see Table S2 for atomic charges based on natural bond orbital analysis). As a consequence, the $M^+ \cdots RF$ interaction is relatively unchanged for complexation at the O2 binding site, leading to a minor S_1 shift upon metalation. In

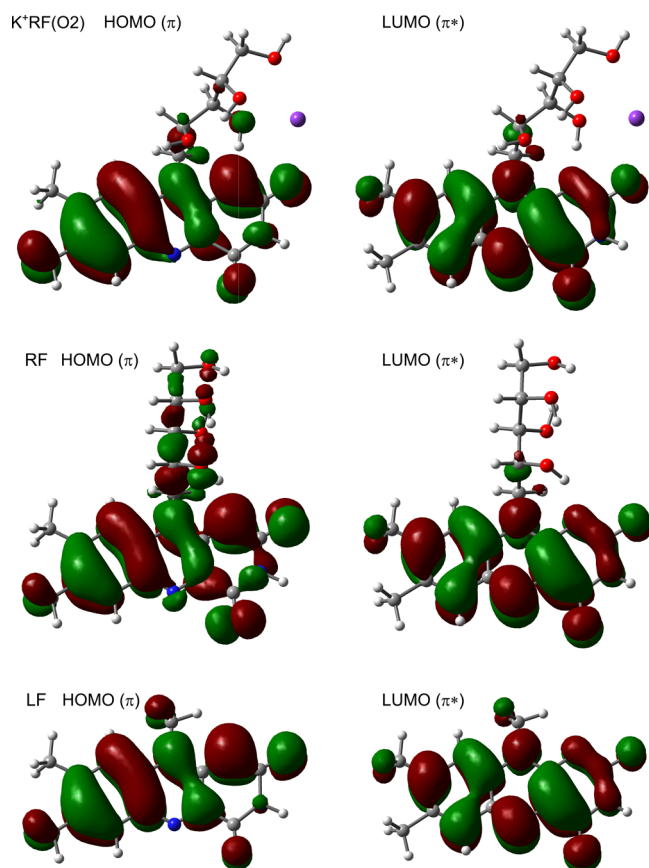


Figure 4. Natural transition orbitals of $K^+RF(O_2)$, RF, and LF computed at the PBE0/cc-pVDZ level.

contrast, the $M^+ \cdots RF$ interaction at the $O4+$ site is strongly enhanced upon S_1 excitation by the charge reorganization, which induces the large S_1 red-shift upon metal complexation.

The computed adiabatic S_1 origins of RF and the $O2(1)$ isomer of K^+RF differ only by 73 cm^{-1} (Table 3). Unfortunately, no experimental spectrum of neutral RF in the gas phase is available, and thus, the experimental S_1 spectrum presented herein can only be compared to the spectra recorded in the condensed phase and to data of related ionic complexes obtained in the gas phase. Absorption measurements of RF in the condensed phase show that the maximum of the first absorption band of RF is not strongly affected by the solvent and its pH value.^{25,43,44} The S_1 origin of isolated K^+RF at $22\,670\text{ cm}^{-1}$ ($\sim 441\text{ nm}$) occurs in between the determined absorption maxima for different solvents ranging from 449 (benzene) to 439 nm (dioxane).²⁶ This observation confirms that metalation at $O2$ has little impact on the S_1 energy. In water, the presence of Na^+ was found to shift the maximum of the S_1 absorption band by only 1 nm from 446 to 447 nm ,¹⁸ which—based on our data—may be taken as evidence that alkali ions prefer to bind to the $O2$ site also in aqueous solution. On the other hand, the maximum of the first absorption band of riboflavin monoanions (deprotonated at $N3$) in the gas phase is significantly red-shifted by $\sim 60\text{ nm}$,²¹ indicating that the charge (protonation) state of the chromophore may substantially affect the photophysical properties of RF (for a comparison to K^+RF , see Figure S7). In addition, the VISPD spectrum of K^+RF recorded at cryogenic temperatures is compared in Figure S8 to an absorption spectrum of RF in aqueous solution recorded at

room temperature, illustrating the drastic effects of solvation and elevated temperature on the spectral resolution and thus the appearance of the spectrum.

It is instructive to compare the geometric, vibrational, electronic, and optical properties of K^+RF to those recently reported for K^+LF .^{54,56} Both complexes show similarities in terms of computed values for electronic excitation, including excitation energies, oscillator strengths, and orbitals. This similarity is reflected in the minor S_1 origin difference of only 136 cm^{-1} for the $O2+$ isomers. On the other hand, introducing the ribityl chain at $N10$ changes the geometry significantly. While the $O2+/O4+$ isomers of K^+LF have C_s symmetry in the S_0 and S_1 states, $K^+RF(O2/O4+)$ has reduced C_1 symmetry in both S_0 and S_1 not only because the side chain is out-of-plane but also because the aromatic ring system is (slightly) bent in S_0 and S_1 (more pronounced for $O2$ than for $O4+$), which relaxes the selection rules for both electronic and vibrational transitions.

The different structural environments of the K^+ cation in K^+RF and K^+LF due to the interaction with the ribityl group in the former complex are also evident from the low-frequency inter- and intramolecular vibrational structure of the S_1 band of the $O2+$ isomer, which is compared as a function of S_1 internal energy in the expanded view in Figure 5. The spectra are

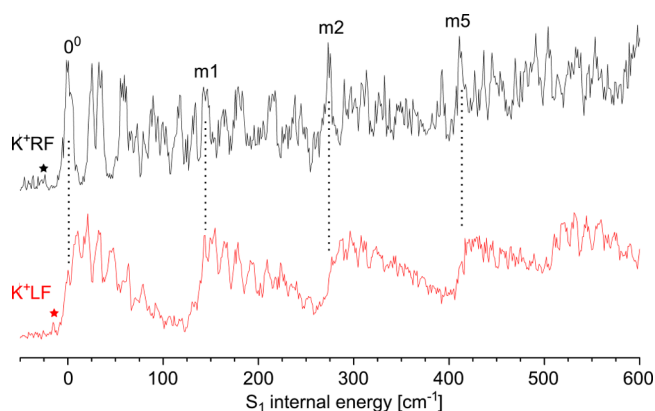


Figure 5. VISPD spectrum of the $S_1 \leftarrow S_0 (\pi\pi^*)$ transition of K^+RF (black) assigned to the $O2$ isomer compared to corresponding spectrum of K^+LF (red)⁵⁶ as a function of S_1 internal energy. Both spectra are recorded in the K^+ fragment channel under the same experimental conditions (Figure 3).

obtained with the same experimental setup (BerlinTrap) under comparable experimental conditions (same OPO laser and trap temperature). Interestingly, the density of low-frequency transitions decreases significantly from K^+LF to the more complex K^+RF ion. In particular, the K^+LF spectrum shows barely resolved progressions with rather low frequencies of $<10\text{ cm}^{-1}$ starting from the barely resolved S_1 origin band. This rather dense structure in low-frequency intermolecular modes of K^+LF has tentatively been attributed to a wide and shallow anharmonic double minimum potential for the in-plane bending mode of the metal ion, which corresponds to the $O2 \leftrightarrow O2+$ isomerization coordinate connecting the nearly isoenergetic $O2$ and $O2+$ isomers via low barriers, a conclusion supported by computed potential energy surfaces. Clearly, such low-frequency modes are not observed in the K^+RF spectrum, for which the 0^0 band is well-resolved and the first intense mode above the S_1 origin is observed at 24 cm^{-1} , i.e., at a much higher frequency compared to K^+LF . Apparently, the addi-

tional interaction of K^+ with the ribityl side chain via the multiple $M^+ \cdots OH$ bonds not only drastically increases the interaction strength at the O2 binding site but also makes the complex more rigid along the metal bending coordinate. This effect probably prevents the formation of a double minimum potential with O2 and O2+ minima, leading to a single O2 configuration in K^+RF . Indeed, the first three transitions above the S_1 origin at 24, 33, and 57 cm^{-1} are in good agreement with computed S_1 frequencies of the most stable O2(1) isomer of K^+RF (27, 33, and 49 cm^{-1} , respectively, denoted n1–n3). The first mode at 27 cm^{-1} (n1) is a butterfly mode with bending along the N5–N10 axis of the tricyclic ring, very similar to the butterfly mode of $H^+LF(N1)$, which also has a slightly bent isoalloxazine ring.⁵⁵ This mode also comprises a twisting motion of the ribityl chain along with the metal ion. At this stage, it is noted that K^+LF is a somewhat intermediate case in the series of M^+LF complexes with alkali ions. The M^+LF complexes with $M = Li, Na, Rb,$ and Cs also show well-resolved 0^0 band origins and do not show such low-frequency modes⁵⁶ because they have either no O2+ isomer (Rb and Cs) or a deeper and thus more isolated O2 potential minimum (Li and Na), giving rise to more regular S_1 spectra in the low-frequency range. The fact that $K^+RF(O2)$ also has a less congested S_1 spectrum than $K^+LF(O2+)$ supports the previous interpretation of the shallow double minimum potential of the latter complex.⁵⁶ Interestingly, also the weak but clearly visible hot bands in the K^+RF spectrum correspond to higher frequencies than in the case of K^+LF . From the intensities of the lowest-frequency mode (27 and 8 cm^{-1} for K^+RF and K^+LF , respectively) marked by asterisks in Figure 5, we estimate an upper limit for the ion temperature as $T \leq 30$ K.

While the low-frequency vibrational patterns in the K^+LF and K^+RF spectra differ strongly, they are both reproduced in combination with intramolecular modes associated with the isoalloxazine ring. These (near) in-plane modes of the chromophore (denoted m1, m2, etc.) have strong Franck–Condon (FC) activity upon S_1 excitation and are relatively independent of the metal-binding site and the substituent at N10.^{52–56} These intense transitions observed in the spectrum of K^+LF at 143, 274, and 416 cm^{-1} match very well with those in the K^+RF spectrum at 145, 274, and 413 cm^{-1} , as indicated by the vertical dotted lines in Figure 5. A more detailed description of the normal coordinates of these vibrations is available in our previous reports on related flavin complexes.^{51–56} Interestingly, while for $K^+LF(O2+)$ the computed inter- and intramolecular modes are mostly isolated and uncoupled, many of the low-frequency modes for K^+RF are more strongly coupled due to the presence of the flexible ribityl chain. Especially the intermolecular $M^+ \cdots RF$ bend and stretch modes (β and σ) strongly couple to the ribityl group because of the strong $M^+ \cdots$ ribityl interaction. Furthermore, the m1 mode of K^+RF computed at 161 cm^{-1} clearly couples to the $M^+ \cdots RF$ stretching mode (σ), and thus, its frequency is significantly larger than that of m1 in $K^+LF(O2+)$ (140 cm^{-1} in S_1). Table 5 compares the measured and computed frequencies for the low-frequency in-plane modes of a $K^+RF(O2)$ to those of LF and $K^+LF(O2+/O4+)$. In general, the intramolecular frequencies computed for K^+RF overestimate slightly but systematically the experimental ones, with maximum and mean deviations of 24 and 15 cm^{-1} , respectively. This effect is also visible in corresponding FC simulations shown in Figure 6, in which we compare the VISPD spectrum of K^+RF with that computed for the most

Table 5. Measured In-Plane Intramolecular Frequencies (in cm^{-1}) in the S_1 State of LF, K^+RF , and K^+LF Compared to Frequencies Computed at the PBE0/cc-pVDZ Level^a

	LF		K^+RF O2(1)		K^+LF O2+		K^+LF O4+	
	calc	exp	calc	exp	calc	exp	calc	exp
m1	165	164	161	145	140	143	202	194
m2	276	274	282	274	274	274	287	286
m3	294		298	274	295	296	295	302
m4	322		322		325	316	332	335
m5	409	403	425	413	416	416	450	443
m6	444	440	443		456	457	421	415
m7	489		493		496		495	
m8	521	513	545		522	522	529	

^aData for LF and K^+LF are taken from refs 32 and 54 and 56, respectively.

stable O2(1) isomer. As can be seen, the FC simulations reproduce reasonably well the complexity of the spectrum, as well as the vibrational pattern of both the low-frequency modes (n1–n3) and the intramolecular in-plane skeletal modes (m1–m8). The high density of low-frequency modes arises from the lack of any structural symmetry and large geometry changes upon S_1 excitation. The experimental intensities may suffer to some extent from saturation effects, as shown previously in studies of the effect of laser intensity on the relative intensity of vibronic transitions in related flavin complexes.⁵⁶ Moreover, some of the low-frequency out-of-plane modes may be rather anharmonic, and thus, the harmonic FC simulations may not quantitatively reproduce both frequency and intensity. Unfortunately, the FC simulations are not sensitive enough to unambiguously determine the conformation of the ribityl side chain of the observed $K^+RF(O2)$ isomer, as shown in Figure S9, where we provide such simulated spectra for the low-energy O2(1–4) isomers of K^+RF . Nonetheless, because the S_1 origins of these isomers differ significantly (Table 3), the experimental VISPD spectrum in the vicinity of the S_1 origin is probably produced by a single isomer only, and this view is also consistent with the observed and predicted density of vibronic transitions and their assignment to the most stable O2(1) isomer. In the future, isomer-selective double-resonance experiments may address this question in more detail.^{68–70,73}

The rich vibronic activity observed in the measured and computed S_1 spectra of K^+RF is induced by the significant geometry changes triggered by electronic $\pi\pi^*$ excitation (Table S3). As the involved molecular orbitals are mostly located on the isoalloxazine chromophore, these geometry changes are similar for related flavin complexes, and particularly the in-plane intramolecular modes have similar frequencies and vibronic intensities, as shown in Figure 5 for K^+RF and K^+LF . Indeed, the bond-length changes upon $S_1 \leftarrow S_0$ excitation of K^+LF and K^+RF are nearly identical for the aromatic ring system (Table S4). The maximum difference in the bond-length change within rings I–III of these two flavin complexes is 0.9 pm. For the O2(1) isomer of K^+RF , the largest structural change is an elongation of the N1–K bond (by 5.1 pm), while the O2–K bond contracts slightly (by 1.6 pm). On the other hand, the bond lengths of K to the ribityl chain are less affected (<1.0 pm), with the notable exception of the contraction of the Oa–K bond by 4.7 pm. This observation is consistent with the small change in the $K^+ \cdots RF$ interaction strength upon S_1 excitation. In contrast, the K–N5 bond length of the $K^+RF(O4+)$ isomer contracts significantly (by

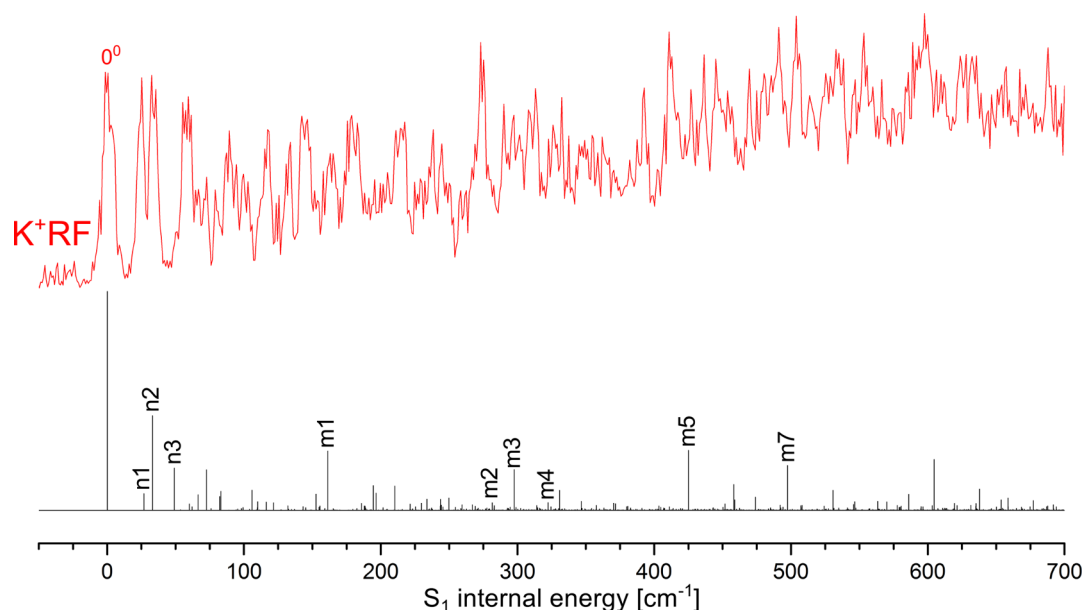


Figure 6. VISPD spectrum of the $S_1 \leftarrow S_0$ ($\pi\pi^*$) transition of K^+RF recorded at $T = 6$ K compared to Franck–Condon simulations of the most stable O2 isomer. Both spectra are plotted as a function of S_1 internal energy.

15.9 pm) because of the strong increase in $K^+\cdots RF$ interaction strength upon S_1 excitation at this metal-binding site, as evident from the large predicted S_1 red-shift for this isomer.⁵⁴

The rich vibronic activity in the VISPD spectrum of K^+RF is partly attributed to the reduced C_1 symmetry, which makes all transitions FC allowed. We can safely exclude tagged complexes, which may possibly form in the ion trap,^{52–56} as carriers for some of the vibronic transition. For example, VISPD of $K^+RF\text{--}He$ or $K^+RF\text{--}N_2$ will also produce transitions in the monitored K^+ fragment channel and thus may increase the density of transitions. However, at $T = 6$ K no tagged complexes are formed in the ion trap (Figure S1), probably because of the relatively weak interaction of He and N_2 with K^+ , and thus, the VISPD signal attributed to K^+RF is free from such a contamination. A further possibility is that some peaks may arise from vibronic coupling to close-lying higher electronic states. For example, the S_2 ($n\pi^*$) state of the most stable O2(1) isomer of K^+RF is vertically only 860 cm^{-1} above the S_1 ($\pi\pi^*$) state, and although its oscillator strength is close to zero ($f = 0.002$), it may gain intensity via vibronic coupling. Such coupling has been invoked from calculations and spectroscopic experiments of bare RF.^{25,44} The detection of the second optically bright S_4 ($\pi\pi^*$) state of this isomer is unlikely, because this state is computed to be vertically 4168 cm^{-1} above S_1 . Finally, although some of the computed O2 isomers of K^+RF are low in energy, there is no clear evidence for the presence of a second isomer, at least in the spectral range near the S_1 origin, although we cannot exclude transitions from such isomers in the more-congested, higher-energy part of the observed S_1 band.

The width of the narrowest transitions in the VISPD spectrum (5 cm^{-1}) provides a rough estimate for the lower limit of the S_1 lifetime of K^+RF as $\tau \geq 1$ ps. Spectroscopic experiments of bare RF in solution report a lifetime on the order of 10–20 fs for the FC state involved in S_1 excitation, which has been attributed to fast coupling of the $\pi\pi^*$ state with the nearby $n\pi^*$ state.²⁵ It is unclear at the moment whether solvation or metal complexation causes the rather different lifetime of the initially excited S_1 state of RF.

4. CONCLUDING REMARKS

In summary, the interaction of alkali metal ions with riboflavin and its impact on the geometrical, vibrational, and optical properties of RF are characterized by vibrational and electronic spectroscopy of isolated M^+RF complexes produced in an ESI source combined with DFT calculations. IRMPD spectra for M^+RF with $M = Li, Na$, and Cs analyzed in the informative CO stretch range illustrate that the M^+ cation preferentially binds to one of the two available CO groups of the RF chromophore. While there is some weak evidence for the preference for the O2 binding site, the O4+ isomer cannot be ruled out from IR spectroscopy. On the other hand, optical spectroscopy of cryogenic M^+RF with $M = K$ (produced in a similar ESI source) clearly shows that the population is dominated by only the O2 isomer, while that of the O4+ isomer is below the detection limit. In this respect, optical spectroscopy for this example is more sensitive to isomeric structure than IR spectroscopy. Actually, the comparison of the IRMPD spectra of M^+RF and M^+LF would lead to a wrong isomer assignment, indicating that optical spectroscopy and DFT calculations are crucial for the correct isomer assignment in this particular case. The exclusive observation of the O2 isomer is consistent with the thermochemical prediction of DFT calculations, which show that the O2 isomers of M^+RF are strongly stabilized by the interaction of M^+ with the ribityl side chain via multiple ionic $M^+\cdots OH$ contacts to the hydroxyl groups of the sugar residue. The observed VISPD spectrum of K^+RF with a band origin at 22 670 cm^{-1} (441.11 nm) is readily assigned to the bright $S_1 \leftarrow S_0$ ($\pi\pi^*$) transition of the O2 isomer of K^+RF . Significantly, the VISPD spectrum exhibits vibrational resolution because of cryogenic cooling down to $T \leq 30$ K, which allows for a detailed analysis of the vibrational structure of both low-frequency out-of-plane and higher-frequency in-plane modes. Comparison of this transition of K^+RF with that of K^+LF illustrates that methyl \rightarrow ribityl substitution at N10 has essentially no impact on the electronic structure because the involved transition orbitals are largely located on the isoalloxazine chromophore. On the other hand, methyl \rightarrow

ribityl substitution has a significant impact on the geometry, vibrational structure, and potential for $O_2 \leftrightarrow O_2^+$ isomerization because of the additional $M^+ \cdots$ ribityl interaction and the loss of structural symmetry due to nonplanarity of the aromatic chromophore. Finally, although the VISPD spectrum is consistent with an assignment of the most stable $O_2(1)$ isomer of K^+RF , the orientation of the flexible ribityl side chain is not determined unambiguously yet. To this end, isomer-selective double-resonance spectroscopy (IR-IR, IR-VIS, and VIS-VIS), along with more sophisticated computational analysis, may be employed in future work to unambiguously determine the side-chain configuration. In contrast to M^+RF , the N1 isomer is the most stable global minimum for H^+RF ,⁵⁰ and this different behavior of the proton and alkali ions is readily explained by the large ionic radii of M^+ as compared to H^+ and the difference in chemical bonding, which is mostly electrostatic for M^+ and covalent for H^+ .

■ ASSOCIATED CONTENT

Supporting Information

The Supporting Information is available free of charge at <https://pubs.acs.org/doi/10.1021/acs.jpca.1c01846>.

Mass spectra of K^+RF , structures of RF and M^+RF , computed IR spectra of all M^+RF , IRMPD spectra of Li^+LF and Li^+RF , comparison of the VISPD spectrum of K^+RF to the spectrum for deprotonated RF and to the absorption spectrum of RF in solution, FC simulations for $K^+RF(O_2)$ isomers, binding energies and relative energies of relevant M^+RF isomers, atomic charges for RF and K^+RF , and Cartesian coordinates and energies of all relevant structures (PDF)

■ AUTHOR INFORMATION

Corresponding Author

Otto Dopfer – Institut für Optik und Atomare Physik,
Technische Universität Berlin, D-10623 Berlin, Germany;
✉ orcid.org/0000-0002-9834-4404; Email: dopfer@physik.tu-berlin.de; Fax: +49 30 314 23018

Author

David Müller – Institut für Optik und Atomare Physik,
Technische Universität Berlin, D-10623 Berlin, Germany

Complete contact information is available at:
<https://pubs.acs.org/doi/10.1021/acs.jpca.1c01846>

Notes

The authors declare no competing financial interest.

■ ACKNOWLEDGMENTS

This work was supported by Deutsche Forschungsgemeinschaft (DFG, Project DO 729/6-2). The IRMPD experiments at FELIX were supported by funding from the European Community's Seventh Framework Program (FP7/2007-2013) under Grant agreement 226716 (FELIX Project 021-2011). We gratefully acknowledge the support of Giel Berden, Jos Oomens, Britta Redlich, and their co-workers from the FELIX laboratory as well as Alan Günther and Judith Langer (TU Berlin) in recording the IRMPD spectrum of Na^+RF . The IRMPD experiments at CLIO were supported by funding from the European Union's Seventh Framework Program (FP7/2012-2015) under Grant agreement 312284 (CLIO Project IC 14-019). We gratefully acknowledge the support of Philippe

Maitre and co-workers from the CLIO laboratory and Aude Bouchet and Johanna Klyne (TU Berlin) in recording the IRMPD spectra of Li^+RF and Cs^+RF . We also thank Pablo Nieto and Carlsson Kluth for initial ground-state computations for M^+RF . O.D. thanks Dan Neumark for many scientific discussions and his longstanding friendship and support.

■ REFERENCES

- (1) Heelis, P. F. The Photophysical and Photochemical Properties of Flavins (Isoalloxazines). *Chem. Soc. Rev.* **1982**, *11*, 15.
- (2) Massey, V. The Chemical and Biological Versatility of Riboflavin. *Biochem. Soc. Trans.* **2000**, *28*, 283–296.
- (3) Losi, A. Flavin-Based Blue-Light Photosensors. A Photobiophysics Update. *Photochem. Photobiol.* **2007**, *83*, 1283–1300.
- (4) Sancar, A. Structure and Function of DNA Photolyase and Cryptochrome Blue-Light Photoreceptors. *Chem. Rev.* **2003**, *103*, 2203–2237.
- (5) Buckel, W.; Thauer, R. K. Flavin-Based Electron Bifurcation, A New Mechanism of Biological Energy Coupling. *Chem. Rev.* **2018**, *118*, 3862–3886.
- (6) Romero, E.; Gómez Castellanos, J. R.; Gadda, G.; Fraaije, M. W.; Mattevi, A. Same Substrate, Many Reactions: Oxygen Activation in Flavoenzymes. *Chem. Rev.* **2018**, *118*, 1742–1769.
- (7) Silva, E.; Edwards, A. M. *Flavins, Photochemistry and Photobiology*; RSC Publishing: Cambridge, 2006.
- (8) Rutter, W. J.; Dalziel, K.; Viervoll, H.; Zackrisson, M.; Ernster, L.; Diczfalusy, E. The Interaction of Riboflavin, FMN, and FAD with Various Metal Ions. The Riboflavin Catalyzed Photochemical Reduction of FeIII, and Photooxidation of FeII. *Acta Chem. Scand.* **1958**, *12*, 438–446.
- (9) Baarda, I. F.; Metzler, D. E. Complexes of Riboflavin with Silver and Other Metal Ions. *Biochim. Biophys. Acta* **1961**, *50*, 463–471.
- (10) Bamberg, P.; Hemmerich, P. Farbe und Konstitution der Isoalloxazin-Silber-Komplexe. Zum Verhalten des Riboflavins gegen Metallionen II. *Helv. Chim. Acta* **1961**, *44*, 1001–1011.
- (11) Varnes, A. W.; Dodson, R. B.; Wehry, E. L. Interactions of Transition-Metal Ions with Photoexcited States of Flavins. Fluorescence Quenching Studies. *J. Am. Chem. Soc.* **1972**, *94*, 946–950.
- (12) Lauterwein, J.; Hemmerich, P.; Lhoste, J. M. Flavoquinone-Metal Complexes. I. Structure and Properties. *Inorg. Chem.* **1975**, *14*, 2152–2161.
- (13) Lauterwein, J.; Hemmerich, P.; Lhoste, J. M. Flavoquinone-Metal Complexes. II. Paramagnetic Interactions. *Inorg. Chem.* **1975**, *14*, 2161–2168.
- (14) Benecky, M.; Yu, T.-J.; Watters, K. L.; McFarland, J. T. Metal-Flavin Complexation. A Resonance Raman Investigation. *Biochim. Biophys. Acta, Protein Struct.* **1980**, *626*, 197–207.
- (15) Fukuzumi, S.; Kojima, T. Control of Redox Reactivity of Flavin and Pterin Coenzymes by Metal Ion Coordination and Hydrogen Bonding. *JBIC, J. Biol. Inorg. Chem.* **2008**, *13*, 321–333.
- (16) Ahmad, I.; Anwar, Z.; Ahmed, S.; Sheraz, M. A.; Khattak, S.-U.-R. Metal Ion Mediated Photolysis Reactions of Riboflavin: A Kinetic Study. *J. Photochem. Photobiol., B* **2017**, *173*, 231–239.
- (17) Spence, J. T.; Peterson, E. R. Infra-Red Spectra of Metal Complexes of Riboflavin. *J. Inorg. Nucl. Chem.* **1962**, *24*, 601–608.
- (18) Lewandowski, D.; Schroeder, G.; Sawczak, M.; Ossowski, T. Fluorescence Properties of Riboflavin-Functionalized Mesoporous Silica SBA-15 and Riboflavin Solutions in Presence of Different Metal and Organic Cations. *J. Phys. Chem. Solids* **2015**, *85*, 56–61.
- (19) Stockett, M. H. Photo-induced Proton-coupled Electron Transfer and Dissociation of Isolated Flavin Adenine Dinucleotide Mono-Anions. *Phys. Chem. Chem. Phys.* **2017**, *19*, 25829–25833.
- (20) Giacomozzi, L.; Kjær, C.; Langeland Knudsen, J.; Andersen, L. H.; Brøndsted Nielsen, S.; Stockett, M. H. Absorption and Luminescence Spectroscopy of Mass-selected Flavin Adenine Dinucleotide Mono-anions. *J. Chem. Phys.* **2018**, *148*, 214309.
- (21) Bull, J. N.; Carrascosa, E.; Giacomozzi, L.; Bieske, E. J.; Stockett, M. H. Ion Mobility Action Spectroscopy of Flavin Dianions

Reveals Deprotomer-dependent Photochemistry. *Phys. Chem. Chem. Phys.* **2018**, *20*, 19672–19681.

(22) Matthews, E.; Dessent, C. E. H. Observation of Near-Threshold Resonances in the Flavin Chromophore Anions Alloxazine and Lumichrome. *J. Phys. Chem. Lett.* **2018**, *9*, 6124–6130.

(23) Matthews, E.; Cercola, R.; Dessent, C. E. H. Protomer-Dependent Electronic Spectroscopy and Photochemistry of the Model Flavin Chromophore Alloxazine. *Molecules* **2018**, *23*, 2036.

(24) Lincke, K.; Langeland, J.; Madsen, A. Ø.; Kiefer, H. V.; Skov, L.; Gruber, E.; Mikkelsen, K. V.; Andersen, L. H.; Nielsen, M. B.; et al. Elucidation of the Intrinsic Optical Properties of Hydrogen-Bonded and Protonated Flavin Chromophores by Photodissociation Action Spectroscopy. *Phys. Chem. Chem. Phys.* **2018**, *20*, 28678–28684.

(25) Weigel, A.; Dobryakov, A. L.; Veiga, M.; Pérez Lustres, J. L. Photoinduced Processes in Riboflavin: Superposition of $\pi\pi^*$ - $n\pi^*$ States by Vibronic Coupling, Transfer of Vibrational Coherence, and Population Dynamics under Solvent Control. *J. Phys. Chem. A* **2008**, *112*, 12054–12065.

(26) Zirak, P.; Penzkofer, A.; Mathes, T.; Hegemann, P. Photodynamics of Roseoflavin and Riboflavin in Aqueous and Organic Solvents. *Chem. Phys.* **2009**, *358*, 111–122.

(27) Sikorska, E.; Khmelinskii, I. V.; Prukala, W.; Williams, S. L.; Patel, M.; Worrall, D. R.; Bourdelande, J. L.; Koput, J.; Sikorski, M.; et al. Spectroscopy and Photophysics of Lumiflavins and Lumichromes. *J. Phys. Chem. A* **2004**, *108*, 1501–1508.

(28) Wolf, M. M. N.; Schumann, C.; Gross, R.; Domratheva, T.; Diller, R. Ultrafast Infrared Spectroscopy of Riboflavin. Dynamics, Electronic Structure, and Vibrational Mode Analysis. *J. Phys. Chem. B* **2008**, *112*, 13424–13432.

(29) Zhang, T.; Papon, K.; Ochran, R.; Ridge, D. P. Stability of Flavin Semiquinones in the Gas Phase. The Electron Affinity, Proton Affinity, and Hydrogen Atom Affinity of Lumiflavin. *J. Phys. Chem. A* **2013**, *117*, 11136–11141.

(30) Guyon, L.; Tabarin, T.; Thuillier, B.; Antoine, R.; Broyer, M.; Boutou, V.; Wolf, J. P.; Dugourd, P. Femtosecond Pump-Probe Experiments on Trapped Flavin. Optical Control of Dissociation. *J. Chem. Phys.* **2008**, *128*, 075103.

(31) Klaumünzer, B.; Kröner, D.; Lischka, H.; Saalfrank, P. Non-adiabatic Excited State Dynamics of Riboflavin after Photoexcitation. *Phys. Chem. Chem. Phys.* **2012**, *14*, 8693–8702.

(32) Vdovin, A.; Slenczka, A.; Dick, B. Electronic Spectroscopy of Lumiflavin in Superfluid Helium Nanodroplets. *Chem. Phys.* **2013**, *422*, 195–203.

(33) Quick, M.; Weigel, A.; Ernsting, N. P. Fluorescence Following Excited-State Protonation of Riboflavin at N(5). *J. Phys. Chem. B* **2013**, *117*, 5441–5447.

(34) Weigel, A.; Dobryakov, A.; Klaumünzer, B.; Sajadi, M.; Saalfrank, P.; Ernsting, N. P. Femtosecond Stimulated Raman Spectroscopy of Flavin after Optical Excitation. *J. Phys. Chem. B* **2011**, *115*, 3656–3680.

(35) Sikorska, E.; Khmelinskii, I.; Komasa, A.; Koput, J.; Ferreira, L. F. V.; Herance, J. R.; Bourdelande, J. L.; Williams, S. L.; Worrall, D. R.; et al. Spectroscopy and Photophysics of Flavin Related Compounds. Riboflavin and iso-(6,7)-Riboflavin. *Chem. Phys.* **2005**, *314*, 239–247.

(36) Neiss, C.; Saalfrank, P.; Parac, M.; Grimme, S. Quantum Chemical Calculation of Excited States of Flavin-Related Molecules. *J. Phys. Chem. A* **2003**, *107*, 140–147.

(37) Hasegawa, J.; Bureekaew, S.; Nakatsuji, H. SAC-CI Theoretical Study on the Excited States of Lumiflavin. Structure, Excitation Spectrum, and Solvation Effect. *J. Photochem. Photobiol., A* **2007**, *189*, 205–210.

(38) Salzmann, S.; Marian, C. M. Effects of Protonation and Deprotonation on the Excitation Energies of Lumiflavin. *Chem. Phys. Lett.* **2008**, *463*, 400–404.

(39) Salzmann, S.; Martinez-Junza, V.; Zorn, B.; Braslavsky, S. E.; Mansurova, M.; Marian, C. M.; Gärtner, W. Photophysical Properties of Structurally and Electronically Modified Flavin Derivatives

Determined by Spectroscopy and Theoretical Calculations. *J. Phys. Chem. A* **2009**, *113*, 9365–9375.

(40) Salzmann, S.; Tatchen, J.; Marian, C. M. The Photophysics of Flavins: What Makes the Difference Between Gas Phase and Aqueous Solution? *J. Photochem. Photobiol., A* **2008**, *198*, 221–231.

(41) Klaumünzer, B.; Kröner, D.; Saalfrank, P. (TD-)DFT Calculation of Vibrational and Vibronic Spectra of Riboflavin in Solution. *J. Phys. Chem. B* **2010**, *114*, 10826–10834.

(42) Sikorska, E.; Khmelinskii, I. V.; Koput, J.; Bourdelande, J. L.; Sikorski, M. Electronic Structure of Isoalloxazines in their Ground and Excited States. *J. Mol. Struct.* **2004**, *697*, 137–141.

(43) Drössler, P.; Holzer, W.; Penzkofer, A.; Hegemann, P. pH Dependence of the Absorption and Emission Behaviour of Riboflavin in Aqueous Solution. *Chem. Phys.* **2002**, *282*, 429–439.

(44) Sun, M.; Moore, T. A.; Song, P. S. Molecular Luminescence Studies of Flavins. I. The Excited States of Flavins. *J. Am. Chem. Soc.* **1972**, *94*, 1730–1740.

(45) Wolf, M. M. N.; Zimmermann, H.; Diller, R.; Domratheva, T. Vibrational Mode Analysis of Isotope-Labeled Electronically Excited Riboflavin. *J. Phys. Chem. B* **2011**, *115*, 7621–7628.

(46) Climent, T.; González-Luque, R.; Merchán, M.; Serrano-Andrés, L. Theoretical Insight into the Spectroscopy and Photochemistry of Isoalloxazine, the Flavin Core Ring. *J. Phys. Chem. A* **2006**, *110*, 13584–13590.

(47) Karasulu, B.; Götze, J. P.; Thiel, W. Assessment of Franck-Condon Methods for Computing Vibrationally Broadened UV-vis Absorption Spectra of Flavin Derivatives: Riboflavin, Roseoflavin, and 5-Thioflavin. *J. Chem. Theory Comput.* **2014**, *10*, 5549–5566.

(48) Wu, M.; Eriksson, L. A. Absorption Spectra of Riboflavin-A Difficult Case for Computational Chemistry. *J. Phys. Chem. A* **2010**, *114*, 10234–10242.

(49) Günther, A.; Nieto, P.; Berden, G.; Oomens, J.; Dopfer, O. IRMPD Spectroscopy of Metalated Flavins: Structure and Bonding of M^{q+} -Lumichrome Complexes ($M^{q+} = Li^+-Cs^+, Ag^+, Mg^{2+}$). *Phys. Chem. Chem. Phys.* **2014**, *16*, 14161–14171.

(50) Langer, J.; Günther, A.; Seidenbecher, S.; Berden, G.; Oomens, J.; Dopfer, O. Probing Protonation Sites of Isolated Flavins Using IR Spectroscopy: From Lumichrome to the Cofactor Flavin Mononucleotide. *ChemPhysChem* **2014**, *15*, 2550–2562.

(51) Nieto, P.; Günther, A.; Berden, G.; Oomens, J.; Dopfer, O. IRMPD Spectroscopy of Metalated Flavins: Structure and Bonding of Lumiflavin Complexes with Alkali and Coinage Metal Ions. *J. Phys. Chem. A* **2016**, *120*, 8297–8308.

(52) Nieto, P.; Müller, D.; Sheldrick, A.; Günther, A.; Miyazaki, M.; Dopfer, O. Effect of Alkali Ions on Optical Properties of Flavins: Vibronic Spectra of Cryogenic M^+ Lumichrome Ions ($M = Li-Cs$) in the Gas Phase. *Phys. Chem. Chem. Phys.* **2018**, *20*, 22148–22158.

(53) Sheldrick, A.; Müller, D.; Günther, A.; Nieto, P.; Dopfer, O. Optical Spectroscopy of Isolated Flavins: Photodissociation of Protonated Lumichrome. *Phys. Chem. Chem. Phys.* **2018**, *20*, 7407–7414.

(54) Müller, D.; Nieto, P.; Miyazaki, M.; Dopfer, O. Effect of Alkali Ions on Optical Properties of Flavins: Vibronic Spectra of Cryogenic M^+ Lumiflavin Complexes ($M = Li-Cs$). *Faraday Discuss.* **2019**, *217*, 256–275.

(55) Müller, D.; Dopfer, O. Vibronic Optical Spectroscopy of Cryogenic Flavin Ions: The O2+ and N1 Tautomers of Protonated Lumiflavin. *Phys. Chem. Chem. Phys.* **2020**, *22*, 18328.

(56) Müller, D.; Dopfer, O. Optical Spectroscopy of Cryogenic Metalated Flavins: The O2(+) Isomers of M^+ Lumiflavin ($M = Li-Cs$). *J. Photochem. Photobiol.* **2020**, *3–4*, 100009.

(57) Takahashi, M.; Ishikawa, Y.; Nishizawa, J. I.; Ito, H. Low-Frequency Vibrational Modes of Riboflavin and Related Compounds. *Chem. Phys. Lett.* **2005**, *401*, 475–482.

(58) Maitre, P.; Le Caër, S.; Simon, A.; Jones, W.; Lemaire, J.; Mestdag, H.; Heninger, M.; Mauclair, G.; Boissel, P.; Prazeres, R.; et al. Ultrasensitive Spectroscopy of Ionic Reactive Intermediates in the Gas Phase Performed with the First Coupling of an IR FEL with

an FTICR-MS. *Nucl. Instrum. Methods Phys. Res., Sect. A* **2003**, 507, 541–546.

(59) Oepts, D.; van der Meer, A. F. G.; van Amersfoort, P. W. The Free-Electron-Laser User Facility FELIX. *Infrared Phys. Technol.* **1995**, 36, 297–308.

(60) Valle, J. J.; Eyler, J. R.; Oomens, J.; Moore, D. T.; van der Meer, A. F. G.; von Helden, G.; Meijer, G.; Hendrickson, C. L.; Marshall, A. G.; Blakney, G. T. Free Electron Laser-Fourier Transform Ion Cyclotron Resonance Mass Spectrometry Facility for Obtaining Infrared Multiphoton Dissociation Spectra of Gaseous Ions. *Rev. Sci. Instrum.* **2005**, 76, 023103.

(61) Bouchet, A.; Klyne, J.; Piani, G.; Dopfer, O.; Zehnacker, A. Diastereo-specific Conformational Properties of Neutral, Protonated and Radical Cation Forms of (1 R, 2 S)-Cis-and (1 R, 2 R)-Trans-Amino-Indanol by Gas Phase Spectroscopy. *Phys. Chem. Chem. Phys.* **2015**, 17, 25809–25821.

(62) Chiavarino, B.; Crestoni, M. E.; Schütz, M.; Bouchet, A.; Piccirillo, S.; Steinmetz, V.; Dopfer, O.; Fornarini, S. Cation- π Interactions in Protonated Phenylalkylamines. *J. Phys. Chem. A* **2014**, 118, 7130–7138.

(63) Günther, A.; Nieto, P.; Müller, D.; Sheldrick, A.; Gerlich, D.; Dopfer, O. BerlinTrap: A New Cryogenic 22-Pole Ion Trap Spectrometer. *J. Mol. Spectrosc.* **2017**, 332, 8–15.

(64) Frisch, M. J.; Trucks, G. W.; Schlegel, H. B.; Scuseria, G. E.; Robb, M. A.; Cheeseman, J. R.; Scalmani, G.; Barone, V.; Petersson, G. A., et al. *Gaussian 16*, Revision C.01; Gaussian, Inc.: Wallingford, CT, 2016.

(65) Lim, I. S.; Schwerdtfeger, P.; Metz, B.; Stoll, H. All-Electron and Relativistic Pseudopotential Studies for the Group 1 Element Polarizabilities from K to Element 119. *J. Chem. Phys.* **2005**, 122, 104103.

(66) Oomens, J.; Sartakov, B. G.; Meijer, G.; von Helden, G. von Gas-Phase Infrared Multiple Photon Dissociation Spectroscopy of Mass-selected Molecular Ions. *Int. J. Mass Spectrom.* **2006**, 254, 1–19.

(67) Platenkamp, R. J.; van Osnabrugge, H. D.; Visser, A. J. W. G. High-Resolution Fluorescence and Excitation Spectroscopy of N₃-Undecylfluoranthene in n-Decane. *Chem. Phys. Lett.* **1980**, 72, 104–111.

(68) Rizzo, T. R.; Stearns, J. a.; Boyarkin, O. V. Spectroscopic Studies of Cold, Gas-Phase Biomolecular Ions. *Int. Rev. Phys. Chem.* **2009**, 28, 481–515.

(69) Boyarkin, O. V. Cold Ion Spectroscopy for Structural Identifications of Biomolecules. *Int. Rev. Phys. Chem.* **2018**, 37, 559–606.

(70) Ishiuchi, S.; Wako, H.; Kato, D.; Fujii, M. High-Cooling-Efficiency Cryogenic Quadrupole Ion Trap and UV-UV Hole Burning Spectroscopy of Protonated Tyrosine. *J. Mol. Spectrosc.* **2017**, 332, 45–51.

(71) Zagorec-Marks, W.; Smith, J. E. T.; Foreman, M. M.; Sharma, S.; Weber, J. M. Intrinsic Electronic Spectra of Cryogenically Prepared Protoporphyrin IX Ions in Vacuo - Deprotonation-induced Stark Shifts. *Phys. Chem. Chem. Phys.* **2020**, 22, 20295–20302.

(72) Weichman, M. L.; Neumark, D. M. Slow Photoelectron Velocity-Map Imaging of Cryogenically Cooled Anions. *Annu. Rev. Phys. Chem.* **2018**, 69, 101–124.

(73) Bouchet, A.; Klyne, J.; Ishiuchi, S.; Dopfer, O.; Fujii, M.; Zehnacker, A. Stereochemistry-dependent Structure of Hydrogen-bonded Protonated Dimers: the Case of 1-Amino-2-Indanol. *Phys. Chem. Chem. Phys.* **2018**, 20, 12430–12443.

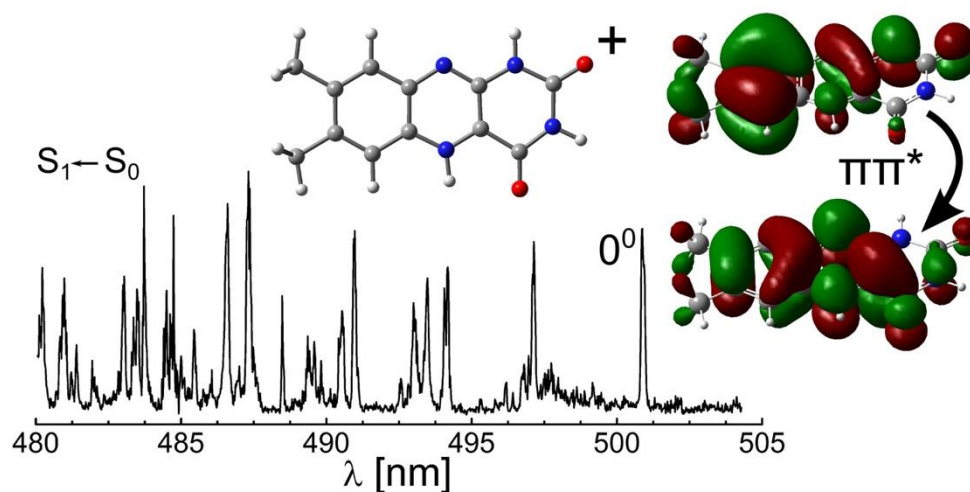
4.5. Optical spectroscopy of isolated flavins: photodissociation of protonated lumichrome

Alexander Sheldrick, David Müller, Alan Günther, Pablo Nieto and Otto Dopfer

Phys. Chem. Chem. Phys., 2018, **20**, 7407

<https://doi.org/10.1039/C8CP00590G>

Reproduced with permission of the PCCP Owner Societies



Declaration of Contribution

The experimental data were acquired by David Müller and Alexander Sheldrick. Computational data were acquired by Alexander Sheldrick, Pablo Nieto, and David Müller. The manuscript was written by Pablo Nieto and reviewed by all co-authors. All work was supervised by Otto Dopfer.



Cite this: *Phys. Chem. Chem. Phys.*,
2018, 20, 7407

Received 26th January 2018,
Accepted 21st February 2018

DOI: 10.1039/c8cp00590g

rsc.li/pccp

Optical spectroscopy of isolated flavins: photodissociation of protonated lumichrome†

Alexander Sheldrick, David Müller, Alan Günther, Pablo Nieto and Otto Dopfer *

The optical properties of flavins strongly depend on the charge and oxidation states as well as the environment. Herein, the electronic spectrum of cold protonated lumichrome, the smallest flavin molecule, is recorded by means of photodissociation in the visible range (VISPD) in a cryogenic ion trap tandem mass spectrometer coupled to an electrospray ionization source. The vibronic spectrum is assigned to the $S_1 \leftarrow S_0$ ($\pi\pi^*$) transition of the most stable N5-protonated isomer by comparison with quantum chemical calculations at the PBE0/cc-pVDZ level in combination with multi-dimensional Franck–Condon simulations. Analysis of the geometric and electronic structures of neutral and protonated lumichrome explains the large red shift of the band origin upon protonation ($\Delta S_1 \sim -6000\text{ cm}^{-1}$), which corresponds to the increase in proton affinity upon S_1 excitation as a result of charge transfer. N5 protonation greatly modifies the structure of the central pyrazine ring of the chromophore. The orbitals involved in $S_1 \leftarrow S_0$ excitation include an important fraction of the probability at the central ring and they are, hence, largely influenced by the positive charge of the attached proton. The rich vibronic spectrum indicates the large geometry change upon S_1 excitation. This combined experimental and computational approach is shown to be suitable to determine the optical properties of flavins as a function of oxidation, protonation, metalation, and microsolvation state.

1. Introduction

Flavins are a family of yellow bioorganic dye molecules derived from the 7,8-dimethyl-10-alkylisoalloxazine chromophore (isolumichrome = iso-LC for $R = H$). Due to the ability of the chromophore to absorb in a wide spectral range, flavins play a vital role in many biological processes.^{1,2} Flavins only differ by

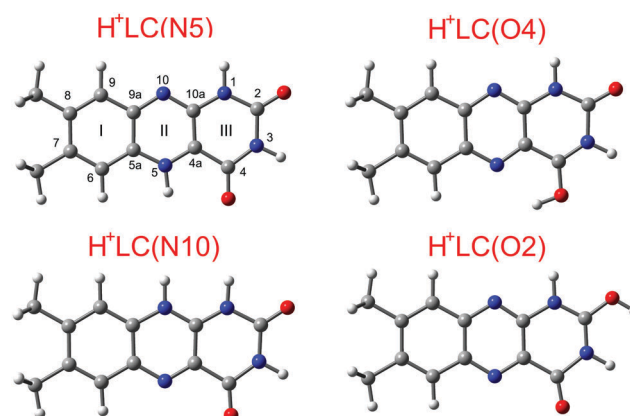


Fig. 1 Lowest-energy structural isomers of protonated lumichrome (H^+LC) calculated at the PBE0/cc-pVDZ level. Atomic and ring numbers are indicated for $H^+LC(N5)$ according to IUPAC notation.

the substituent (R) attached to the N10 position of the chromophore (Fig. 1). The most prominent members of the flavin family include lumichrome (LC, no substituent at N10 but H at N1), lumiflavin (LF, $R = \text{methyl}$), riboflavin (RF, $R = \text{ribityl}$, vitamin B_2), and flavin mononucleotide (FMN, $R = \text{ribophosphate}$). The range of the absorption sensitively depends on the substituent, the protonation, metalation, and oxidation state, as well as the solvent environment. Thus, the absorption spectrum has been shown to be a valuable indicator to determine changes in the electronic structure of the flavin.^{2–8} The ability of flavins to serve as electron donors and acceptors depending on environment and their wide absorption bands have made them an integral part of many biological processes.² Examples of the latter have been found in fungi, where flavins act as blue light receptors or as light sensory modules in plants and bacteria.^{9,10} Their potential as redox reaction partners has also been studied in the respiratory chain¹¹ and in the repair of DNA.¹² They are also the most important components of flavoproteins, where they occur as catalyst in the oxidation of glucose by GOx enzymes.^{11,13}

Technische Universität Berlin, Institut für Optik und Atomare Physik,
Hardenbergstr. 36, Berlin D-10623, Germany. E-mail: dopfer@physik.tu-berlin.de;
Fax: +49 30 314 23018

† Electronic supplementary information (ESI) available. See DOI: 10.1039/c8cp00590g

The photochemical properties of flavins has been the subject of extensive research since their structure was determined by chemical synthesis more than 80 years ago.^{14,15} In fact, the Nobel prize in chemistry in 1937 was awarded to Paul Karrer for his pioneering investigations on flavins.¹⁶ Most of the studies on flavins and their complexes has been carried out in solution.^{4–8,11} There is, however, some question on the considerable influence of both solvent and counter ions on the flavin properties.^{4–8,11} Hence, spectroscopic experiments on flavin molecules and their aggregates isolated in the gas phase are required to obtain information about the intrinsic structural, electronic, and chemical properties of the optically active species. To this end, basic properties, such as their geometric and electronic structure, stability, and their interaction with the solvent must be characterized at the molecular level. However, due to their difficult generation in the gas phase, experiments on isolated flavins have been extremely rare. The few available studies include a fluorescence spectrum of LF embedded in superfluid He droplets,¹⁷ the determination of the proton and electron affinities of LF by mass spectrometry,¹⁸ and the photo- and collision-induced fragmentation of protonated FMN.¹⁹ Very recently, the optical spectrum and fragmentation pattern of flavin adenine dinucleotide anions (FAD[−]) has been reported.²⁰ The FAD[−] spectrum recorded at room temperature shows a rather broad (~100 nm) band centered around 440 nm and does not provide any structural information. The preferred metalation site and binding energy of alkali and coinage metal ions attached to LC²¹ and LF²² in the ground electronic state (S₀) has recently been determined in our group by infrared multiphoton dissociation (IRMPD) spectroscopy in a room temperature ion trap and quantum chemical calculations at the B3LYP/cc-pVDZ level. Similarly, the preferred protonation site in the S₀ state of several isolated flavins, including LC, LF, RF, and FMN, was determined at room temperature using the same experimental and computational approach.²³ The determined protonation site strongly depends on the substituent, and for protonated lumichrome (H⁺LC) the analysis of the IRMPD spectrum revealed the N5 position as the most stable protonation site. No evidence was obtained for other less favorable protonation sites and the presence of iso-LC protomers, although theory predicts them to be low in energy (Table 1).²³

Table 1 Proton affinities (PA) and relative energies (ΔE_0) in kJ mol^{−1} calculated at the PBE0/cc-pVDZ level compared to corresponding values determined at the B3LYP/cc-pVDZ level

Isomer	PBE0/cc-pVDZ		B3LYP/cc-pVDZ ^a	
	PA	ΔE_0	PA	ΔE_0
LC		0		0
iso-LC		54.9		53.5
H ⁺ LC(N5)	930.6	0	935.0	0
H ⁺ LC(O4)	911.3	19.3	914.2	20.8
H ⁺ LC(N10)	899.1	31.5	904.3	30.7
H ⁺ LC(O2)	861.1	69.5	865.7	69.3
H ⁺ iso-LC(O4)	926.5	59.0	930.0	58.5
H ⁺ iso-LC(N5)	907.2	78.3	912.2	76.3

^a Ref. 23.

Although the optical absorption properties of isolated flavin ions are of paramount importance for understanding many biochemical processes, they are completely unexplored. The case of LC as the smallest representative of the flavin class of molecules is particularly interesting. The lowest optical excitation was predicted to be a dark $n\pi^*$ transition, and only higher-energy bright $\pi\pi^*$ transitions were observed in the liquid phase.²⁴ Protonation of LC is expected to have a substantial effect on its electronic structure and molecular orbitals. Hence, large electronic shifts upon protonation are expected in the absorption spectrum of LC. The detailed analysis of these effects is the aim of the present investigation. We combine electrospray ionization with cryogenic ion trapping to characterize cold H⁺LC ions in the gas phase *via* optical photodissociation spectroscopy in the visible range (VISPD) performed in a tandem mass spectrometer. The vibronic spectrum, along with a very brief preliminary analysis, was presented in an earlier report to illustrate of the capabilities of the recently constructed cryogenic ion trap spectrometer (BerlinTrap).²⁵ While vibrational IR spectroscopy of large biomolecular ions can readily be performed at room temperature without substantial loss in spectral resolution, cooling down to low temperature is definitively required for optical spectroscopy in order to avoid hot band transitions leading to spectral congestion,^{25–33} in the worst case leading to unresolved vibronic fine structure. Significantly, the VISPD spectrum of cold H⁺LC ions corresponds to the first optical spectrum of any flavin molecule recorded in the gas phase.²⁵ Herein, we present the detailed analysis of the experimental spectrum through comparison with quantum chemical simulations. To this end, density functional theory (DFT) calculations for the electronic structure of the lowest electronic states are combined with multidimensional Franck–Condon (FC) simulations to assign the observed vibronic spectrum. The computational analysis provides details of the geometrical, vibrational, and electronic properties of the ground, first, and second excited singlet states of H⁺LC (S_n, *n* = 0–2). Comparison with LC reveals the large effects of protonation on the electronic structure of this simplest flavin molecule.

2. Experimental and computational details

A detailed description of the employed experimental apparatus (BerlinTrap) employed for VISPD spectroscopy of H⁺LC has been given elsewhere.²⁵ Briefly, the central parts of the BerlinTrap setup include (i) an electrospray ionization (ESI) source to generate ions, (ii) a quadrupole mass spectrometer to size-select the desired ions, (iii) a cryogenic 22-pole ion trap to store and cool the ions *via* He buffer gas, and (iv) a reflectron time-of-flight mass spectrometer (ReTOF-MS) to analyze the product ions. H⁺LC ions are generated in the ESI source by spraying a LC-containing solution at a 2 mL h^{−1} rate. The analyte solution consists of 2 mg LC (Sigma Aldrich, >99% purity), 17 mL MeOH, and 2.5 mL formic acid. H⁺LC ions are then mass selected (*m/z* 243) and guided *via* several linear RF multipoles to a 22-pole trap, where they are stored for 90 ms and cooled down to 25 K by means of He buffer gas cooling.

After extraction from the trap, the cold H^+LC ions are irradiated at the extraction region of the orthogonal ReTOF-MS , and both fragment and parent ions are simultaneously detected using a microchannel plate detector. Laser radiation is provided by a commercial optical parametric oscillator (OPO) laser system (Continuum, Panther EX-OPO) pumped by the third harmonic of a Nd:YAG laser (Continuum, Powerlite DLS 9010). Typical OPO laser intensities are 3–5 mJ per pulse at an area of around 2 cm^2 . The laser wavelength (bandwidth $2\text{--}3\text{ cm}^{-1}$) is tuned in 0.02 nm steps and calibrated with a grating spectrometer (Bristol Instruments, 821). The mass discriminated ion signals registered at the microchannel plate are digitalized and converted to action spectra *via* homemade LabVIEW programs. The VISPD spectra are obtained by adding the acquired fragment signals and linear normalization by both parent ion signal and laser intensity. In this way, VISPD spectra of H^+LC are recorded in the $19\,700\text{--}20\,800\text{ cm}^{-1}$ spectral range.

DFT calculations at the PBE0/cc-pVDZ level are carried out for the optimization of the ground states for LC, iso-LC, H^+LC , and $\text{H}^+\text{iso-LC}$ using GAUSSIAN09.³⁴ The PBE0 functional is employed as a computationally economic method, because it shows good results as found by Medvedev *et al.*³⁵ who compared various levels of theory to the computationally more expensive CCSD level. Furthermore, the PBE0 data agree well with the structures and energies obtained at the B3LYP level previously used for the IR spectroscopic characterization of flavin ions^{21–23} but yields much better predictions for excited state energies with respect to adiabatic electronic transitions and vibronic bands. Vertical excitation energies are calculated with the time-dependent DFT (TD-DFT) method at the optimized ground state geometry. Geometries of the excited electronic states are optimized at the same level of theory using the corresponding ground state structures as the starting point. The natural transition orbital method³⁶ is used to calculate the orbitals involved in the lowest electronic excitations. Calculated proton affinities and relative energies are corrected for harmonic zero-point vibrational energies. Vibronic spectra based on multidimensional FC simulations are simulated for $T = 0\text{ K}$ using PGOPHER.³⁷ The resulting stick spectra are convoluted with a Lorentzian line profile using a FWHM of 6 cm^{-1} to facilitate convenient comparison with the experimental VISPD spectrum.

3. Results and discussion

A variety of low-energy H^+LC and iso- H^+LC isomers with different protonation sites are considered to assign the measured VISPD spectrum.²³ The proton may attach to the various available nucleophilic sites of LC (Fig. 1) and iso-LC (Fig. S1 in ESI[†]), such as the lone pairs of the O atoms of the two CO groups (denoted O2 and O4) and the lone pairs of the two heterocyclic N atoms (N10 and N5 for LC, N5 and N1 for iso-LC). LC is calculated to be $\Delta E_0 = 54.9\text{ kJ mol}^{-1}$ more stable than iso-LC. As a result, only the formation of H^+LC may be expected. However, iso- H^+LC may still be present in solution because of solvent stabilization effects and thus they may also be generated in the

ESI source. In our previous IRMPD experiments on M^+LC ions produced by ESI, isomers with relative free energies as high as 37 kJ mol^{-1} were identified.²¹ Therefore, the most stable N5 and O4 isomers of $\text{H}^+\text{iso-LC}$ are also considered here. The calculated proton affinities (PA) and relative energies (ΔE_0) of all considered $\text{H}^+(\text{iso-})\text{LC}$ isomers in Table 1 show good agreement between the PBE0 and B3LYP levels.²³ $\text{H}^+\text{LC}(\text{N5})$ is the global minimum structure, corresponding to $\text{PA} = 930.6\text{ kJ mol}^{-1}$. The other three O4, N10, and O2 isomers of H^+LC have relative energies of $\Delta E_0 = +19.3$, $+31.5$, and $+69.5\text{ kJ mol}^{-1}$, respectively. Although the $\text{H}^+\text{iso-LC}$ and H^+LC isomers have somewhat different PAs for the same protonation site, the relative energies of all $\text{H}^+\text{iso-LC}$ isomers are still relatively high, with $\Delta E_0 = +59.0$ and $+78.3\text{ kJ mol}^{-1}$ for the O4 and N5 isomers of $\text{H}^+\text{iso-LC}$, because of the large energy gap between the two neutral molecules.

The VISPD spectrum of the $\text{S}_1 \leftarrow \text{S}_0$ transition of H^+LC recorded between $19\,700$ and $20\,800\text{ cm}^{-1}$ is obtained by monitoring the two predominant fragment ion signals (m/z 172 and 198, Fig. S2 in ESI[†]), linearly normalized for laser power and parent ion intensity (m/z 243). The range close to the adiabatic S_1 origin transition is plotted in Fig. 2, while a larger range is shown in Fig. S3 in ESI[†]. No VISPD signal is observed down to $19\,600\text{ cm}^{-1}$. The action spectra recorded in both fragment channels are essentially the same (Fig. S4 in ESI[†]), which provides a first hint (but no proof) that the observed spectrum is produced by a single isomer. The branching ratio is around 3:1 for m/z 198 and 172. The same major fragment ions are observed for IRMPD activation,²³ which indicates that optical activation into the S_1 state is followed by internal conversion to the S_0 ground electronic state and subsequent statistical dissociation. The m/z 198 fragment ion corresponds to formal loss of $\text{CO} + \text{NH}_3$ or $\text{HCN} + \text{H}_2\text{O}$, whereas the m/z 172 ion arises from formal loss of $\text{CONH} + \text{CO}$.²³ The 22-pole trap temperature is kept at 25 K to maximize the VISPD signal. This temperature is low enough to minimize the appearance of hot bands, which are below the

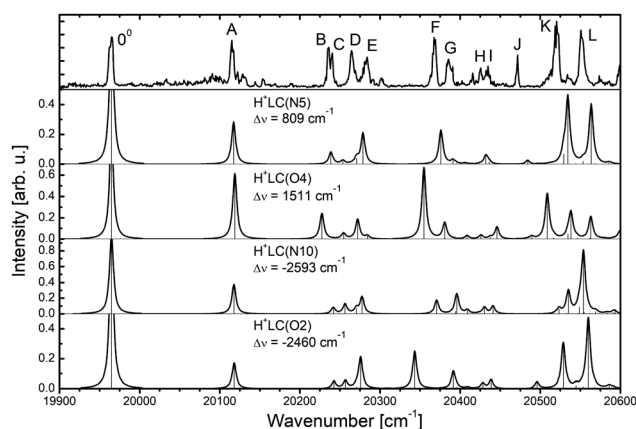


Fig. 2 Comparison between experimental VISPD spectrum recorded for H^+LC and Franck-Condon simulations for the isomers shown in Fig. 1 calculated at the PBE0/cc-pVDZ level using a convolution width of 6 cm^{-1} . Isomers are ordered from top to bottom according to their relative energy (Table 1). The energy scale of the simulated spectra is shifted by $\Delta\nu$ to match the frequencies of calculated and observed S_1 origins at $19\,962\text{ cm}^{-1}$.

detection limit. The S_1 band origin is recorded at $19\,962\text{ cm}^{-1}$. Toward higher frequency, many intense vibronic transitions (labeled A–L in Fig. 2) are observed, which indicate a large geometry change upon electronic excitation. The measured bands have a width of around 6 cm^{-1} (FWHM), which is composed of the laser bandwidth ($\sim 2\text{--}3\text{ cm}^{-1}$) and unresolved rotational structure. The measured spectrum reveals a substantial redshift of the first electronic transition of H^+LC compared to that of neutral LC. Although no experimental data are available for isolated LC, the maximum of its first absorption band in solution was found to be in the $379\text{--}385\text{ nm}$ range ($\sim 26\,000\text{ cm}^{-1}$) depending on the solvent.²⁴ Thus, the large red shift of around $\sim 6000\text{ cm}^{-1}$ demonstrates that protonation of the aromatic chromophore strongly changes both its geometric and electronic configuration.

To determine the isomer observed in the experimental spectrum, we consider next to the proton affinities also the positions of the adiabatic $S_1 \leftarrow S_0$ origin transitions and the vibronic spectra simulated within the Franck–Condon approximation. The resulting vibronic spectra are compared to the measured VISPD spectrum in Fig. 2 for the considered H^+LC isomers and in Fig. S5 in ESI† for the iso- H^+LC isomers. For convenient comparison between experimental and computed vibronic spectra, the computed spectra are shifted in these figures by a constant amount ($\Delta\nu$) to match the calculated and experimental S_1 origins, $\Delta\nu = S_1^{\text{exp}} - S_1^{\text{calc}}$ with $S_1^{\text{exp}} = 19\,962\text{ cm}^{-1}$. All adiabatic S_1 energies are listed in Table 2, along with the corresponding $\Delta\nu$ shifts. From this comparison, the observed VISPD spectrum is clearly assigned to the $S_1 \leftarrow S_0$ transition of the most stable $\text{H}^+\text{LC}(\text{N5})$ isomer. First, considering the absolute position of the predicted S_1 origins, the best match with the observed value is obtained for $\text{H}^+\text{LC}(\text{N5})$, with a deviation of only $\Delta\nu = 809\text{ cm}^{-1}$. The comparison is much less favorable for all other isomers of both H^+LC ($\Delta\nu = 1511, -2593, -2460\text{ cm}^{-1}$ for O4, N10, O2) and iso- H^+LC ($\Delta\nu = 2408$ and 4525 cm^{-1} for O4 and N5). Second, also the vibronic pattern predicted for $\text{H}^+\text{LC}(\text{N5})$ shows the best agreement with the experimental spectrum with respect to both position and relative intensity of the transitions. In particular, $\text{H}^+\text{LC}(\text{N5})$ is the only isomer able to reproduce the high intensity doublet K and L at around $20\,550\text{ cm}^{-1}$, thus confirming the assignment of the observed VISPD spectrum to the $S_1 \leftarrow S_0$ transition of $\text{H}^+\text{LC}(\text{N5})$. The observed deviations between experimental and computed vibronic intensities may

Table 2 Adiabatic S_1 energies of LC and various isomers of H^+LC and $\text{H}^+\text{iso-LC}$ calculated at the PBE0/cc-pVDZ level, along with the shifts from the experimental S_1 origin of H^+LC (in cm^{-1})

Isomer	S_1	$\Delta\nu$
LC	24 826	
H^+LC (exp)	19 962	0
$\text{H}^+\text{LC}(\text{N5})$	19 153	809
$\text{H}^+\text{LC}(\text{O4})$	18 451	1511
$\text{H}^+\text{LC}(\text{N10})$	22 555	−2593
$\text{H}^+\text{LC}(\text{O2})$	22 422	−2460
$\text{H}^+\text{iso-LC}(\text{O4})$	17 554	2408
$\text{H}^+\text{iso-LC}(\text{N5})$	15 437	4525

arise from several factors, including deficiencies in the electronic structure calculations, deviations from the harmonic FC principle, vibronic coupling, and mode-dependent dissociation cross sections and competing radiative and nonradiative relaxation channels. The assignment to the N5 isomer confirms the conclusion obtained from our previous IRMPD experiments combined with B3LYP/cc-pVDZ calculations.²³

After identification of $\text{H}^+\text{LC}(\text{N5})$ as carrier of the observed VISPD spectrum, we consider in Fig. 3 and Table 3 in more detail the assignment of the vibrational transitions. A full set of normal modes for the S_0 and S_1 states of $\text{H}^+\text{LC}(\text{N5})$ can be found in Table S1 in the ESI.† The notation of the vibrations follows the Mulliken convention. The $S_1 \leftarrow S_0$ transition has $\pi\pi^*$ character and the N5 isomer belongs to the C_s point group. Therefore, all vibronic transitions originating from the ground vibrational level in the S_0 electronic state terminate in S_1 vibrational states with a' symmetry. The agreement between experimental and calculated vibrational frequencies is very good. The maximum and mean deviations of 12 and 4 cm^{-1} , respectively, are small considering the experimental peak width (6 cm^{-1}) and the harmonic approximation employed for the FC analysis. Most of the vibronic transitions are fundamentals of the lowest frequency a' modes of $\text{H}^+\text{LC}(\text{N5})$, $44^1\text{--}53^1$, and only fundamentals, overtones, and combination bands of these in-plane modes are observed. Graphical representations of these normal coordinates are given in Fig. S6 in ESI.† Briefly, bands A and D are identified as short progression in mode 53 with one and two quanta, respectively. This mode involves in-plane bending of the outer aromatic rings I and III around the central ring II. The B/C doublet is assigned to in-plane rocking modes of the methyl groups attached to C7 (mode 52) and C8 (mode 51). Both modes also include the shear deformation of ring II along the N5–N10 direction. Mode 50 (band E) involves a uniform stretching of the three chromophore rings along the long molecular axis. Mode 49 (band F) is described by the compression of ring III combined with the scissoring motion of the two carbonyl groups. Combination bands 53^152^1 and 53^150^1 are assigned to bands G and H, respectively. Band G also contains a minor contribution of the 48^1 fundamental associated with a shear deformation of ring I along the C6–C9 axis. A hindered rotation

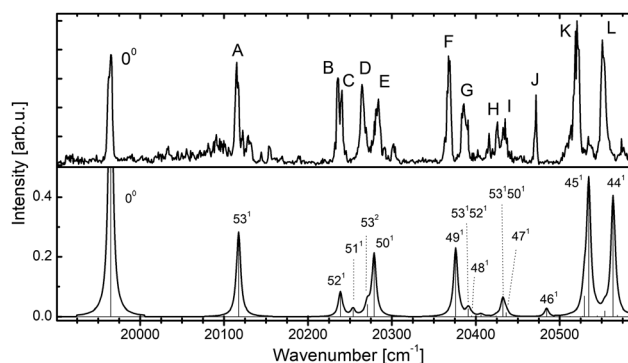


Fig. 3 Experimental VISPD spectrum of H^+LC (top) compared to the Franck–Condon simulation of the identified $\text{H}^+\text{LC}(\text{N5})$ isomer (bottom) along with vibrational assignments (Table 3).

Table 3 Experimental frequencies for vibronic transitions observed in the VISPD spectrum of the S_1 state of H^+LC compared to frequencies of the $H+LC(N5)$ isomer computed at the PBE0/cc-pVDZ level, along with the mode assignment

Band	ν (exp.)	ν (calc.)	Assignment
	19 962	19 153	0^0
A	+154	153.1	53^1
B	+274	273.9	52^1
C	+278	289.0	51^1
D	+303	306.2	53^2
E	+321	314.7	50^1
F	+406	411.7	49^1
G	+425	427.0	$53^1 52^1$
		430.8	48^1
H	+464	467.8	$53^1 50^1$
I	+473	471.5	47^1
J	+509	519.9	46^1
K	+558	569.8	45^1
L	+590	598.6	44^1

of the rigid ring II (mode 47), and the elongation of ring III along the N1–C4 axis combined with the elongation of rings I and II along the long molecular axis (mode 46), are assigned to bands I and J, respectively. Two complex delocalized deformation modes of all three rings are attributed to the very intense bands K (45^1) and L (44^1). The intensities for most vibronic transitions are well reproduced by the FC simulations. Nevertheless, the intensities calculated for all transitions involving vibrations 52, 51, and 46 are slightly underestimated. There are also a number of reproducible low-intensity bands around transition A that could not be explained by the FC simulations. All obvious efforts to rationalize these transitions by hot bands using FC simulations at finite temperature or by other isomers failed.

The structures calculated for LC in the S_0 and S_1 states are given in Fig. S7 (ESI[†]), while the S_0 geometry of $H^+LC(N5)$ is shown in Fig. S8 in ESI[†]. The relative changes of the geometry induced by N5 protonation of LC in the S_0 state are visualized in Fig. 4(a). Positive numbers imply distance elongation upon protonation, while negative numbers indicate distance contraction. Although the excess positive charge has an influence throughout the whole chromophore, the most prominent feature is a compression of ring II along the N5–N10 axis (-8.3 pm), along with an elongation of the same ring along the C5a–C10a axis (6.7 pm). Ring III is also contracted noticeably along the C2–C4a distance (-6.1 pm). In contrast, a relatively smaller deformation is induced in ring I. N5 protonation also affects the length of the C2O (-1.2 pm) and C4O (0.5 pm) bonds of the two carbonyl groups. The latter effect is used in previous studies as sensitive indicator for determination of the protonation site by means of IRMPD spectroscopy and B3LYP calculations of the C=O stretch fundamentals.²³

The geometry change upon $S_1 \leftarrow S_0$ electronic excitation of $H^+LC(N5)$ is shown in Fig. 4(b) and will be used to rationalize the relative FC intensities of the simulated and observed vibronic transitions. Electronic excitation has an even more drastic effect on the geometry of the chromophore than protonation. The consequences of electronic excitation are substantial throughout the whole chromophore, and are particularly strong in rings I

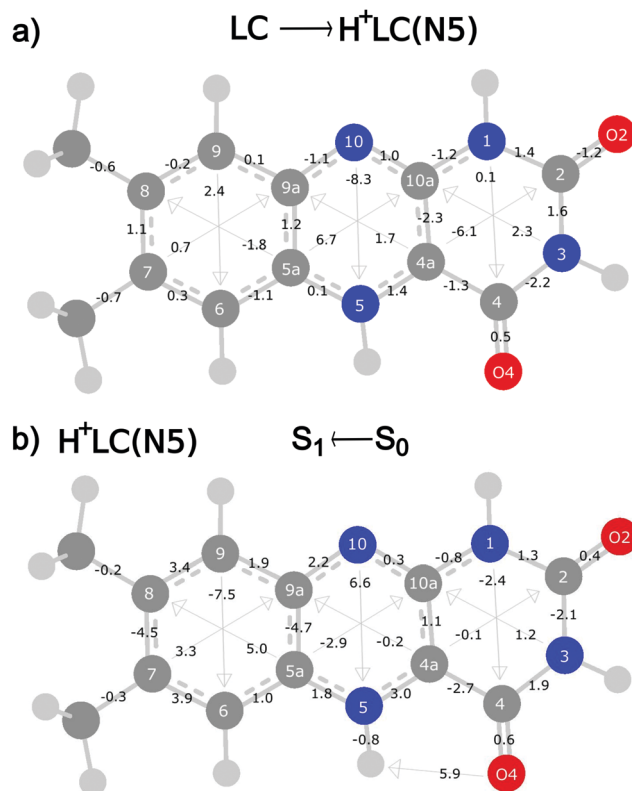


Fig. 4 (a) Relative structural changes (in pm) of $H^+LC(N5)$ with respect to neutral LC in the ground electronic state (S_0) to illustrate the structural effects of protonation. Positive values indicate elongation upon protonation. (b) Relative structural changes (in pm) of the S_1 state with respect to the S_0 state of $H^+LC(N5)$ to illustrate the structural effects of electronic $\pi\pi^*$ excitation. Positive values indicate elongation upon excitation. Absolute geometries are available in Fig. S7 and S8 in ESI[†].

and II. In this case, the expansion of ring II along the N5–N10 axis (6.6 pm) is accompanied by a compression of the same ring along the C5a–C10a axis (-2.9 pm). Ring I is greatly contracted along the C9–C6 distance (-7.5 pm) and expanded along the C7–C9a (3.3 pm) and the C8–C5a (5.0 pm) directions. In contrast, only a smaller deformation is induced in ring III, with a contraction along the N1–C4 axis (-2.4 pm) and an elongation of the N3–C10a distance (1.2 pm). $S_1 \leftarrow S_0$ excitation also moderately affects the length of the C2O (0.4 pm) and C4O (0.6 pm) bonds to the two carbonyl groups. The deformation induced by $S_1 \leftarrow S_0$ excitation is very similar to the 45 normal mode of the S_1 state. Therefore, a large FC factor is expected for this fundamental, and the associated band K assigned to 45^1 is indeed the most intense vibronic transition in both the experimental and simulated VISPD spectrum in Fig. 2. Similarly, the modes 49 and 50 also include a compression of ring I, which explains their high FC factors and the large intensities of the corresponding bands F and E, respectively.

In a next step, we consider the nature of the lowest electronic singlet excitations in LC and $H^+LC(N5)$. The energies and oscillator strengths (f) for the first two vertical transitions originating from their optimized S_0 ground state geometries are listed in Table 4. For all but one transition, adiabatic

Table 4 Transition energies ($\Delta\nu$) and oscillator strengths (f) for the vertical (adiabatic) transitions originating from the electronic ground state of LC and $H^+LC(N5)$ calculated at the PBE0/cc-pVDZ level

Isomer	Transition	$\Delta\nu$ [cm^{-1}]	$f (\times 10^{-3})$
LC	$S_1 \leftarrow S_0$ ($n\pi^*$)	28 213 (24 826)	1.3
	$S_2 \leftarrow S_0$ ($\pi\pi^*$)	28 745 (—) ^a	86.4
$H^+LC(N5)$	$S_1 \leftarrow S_0$ ($\pi\pi^*$)	22 026 (19 153)	47.7
	$S_2 \leftarrow S_0$ ($n\pi^*$)	25 696 (20 767)	0.3

^a All efforts to optimize this state failed.

energies are given as well. The orbitals involved in these $S_1 \leftarrow S_0$ and $S_2 \leftarrow S_0$ transitions are shown in Fig. 5. In agreement with previous calculations,²⁴ the lowest excited singlet state (S_1) of LC corresponds to a very weak $n\pi^*$ excitation from HOMO to LUMO at $28\,213\text{ cm}^{-1}$ ($f = 1.3 \times 10^{-3}$). Very close in energy at $28\,745\text{ cm}^{-1}$ is the optically bright S_2 state arising from $\pi\pi^*$ excitation (HOMO–1 to LUMO) with $f = 86 \times 10^{-3}$. For this reason, only the $S_2 \leftarrow S_0$ transition of LC is observed in solution near $\sim 380\text{ nm}$ ($\sim 26\,000\text{ cm}^{-1}$),²⁴ with the band maximum depending somewhat on the solvent. For $H^+LC(N5)$, the energy order of $\pi\pi^*$ and $n\pi^*$ excitation changes (Table 4), and the optically bright $\pi\pi^*$ transition ($f = 48 \times 10^{-3}$) becomes the

lowest singlet excited state (S_1) at $22\,026\text{ cm}^{-1}$, while the dark $n\pi^*$ state (S_2) is much higher in energy ($25\,696\text{ cm}^{-1}$, $f = 0.3 \times 10^{-3}$). As a result, the computed red shift in the vertical excitation energy for the $\pi\pi^*$ state upon protonation (-6719 cm^{-1}) is much larger than that for the $n\pi^*$ state (-2517 cm^{-1}). The experimental red shift observed for the $\pi\pi^*$ transition is of the order of -6000 cm^{-1} , in excellent agreement with the theoretical predictions. Large shifts upon protonation of aromatic molecules were observed previously, providing that protonation occurs at the aromatic chromophore.³⁸ Since all orbitals involved in S_1 and S_2 excitation of LC and $H^+LC(N5)$ involve electron density near N5 (Fig. 5), a considerable electronic shift is expected for both transitions upon N5 protonation. However, the n orbital (HOMO) is clearly influenced to a larger extent than the π orbital (HOMO–1), because the former is mostly localized at the central ring II, whose geometry is greatly modified upon N5 protonation. In contrast, a large part of the HOMO–1 orbital is localized at ring I that is less affected by N5 protonation, as discussed above. Thus, from the shapes of the orbitals, one can readily rationalize that for $H^+LC(N5)$ the $n\pi^*$ transition is more than 3000 cm^{-1} higher in energy than the $\pi\pi^*$ transition.

4. Concluding remarks

We report the first optical spectrum of a flavin molecule isolated in the gas phase. The electronic spectrum of the $S_1 \leftarrow S_0$ ($\pi\pi^*$) transition of protonated lumichrome (H^+LC), the simplest member of the flavin family, is obtained by photodissociation spectroscopy in the visible range near 500 nm , with an S_1 origin located at $19\,962\text{ cm}^{-1}$. The VISPD spectrum is recorded in a recently commissioned cryogenic ion trap tandem mass spectrometer coupled to an electrospray ionization source (BerlinTrap), suitable for spectroscopy of cryogenic biomolecular ions and their clusters.²⁵ Cooling the ions down to temperatures below 30 K ensures the absence of hot band transitions and thus yields a vibrationally resolved electronic spectrum of the first excited singlet state. The analysis of the measured vibronic spectrum using TD-DFT calculations coupled to multidimensional FC simulations provides a reliable structural, vibrational, and electronic assignment, and the salient results may be summarized as follows.

(1) The carrier of the observed VISPD spectrum is the most stable $H^+LC(N5)$ isomer, in line with the thermochemical predictions and the analysis of the IRMPD spectrum recorded at room temperature.²³ There is no indication for the contribution of other less stable isomers to the VISPD spectrum in this spectral range. (2) The S_1 state of $H^+LC(N5)$ is assigned to optically bright $\pi\pi^*$ excitation. S_1 excitation has a large effect on the structure of the aromatic chromophore, leading to intense and rich vibronic activity according to the FC principle. All FC-allowed low-frequency fundamentals are identified in the VISPD spectrum, and their excitation is correlated with the calculated geometry change. (3) N5 protonation of LC induces a drastic change in both its geometry and electronic structure. In particular, the bright $\pi\pi^*$ state experiences a rather large red shift of around -6000 cm^{-1} (30%) upon protonation from the broad absorption of LC in the

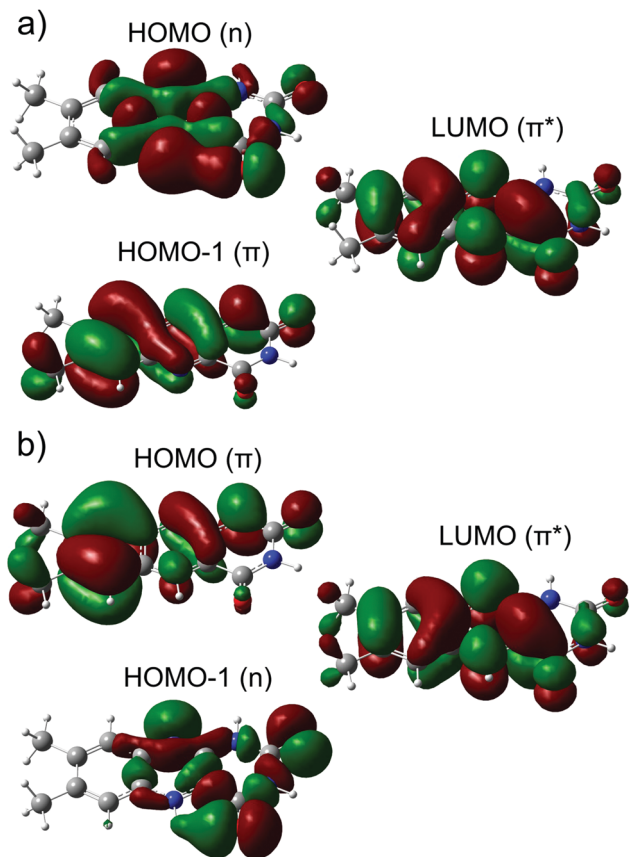


Fig. 5 Molecular orbitals involved in the $S_1 \leftarrow S_0$ (LUMO \leftarrow HOMO, $n\pi^*$) and $S_2 \leftarrow S_0$ (LUMO \leftarrow HOMO–1, $\pi\pi^*$) transitions of LC (a) compared to those of the corresponding $S_1 \leftarrow S_0$ (LUMO \leftarrow HOMO, $\pi\pi^*$) and $S_2 \leftarrow S_0$ (LUMO \leftarrow HOMO–1, $n\pi^*$) transitions of $H^+LC(N5)$ (b), respectively (TD-DFT, PBE0/cc-pVDZ).

liquid phase (~ 380 nm, $\sim 26\,000$ cm $^{-1}$).²⁴ This large shift is readily rationalized by the strong interaction of the proton directly attached to the central ring of the aromatic chromophore with the orbitals involved in the transition and the resulting charge transfer.³⁸ In particular, the energy of the LUMO (π^*) is strongly lowered, giving rise to the large red shift of the $\pi\pi^*$ state. Because the close lying optically dark $n\pi^*$ state of LC is significantly less affected by N5 protonation, the energetic order of the two lowest electronic singlet states ($n\pi^*$, $\pi\pi^*$) changes between LC and H⁺LC(N5). Similar large red shifts in electronic excitations upon protonation have been reported for other aromatic molecules, in which the proton is directly attached to the aromatic chromophore (e.g., naphthalene)^{38,39} and not to the side chain (e.g., amino acids).⁴⁰

As a more general conclusion, the analysis of the first optical spectrum of an isolated flavin molecule (here protonated lumichrome) illustrates that their intrinsic optical properties depend extremely sensitively on external perturbations (here protonation). The developed combined spectroscopic and computational approach is demonstrated to be a powerful tool to characterize these effects at the molecular level with high spectroscopic precision. Thus, cryogenic ion trap spectroscopy combined with quantum chemical calculations offers the opportunity to unravel the individual impact of oxidation, charge state, metalation, counter ions, and stepwise microsolvation on the photochemical properties of this fundamental class of biomolecules, thereby improving our molecular-level understanding of biochemical processes involving flavins. Currently, this strategy is applied to larger protonated²³ and metalated^{21,22} flavins to probe the perturbation of the electronic structure as a function of the flavin substituent, and the charge, type, binding site, and bond strength of the metal ion.

Conflicts of interest

There are no conflicts to declare.

Acknowledgements

This work was supported by Deutsche Forschungsgemeinschaft (DFG, grant number DO 729/6). We thank Dieter Gerlich, TU Chemnitz, and Deutsche Forschungsgemeinschaft for the generous continuous loan of the ESI source, the 22-pole trap, and several turbomolecular pumps.

References

- 1 P. F. Heelis, *Chem. Soc. Rev.*, 1982, **11**, 15.
- 2 *Flavins: Photochemistry and Photobiology*, ed. E. Silva and A. M. Edwards, RSC Pub., Cambridge, UK, 2006.
- 3 W. J. Rutter, *Acta Chem. Scand.*, 1958, **12**, 438.
- 4 M. Benecky, T. Y. Yu, K. L. Watters and J. T. McFarland, *Biochim. Biophys. Acta*, 1980, **626**, 197.
- 5 J. Lauterwein, P. Hemmerich and J. M. Lhoste, *Inorg. Chem.*, 1975, **14**, 2152.
- 6 J. Lauterwein, P. Hemmerich and J. M. Lhoste, *Inorg. Chem.*, 1975, **14**, 2161.
- 7 F. Müller, P. Hemmerich and A. Ehrenberg, *Eur. J. Biochem.*, 1968, **5**, 158.
- 8 P. Hemmerich and J. Lauterwein, in *The Structure and Reactivity of Flavin-Metal Complexes*, ed. G. L. Eichhorn, Elsevier Scientific Pub. Co, Amsterdam, London, New York, 1973.
- 9 A. Losi and W. Gartner, *Photochem. Photobiol.*, 2011, **87**, 491.
- 10 T. E. Swartz, T. S. Tseng, M. A. Frederickson, G. Paris, D. J. Commerci, G. Rajashekar, J. G. Kim, M. B. Mudgett, G. A. Splitter, R. A. Ugalde, F. A. Goldbaum, W. R. Briggs and R. A. Bogomolni, *Science*, 2007, **317**, 1090.
- 11 V. Massey, *Biochem. Soc. Trans.*, 2000, **28**, 283.
- 12 M. Sugiyama, *Environ. Health Perspect.*, 1991, **92**, 63.
- 13 V. Piano, B. A. Palfey and A. Mattevi, *Trends Biochem. Sci.*, 2017, **42**(6), 457.
- 14 R. Kuhn and F. Weygand, *Ber. Dtsch. Chem. Ges. B*, 1934, **67**, 2084.
- 15 P. Karrer, K. Schopp and F. Benz, *Helv. Chim. Acta*, 1935, **18**, 426.
- 16 *Nobel Lectures: Chemistry 1922–1941*, Elsevier Publishing Company, Amsterdam, 1966.
- 17 A. Vdovin, A. Slenczka and B. Dick, *Chem. Phys.*, 2013, **422**, 195.
- 18 T. Zhang, K. Papson, R. Ochran and D. P. Ridge, *J. Phys. Chem. A*, 2013, **117**, 11136.
- 19 L. Guyon, T. Tabarin, B. Thuillier, R. Antoine, M. Broyer, V. Boutou, J. P. Wolf and P. Dugourd, *J. Chem. Phys.*, 2008, **128**, 75103.
- 20 M. H. Stockett, *Phys. Chem. Chem. Phys.*, 2017, **19**, 25829.
- 21 A. Günther, P. Nieto, G. Berden, J. Oomens and O. Dopfer, *Phys. Chem. Chem. Phys.*, 2014, **16**, 14161.
- 22 P. Nieto, A. Günther, G. Berden, J. Oomens and O. Dopfer, *J. Phys. Chem. A*, 2016, **120**, 8297.
- 23 J. Langer, A. Günther, S. Seidenbecher, G. Berden, J. Oomens and O. Dopfer, *ChemPhysChem*, 2014, **15**, 2550.
- 24 E. Sikorska, I. V. Khmelinskii, W. Prukala, S. L. Williams, M. Patel, D. R. Worrall, J. L. Bourdelande, J. Koput and M. Sikorski, *J. Phys. Chem. A*, 2004, **108**, 1501.
- 25 A. Günther, P. Nieto, D. Müller, A. Sheldrick, D. Gerlich and O. Dopfer, *J. Mol. Spectrosc.*, 2017, **332**, 8.
- 26 E. Garand, M. Z. Kamrath, P. A. Jordan, A. B. Wolk, C. M. Leavitt, A. B. McCoy, S. J. Miller and M. A. Johnson, *Science*, 2012, **335**, 694.
- 27 I. Alata, J. Bert, M. Broquier, C. Dedonder, G. Feraud, G. Grégoire, S. Soorkia, E. Marceca and C. Jouvét, *J. Phys. Chem. A*, 2013, **117**, 4420.
- 28 E. K. Campbell, M. Holz, D. Gerlich and J. P. Maier, *Nature*, 2015, **523**, 322.
- 29 J. G. Redwine, Z. A. Davis, N. L. Burke, R. A. Oglesbee, S. A. McLuckey and T. S. Zwier, *Int. J. Mass Spectrom.*, 2013, **348**, 9.
- 30 A. B. Wolk, C. M. Leavitt, E. Garand and M. A. Johnson, *Acc. Chem. Res.*, 2014, **47**, 202.
- 31 J. Roithová, A. Gray, E. Andris, J. Jašík and D. Gerlich, *Acc. Chem. Res.*, 2016, **49**, 223.

- 32 K. R. Asmis and J. Sauer, *Mass Spectrom. Rev.*, 2007, **26**, 542.
- 33 T. R. Rizzo, J. A. Stearns and O. V. Boyarkin, *Int. Rev. Phys. Chem.*, 2009, **28**, 481.
- 34 M. J. Frisch, G. W. Trucks, H. B. Schlegel, G. E. Scuseria, M. A. Robb, J. R. Cheeseman, G. Scalmani, V. Barone, B. Mennucci and G. A. Petersson, *et al.*, *Gaussian 09, Revision D.01*, Wallingford CT, 2009.
- 35 M. G. Medvedev, I. S. Bushmarinov, J. Sun, J. P. Perdew and K. A. Lyssenko, *Science*, 2017, **355**, 49.
- 36 R. L. Martin, *J. Chem. Phys.*, 2003, **118**, 4775.
- 37 C. M. Western, *J. Quant. Spectrosc. Radiat. Transfer*, 2017, **186**, 221.
- 38 I. Alata, R. Omidyan, M. Broquier, C. Dedonder, O. Dopfer and C. Jouvet, *Phys. Chem. Chem. Phys.*, 2010, **12**, 14456.
- 39 U. J. Lorenz, N. Solca, J. Lemaire, P. Maitre and O. Dopfer, *Angew. Chem., Int. Ed.*, 2007, **46**, 6714.
- 40 O. V. Boyarkin, S. R. Mercier, A. Kamariotis and T. R. Rizzo, *J. Am. Chem. Soc.*, 2006, **128**, 2816.

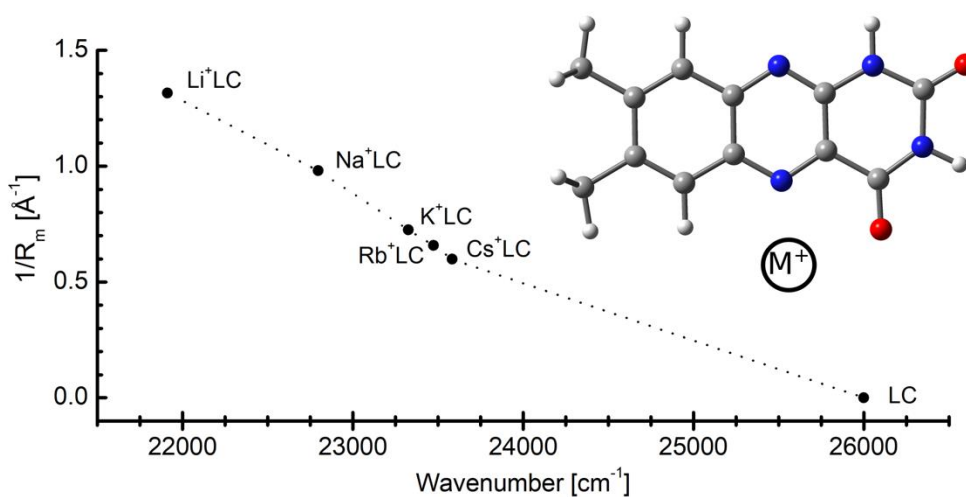
4.6. Effect of alkali ions on optical properties of flavins: vibronic spectra of cryogenic M⁺lumichrome ions (M = Li-Cs) in the gas phase

Pablo Nieto, David Müller, Alexander Sheldrick, Alan Günther, Mitsuhiro Miyazaki and Otto Dopfer

Phys. Chem. Chem. Phys., 2018, 20, 22148-22158

<https://doi.org/10.1039/C8CP03950J>

Reproduced with permission of the PCCP Owner Societies



Declaration of Contribution

The experimental data were acquired by David Müller and Alexander Sheldrick. Computational data were acquired by Pablo Nieto, Mitsuhiro Miyazaki, Alexander Sheldrick, and David Müller. The manuscript was written by Pablo Nieto and reviewed by all co-authors. All work was supervised by Otto Dopfer.



Cite this: *Phys. Chem. Chem. Phys.*,
2018, 20, 22148

Effect of alkali ions on optical properties of flavins: vibronic spectra of cryogenic M^+ lumichrome ions ($M = \text{Li} - \text{Cs}$) in the gas phase†

Pablo Nieto,^a David Müller,^a Alexander Sheldrick,^a Alan Günther,^a
Mitsuhiko Miyazaki^{ab} and Otto Dopfer^{ab*}

The photochemical properties of flavins depend sensitively on their environment and are strongly modified by coordination with metal ions. Herein, the electronic spectra of cold complexes of the smallest flavin molecule (lumichrome, LC, $\text{C}_{12}\text{N}_4\text{O}_2\text{H}_{10}$) with alkali ions ($M^+\text{LC}$, $M = \text{Li} - \text{Cs}$) are measured by photodissociation in the visible range (VISPD) in a cryogenic ion trap coupled to a tandem mass spectrometer and an electrospray ionization source. The observed vibronic spectra of all ions are assigned to the optically bright $S_1 \leftarrow S_0$ ($\pi\pi^*$) transition of the most stable O4 isomer of $M^+\text{LC}$ by comparison with quantum chemical calculations at the PBE0/cc-pVDZ level coupled to multidimensional Franck–Condon simulations. The rich vibronic spectra indicate substantial geometry changes upon S_1 excitation. Large red shifts of the S_1 origins upon metal complexation and progressions in the intermolecular in-plane metal stretch and bend modes demonstrate that the strength of the metal–flavin interaction in $M^+\text{LC}(\text{O4})$ strongly increases by S_1 excitation. The stronger $M^+ \cdots \text{LC}$ bond in the S_1 state of $M^+\text{LC}(\text{O4})$ is rationalized by the charge reorganization upon $\pi\pi^*$ excitation of the LC chromophore. The computations confirm that the optical properties of LC can be strongly modulated by metalation *via* both the type and binding site of the metal ion.

Received 21st June 2018,
Accepted 6th August 2018

DOI: 10.1039/c8cp03950j

rsc.li/pccp

1. Introduction

Flavins are yellow bioorganic dye molecules derived from the heterocyclic 7,8-dimethyl-10-alkylisoalloxazine chromophore (iso-lumichrome = iso-LC = $\text{C}_{12}\text{N}_4\text{O}_2\text{H}_{10}$, $R = \text{H}$ at N10, Fig. 1). The most fundamental members of the flavin family are lumichrome (LC, no substituent at N10 but H at N1), lumiflavin (LF, $R = \text{methyl}$ at N10), riboflavin (RF, $R = \text{ribityl}$ at N10, vitamin B_2), and flavin mononucleotide (FMN, $R = \text{ribosephosphate}$ at N10). Because the tricyclic aromatic flavin chromophore can absorb in a wide spectral range of the optical part of the electromagnetic spectrum, nature utilizes flavins and flavo-proteins for many photochemical phenomena, redox reactions, and biocatalytic processes.^{1–5} Examples include the repair of DNA, blue light receptors (BLUF), light-oxygen-voltage (LOV) sensing, the respiratory chain, and the catalytic oxidation of glucose by GOx enzymes. The importance of flavins was

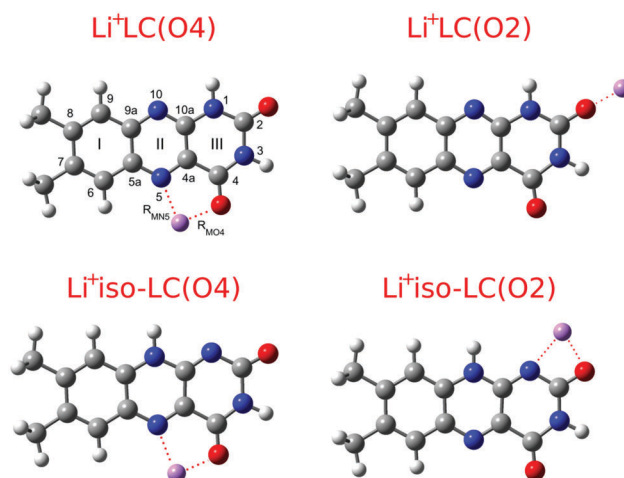


Fig. 1 Lowest-energy structural isomers of Li^+LC ($\text{LC} = \text{C}_{12}\text{N}_4\text{O}_2\text{H}_{10}$, O atoms are red, N atoms are blue) calculated at the PBE0/cc-pVDZ level. Atomic and ring numbers according to IUPAC notation are indicated for $\text{Li}^+\text{LC}(\text{O4})$. The $M - \text{N5}$ (R_{MN5}) and $M - \text{O4}$ (R_{MO4}) bond distances are also indicated.

^a Institut für Optik und Atomare Physik, Technische Universität Berlin, Hardenbergstr. 36, Berlin D-10623, Germany. E-mail: dopfer@physik.tu-berlin.de; Fax: +49 30 314 23018

^b Laboratory for Chemistry and Life Science, Institute of Innovative Research, Tokyo Institute of Technology, 4259, Nagatsuta-cho, Midori-ku, Yokohama, Japan

† Electronic supplementary information (ESI) available. See DOI: 10.1039/c8cp03950j

appreciated by (i) the Nobel prize in chemistry in 1937 awarded to Karrer for his pioneering synthesis and characterization of flavins, and (ii) the Nobel prize in chemistry in 2015 awarded to

Lindahl, Modrich, and Sancar for unraveling the mechanism of DNA repair involving the enzyme photolyase with its fully reduced flavin-adenine dinucleotide (FADH[−]) chromophore. A variety of biochemical processes involving flavins are based on strong metal–flavin interactions.^{6–15}

The optical absorption of flavins sensitively depends on the substituent (R), the protonation, metalation, and oxidation state, and the solvent environment. Therefore, the absorption spectrum is a valuable indicator for changes in the electronic structure of the flavin. To this end, the photochemical properties of flavins were extensively characterized in the condensed phase.^{16–18} In contrast, spectroscopic studies of flavins and their aggregates isolated in the gas phase, which are required to separate the intrinsic structural, electronic, and chemical properties of the optically active flavin chromophore from the strong effects of the environment (*e.g.*, solvation, ions), have not been performed until recently. Apart from our contributions outlined below,^{19–23} the few available studies from other groups include a fluorescence spectrum of LF embedded in He droplets,²⁴ the measurement of proton and electron affinities of LF by mass spectrometry,²⁵ and photo- and collision-induced fragmentation of protonated FMN.²⁶ Very recently, the optical absorption and emission spectra of the mono-anion of flavin adenine dinucleotide (FAD) have been reported in the 210–550 nm range, covering the first four excited singlet states (S₁–S₄).^{27,28} However, the spectra recorded at room temperature exhibit rather broad and unstructured absorption and emission bands, which are similar to those in solution and do not provide any detailed structural or vibronic information.

A few years ago, we initiated a research program to systematically characterize the geometric and electronic structure of protonated and metalated flavins in the gas phase in the electronic ground (S₀) and first excited singlet states (S₁).^{19–23} In this approach, the flavin ions are generated in electrospray ionization sources attached to tandem mass spectrometers. Their geometric and vibrational structures in the S₀ state are initially probed by infrared multiple photon dissociation (IRMPD) spectroscopy of mass-selected ions performed at room temperature in a Fourier-transform ion cyclotron resonance mass spectrometer coupled to an IR free electron laser.^{19–21} In a second step, the vibronic structure in the S₁ state is measured by visible photodissociation (VISPD) of mass-selected ions in a tandem mass spectrometer (quadrupole/time-of-flight) coupled to a recently commissioned cryogenic ion trap (*T* = 4–300 K), using dye and optical parametric oscillator (OPO) lasers.^{22,23} Significantly, both the IRMPD and VISPD spectra display vibrational resolution and thus provide for the first time very detailed information about (i) the preferred protonation and metalation sites and (ii) the effects of protonation and metalation on the geometric and electronic structure of isolated flavins. This information is extracted by comparison of the experimental spectra with results from density functional theory (DFT) calculations.

Herein, we present the vibronic VISPD spectra of the S₁ state of cryogenic M⁺LC complexes with alkali ions (M = Li–Cs). The previous IRMPD studies indicate two major binding sites of M⁺ to LC.²⁰ In the most stable O4 isomer, the M⁺ ion binds to the

lone pairs of O4 and N5 in a O4–M⁺–N5 chelate type bonding, while in the less stable O2 isomer M⁺ forms a linear C–O2–M⁺ bond (Fig. 1). The analysis of the IRMPD spectra in the informative C=O stretch range reveals that the O4 isomer is clearly present for all alkali ions, while the O2 isomer is positively identified only for M = K–Cs. No evidence was obtained for the presence of M⁺iso-LC complexes. For alkali ions, the M⁺–LC interaction is mainly electrostatic in nature, and the bond strength scales with the inverse ionic radius of M⁺.²⁰ The interaction with coinage metals ions (M = Cu and Ag) is stronger because of additional covalent contributions to the M⁺–LC bond involving transition metals. Interestingly, the only structure found for protonated LC (H⁺LC) is the N5 isomer, in which the proton forms a covalent N5–H bond.¹⁹ The proton is too small to benefit from the interaction with the lone pairs of both N5 and O4. Thus, the resulting two deep H⁺LC(N5) and H⁺LC(O4) minima are well separated by a large barrier, and only H⁺LC(N5) is detected in the IRMPD experiment. This isomer assignment was subsequently confirmed by the analysis of the optical spectrum of the S₁ state of H⁺LC.^{22,23}

As outlined above, the optical absorption properties of isolated flavins are relevant for many photochemical processes and are essentially unexplored. The electronic structure is dominated by ππ* excitation of the aromatic π electrons and nπ* excitation of the in-plane lone pair electrons of the various O and N atoms of the heterocyclic chromophore.^{3,16,29–31} The case of LC as the smallest flavin is particularly interesting.³⁰ The lowest excited singlet state (S₁) was predicted to be a dark nπ* state. Consequently, only the nearby optically bright ππ* transitions were observed in the liquid phase.¹⁶ No gas phase spectrum of isolated LC has been reported so far. The analysis of our recent vibronic VISPD spectrum of cryogenic H⁺LC(N5) ions recorded at *T* ~ 25 K reveals important effects of N5-protonation on the electronic structure and molecular orbitals of LC.²³ In particular, a large red shift of the optically bright S₁ ← S₀ (ππ*) transition upon protonation (ΔS₁ ~ −6000 cm^{−1}) is observed, in agreement with the quantum chemical predictions. Significantly, N5-protonation of LC switches the energetic order of the lowest nπ* (dark) and ππ* (bright) states from S₁/S₂ to S₂/S₁.²³ Herein, we extend this work for H⁺LC to M⁺LC complexes with the alkali ions M = Li–Cs, using the same experimental and computational strategy, to further explore the effects of a metal cation on the optical absorption of this chromophore as a function of the interaction strength and the binding site. Significantly, these VISPD spectra are the first optical spectra of any isolated metal–flavin complex. Thus, the results provide a first impression of the M⁺···flavin interaction and its dependence on electronic excitation.

2. Experimental and computational details

VISPD spectra of cryogenic M⁺LC ions are recorded in the BerlinTrap tandem mass spectrometer described elsewhere.²² Briefly, the BerlinTrap setup includes (i) an electrospray ionization

(ESI) source to produce the ions, (ii) a mini-quadrupole to accumulate the ions, (iii) a quadrupole mass filter to select the ions under study, (iv) a cryogenic 22-pole ion trap to store and cool the ions by means of He buffer gas, and (v) a reflectron time-of-flight mass spectrometer (ReTOF-MS) to detect the parent and fragment ions. M^+LC ions are generated in the ESI source by spraying a solution containing LC at a rate of 2 mL h^{-1} . For the production of M^+LC , 2 mg LC are added to 19 mL methanol and 1 mL water (to increase salt solubility), with 0.14–0.10 mmol of alkali salt (LiCl–CsCl, Sigma Aldrich, >99.9% purity), giving average mole ratios of about 1:12 of neutral LC to metal salt (to optimize the yield of M^+LC ions). The M^+LC ions generated are mass selected and guided to the cryogenic 22-pole trap mounted on a coldhead, where they are cooled down to 25 K using pulsed He buffer gas and stored for 90 ms. After extraction from the trap, the cold M^+LC ions are irradiated at the extraction region of the orthogonal ReTOF-MS, and both fragment and parent ions are simultaneously detected by a microchannel plate. For all M^+LC parent ions, M^+ is the only fragment ion observed upon VISPD (see Fig. 2 for $M = \text{Cs}$). Laser radiation is provided by a commercial OPO laser (Continuum, Panther EX-OPO) pumped by the third harmonic of a Nd:YAG laser (Continuum, Powerlite DLS 9010). Typical OPO laser intensities are 3–5 mJ per pulse at an area of around 2 cm^2 . The laser wavelength (bandwidth $\sim 2 \text{ cm}^{-1}$) is tuned using 0.02 nm steps and calibrated with a wavemeter. In addition, a dye laser (Radiant Dyes, Narrowscan) pumped by the third harmonic of a Nd:YAG laser (Innolas, Spotlight 1000) is used for the Na–Cs experiments to improve the spectral resolution compared to the corresponding spectra recorded with the OPO laser. Coumarin 120 and Stilbene dissolved in ethanol are employed as dye solutions for recording

the spectra of M^+LC with $M = \text{Na}$ and K–Cs , respectively. Pulse energies of 5–9 mJ at a bandwidth of 0.06 cm^{-1} are obtained with this laser. The frequency of the dye laser is also calibrated with the wavemeter. The mass discriminated ion signals registered at the microchannel plate are converted into VISPD action spectra by linear normalization of the integrated M^+ fragment ion signal by both the M^+LC parent ion signal and the laser intensity measured simultaneously with the photodissociation mass spectra. To cover the respective $S_1 \leftarrow S_0$ transitions of M^+LC , their VISPD spectra are recorded in the $21\,300\text{--}24\,700 \text{ cm}^{-1}$ spectral range.

DFT calculations at the PBE0/cc-pVDZ level are carried out for optimizing the electronic ground states (S_0) of LC, iso-LC, and their M^+LC and $M^+\text{iso-LC}$ isomers using GAUSSIAN09.³² Vertical excitation energies of the ground state minima are calculated with the time-dependent DFT approach. Subsequently, geometries of the first excited electronic states ($S_1\text{--}S_3$) are optimized at the same computational level using the corresponding ground state structures as starting point. The computationally economic PBE0 functional is chosen because it reproduces the vibronic $S_1 \leftarrow S_0$ spectrum of the related H^+LC ion well.²³ This functional also yields similar results for the S_0 ground state as the B3LYP functional employed previously for the analysis of the IR spectra of flavin ions^{19–21} but yields much better predictions for the excited state spectra.²³ Harmonic vibrational analysis ensures the identification of minima on the potential energy surface. The natural transition orbitals method³³ is employed to determine the orbitals involved in the lowest electronic excitations. Calculated metal ion binding energies (D_0) and relative energies (ΔE_0) are corrected for harmonic zero-point vibrational energies. Vibronic spectra are simulated for $T = 0 \text{ K}$ utilizing harmonic (unscaled) frequencies by means of multi-dimensional Franck–Condon (FC) simulations as implemented in PGOPHER.³⁴ These stick spectra are convoluted with a Lorentzian line profile using a FWHM of 6 cm^{-1} to enable convenient comparison with the measured VISPD spectra. The atomic charge distribution is evaluated using the natural bond orbital analysis.³⁵

3. Results and discussion

The VISPD spectra of the $S_1 \leftarrow S_0$ transition of all M^+LC ions considered ($M = \text{Li–Cs}$) are recorded in the LC loss channel, which is the only fragmentation channel observed upon photodissociation. As an example, the laser-on and laser-off mass spectra of Cs^+LC (m/z 375) obtained with the laser frequency tuned resonantly to its $S_1 \leftarrow S_0$ band origin at $23\,571 \text{ cm}^{-1}$ are shown in Fig. 2. The only laser-induced fragment ion observed is Cs^+ (m/z 133). The other minor fragment ion at m/z 258 is not affected by laser action and is thus concluded to result from metastable decay and/or collision-induced dissociation. The VISPD spectra of all M^+LC ions recorded in the vicinity of the S_1 origin are compared in Fig. 3 to that of H^+LC .²³ These spectra are referenced to the S_1 origins, and spectra at the absolute wavenumber scale are available in Fig. S1 in ESI† to show the complete covered range. The 22-pole trap temperature is kept at

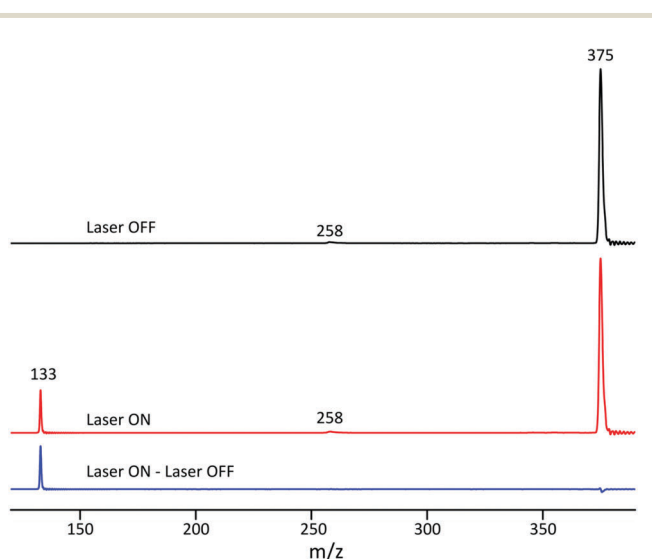


Fig. 2 Photodissociation mass spectra of Cs^+LC (m/z 375). Laser ON, laser OFF, and difference mass spectra with the laser frequency tuned resonantly to the $S_1 \leftarrow S_0$ band origin at $23\,571 \text{ cm}^{-1}$. The only laser-induced fragment ion is Cs^+ (m/z 133). The laser-induced loss of LC is observed for all M^+LC with alkali ions. A low-intensity fragment ion not sensitive to laser action is observed at m/z 258 and arises from metastable decay or collision-induced dissociation.

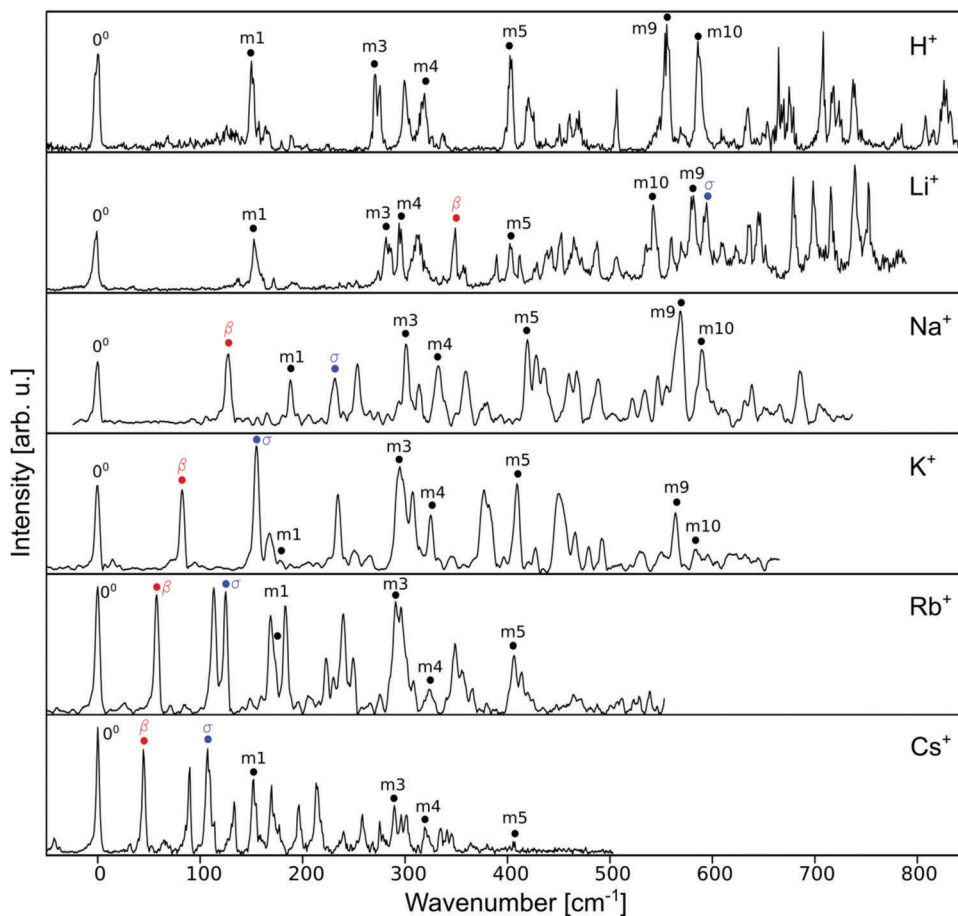


Fig. 3 Experimental VISPD spectra of the $S_1 \leftarrow S_0$ transition of M^+LC ($M = H, Li\text{--}Cs$) plotted as a function of S_1 internal energy. The spectra of H^+LC and Li^+LC are recorded with the OPO laser, while the dye laser is used for the spectra of M^+LC with $M = Na\text{--}Cs$. The S_1 origin energies (0^0) are 19 962 (H), 21 911 (Li), 22 786 (Na), 23 315 (K), 23 465 (Rb), and 23 571 cm^{-1} (Cs). Spectra at the absolute wavenumber scale are available in Fig. S1 in ESI†. Positions and assignments of vibronic transitions are listed in Table S1 in ESI†. Intramolecular LC modes are denoted as m1–m10, while β and σ are intermolecular in-plane $M^+ \cdots LC$ bend and stretch modes. The spectrum of H^+LC is reproduced from ref. 23.

25 K for all measurements (except for Li^+LC , for which the trap is held at 6 K) to maximize the trapped ion and VISPD signals. This temperature is low enough to nearly completely suppress the appearance of hot bands for all M^+LC ions except for Cs^+LC . Cs^+LC has the lowest vibrational frequencies, because it has the weakest $M^+ \cdots LC$ bond and the highest mass. VISPD spectra of Cs^+LC recorded for various ion trap temperatures ($T = 25, 50, 100$ K) illustrate the drastic effect of cooling the rotational and vibrational temperature of the ions on the widths of the vibronic transitions and the intensity of hot bands (Fig. S2 in ESI†). A FC analysis of the relative intensity of the 53_1^0 hot band originating from the lowest frequency mode in S_0 ($\beta = 42$ cm^{-1}) yields a vibrational temperature of 29 ± 3 K for a nominal trap temperature measured as 25 ± 1 K. Similar ion temperatures of 33 ± 3 and 31 ± 3 K are obtained for K^+LC and Rb^+LC from the analysis of the hot band intensities. For M^+LC with $M = Li$ and Na no hot bands are detected. The widths of the peaks in the M^+LC spectra with $M = Na\text{--}Cs$ recorded with the dye laser (bandwidth ~ 0.06 cm^{-1}) are $\sim 3\text{--}4.5$ cm^{-1} at $T = 25$ K and arise mostly from unresolved rotational structure (and possibly from a finite lifetime). The Li^+LC spectrum exhibits slightly larger

widths (~ 5 cm^{-1} for the S_1 origin), because it is measured with the OPO laser (bandwidth ~ 2 cm^{-1}). The S_1 origin of all M^+LC ions is accompanied by rich vibronic structure, indicating a large geometry change upon electronic excitation. The S_1 origin energies of 21 911 (Li), 22 786 (Na), 23 315 (K), 23 465 (Rb), and 23 571 cm^{-1} (Cs) increase substantially with increasing size of the alkali ion. Unfortunately, no experimental spectrum is available for isolated LC. The maximum of its first absorption band in solution (assigned to the lowest $\pi\pi^*$ state, S_2) lies in the 379–385 nm range ($\sim 26\,000$ cm^{-1}) depending on the solvent.¹⁶ Assuming this value as an experimental reference energy for the lowest $\pi\pi^*$ state of isolated LC, the large derived S_1 red shifts of -2429 (Cs) and -4089 cm^{-1} (Li) for M^+LC illustrate that metalation of the aromatic chromophore significantly changes both its geometric and electronic structure. On the other hand, the S_1 red shifts of M^+LC are smaller than that of H^+LC (~ -6000 cm^{-1} for the observed N5-protonated isomer), indicating that the effects of alkali metal complexation are less pronounced than that of protonation.²³

Quantum chemical calculations are used to derive the isomer and vibronic assignments of the measured VISPD spectra.

The M^+ cation can bind to the various available nucleophilic sites of LC and iso-LC (Fig. 1), including the lone pairs of the O atoms of the two CO groups (denoted O2 and O4), the lone pairs of the two heterocyclic N atoms (N5 and N10 for LC, N1 and N5 for iso-LC), and π -stacking to the three aromatic rings (I–III).²⁰ However, only isomers with M^+ attached to the CO groups of LC are found experimentally by IRMPD spectroscopy.²⁰ Consequently, only these will be considered in detail here. Although LC is predicted to be $\Delta E_0 = 55 \text{ kJ mol}^{-1}$ more stable than iso-LC, M^+ iso-LC complexes may still be present in solution and in the ESI spray because of enhanced solvent stabilization. In fact, our previous IRMPD experiments on M^+ LC reveal the presence of isomers with relative energies as high as 40 kJ mol^{-1} in the ESI source.²⁰ The binding and relative energies D_0 and ΔE_0 of all considered M^+ LC isomers calculated at the PBE0 level agree well with those at the B3LYP level.²⁰ The M^+ LC(O4) isomer, in which M^+ binds in a chelate to the lone pairs of both O4 and N5, is the global minimum for all alkali ions,²⁰ with D_0 ranging from 296 kJ mol^{-1} for Li^+ down to 140 kJ mol^{-1} for Cs^+ . The M^+ LC(O2) isomers, in which M^+ binds in a linear fashion to O2, are systematically less stable local minima, whereby the energy gap to the O4 minimum decreases from 73 kJ mol^{-1} (Li) to 34 kJ mol^{-1} (Cs). The geometric and vibrational properties of the O4 and O2 isomers of M^+ LC in the S_0 ground electronic state are discussed in detail elsewhere.²⁰ In general, the $M^+ \cdots \text{LC}$ bond is mostly electrostatic in nature. Hence, the bond strength, and several other structural and spectroscopic parameters, show a monotonic dependence on the inverse ionic radius of M^+ ($1/R_M$).^{20,21,36} While the most stable M^+ LC(O4) isomer is identified in the IRMPD spectra of all alkali ions, the M^+ LC(O2) local minimum is positively identified only for $M = \text{K–Cs}$.²⁰ The O2 isomer of M^+ iso-LC (O2/N1 chelate) is slightly more stable (by $2\text{--}12 \text{ kJ mol}^{-1}$) than the corresponding O4 isomer (O4/N5 chelate). Both M^+ iso-LC isomers are less stable than the M^+ LC(O4) global minimum by around $45\text{--}60 \text{ kJ mol}^{-1}$. This energy difference is mainly coming from the difference in stability of LC and iso-LC.

To identify the M^+ LC isomers observed in the VISPD spectra, both the positions of the adiabatic $S_1 \leftarrow S_0$ origin transitions and the vibronic spectra simulated within the FC approximation are considered next. In Fig. 4 the experimental S_1 origins extracted from the VISPD spectra are compared with the adiabatic S_1 origins calculated for all considered isomers and plotted *versus* the inverse ionic radii ($1/R_M$)^{20,36} of M^+ . A monotonic dependence of the metalation-induced S_1 shift on $1/R_M$ is expected, because the $M^+ \cdots \text{LC}$ bonding is mostly electrostatic for all alkali ions.²⁰ The data points for the O4 and N5 isomers of H^+ LC discussed elsewhere²³ are also included for completeness. The experimental VISPD spectra of M^+ LC are compared in Fig. 5 to the simulated $S_1 \leftarrow S_0$ vibronic spectra as a function of the S_1 internal energy. The computed spectra have to be shifted by a constant amount to match the calculated and experimental S_1 origins, $\Delta\nu = S_1^{\text{exp}} - S_1^{\text{calc}}$. All values for S_1^{exp} , S_1^{calc} , and $\Delta\nu$ are listed in Table 2. The spectra of the calculated isomers are ordered from top to bottom according to their relative energy (Table 1).

From Fig. 4, it is evident that the adiabatic S_1 energies calculated for the M^+ LC(O4) isomer closely reproduce the trend

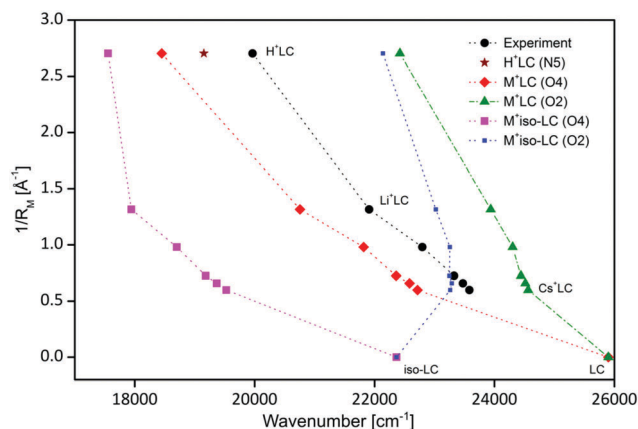


Fig. 4 Measured adiabatic $S_1 \leftarrow S_0$ ($\pi\pi^*$) transition energies of M^+ LC (black dots) compared to values calculated for the various M^+ LC and M^+ iso-LC conformers ($M = \text{H, Li–Cs}$) (colored symbols) *versus* the inverse radius of the cation.^{20,36} The values for the O4 ($M = \text{Li–Cs}$) and N5 ($M = \text{H}$)²³ conformers reproduce the experimental trend best except for a nearly constant shift ranging from $+1154$ (Li) to $+854 \text{ cm}^{-1}$ (Cs) and down to $+809 \text{ cm}^{-1}$ for the protonated species (Table 2). The data point calculated for LC corresponds to the S_2 state, because S_2 is the lowest bright $\pi\pi^*$ state for LC.

of the experimental data, with a small and roughly constant deviation of $\Delta\nu = 1004 \pm 150 \text{ cm}^{-1}$ ($\sim 5\%$, $\sim 0.1 \text{ eV}$). The deviation $\Delta\nu$ becomes slightly smaller with decreasing interaction ($\Delta\nu = 1154, 969, 955, 881, \text{ and } 854 \text{ cm}^{-1}$ for Li to Cs). In addition, extrapolation to zero interaction ($R_M \rightarrow \infty$) converges smoothly to the value computed for the corresponding S_2 state of LC (*i.e.*, the lowest bright $\pi\pi^*$ state). (Here, we note that the S_1 state of LC is in fact predicted to be a dark $n\pi^*$ state at 24826 cm^{-1} , which however is calculated to be very close to the optically bright $\pi\pi^*$ state (S_2), with an adiabatic energy difference of 1073 cm^{-1}). The energies of the S_1 origins computed for the M^+ LC(O2) isomers exhibit a largely different dependence as a function of $1/R_M$. In addition, they are significantly larger than the experimental values ($-\Delta\nu = 2026, 1517, 1126, 1050, \text{ and } 992 \text{ cm}^{-1}$ for Li to Cs). For both reasons, we can exclude the O2 isomers. The S_1 origins of M^+ iso-LC(O4) are systematically lower than the measured values by around 4000 cm^{-1} ($\Delta\nu = 3966, 4085, 4131, 4097, 4043 \text{ cm}^{-1}$ for Li to Cs), and this large difference of $\sim 0.5 \text{ eV}$ allows us to exclude also this isomer as carrier of the measured VISPD spectra. Finally, although the S_1 origins of M^+ iso-LC(O2) are closer to the observed ones ($\Delta\nu = -1111, -470, 67, 176, 309 \text{ cm}^{-1}$ for Li to Cs), the largely varying deviations indicate that this isomer is also not responsible for the observed spectra. The large differences in the computed S_1 origins of M^+ LC(O4) and M^+ LC(O2) illustrate that the optical absorption properties and thus the photochemical behaviour of flavins can indeed be drastically manipulated by metal complexation, because they strongly depend on both the type of metal ion and the metalation site.

The comparison of the computed vibronic spectra of the various isomers with the measured VISPD spectra in Fig. 5 confirms the assignment to the most stable M^+ LC(O4) isomer derived from the analysis of the S_1 origins. Clearly, all intense vibrational features are well reproduced in position and relative

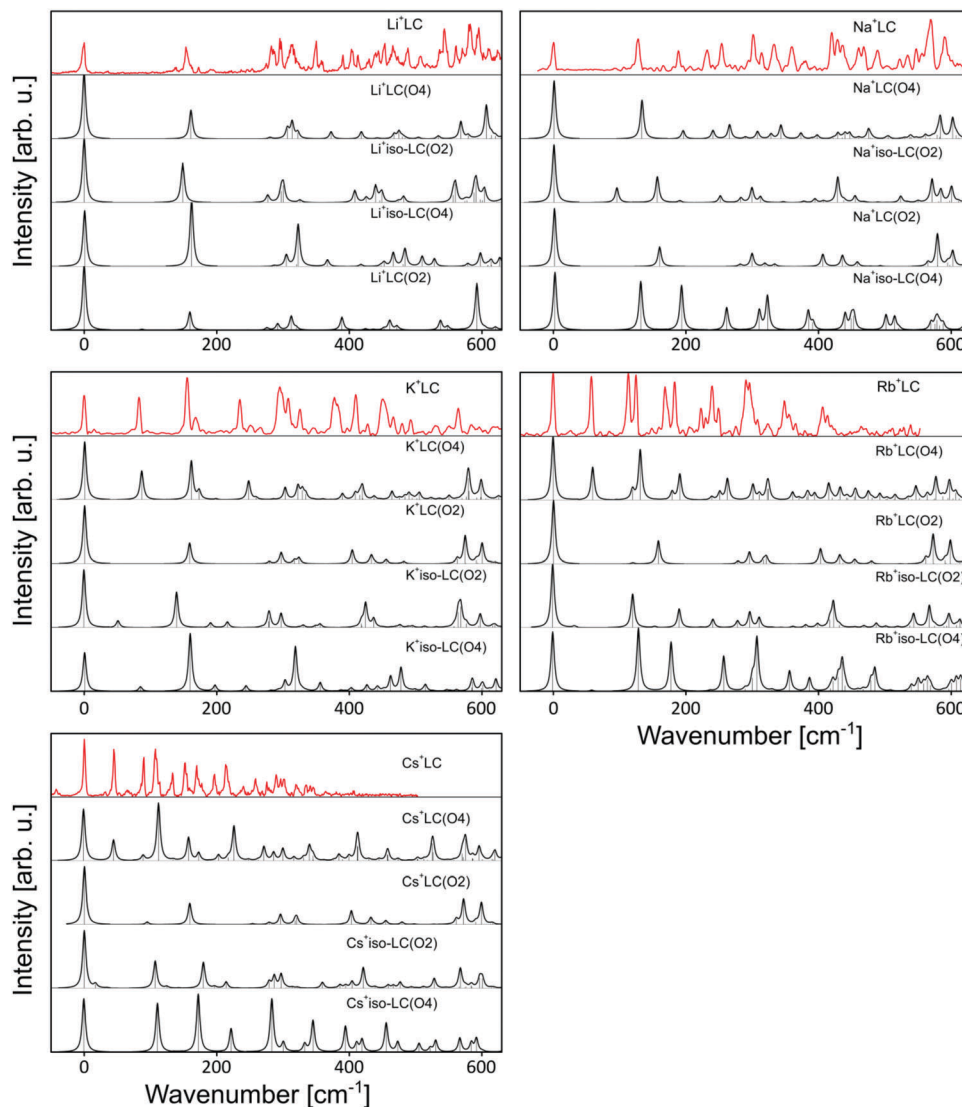


Fig. 5 Comparison between experimental VISPD spectra recorded for M^+LC ($M = Li-Cs$) as a function of S_1 internal energy (Fig. 3) compared to Franck-Condon simulations for the isomers shown in Fig. 1 using a convolution width of 6 cm^{-1} . Isomers are ordered from top to bottom according to their relative energy (Table 1).

intensity only for this isomer for all metal ions. For example, for $M = K-Cs$ only the $M^+LC(O4)$ spectrum can reproduce the first vibronic band. On the other hand, the first vibronic band predicted for $M^+iso-LC(O2)$ with $M = Na-Cs$ is not detected in the experiment. Hence, from the overall analysis of the relative energies, binding energies, S_1 energies, and vibronic spectra, we clearly favor an assignment of the VISPD spectra to the most stable $M^+LC(O4)$ isomer, which is also the dominant isomer identified by IRMPD spectroscopy.²⁰ The presence of other isomers in the VISPD spectra in the same spectral range is unlikely, considering the large differences in their predicted S_1 origins (Fig. 4 and Table 2).

After the identification of the $M^+LC(O4)$ isomer as the carrier of the observed VISPD spectra for all alkali metals, we focus in Fig. 6 on the detailed assignment of the vibronic transitions. Numerical values for the positions of all intense experimental

bands and their vibronic assignments are given in Table S1 in ESI.† Complete lists of all vibrational frequencies calculated for the S_0 and S_1 states of $M^+LC(O4)$ are available in Table S2 in ESI.† The numbering of the vibrational modes follows the Mulliken notation. The $M^+LC(O4)$ structures with their planar aromatic rings have C_s symmetry, and the $S_1 \leftarrow S_0$ transition has $\pi\pi^*$ character. Consequently, according to the FC principle, all vibronic transitions originating from the ground vibrational state in the S_0 electronic ground state terminate in S_1 vibrational states with a' symmetry, *i.e.* only in-plane modes (a') are observed and assigned. The maximum deviations between the experimental and calculated harmonic vibrational frequencies are less than 20 cm^{-1} , with mean deviations of around $5-10\text{ cm}^{-1}$ for $M = Li-Cs$. These differences are small considering the experimental peak width ($\sim 5\text{ cm}^{-1}$) and the harmonic approximation employed for the FC analysis. Most of the vibronic transitions

Table 1 Binding energies (D_0) and relative energies (ΔE_0) in kJ mol^{-1} calculated at the PBE0/cc-pVDZ level compared to corresponding values determined at the B3LYP/cc-pVDZ level^a

Isomer	PBE0/cc-pVDZ		B3LYP/cc-pVDZ		Isomer	PBE0/cc-pVDZ		B3LYP/cc-pVDZ	
	D_0	ΔE_0	D_0	ΔE_0		D_0	ΔE_0	D_0	ΔE_0
LC		0			K ⁺ LC(O4)	173.6	0	177.4	0
iso-LC		54.9			K ⁺ LC(O2)	131.8	41.8	137.4	40.0
Li ⁺ LC(O4)	296.0	0	304.0	0	K ⁺ iso-LC(O2)	182.4	46.1		
Li ⁺ iso-LC(O2)	294.4	56.5			K ⁺ iso-LC(O4)	170.9	57.6		
Li ⁺ iso-LC(O4)	292.0	58.9			Rb ⁺ LC(O4)	155.4	0	156.6	0
Li ⁺ LC(O2)	222.7	73.3	232.5	71.5	Rb ⁺ LC(O2)	116.8	38.6	120.2	36.4
Na ⁺ LC(O4)	217.6	0	223.6	0	Rb ⁺ iso-LC(O2)	164.8	45.5		
Na ⁺ iso-LC(O2)	221.6	50.9			Rb ⁺ iso-LC(O4)	153.1	57.3		
Na ⁺ LC(O2)	161.1	56.4	168.0	55.6	Cs ⁺ LC(O4)	140.3	0	140.3	0
Na ⁺ iso-LC(O4)	213.5	59.0			Cs ⁺ LC(O2)	106.3	34.0	108.8	31.5
					Cs ⁺ iso-LC(O2)	150.8	44.4		
					Cs ⁺ iso-LC(O4)	138.7	56.5		

^a B3LYP values are from ref. 20.

Table 2 Experimental and predicted adiabatic S_1 energies of LC and various isomers of M^+ LC and M^+ iso-LC calculated at the PBE0/cc-pVDZ level, along with the shifts from the experimental S_1 origin (in cm^{-1})

Isomer	$S_1 \leftarrow S_0$	$\Delta\nu$	Isomer	$S_1 \leftarrow S_0$	$\Delta\nu$
LC(exp)	$\sim 26\,000$ (S_2) ^a		K ⁺ LC(exp)	23 315	0
LC	25 899 (S_2) ^b		K ⁺ LC(O4)	22 360	955
iso-LC	22 366		K ⁺ LC(O2)	24 441	-1126
H ⁺ LC(exp) ^c	19 962	0	K ⁺ iso-LC(O2)	23 248	67
H ⁺ LC(N5) ^c	19 153	869	K ⁺ iso-LC(O4)	19 184	4131
H ⁺ LC(O4) ^c	18 451	1511	Rb ⁺ LC(exp)	23 465	0
Li ⁺ LC(exp)	21 911	0	Rb ⁺ LC(O4)	22 584	881
Li ⁺ LC(O4)	20 757	1154	Rb ⁺ LC(O2)	24 515	-1050
Li ⁺ iso-LC(O2)	23 022	-1111	Rb ⁺ iso-LC(O2)	23 289	176
Li ⁺ iso-LC(O4)	17 945	3966	Rb ⁺ iso-LC(O4)	19 368	4097
Li ⁺ LC(O2)	23 937	-2026	Cs ⁺ LC(exp)	23 571	0
Na ⁺ LC(exp)	22 786	0	Cs ⁺ LC(O4)	22 717	854
Na ⁺ LC(O4)	21 817	969	Cs ⁺ LC(O2)	24 563	-992
Na ⁺ iso-LC(O2)	23 256	-470	Cs ⁺ iso-LC(O2)	23 262	309
Na ⁺ LC(O2)	24 303	-1517	Cs ⁺ iso-LC(O4)	19 528	4043
Na ⁺ iso-LC(O4)	18 701	4085			

^a Vertical value from experiments in solution for the S_2 ($\pi\pi^*$) state (exact value depends on solvent).¹⁶ ^b This value corresponds to the adiabatic energy of the optically bright $\pi\pi^*$ (S_2) state. For LC, this state is higher than the optically dark $n\pi^*$ (S_1) state at $24\,826\text{ cm}^{-1}$. ^c From ref. 23.

are fundamentals of the lowest frequency a' modes (42^1 – 53^1 for Li–Cs), and all other assigned modes are overtones and combination bands of these in-plane modes. At this point, we note that there is weak vibronic structure in the VISPD spectra which cannot be reproduced by the FC simulations at $T = 0\text{ K}$. This additional signal is most pronounced in the Li⁺LC spectrum in the 100 – 300 cm^{-1} range above the S_1 origin. Similar signal was also observed in the H⁺LC spectrum. The relative intensity of this signal strongly depends on the experimental conditions. According to the calculations, this signal cannot be ascribed to S_1 vibronic bands of other M^+ LC isomers and also not to hot bands of M^+ LC(O4). Alternative options including (i) vibronic bands of a higher electronic state of the M^+ LC(O4) isomer and (ii) vibronic coupling of the bright S_1 state of M^+ LC(O4) with another, possibly dark state, can also be excluded. Thus, we tentatively assign this signal to S_1 spectra of tagged M^+ LC(O4)– L_n clusters with weakly bonded ligands L (e.g., $L = \text{He}$ and N_2)

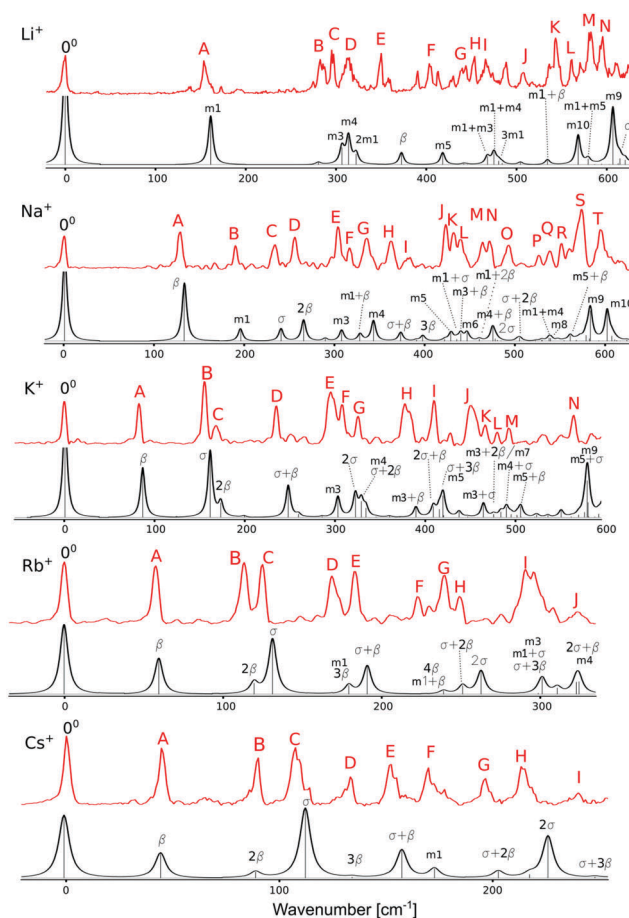


Fig. 6 Experimental VISPD spectra of M^+ LC ($M = \text{Li–Cs}$) as a function of S_1 internal energy (Fig. 3) (top) compared with the Franck–Condon simulation of the identified M^+ LC(O4) conformer (bottom) along with vibrational assignments (Table S1 in ESI†).

formed in the 22-pole trap. Such clusters are formed in various abundances depending on the experimental conditions, as observed in the mass spectra (not shown here). Their formation is only significant for Li⁺LC (and H⁺LC) because of the large binding energies of L to the small M^+ (H^+) ion.

Table 3 Frequencies (cm^{-1}) of relevant low-energy vibrations of $\text{M}^+\text{LC}(\text{O4})$ and LC in the S_0 and S_1 states calculated at the PBE0/cc-pVDZ level compared to available experimental S_1 frequencies. A complete set of calculated frequencies is given in Table S2 in ESI. For comparison, values are also given for $\text{H}^+\text{LC}(\text{N5})$ and LC

Mode	Li			Na			K			Rb			Cs			H			LC	
	S_0	S_1	exp	S_0	S_1	exp	S_0	S_1	exp	S_0	S_1	exp	S_0	S_1	exp	S_0	S_1	exp	S_0	S_1
β	354	373	350	123	132	128	79	86	83	55	60	57	42	45	45	1151	1143			
σ	598	615	595	233	240	232	156	161	155	122	132	125	104	114	108	3455	3555			
m1	159	161	157	187	195	189	190	199		176	180	182	171	174	170	153	153	154	159	158
m2	294	280		303	289		299	285		297	283		296	283		305	289	278	289	278
m3	310	306	288	314	307	301	309	303	295	308	301	293	308	301		283	274	274	303	296
m4	325	314	299	344	342	333	336	328	325	334	325	323	333	322		330	315	321	328	314
m5	414	418	403	428	428	420	419	419	410	416	416		414	413		413	412	406	406	404
m6	446	446		445	445	436	440	437		440	435		439	434		432	431		436	430
m7	481	480		479	477		478	476	466	478	475		478	475		474	472		475	471
m8	496	505		541	538	534	539	535		538	534		537	533		525	520	509	529	522
m9	623	607	596	616	582	569	613	579	565	612	577		612	576		573	570	558	607	564
m10	568	569	548	586	601	590	585	598		584	598		584	597		609	599	590	581	592

In a next step, we discuss the relevant low-frequency in-plane normal modes of the $\text{M}^+\text{LC}(\text{O4})$ isomer and compare their frequencies as a function of M^+ . They are listed in Table 3 with an M^+ -independent notation, and graphical representations are shown in Fig. S3 in ESI.† The two in-plane intermolecular modes of the metal ion are the $\text{M}^+\cdots\text{LC}$ stretch (σ) and in-plane bend (β). Their frequencies change drastically with M^+ , because both the reduced mass and the force constants change according to the strongly varying binding energy and angular anisotropy of the $\text{M}^+\cdots\text{LC}$ potential. For example, $\beta = 373\text{--}45\text{ cm}^{-1}$ and $\sigma = 615\text{--}114\text{ cm}^{-1}$ are computed for $\text{M}^+\text{LC}(\text{O4})$ with Li–Cs in the S_1 state, as a result of the strongly decreasing interaction and increasing mass with increasing size of the metal ion. On the other hand, the frequencies of the skeleton vibrations of LC do not change much with M^+ (as long as they do not strongly couple with the intermolecular metal modes). As a result, the frequency order of the metal and LC modes changes with M^+ , and we introduce an additional to describe the normal modes of $\text{M}^+\cdots\text{LC}$, which is independent of M^+ (m1, m2, m3, ... for the lowest frequency a' modes, Fig. S3 in ESI†). In addition, these M^+LC modes do not differ much from those of LC and H^+LC , because both protonation and metalation have not a large impact on these. Briefly, mode m1 with a calculated S_1 frequency of $161\text{--}199\text{ cm}^{-1}$ for Li–Cs involves in-plane bending of the outer aromatic rings I and III around the central ring II. Its larger frequency variation is caused by M^+ -dependent mixing with σ and β . Mode m2 with $280\text{--}289\text{ cm}^{-1}$ is a scissoring motion of the methyl groups at C7 and C8. Mode m3 with $301\text{--}307\text{ cm}^{-1}$ is associated with a shear deformation of ring II along the N5–N10 axis, while mode m4 with $314\text{--}342\text{ cm}^{-1}$ is described by a uniform stretching of the three aromatic rings along the long molecular axis. Mode m5 at $413\text{--}428\text{ cm}^{-1}$ involves a compression of ring III combined with a scissoring motion of the two carbonyl groups. Modes m9 and m10 with $576\text{--}607$ and $569\text{--}601\text{ cm}^{-1}$ are two complex delocalized deformation modes of all three rings.

The low-frequency part of the $\text{M}^+\text{LC}(\text{O4})$ spectra with $\text{M} = \text{Na}\text{--}\text{Cs}$ is dominated by progressions and combinations of the intermolecular β and σ modes, indicative of substantial geometry changes of the $\text{M}^+\cdots\text{LC}$ bond upon S_1 excitation.

For example, all but one transition in the $\text{Cs}^+\text{LC}(\text{O4})$ spectrum can be assigned to $n\beta + m\sigma$ with $n \leq 3$ and $m \leq 2$. Bands A, B, and D are due to $n\beta$, bands C and H arise from $m\sigma$, and bands E, G, and I are combination bands of β and σ . The remaining band F is due to the intramolecular m1 mode of LC. The $\text{M}^+\text{LC}(\text{O4})$ spectra with $\text{M} = \text{Na}\text{--}\text{Rb}$ exhibit similar intermolecular $n\beta + m\sigma$ transitions but contain more intramolecular LC bands (mainly m1–m5, m9, m10) toward higher frequency, because they are recorded in a more extended frequency range. Interestingly, the $\text{Li}^+\text{LC}(\text{O4})$ spectrum is dominated by intramolecular LC modes, and the β and σ modes with their high frequencies are less pronounced in the VISPD spectrum. In general, the computed metal frequencies $\beta = 45, 60, 86, 132$, and 373 cm^{-1} and $\sigma = 114, 132, 161, 240$, and 615 cm^{-1} (Cs–Li) agree very well with the measured ones ($\beta = 45, 57, 83, 128, 350\text{ cm}^{-1}$, $\sigma = 108, 125, 155, 232, 595\text{ cm}^{-1}$), indicating that the computational level describes the $\text{M}^+\cdots\text{LC}$ interaction in the S_1 excited state to high accuracy. In addition, both in-plane metal frequencies are slightly larger in the S_1 state than in the S_0 state ($\beta = 42, 55, 79, 123, 354\text{ cm}^{-1}$, $\sigma = 104, 122, 156, 233, 598\text{ cm}^{-1}$), because the $\text{M}^+\cdots\text{LC}$ interaction increases by S_1 excitation. This observation is consistent with the computed (and observed) S_1 red shifts upon metalation, because these correspond directly to the increase in the binding energy upon S_1 excitation ($\Delta D_0 = -\Delta S_1$). This strengthening of the $\text{M}^+\cdots\text{LC}$ interaction amounts to $\Delta D_0 = 34.8, 24.4, 18.1, 16.3$, and 12.9 kJ mol^{-1} for $\text{M}^+\text{LC}(\text{O4})$ with $\text{M} = \text{Li}\text{--}\text{Cs}$, which corresponds to 9–12%. Interestingly, the $\text{Li}^+\text{LC}(\text{O4})$ spectrum closely resembles that of $\text{H}^+\text{LC}(\text{N5})$, possibly because both Li^+ and H^+ bind very strongly to the LC chromophore so that electronic S_1 excitation does not affect much the geometry of the cation $\cdots\text{LC}$ bond in these two ions.

In a next step, we consider in more detail the geometry changes of $\text{M}^+\text{LC}(\text{O4})$ induced by S_1 excitation, which are already indicated by the vibrational analysis. To this end, the geometry of the S_0 state and its change upon S_1 excitation are shown in Fig. 7 for $\text{Li}^+\text{LC}(\text{O4})$, while corresponding structures for $\text{M} = \text{Na}\text{--}\text{Cs}$ are given in Fig. S4 in ESI.† Specifically, the structural changes of LC induced by metalation at the O4 position in the S_0 state are described in Fig. 7(top) (and Fig. S4(top) in ESI†), where relative

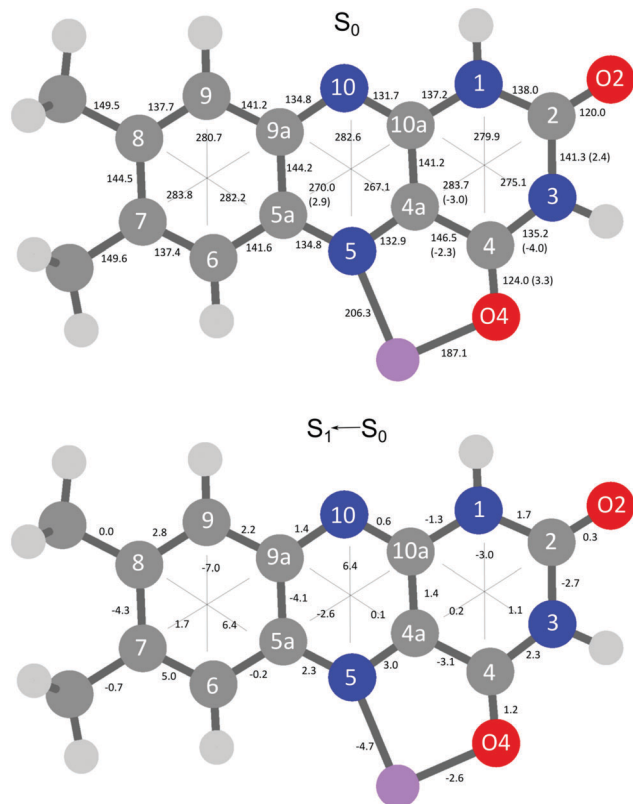


Fig. 7 (top) Geometry of the ground state (S₀) of Li⁺LC (absolute values) and relative changes ≥ 2 pm compared to bare LC calculated at the PBE0/cc-pVDZ level. (bottom) Geometry changes of Li⁺LC(O4) upon S₁ excitation (distances relative to S₀). All values are given in pm. Positive values correspond to elongations; negative values indicate contractions upon S₁ excitation.

changes ≥ 2.0 pm with respect to neutral LC are given in parentheses. The metal ion binds slightly closer (and stronger) to O4 than to N5 (187.1 and 206.3 pm for Li) and the induced geometry changes are more important for ring III than for ring II, as discussed in detail previously.^{20,23} The geometry change of Li⁺LC(O4) upon S₁ excitation of Li⁺LC(O4) visualized in Fig. 7(bottom) (and in Fig. S4(bottom) in ESI[†] for M = Na–Cs) is even more drastic than that induced by metalation. The consequences of S₁ excitation are substantial throughout the whole chromophore and particularly strong in rings I and II. The expansion of ring II along the N5–N10 axis (6.4 pm) is accompanied by a compression of the same ring along the C5a–C10a axis (−2.6 pm). Ring I is greatly contracted along the C9–C6 distance (−7.0 pm) and expanded along the C7–C9a (1.7 pm) and the C8–C5a (6.4 pm) directions. In contrast, only a smaller deformation is induced in ring III, with a contraction along the N1–C4 axis (−3.0 pm) and an elongation of the N3–C10a distance (1.1 pm). S₁ ← S₀ excitation also moderately affects the bond length of the C4O carbonyl group (1.2 pm). The structural changes of the LC moiety upon S₁ excitation of M⁺LC(O4) are relatively independent of M⁺, because the orbitals involved in electronic $\pi\pi^*$ excitation are localized on the LC chromophore and not on M⁺ (Fig. 8). On the other hand, charge

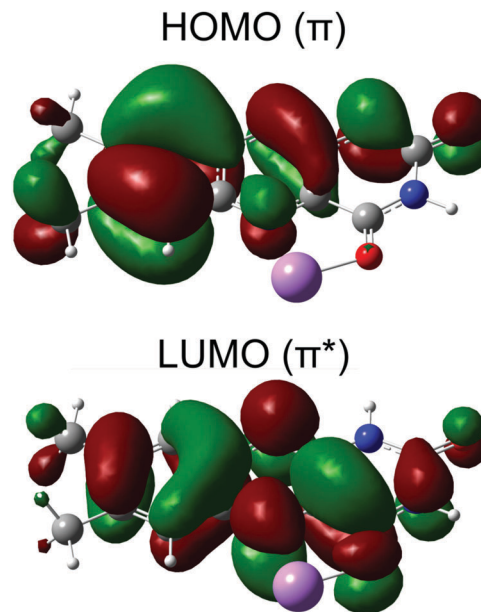


Fig. 8 Molecular orbitals involved in the S₁ ← S₀ transition (LUMO ← HOMO, $\pi\pi^*$) of Li⁺LC(O4) calculated at the PBE0/cc-pVDZ level.

reorganization involved in S₁ excitation of LC has a strong impact on the geometry of the M⁺···LC bond in M⁺LC(O4), which depends somewhat on the interaction strength. As a result of the drastic increase in the M⁺···LC interaction upon S₁ excitation (as indicated by the S₁ red shift), the intermolecular R_{MN5} and R_{MO4} distances contract for all metals. The contraction of the M–O4 bond is more pronounced for the heavier alkali ions ($\Delta R_{\text{MO4}} = -2.6, -3.4, -5.0, -5.7, -7.1$ pm for Li–Cs). Interestingly, the M–N5 bond contraction is of similar magnitude but exhibits a nonmonotonic behaviour, with the smallest contraction obtained for K ($\Delta R_{\text{MN5}} = -4.7, -4.6, -4.4, -4.9$, and -5.2 pm from Li to Cs), because also the N5–M–O4 chelate angle changes at the same time.²⁰ These large changes in the M–N5 and M–O4 bond lengths upon S₁ excitation are consistent with the long FC progressions of the M⁺···LC intermolecular modes β and σ observed in the vibronic VISPD spectra of the S₁ ← S₀ transition.

The HOMO and LUMO orbitals involved in the S₁ ← S₀ transition of M⁺LC(O4) in Fig. 8 (shown for M = Li) illustrate its character as optically allowed $\pi\pi^*$ excitation. Clearly, both orbitals are localized on the aromatic LC chromophore and have essentially no amplitude on M⁺. Hence, the calculated oscillator strengths for S₁ excitation of M⁺LC(O4) are roughly constant ($f \times 10^3 = 31, 40, 45, 49, 51$ for M = Li–Cs). The same HOMO and LUMO orbitals have previously been identified to be responsible for the S₁ ← S₀ transition of H⁺LC(N5) by the same computational and spectroscopic approach ($f \times 10^3 = 48$).²³ As discussed earlier, the experimental S₁ red shift of M⁺LC(O4) observed for the lowest $\pi\pi^*$ transition is in the 2429–4089 cm^{−1} range for Cs–Li, in good agreement with computed red shifts of 3182–5142 cm^{−1}. S₁ excitation of LC shifts electron density from ring I to ring II, in particular also to N5 and O4. For example, the atomic charges on O4 and N5 in LC are −0.565 and −0.386 *e* in S₀ and −0.595 and −0.477 *e* in the $\pi\pi^*$ excited state (S₂), respectively

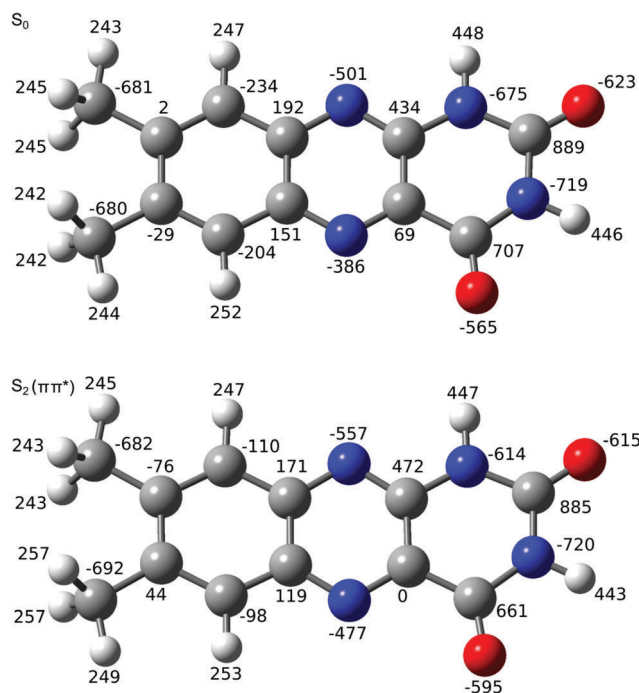


Fig. 9 Atomic charges (in units of $10^{-3} e$) of LC in the S_0 and first $\pi\pi^*$ excited state (S_2) evaluated at the PBE0/cc-pVDZ level using natural bond orbital analysis.

(Fig. 9 and Table 4). Hence, in the O4–M⁺–N5 chelate, this charge transfer enhances the electrostatic interaction of LC with the nearby M⁺ cation in the S_1 state of the M⁺LC(O4) isomer, which results in the large S_1 red shift (Fig. 4). On the other hand, $\pi\pi^*$ excitation has little impact on the partial charge of the O2 atom of LC ($\Delta q < 0.01 e$). Thus, the S_1 shifts of the less stable M⁺LC(O2) isomers are substantially smaller. Finally, formation of the M⁺–LC bond is accompanied by modest charge transfer from M⁺ to LC, which increases with the binding energy of the M⁺···LC bond (Table 4). For example, $q_M = 0.915$ and $0.898 e$ for M⁺LC(O4) with M = Cs and Li, respectively. As this bond becomes stronger in the S_1 excited state, the corresponding charge transfer from M⁺ to LC increases ($q_M = 0.898$ and $0.854 e$ for M = Cs and Li).

It is instructive to compare the properties of M⁺LC with those of the related H⁺LC ions. While M⁺LC(O4) corresponds to a single global minimum, in which M⁺ binds in a chelate to the lone pairs of both O4 and N5, the much smaller size of the proton leads to the interaction with either O4 or N5. Both H⁺LC

minima are very deep ($D_0 = 911$ and 931 kJ mol^{-1} for O4 and N5) and separated by a large barrier (67 kJ mol^{-1} for N5 → O4 tautomerization). Only the more stable H⁺LC(N5) isomer is observed experimentally.^{19,23} Because of the stronger bond of H⁺ to LC, the computed S_1 red shifts of both H⁺LC(N5) and H⁺LC(O4) are larger than those of M⁺LC(O4), in good agreement with available experimental data for the same $\pi\pi^*$ excitation (Fig. 4 and Table 2).

4. Concluding remarks

The vibronic spectra of M⁺LC with M = Li–Cs are recorded by VISPD spectroscopy in a cryogenic ion trap. Significantly, these vibrationally resolved electronic spectra are the first optical spectra of any metalated flavin in the gas phase and thus provide a first impression of the effects of metalation on the intrinsic electronic structure of flavins. The analysis of the rich vibronic spectra using DFT calculations coupled to multi-dimensional FC simulations provides a reliable assignment of the observed band system to the first optically bright $\pi\pi^*$ transition ($S_1 \leftarrow S_0$) of the M⁺LC(O4) global minima identified previously by IRMPD spectroscopy in a 300 K trap.²⁰ Large red shifts in the S_1 band origins and intense progressions in the intermolecular M⁺···LC bend and stretch modes provide a quantitative measure for the substantial increase in the strength of the metal–flavin interaction upon $\pi\pi^*$ excitation of M⁺LC(O4). The large S_1 red shifts of M⁺LC(O4) can be rationalized by the orbitals involved in the $\pi\pi^*$ transition and the resulting changes in the charge distribution. The large differences in the energies of the $\pi\pi^*$ transition of M⁺LC(O4) and M⁺LC(O2) demonstrate that the photochemical properties of flavins can indeed drastically be tuned by metal complexation *via* both the type and binding site of the metal ion. The current study may be extended in several directions. First, the IRMPD spectra suggest that the less stable M⁺LC(O2) local minima can also be produced by ESI (at least for M = K–Cs).²⁰ Their predicted S_1 origins are at substantially higher energies compared to those detected here for M⁺LC(O4), and we are currently searching for them (Table 2 and Fig. 4). Although they may occur in a spectral range where they may overlap with the second $\pi\pi^*$ state of M⁺LC(O4), the FC analysis will provide a clear isomer assignment. Second, effects of solvation on the optical properties of metal–flavin complexes may separately be determined by applying the same experimental and computational strategy to microsolvated clusters, in which in a controlled fashion a variable number of polar or nonpolar solvent ligands are attached to the cryogenic flavin ions. In this way, a more complete picture of the photophysical properties of flavins can be derived at the molecular level.

Conflicts of interest

There are no conflicts to declare.

Acknowledgements

This work was supported by Deutsche Forschungsgemeinschaft (DFG, DO 729/6). M. M. is grateful for a senior research

Table 4 Atomic charges (in units of e) of selected atoms of M⁺LC(O4) and LC in the S_0 and first $\pi\pi^*$ excited singlet state evaluated at the PBE0/cc-pVDZ level using natural bond orbital analysis

	q_M		q_{N5}		q_{O4}		q_{O2}	
	S_0	S_1	S_0	S_1	S_0	S_1	S_0	S_1
Li	0.898	0.854	−0.524	−0.641	−0.728	−0.746	−0.577	−0.559
Na	0.921	0.903	−0.519	−0.617	−0.704	−0.736	−0.570	−0.565
K	0.921	0.904	−0.493	−0.592	−0.704	−0.741	−0.575	−0.568
Rb	0.927	0.911	−0.485	−0.583	−0.698	−0.737	−0.577	−0.570
Cs	0.915	0.898	−0.472	−0.571	−0.699	−0.742	−0.579	−0.571
LC			−0.386	−0.477	−0.565	−0.595	−0.623	−0.615

fellowship from the Alexander von Humboldt Foundation (2017–2019). O. D. acknowledges travel support from the World Research Hub Initiative (WRHI) of Tokyo Institute of Technology (Japan). Part of the computations was performed at the Research Center of Computational Chemistry in Okazaki (Japan).

References

- 1 E. Silva and A. Edwards, *Flavins, Photochemistry, and Photobiology*, RSC Publishing, Cambridge, 2006.
- 2 K. H. Dudley, P. Hemmerich, F. Müller and A. Ehrenberg, *Helv. Chim. Acta*, 1964, **47**, 1354–1383.
- 3 P. F. Heelis, *Chem. Soc. Rev.*, 1982, **11**, 15–39.
- 4 V. Massey, *Biochem. Soc. Trans.*, 2000, **28**, 283–296.
- 5 W. Buckel and R. K. Thauer, *Chem. Rev.*, 2018, **118**, 3862–3886.
- 6 W. J. Rutter, *Acta Chem. Scand.*, 1958, **12**, 438–446.
- 7 I. F. Baarda and D. E. Metzler, *Biochim. Biophys. Acta*, 1961, **50**, 463–471.
- 8 P. Bamberg and P. Hemmerich, *Helv. Chim. Acta*, 1961, **44**, 1001–1011.
- 9 F. Müller, P. Hemmerich and A. Ehrenberg, *Eur. J. Biochem.*, 1968, **5**, 158–164.
- 10 A. W. Varnes, E. L. Wehry and R. B. Dodson, *J. Am. Chem. Soc.*, 1972, **94**, 946–950.
- 11 J. Lauterwein, P. Hemmerich and J. M. Lhoste, *Inorg. Chem.*, 1975, **14**, 2152–2161.
- 12 J. Lauterwein, P. Hemmerich and J. M. Lhoste, *Inorg. Chem.*, 1975, **14**, 2161–2168.
- 13 M. Benecky, T. Y. Yu, K. L. Watters and J. T. McFarland, *Biochim. Biophys. Acta*, 1980, **626**, 197–207.
- 14 S. Fukuzumi and T. Kojima, *J. Biol. Inorg. Chem.*, 2008, **13**, 321–333.
- 15 I. Ahmad, Z. Anwar, S. Ahmed, M. A. Sheraz and S. Khattak, *J. Photochem. Photobiol., B*, 2017, **173**, 231–239.
- 16 E. Sikorska, I. V. Khmelinskii, W. Prukala, S. L. Williams, M. Patel, D. R. Worrall, J. L. Bourdelande, J. Koput and M. Sikorski, *J. Phys. Chem. A*, 2004, **108**, 1501–1508.
- 17 A. Tyagi and A. Penzkofer, *J. Photochem. Photobiol., A*, 2010, **215**, 108–117.
- 18 A. Tyagi and A. Penzkofer, *Photochem. Photobiol.*, 2011, **87**, 524–533.
- 19 J. Langer, A. Günther, S. Seidenbecher, G. Berden, J. Oomens and O. Dopfer, *ChemPhysChem*, 2014, **15**, 2550–2562.
- 20 A. Günther, P. Nieto, G. Berden, J. Oomens and O. Dopfer, *Phys. Chem. Chem. Phys.*, 2014, **16**, 14161–14171.
- 21 P. Nieto, A. Günther, G. Berden, J. Oomens and O. Dopfer, *J. Phys. Chem. A*, 2016, **120**, 8297–8308.
- 22 A. Günther, P. Nieto, D. Müller, A. Sheldrick, D. Gerlich and O. Dopfer, *J. Mol. Spectrosc.*, 2017, **332**, 8–15.
- 23 A. Sheldrick, D. Müller, A. Günther, P. Nieto and O. Dopfer, *Phys. Chem. Chem. Phys.*, 2018, **20**, 7407–7414.
- 24 A. Vdovin, A. Slenczka and B. Dick, *Chem. Phys.*, 2013, **422**, 195–203.
- 25 T. L. Zhang, K. Papson, R. Ochran and D. P. Ridge, *J. Phys. Chem. A*, 2013, **117**, 11136–11141.
- 26 L. Guyon, T. Tabarin, B. Thuillier, R. Antoine, M. Broyer, V. Boutou, J. P. Wolf and P. Dugourd, *J. Chem. Phys.*, 2008, **128**, 075103.
- 27 M. H. Stockett, *Phys. Chem. Chem. Phys.*, 2017, **19**, 25829–25833.
- 28 L. Giacomozzi, C. Kjær, J. Langeland Knudsen, L. H. Andersen, S. Brøndsted Nielsen and M. H. Stockett, *J. Chem. Phys.*, 2018, **148**, 214309.
- 29 E. Sikorska, I. Khmelinskii, D. Worrall, J. Koput and M. Sikorski, *J. Fluoresc.*, 2004, **14**, 57–64.
- 30 S. Salzmann and C. M. Marian, *Chem. Phys. Lett.*, 2008, **463**, 400–404.
- 31 J. Hasegawa, S. Bureekaew and H. Nakatsuji, *J. Photochem. Photobiol., A*, 2007, **189**, 205–210.
- 32 M. J. Frisch, *et al.*, *GAUSSIAN09, Rev. D.01*, Gaussian, Inc., Wallingford CT, 2009.
- 33 R. L. Martin, *J. Chem. Phys.*, 2003, **118**, 4775–4777.
- 34 C. M. Western, *J. Quant. Spectrosc. Radiat. Transfer*, 2017, **186**, 221–242.
- 35 E. D. Glendening, J. K. Badenhoop, A. E. Reed, J. E. Carpenter, J. A. Bohmann, C. M. Morales, C. R. Landis and F. Weinhold, *NBO 6.0, Theoretical Chemistry*, University of Wisconsin, Madison, 2013.
- 36 R. D. Shannon, *Acta Crystallogr., Sect. A: Cryst. Phys., Diffraction, Theor. Gen. Crystallogr.*, 1976, **32**, 751–767.

5. Results and Discussion

In this section, the major results presented in chapter 4 are summarized and discussed. In particular, the effect of protonation and metalation on the photophysical properties of differently sized flavins is investigated. Importantly, these results provide precise information of the bare flavin molecule and its complexes, free from any disturbing external factors such as solvation. The discussion in this chapter extends the previously published IRMPD results by our group, which provided the preferred metalation (with alkali and coinage metals) and protonation sites of various flavins.^{110–112} The analysis of the measured high-resolution optical spectra of cryogenically-cooled flavins provides precise insight into excited-state properties such as the geometric, vibrational, and electronic structure.^{113–118}

5.1. Assignment of VISPD Spectra

In chapter 4, vibronic VISPD spectra of M^+LC and M^+LF with $M=Li-Cs$, H^+LC and H^+LF , and K^+RF are presented. All spectra are recorded employing the BerlinTrap apparatus at cryogenic temperatures ($T < 25$ K).⁸⁸ Hence, the spectra provide vibronic resolution in combination with well-resolved electronic origin transitions (0^0). All measured spectra are assigned to S_1 ($\pi\pi^*$) excitations. The origins of the respective molecules are summarized in Table 6. In the individual publications (chapter 4), the isomers were assigned and a summary is given in Table 6.

Table 6. Experimentally determined S_1 origin energies (in cm^{-1}) of M^+LF , M^+LC , H^+LF , H^+LC , and K^+RF . ^a Measured in He nanodroplets.^{54 b,c} Measured in the condensed phase.^{20,21}

M/H	LF N1	O2+	O2	O4+	LC O4+	N5	RF O2
neutral				21511 ^a		26000±1000 ^b	22500±2500 ^c
H	23202	23128				19962	
Li		23202		17645	21911		
Na		23037		18310	22786		
K		22806		18778	23315		22670
Rb			22355	18914	23465		
Cs			22323	19031	23571		

A joint approach employing VISPD spectroscopy of cryogenically cooled ions and quantum chemical TD-DFT calculations is applied to unravel the photophysical properties of protonated and metalated flavins with various complexity. First, DFT calculations are carried out for metalated ($M^+LC/M^+LF/M^+RF$, $M = Li-Cs$) and protonated (H^+LF/H^+LC) flavins to determine their structure in the S_0 state. Second, to investigate the photophysical properties, the calculations are extended to TD-DFT for excited states. It is instructive to compute excitation energies (vertical/adiabatic) to predict absorption spectra of the most probable isomers. The excited state calculations presented within this thesis are mostly applied to low-energy isomers which have been predicted previously.^{110–112} The measured VISPD spectra are compared to the quantum chemical calculations. For the sake of comparison, relevant binding energies and relative energies of M^+LC , M^+LF , and M^+RF are summarized in Table 7.

Table 7. Binding energies and relative energies (in parentheses) of M⁺RF, M⁺LF, and M⁺LC with M = Li-Cs computed with PBE0/cc-pVDZ. All values are given in kJ mol⁻¹.

M	Isomer	M ⁺ RF	M ⁺ LF	M ⁺ LC
Li	O2	411.4 (0.0)	279.7 (20.4)	227.2 (73.3)
	O2+	-	289.5 (10.6)	-
	O4+	298.3 (113.1)	300.1 (0.0)	296.0 (0.0)
Na	O2	292.7 (0.0)	209.5 (10.2)	161.1 (56.4)
	O2+	-	214.2 (5.5)	-
	O4+	217.0 (75.7)	219.7 (0.0)	217.6 (0.0)
K	O2	254.3 (0.0)	175.9 (0.1)	131.8 (41.8)
	O2+	-	175.5 (0.5)	-
	O4+	173.2 (81.1)	176.0 (0.0)	173.6 (0.0)
Rb	O2	220.7 (0.0)	158.9 (0.0)	116.8 (38.6)
	O4+	154.7 (66.0)	157.9 (1.0)	155.4 (0.0)
Cs	O2	209.3 (0.0)	146.8 (0.0)	106.3 (34.0)
	O4+	141.8 (67.5)	143.9 (2.9)	140.3 (0.0)

Flavins offer a variety of nucleophilic binding sites. The metal ion and the proton can benefit from the lone pairs of the nitrogen (N1, N5) and oxygen (O2, O4) atoms. In contrast, the interaction of M⁺/H⁺ with the aromatic π electron system is weaker and is thus not considered here anymore.^{110–112} For RF, additional attractive lone pairs from the OH groups of the ribityl chain are available.

The computed binding energies depend on the functional group of the flavins and on the binding site and size of M⁺/H⁺. The M⁺...FI (FI) interaction is mostly electrostatic in nature and thus increases with decreasing ionic radius (*e.g.*, from 300 to 144 kJ mol⁻¹ for the O4+ isomer of M⁺LF with M = Li-Cs, respectively).

For the O4+ isomers, the binding energy is hardly affected by the different functional groups (*e.g.*, 298, 300, and 296 kJ mol⁻¹ for Li⁺RF, Li⁺LF, and Li⁺LC, respectively) because the relevant functional groups are far away from the O4-M-N5 chelate. For the O2 binding site, the binding energy for M⁺RF is substantially higher than for M⁺LF and M⁺LC because of the possible multiple interactions of the metal cation with the OH groups of the ribityl chain. For M⁺LC, the O2+ binding site is not feasible because of steric hindrance with the hydrogen atom at N1. For M⁺LF, the O2+ binding site is not feasible for the heavier atoms (Rb and Cs) because of the repulsive interaction of the bulky metal with the nearby CH₃ group at N10. For the M⁺LF(O2+) isomers, the smaller metals (Li, Na, and K) can bind to both the lone pairs of N1 and O2 to form a chelate of the form N1-M-O2. Both M⁺LC and M⁺LF form isomers in which the metal binds to O2 to form nearly linear C2-O2-M bonds. The proton is too small to form a chelate of the form O-H-N. Hence, distinct protomers can be produced and trapped in their own deep potential wells with large tautomerization barriers V_b (*e.g.*, $V_b = 156$ kJ mol⁻¹ for O2+ \rightarrow N1, $V_b = 67$ kJ mol⁻¹ for N5 \rightarrow O4).^{114,118} The proton binds covalently to the flavins and the proton affinities (PA) are summarized in Table 8.^{114,118}

Table 8. Proton affinities (PA) and relative energies (E_0) for the S_0 state of various protomers of H⁺LC and H⁺LF computed at the PBE0/cc-pVDZ level. All values are given in kJ mol⁻¹.

H ⁺ LC	PA (E_0)	H ⁺ LF	PA (E_0)
N5	930.6 (0)	O2+	971.7 (0.0)
O4+	911.3 (19.3)	N1	956.7 (15.0)
O2	899.1 (69.5)	O2-	945.6 (26.1)
N10	861.1 (31.5)	O4+	936.1 (35.6)
		N5	919.8 (51.9)

5.2. Nature and Order of Electronic States

The excited state manifolds of flavins comprise several $n\pi^*$ and $\pi\pi^*$ states. Transitions of $n\pi^*$ character arise from nonbonding lone pair electrons at the N heteroatoms and the carbonyl O atoms into π^* orbitals. In addition, $\pi\pi^*$ excitations arise from the aromatic π electron system. In particular, $\pi\pi^*$ transitions are optically bright, whereas $n\pi^*$ transitions are optically dark. The oscillator strength (f) is an indicator of the probability for an electronic excitation. In general, dark $n\pi^*$ states have an oscillator strength close to zero and are not detected in our experiment.

It is instructive to evaluate the nature and the order of low-lying singlet excited states. Herein, these are analysed depending on the size and site of metalation with alkali cations, and on the type of flavin (*e.g.*, LC, LF, and RF), and additionally for protonated H⁺LF/LC. For the sake of completeness, the same calculations are carried out for the neutral flavins to reveal the effect of metalation/protonation on the electronic structure of neutral flavins.

The first excited singlet state S_1 of all identified M⁺Fl/H⁺Fl isomers corresponds to an optically bright $\pi\pi^*$ excitation. Clearly, metalation and protonation can alter the order of electronic states with respect to the neutral flavin. For example, the S_1 state of LC is of $n\pi^*$ character, but protonation at N5 changes the order of electronic states and the lowest singlet excitation becomes a $\pi\pi^*$ transition. Furthermore, for H⁺LF the S_1 and S_3 states are of $\pi\pi^*$ character for both, the O2+ and N1 tautomers, whereas for LF the S_3 state is optically dark. A similar behaviour is observed for the M⁺LF(O2(+)) isomers. For example, the S_3 states of Li⁺LF(O2+) and Na⁺LF(O2+) have $\pi\pi^*$ character. As described, the S_3 state of LF is attributed to an optically dark $n\pi^*$ state.

The optimization of excited state geometries is often demanding. However, it is required to obtain adiabatic excitation energies (E_a). In this thesis, all reported E_a values are corrected for harmonic zero - point vibrational energies of ground and excited state. In the following they are compared to experimental data.

5.3. Comparison S_1 Adiabatic Excitation Energies

In this section, the S_1 adiabatic excitation energies determined for various flavins are compared with each other and to their experimentally determined electronic origin transition energies. This comparison shows not only the effect of metalation and protonation but also supports the previously made isomer assignments that were based on quantum chemical calculations. The computed adiabatic S_1 origins and the extracted experimental S_1 origins are shown for H^+LC , H^+LF , M^+LC , and M^+LF with $M=Li-Cs$ as a function of the inverse ionic radius of the metal ion and the proton in Figure 13 to demonstrate the dependence of the transition energies on the size of M^+/H^+ . Also included are the predicted adiabatic excitation energies of the first bright state of LF and LC as well as the experimentally determined origin transition of the neutral flavins.^{21,54}

Unfortunately, studies on bare gas-phase neutral flavins are scarce due to the difficulty to transfer them into the gas phase with sufficient abundance. To the best of our knowledge, no optical spectra of bare gas-phase neutral LC and RF are reported in the literature to date. For LF, Vdovin *et al.* presented high-resolution fluorescence and dispersed emission spectra of LF doped into superfluid He nanodroplets ($LF@He_N$).⁵⁴ The authors estimate the effect of the He environment on the transition energy to be less than 1 % ($<250\text{ cm}^{-1}$). Hence, the S_1 origin transition of $LF@He_N$ at 21511 cm^{-1} can be safely used as the electronic origin transition of bare neutral LF. The absorption properties of LC have been extensively studied in the condensed phase but not in the gas phase.²¹ As expected, the absorption spectra recorded in the condensed phase are rather broad and somewhat sensitive to the surrounding solvent conditions. However, the first absorption band is hardly affected by the type of solvent and is experimentally found at around 26000 cm^{-1} . Hence, this value is used as the reference point of neutral LC. No gas-phase spectrum of bare RF has been reported yet. In the condensed phase, the maximum of the first absorption band is observed at around 22500 cm^{-1} (RF in methanol) and this value is used as the reference value for neutral RF.²¹ The shift of the measured S_1 band origins with respect to those of neutral flavins is given as ΔS_1 . Of course, the accuracy of the observed ΔS_1 shifts upon metalation and protonation is highest in the case of LF, because the S_1 origin transition of $LF@He_N$ reported by Vdovin *et al.* is closest to the bare gas phase molecule compared to those from the condensed phase studies for LC and RF.

The experimentally extracted S_1 origins which are assigned to the $M^+LF(O4+)$ isomers are significantly red - shifted with respect to the S_1 origin transition of $LF@He_N$. In more detail, the ΔS_1 shifts upon metal complexation with M^+ amount up to 18.0 % for $Li^+LF(O4+)$. In contrast, a smaller ΔS_1 blue shift is observed for the $M^+LF(O2(+))$ isomers. The largest ΔS_1 shift for the $O2/O2+$ binding site is observed for $Li^+LF(O2+)$ and amounts to only 8.0 %. For LC, the observed ΔS_1 shift is of the same order of magnitude (*e.g.*, 20.2 % for $Li^+LC(O4+)$ and 9.3 % for $Cs^+LC(O4+)$). For K^+RF the ΔS_1 shift is less than 1 %.

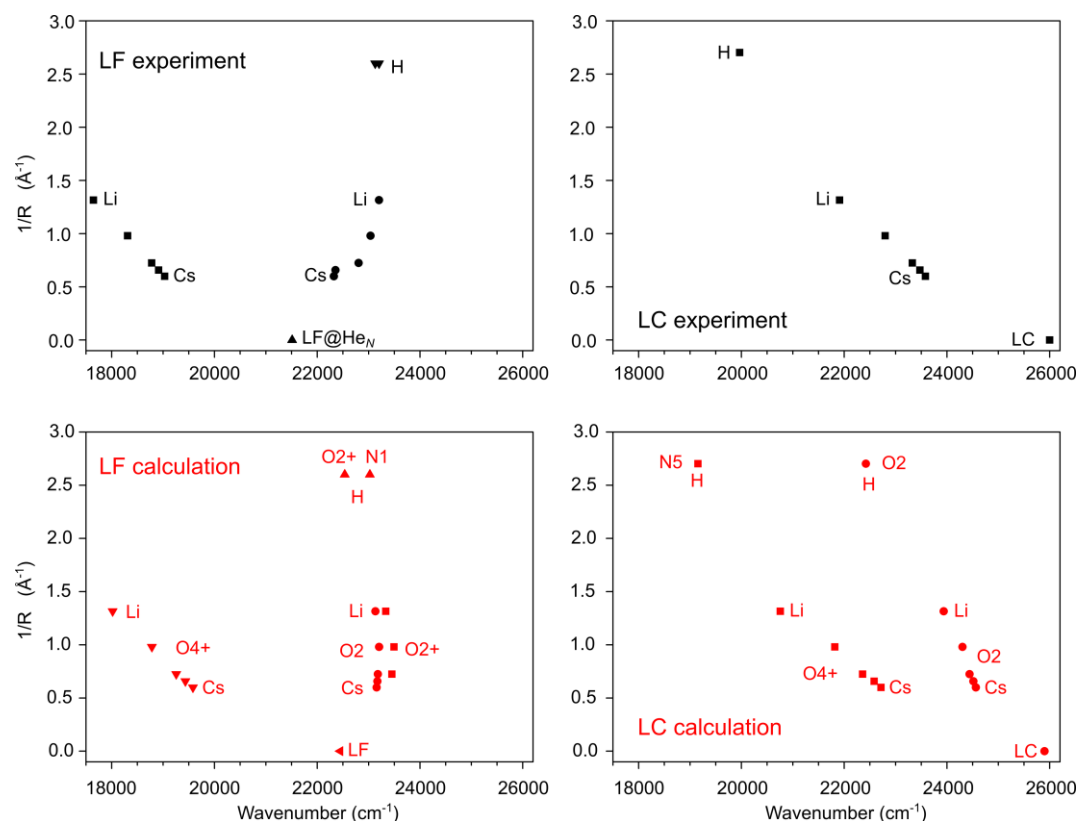


Figure 13. Comparison of computed adiabatic S1 energies (PBE0/cc-pVDZ) to experimental band origins of M⁺LF, M⁺LC, H⁺LF, and H⁺LC as a function of the inverse ionic radius. The experimental values for neutral LF@He_N and LC (from the condensed phases) are taken from Ref. ⁵⁴ and ²¹, respectively. The radii of the proton and the metal ion are summarized in Table 9.

Table 9. Ionic radius of the alkali metals and the proton. Here, the radius for H⁺ is defined as half of the distance of H₂. Values are given in pm.¹³⁸

	R
H	37
Li	76
Na	102
K	138
Rb	152
Cs	167

As a first step, adiabatic excitation energies of M⁺LF/LC(O2/O2+/O4+) are compared with each other. It must be kept in mind that the O2+ isomer of M⁺LF with M=Rb and Cs is not stable due to steric effects with the CH₃ group at N10. In addition, no stable O2+ isomer is predicted for M⁺LC with M=Li - Cs for the same reason because for LC an H atom is at N1 instead of a substituent at N10, and the O2+ binding site is not feasible for M⁺LC.

The magnitude and direction of the ΔS₁ shifts can be rationalized by the orbitals contributing to the electronic excitation and the charge reorganization. The natural transition orbital approach allows obtaining a qualitative picture of the electronic excitation.¹³⁶ The computed orbitals fully support the

experimental data and are in line with computed quantities. In detail, the orbitals of interest for LC, LF, and RF are very similar and basically delocalized over the complete aromatic ring system (Figure 14). Importantly, the orbitals presented within this thesis for LF and RF computed with PBE0/cc-pVDZ are in good agreement with the orbitals reported in the literature.^{64,73} For example, the HOMO and LUMO orbitals for RF have been calculated at different levels of theory (*e.g.*, B3LYP and PBE0 with 6-311+G(2d,2p) basis set).⁷³ As a general result, only a minor contribution is observed on the ribityl chain for the HOMO orbitals and essentially no contribution is observed on the ribityl chain for the LUMO orbital, in full agreement with the orbitals presented within this thesis.

However, no comparable orbitals for metalated flavins have been reported in the literature yet. The orbitals of the ionic complexes presented in this thesis are very similar to those of the neutral flavins. These orbitals are also highly delocalized over the complete chromophore. As for the neutral flavins, there is only modest contribution of the orbital wavefunction on the CH₃ (LF) and on the ribityl group (RF). The partial charge of LF in the S₀ and S₁ state using the natural bond orbital analysis is shown in Figure 15.¹¹⁶

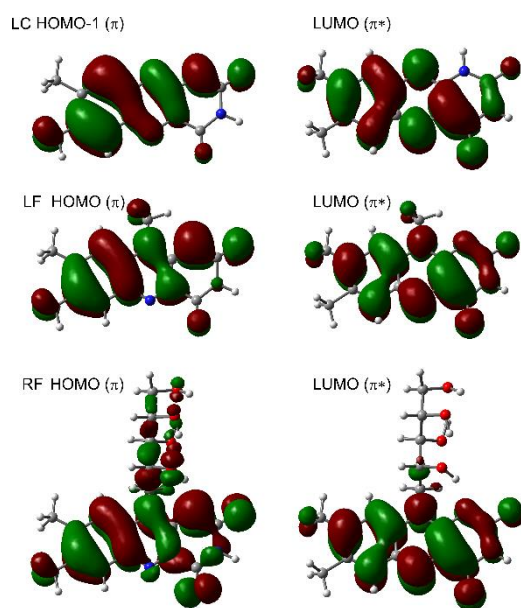


Figure 14. Natural transition orbitals of LC, LF, and RF calculated at the PBE0/cc-pVDZ level.

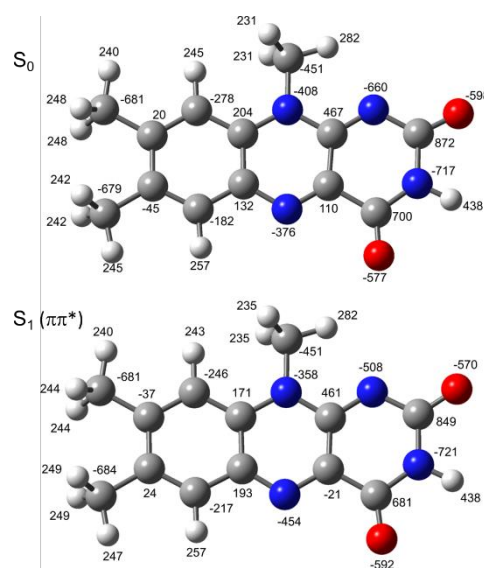


Figure 15. Atomic charge distribution of LF (in 10⁻³ e) in the S₀ and S₁ states using the natural bond orbital analysis.

M⁺LF and M⁺LC

The predicted S₁ energies of the O2/O2⁺ isomers of M⁺LC and M⁺LF are generally higher in energy than those of the O4⁺ isomers. The predicted S₁ energies of the M⁺LC(O4⁺) and M⁺LC(O2) are blue - shifted with respect to those of M⁺LF(O4⁺) and M⁺LF(O2⁺)), respectively, because the orbitals are more delocalized for LF than for LC with some minor contribution on the methyl group at N10. This

reduces the energy of the orbitals and results in a lower $\pi\pi^*$ transition. The predicted adiabatic excitation energies of the $M^+LC(O4+)$ and $M^+LF(O4+)$ isomers exhibit essentially the same dependence on the metal ion size, because the orbitals contributing to the electronic excitation are essentially the same, and the relevant N5-M-O4 chelate is far away from the CH_3/H groups. In particular, for both, $M^+LC(O4+)$ and $M^+LF(O4+)$, the excitation energy increases in the series from Li to Cs, because of the stronger bond for the smaller metals to the flavin.

Despite being less stable than the $M^+LC(O4+)$ isomers, the S_1 energies of the $M^+LC(O2)$ are also included in Figure 13 for comparison ($E_0 = 34.0-73.3$ kJ mol⁻¹ for Cs to Li). The computed adiabatic S_1 energies of $M^+LC(O2)$ exhibit a less pronounced dependence on the size of the metal ion than the $O4+$ isomers, because of the larger charge transfer at $O4/N5$ compared to $O2$.¹¹⁷ Interestingly, the S_1 energies of the $M^+LF(O2(+))$ isomers are clearly less affected by the different alkali ions with respect to the $O4+$ isomers and range only within 72 cm⁻¹ ($O2$) and 160 cm⁻¹ ($O2+$). This observation can be explained by the molecular orbital wavefunction, which shows large changes at N5 and O4, but only minor changes at N1 and O2 for all investigated flavins.

H⁺LF and H⁺LC

The excitation energies of H^+LF and H^+LC are included in Figure 13 as well to illustrate the effect of different protonation sites on the excitation energies. The flavin chromophore provides several protonation sites. As expected from the small proton size, distinct protomers (*e.g.*, $O2+$ and N1 for H^+LF) can be formed, but no chelate. The predicted S_1 energies of the two lowest-energy protomers of H^+LF ($O2+$ and N1, $E_0 = 15.0$ kJ mol⁻¹) differ by only 490 cm⁻¹. Due to the same binding site, the predicted S_1 energies are close to the energies of the $O2(+)$ isomers of M^+LF . For example, they are slightly red-shifted by 800 and 310 cm⁻¹ with respect to the S_1 energy of $Li^+LF(O2+)$ for $H^+LF(O2+)$ and $H^+LF(N1)$, respectively. In contrast, the predicted S_1 energies of $H^+LF(N1/O2+)$ are significantly blue - shifted with respect to those of the $M^+LF(O4+)$ isomers.

Protonation of LC at N5 has a larger impact on the S_1 energy than metalation at $O4+$ for LC, because of the much stronger bond of the proton to LC than M^+ to LC (Table 7 and Table 8). For example, the S_1 energy of $H^+LC(N5)$ is computed at 19153 cm⁻¹, and hence red-shifted by 1604 cm⁻¹ compared to the S_1 energy of $Li^+LC(O4+)$. It can be concluded that different protonation sites result in strongly differing absorption shifts when compared to the neutral molecule. On the one hand, protonation at $O2+$ and N1 for LF results in a marginal shift with respect to neutral LF. On the other hand, protonation at N5 for LC results in a shift as big as 6746 cm⁻¹ compared to neutral LC. The redshifts and blueshifts are confirmed by the molecular orbital wavefunction in Figure 14, which shows only minor changes at N1/O2 for LF and significant changes at N5 for LC. Finally, all computed S_1 energies of the cationic complexes converge smoothly to the first bright $\pi\pi^*$ state of neutral LC(S_2) and LF(S_1).

K⁺RF

Finally, the S_1 energies of K⁺RF are described for comparison. The number of low-energy isomers is larger than that of M⁺LC/M⁺LF because many different orientations of the flexible ribityl chain at N10 are possible. Importantly, we have not applied a systematic global optimization approach and may thus not have found the true global minimum structure both, for RF and M⁺RF with M=Li-Cs. The calculated S_1 energies of the four most stable O2 isomers ($E_0 = 11.1 \text{ kJ mol}^{-1}$) of K⁺RF range within only 995 cm^{-1} (Figure 16). This means that the orientation of the ribityl chain hardly affects the predicted S_1 energy of the O2 isomers, because only a minor contribution of the orbital wavefunction is observed on the ribityl chain (Figure 14). In addition, these values are close to the predicted S_1 energies of the K⁺LF(O2(+)) isomers. Consequently, methyl (LF) \rightarrow ribityl (RF) substitution hardly affects the predicted S_1 energies for the O2(+) isomers, because basically the same orbitals are involved in the electronic excitation. In contrast, the predicted S_1 energy of one reported O4+ isomer of K⁺RF is significantly red - shifted with respect to the O2 isomers. Finally, the predicted S_1 energies for K⁺RF follow the same trend (pronounced red shift for the O4+ isomers, smaller blue shift for the N1/O2(+) isomers) as for M⁺LC, M⁺LF, H⁺LC, and H⁺LF. As for M⁺LF and M⁺LC, this observation can be rationalized by the large changes of the orbitals at O4/N5 and the minor changes at N1/O2.

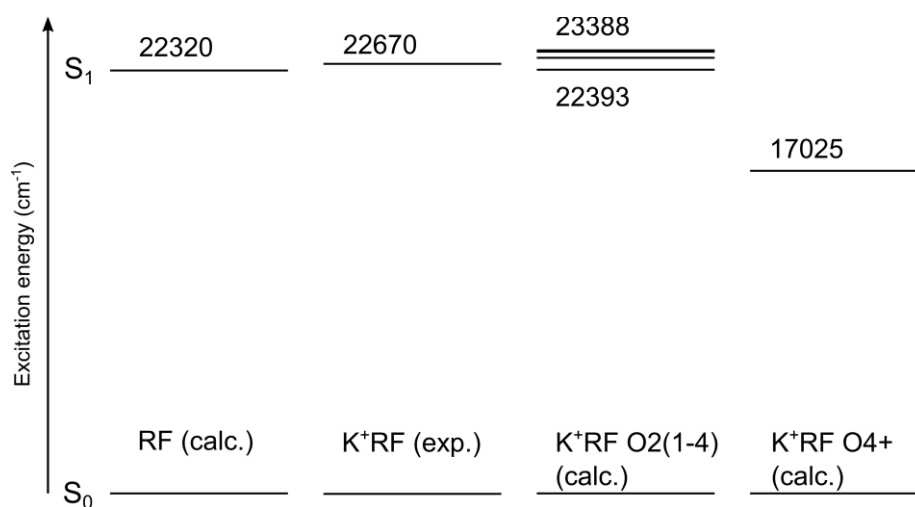


Figure 16. Comparison of computed adiabatic S_1 origins (PBE0/cc-pVDZ) of RF, K⁺RF(O2), and K⁺RF(O4+) to the experimental band origin of K⁺RF. The adiabatic S_1 origins for the four most stable O2 isomers K⁺RF(O2(1-4)) range between 22393 and 23388 cm^{-1} , which are indicated by four levels. The predicted S_1 origin of the O4+ isomer is significantly red - shifted with respect to all other quantities shown in this figure.

5.4. Comparison of Experimental S_1 Energies to Computed S_1 Energies

A comparison of the predicted S_1 energies for the O2/O2+/O4+ isomers and the experimentally extracted (and assigned) transition energies shows excellent agreement (to within 0.1 eV) both for M⁺LC and M⁺LF (Figure 13). Both, the experimental and computed curves converge smoothly to the values of the neutral flavin (*e.g.*, $R \rightarrow \infty$, no metal). The minor deviations between experimental and

computed data are a strong indicator for the reliability of the excited state calculations at the PBE0/cc - pVDZ computational level for this type of flavin ions. Regarding the protonated flavins, the predicted S_1 origin transitions of $H^+LF(N1/O2^+)$ and $H^+LC(N5)$ also show good agreement to the experimentally extracted origin transitions with a maximum deviation of only 809 cm^{-1} for H^+LC . The experimental S_1 origin of K^+RF matches the predicted origin transitions of the four most stable $O2(1 - 4)$ isomers (maximum deviation 718 cm^{-1} , Figure 16). In contrast to that, for K^+RF the calculated S_1 origin transition of the less stable $O4^+$ is significantly red - shifted to the measured spectrum. Hence, this isomer can be excluded to be responsible for the measured VISPD spectrum, as such big discrepancies have not been observed for related flavin ions.^{113–118} The shift of the measured S_1 band origins with respect to those of neutral flavins (ΔS_1) is indicative of a change in the $M^+/H^+...Fl$ interaction strength upon electronic excitation and will be discussed in the following section.

5.5. Introduction into Flavin Photophysics

Aided by electronic spectroscopy of cryogenically cooled ions, low-energy isomers can be investigated in an isomer-selective manner because the photophysical properties of flavins are highly sensitive to the site of protonation/metalation, as can be seen in Figure 13. For example, different metalation/protonation sites result in very different absorption ranges. Other sophisticated experimental approaches, such as double resonance techniques (IR-IR, IR-VIS, VIS-VIS), are also suitable to differentiate low-energy isomers.^{56,57,61} Double resonance experiments may be applied in future research at the BerlinTrap apparatus.

In particular, the ΔS_1 shift is a direct measure of the change of the $M^+...Fl$ interaction strength upon electronic excitation. This relation is shown schematically in Figure 17 for M^+LF . Here, the

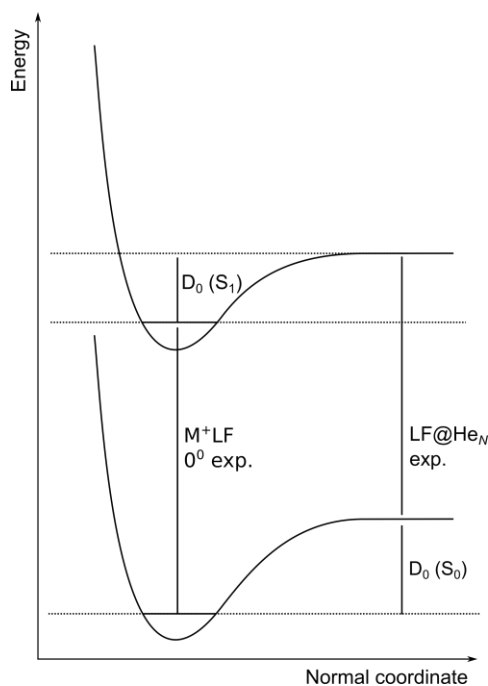


Figure 17. Schematic representation of the ground and first excited state potential energy surface. The change in interaction strength upon electronic excitation is determined as $\Delta S_1 = -\Delta D_0$. The S_1 origin of neutral LF is taken from Ref. ⁵⁴. The S_1 origin transitions of M^+LF with $M = Li-Cs$ are obtained in this thesis and the D_0 values for the S_0 state are computed at the PBE0/cc-pVDZ level of theory.

change in interaction strength can be described as $\Delta S_1 = -\Delta D_0$, where ΔD_0 indicates the change in binding energy for the S_0 and S_1 state. Importantly, the change in interaction strength is based on the computed binding energy (D_0) for the electronic ground state S_0 . For example, the interaction strength for $M^+LF(O4^+)$ increases significantly up to 20 % for Cs^+LF in the S_1 state with respect to the S_0 state.

Following the same approach, the $M^+...F$ interaction strength for $M^+LF(O2(+))$ in the S_1 states is reduced, but to a smaller extent. For example, for $Na^+LF(O2+)$ it is reduced in the S_1 state by 8.5 %. For $M^+LC(O4+)$, a similar trend as for $M^+LF(O4+)$ is observed. The changes on the interaction strength for M^+LC and M^+LF upon electronic excitation are summarized in Table 10 and shown in Figure 18. The change in interaction strength can be rationalized by the charge reorganization upon $\pi\pi^*$ excitation at the N1/O2 and N5/O4 atoms. For example, the negative charge at the O2 atom is slightly reduced and the negative charge at the N5 atom is substantially increased. This behaviour increases the interaction in the S_1 state which in turn results in the observed ΔS_1 shifts. The increase in binding energy is largest for the O4+ isomers of Li^+LF and Li^+LC , because the charge transfer from Li^+ to the flavin is most pronounced for these complexes.^{116,117} However, the relative change in binding energy remains nearly the same from Li to Cs (*e.g.*, from 15.4 to 20.6 % for the O4+ isomer of LF from Li-Cs, Table 10), because of the decreasing binding energy with increasing metal size. The small ΔS_1 blue shift observed for K^+RF is indicative of a slightly reduced $K^+...RF$ interaction in the S_1 state. Clearly, the optical response for the different binding sites originates from a change in the interaction strength and not from a change of the HOMO/LUMO orbitals involved in the electronic excitation, as they are essentially the same for all investigated complexes with no contribution of the orbital wavefunction on M^+/H^+ .

Interestingly, both investigated protonated complexes show a very different behaviour. For example, only a minor ΔS_1 blue shift is observed for $H^+LF(N1/O2+)$, whereas for H^+LC a ΔS_1 red shift as much as 6000 cm^{-1} is observed. As a result, the direction and magnitude of ΔS_1 depends significantly on the protonation.

The same approach is applied to protonated H^+LF and H^+LC . On

the one hand, for H^+LF , the small ΔS_1 blue shifts for the O2+ and N1 tautomers are caused by a reduced proton affinity upon S_1 excitation. On the other hand, the pronounced ΔS_1 red shift for H^+LC is associated to an increase in proton affinity upon electronic excitation. These results are similar to those of the metalated flavins. As a general remark, large ΔS_1 shifts, as observed for the $M^+LF(O4+)$ isomers, may also be determinable at elevated temperatures. However, the ΔS_1 shifts of the O2(+) isomers of M^+LF are significantly smaller ($\Delta S_1 = 812\text{-}1691\text{ cm}^{-1}$ for Cs-Li, respectively) and can only be observed when the molecules are cold.

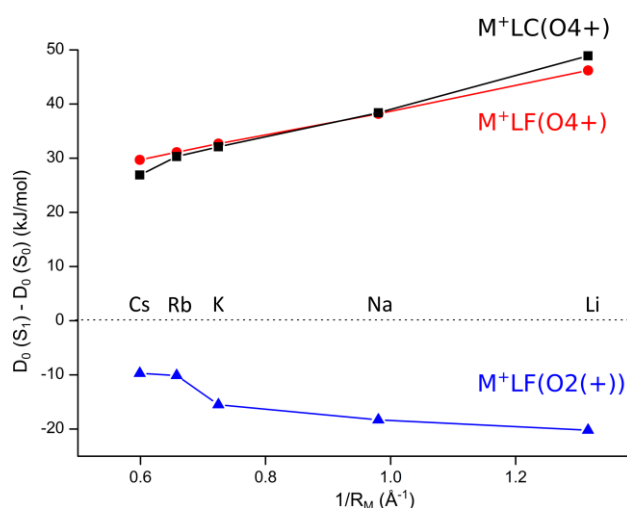


Figure 18. Change in binding energy from the S_0 to the S_1 state. Values are summarized in Table 10.

To conclude, the interaction strength in the excited state can be probed to high precision by evaluating the ΔS_1 shifts. The VISPD spectra exhibit small ΔS_1 blue shifts for the N1/O2/O2+ binding site and pronounced ΔS_1 red shifts for the N5/O4+ binding site. Furthermore, the direction of the ΔS_1 shift is independent of the functional group of the flavin because the shift originates from a change in the interaction strength and the orbitals involved in the electronic excitation are essentially the same for all flavins (Figure 14). Several quantum chemical calculations support this statement, which are analysed in more detail in the following sections.

Table 10. Change in binding energy in the S_1 state with respect to the electronic ground state S_0 (ΔD_0). For M^+LF , the experimental S_1 transition of $LF@He_N$ and the computed ground state binding energies are used. For M^+LC the absorption maximum of LC in solution (26000 cm^{-1}) and the computed ground state binding energies are used. Values are given in kJ mol^{-1} and % (in parentheses). Positive values indicate an increase in binding energy, whereas negative values indicate a decrease in binding energy in the S_1 state.

M	Isomer	M^+LF	M^+LC
Li	O2+	-20.2 (-7.0)	
	O4+	46.2 (15.4)	48.9 (16.5)
Na	O2+	-18.3 (-8.5)	
	O4+	38.2 (17.4)	38.4 (17.7)
K	O2+	-15.5 (-8.8)	
	O4+	32.7 (18.6)	32.1 (18.5)
Rb	O2	-10.1 (-6.4)	
	O4+	31.1 (19.7)	30.3 (19.5)
Cs	O2	-9.7 (-6.6)	
	O4+	29.7 (20.6)	26.9 (19.2)

5.6. Analysis of VISPD Spectra

To investigate the vibrational structure of the measured VISPD spectra, the harmonic normal modes and frequencies of the ground and excited states are computed. For example, the informative intermolecular bend and stretch modes (β and σ) and the first in-plane mode of the flavin chromophore (denoted m1) are shown in Figure 19. As expected from the change in $M^+...F$ interaction strength upon $\pi\pi^*$ excitation, the computed values for β and σ differ for the S_0 and S_1 state (Table 11). For a pseudodiatomic model, a higher binding energy results in a larger force constant k , which in turn results in higher frequencies ($\omega = \sqrt{k/\mu}$), with the reduced mass μ . On the one hand, the β and σ frequencies are systematically higher in the S_1 state for the O4+ isomers both, for M^+LC and M^+LF . On the other hand, the β and σ modes for the $M^+LF(O2(+))$ isomers differ to a smaller extent in the two electronic states. To illustrate this fact, the change in the σ mode ($\sigma(S_1)-\sigma(S_0)$) is shown in Figure 20 for M^+LC and M^+LF . The modes related to the excess proton (σ_{OH} and β_{OH}) of the protonated flavins are not within the measured spectral range because of their high PA and small reduced mass. Hence, these modes do not play a role in the further discussion. For $K^+RF(O2)$, the intermolecular β and σ modes couple to the ribityl chain due to the strong $K^+...RF$ interaction. Therefore, these modes are not

suitable for a similar qualitative statement as for M^+LC and M^+LF . The individual modes are described in detail in the publications.^{113–118}

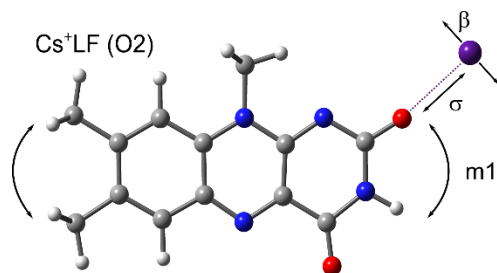


Figure 19. Intermolecular (β and σ) bend and stretch modes and first in-plane intramolecular (m1) mode of the flavin chromophore for $Cs^+LF(O2)$.

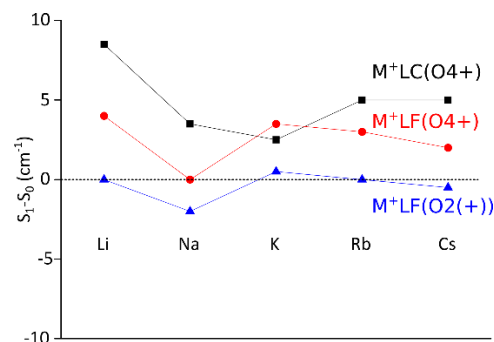


Figure 20. Difference of computed frequencies of the σ mode between the S_1 and S_0 state. For the $O2(+)$ isomers, the values for the S_0 and S_1 state do not differ much. For the $O4+$ isomer, the values are systematically larger in the S_1 state compared to the S_0 state.

Table 11. Computed intramolecular β and σ modes of M^+LC and M^+LF ($M=Li-Cs$) of the identified $O2(+)/O4+$ isomers for the S_0 and S_1 state computed at the PBE0/cc-pVDZ level compared to experimental values. Values are given in cm^{-1} .

	Isomer	Li			Na			K			Rb			Cs		
		S_0	S_1	exp	S_0	S_1	exp	S_0	S_1	exp	S_0	S_1	exp	S_0	S_1	exp
β	LC(O4+)	354	373	350	123	132	128	79	86	83	55	60	57	42	45	45
	LF(O4+)	320	375	368	121	134	128	71	86	82	48	60	57	36	45	45
	LF(O2(+))	235	236		85	93		43	26		18	20	21	16	18	16
σ	LC(O4+)	598	615	595	233	240	232	156	161	155	122	132	125	104	114	108
	LF(O4+)	618	626	610	240	240	234	155	162	157	124	130	124	107	111	108
	LF(O2(+))	585	585		264	260		215	216		127	127	118	104	103	95

The vibrational structure of the $S_1 \leftarrow S_0$ transition in the measured VISPD spectra is further analysed with the help of multidimensional Franck-Condon (FC) simulations which are carried out for $T=0$ K. Hence, the computed spectra do not contain any hot band contribution from vibrationally excited states of the electronic ground state. Typically, both the measured VISPD spectra and the FC simulations are shifted to match their 0^0 transitions for better comparison and are plotted as a function of S_1 internal energy. In addition to the good agreement between experimental and predicted S_1 energies (to within 0.1 eV), the comparison of measured VISPD spectra and computed FC spectra further supports the isomer assignment.

All measured VISPD spectra of protonated and metalated flavins presented in this thesis exhibit strong vibronic activity above the 0^0 origin transition, which is indicative of substantial geometry changes upon electronic excitation. The computed geometries for the ground and excited state and

the associated geometry changes upon electronic excitation are in line with the observed VISPD spectra and will be outlined in the following section.

To simulate vibronic spectra, the determination of the symmetry of the initial and final electronic state is highly beneficial because the application of selection rules reduces computational resources. For the neutral flavins, both LC and LF have C_s symmetry in the ground and the first $\pi\pi^*$ state (S_2 and S_1 for LC and LF, respectively). In contrast, RF has a reduced C_1 symmetry in the $S_{0,1}$ states due to the ribityl chain at N10. However, the tricyclic ring of the flavin chromophore is also slightly nonplanar. In this thesis, the first computed vibronic spectra of metalated flavins are reported. The symmetry of the identified isomers of the protonated and metalated flavins for the S_0 and S_1 state is summarized in Table 12. The ionic complexes have either C_s or C_1 symmetry depending on the metal/proton binding site, the functional group, and the size of M^+/H^+ . The vibrational structure is analysed in more detail to extract information about geometric, vibrational, and electronic structure of the excited state.

Both the O4+ and the O2 isomers of M^+LF and M^+LC have C_s symmetry in the S_0 and S_1 state. Furthermore, the $H^+LF(O2^+)$ and $H^+LC(N5)$ protomers also show C_s symmetry for both electronic states. As expected from the C_s symmetry in both states, the simulated spectra of these isomers are dominated by progressions and combination bands of in-plane modes with a' symmetry, which include the intermolecular bending and stretching modes β and σ as well as the intramolecular in-plane modes of the flavin skeleton (denoted m_1, m_2, \dots). The computed FC simulations do not show significant FC activity for modes with a'' symmetry (out-of-plane) with even quanta. The in-plane σ_{OH} and β_{OH} modes of the protonated flavins associated with the excess proton are not within the investigated spectral range and are not considered in the discussion. As an example, the intermolecular β and σ modes as well as the first FC active in-plane intramolecular flavin mode, m_1 , are shown in Figure 19 for $Cs^+LF(O2)$.

The symmetry depends somewhat on the binding motif and on the size of the ligand (Figure 21). In detail, protonation and complexation with smaller alkali metals (Li, Na) can result in a reduction of symmetry. In the case of $Li^+LF(O2^+)$, for example, geometry optimizations predict that the complex has C_s symmetry for the S_0 , and C_1 symmetry for the S_1 state. A similar observation is made for $Na^+LF(O2^+)$. However, both the S_0 and S_1 state have C_1 symmetry. The N1 protomer of LF also shows C_1 symmetry in both electronic states. Interestingly, with increasing metal size ($Na \rightarrow K$), the O2+ isomer of K^+LF again has C_s symmetry in both electronic states.

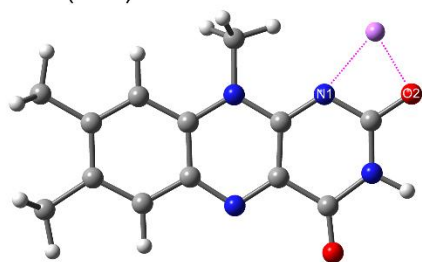
Clearly, for all optimized geometries with C_1 symmetry, the molecule is bent along the N5-N10 axis. This butterfly-type deformation is more pronounced in the excited state geometry. For example, deformation of $H^+LF(N1)$ results in a bending angle of 177° and 173° for the S_0 and S_1 state, respectively. In addition to the bending of the flavin chromophore, the CH_3 group at N10 rotates out of the plane as well. This can be rationalized by steric effects with the small alkali cation and the proton with the nearby methyl group at N10. The origin of the butterfly-type deformation remains

unanswered here. Maybe, the strong charge transfer to N5 upon electronic excitation causes strong electron repulsion which in turn results in the bending along N5-N10. Of course, the reduction in symmetry relaxes the selection rules for vibronic transitions and the number of FC-allowed transitions increases significantly as the a'' modes become FC-allowed and active.

Table 12. Symmetry of H⁺LC, H⁺LF, M⁺LC, M⁺LF, and M⁺RF for the S₀ and S₁ state computed at the PBE0/cc-pVDZ level. The O4+ isomers of M⁺LC/M⁺LF have C_s symmetry in both states. For the N1/O2+ binding site, the symmetry depends on the size of the ligand.

M/H	LF N1		O2+		O2		O4+		LC O4+	N5	RF O2
	S ₀	S ₁	S ₀	S ₁	S _{0,1}	S _{0,1}	S _{0,1}	S _{0,1}	S _{0,1}	S _{0,1}	S _{0,1}
H	C ₁	C ₁	C _s	C _s	C _s	C _s	C _s	C _s	C _s	C _s	C ₁
Li			C _s	C ₁	C _s	C _s	C _s	C _s			C ₁
Na			C ₁	C ₁	C _s	C _s	C _s	C _s			C ₁
K			C _s	C _s	C _s	C _s	C _s	C _s			C ₁
Rb					C _s	C _s	C _s	C _s			C ₁
Cs					C _s	C _s	C _s	C _s			C ₁

Li⁺LF (O2+)



Cs⁺LF (O2)

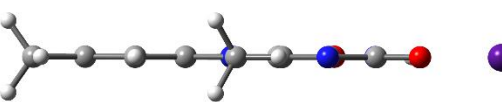
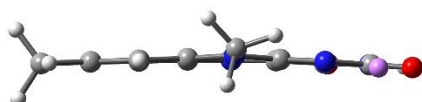
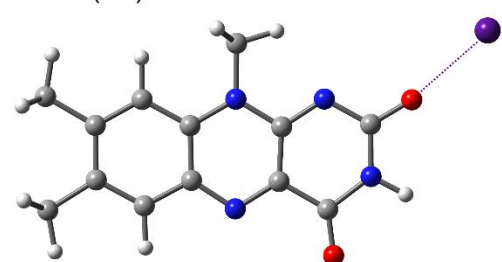


Figure 21. Side and front view of Li⁺LF(O2+) and Cs⁺LF(O2). Shown are optimized S₁ geometries computed at the PBE0/cc-pVDZ level. Clearly, Li⁺LF(O2+) has C₁ symmetry, and Cs⁺LF(O2) has C_s symmetry.

In this thesis, the informative β and σ modes are extracted from the VISPD spectra and compared to predicted frequencies for the S₁ state to probe the interaction strength (Table 11). Importantly, the overall agreement between experiment and calculation is good, which demonstrates that the M⁺...Fl interaction is probed to high precision by the chosen computational level of theory. As expected, the intermolecular frequencies (β and σ) depend on the metal size. Both modes increase in frequency in the series from Cs to Li. This fact can be rationalized by the metal dependent bond strength and the decreasing reduced mass ($\omega = \sqrt{k/\mu}$). In contrast, the intramolecular modes of the flavin skeleton

are hardly affected for all investigated isomers. Importantly, the m1 mode has been identified as the dominant progression in the spectrum of LF@He_N.⁵⁴ Essentially no amplitude of the orbital wavefunction for the HOMO/LUMO orbitals is observed for the ionic complexes on M⁺/H⁺. Consequently, M⁺/H⁺ does not have a drastic effect on the electronic structure of the neutral flavin molecule. Therefore, both LF@He_N and M⁺LF/H⁺LF/M⁺LC/H⁺LC show similar vibrational activity, especially for the intramolecular modes of the flavin skeleton.^{54,113–118}

The vibrational activity of the identified O4+ isomers of M⁺LC and M⁺LF is very similar. Due to the same binding site and a similar binding energy, the computed and measured frequencies differ only slightly. This can be understood, because the substituent R at N10 (CH₃ for LF) and at N1 (H for LC) is far away from the O4+ binding site, and the orbitals involved in the electronic excitation are essentially the same. Indeed, the measured frequencies for the β and σ modes are very similar for the O4+ isomers of M⁺LC and M⁺LF (Table 11).

In contrast, metalation and protonation at the O2+/N1 binding site changes the vibronic activity drastically with respect to the O4+ binding site. Due to the more pronounced folding of the molecule along the N5-N10 axis in the excited state, low-energy modes associated with a butterfly-type deformation are predicted and observed. For example, for Li⁺LF(O2+), the progression above the S₁ origin transition is assigned to this butterfly-type mode, that is well reproduced by the FC simulations

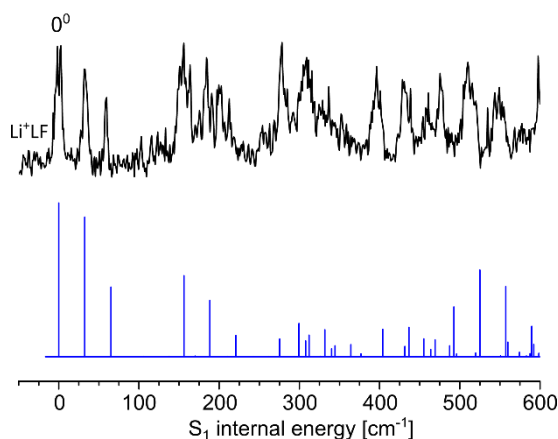


Figure 22. Comparison between VISP spectrum of Li⁺LF and FC simulations of the O2+ isomer as a function of S₁ internal energy. The bending of the chromophore along the N5-N10 axis upon electronic excitation can be seen in the short low-frequency progression.

(Figure 22). The same butterfly mode is predicted and observed for H⁺LF(N1). With increasing metal size, the O2+ binding site becomes less attractive, and is not even feasible for the heavier metals Rb and Cs because of their large radius. Interestingly, the O2 and O2+ isomers of K⁺LF are nearly iso-energetic ($E_0=0.4$ kJ mol⁻¹), and the O2+ isomer shows C_s symmetry in both the S₀ and S₁ state. Consequently, FC simulations do not contain such low-frequency modes.¹¹³ However, the measured VISP spectrum of K⁺LF recorded in the higher energy region shows low-frequency modes in the order of 8-10 cm⁻¹. These low-frequency modes could be attributed to the very shallow double minimum potential along the bending coordinate. Interestingly, in the case of K⁺RF, such low-frequency modes are not observed because of the different environment of the K⁺ cation.¹¹⁵

5.7. Geometry Changes upon Electronic Excitation

The computed geometry changes from S_0 to S_1 are in reasonable agreement with the measured spectra. For example, for $H^+LF(N1)$, $Li^+LF(O2+)$, and $Na^+LF(O2+)$ the change in the butterfly angle of the flavin chromophore is in line with the observed low-frequency modes.^{113,114} Furthermore, for the $O4+$ isomers the $N5-M-O4$ chelate changes substantially upon $\pi\pi^*$ excitation.^{116,117} These changes give rise to the pronounced progression in the in-plane β and σ mode. The geometry changes for M^+LC and M^+LF of the $N5-M$ and $O4-M$ bond length are summarized in Table 13. Clearly, almost all bond lengths become shorter upon electronic excitation. For $M^+LC(O4+)$ the $N5-M$ and $O4-M$ bond lengths contract substantially. In contrast, for $M^+LF(O4+)$ the $M-O4$ bond length is hardly affected (<1.1 pm) and the $M-N5$ bond length contracts up to 16.0 pm for $Cs^+LF(O4+)$. These results are in line with the strong vibronic activity and the increased interaction in the S_1 state.

Clearly, the behaviour is different at the $O2$ binding site. For $M^+LF(O2)$ with $M=Rb$ and Cs , S_1 excitation results in a decrease of the interaction with the $N1$ lone pair. Consequently, the $N1-M$ bond length increases substantially, which results in a more linear $C2-O2-M$ angle. This geometry change causes the pronounced progression in the β mode which is observed both computationally and experimentally. Furthermore, the elongated $N1-M$ bond length supports the reduced $M^+...LF$ interaction in the S_1 state associated with the small ΔS_1 blue shift.

Table 13. Selected bond length changes upon electronic excitation for the identified $O4+/O2/O2+$ isomers of M^+LC and M^+LF . All values are given in picometer. Negative values indicate contractions, positive values indicate elongations upon electronic excitation.

	O4+				O2		O2+	
	M-O4		M-N5		M-O2	M-N1	M-O2	M-N1
	LC	LF	LC	LF	LF	LF	LF	LF
Li	-2.6	0.1	-4.7	-5.9			-0.7	-0.4
Na	-3.4	-0.2	-4.6	-7.6			-1.1	1.4
K	-5.0	-0.6	-4.4	-10.5			-1.5	9.8
Rb	-5.7	-0.8	-4.9	-11.8	-0.5	9.8		
Cs	-7.1	-1.1	-5.2	-16.0	-0.3	9.6		

6. Conclusion and Outlook

The investigation of bare molecules in the gas phase free from their natural environment provides detailed information about their intrinsic properties. In this thesis, the first high-resolution optical spectra of protonated and metalated (complexation with alkali metals $M=Li, Na, K, Rb$, and Cs) flavin molecules isolated in the gas phase are reported. These flavins include lumichrome (LC), lumiflavin (LF), and the biologically relevant riboflavin (RF, vitamin B_2).^{113–118} These results provide a significant step forward, because most of the earlier experiments have been conducted in solution and at room temperature, and thus only produced low-resolution spectra with limited information.

The high-resolution spectra are recorded by means of electronic photodissociation (VISPD) spectroscopy employing the BerlinTrap apparatus, a tandem mass spectrometer coupled to an electrospray ionization source and a cryogenic 22-pole ion trap.^{87,88} Here, the experimental setup is equipped with two types of tunable laser sources operating in the VIS range, namely a dye laser and an OPO laser, to conduct action spectroscopy. All investigated molecules are cooled within the trap to cryogenic temperatures ($T < 25\text{ K}$) by means of helium buffer gas.⁸⁹ Cooling of the ions ensures that all measured spectra show well resolved electronic origin transitions and vibrational resolution even for such large biomolecules. Furthermore, the contribution of hot bands is almost completely suppressed for all investigated complexes. A combined approach of quantum chemical calculations and experimental data provides detailed information about the geometric, vibrational, and electronic structure of the various flavin ions. In particular, systematic trends at the molecular level are identified. Additionally, it was found that the metals bind mostly electrostatically to the flavins while the proton binds covalently to them.

The vibronic spectra are assigned to $S_1 \leftarrow S_0 (\pi\pi^*)$ transition of the most stable isomers/protomers, which have been identified by IRMPD spectroscopy and DFT calculations.^{110–112} To shed further light on the intrinsic properties of the metalated and protonated flavins, the vibrational structure is analyzed by TD-DFT quantum chemical calculations coupled to multidimensional Franck-Condon simulations.

The optical response of the investigated complexes is highly sensitive to the size and site of metalation, and on the site of protonation. In addition, the flavin specific functional group at N10/N1 can affect the optical response. The experimentally extracted S_1 origin transitions are compared to those obtained for neutral flavins (ΔS_1). This comparison shows either pronounced ΔS_1 blue shifts for the O2/O2+/N1 binding site and substantially smaller red shifts for the O4+/N5 binding site, independent of the functional group of the different flavins and the size of the metal/proton. This demonstrates the sensitive photophysical properties of the flavins with respect to the binding site of the alkali metal or proton. As a result, these ΔS_1 shifts are associated with a change in the intermolecular interaction strength upon $\pi\pi^*$ excitation. The ΔS_1 red shifts are connected to an increase in binding energy and proton affinity, whereas the ΔS_1 blue shifts is indicative for a decrease

of them. For example, the $\text{Cs}^+\dots\text{LF}$ interaction strength increase up to 20 % for the O4+ isomer, but decrease by only 6.6 % for the O2 isomer. Clearly, this variation in photophysical response is not determined by the HOMO and LUMO orbitals contributing to the electronic excitation for this type of flavin ions, as the orbitals are essentially the same for all investigated complexes and mostly localized on the flavin chromophore. The change in interaction strength can be rationalized by charge transfer upon $\pi\pi^*$ excitation. Because the orbitals do not cover the metal/proton, and also not the relevant functional group at N10, the intramolecular vibronic structure is very similar in terms of peak positions for all investigated complexes. In addition, the intramolecular structure of LF doped in superfluid He nanodroplets (LF@He_n) and the $\text{M}^+\text{LF}/\text{H}^+\text{LF}$ complexes investigated in this thesis are very similar, demonstrating that in both cases the same electronic state is excited.⁵⁴

In contrast, the intermolecular structure is highly sensitive to the size and site of metalation. As a result, the observed low-frequency bend and stretch modes are connected with substantial geometry changes upon electronic excitation. For example, for the O4+ isomers, the $\text{M}^+\dots\text{LF}/\text{M}^+\dots\text{LC}$ bond decreases substantially which in turn results in a change of the N5-M-O4 chelate. This view is in full agreement with the observed ΔS_1 red shift and the associated change in binding energy in the S_1 excited state. Furthermore, substitution from methyl to ribityl at N10 has substantial impact on the geometry and vibrational structure for K^+LF and K^+RF . This could be explained by the strong interaction of the K^+ cation and the ribityl chain. Clearly, the side chain influences the soft potential for $\text{O2} \leftrightarrow \text{O2}^+$ as observed for K^+LF , which in turn results in a less congested spectrum for K^+RF . Overall, this demonstrates that vibrational activity can be modulated by different properties (*e.g.*, functional group, binding site and size).

The strongly different optical absorption ranges for different binding sites allow to investigate flavins in a isomer-selective fashion, which is virtually not possible for IRMPD spectroscopy carried out at room temperature, because of strongly overlapping spectra for IRMPD experiments. However, even for similar binding sites, low-energy protomers can be separated by cryogenic optical spectroscopy. Due to the much smaller size of the proton compared to the alkali metals, it cannot form a N-H-O chelate. In contrast, it binds preferably to one of the nitrogen or oxygen atoms (OH, NH), which in turn results in steep potential wells with large tautomerization barriers. Clearly, these distinct low-energy protomers, like $\text{H}^+\text{LF}(\text{N1}/\text{O2}^+)$, can be distinguished by cryogenic optical spectroscopy because of their different vibrational activity. This can be rationalized by the C_s symmetry for the O2^+ protomer and the C_1 symmetry for the N1 protomer in both electronic states. The butterfly-type out-of-plane structure computed for the N1 protomer is more pronounced in the S_1 state, which gives rise to many out-of-plane modes and a more congested spectrum than for the planar O2^+ protomer. To conclude, the experimental and computational approach used here is clearly better suitable to assign low-energy isomers than the previously applied IRMPD technique.

In this thesis, many new findings in the field of cryogenic optical spectroscopy of flavins have been found. Of course, research is a dynamic process and many possible directions are possible. Most isomers, which are identified in this thesis, were investigated in an isomer-selective manner. Unfortunately, this single-laser approach has some limitations, because with increasing complexity of the flavin and its complexes, the number of possible low-energy isomers can increase substantially. This can already be observed for K⁺RF, because of the flexible ribityl side chain of RF. To investigate molecules in a truly isomer-selective fashion, the implementation of double-resonance experiments (*e.g.*, IR-VIS, VIS-VIS) could be beneficial.^{56,57,59,61,139} The addition of He, H₂, Ne, or Ar to the buffer gas allows to perform IR-spectroscopy of complexes with weakly bound ligands at cryogenic temperatures.¹⁴⁰

Here, the simplest flavins LC, LF, and RF have been investigated. This research could be extended in many directions. First, the investigation of more complex molecules such as FAD and FMN is important because of their biophysical relevance in flavoproteins.² Second, complexation of flavins with metals such as Fe, Cu, or Mg could be interesting because they occur in biological systems.^{2,29} Third, so far only cations have been investigated at the BerlinTrap. However, many flavins occur in the anionic form in their biological environment.² Therefore, the investigation of anionic complexes could be a further step to biologically more relevant systems. Fourth, the investigation of hydrated flavins could be a further step to biologically more realistic systems.

The recorded high-resolution spectra can generally serve as a benchmark for computational methods. At this point, the origin of some spectral features is not clear and could possibly be understood by employing a more precise theoretical description. To this end, the treatment of vibronic coupling or hindered internal methyl rotation could improve the agreement between experiment and calculations.¹⁴¹

The BerlinTrap can be continuously developed and improved. The installation of a wired quadrupole could increase the overlap of the ions and a laser, which is also important for future double resonance experiments.

References

- (1) J. M. Berg, J. L. Tymoczko, G. J. Gatto, L. Stryer, *Biochemistry*, Macmillan international, **2019**
- (2) E. Silva and A. Edwards, *Flavins: Photochemistry and photobiology*, RSC Publishing, **2003**
- (3) J.-P. Schermann, *Spectroscopy and modelling of biomolecular building blocks*, Elsevier, **2008**
- (4) P. Karrer, K. Schöpp, F. Benz, *Helv. Chim. Acta*, **1935**, *18*, 426–429
- (5) G. F. Ball, *Vitamins in foods, Analysis, bioavailability, and stability*; Taylor & Francis, **2006**
- (6) K. H. Dudley, A. Ehrenberg, P. Hemmerich, F. Müller, *Helv. Chim. Acta*, **1964**, *47*, 1354–1383
- (7) P. F. Heelis, *Chem. Soc. Rev.*, **1982**, *11*, 15
- (8) V. Massey, *Biochem. Soc. Trans.*, **2000**, *28*, 283–296
- (9) W. Buckel, R. K. Thauer, *Chem. Rev.*, **2018**, *118*, 3862–3886
- (10) T. E. Swartz, T. Tseng, M. A. Frederickson, G. Paris, D. J. Comerci, G. Rajashekara, J. Kim, M. B. Mudgett, G. A. Splitter, et al., *Science*, **2007**, *317*, 1090–1093
- (11) T. E. Swartz, S. B. Corchnoy, J. M. Christie, J. W. Lewis, I. Szundi, W. R. Briggs, R. A. Bogomolni, *J. Biol. Chem.*, **2001**, *276*, 36493–36500
- (12) E. Romero, J. R. Gómez Castellanos, G. Gadda, M. W. Fraaije, A. Mattevi, *Chem. Rev.*, **2018**, *118*, 1742–1769
- (13) D. Zhong, *Annu. Rev. Phys. Chem.*, **2015**, *66*, 691–715
- (14) A. Sancar, *Chem. Rev.*, **2003**, *103*, 2203–2237
- (15) A. Losi, *Photochem Photobiol*, **2007**, *83*, 1283–1300
- (16) A. Losi, W. Gärtner, *Photochem Photobiol*, **2011**, *87*, 491–510
- (17) C. Bialas, L. E. Jarocho, K. B. Henbest, T. M. Zollitsch, G. Kodali, C. R. Timmel, S. R. Mackenzie, P. L. Dutton, C. C. Moser, et al., *J. Am. Chem. Soc.*, **2016**, *138*, 16584–16587
- (18) M. Liedvogel, H. Mouritsen, *J. R. Soc., Interface*, **2010**, *7*, 147–162
- (19) L. Guyon, T. Tabarin, B. Thuillier, R. Antoine, M. Broyer, V. Boutou, J. P. Wolf, P. Dugourd, *J. Chem. Phys.*, **2008**, *128*, 75103
- (20) E. Sikorska, I. Khmelinskii, A. Komasa, J. Koput, L. F. Ferreira, J. R. Herance, J. L. Bourdelande, S. L. Williams, D. R. Worrall, et al., *Chem. Phys.*, **2005**, *314*, 239–247
- (21) E. Sikorska, I. V. Khmelinskii, W. Prukła, S. L. Williams, M. Patel, D. R. Worrall, J. L. Bourdelande, J. Koput, M. Sikorski, et al., *J. Phys. Chem. A*, **2004**, *108*, 1501–1508
- (22) E. Sikorska, I. V. Khmelinskii, D. R. Worrall, J. Koput, M. Sikorski, *J. Fluoresc.*, **2004**, *14*, 57–64
- (23) P. Zirák, A. Penzkofer, T. Mathes, P. Hegemann, *Chem. Phys.*, **2009**, *358*, 111–122
- (24) P. Drössler, W. Holzer, A. Penzkofer, P. Hegemann, *Chem. Phys.*, **2002**, *282*, 429–439
- (25) A. Tyagi, A. Penzkofer, *J. Photochem. Photobiol., A*, **2010**, *215*, 108–117
- (26) A. Tyagi, A. Penzkofer, *Photochem Photobiol*, **2011**, *87*, 524–533
- (27) S. Ghisla, *Biochemistry*, **1974**, *13*, 589–597
- (28) A. W. Varnes, R. B. Dodson, E. L. Wehry, *J. Am. Chem. Soc.*, **1972**, *94*, 946–950
- (29) D. Lewandowski, G. Schroeder, M. Sawczak, T. Ossowski, *J. Phys. Chem. Solids*, **2015**, *85*, 56–61
- (30) I. Ahmad, Z. Anwar, S. Ahmed, M. A. Sheraz, S.-U.-R. Khattak, *J. Photochem. Photobiol., B*, **2017**, *173*, 231–239
- (31) W. J. Rutter, K. Dalziel, H. Viervoll, M. Zackrisson, L. Ernster, E. Diczfalussy, *Acta Chem. Scand.*, **1958**, *12*, 438–446
- (32) I. F. Baarda, D. E. Metzler, *Biochim. Biophys. Acta*, **1961**, *50*, 463–471
- (33) P. Bamberg, P. Hemmerich, *Helv. Chim. Acta*, **1961**, *44*, 1001–1011
- (34) J. Lauterwein, P. Hemmerich, J. M. Lhoste, *Inorg. Chem.*, **1975**, *14*, 2152–2161
- (35) J. Lauterwein, P. Hemmerich, J. M. Lhoste, *Inorg. Chem.*, **1975**, *14*, 2161–2168
- (36) M. Benecky, T. Yu, K. L. Watters, J. T. McFarland, *Biochim. Biophys. Acta*, **1980**, *626*, 197–207

- (37) S. Fukuzumi, T. Kojima, *J. Biol. Inorg. Chem.*, **2008**, *13*, 321–333
- (38) J. T. Spence, E. R. Peterson, *J. Inorg. Nucl. Chem.*, **1962**, *24*, 601–608
- (39) W. Holzer, A. Penzkofer, M. Fuhrmann, P. Hegemann, *Photochem Photobiol*, **2002**, *75*, 479–487
- (40) S. Ghisla, C. Thorpe, V. M. Massey, *Biochemistry*, **1984**, *23*, 3154–3161
- (41) E. Sikorska, I. V. Khmelinskii, J. Koput, J. L. Bourdelande, M. Sikorski, *J. Mol. Struct.*, **2004**, *697*, 137–141
- (42) E. Sikorska, I. V. Khmelinskii, W. Prukala, S. L. Williams, D. R. Worrall, J. L. Bourdelande, A. Bednarek, J. Koput, M. Sikorski, et al., *J. Mol. Struct.*, **2004**, *689*, 121–126
- (43) M. Sun, T. A. Moore, P. S. Song, *J. Am. Chem. Soc.*, **1972**, *94*, 1730–1740
- (44) A. Weigel, A. L. Dobryakov, M. Veiga, J. L. Pérez Lustres, *J. Phys. Chem. A*, **2008**, *112*, 12054–12065
- (45) M. M. Wolf, C. Schumann, R. Gross, T. Domratcheva, R. Diller, *J. Phys. Chem. B*, **2008**, *112*, 13424–13432
- (46) M. Quick, A. Weigel, N. P. Ernsting, *J. Phys. Chem. B*, **2013**, *117*, 5441–5447
- (47) M. M. Wolf, H. Zimmermann, R. Diller, T. Domratcheva, *J. Phys. Chem. B*, **2011**, *115*, 7621–7628
- (48) M. H. Stockett, *Phys. Chem. Chem. Phys.*, **2017**, *19*, 25829–25833
- (49) L. Giacomozzi, C. Kjær, J. Langeland Knudsen, L. H. Andersen, S. Brøndsted Nielsen, M. H. Stockett, *J. Chem. Phys.*, **2018**, *148*, 214309
- (50) J. N. Bull, E. Carrascosa, L. Giacomozzi, E. J. Bieske, M. H. Stockett, *Phys. Chem. Chem. Phys.*, **2018**, *20*, 19672–19681
- (51) E. Matthews, R. Cercola, C. E. Dessent, *Molecules*, **2018**, *23*, 2033
- (52) E. Matthews, C. E. Dessent, *J. Phys. Chem. Lett.*, **2018**, *9*, 6124–6130
- (53) K. Lincke, J. Langeland, A. Ø. Madsen, H. V. Kiefer, L. Skov, E. Gruber, K. V. Mikkelsen, L. H. Andersen, M. B. Nielsen, et al., *Phys. Chem. Chem. Phys.*, **2018**, *20*, 28678–28684
- (54) A. Vdovin, A. Slenczka, B. Dick, *Chem. Phys.*, **2013**, *422*, 195–203
- (55) L. Kammler, M. van Gastel, *J. Phys. Chem. A*, **2012**, *116*, 10090–10098
- (56) T. R. Rizzo, J. a. Stearns, O. V. Boyarkin, *Int. Rev. Phys. Chem.*, **2009**, *28*, 481–515
- (57) O. V. Boyarkin, *Int. Rev. Phys. Chem.*, **2018**, *37*, 559–606
- (58) R. J. Platenkamp, H. D. van Osnabrugge, A.J.W.G. Visser, *Chem. Phys. Lett.*, **1980**, *72*, 104–111
- (59) M. L. Weichman, D. M. Neumark, *Annu. Rev. Phys. Chem.*, **2018**, *69*, 101–124
- (60) W. Zagorec-Marks, J. E. Smith, M. M. Foreman, S. Sharma, J. M. Weber, *Phys. Chem. Chem. Phys.*, **2020**, *22*, 20295–20302
- (61) S. Ishiuchi, H. Wako, D. Kato, M. Fujii, *J. Mol. Spectrosc.*, **2017**, *332*, 45–51
- (62) C. Neiss, P. Saalfrank, M. Parac, S. Grimme, *J. Phys. Chem. A*, **2003**, *107*, 140–147
- (63) J. Hasegawa, S. Bureekaew, H. Nakatsuji, *J. Photochem. Photobiol., A*, **2007**, *189*, 205–210
- (64) S. Salzmann, C. M. Marian, *Chem. Phys. Lett.*, **2008**, *463*, 400–404
- (65) S. Salzmann, V. Martinez-Junza, B. Zorn, S. E. Braslavsky, M. Mansurova, C. M. Marian, W. Gärtner, *J. Phys. Chem. A*, **2009**, *113*, 9365–9375
- (66) S. Salzmann, J. Tatchen, C. M. Marian, *J. Photochem. Photobiol., A*, **2008**, *198*, 221–231
- (67) B. Klaumünzer, D. Kröner, P. Saalfrank, *J. Phys. Chem. B*, **2010**, *114*, 10826–10834
- (68) B. Klaumünzer, D. Kröner, H. Lischka, P. Saalfrank, *Phys. Chem. Chem. Phys.*, **2012**, *14*, 8693–8702
- (69) B. Karasulu, J. P. Götze, W. Thiel, *J. Chem. Theory Comput.*, **2014**, *10*, 5549–5566
- (70) M. P. Kabir, Y. Orozco-Gonzalez, S. Gozem, *Phys. Chem. Chem. Phys.*, **2019**, *21*, 16526–16537
- (71) N. H. List, F. M. Pimenta, L. Holmegaard, R. L. Jensen, M. Etzerodt, T. Schwabe, J. Kongsted, P. R. Ogilby, O. Christiansen, et al., *Phys. Chem. Chem. Phys.*, **2014**, *16*, 9950–9959
- (72) L. Zanetti-Polzi, M. Aschi, I. Daidone, A. Amadei, *Chem. Phys. Lett.*, **2017**, *669*, 119–124
- (73) M. Wu, L. A. Eriksson, *J. Phys. Chem. A*, **2010**, *114*, 10234–10242

- (74) K. Zenichowski, M. Gothe, P. Saalfrank, *J. Photochem. Photobiol., A*, **2007**, *190*, 290–300
- (75) A. Udvarhelyi, M. Olivucci, T. Domratcheva, *J. Chem. Theory Comput.*, **2015**, *11*, 3878–3894
- (76) Y.-K. Choe, S. Nagase, K. Nishimoto, *Journal of computational chemistry*, **2007**, *28*, 727–739
- (77) Y. J. Zheng, R. L. Ornstein, *J. Am. Chem. Soc.*, **1996**, *118*, 9402–9408
- (78) T. Kottke, J. Heberle, D. Hehn, B. Dick, P. Hegemann, *Biophys. J.*, **2003**, *84*, 1192–1201
- (79) R. K. Kar, V. A. Borin, Y. Ding, J. Matysik, I. Schapiro, *Photochem Photobiol*, **2019**, *95*, 662–674
- (80) W. Koch, M. C. Holthausen, *A Chemist's Guide to Density Functional Theory*, Wiley-VCH, **2015**
- (81) P. R. Bunker, P. Jensen, *Molecular symmetry and spectroscopy*, NRC Research Press, **2006**
- (82) R. E. Smalley, *Laser Chem.*, **1983**, *2*, 167–184
- (83) J. B. Fenn, M. Mann, C. K. Meng, S. F. Wong, C. M. Whitehouse, *Science*, **1989**, *246*, 64–71
- (84) T. D. Veenstra, *Biophys. Chem.*, **1999**, *79*, 63–79
- (85) S. Crotti, R. Seraglia, P. Traldi, *Eur. J. Mass Spectrom.*, **2011**, *17*, 85–99
- (86) K. Tanaka, H. Waki, Y. Ido, S. Akita, Y. Yoshida, T. Yoshida, T. Matsuo, *Rapid Commun. Mass Spectrom.*, **1988**, *2*, 151–153
- (87) A. Günther, *Entwicklung eines neuartigen kryogenen 22-Pol Ionenfallenspektrometers (BerlinTrap) und spektroskopische Analyse von isolierten Flavinionenkomplexen*, Technische Universität Berlin, **2017**
- (88) A. Günther, P. Nieto, D. Müller, A. Sheldrick, D. Gerlich, O. Dopfer, *J. Mol. Spectrosc.*, **2017**, *332*, 8–15
- (89) D. Gerlich, in *Advances in Chemical Physics*, John Wiley & Sons, Inc, **1992**, 1–176
- (90) A. B. Wolk, C. M. Leavitt, E. Garand, M. A. Johnson, *Acc. Chem. Res.*, **2014**, *47*, 202–210
- (91) J. Roithová, A. Gray, E. Andris, J. Jašík, D. Gerlich, *Acc. Chem. Res.*, **2016**, *49*, 223–230
- (92) C. M. Choi, D. H. Choi, N. J. Kim, J. Heo, *Int. J. Mass Spectrom.*, **2012**, *314*, 18–21
- (93) O. V. Boyarkin, S. R. Mercier, A. Kamariotis, T. R. Rizzo, *J. Am. Chem. Soc.*, **2006**, *128*, 2816–2817
- (94) A. Svendsen, U. J. Lorenz, O. V. Boyarkin, T. R. Rizzo, *Rev. Sci. Instrum.*, **2010**, *81*, 73107
- (95) K. R. Asmis, J. Sauer, *Mass Spectrom. Rev.*, **2007**, *26*, 542–562
- (96) J. Roithová, A. Gray, E. Andris, J. Jašík, D. Gerlich, *Acc. Chem. Res.*, **2016**, *49*, 223–230
- (97) C. A. Rice, F.-X. Hardy, O. Gause, J. P. Maier, *J. Phys. Chem. Lett.*, **2014**, *5*, 942–945
- (98) W. Paul, *Rev. Mod. Phys.*, **1990**, *62*, 531–540
- (99) R. Wester, *J. Phys. B: At., Mol. Opt. Phys.*, **2009**, *42*, 154001
- (100) O. Asvany, S. Schlemmer, *Int. J. Mass Spectrom.*, **2009**, *279*, 147–155
- (101) S. Trippel, J. Mikosch, R. Berhane, R. Otto, M. Weidemüller, R. Wester, *Phys. Rev. Lett.*, **2006**, *97*, 193003
- (102) K. Hirsch, J. T. Lau, P. Klar, A. Langenberg, J. Probst, J. Rittmann, M. Vogel, V. Zamudio-Bayer, T. Möller, et al., *J. Phys. B: At., Mol. Opt. Phys.*, **2009**, *42*, 154029
- (103) O. V. Boyarkin, V. Kopysov, *Rev. Sci. Instrum.*, **2014**, *85*, 33105
- (104) J. Jašík, J. Žabka, J. Roithová, D. Gerlich, *Int. J. Mass Spectrom.*, **2013**, *354–355*, 204–210
- (105) A. I. González Flórez, D.-S. Ahn, S. Gewinner, W. Schöllkopf, G. von Helden, *Phys. Chem. Chem. Phys.*, **2015**, *17*, 21902–21911
- (106) J. P. Toennies, A. F. Vilesov, *Angew. Chem.*, **2004**, *116*, 2674–2702
- (107) P. R. Berman, V. S. Malinovsky, *Principles of Laser Spectroscopy and Quantum Optics*, Princeton University Press, **2011**
- (108) J. H. Gross, *Mass Spectrometry*, Springer, **2011**
- (109) R. E. March, *J. Mass Spectrom.*, **1997**, *32*, 351–369
- (110) A. Günther, P. Nieto, G. Berden, J. Oomens, O. Dopfer, *Phys. Chem. Chem. Phys.*, **2014**, *16*, 14161–14171
- (111) P. Nieto, A. Günther, G. Berden, J. Oomens, O. Dopfer, *J. Phys. Chem. A*, **2016**, *120*, 8297–8308

- (112) J. Langer, A. Günther, S. Seidenbecher, G. Berden, J. Oomens, O. Dopfer, *ChemPhysChem*, **2014**, 15, 2550–2562
- (113) D. Müller, O. Dopfer, *J. Photochem. Photobiol.*, **2020**, 3-4, 100009
- (114) D. Müller, O. Dopfer, *Phys. Chem. Chem. Phys.*, **2020**, 22, 18328
- (115) D. Müller, O. Dopfer, *J. Phys. Chem. A*, **2021**, 125, 3146–3158
- (116) D. Müller, P. Nieto, M. Miyazaki, O. Dopfer, *Faraday Discuss.*, **2019**, 217, 256–275
- (117) P. Nieto, D. Müller, A. Sheldrick, A. Günther, M. Miyazaki, O. Dopfer, *Phys. Chem. Chem. Phys.*, **2018**, 20, 22148–22158
- (118) A. Sheldrick, D. Müller, A. Günther, P. Nieto, O. Dopfer, *Phys. Chem. Chem. Phys.*, **2018**, 20, 7407–7414
- (119) D. Oepts, A. F. van der Meer, P. W. van Amersfoort, *Infrared Phys. Technol.*, **1995**, 36, 297–308
- (120) J. J. Valle, J. R. Eyler, J. Oomens, D. T. Moore, A. F. van der Meer, G. von Helden, G. Meijer, C. L. Hendrickson, A. G. Marshall, et al., *Rev. Sci. Instrum.*, **2005**, 76, 23103
- (121) P. Maître, S. Le Caër, A. Simon, W. Jones, J. Lemaire, H. Mestdag, M. Heninger, G. Mauclair, P. Boissel, et al., *Nucl. Instrum. Methods Phys. Res., Sect. A*, **2003**, 507, 541–546
- (122) M. Dole, L. L. Mack, R. L. Hines, R. C. Mobley, L. D. Ferguson, M. B. Alice, *J. Chem. Phys.*, **1968**, 49, 2240–2249
- (123) J. V. Iribarne, *J. Chem. Phys.*, **1976**, 64, 2287
- (124) O. Asvany, S. Brünken, L. Kluge, S. Schlemmer, *Appl. Phys. B*, **2014**, 114, 203–211
- (125) W. Kohn, L. J. Sham, *Phys. Rev.*, **1965**, 140, 1133–1138
- (126) E. Runge, E. K. Gross, *Phys. Rev. Lett.*, **1984**, 52, 997–1000
- (127) F. Jensen, *Comput. Mol. Sci.*, **2013**, 3, 273–295
- (128) C. Adamo, V. Barone, *J. Chem. Phys.*, **1999**, 110, 6158–6170
- (129) C. Adamo, G. E. Scuseria, V. Barone, *J. Chem. Phys.*, **1999**, 111, 2889–2899
- (130) M. G. Medvedev, I. S. Bushmarinov, J. Sun, J. P. Perdew, K. A. Lyssenko, *Science*, **2017**, 355, 49–52
- (131) T. H. Dunning, *J. Chem. Phys.*, **1989**, 90, 1007–1023
- (132) M. J. Frisch, G. W. Trucks, H. B. Schlegel, G. E. Scuseria, M. A. Robb, J. R. Cheeseman, G. Scalmani, V. Barone, G. A. Petersson, et al., *Gaussian 16, Revision C.01*; Gaussian, Inc., Wallingford, CT, **2016**
- (133) I. S. Lim, P. Schwerdtfeger, B. Metz, H. Stoll, *J. Chem. Phys.*, **2005**, 122, 104103
- (134) G. Herzberg, *Molecular spectra and molecular structure*, Krieger, **1992**
- (135) C. M. Western, *J. Quant. Spectrosc. Radiat. Transfer*, **2017**, 186, 221–242
- (136) R. L. Martin, *J. Chem. Phys.*, **2003**, 118, 4775–4777
- (137) A. E. Reed, L. A. Curtiss, F. Weinhold, *Chem. Rev.*, **1988**, 88, 899–926
- (138) R. D. Shannon, *Acta Crystallogr.*, **1976**, 32, 751–767
- (139) A. Bouchet, J. Klyne, S.-i. Ishiuchi, O. Dopfer, M. Fujii, A. Zehnacker, *Phys. Chem. Chem. Phys.*, **2018**, 20, 12430–12443
- (140) J. Jašík, R. Navrátil, I. Němec, J. Roithová, *J. Phys. Chem. A*, **2015**, 119, 12648–12655
- (141) P. J. Breen, J. A. Warren, E. R. Bernstein, J. I. Seeman, *Acc. Chem. Res.*, **1987**, 87, 1917–1926

Appendix

Electronic Supporting Information (ESI)

**Effect of alkali ions on optical properties of flavins:
Vibronic spectra of cryogenic M⁺lumiflavin complexes (M=Li-Cs)**

David Müller,^a Pablo Nieto,^a Mitsuhiro Miyazaki,^{a,b} Otto Dopfer^{a,c,*}

a) Institut für Optik und Atomare Physik, Technische Universität Berlin, Hardenbergstr. 36, 10623 Berlin, Germany.

b) Laboratory for Chemistry and Life Science, Institute of Innovation Research, Tokyo Institute of Technology, 4259, Nagatsuta-cho, Midori-ku, Yokohama, Japan.

c) Tokyo Tech World Research Hub Initiative (WRHI), Institute of Innovation Research, Tokyo Institute of Technology, 4259, Nagatsuta-cho, Midori-ku, Yokohama, Japan.

* corresponding author: dopfer@physik.tu-berlin.de; Fax: +49 30 314 23018

Figure S1. Photodissociation mass spectra of Na^+LF with laser off and on (resonant to S_1 origin at 18310 cm^{-1}). The photodissociation efficiency is around 2%.

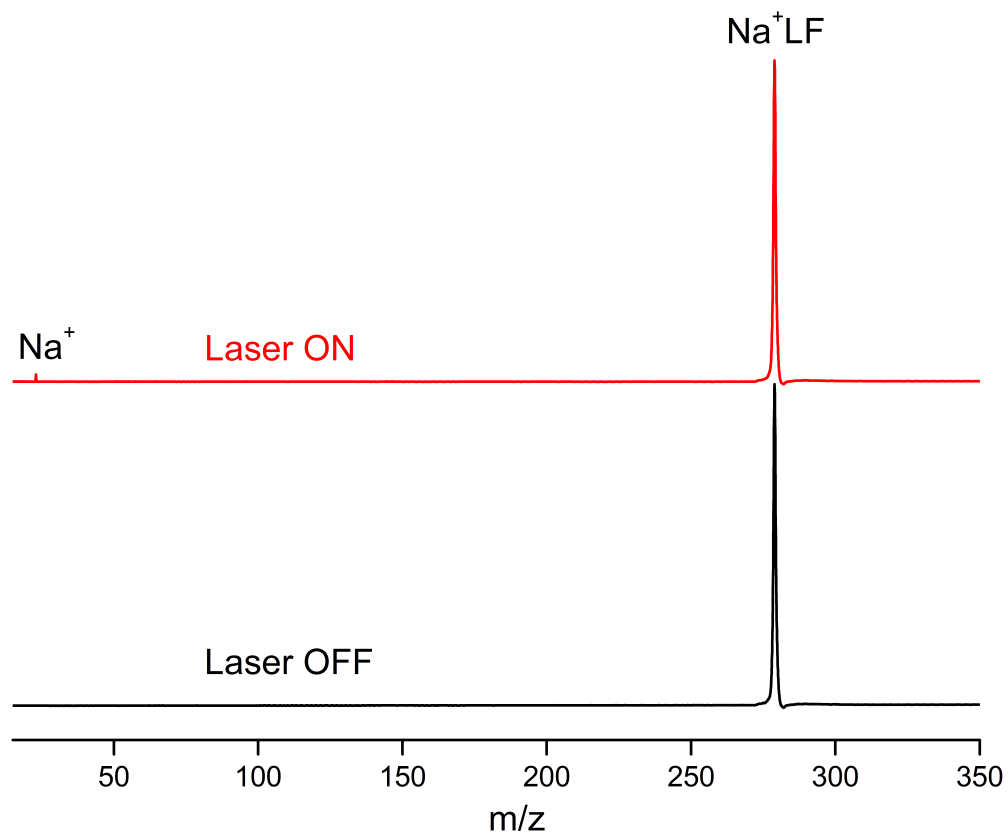
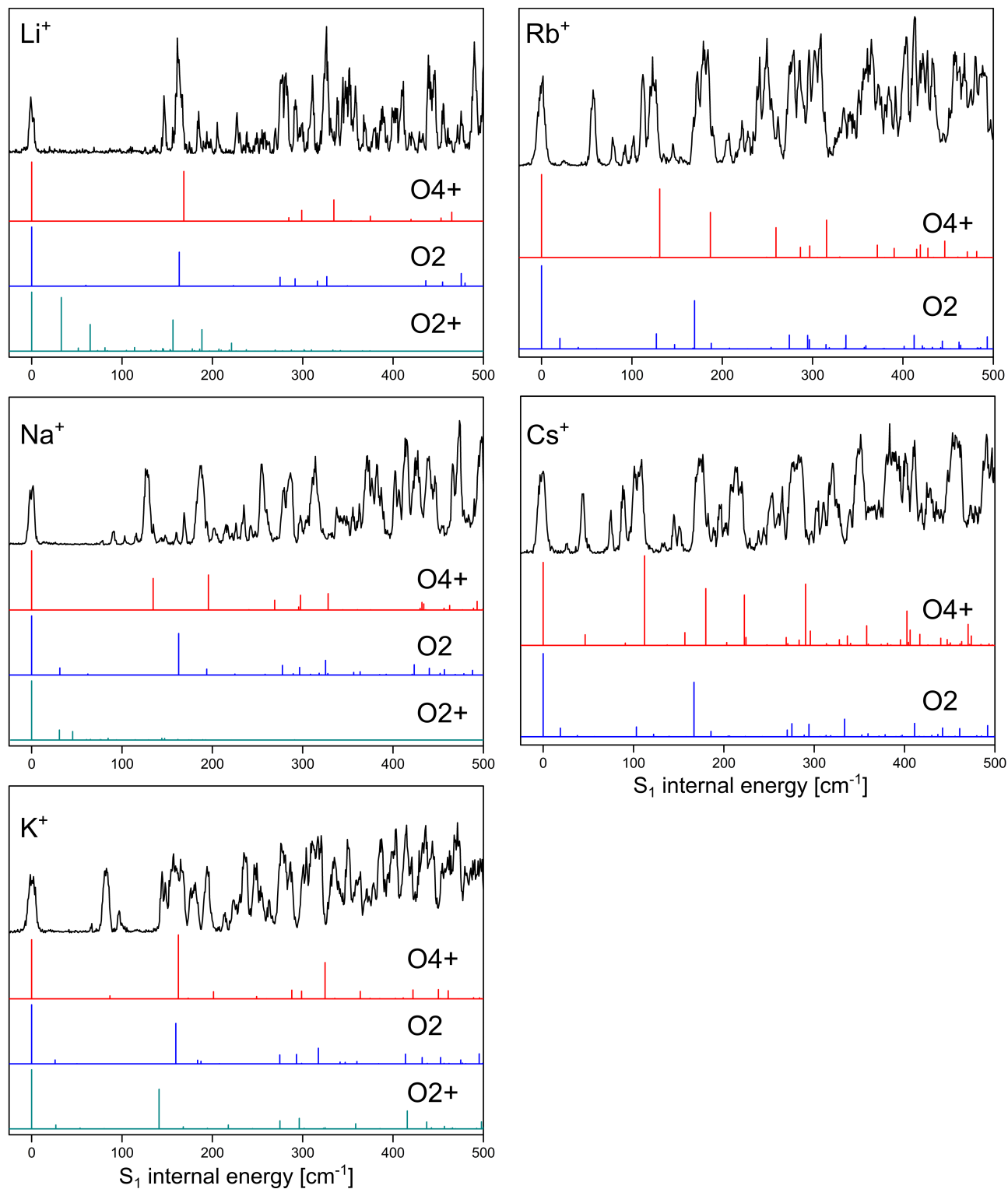


Figure S2. Comparison between measured VISPD spectra of M^+LF with $M=(Li-Cs)$ and Franck-Condon (FC) simulations for the three most stable isomers shown in Figure 1 as a function of S_1 internal energy. Clearly, the FC simulations of the O4+ isomer fits best, in particular when comparing the main (i.e., intense) transitions.



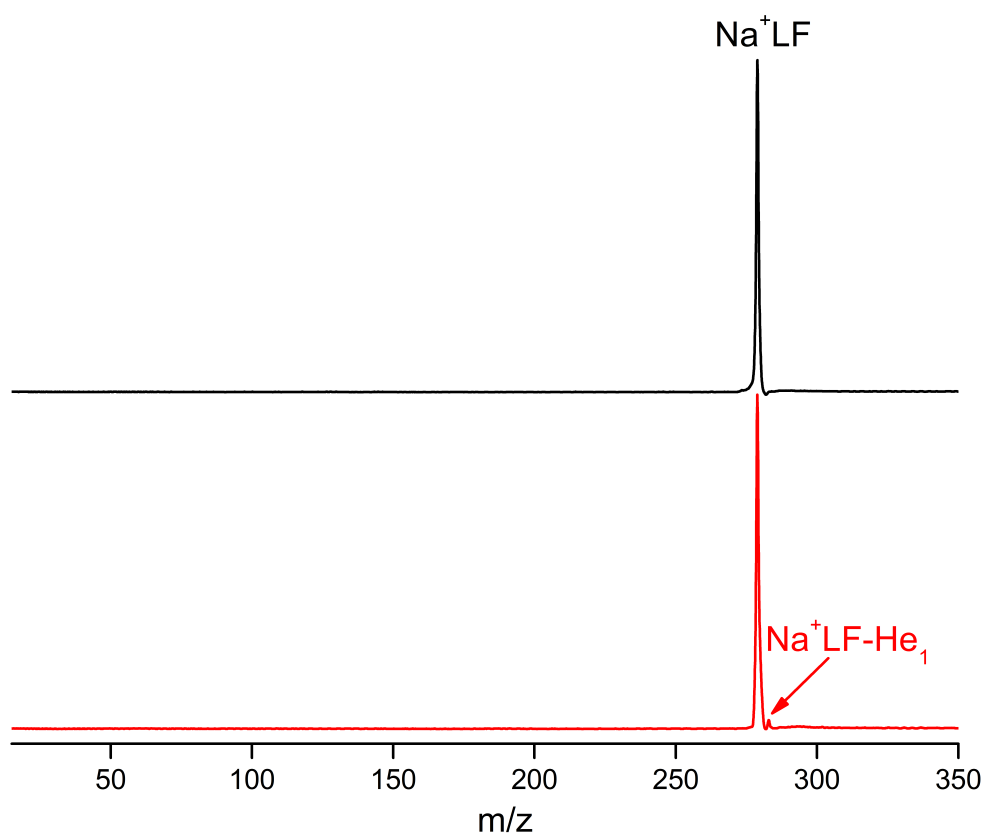


Figure S3. Laser-off mass spectra of trapping mass-selected Na^+LF ions measured at trap temperatures of 13 K (black) and 6 K (red). At $T=6$ K, He-tagged complexes of the type $\text{Na}^+\text{LF-He}_1$ are observed (2% of Na^+LF). At $T=13$ K, no such complexes are formed in the cryogenic 22-pole trap.

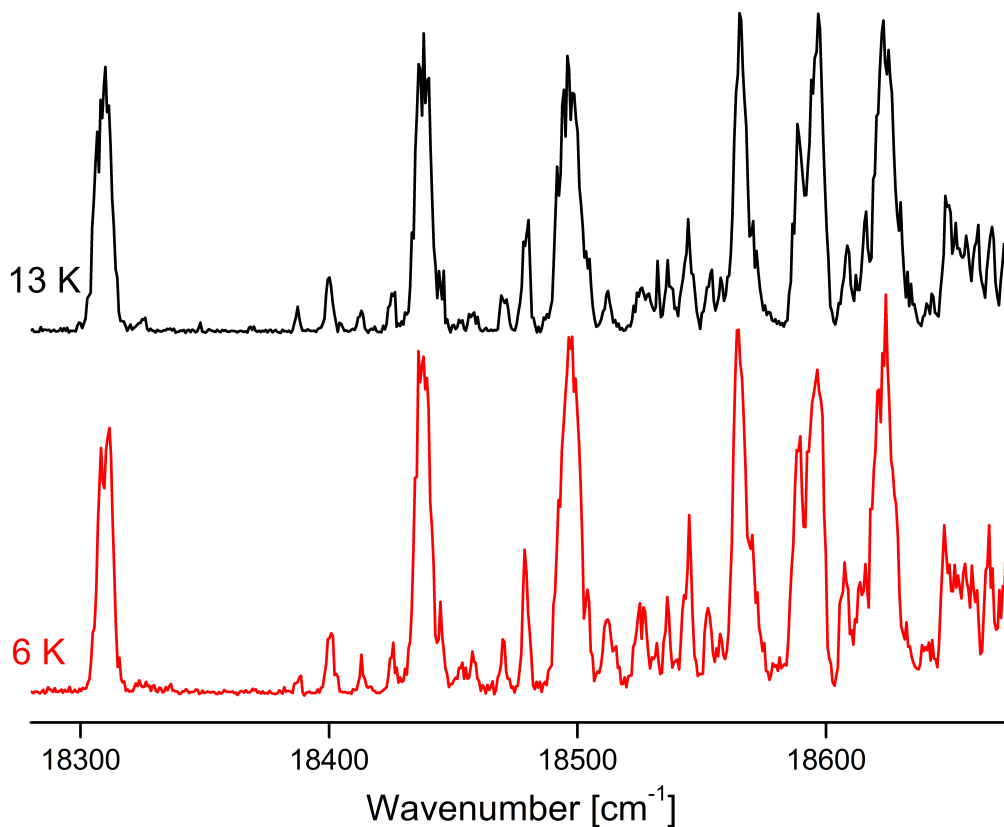
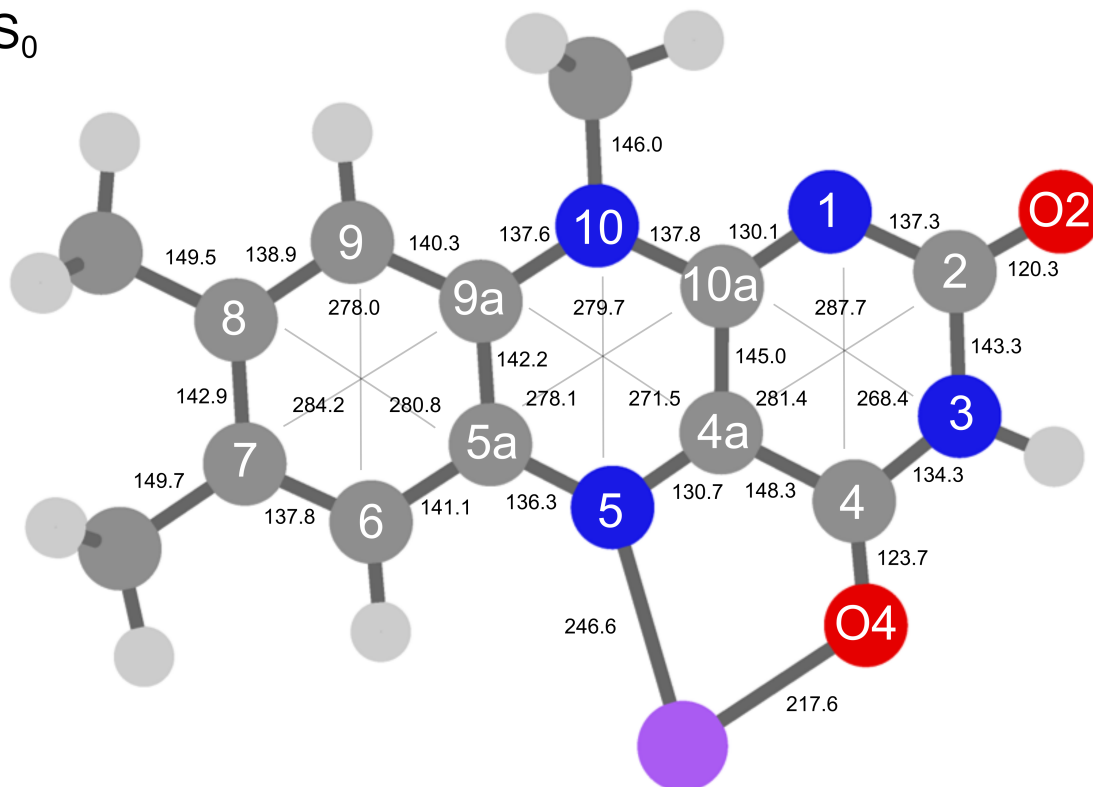


Figure S4. VISPD spectra of Na^+LF after mass-selection, trapping, and cooling at trap temperatures of $T=13$ K (black, no He adducts formed) and at $T=6$ K (red, He adducts formed). The spectra are very similar indicating that the contribution of the He adducts to the VISPD spectrum at 6 K is negligible.

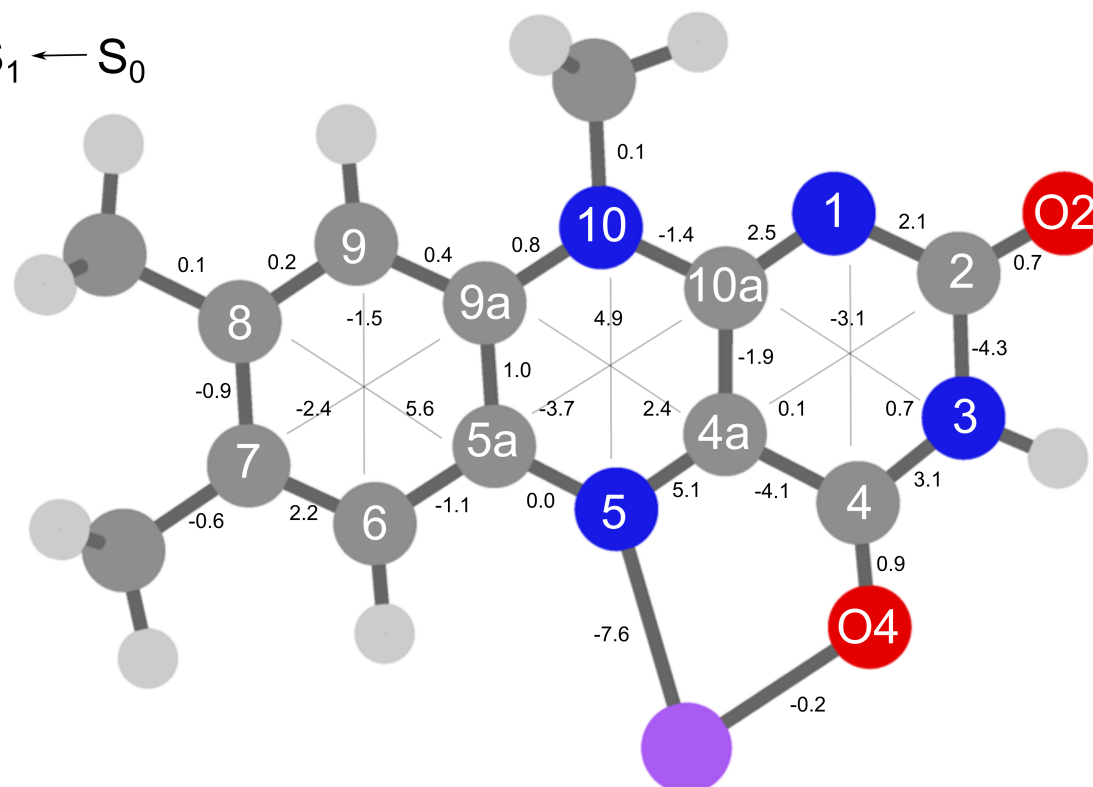
Figure S5. (Top) Absolute distances (in pm) of M^+LF ($M=Na-Cs$) and LF in its S_0 state calculated at the PBE0/cc-pVDZ level. (Bottom) Relative changes in bond distances upon electronic S_1 excitation. Positive (negative) values indicate elongations (contractions).

Na^+LF

S_0

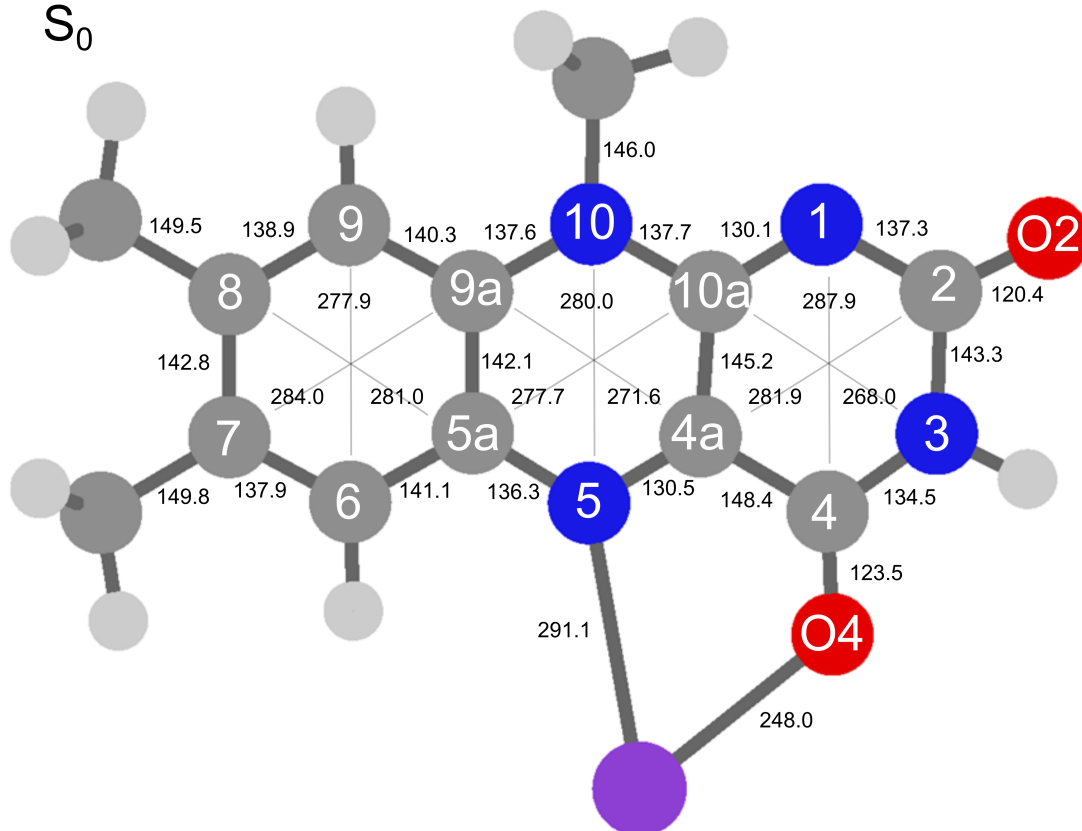


$S_1 \leftarrow S_0$

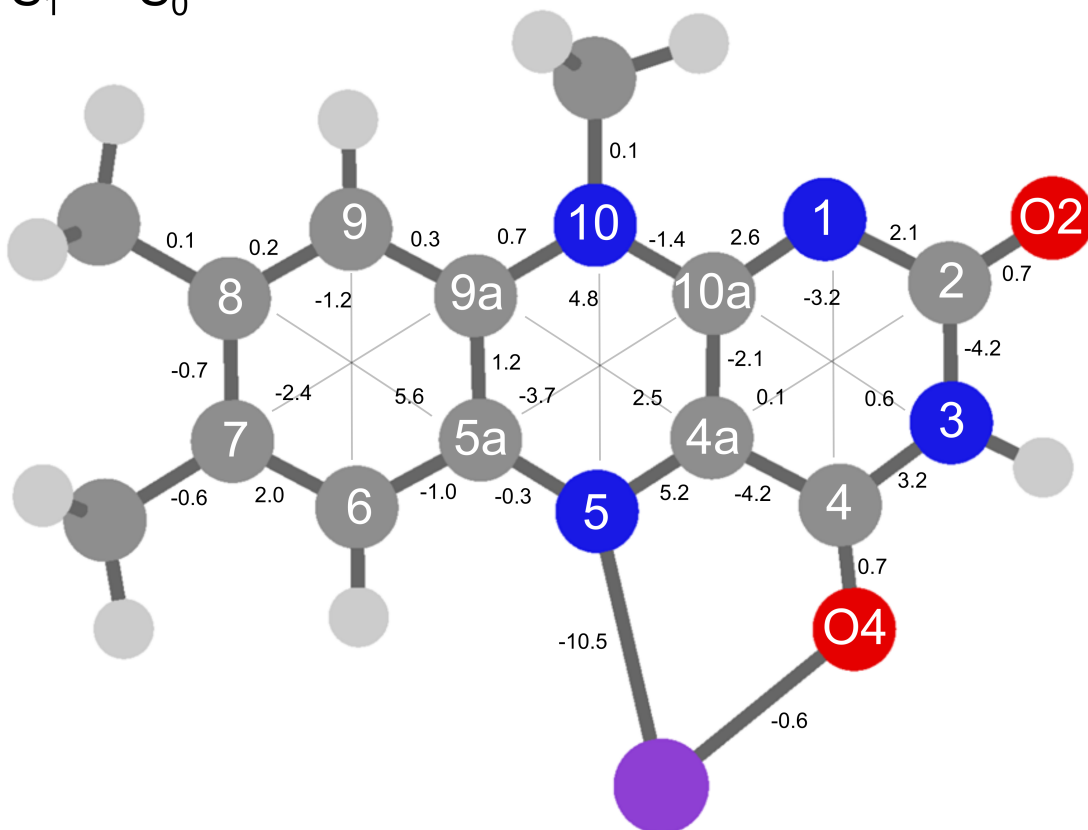


K⁺LF

S₀

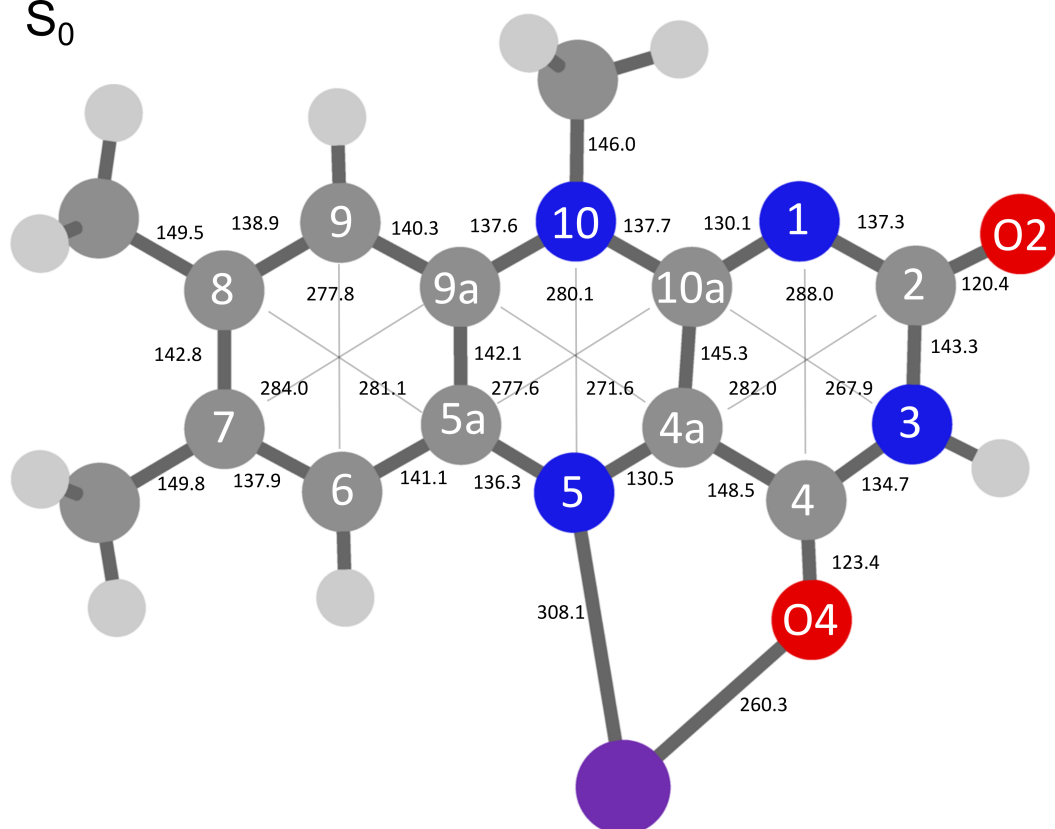


S₁ ← S₀

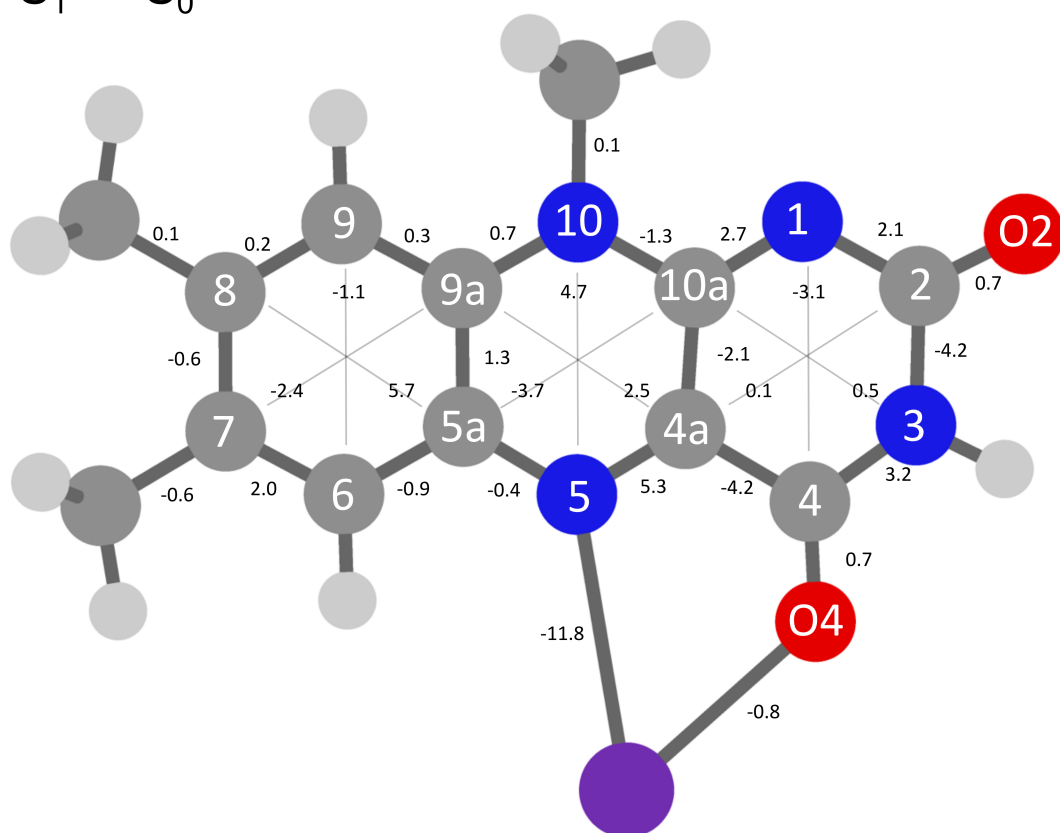


Rb⁺LF

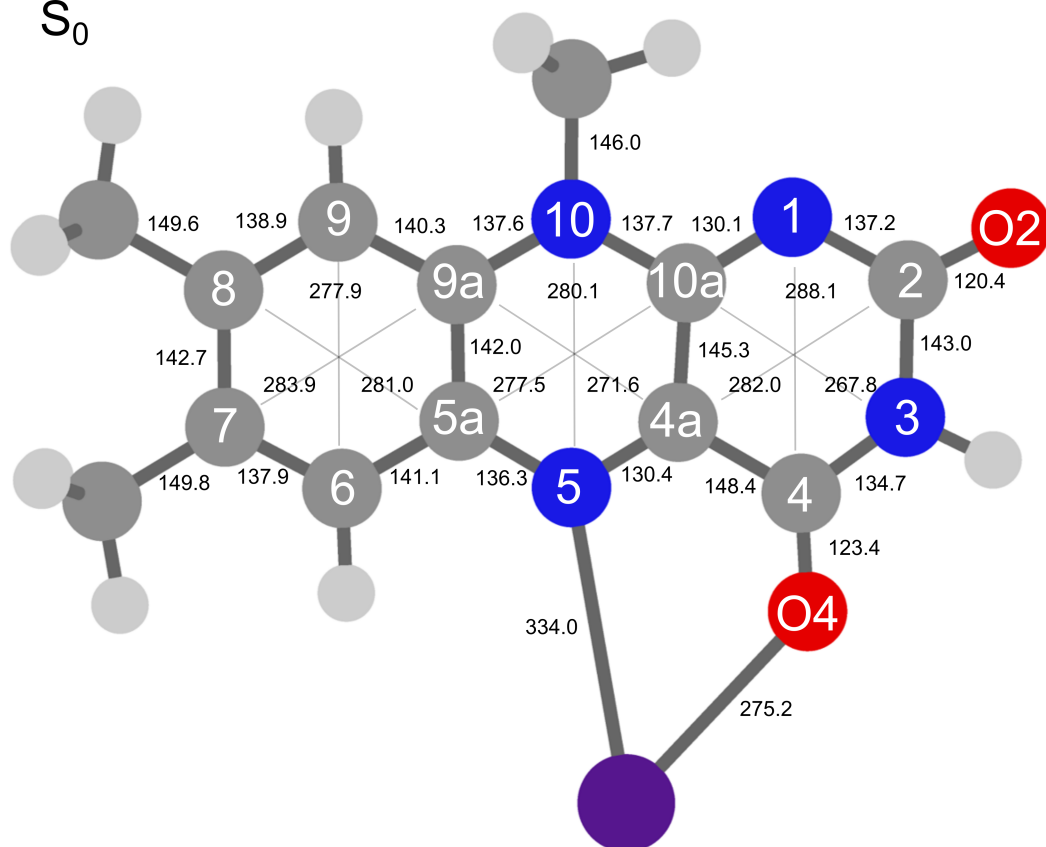
S₀



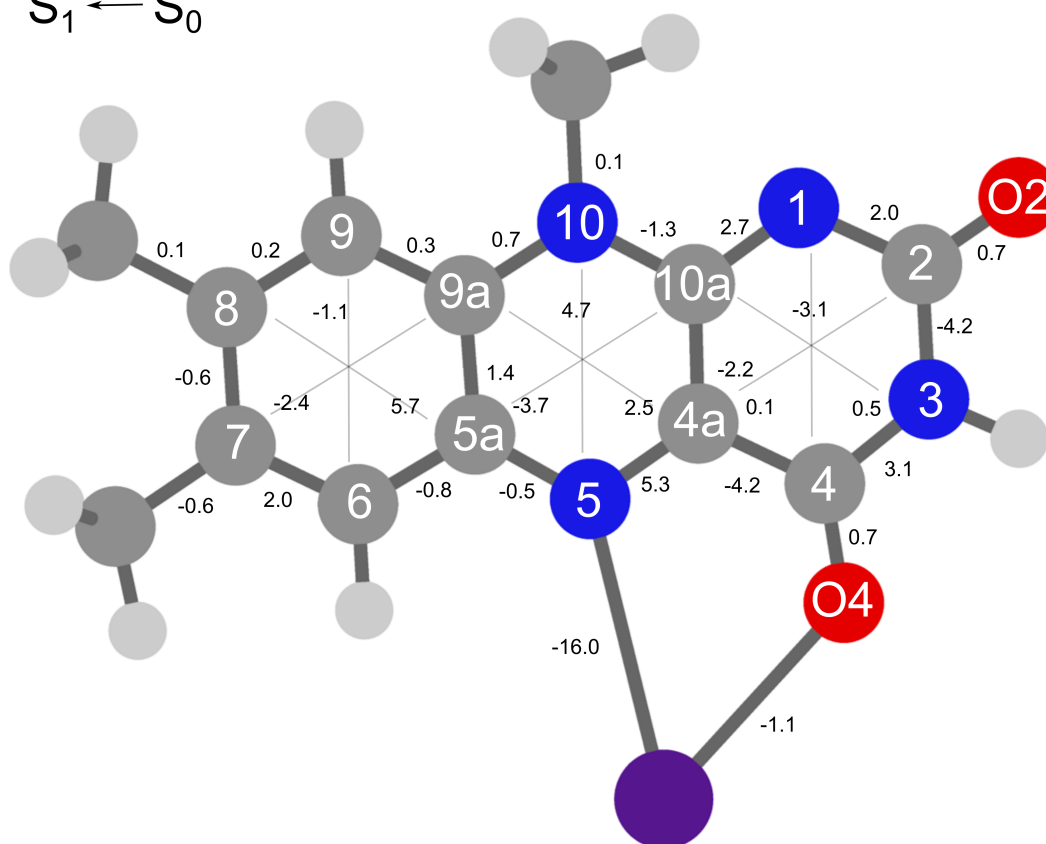
S₁ ← S₀



Cs⁺LF
S₀

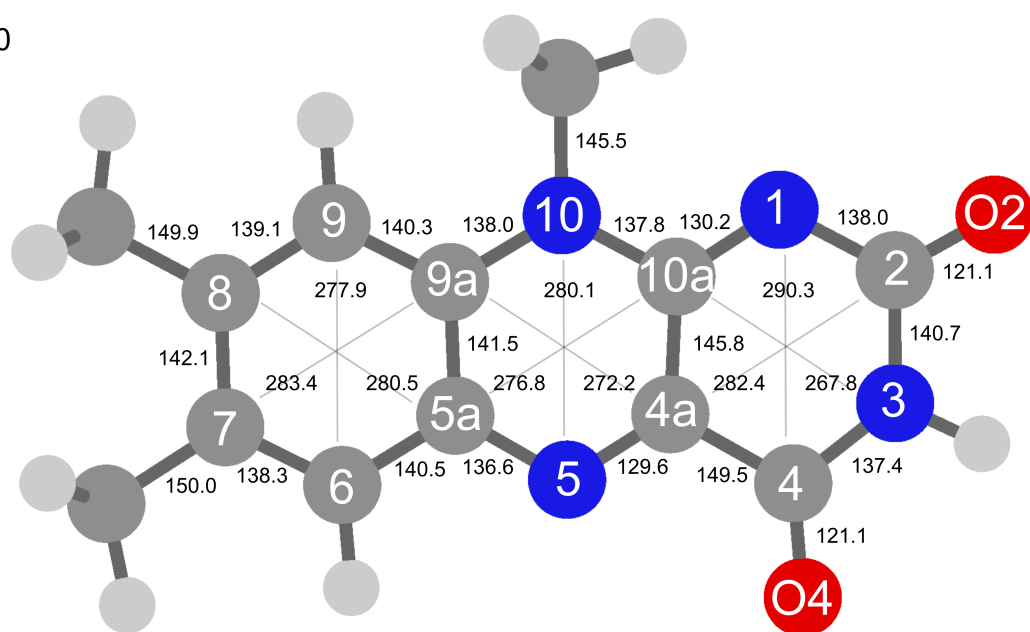


S₁ ← S₀



LF

S_0



$S_1 \leftarrow S_0$

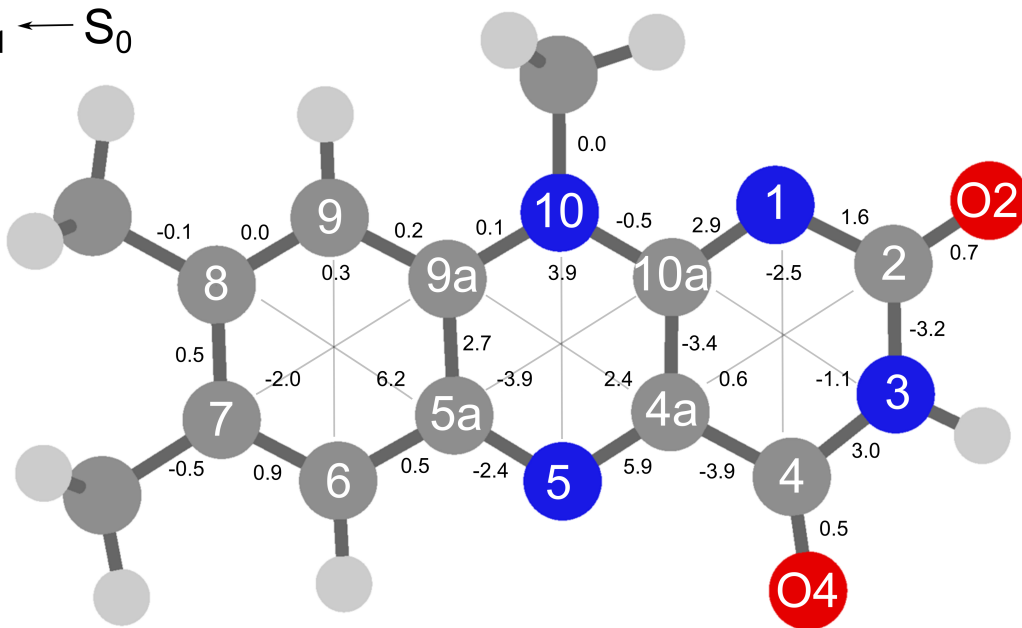


Figure S6. Dependence of the S_1 origin intensities of M^+LF with $M=Li-Cs$ on the laser pulse energy compared to a fit to a polynomial with degree $n=1$ (linear, $M=Na-Cs$) and $n=1-3$ (linear, quadratic, cubic; $M=Li$). While for $M=Na-Cs$, the linear fit reproduces the experimental data points well, for Li clearly a quadratic (blue) to cubic (pink) function fits much better.

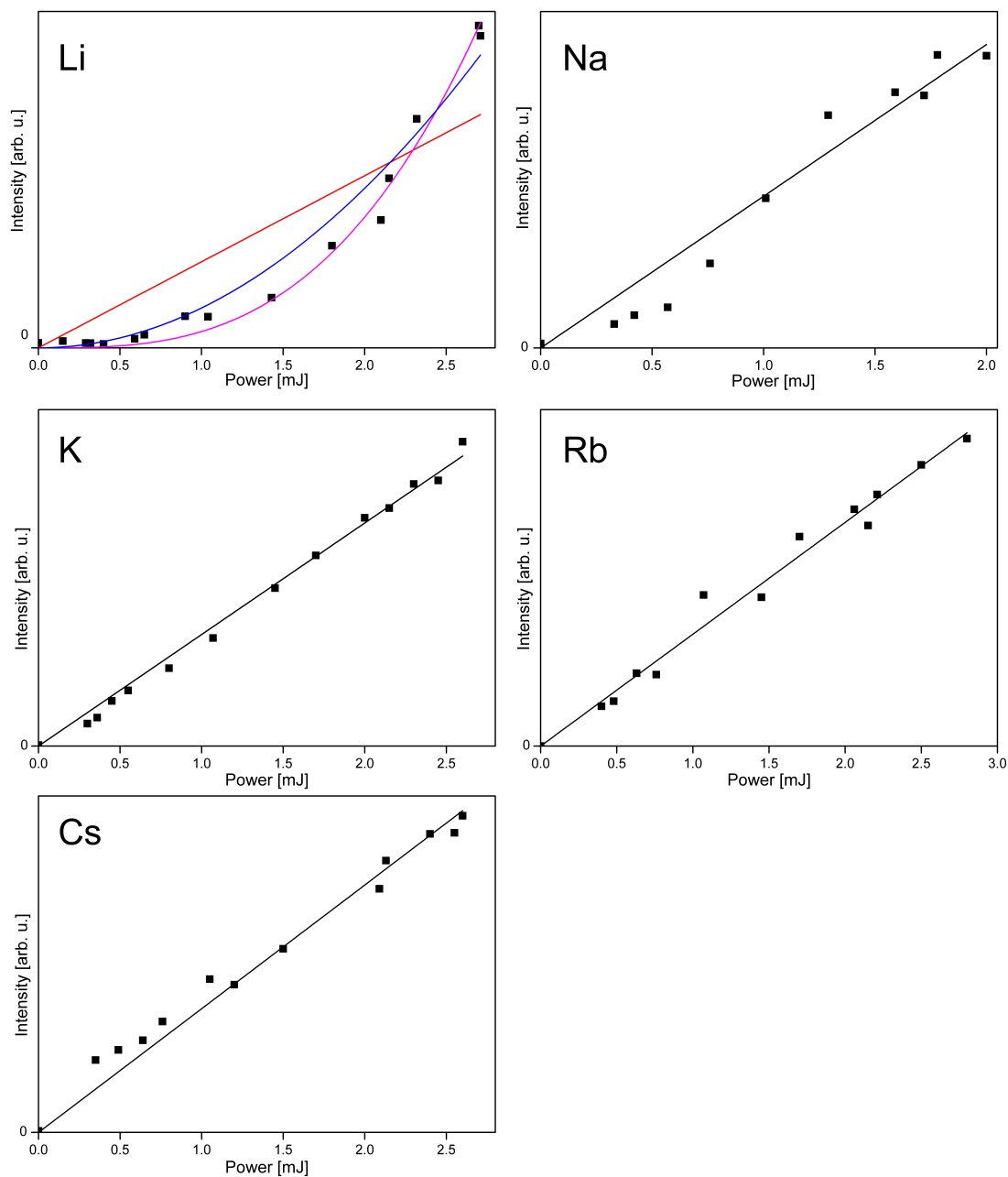


Table S1. Experimental frequencies for vibronic transitions (in cm^{-1}) observed in the VISPD spectra of the S_1 states of M^+LF ($M=\text{Li-Cs}$) compared to harmonic frequencies of the $M^+LF(O4^+)$ isomers computed at the PBE0/cc-pVDZ level, along with the mode assignment. The normal modes \square , \square , and m1 etc. are similar to those of $M^+LC(O4^+)$ discussed in Nieto et al. PCCP **20**, 22148 (2018). The m4* mode is special to the LF chromophore and corresponds to the in-plane bend of the CH_3 group at N10.

Li^+LF

	\square (exp)	\square (calc)	Assignment
	17645	18022	0^0
A	163	167	m1
B	281	284	m2
C	292	297	m3
D	311	318	m4
E	326	334	2m1
F	368	375	\square
G	410	419	m5
H	440	447	m6
I	446	451	m1+m2
J	456	464	m1+m3
K	477	485	m1+m4
L	490	501	3m1
		501	m7
M	503	515	m8
N	533	542	\square +m1

Na⁺LF

	ν (exp)	ν (calc)	Assignment
	18310	18784	ν_0
A	128	134	ν
B	187	194	m1
C	234	240	ν
D	256	268	2ν
E	279	295	m2
F	286	298	m3
G	313	328	m1+ ν
H	338	343	m4
I	355	361	m4*
J	363	374	$\nu + \nu$
K	371	388	2m1
L	382	402	3ν
M	407	429	m2+ ν
N	414	432	m3+ ν
O	426	434	m1+ ν
		433	m6
P	439	462	m1+2 ν
Q	447	455	m5
R	465	489	m1+m2
S	473	492	m1+m3
T	497	498	m7

K⁺LF

	\square (exp)	\square (calc)	Assignment
	18778	19279	0^0
A	82	86	\square
B	157	162	\square
C	164	172	$2\square$
D	194	202	m1
E	236	248	$\square + \square$
F	247	258	$3\square$
G	278	288	m1+ \square
H	286	287	m2
I	302	295	m3
J	311	324	$2\square$
K	318	334	$\square + 2\square$
L	335	332	m4
M	350	364	m1+ \square
N	360	360	m4*
O	371	373	m2+ \square
P	378	381	m3+ \square
Q	386	404	2m1
R	401	420	$3\square + \square$
S	415	418	m4+ \square
	415	421	m6
T	435	449	m2+ \square
U	443	450	m5
		457	m3+ \square

Rb⁺LF

	λ (exp)	λ (calc)	Assignment
	18914	19451	0^0
A	57	60	π
B	112	120	2π
C	124	130	π
D	172	180	3π
E	179	190	$\pi+\pi$
F	184	185	m1
G	240	245	m1+ π
H	249	260	2π
I	285	285	m2
J	296	296	m3
K	303	315	m1+ π
L	308	320	$2\pi+\pi$
M	335	330	m4
N	361	360	m4*
O	366	370	2m1
P	402	415	m2+ π
Q	413	419	m6
R	422	426	m3+ π
S	457	460	m4+ π
	458	450	m5
T	468	470	m1+m2
U	480	481	m1+m3
V	489	495	m7

Cs⁺LF

	ν (exp)	ν (calc)	Assignment
	19031	19658	0^0
A	44	45	ν
B	88	90	2ν
C	108	111	ν
D	148	156	$\nu + \nu$
E	175	179	m1
F	196	201	$2\nu + \nu$
G	214	222	2ν
		224	m1 + ν
H	254	267	$2\nu + \nu$
I	264	269	$2\nu + m1$
J	276	283	m2
	284	294	m3
	280	290	m1 + ν
K	299	312	$2\nu + 2\nu$
L	311	314	$3\nu + m1$
M	320	328	m4
N	350	360	m4*
		358	2m1
O	387	401	$2\nu + m1$
P	401	416	m5
Q	410	449	m6
R	427	439	m4 + ν
S	457	462	m1 + m2
		473	m1 + m3
T	493	505	$2\nu + m2$
		516	$2\nu + m3$

Table S2. Low-energy intramolecular in-plane vibrational frequencies (in cm^{-1}) in the S_1 state of LF and $M^+LF(O4^+)$ with $M=\text{Li-Cs}$ calculated at the PBE0/cc-pVDZ level compared to experimental data.

	Li		Na		K		Rb		Cs		LF	
mode	S_1	exp	S_1	exp	S_1	exp	S_1	exp	S_1	exp	S_1	exp ^a
m1	167	163	194	187	202	194	185	184	179	175	165	164
m2	284	281	295	279	287	286	285	285	283	276	276	274
m3	297	292	298	286	295	302	296	296	294	284	294	
m4	318	311	343	338	332	335	330	335	328	320	322	
m4*	352	?	361	355	360	360	360	361	360	350	358	
m5	419	410	455	447	450	443	450	458	416	401	409	403
m6	447	440	433	426	421	415	419	413	449	410	444	440
m7	501	490	498	497	495		495	489	494		489	
m8	515	503	532		529		528		527		521	513
m9	550		550		549		548		548		545	
m10	577		615		613		613		612		603	593

^a Values from He droplet spectrum (Vdovin et al., Chem. Phys. **422**, 195 (2013)).

Table S3. Harmonic vibrational frequencies (cm^{-1}) of LF and $\text{M}^+\text{LF}(\text{O4}^+)$ with $\text{M}=\text{Li}-\text{Cs}$ in the S_0 and S_1 states (Mulliken notation) calculated at the PBE0/cc-pVDZ level.

Li^+LF

S_0 a''	a'	S_1 a''	a'
46.85	164.09	45.80	166.92
64.48	285.88	57.73	283.96
101.47	298.62	90.87	297.11
120.86	320.32	112.89	317.69
135.00	335.66	119.11	351.67
161.78	362.05	147.99	374.52
176.86	410.92	169.39	419.09
190.42	444.09	198.42	446.95
194.68	500.34	200.01	500.61
215.65	509.69	217.53	515.39
252.45	556.19	232.78	549.96
340.73	582.01	338.71	577.23
383.39	617.92	357.70	625.65
459.44	646.66	416.33	639.86
537.63	697.44	492.65	691.88
638.62	760.18	621.71	746.80
679.01	798.10	645.33	795.03
752.12	855.69	680.04	845.84
769.85	886.93	731.71	888.00
791.25	997.73	759.06	997.64
829.29	1013.00	776.78	1013.32
873.94	1027.44	876.62	1021.82
884.24	1036.67	885.79	1032.01
1027.15	1107.54	1012.24	1101.12
1052.28	1179.32	1043.14	1176.54
1132.73	1211.87	1128.75	1192.69
1438.96	1221.30	1432.09	1224.94
1454.57	1267.25	1450.63	1250.94
1476.59	1278.79	1467.44	1276.38
3134.01	1343.95	3118.36	1300.80
3138.19	1363.63	3131.67	1342.36
3175.52	1376.22	3172.87	1363.82
	1388.08		1376.96
	1396.39		1387.87
	1402.34		1393.48
	1423.46		1406.25
	1436.04		1414.53
	1452.02		1418.02
	1463.86		1441.58
	1490.98		1457.05
	1495.85		1468.45
	1524.91		1488.39
	1548.71		1522.23
	1594.36		1531.60
	1630.44		1563.26
	1667.54		1610.16
	1709.16		1675.88
	1769.57		1716.74
	1870.70		1783.13
	3061.91		3051.13
	3063.68		3059.58
	3080.78		3080.45
	3173.74		3175.03
	3181.08		3179.01
	3204.75		3212.94
	3221.60		3230.14
	3252.45		3247.13
	3584.82		3614.12

Na⁺LF

S ₀ a''	a'	S ₁ a''	a'
40.66	121.09	41.18	133.81
62.83	180.67	54.05	194.08
71.99	240.50	62.86	240.31
101.53	296.25	99.92	294.68
134.75	300.06	118.95	297.53
146.50	346.49	121.54	343.05
165.62	357.71	158.87	360.71
175.42	425.82	176.81	432.95
193.12	452.63	193.81	454.74
211.54	505.12	217.30	497.95
252.78	528.12	233.06	531.67
339.89	553.90	338.13	550.14
381.65	609.82	351.41	615.07
458.18	644.18	415.97	637.05
532.04	686.17	490.23	677.91
638.58	761.41	621.77	746.62
678.75	795.26	647.13	790.41
750.87	850.00	680.85	838.44
771.43	885.49	733.19	885.92
788.95	999.32	757.77	998.37
829.12	1019.14	773.94	1016.02
873.03	1028.13	875.89	1022.83
880.41	1035.85	877.21	1029.60
1027.32	1106.43	1013.70	1101.79
1052.76	1177.00	1043.50	1176.27
1133.49	1216.41	1129.12	1190.05
1439.70	1220.46	1433.77	1223.74
1455.05	1267.68	1451.34	1248.19
1477.76	1276.40	1467.35	1274.52
3133.54	1340.31	3120.46	1297.74
3137.06	1364.38	3129.47	1336.38
3173.74	1378.51	3171.21	1364.61
	1389.01		1379.03
	1397.45		1391.31
	1403.27		1393.56
	1422.12		1404.36
	1436.34		1411.85
	1451.12		1421.91
	1463.99		1439.38
	1481.84		1453.24
	1489.16		1468.35
	1521.62		1486.17
	1547.72		1502.78
	1597.24		1530.67
	1630.79		1563.33
	1670.05		1602.30
	1710.43		1667.46
	1779.38		1729.31
	1866.28		1771.41
	3061.52		3052.51
	3062.68		3058.09
	3079.98		3079.95
	3170.67		3173.37
	3179.69		3176.37
	3197.99		3206.71
	3221.70		3232.83
	3251.67		3246.74
	3591.73		3619.24

K⁺LF

S ₀ a''	a'	S ₁ a''	a'
33.28	71.25	35.14	86.20
53.30	154.94	48.52	161.94
63.03	199.72	52.51	201.59
101.23	289.03	94.57	287.33
134.90	299.02	112.43	294.64
141.10	336.12	124.24	332.25
160.82	357.19	157.08	359.95
175.04	414.70	173.93	421.37
192.66	449.56	194.07	450.45
209.95	503.87	216.74	495.40
252.38	525.99	234.14	528.73
338.54	550.79	336.64	548.86
380.45	608.75	346.57	613.03
457.57	643.77	414.32	637.05
528.38	683.14	485.85	674.90
638.46	761.81	620.38	746.07
678.88	794.07	645.42	788.22
749.01	846.78	678.68	834.97
772.13	884.78	732.54	884.78
787.73	999.41	757.28	998.54
828.84	1020.75	772.29	1016.98
873.35	1028.00	874.19	1022.83
880.70	1035.53	875.49	1028.62
1027.55	1106.46	1014.07	1101.36
1053.10	1175.68	1043.35	1175.17
1133.95	1214.19	1129.22	1187.02
1440.11	1221.46	1434.04	1222.80
1455.35	1267.09	1452.28	1244.86
1478.20	1275.12	1467.47	1271.92
3132.97	1338.20	3120.05	1296.11
3136.05	1363.92	3128.28	1332.59
3172.53	1378.62	3170.76	1364.15
	1389.26		1377.59
	1397.44		1391.08
	1402.91		1393.71
	1421.19		1402.47
	1436.36		1411.56
	1450.53		1421.95
	1464.07		1438.02
	1476.99		1452.71
	1487.38		1468.05
	1522.16		1485.12
	1547.34		1498.49
	1598.63		1531.31
	1629.97		1561.82
	1669.58		1595.82
	1710.69		1663.38
	1774.86		1725.81
	1864.14		1766.56
	3061.00		3051.90
	3061.84		3057.42
	3079.43		3080.29
	3168.33		3172.57
	3178.54		3173.89
	3200.43		3208.25
	3221.63		3234.10
	3250.50		3247.29
	3594.23		3620.17

Rb⁺LF

S ₀ a''	a'	S ₁ a''	a'
27.69	48.35	29.52	59.59
49.43	124.38	45.31	129.78
62.77	183.28	51.22	184.94
101.25	286.87	93.20	285.01
134.94	298.76	111.07	296.24
139.16	333.44	122.99	329.65
159.40	357.14	155.39	360.12
175.00	412.17	171.14	418.75
192.60	448.92	190.75	449.73
209.84	503.67	216.80	494.86
252.42	525.34	233.67	527.77
338.41	550.12	335.37	548.31
380.40	608.52	346.61	612.58
457.50	643.68	414.62	637.23
527.81	682.45	485.87	673.84
638.67	761.98	621.10	746.11
678.83	793.89	645.64	787.77
748.37	846.25	678.70	834.19
772.79	884.64	733.12	884.60
787.14	999.56	757.15	998.54
828.79	1021.35	771.33	1017.26
873.52	1028.36	873.27	1022.88
882.00	1035.55	874.37	1028.21
1027.69	1106.49	1014.62	1101.72
1053.22	1175.28	1043.54	1175.22
1134.15	1213.54	1129.31	1186.87
1440.29	1222.23	1434.71	1222.31
1455.50	1267.16	1451.73	1244.15
1478.39	1274.83	1467.33	1272.74
3132.74	1337.87	3121.10	1296.12
3135.65	1363.97	3127.38	1332.46
3172.10	1378.88	3169.31	1364.23
	1389.39		1379.75
	1397.56		1391.41
	1403.20		1393.56
	1420.92		1402.39
	1436.53		1411.78
	1450.50		1422.38
	1464.22		1438.16
	1474.86		1451.84
	1487.04		1468.18
	1522.68		1484.59
	1547.48		1496.58
	1599.66		1531.78
	1630.20		1562.26
	1670.35		1594.69
	1711.23		1662.68
	1778.38		1730.02
	1863.30		1764.05
	3060.77		3052.84
	3061.60		3056.68
	3079.21		3079.09
	3167.70		3171.84
	3178.20		3173.81
	3203.00		3208.67
	3221.48		3233.74
	3250.16		3245.56
	3596.31		3622.73

Cs⁺LF

S₀ a''	a'	S₁ a''	a'
24.53	36.18	26.45	45.23
47.98	106.71	44.41	111.28
63.24	177.42	51.55	178.82
100.53	285.73	92.01	283.06
135.61	296.81	110.42	294.32
138.26	331.32	124.88	327.50
159.04	357.34	155.59	359.86
175.36	409.88	172.01	415.68
194.52	448.72	193.16	449.16
210.78	503.77	216.64	494.24
251.98	525.09	234.41	527.09
338.65	549.17	335.11	547.99
379.68	608.29	346.09	611.82
457.37	643.61	414.29	637.22
526.89	681.66	485.06	673.13
638.44	761.90	620.19	745.89
678.84	793.90	644.64	787.38
748.08	845.29	678.14	833.49
773.30	884.19	733.01	884.13
787.03	999.95	757.30	998.65
829.63	1021.47	771.70	1017.51
874.58	1028.02	873.79	1022.56
884.48	1035.97	874.56	1028.16
1027.67	1106.28	1014.38	1101.42
1052.86	1174.85	1043.30	1174.59
1134.63	1212.36	1129.38	1185.38
1440.37	1221.89	1434.45	1222.12
1456.16	1265.86	1452.85	1243.50
1478.52	1273.66	1467.51	1271.27
3132.24	1338.00	3120.01	1295.11
3134.66	1363.34	3127.08	1331.85
3172.58	1379.19	3169.73	1364.31
	1389.12		1377.80
	1396.30		1390.94
	1402.75		1393.79
	1420.67		1402.13
	1436.69		1411.96
	1450.29		1421.98
	1464.76		1437.64
	1474.40		1452.03
	1486.57		1468.08
	1523.24		1484.62
	1547.35		1496.70
	1600.76		1532.39
	1629.71		1561.31
	1669.89		1592.47
	1711.68		1661.65
	1775.12		1725.79
	1863.00		1763.29
	3059.90		3051.90
	3061.46		3056.62
	3079.78		3079.83
	3166.70		3171.88
	3178.14		3173.18
	3207.69		3211.63
	3221.55		3234.35
	3250.23		3246.61
	3596.70		3623.06

LF

S ₀ a''	a'	S ₁ a''	a'
44.12	164.63	-36.80	164.70
63.49	278.64	47.65	276.27
101.17	295.23	62.18	293.63
124.45	325.76	99.41	321.95
136.53	354.64	125.23	357.65
152.60	405.04	145.50	408.51
173.49	444.67	157.24	444.31
192.34	502.42	186.72	489.35
208.16	517.89	211.58	520.79
249.83	545.57	240.34	544.73
334.97	606.65	321.66	602.81
379.05	642.39	336.71	635.25
456.38	679.87	415.38	668.92
519.95	763.83	477.25	742.81
638.38	794.02	615.94	783.00
674.99	842.21	652.15	830.00
731.99	883.28	674.17	878.13
780.20	1000.62	738.58	999.58
788.18	1020.38	761.60	1014.18
836.46	1036.16	773.10	1018.56
866.02	1040.18	858.96	1026.85
925.25	1108.42	899.87	1096.28
1030.99	1176.49	1019.18	1174.61
1056.48	1204.99	1043.60	1189.12
1137.55	1235.73	1130.81	1202.07
1443.48	1267.87	1438.58	1243.78
1458.75	1273.70	1453.48	1265.39
1480.40	1337.58	1467.07	1289.83
3121.66	1363.66	3109.02	1337.17
3126.09	1383.05	3115.47	1360.96
3156.35	1390.32	3149.30	1381.40
	1397.39		1390.85
	1408.38		1394.29
	1414.97		1397.55
	1429.25		1416.21
	1439.09		1422.54
	1451.97		1428.25
	1466.90		1452.73
	1479.05		1464.10
	1527.08		1478.06
	1551.50		1486.67
	1617.39		1540.63
	1632.00		1554.83
	1678.15		1575.29
	1713.97		1651.06
	1836.54		1737.38
	1848.67		1809.22
	3052.84		3044.10
	3055.10		3048.55
	3069.11		3066.56
	3165.21		3157.68
	3166.04		3171.41
	3210.65		3223.92
	3224.44		3226.81
	3238.45		3233.27
	3619.17		3632.26

Table S4. Selected atomic charges (in e) of $M^+LF(O4^+)$ and LF in the S_0 and S_1 states using natural bond orbital analysis (PBE0/cc-pVDZ).

	q_M		q_{N5}		q_{O4}		q_{O2}		q_{N1}	
	S_0	S_1	S_0	S_1	S_0	S_1	S_0	S_1	S_0	S_1
Li	0.881	0.860	-0.519	-0.619	-0.738	-0.744	-0.536	-0.497	-0.632	-0.482
Na	0.922	0.908	-0.494	-0.595	-0.723	-0.733	-0.545	-0.505	-0.636	-0.481
K	0.922	0.909	-0.467	-0.569	-0.725	-0.736	-0.550	-0.509	-0.639	-0.481
Rb	0.928	0.915	-0.459	-0.561	-0.721	-0.732	-0.553	-0.511	-0.640	-0.482
Cs	0.917	0.906	-0.446	-0.550	-0.724	-0.736	-0.555	-0.513	-0.641	-0.483
LF			-0.376	-0.454	-0.577	-0.592	-0.598	-0.570	-0.660	-0.508

Table S5. Vertical transition energies (λ in cm^{-1} , λ in nm) and oscillator strength (f) for the first four excited singlet states of $M^+LF(O2)$ with $M=Li-Cs$ and $M^+LF(O2^+)$ with $M=Li-K$ calculated at the PBE0/cc-pVDZ level.^a

O2	S_1 ($\pi\pi^*$)			S_2 ($n\pi^*$)			S_3 ($n\pi^*/\pi\pi^*$)			S_4 ($n\pi^*/\pi\pi^*$)		
	λ	λ	F	λ	λ	f	λ	λ	f	λ	λ	f
Li	25735	388.57	0.174	27090	369.14	0.001	29171	342.81	0.263	29344	340.79	0.000
Na	25746	388.41	0.193	27077	369.32	0.001	29267	341.68	0.000	29581	338.06	0.240
K	25698	389.14	0.204	27066	369.47	0.001	29202	342.44	0.000	29722	336.45	0.234
Rb	25674	389.50	0.210	27055	369.62	0.001	29162	342.91	0.000	29802	335.55	0.234
Cs	25650	389.87	0.216	27039	369.83	0.001	29129	343.30	0.000	29839	335.13	0.234

O2+	S_1 ($\pi\pi^*$)			S_2 ($n\pi^*$)			S_3 ($n\pi^*/\pi\pi^*$)			S_4 ($n\pi^*/\pi\pi^*$)		
	λ	λ	F	λ	λ	f	λ	λ	f	λ	λ	f
Li	26159	382.28	0.138	27728	360.64	0.001	29175	342.76	0.303	29916	334.27	0.000
Na	26191	381.81	0.165	27332	365.87	0.005	29443	339.64	0.235	29762	336.00	0.040
K	26063	383.69	0.191	27161	368.18	0.001	29413	339.99	0.000	29697	336.73	0.250

^a The character of the S_3/S_4 states depend on the metal. The optically bright $\pi\pi^*$ states have large f values, while the optically dark $n\pi^*$ states have f values close to 0.

Electronic Supporting Information

Optical Spectroscopy of Cryogenic Metalated Flavins: The O2(+) Isomers of M⁺Lumiflavin (M=Li-Cs)

David Müller and Otto Dopfer*

Institut für Optik und Atomare Physik, Technische Universität Berlin, Hardenbergstr. 36, D-10623 Berlin, Germany

* corresponding author: dopfer@physik.tu-berlin.de; Fax: +49 30 314 23018

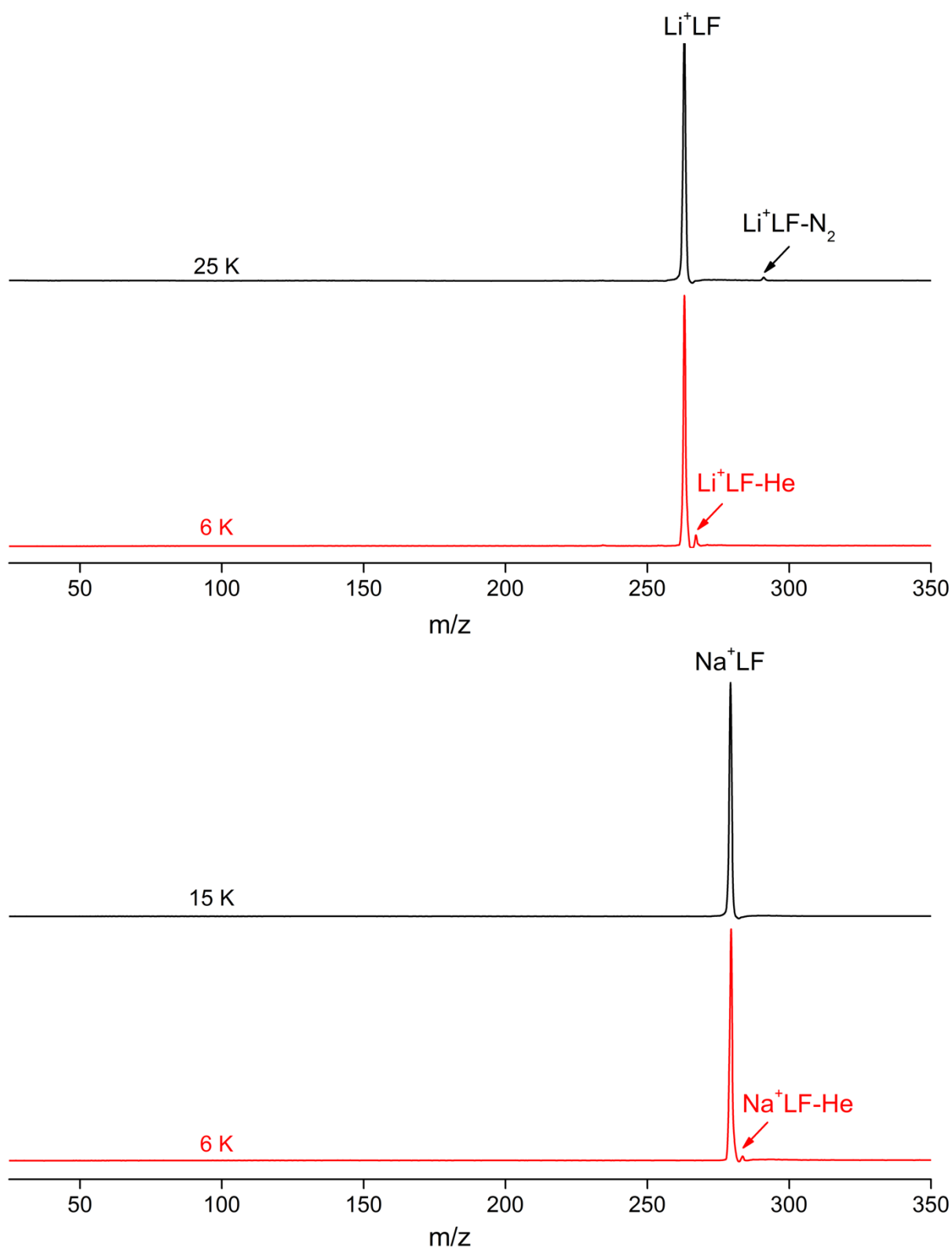


Figure S1. Laser-off mass spectra of mass-selected Li^+LF and Na^+LF ions trapped in the 22-pole recorded at trap temperatures of 15 or 25 K (black) and 6 K (red). At $T=6$ K, $\text{Na}^+\text{LF-He}$ (1.6%) and Li-LF-He (2%) clusters are formed in the trap. At 15 and 25 K, these He clusters disappear but instead $\text{Li}^+\text{LF-N}_2$ clusters are formed in the trap (1.3%).

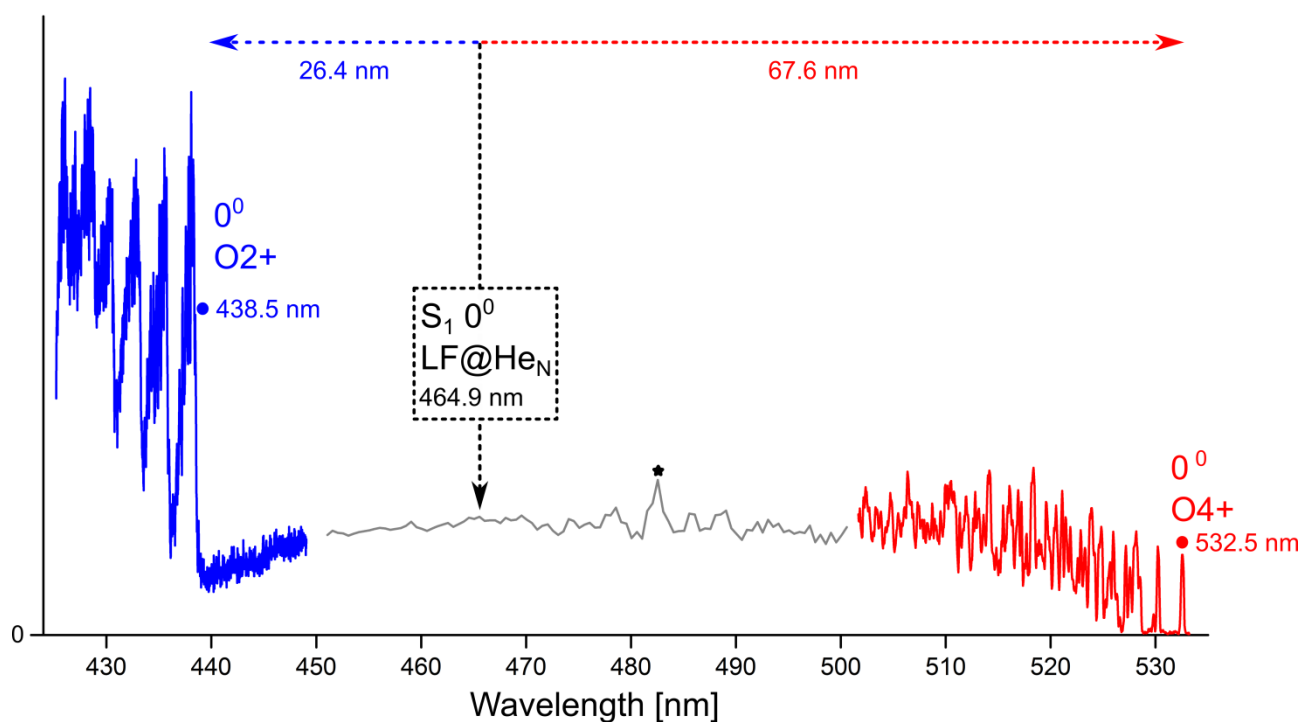


Figure S2. Overview VISPD spectrum of K⁺LF. The red part is attributed to the S₁←S₀ (ππ*) transition of the O4+ isomer. The blue part is attributed to the S₁←S₀ (ππ*) of the O2+ isomer. The 0⁰ origins of both isomers are marked. The value of the S₁ band origin of LF@He_N at 464.9 nm is marked with an arrow, along with shifts of the 0⁰ transitions of the K⁺LF complexes. The grey range is measured at an enlarged step size of 0.5 nm. The peak marked with an asterisk is an artefact and arises from a drop in the laser intensity.

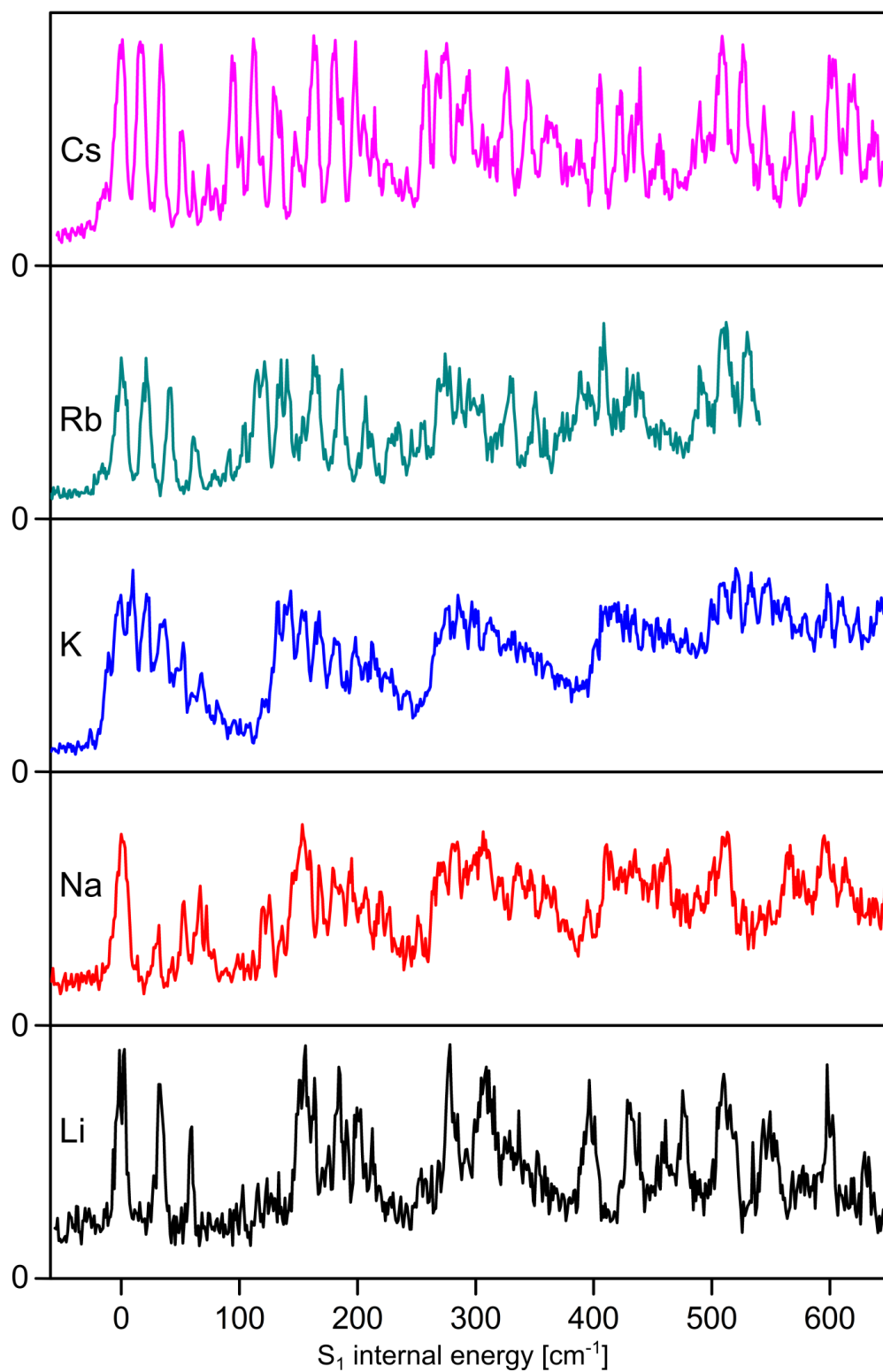
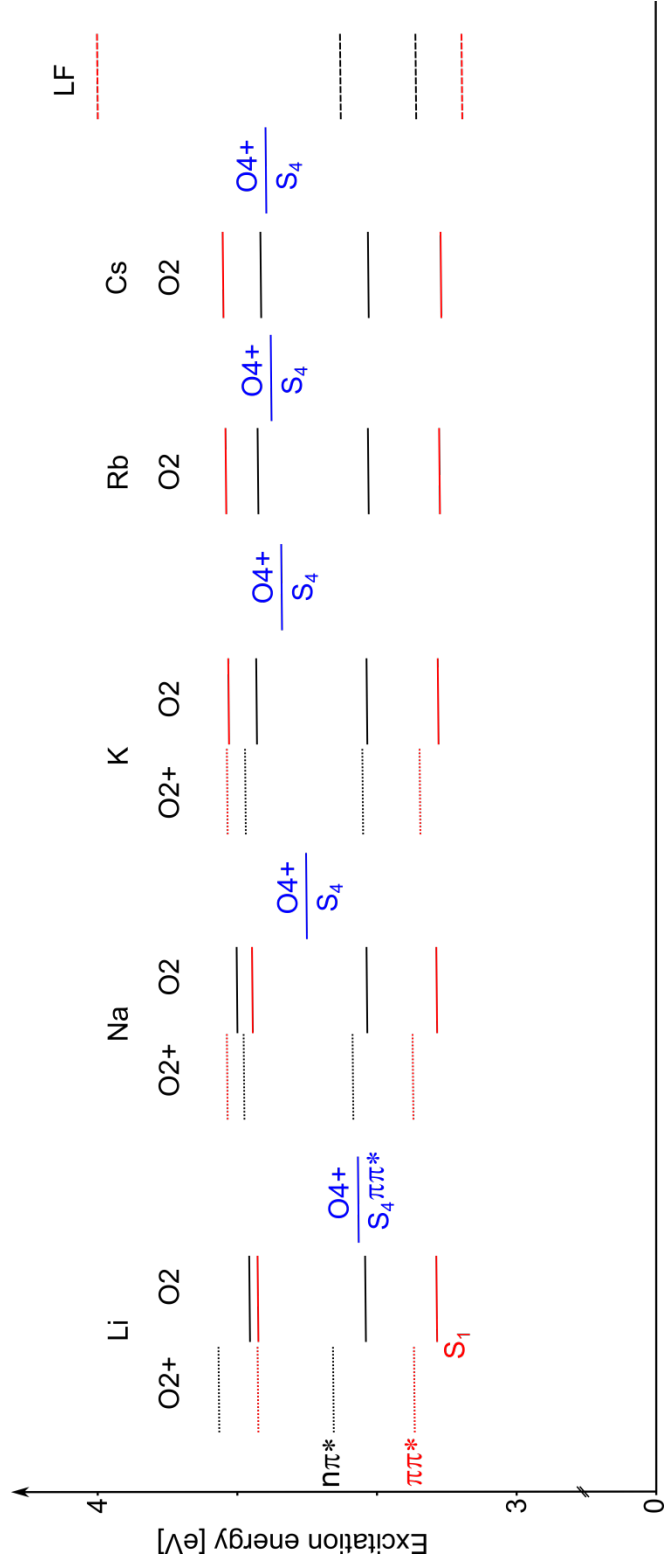


Figure S3. VISP spectra of M^+LF ($M=\text{Li-Cs}$) recorded at a trap temperature of $T=6$ K plotted as a function of S_1 internal energy.

Figure S4. Vertical S_1 - S_4 excitation energies (PBE0/cc-pVDZ) of $M^+LF(O_2/O_2^+)$ with $M=Li-Cs$ and LF originating from the optimized S_0 ground state. Red data is associated with bright $\pi\pi^*$ transitions, black data corresponds to dark $n\pi^*$ transitions. Blue data corresponds to the second optically bright state S_4 ($\pi\pi^*$) of the O_4^+ isomer. The $S_{2/3}$ states of the O_4^+ isomer are optically dark $n\pi^*$ states and not visualized. Oscillator strengths and excitation energies are presented in Table S2.



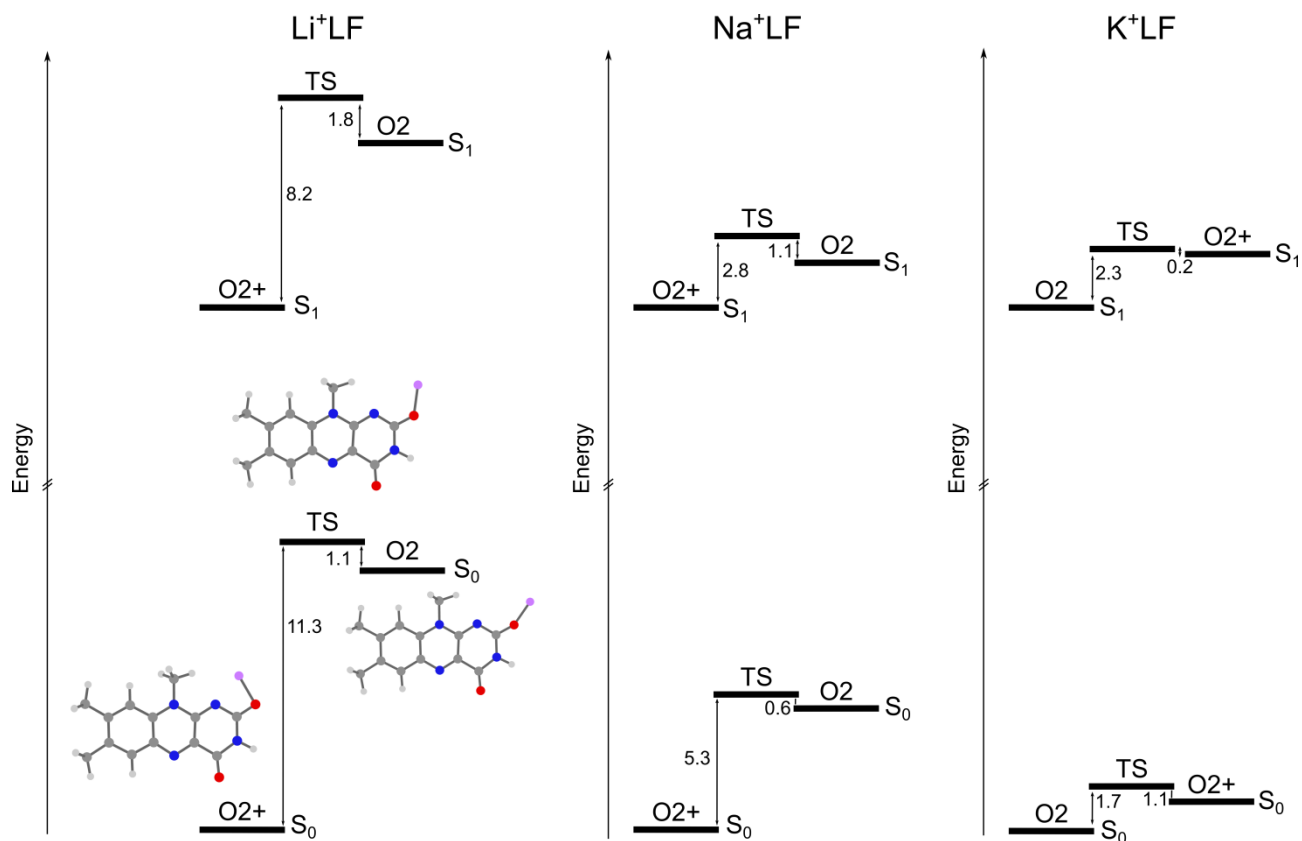


Figure S5. Potential energy diagram (without zero-point energy corrections) of Li^+LF (left), Na^+LF (middle), and K^+LF (right) for the O_2 and O_2^+ isomers and the transition state (TS) in the electronic ground state (S_0) and the first excited singlet state (S_1) computed at the PBE0/cc-pVDZ level. Values are given in kJ/mol.

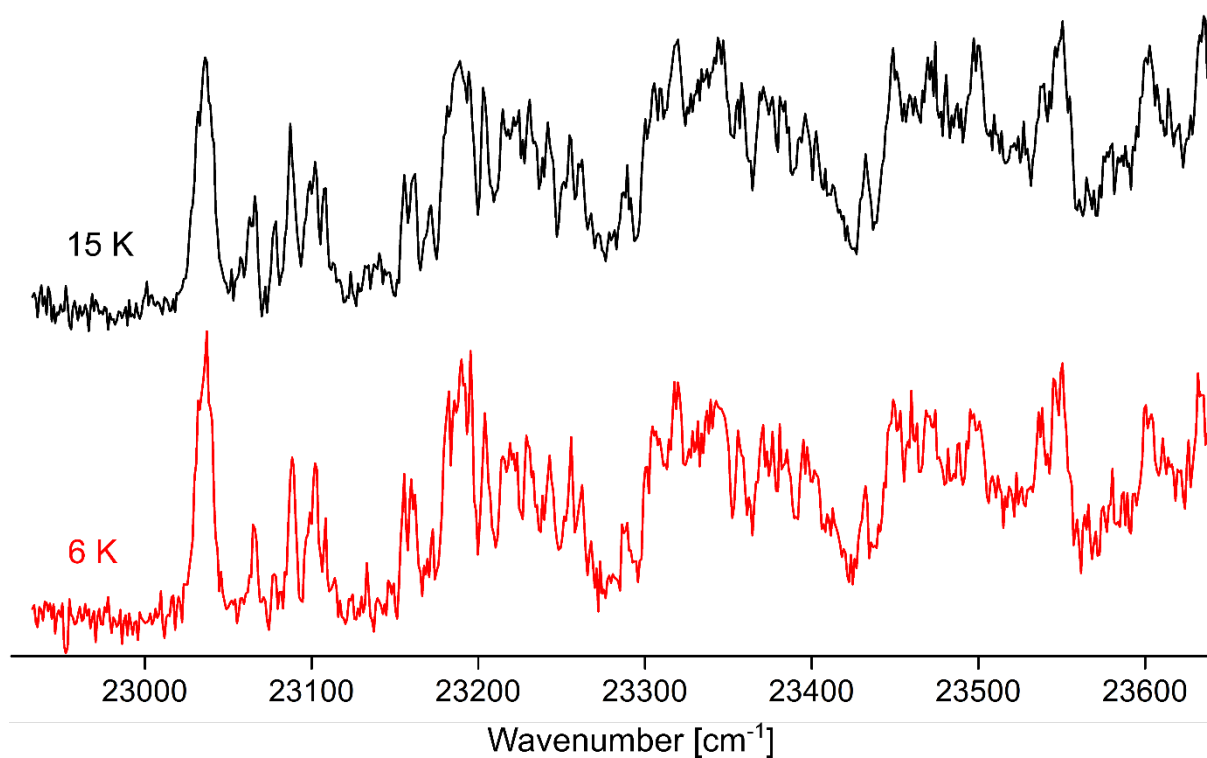


Figure S6. VISPD spectra of Na⁺LF recorded at trap temperatures of 15 K (black) and 6 K (red). Both spectra are essentially the same in terms of band positions and relative intensities. Hence, the minor presence of Na⁺LF-He clusters at 6 K (Figure S1) cannot be responsible for peaks observed in the measured VISPD spectra.

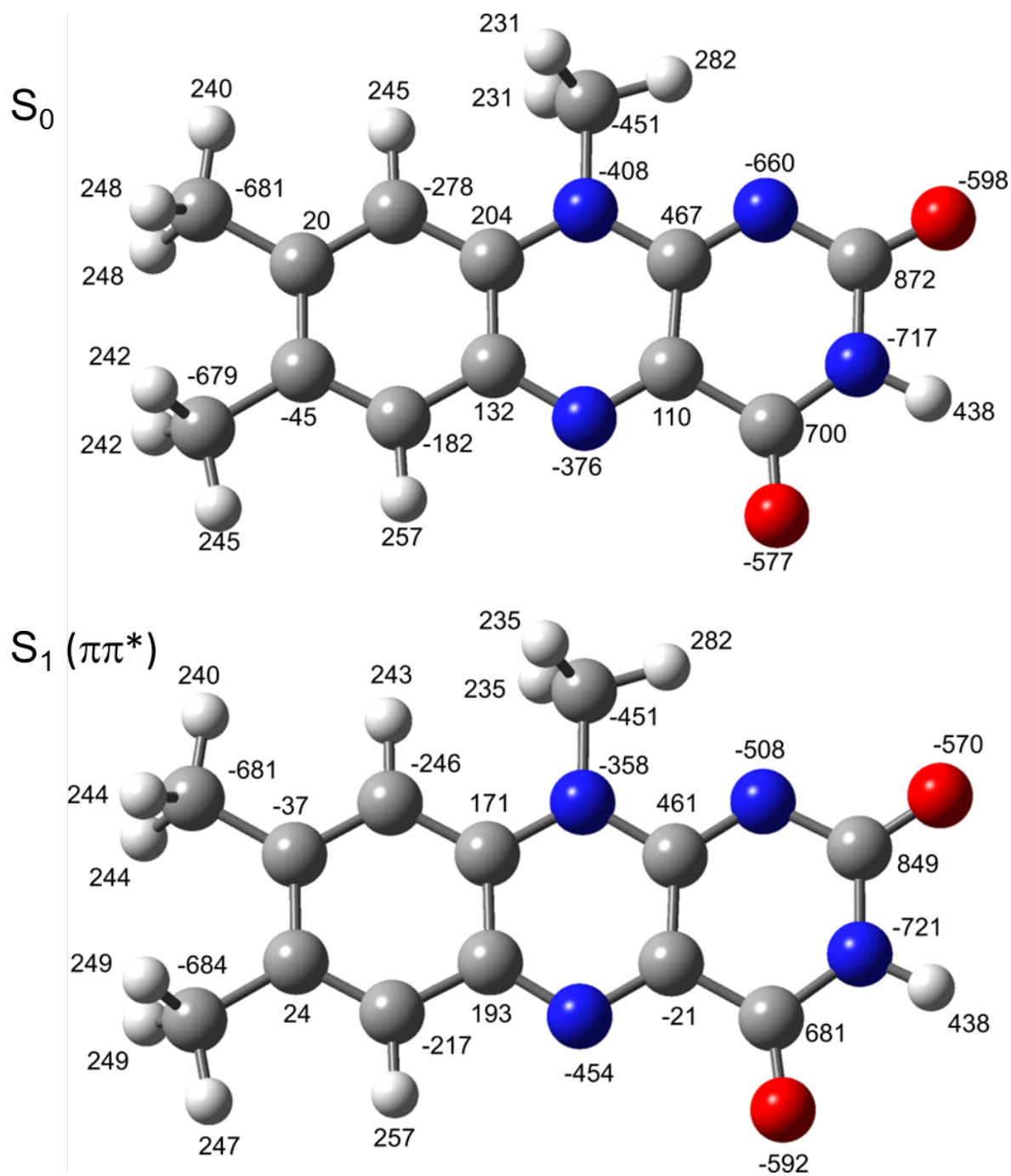


Figure S7. NBO atomic charge distribution of LF (in $10^{-3} e$, PBE0/cc-pVDZ) in the S_0 and S_1 state.

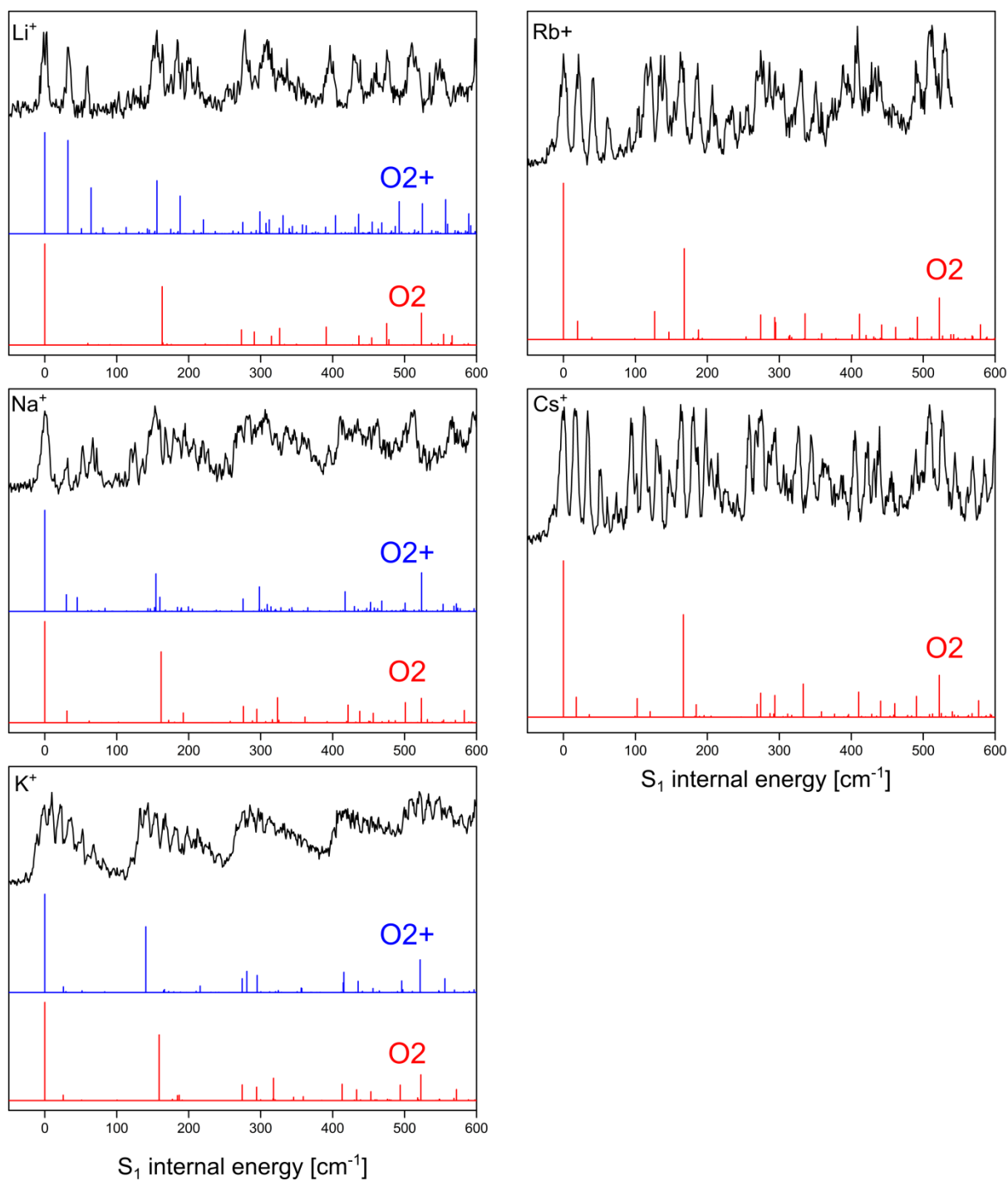


Figure S8. Comparison between VISP spectra of M^+LF with $M=Li-Cs$ and Franck-Condon simulations (PBE0/cc-pVDZ) for the $O_2(+)$ isomers as a function of S_1 internal energy.

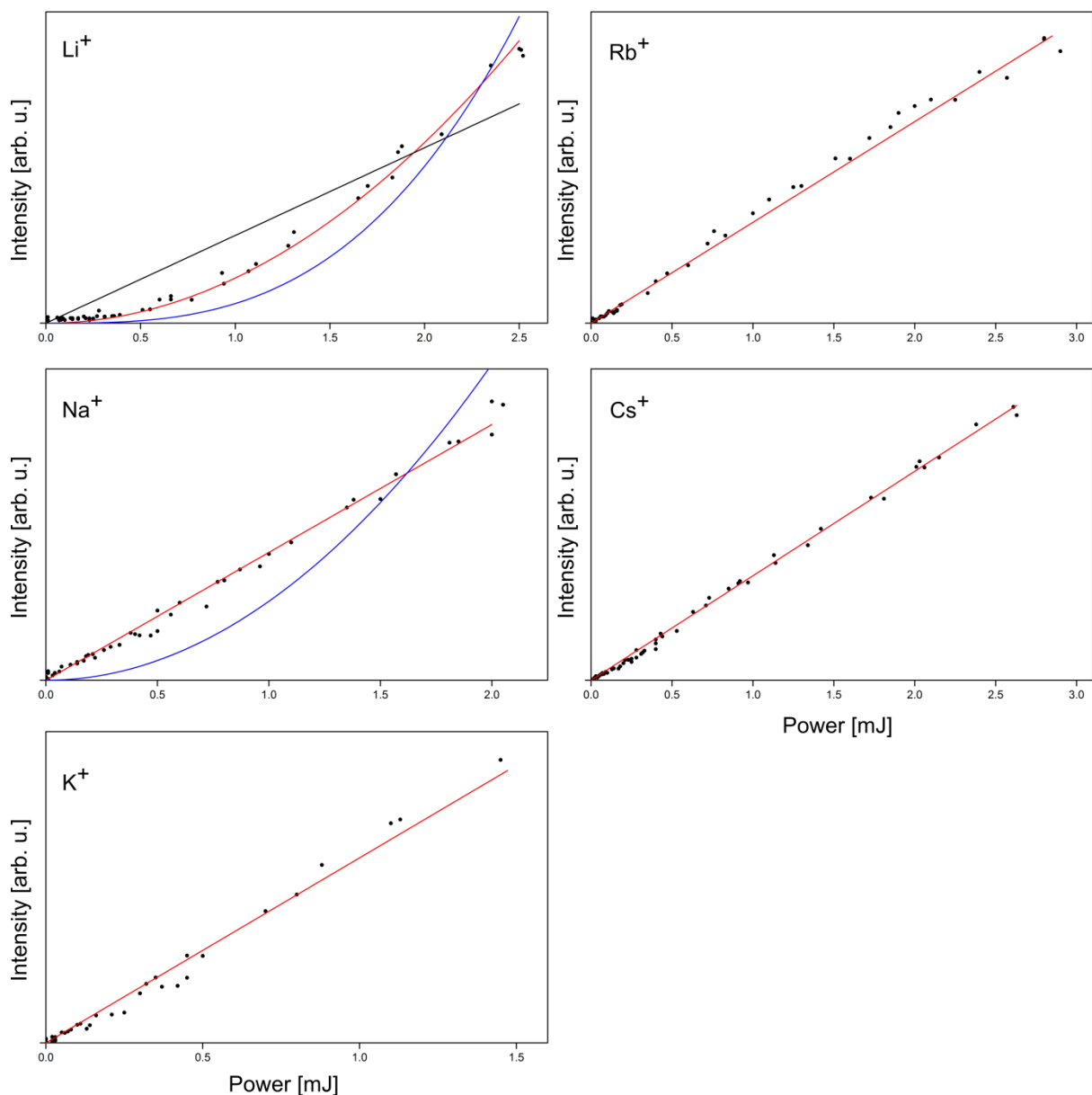


Figure S9. Dependence of the photodissociation yield measured at the S_1 origins of M^+LF on the OPO laser pulse energy. For M^+LF with $M=\text{Na}-\text{Cs}$, a linear power dependence is observed, which is indicative for a single-photon VISPD process. In contrast, for Li^+LF a nonlinear power dependence is observed. A quadratic function (red) fits better than the linear (black) and cubic (blue) function, indicative of a two-photon VISPD process. The photon energy at $S_1 0^0$ (23202 cm^{-1}) is clearly smaller than the binding energy in the S_0 state (24200 cm^{-1}). Consequently, single-photon absorption is not sufficient to fragment the Li^+LF parent ion.

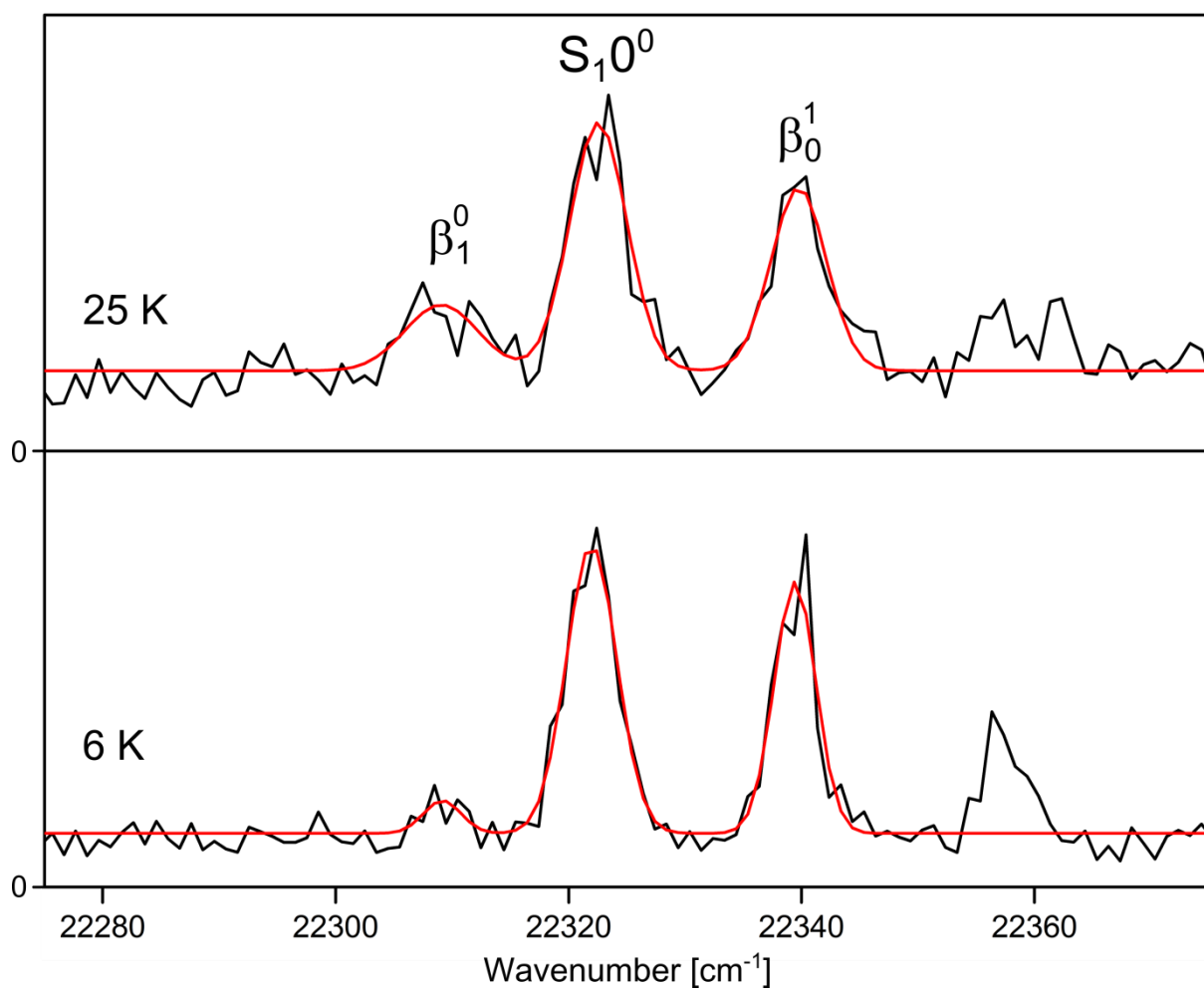


Figure S10. VISPD spectra of Cs^+LF recorded at trap temperatures of 6 and 25 K. An analysis of the hot band intensity and the fundamental of the in-plane β mode yields an effective ion temperature of 11 ± 4 K at a nominal trap temperature of 6 K.

Table S1. Absolute distances (in pm) of the O2(+) isomers of M⁺LF with M=Li-Cs in the S₀ and S₁ state (PBE0/cc-pVDZ). Relative changes upon electronic excitation are tabulated (in picometer) as Δ. Values below the line correspond to geometries and changes of the diagonal bonds of the tricyclic aromatic rings. Methyl groups are labelled M1-M3.

Li	O2 S ₀	O2 S ₁	Δ pm	O2+ S ₀	O2+ S ₁	Δ pm
O4-C4	120.3	120.9	0.6	120.1	120.7	0.6
C4-N3	139.5	141.5	2.0	139.6	141.1	1.5
C4-C4a	148.6	146.2	-2.4	149.0	146.9	-2.1
C4a-N5	130.5	134.0	3.5	130.4	133.9	3.5
N5-C5a	135.1	136.2	1.1	135.0	136.4	1.4
N1-M+	352.1	360.4	8.3	208.4	208.0	-0.4
O2-M+	172.6	171.6	-1.0	185.4	184.7	-0.7
C5a-C6	141.2	139.6	-1.6	141.2	139.9	-1.3
C6-C7	137.8	142.8	5.0	137.9	143.3	5.4
C7-M1	149.8	148.3	-1.5	149.7	148.1	-1.6
C7-C8	143.0	141.4	-1.6	142.9	141.3	-1.6
C8-M2	149.5	149.7	0.2	149.5	149.7	0.2
C8-C9	139.0	139.1	0.1	139.2	139.0	-0.2
C9-C9a	140.1	142.9	2.8	140.0	143.5	3.5
C9a-C5a	142.2	141.3	-0.9	142.0	140.5	-1.5
N10-M3	146.0	145.3	-0.7	145.8	145.0	-0.8
C9a-N10	138.2	137.6	-0.6	138.7	138.1	-0.6
N10-C10a	136.2	139.7	3.5	136.0	139.8	3.8
C10a-C4a	144.1	142.2	-1.9	144.2	142.1	-2.1
C10a-N1	133.1	132.7	-0.4	133.6	133.2	-0.4
N1-C2	134.1	135.5	1.4	137.3	138.1	0.8
C2-N3	137.0	135.1	-1.9	136.0	134.7	-1.3
C2-O2	126.0	126.2	0.2	124.6	125.1	0.5
N1-C4	289.4	287.0	-2.4	289.1	286.8	-2.3
C2-C4a	277.7	279.1	1.4	277.7	279.0	1.3
N3-C10a	268.1	265.9	-2.2	272.0	269.2	-2.8
N10-N5	279.2	285.5	6.3	278.7	285.1	6.4
C10a-C5a	275.4	272.5	-2.9	275.6	272.1	-3.5
C4a-C9a	271.5	272.7	1.2	271.8	272.6	0.8
C9-C6	279.3	275.4	-3.9	279.3	274.8	-4.5
C9a-C7	283.5	282.7	-0.8	283.5	282.9	-0.6
C5a-C8	280.5	288.9	8.4	280.2	289.5	9.3

Na	O2 S ₀	O2 S ₁	Δ pm	O2+ S ₀	O2+ S ₁	Δ pm
O4-C4	120.4	121.0	0.6	120.2	120.8	0.6
C4-N3	139.2	141.3	2.1	139.1	140.7	1.6
C4-C4a	148.7	146.0	-2.7	148.9	146.6	-2.3
C4a-N5	130.3	134.2	3.9	130.2	134.0	3.8
N5-C5a	135.3	136.0	0.7	135.2	136.2	1.0
N1-M+	382.5	394.6	12.1	249.4	250.8	1.4
O2-M+	207.4	206.7	-0.7	217.5	216.4	-1.1
C5a-C6	141.1	139.4	-1.7	141.1	139.5	-1.6
C6-C7	137.9	142.3	4.4	137.9	143.0	5.1
C7-M1	149.8	148.4	-1.4	149.8	148.2	-1.6
C7-C8	142.8	141.6	-1.2	142.8	141.6	-1.2
C8-M2	149.6	149.7	0.1	149.5	149.7	0.2
C8-C9	139.0	139.1	0.1	139.2	139.0	-0.2
C9-C9a	140.1	142.5	2.4	140.0	143.0	3.0
C9a-C5a	142.0	142.1	0.1	141.9	141.2	-0.7
N10-M3	145.9	145.3	-0.6	145.6	144.9	-0.7
C9a-N10	138.2	137.5	-0.7	138.7	137.9	-0.8
N10-C10a	136.5	139.6	3.1	136.3	140.0	3.7
C10a-C4a	144.4	142.3	-2.1	144.5	142.3	-2.2
C10a-N1	132.6	132.6	0.0	133.2	133.0	-0.2
N1-C2	134.9	136.5	1.6	137.5	138.5	1.0
C2-N3	137.6	135.5	-2.1	136.9	135.4	-1.5
C2-O2	125.0	125.2	0.2	124.0	124.4	0.4
N1-C4	289.6	287.1	-2.5	289.9	287.5	-2.4
C2-C4a	278.7	280.1	1.4	278.8	280.1	1.3
N3-C10a	268.0	265.9	-2.1	270.4	267.9	-2.5
N10-N5	279.2	285.5	6.3	278.7	285.0	6.3
C10a-C5a	275.8	272.8	-3.0	276.0	272.9	-3.1
C4a-C9a	271.6	273.1	1.5	271.9	272.9	1.0
C9-C6	279.1	276.0	-3.1	279.0	275.4	-3.6
C9a-C7	283.5	282.3	-1.2	283.5	282.5	-1.0
C5a-C8	280.4	288.5	8.1	280.2	289.1	8.9

K	O2 S ₀	O2 S ₁	Δ pm	O2+ S ₀	O2+ S ₁	Δ pm
O4-C4	120.5	121.1	0.6	120.3	120.9	0.6
C4-N3	139.0	141.3	2.3	138.9	140.8	1.9
C4-C4a	148.7	145.9	-2.8	148.9	146.3	-2.6
C4a-N5	130.3	134.2	3.9	130.2	134.1	3.9
N5-C5a	135.4	135.9	0.5	135.3	136.0	0.7
N1-M+	422.9	431.7	8.8	299.7	309.5	9.8
O2-M+	239.1	238.6	-0.5	246.2	244.7	-1.5
C5a-C6	141.1	139.4	-1.7	141.1	139.4	-1.7
C6-C7	137.9	142.1	4.2	137.9	142.5	4.6
C7-M1	149.8	148.5	-1.3	149.8	148.3	-1.5
C7-C8	142.8	141.8	-1.0	142.7	141.8	-0.9
C8-M2	149.6	149.7	0.1	149.6	149.7	0.1
C8-C9	139.0	139.0	0.0	139.1	138.9	-0.2
C9-C9a	140.1	142.3	2.2	140.0	142.6	2.6
C9a-C5a	142.0	142.3	0.3	141.8	141.9	0.1
N10-M3	145.8	145.3	-0.5	145.5	145.0	-0.5
C9a-N10	138.2	137.5	-0.7	138.6	137.7	-0.9
N10-C10a	136.6	139.5	2.9	136.6	140.0	3.4
C10a-C4a	144.5	142.4	-2.1	144.7	142.4	-2.3
C10a-N1	132.4	132.5	0.1	132.9	132.8	-0.1
N1-C2	135.2	136.9	1.7	137.1	138.3	1.2
C2-N3	137.9	135.7	-2.2	137.4	135.6	-1.8
C2-O2	124.7	124.9	0.2	123.9	124.3	0.4
N1-C4	289.6	287.0	-2.6	290.1	287.5	-2.6
C2-C4a	279.2	280.6	1.4	279.0	280.3	1.3
N3-C10a	267.9	265.9	-2.0	269.6	267.2	-2.4
N10-N5	279.3	285.4	6.1	278.8	285.2	6.4
C10a-C5a	275.9	272.9	-3.0	276.4	273.2	-3.2
C4a-C9a	271.6	273.2	1.6	271.8	273.4	1.6
C9-C6	279.0	276.3	-2.7	279.0	276.0	-3.0
C9a-C7	283.5	282.2	-1.3	283.5	282.3	-1.2
C5a-C8	280.4	288.3	7.9	280.2	288.6	8.4

Rb	O2 S ₀	O2 S ₁	Δ pm
O4-C4	120.5	121.1	0.6
C4-N3	139.0	141.3	2.3
C4-C4a	148.7	145.9	-2.8
C4a-N5	130.2	134.3	4.1
N5-C5a	135.4	135.9	0.5
N1-M+	434.9	444.7	9.8
O2-M+	251.8	251.3	-0.5
C5a-C6	141.1	139.4	-1.7
C6-C7	137.9	142.0	4.1
C7-M1	149.8	148.5	-1.3
C7-C8	142.8	141.8	-1.0
C8-M2	149.6	149.7	0.1
C8-C9	139.0	139.0	0.0
C9-C9a	140.1	142.2	2.1
C9a-C5a	141.9	142.5	0.6
N10-M3	145.8	145.3	-0.5
C9a-N10	138.2	137.5	-0.7
N10-C10a	136.6	139.4	2.8
C10a-C4a	144.6	142.4	-2.2
C10a-N1	132.3	132.5	0.2
N1-C2	135.3	137.1	1.8
C2-N3	138.0	135.8	-2.2
C2-O2	124.5	124.7	0.2
N1-C4	289.6	287.1	-2.5
C2-C4a	279.3	280.8	1.5
N3-C10a	267.8	265.9	-1.9
N10-N5	279.3	285.4	6.1
C10a-C5a	275.9	273.0	-2.9
C4a-C9a	271.6	273.3	1.7
C9-C6	278.9	276.4	-2.5
C9a-C7	283.5	282.1	-1.4
C5a-C8	280.4	288.2	7.8

Cs	O2 S ₀	O2 S ₁	Δ pm
O4-C4	120.5	121.1	0.6
C4-N3	138.9	141.2	2.3
C4-C4a	148.7	145.9	-2.8
C4a-N5	130.2	134.3	4.1
N5-C5a	135.4	135.9	0.5
N1-M+	451.1	460.7	9.6
O2-M+	267.7	267.4	-0.3
C5a-C6	141.1	139.4	-1.7
C6-C7	137.9	141.9	4.0
C7-M1	149.8	148.6	-1.2
C7-C8	142.8	141.8	-1.0
C8-M2	149.6	149.7	0.1
C8-C9	139.0	139.0	0.0
C9-C9a	140.1	142.1	2.0
C9a-C5a	141.9	142.6	0.7
N10-M3	145.8	145.3	-0.5
C9a-N10	138.2	137.5	-0.7
N10-C10a	136.7	139.4	2.7
C10a-C4a	144.6	142.4	-2.2
C10a-N1	132.3	132.5	0.2
N1-C2	135.4	137.2	1.8
C2-N3	138.1	135.8	-2.3
C2-O2	124.5	124.7	0.2
N1-C4	289.7	287.1	-2.6
C2-C4a	279.4	280.8	1.4
N3-C10a	267.8	265.9	-1.9
N10-N5	279.3	284.4	5.1
C10a-C5a	276.0	273.0	-3.0
C4a-C9a	271.6	273.4	1.8
C9-C6	278.9	276.5	-2.4
C9a-C7	283.5	282.1	-1.4
C5a-C8	280.4	288.1	7.7

Table S2. Vertical transition energies (ν in cm^{-1} , λ in nm) and oscillator strength (f) for the first four excited singlet states of $\text{M}^+\text{LF}(\text{O}_2)$ with $\text{M}=\text{Li-Cs}$ and $\text{M}^+\text{LF}(\text{O}_2^+)$ with $\text{M}=\text{Li-K}$ and LF calculated at the PBE0/cc-pVDZ level.

O2	S_1 ($\pi\pi^*$)			S_2 ($n\pi^*$)			S_3 ($n\pi^*/\pi\pi^*$)			S_4 ($n\pi^*/\pi\pi^*$)		
	ν	λ	f	ν	λ	f	ν	λ	f	ν	λ	f
Li	25735	388.57	0.174	27090	369.14	0.001	29171	342.81	0.263	29344	340.79	0.000
Na	25746	388.41	0.193	27077	369.32	0.001	29267	341.68	0.000	29581	338.06	0.240
K	25698	389.14	0.204	27066	369.47	0.001	29202	342.44	0.000	29722	336.45	0.234
Rb	25674	389.50	0.210	27055	369.62	0.001	29162	342.91	0.000	29802	335.55	0.234
Cs	25650	389.87	0.216	27039	369.83	0.001	29129	343.30	0.000	29839	335.13	0.234

O2+	S_1 ($\pi\pi^*$)			S_2 ($n\pi^*$)			S_3 ($n\pi^*/\pi\pi^*$)			S_4 ($n\pi^*/\pi\pi^*$)		
	ν	λ	f	ν	λ	f	ν	λ	f	ν	λ	f
Li	26159	382.28	0.138	27728	360.64	0.001	29175	342.76	0.303	29916	334.27	0.000
Na	26191	381.81	0.165	27332	365.87	0.005	29443	339.64	0.235	29762	336.00	0.040
K	26063	383.69	0.191	27161	368.18	0.001	29413	339.99	0.000	29697	336.73	0.250

	S_1 ($\pi\pi^*$)			S_2 ($n\pi^*$)			S_3 ($n\pi^{**}$)			S_4 ($\pi\pi^*$)		
	ν	λ	f	ν	λ	f	ν	λ	f	ν	λ	f
LF	25236	396.26	0.213	26121	382.84	0.000	27585	362.51	0.000	32250	310.08	0.136

Table S3. Experimental frequencies for vibronic transitions (in cm^{-1}) observed in the VISPD spectra of the S_1 states of M^+LF ($M=\text{Li-Cs}$) compared to harmonic frequencies of the $M^+LF(\text{O}_2/\text{O}_2^+)$ isomers computed at the PBE0/cc-pVDZ level, along with the mode assignment. Mode n1 is a butterfly out-of-plane mode.

Li	ν (exp)	ν (calc)	Assignment
	23202		0^0
A	32	32	n1
B	60		2n1
C	102		
D	127		
E	156	156	m1
F	184		m1+ n1
G	200		
H	212		m1+2n1
I	254		
J	278	275	m2
K	304	299	m3
L	312		m2+n1; 2m1
M	325	326	m4
N	336		m3+n1; m2+2n1
O	352		m4+n1; m3+2n1
P	396	404	m5
Q	433		m5+n1; m2+m1
R	461		m5+2n1; m3+m1
S	475	493	m7
T	510	525	m8; m7+n1
U	534		m7+2n1
V	548		m8+n1; 2m2
W	554		m6+m1
X	568		m8+2n1
Y	580		2m2+n1

Na	v (exp)	v (calc)	Assignment
	23037		0 ⁰
A	31	30	n1
B	53	45	n2
C	69		
D	122		
E	136	147	
F	153	155	m1
G	159	160	
H	167	168	
I	180		
J	195		
K	206		
L	218		
M	227		
N	251		
O	271	276	m2
P	283	298	m3
Q	298		
R	303		
S	323		
T	335		
U	347		
V	362		
W	374		
X	394		
Y	414	416	m5
Z	432		
A'	457		
B'	462	468	m6
C'	487		
D'	502	501	m7
E'	513	524	m8
F'	529		
G'	546		
H'	566		
I'	575		
J'	597		

K	ν (exp)	ν (calc)	Assignment
	22806		0^0
A	8		
B	20		
C	30		
D	33		
E	42		
F	48		
G	55		
H	62		
I	70		
J	77		
K	126		
L	132		
M	137		
N	143	140	m1
O	153		
P	165		
Q	178		
R	193		
S	202		
T	208		

Rb	v (exp)	v (calc)	Assignment
	22355		0^0
A	21	20	β
B	41		2β
C	62		3β
D	78		
E	91		
F	104		
G	118	127	σ
H	137		$\sigma+\beta$
I	164	168	$m1; \sigma+2\beta$
J	186		$m1+\beta$
K	209		$m1+2\beta$
L	231		$2\sigma; m1+3\beta$
M	251		$2\sigma+2\beta$
N	270	274	$m2$
O	276		$m1+\sigma$
P	286		$m2+\beta$
Q	294	294	$m3$
R	302		$m1+\sigma$
S	317	317	$m4$
T	329		$2m1$
U	349		$2m1+\beta$
V	351	359	$m4^*$
W	391		$m2+\sigma; m1+2\sigma;$
X	408	412	$m5$
Y	433		$m2+m1$
Z	440	445	$m6$
A'	460		$m3+m1$
B'	492	492	$m7$
C'	510	522	$m8$
D'	530		$m8+\beta$

Cs	ν (exp)	ν (calc)	Assignment
	22323		0^0
A	16	18	β
B	33		2β
C	51		3β
D	60		
E	75		
F	95	102	σ
G	112		$\sigma+\beta$
H	132		$\sigma+2\beta$
I	149		$\sigma+3\beta$
J	163	167	m1
K	181		$m1+\beta$
L	198		$m1+2\beta$
M	206		$2\sigma+\beta$
N	215		$m1+3\beta$
O	226		$2\sigma+2\beta$
P	241		$2\sigma+3\beta$
Q	258		$m1+\sigma$
R	272	274	m2
S	294	294	$m3; m2+\beta$
T	307		$m2+2\beta$
U	327		$2m1$
V	345		$2m1+\beta$
W	360		$2m1+ 2\beta$
X	364	359	$m4^*; m2+\sigma$
Y	387		$m4^*+\beta;$
Z	405	410	m5
A'	422		$m5+\beta$
B'	432		$m1+m2$
C'	439		$m5+2\beta$
D'	455		$m1+m3$
E'	489	491	$m7; 3m1$
F'	507	522	$m8; m7+\beta; 3m1+\beta$
G'	526		$m8+\beta$
H'	544	540	$m9; m8+2\beta$
I'	568		$m5+m1$
J'	585		$2m3$

Table S4. Calculated harmonic vibrational frequencies of $M^+LF(O_2/O_2^+)$ with $M=Li-Cs$ for the S_0 and S_1 states (PBE0/cc-pVDZ). Frequencies are listed according to symmetry following the Mulliken notation.

Li⁺LF(O₂)

S_0 a''	a'	S_1 a''	a'
41.00	54.64	37.38	59.89
61.69	163.85	53.09	163.17
90.10	280.49	82.04	273.36
102.66	298.87	87.88	291.14
135.72	327.02	97.38	315.02
156.99	352.68	144.97	349.57
168.98	392.14	158.38	391.09
175.61	446.59	170.84	443.88
194.27	488.44	181.37	475.24
207.90	528.57	206.83	523.58
262.78	548.09	220.91	537.51
344.11	565.20	319.55	566.00
394.26	638.74	341.77	623.81
462.87	675.64	394.89	668.82
531.83	715.76	459.69	711.66
640.21	764.64	604.56	748.58
675.86	815.77	652.01	809.46
734.36	858.95	707.02	848.82
781.84	892.51	727.65	889.76
785.78	1002.17	766.62	993.92
837.77	1024.05	790.98	1010.17
867.45	1036.03	863.04	1026.87
923.63	1086.67	906.38	1065.74
1030.54	1112.48	993.60	1113.02
1054.76	1180.92	1039.53	1177.20
1135.32	1201.65	1128.00	1182.33
1440.03	1242.48	1419.57	1217.24
1456.38	1261.84	1450.73	1245.64
1475.94	1299.02	1473.00	1276.77
3132.94	1335.88	3093.07	1323.58
3135.53	1354.95	3130.24	1342.07
3176.14	1386.91	3144.84	1354.88
	1392.46		1370.20
	1396.36		1381.91
	1404.77		1392.96
	1423.82		1396.14
	1434.55		1407.12
	1449.72		1420.38
	1463.91		1435.93
	1484.08		1460.53
	1497.69		1469.49
	1531.07		1479.41
	1552.90		1501.74
	1573.36		1534.73
	1625.27		1553.01
	1644.23		1598.65
	1702.97		1684.39
	1705.08		1694.54
	1872.69		1834.07
	3060.99		3033.95
	3062.17		3058.28
	3086.19		3063.58
	3176.53		3171.90
	3177.25		3184.80
	3232.64		3225.32
	3237.73		3228.67
	3246.32		3239.51
	3610.73		3610.69

Li⁺LF(O2⁺)

S₀ a''	a'	S₁ a''	a''
15.43	158.04	32.19	702.00
55.70	234.52	50.99	732.47
80.09	283.26	71.36	742.31
102.44	304.77	80.93	770.74
132.32	336.13	104.92	788.54
144.78	358.85	130.78	792.86
158.95	404.96	146.17	847.45
183.45	454.57	152.98	864.82
189.53	494.09	155.99	885.11
203.73	528.15	179.40	902.45
262.10	546.93	193.83	988.25
341.98	584.60	215.61	991.88
394.00	621.66	236.47	1012.22
462.04	646.01	275.27	1028.55
529.95	698.97	299.01	1040.02
639.52	760.57	307.39	1052.08
677.85	794.56	325.90	1104.25
735.11	856.70	339.17	1121.18
779.25	888.15	361.69	1179.28
789.67	1002.60	390.22	1182.04
830.97	1024.50	403.92	1221.77
864.34	1037.96	448.12	1248.46
924.33	1065.99	451.67	1278.10
1029.84	1105.47	492.54	1320.35
1054.48	1181.83	524.83	1340.12
1127.53	1202.25	537.99	1348.35
1439.37	1242.43	584.79	1374.69
1455.72	1264.02	598.60	1383.02
1463.23	1303.86	616.70	1394.96
3133.73	1330.04	638.41	1397.26
3136.98	1358.85	646.00	1413.25
3178.06	1386.23	694.36	1415.62
	1395.87		1429.26
	1398.10		1447.70
	1407.96		1450.52
	1423.99		1461.82
	1433.05		1463.14
	1449.09		1468.65
	1466.01		1482.95
	1481.82		1502.01
	1490.57		1528.68
	1524.75		1553.46
	1553.24		1608.27
	1567.33		1688.13
	1631.42		1721.19
	1645.67		1843.80
	1702.82		3029.35
	1725.87		3060.30
	1881.10		3062.03
	3061.49		3086.44
	3063.23		3133.37
	3091.50		3152.28
	3177.09		3173.55
	3178.96		3187.74
	3233.74		3222.09
	3246.13		3228.47
	3254.70		3237.36
	3597.40		3602.55

Na⁺LF(O2)

S₀ a''	a'	S₁ a''	a'
29.49	26.09	27.83	30.84
61.83	160.83	51.20	161.74
68.73	262.54	67.99	257.76
101.01	282.25	86.06	276.06
134.65	299.08	94.24	294.62
151.81	326.85	145.49	316.34
161.53	362.98	156.76	361.57
173.59	427.08	160.64	421.39
193.00	449.88	182.32	444.34
207.96	510.84	210.39	500.95
260.32	527.12	221.88	523.43
342.55	547.69	321.41	538.57
391.73	624.76	338.03	618.30
461.71	649.54	397.81	636.16
529.70	680.84	464.04	672.76
640.33	762.52	609.47	740.61
675.49	801.51	653.49	793.84
732.96	848.47	707.39	836.68
781.75	890.99	722.05	887.36
787.98	1002.10	767.77	994.35
837.53	1023.69	788.86	1008.09
866.64	1037.02	860.53	1023.70
924.10	1075.91	907.83	1053.63
1030.67	1111.08	996.42	1109.74
1055.23	1180.52	1039.52	1178.47
1135.41	1203.28	1127.93	1183.42
1440.71	1242.67	1422.20	1211.10
1456.81	1263.03	1450.79	1248.94
1476.16	1296.35	1471.43	1277.49
3132.17	1340.31	3096.17	1325.12
3134.74	1352.82	3127.67	1335.30
3172.99	1387.45	3143.58	1356.87
	1393.61		1367.06
	1396.63		1378.71
	1405.93		1392.63
	1422.32		1396.87
	1434.41		1399.10
	1447.68		1420.92
	1463.80		1432.70
	1479.12		1460.69
	1490.64		1468.50
	1525.84		1477.96
	1552.30		1499.65
	1577.71		1526.79
	1625.13		1548.07
	1649.91		1589.73
	1705.90		1684.47
	1721.19		1707.66
	1868.91		1829.02
	3060.43		3036.06
	3061.50		3056.58
	3083.75		3063.00
	3174.64		3169.94
	3175.95		3183.26
	3231.78		3225.22
	3234.84		3229.08
	3244.83		3238.83
	3614.58		3615.76

Na⁺LF(O2+)

S₀ a''	a''	S₁ a''	a''
31.44	1039.10	29.95	1022.86
54.71	1054.90	45.09	1039.68
65.38	1062.14	64.78	1047.00
85.25	1105.32	76.28	1106.20
100.32	1129.16	83.83	1122.12
126.05	1181.29	93.32	1181.29
136.78	1205.20	143.41	1184.18
150.67	1241.75	146.74	1216.64
160.22	1265.29	154.51	1251.44
169.26	1301.15	159.91	1279.25
184.58	1335.44	167.60	1320.84
202.86	1355.84	189.32	1335.03
260.42	1386.87	215.11	1351.54
264.18	1395.67	259.74	1371.55
285.43	1397.94	275.70	1384.99
304.00	1412.95	298.24	1394.40
339.11	1422.31	310.53	1399.28
347.93	1432.71	336.00	1413.73
366.88	1440.13	339.77	1416.15
393.27	1446.78	365.59	1419.41
417.80	1456.44	393.59	1437.07
460.59	1463.53	417.46	1450.60
470.72	1467.61	451.75	1460.01
507.55	1473.03	468.27	1463.21
524.81	1485.89	500.67	1467.59
532.82	1522.47	523.60	1481.68
549.64	1552.57	538.99	1496.16
610.35	1569.64	604.08	1516.01
639.81	1628.33	609.70	1548.69
643.49	1648.89	627.40	1600.27
678.40	1704.08	649.42	1689.04
690.42	1737.07	683.83	1726.52
736.43	1876.03	705.37	1836.80
761.42	3061.11	729.60	3031.11
779.20	3062.61	739.81	3058.21
791.04	3085.47	770.19	3058.85
795.39	3133.19	788.35	3088.92
832.64	3136.17	793.94	3131.11
851.80	3175.41	840.44	3145.90
863.48	3177.68	860.93	3171.49
886.21	3179.94	883.08	3186.36
924.64	3232.83	904.79	3222.83
1002.86	3234.16	990.18	3229.15
1024.15	3243.53	992.46	3236.49
1030.08	3603.45	1009.77	3608.05

K⁺LF(O2)

S ₀ a''	a'	S ₁ a''	a'
22.97	23.03	22.71	25.59
61.23	159.79	50.23	158.93
62.46	190.98	62.08	186.87
100.48	280.43	88.69	274.43
134.58	298.83	95.45	294.32
146.30	327.17	145.91	317.32
157.16	360.44	152.45	359.26
172.00	417.52	159.41	413.21
191.84	447.56	182.46	444.73
207.21	506.23	208.81	493.83
259.13	526.24	221.32	522.66
341.84	547.46	321.71	539.19
390.46	619.75	335.97	615.11
461.06	646.53	398.64	630.86
528.96	681.01	465.23	672.72
639.69	762.45	611.14	739.64
673.21	799.84	652.19	791.68
730.49	847.35	703.12	835.18
781.33	890.26	721.59	886.23
788.19	1001.96	767.05	994.89
836.17	1023.49	786.79	1006.88
866.74	1036.97	859.82	1022.50
923.90	1071.85	907.90	1049.33
1030.71	1110.42	997.96	1108.63
1055.31	1180.15	1039.44	1178.39
1135.29	1203.69	1127.62	1183.96
1440.88	1242.45	1423.80	1208.27
1456.91	1263.39	1450.81	1249.52
1476.30	1294.43	1470.59	1277.06
3131.72	1341.96	3097.77	1325.63
3134.26	1351.79	3126.59	1330.62
3171.65	1387.56	3143.21	1356.71
	1392.90		1366.20
	1396.72		1377.97
	1405.65		1391.99
	1421.68		1395.89
	1434.26		1398.98
	1446.43		1420.95
	1462.97		1431.77
	1475.63		1460.77
	1488.54		1468.03
	1524.44		1477.04
	1551.98		1497.15
	1579.94		1525.24
	1624.00		1546.30
	1651.08		1585.49
	1706.21		1682.37
	1715.93		1699.30
	1866.57		1826.58
	3060.13		3037.16
	3061.12		3055.91
	3082.52		3062.76
	3174.08		3169.19
	3175.34		3182.57
	3231.17		3224.79
	3232.53		3229.07
	3244.53		3238.67
	3616.08		3617.30

K⁺LF(O2+)

S ₀ a''	a'	S ₁ a''	a'
10.36	42.76	14.63	25.86
51.90	143.90	41.65	140.38
58.08	215.46	55.59	215.86
92.44	281.43	82.51	274.32
133.62	300.72	89.65	295.00
142.03	336.14	141.87	324.57
150.05	357.78	147.71	357.21
163.98	416.12	162.34	415.74
187.09	461.00	173.93	456.96
204.18	505.65	195.63	496.00
258.77	527.55	216.21	521.67
339.70	548.00	315.07	538.46
390.42	611.25	337.36	609.40
460.24	642.75	394.94	626.92
526.45	685.22	456.16	677.39
639.83	761.68	608.23	737.31
677.40	796.30	651.08	789.32
735.12	847.17	709.05	835.35
779.35	886.90	725.28	883.37
790.09	1002.39	767.47	993.66
832.14	1023.67	790.40	1005.70
863.06	1038.35	858.13	1020.84
924.48	1061.56	906.41	1046.30
1030.26	1107.66	993.38	1107.97
1055.08	1181.02	1039.29	1180.40
1130.57	1205.17	1123.68	1185.77
1440.49	1241.98	1419.56	1211.52
1456.77	1265.06	1450.43	1252.93
1467.86	1298.33	1463.18	1279.05
3132.56	1337.82	3092.77	1324.05
3135.39	1354.65	3128.71	1331.64
3169.52	1387.13	3136.42	1355.09
	1392.80		1367.89
	1396.45		1379.57
	1411.49		1393.67
	1420.07		1397.09
	1432.65		1403.35
	1444.47		1421.74
	1463.68		1429.37
	1470.34		1459.61
	1485.32		1467.21
	1521.78		1478.75
	1552.09		1494.20
	1570.56		1514.53
	1626.82		1545.78
	1649.64		1590.81
	1704.70		1687.48
	1731.37		1716.90
	1872.56		1832.66
	3060.67		3033.73
	3062.00		3057.28
	3083.91		3060.03
	3174.46		3169.84
	3176.78		3184.77
	3231.91		3229.56
	3241.51		3230.15
	3243.90		3238.26
	3605.57		3609.50

Rb⁺LF(O2)

S₀ a''	a'	S₁ a''	a'
20.40	17.68	19.29	19.71
58.94	127.40	49.60	126.91
62.11	170.35	59.38	167.97
101.08	280.23	90.05	274.27
135.32	298.87	96.48	293.72
144.07	327.15	144.90	317.25
158.88	359.62	150.43	358.90
173.29	415.47	159.60	411.60
192.52	447.33	182.72	444.60
207.35	505.43	210.91	491.97
259.04	525.91	222.63	522.50
341.50	547.36	322.04	539.50
390.12	618.45	335.55	613.93
460.83	646.11	399.11	630.13
528.36	680.78	466.13	672.27
639.81	762.56	611.93	739.35
673.40	799.42	652.65	791.04
730.39	846.93	702.24	834.72
781.26	890.14	722.07	885.89
788.61	1002.09	767.58	995.06
836.54	1023.64	786.77	1006.39
866.44	1037.15	859.13	1022.22
923.93	1070.28	907.90	1047.90
1030.70	1110.46	998.77	1108.41
1055.40	1180.11	1039.35	1178.24
1135.75	1203.81	1128.07	1184.49
1440.99	1242.45	1424.60	1206.97
1457.19	1263.18	1450.66	1250.01
1476.90	1293.70	1470.56	1277.16
3131.51	1343.05	3098.63	1325.69
3134.10	1351.39	3126.07	1328.43
3170.84	1387.53	3143.15	1356.62
	1393.11		1366.26
	1396.98		1378.14
	1406.15		1391.99
	1421.58		1395.75
	1434.29		1399.15
	1445.90		1420.89
	1462.71		1431.64
	1474.16		1460.85
	1487.89		1467.74
	1524.33		1477.07
	1551.97		1496.39
	1581.62		1525.21
	1624.16		1545.60
	1652.34		1583.91
	1706.58		1681.28
	1721.70		1703.69
	1865.99		1825.68
	3059.99		3037.72
	3061.01		3055.53
	3081.88		3062.78
	3173.76		3168.76
	3175.13		3182.29
	3231.05		3224.72
	3231.65		3229.22
	3244.17		3238.41
	3617.38		3618.90

Cs⁺LF(O2)

S₀ a''	a'	S₁ a''	a'
18.21	16.00	17.62	18.01
57.97	104.29	49.76	102.59
61.93	167.80	58.46	166.64
101.04	280.33	91.27	274.21
135.59	298.61	97.74	293.76
142.94	327.20	143.63	317.25
158.68	359.25	149.29	358.61
173.57	413.83	159.52	410.43
192.59	447.16	182.10	444.62
207.65	504.63	211.71	490.63
258.47	525.81	223.52	522.44
341.41	547.30	322.26	539.88
389.66	616.89	335.07	612.68
460.74	645.49	399.57	629.44
528.23	680.53	466.69	671.93
639.72	762.51	612.44	739.14
673.28	798.92	652.55	790.42
730.17	846.51	701.32	834.29
781.23	889.97	722.44	885.71
788.26	1001.85	767.13	995.17
836.61	1023.33	786.25	1005.96
866.64	1037.21	859.22	1021.97
923.82	1069.35	908.07	1047.00
1030.71	1110.61	999.38	1108.27
1055.23	1179.90	1039.42	1178.27
1135.78	1203.94	1128.00	1184.80
1440.93	1242.32	1425.09	1206.12
1456.94	1263.65	1450.37	1250.42
1477.09	1293.22	1470.44	1277.10
3131.37	1343.49	3099.18	1325.08
3133.86	1351.03	3125.59	1327.86
3170.58	1387.55	3143.08	1356.42
	1392.74		1366.36
	1396.83		1378.44
	1405.89		1391.73
	1421.25		1395.46
	1434.27		1399.37
	1445.49		1420.89
	1462.64		1431.46
	1473.33		1460.89
	1487.53		1467.42
	1524.18		1476.83
	1551.87		1495.75
	1582.27		1525.16
	1623.55		1545.27
	1652.50		1582.75
	1706.55		1680.44
	1717.88		1698.48
	1865.43		1825.16
	3059.91		3038.07
	3060.82		3055.18
	3081.63		3062.74
	3173.70		3168.44
	3174.99		3181.99
	3230.82		3224.44
	3230.97		3229.37
	3244.15		3238.63
	3617.52		3619.15

Table S5. Selected atomic charges (in e) of M+LF(O2/O2+) and LF in the S₀ and S₁ states using natural bond orbital analysis (NBO, PBE0/cc-pVDZ).

	q_M		q_{N5}		q_{O4}		q_{O2}		q_{N1}	
	S₀	S₁	S₀	S₁	S₀	S₁	S₀	S₁	S₀	S₁
Li(O2)	0.959	0.956	-0.345	-0.456	-0.532	-0.553	-0.899	-0.905	-0.679	-0.619
Li(O2+)	0.942	0.941	-0.339	-0.457	-0.518	-0.541	-0.765	-0.778	-0.811	-0.771
Na(O2)	0.966	0.966	-0.348	-0.455	0.539	0.558	-0.840	-0.843	-0.686	-0.607
Na(O2+)	0.950	0.948	-0.343	-0.457	-0.527	0.549	-0.742	-0.750	-0.777	-0.722
K(O2)	0.969	0.969	-0.350	-0.455	-0.542	-0.560	-0.825	-0.823	-0.683	-0.598
K(O2+)	0.963	0.962	-0.346	-0.455	-0.533	-0.553	-0.754	-0.763	-0.751	-0.674
Rb(O2)	0.971	0.970	-0.351	-0.454	-0.544	-0.561	-0.813	-0.809	-0.683	-0.595
Cs(O2)	0.970	0.969	-0.351	-0.454	-0.545	-0.562	-0.807	-0.803	-0.682	-0.592
LF			-0.376	-0.454	-0.577	-0.592	-0.598	-0.570	-0.660	-0.508

Cartesian coordinates and energies (in Å and hartree) of optimized geometries of the $S_{0/1}$ states of M^+LF ($M=Li-Cs$).

Li⁺LF(O2) S₀

C	-2.43060000	2.68848700	0.00000000
C	-2.44383000	1.31053700	0.00000000
C	-1.25109100	0.55448800	0.00000000
C	0.00000000	1.22951000	0.00000000
C	0.01718100	2.63061500	0.00000000
C	-1.16720200	3.35796500	0.00000000
C	1.09261900	-0.89096700	0.00000000
C	-0.22375700	-1.47655800	0.00000000
C	-0.31657300	-2.95988300	0.00000000
C	2.14718900	-2.92171200	0.00000000
H	-3.37893000	0.74798400	0.00000000
H	0.96040700	3.17466000	0.00000000
H	0.94992900	-4.58419800	0.00000000
N	1.15409500	0.47011400	0.00000000
N	2.22902800	-1.58341700	0.00000000
N	0.93950700	-3.56759400	0.00000000
N	-1.33589800	-0.79355600	0.00000000
O	-1.33557800	-3.59971000	0.00000000
O	3.18071500	-3.64229000	0.00000000
C	-1.11785400	4.85232600	0.00000000
H	-1.63500600	5.26261000	0.88202200
H	-0.08700100	5.22804700	0.00000000
H	-1.63500600	5.26261000	-0.88202200
C	-3.70729300	3.47119300	0.00000000
H	-3.77699000	4.12430300	0.88420100
H	-3.77699000	4.12430300	-0.88420100
H	-4.57977900	2.80594400	0.00000000
H	2.54528900	1.76285100	0.89752100
C	2.45301700	1.13652000	0.00000000
H	3.22531000	0.36437500	0.00000000
H	2.54528900	1.76285100	-0.89752100
Li	4.88813700	-3.89143300	0.00000000

Sum of electronic and zero-point Energies= -878.330798
Sum of electronic and thermal Energies= -878.313342
Sum of electronic and thermal Enthalpies= -878.312398
Sum of electronic and thermal Free Energies= -878.376073

Li⁺(O2) S₁

C	-2.34036400	2.79565500	0.00000000
C	-2.38801700	1.36856700	0.00000000
C	-1.25270800	0.55551700	0.00000000
C	0.00000000	1.20972000	0.00000000
C	0.05592500	2.63773600	0.00000000
C	-1.08154700	3.43909300	0.00000000
C	1.02393200	-0.94168100	0.00000000
C	-0.28276300	-1.50242300	0.00000000
C	-0.37885300	-2.96122500	0.00000000
C	2.08600100	-2.97813600	0.00000000
H	-3.35383200	0.85837400	0.00000000
H	1.02969200	3.12782300	0.00000000
H	0.86635700	-4.61331300	0.00000000
N	1.14698300	0.45028900	0.00000000
N	2.16146200	-1.62563200	0.00000000
N	0.88481100	-3.59686200	0.00000000
N	-1.42194900	-0.79639200	0.00000000
O	-1.39009400	-3.62415100	0.00000000
O	3.13536200	-3.67948500	0.00000000
C	-0.97213200	4.93210400	0.00000000
H	-1.46027600	5.37138400	0.88472000
H	0.07631000	5.25687900	0.00000000
H	-1.46027600	5.37138400	-0.88472000
C	-3.60532500	3.56992300	0.00000000
H	-3.65565100	4.23880800	0.87772800
H	-3.65565100	4.23880800	-0.87772800
H	-4.49047200	2.92314500	0.00000000
H	2.58799400	1.69590400	0.89830600
C	2.45977700	1.07357600	0.00000000
H	3.20574000	0.27500000	0.00000000
H	2.58799400	1.69590400	-0.89830600
Li	4.80574000	-4.07379700	0.00000000

Sum of electronic and zero-point Energies= -878.225396
Sum of electronic and thermal Energies= -878.207285
Sum of electronic and thermal Enthalpies= -878.206341
Sum of electronic and thermal Free Energies= -878.271725

Li⁺LF(O2+) S₀

C	-2.46038300	2.60564600	0.00000000
C	-2.44422400	1.22715600	0.00000000
C	-1.23537300	0.49835400	0.00000000
C	0.00000000	1.19783700	0.00000000
C	-0.01068900	2.59735600	0.00000000
C	-1.21161100	3.30057100	0.00000000
C	1.13793100	-0.90263500	0.00000000
C	-0.16744600	-1.51542400	0.00000000
C	-0.25784400	-3.00296500	0.00000000
C	2.19357000	-2.97667800	0.00000000
H	-3.36671800	0.64419000	0.00000000
H	0.91796400	3.16581300	0.00000000
H	1.01315200	-4.63696700	0.00000000
N	1.17258100	0.45681100	0.00000000
N	2.27317000	-1.60634000	0.00000000
N	0.99453400	-3.61907000	0.00000000
N	-1.28897300	-0.85063100	0.00000000
O	-1.28045200	-3.63240400	0.00000000
O	3.25941500	-3.62269200	0.00000000
C	-1.19267000	4.79506200	0.00000000
H	-1.71902100	5.19389000	0.88183600
H	-0.17033100	5.19320900	0.00000000
H	-1.71902100	5.19389000	-0.88183600
C	-3.75301200	3.36097300	0.00000000
H	-3.83574000	4.01237400	0.88425300
H	-3.83574000	4.01237400	-0.88425300
H	-4.61142300	2.67783900	0.00000000
H	2.51572900	1.80015800	0.89748000
C	2.44296600	1.17127400	0.00000000
H	3.25510100	0.44434700	0.00000000
H	2.51572900	1.80015800	-0.89748000
Li	4.30071300	-2.08835500	0.00000000

Sum of electronic and zero-point Energies= -878.334518
Sum of electronic and thermal Energies= -878.317251
Sum of electronic and thermal Enthalpies= -878.316307
Sum of electronic and thermal Free Energies= -878.379888

Li⁺LF(O2+) S₁

C	3.52173800	0.77226700	0.02405300
C	2.27414000	1.47525900	-0.02866400
C	1.02564900	0.84487600	-0.04748600
C	1.02697000	-0.55940800	-0.04464700
C	2.26994600	-1.27228400	0.02890400
C	3.50794000	-0.64046500	0.05872400
C	-1.35550600	-0.47285500	-0.04059000
C	-1.24716200	0.94356500	-0.04784900
C	-2.48933500	1.72691400	-0.01793400
C	-3.68051700	-0.41646900	0.07668600
H	2.27026300	2.56734900	-0.06063500
H	2.25212300	-2.36146400	0.07729500
H	-4.54168500	1.42299600	0.07413400
N	-0.18011400	-1.22655600	-0.10933400
N	-2.50630000	-1.14076100	0.02418600
N	-3.65211800	0.93006200	0.03889200
N	-0.09403700	1.62338500	-0.07780300
O	-2.57023500	2.93055500	-0.03759900
O	-4.75006200	-1.05949700	0.16063300
C	4.77768000	-1.42975800	0.13392900
H	5.35794600	-1.17286900	1.03439400
H	4.57815800	-2.50866100	0.16026000
H	5.42680000	-1.22938300	-0.73338300
C	4.78856300	1.53812100	0.04967700
H	5.37333900	1.29591700	0.95582400
H	5.43851100	1.24660200	-0.79530200
H	4.62607000	2.62145900	0.01409400
H	-0.00033200	-3.17663700	0.70553000
C	-0.22347800	-2.66979200	-0.24729800
H	-1.22318200	-2.95567000	-0.58260000
H	0.49611700	-2.99450900	-1.01066500
Li	-3.88118100	-2.68877600	0.22005600

Sum of electronic and zero-point Energies= -878.228194
Sum of electronic and thermal Energies= -878.210245
Sum of electronic and thermal Enthalpies= -878.209301
Sum of electronic and thermal Free Energies= -878.274079

Na⁺LF(O2) S₀

C	-0.47295400	-3.95842800	0.00000000
C	0.59018700	-3.08063100	0.00000000
C	0.40114100	-1.68203300	0.00000000
C	-0.91904600	-1.15905100	0.00000000
C	-2.00226500	-2.04802500	0.00000000
C	-1.79721500	-3.42298100	0.00000000
C	0.00000000	1.04617100	0.00000000
C	1.29685700	0.41120000	0.00000000
C	2.49267100	1.29511700	0.00000000
C	0.87853500	3.16642900	0.00000000
H	1.62265500	-3.43418400	0.00000000
H	-3.02570900	-1.67601600	0.00000000
H	2.92366900	3.30502500	0.00000000
N	-1.08126900	0.21345600	0.00000000
N	-0.20127800	2.35712500	0.00000000
N	2.15142000	2.64433500	0.00000000
N	1.48911200	-0.87792600	0.00000000
O	3.63782800	0.92214400	0.00000000
O	0.76688900	4.41169800	0.00000000
C	-2.97347200	-4.34685800	0.00000000
H	-2.95582300	-5.00667300	0.88209500
H	-3.92410400	-3.79882400	0.00000000
H	-2.95582300	-5.00667300	-0.88209500
C	-0.24922800	-5.43949000	0.00000000
H	-0.70340600	-5.91406100	0.88420800
H	-0.70340600	-5.91406100	-0.88420800
H	0.82177400	-5.67808300	0.00000000
H	-2.96646500	0.44614300	0.89726500
C	-2.42631100	0.77767800	0.00000000
H	-2.33020500	1.86570200	0.00000000
H	-2.96646500	0.44614300	-0.89726500
Na	-0.31761100	6.18011900	0.00000000

Sum of electronic and zero-point Energies= -1033.023721
Sum of electronic and thermal Energies= -1033.005825
Sum of electronic and thermal Enthalpies= -1033.004881
Sum of electronic and thermal Free Energies= -1033.070771

Na⁺LF(O2) S₁

C	-0.35823900	-3.99326900	0.00000000
C	0.70269200	-3.04470900	0.00000000
C	0.50255200	-1.66464900	0.00000000
C	-0.84410100	-1.21250700	0.00000000
C	-1.91065800	-2.15683800	0.00000000
C	-1.69714400	-3.53098100	0.00000000
C	0.00000000	1.01679600	0.00000000
C	1.31160800	0.46440300	0.00000000
C	2.42689500	1.40657100	0.00000000
C	0.73122100	3.20506400	0.00000000
H	1.73943900	-3.38778300	0.00000000
H	-2.93918200	-1.79581800	0.00000000
H	2.75730900	3.44605700	0.00000000
N	-1.08701100	0.14110000	0.00000000
N	-0.29843100	2.30846100	0.00000000
N	2.01026600	2.75719100	0.00000000
N	1.59062400	-0.84808100	0.00000000
O	3.60701100	1.13776200	0.00000000
O	0.50425900	4.43680700	0.00000000
C	-2.84764900	-4.48880300	0.00000000
H	-2.82565100	-5.14564000	0.88449200
H	-3.80921800	-3.95932400	0.00000000
H	-2.82565100	-5.14564000	-0.88449200
C	-0.04490900	-5.44425900	0.00000000
H	-0.49177100	-5.94292600	0.87830300
H	-0.49177100	-5.94292600	-0.87830300
H	1.03460100	-5.63582900	0.00000000
H	-2.98267800	0.31399300	0.89773400
C	-2.44584600	0.65551100	0.00000000
H	-2.38694000	1.74665700	0.00000000
H	-2.98267800	0.31399300	-0.89773400
Na	-0.48660300	6.25036000	0.00000000

Sum of electronic and zero-point Energies= -1032.917993
Sum of electronic and thermal Energies= -1032.899479
Sum of electronic and thermal Enthalpies= -1032.898535
Sum of electronic and thermal Free Energies= -1032.965941

Na⁺LF(O2+) S₀

C	3.80950500	0.57823700	0.04796200
C	2.69071400	1.38438300	0.03184700
C	1.38709500	0.84658200	-0.01160800
C	1.21505000	-0.56101600	-0.04998800
C	2.34756000	-1.38393700	-0.02548700
C	3.62640000	-0.83757100	0.02400100
C	-1.15494000	-0.22687200	-0.04750800
C	-0.86663200	1.18849200	-0.02931400
C	-2.01276500	2.13960000	-0.02893800
C	-3.44814000	0.13718100	0.00488800
H	2.76986300	2.47256500	0.05479800
H	2.25216300	-2.46874600	-0.02921000
H	-4.07441000	2.07711500	-0.01067100
N	-0.07793100	-1.06059500	-0.10641600
N	-2.38533800	-0.73535400	-0.01540700
N	-3.24295700	1.49071300	-0.02198700
N	0.33340500	1.69415200	-0.01774200
O	-1.91537500	3.33808800	-0.03340000
O	-4.60720700	-0.30033400	0.05248500
C	4.81624200	-1.74258400	0.05569800
H	5.42102800	-1.56586200	0.95938500
H	4.52748200	-2.80099100	0.03662700
H	5.47855400	-1.55039500	-0.80349300
C	5.18463800	1.16926200	0.09507100
H	5.73298200	0.83791900	0.99101500
H	5.78315100	0.86097700	-0.77665000
H	5.14446100	2.26559400	0.10823100
H	-0.08850400	-3.00036800	0.73040800
C	-0.27317300	-2.49787700	-0.23051500
H	-1.29999500	-2.67717500	-0.55515300
H	0.41378100	-2.89297000	-0.98826500
Na	-4.19995300	-2.43140000	0.20404600

Sum of electronic and zero-point Energies= -1033.025518
Sum of electronic and thermal Energies= -1033.007671
Sum of electronic and thermal Enthalpies= -1033.006727
Sum of electronic and thermal Free Energies= -1033.071768

Na⁺LF(O2+) S₁

C	3.82405900	0.55940400	0.05231100
C	2.66104000	1.38960300	0.00852900
C	1.35761700	0.89372800	-0.03252100
C	1.21208900	-0.51031700	-0.06021800
C	2.36946300	-1.34888200	-0.00002100
C	3.66416300	-0.84710500	0.05292800
C	-1.15307700	-0.17503000	-0.07273100
C	-0.89527500	1.22408700	-0.05190200
C	-2.05058200	2.12565600	-0.02099800
C	-3.46151800	0.10540300	0.02760100
H	2.77100700	2.47633400	0.00211800
H	2.24018300	-2.43134900	0.01812300
H	-4.11798500	2.02751900	0.04066500
N	-0.05687000	-1.04312000	-0.14677700
N	-2.35944700	-0.73241100	-0.02706000
N	-3.28340300	1.44719800	0.00599100
N	0.32338300	1.78022400	-0.05591800
O	-2.01214700	3.33329000	-0.01866500
O	-4.60017600	-0.39057700	0.09522300
C	4.84643700	-1.76332500	0.11492500
H	5.44337500	-1.59008000	1.02455900
H	4.53740100	-2.81656000	0.11283600
H	5.52010500	-1.60964400	-0.74327400
C	5.16596500	1.18546100	0.10261600
H	5.71505000	0.86307900	1.00582200
H	5.78742800	0.84871100	-0.74670300
H	5.11782700	2.28048900	0.09241900
H	-0.05610100	-3.02314900	0.60951200
C	-0.24500900	-2.46921900	-0.32456000
H	-1.27461000	-2.63914900	-0.64731100
H	0.42890300	-2.84074600	-1.10858200
Na	-4.12289700	-2.49701700	0.22890200

Sum of electronic and zero-point Energies= -1032.918464
Sum of electronic and thermal Energies= -1032.899939
Sum of electronic and thermal Enthalpies= -1032.898994
Sum of electronic and thermal Free Energies= -1032.965877

K*LF(O2) S₀

C	-0.42417200	-4.33651400	0.00000000
C	0.63029800	-3.44800700	0.00000000
C	0.42764700	-2.05159700	0.00000000
C	-0.89711100	-1.54142900	0.00000000
C	-1.97147200	-2.44130800	0.00000000
C	-1.75319100	-3.81424000	0.00000000
C	0.00000000	0.67385100	0.00000000
C	1.30351800	0.05004700	0.00000000
C	2.48998700	0.94655200	0.00000000
C	0.85629100	2.80563600	0.00000000
H	1.66617700	-3.79153400	0.00000000
H	-2.99843100	-2.07907100	0.00000000
H	2.90290300	2.95706200	0.00000000
N	-1.07328500	-0.17066600	0.00000000
N	-0.21473800	1.98077400	0.00000000
N	2.13548400	2.29104500	0.00000000
N	1.50843000	-1.23655100	0.00000000
O	3.63931900	0.58458100	0.00000000
O	0.73028700	4.04634100	0.00000000
C	-2.92063000	-4.74956600	0.00000000
H	-2.89697100	-5.40915000	0.88213700
H	-3.87640800	-4.21047600	0.00000000
H	-2.89697100	-5.40915000	-0.88213700
C	-0.18556300	-5.81539300	0.00000000
H	-0.63476500	-6.29472800	0.88421200
H	-0.63476500	-6.29472800	-0.88421200
H	0.88784700	-6.04308900	0.00000000
H	-2.96070400	0.04316500	0.89724600
C	-2.42370600	0.38007100	0.00000000
H	-2.33894500	1.46923200	0.00000000
H	-2.96070400	0.04316500	-0.89724600
K	-0.28935400	6.20900600	0.00000000

Sum of electronic and zero-point Energies= -899.167974
Sum of electronic and thermal Energies= -899.149879
Sum of electronic and thermal Enthalpies= -899.148934
Sum of electronic and thermal Free Energies= -899.215981

K*LF(O2) S₁

C	-0.18300600	-4.37370500	0.00000000
C	0.84398400	-3.39193000	0.00000000
C	0.59642600	-2.01982800	0.00000000
C	-0.76769200	-1.61332400	0.00000000
C	-1.80022100	-2.59192400	0.00000000
C	-1.53804900	-3.95742700	0.00000000
C	0.00000000	0.64346700	0.00000000
C	1.33047400	0.13713700	0.00000000
C	2.41117200	1.11754000	0.00000000
C	0.65440000	2.86051100	0.00000000
H	1.89183400	-3.69908100	0.00000000
H	-2.84076200	-2.26733600	0.00000000
H	2.67333100	3.16468500	0.00000000
N	-1.05541600	-0.26854800	0.00000000
N	-0.34384300	1.92349400	0.00000000
N	1.94860100	2.45262700	0.00000000
N	1.65404100	-1.16571200	0.00000000
O	3.60061300	0.89045400	0.00000000
O	0.38102700	4.07936100	0.00000000
C	-2.65437500	-4.95485800	0.00000000
H	-2.60968600	-5.61078100	0.88438900
H	-3.63383200	-4.45913600	0.00000000
H	-2.60968600	-5.61078100	-0.88438900
C	0.17761000	-5.81437500	0.00000000
H	-0.25166800	-6.32745300	0.87860100
H	-0.25166800	-6.32745300	-0.87860100
H	1.26299700	-5.96963900	0.00000000
H	-2.95536100	-0.16358800	0.89754700
C	-2.43155900	0.19804300	0.00000000
H	-2.41263600	1.29063000	0.00000000
H	-2.95536100	-0.16358800	-0.89754700
K	-0.65364700	6.22926400	0.00000000

Sum of electronic and zero-point Energies= -899.062355
Sum of electronic and thermal Energies= -899.043663
Sum of electronic and thermal Enthalpies= -899.042718
Sum of electronic and thermal Free Energies= -899.111218

K⁺LF(O2+) S₀

C	0.47244900	-4.12025200	0.00000000
C	1.35213500	-3.05782700	0.00000000
C	0.90313300	-1.72069800	0.00000000
C	-0.48936100	-1.45385400	0.00000000
C	-1.38685600	-2.52893100	0.00000000
C	-0.92759300	-3.84234500	0.00000000
C	0.00000000	0.89160200	0.00000000
C	1.39403500	0.50530200	0.00000000
C	2.41777300	1.58648700	0.00000000
C	0.50782100	3.15131200	0.00000000
H	2.43269600	-3.21084700	0.00000000
H	-2.46257500	-2.35936200	0.00000000
H	2.48963800	3.64410000	0.00000000
N	-0.90432900	-0.13159400	0.00000000
N	-0.42802100	2.14970800	0.00000000
N	1.84935500	2.85368600	0.00000000
N	1.81948100	-0.72499400	0.00000000
O	3.60840800	1.41118800	0.00000000
O	0.16359700	4.34197800	0.00000000
C	-1.91034300	-4.96976100	0.00000000
H	-1.76920600	-5.61466500	0.88199400
H	-2.94699600	-4.60994600	0.00000000
H	-1.76920600	-5.61466500	-0.88199400
C	0.97038200	-5.53282200	0.00000000
H	0.61331600	-6.08402500	0.88426700
H	0.61331600	-6.08402500	-0.88426700
H	2.06707700	-5.56613300	0.00000000
H	-2.79879600	-0.27748100	0.89709700
C	-2.33188900	0.15193400	0.00000000
H	-2.45911800	1.23548900	0.00000000
H	-2.79879600	-0.27748100	-0.89709700
K	-2.29331100	4.49500900	0.00000000

Sum of electronic and zero-point Energies= -899.167848
Sum of electronic and thermal Energies= -899.149696
Sum of electronic and thermal Enthalpies= -899.148752
Sum of electronic and thermal Free Energies= -899.216310

K⁺LF(O2+) S₁

C	0.72911900	-4.10193000	0.00000000
C	1.56099200	-2.94522600	0.00000000
C	1.06747600	-1.64169000	0.00000000
C	-0.34309000	-1.49101200	0.00000000
C	-1.18223000	-2.64429600	0.00000000
C	-0.67919800	-3.93944700	0.00000000
C	0.00000000	0.87477300	0.00000000
C	1.39935300	0.61278500	0.00000000
C	2.30015000	1.76564600	0.00000000
C	0.27781200	3.18188100	0.00000000
H	2.64736700	-3.05660900	0.00000000
H	-2.26469200	-2.51601600	0.00000000
H	2.20478300	3.83208000	0.00000000
N	-0.87243000	-0.21954700	0.00000000
N	-0.55796800	2.08019600	0.00000000
N	1.62121500	2.99932500	0.00000000
N	1.95250000	-0.60879000	0.00000000
O	3.50895400	1.73108700	0.00000000
O	-0.20615000	4.32715200	0.00000000
C	-1.59578300	-5.12297500	0.00000000
H	-1.43276300	-5.75947300	0.88455400
H	-2.64901700	-4.81360200	0.00000000
H	-1.43276300	-5.75947300	-0.88455400
C	1.34866200	-5.44943100	0.00000000
H	1.01855300	-6.03335700	0.87774300
H	1.01855300	-6.03335700	-0.87774300
H	2.44398700	-5.40423500	0.00000000
H	-2.75959700	-0.47843200	0.89758600
C	-2.30931200	-0.02771100	0.00000000
H	-2.50045500	1.04709600	0.00000000
H	-2.75959700	-0.47843200	-0.89758600
K	-2.65282700	4.35796900	0.00000000

Sum of electronic and zero-point Energies= -899.060985
Sum of electronic and thermal Energies= -899.042180
Sum of electronic and thermal Enthalpies= -899.041236
Sum of electronic and thermal Free Energies= -899.110620

Rb⁺LF(O2) S₀

C	5.02661500	0.19744600	0.00000000
C	4.02205900	1.14222600	0.00000000
C	2.65854200	0.77976000	0.00000000
C	2.30480900	-0.59477400	0.00000000
C	3.32280900	-1.55797500	0.00000000
C	4.66143800	-1.18274300	0.00000000
C	0.00000000	0.04036100	0.00000000
C	0.46981300	1.40761800	0.00000000
C	-0.55784900	2.48280100	0.00000000
C	-2.21723800	0.64460600	0.00000000
H	4.24364100	2.21085100	0.00000000
H	3.08145700	-2.61988200	0.00000000
H	-2.60204500	2.66065200	0.00000000
N	0.96358400	-0.92818400	0.00000000
N	-1.27228200	-0.32413100	0.00000000
N	-1.85167400	1.97560600	0.00000000
N	1.72386000	1.75953800	0.00000000
O	-0.32992700	3.66626700	0.00000000
O	-3.43342300	0.37743800	0.00000000
C	5.72519200	-2.23463000	0.00000000
H	6.37765100	-2.13533400	0.88216500
H	5.29970300	-3.24613500	0.00000000
H	6.37765100	-2.13533400	-0.88216500
C	6.46806100	0.60545900	0.00000000
H	6.99620800	0.21479000	0.88421700
H	6.99620800	0.21479000	-0.88421700
H	6.57009700	1.69801600	0.00000000
H	0.96806600	-2.82782000	0.89720900
C	0.57192700	-2.33274000	0.00000000
H	-0.51987900	-2.37264400	0.00000000
H	0.96806600	-2.82782000	-0.89720900
Rb	-5.57652700	-0.94454200	0.00000000

Sum of electronic and zero-point Energies= -894.940572
Sum of electronic and thermal Energies= -894.922362
Sum of electronic and thermal Enthalpies= -894.921418
Sum of electronic and thermal Free Energies= -894.989714

Rb⁺LF(O2) S₁

C	4.50284500	2.30240700	0.00000000
C	3.15299100	2.74179100	0.00000000
C	2.06212100	1.87351800	0.00000000
C	2.35114500	0.47829700	0.00000000
C	3.70111900	0.03279500	0.00000000
C	4.77867400	0.91136100	0.00000000
C	0.00000000	0.08495800	0.00000000
C	-0.18546200	1.49648400	0.00000000
C	-1.56095100	1.98274900	0.00000000
C	-2.26354100	-0.39147900	0.00000000
H	2.92677200	3.80998600	0.00000000
H	3.90878500	-1.03721700	0.00000000
H	-3.48735200	1.24294300	0.00000000
N	1.30286800	-0.41173900	0.00000000
N	-0.96319600	-0.82530700	0.00000000
N	-2.51685800	0.94267800	0.00000000
N	0.80889500	2.39896600	0.00000000
O	-1.92477500	3.13795200	0.00000000
O	-3.20510000	-1.20946500	0.00000000
C	6.18620800	0.40161100	0.00000000
H	6.74261800	0.75201800	0.88433800
H	6.21426900	-0.69580800	0.00000000
H	6.74261800	0.75201800	-0.88433800
C	5.60164800	3.30206000	0.00000000
H	6.25655500	3.16718300	0.87875500
H	6.25655500	3.16718300	-0.87875500
H	5.22430300	4.33154600	0.00000000
H	2.11071400	-2.13440800	0.89743100
C	1.54376600	-1.84470400	0.00000000
H	0.57225900	-2.34501200	0.00000000
H	2.11071400	-2.13440800	-0.89743100
Rb	-4.70770700	-3.22343800	0.00000000

Sum of electronic and zero-point Energies= -894.834993
Sum of electronic and thermal Energies= -894.816186
Sum of electronic and thermal Enthalpies= -894.815242
Sum of electronic and thermal Free Energies= -894.885028

Cs⁺LF(O2) S₀

C	1.07455300	5.50752600	0.00000000
C	-0.08684100	4.76382000	0.00000000
C	-0.06809900	3.35315700	0.00000000
C	1.17844400	2.67469100	0.00000000
C	2.36096200	3.42691400	0.00000000
C	2.32379500	4.81665000	0.00000000
C	0.00000000	0.59428500	0.00000000
C	-1.21138600	1.38391400	0.00000000
C	-2.50482500	0.64949500	0.00000000
C	-1.12678200	-1.40897100	0.00000000
H	-1.06906400	5.23954300	0.00000000
H	3.33179900	2.93354700	0.00000000
H	-3.17581300	-1.28932300	0.00000000
N	1.17453900	1.29271000	0.00000000
N	0.04336000	-0.72795600	0.00000000
N	-2.32849600	-0.72865400	0.00000000
N	-1.24659400	2.68576900	0.00000000
O	-3.59694000	1.15955900	0.00000000
O	-1.16445000	-2.65320100	0.00000000
C	3.60349900	5.59163200	0.00000000
H	3.66647800	6.24858900	0.88217400
H	4.48060800	4.93217700	0.00000000
H	3.66647800	6.24858900	-0.88217400
C	1.03053400	7.00499400	0.00000000
H	1.53823000	7.42191600	0.88421400
H	1.53823000	7.42191600	-0.88421400
H	-0.00413900	7.37045100	0.00000000
H	3.01772700	0.83278300	0.89720900
C	2.44075900	0.56976900	0.00000000
H	2.21228300	-0.49867000	0.00000000
H	3.01772700	0.83278300	-0.89720900
Cs	-0.39485000	-5.21755500	0.00000000

Sum of electronic and zero-point Energies= -891.009821
Sum of electronic and thermal Energies= -890.991545
Sum of electronic and thermal Enthalpies= -890.990601
Sum of electronic and thermal Free Energies= -891.059742

Cs⁺LF(O2) S₁

C	1.31042800	5.48774800	0.00000000
C	0.08908300	4.76581400	0.00000000
C	0.01991400	3.37325700	0.00000000
C	1.25878100	2.66769500	0.00000000
C	2.48484600	3.38597700	0.00000000
C	2.53701200	4.77527100	0.00000000
C	0.00000000	0.64339300	0.00000000
C	-1.18212000	1.43671300	0.00000000
C	-2.45580300	0.72557400	0.00000000
C	-1.13818100	-1.37139300	0.00000000
H	-0.86212800	5.30186200	0.00000000
H	3.42530700	2.83502300	0.00000000
H	-3.17344900	-1.20906500	0.00000000
N	1.23347700	1.29281200	0.00000000
N	0.04711900	-0.68107300	0.00000000
N	-2.30682500	-0.67903700	0.00000000
N	-1.20214200	2.77959000	0.00000000
O	-3.56339000	1.21590300	0.00000000
O	-1.14567100	-2.61826600	0.00000000
C	3.84961900	5.49501600	0.00000000
H	3.95432500	6.14425100	0.88430800
H	4.69191400	4.79096400	0.00000000
H	3.95432500	6.14425100	-0.88430800
C	1.28719400	6.97326500	0.00000000
H	1.82109700	7.37546100	0.87885800
H	1.82109700	7.37546100	-0.87885800
H	0.26526600	7.37068100	0.00000000
H	3.06008700	0.76081700	0.89737500
C	2.46804400	0.52643400	0.00000000
H	2.20137700	-0.53331800	0.00000000
H	3.06008700	0.76081700	-0.89737500
Cs	-0.62038400	-5.23987200	0.00000000

Sum of electronic and zero-point Energies= -890.904309
Sum of electronic and thermal Energies= -890.885445
Sum of electronic and thermal Enthalpies= -890.884501
Sum of electronic and thermal Free Energies= -890.955077

LF S₀

C	3.38348600	0.85042200	-0.00001600
C	2.16039400	1.49512100	-0.00003800
C	0.94383400	0.78947700	-0.00002300
C	0.96364100	-0.62542700	0.00001400
C	2.20235500	-1.28386500	0.00003900
C	3.39646100	-0.57089900	0.00002400
C	-1.43638600	-0.62289000	0.00001000
C	-1.33517300	0.83160900	-0.00002800
C	-2.61876800	1.59714400	-0.00005000
C	-3.75101300	-0.63136900	0.00001400
H	2.09192200	2.58466300	-0.00006900
H	-4.62871600	1.22926700	-0.00003400
N	-0.23791700	-1.30367400	0.00002700
N	-2.54596300	-1.30467200	0.00003100
N	-3.71992900	0.77525500	-0.00002400
N	-0.22368300	1.49765300	-0.00004500
O	-2.68970000	2.80593600	-0.00007600
O	-4.82340100	-1.19474600	0.00003000
C	4.70096100	-1.30875100	0.00004800
H	5.30637400	-1.04711900	0.88291200
H	4.55111300	-2.39638200	0.00013700
H	5.30632200	-1.04725900	-0.88289400
C	4.66497100	1.62989100	-0.00002700
H	5.28059200	1.39850400	0.88434000
H	5.28067800	1.39834400	-0.88429000
H	4.46900600	2.71018700	-0.00013200
H	0.24896700	-3.14193000	0.89746000
C	-0.25734700	-2.75829400	0.00006200
H	-1.30700300	-3.06833300	0.00005100
H	0.24900100	-3.14197200	-0.89729800
H	2.24450900	-2.37242900	0.00007100

Sum of electronic and zero-point Energies= -870.962549
Sum of electronic and thermal Energies= -870.946653
Sum of electronic and thermal Enthalpies= -870.945708
Sum of electronic and thermal Free Energies= -871.005463

LF S₁

C	3.38995800	0.83517600	-0.00001600
C	2.17233200	1.50837000	-0.00003500
C	0.92872600	0.84540600	-0.00001800
C	0.96735000	-0.59631300	0.00002300
C	2.19824700	-1.27370000	0.00004300
C	3.40955600	-0.59124400	0.00002400
C	-1.41105700	-0.55920500	0.00001800
C	-1.35859600	0.86358800	-0.00001800
C	-2.62630000	1.57782700	-0.00002500
C	-3.75333900	-0.64568400	-0.00000300
H	2.13668200	2.59913700	-0.00006600
H	-4.65063100	1.18868000	-0.00006100
N	-0.23642300	-1.27166700	0.00004000
N	-2.51875800	-1.29827300	0.00002900
N	-3.74553000	0.72957900	-0.00003100
N	-0.20134400	1.56862600	-0.00003700
O	-2.77116600	2.78544800	-0.00009700
O	-4.78578300	-1.29253500	0.00000300
C	4.70573500	-1.34114300	0.00004600
H	5.31884800	-1.09640700	0.88355600
H	4.53863900	-2.42681500	0.00008600
H	5.31884000	-1.09647200	-0.88348700
C	4.67190500	1.60455700	-0.00003500
H	5.28542100	1.35750000	0.88238700
H	5.28543600	1.35743300	-0.88242900
H	4.49070500	2.68685500	-0.00007700
H	0.25653000	-3.10295000	0.89629100
C	-0.25808700	-2.72668700	0.00007900
H	-1.30302300	-3.04734700	0.00008500
H	0.25653500	-3.10299800	-0.89610900
H	2.21741800	-2.36347200	0.00007400

Sum of electronic and zero-point Energies= -870.860269
Sum of electronic and thermal Energies= -870.844696
Sum of electronic and thermal Enthalpies= -870.843752
Sum of electronic and thermal Free Energies= -870.902746

Electronic Supporting Information

Vibronic Optical Spectroscopy of Cryogenic Flavin Ions: The O2+ and N1 Tautomers of Protonated Lumiflavin

David Müller and Otto Dopfer*

Institut für Optik und Atomare Physik, Technische Universität Berlin, Hardenbergstr. 36, D-10623 Berlin, Germany

Figure Captions

Figure S1. Photodissociation mass spectrum of H^+LF recorded for excitation wavelength of 23128 cm^{-1} (432.37 nm) assigned to the S_1 origin of the O2^+ tautomer at a trap temperature of $T=6\text{ K}$. The branching ratio depends somewhat on the timing of the high-voltage extraction pulse of the reflectron time-of-flight mass spectrometer. In general, the branching ratio does not depend significantly on the excitation frequency, leading to essentially the same VISPD action spectra monitored in each fragment channel (Figure S2). The suggested assignment of the fragment peaks is provided in Table S1.

Figure S2. VISPD spectra of H^+LF recorded in various fragmentation channels measured at a trap temperature of $T=6\text{ K}$. The spikes between 20500 and 21000 cm^{-1} are not reproducible. The overview spectrum is recorded with the OPO laser at a step size of 0.5 nm (20 cm^{-1} at 500 nm).

Figure S3. Structures of the less stable protomers of H^+LF in the S_0 state obtained at the PBE0/cc-pVDZ level.

Figure S4. Vertical ($\text{S}_1\text{-S}_4$, $\text{T}_1\text{-T}_4$) excitation energies of various H^+LF protomers and LF with respect to the S_0 energy computed at the PBE0/cc-pVDZ level. Triplet energies are reported in Table S7.

Figure S5. Vertical ($\text{S}_1\text{-S}_4$) and adiabatic ($\text{S}_1\text{-S}_2$) excitation energies of various H^+LF protomers and LF with respect to S_0 computed at the PBE0/cc-pVDZ level.

Figure S6. Atomic NBO charge distribution in the S_0 and S_1 states of neutral LF (in 10^{-3} e) evaluated at the PBE0/cc-pVDZ level.

Figure S7. Schematic visualization of in-plane normal modes m1-m12 of LF in the S_1 state calculated at the PBE0/cc-pVDZ level.

Figure S8. Schematic visualization of in-plane normal modes m1-m12 of $\text{H}^+\text{LF}(\text{O2}^+)$ in the S_1 state calculated at the PBE0/cc-pVDZ level.

Figure S9. Laser-induced fluorescence excitation spectrum of the $\text{S}_1 \leftarrow \text{S}_0$ transition of LF in He droplets (Vdovin et al., Chem. Phys. **422**, 195 (2013)) compared to corresponding VISPD spectrum of H^+LF . Corresponding transitions are connected by dotted lines.

Figure S10. Schematic visualization of low energy out-of-plane modes (n1-n8) of $\text{H}^+\text{LF}(\text{N1})$ in the S_1 state calculated at the PBE0/cc-pVDZ level.

Figure S11. Comparison between Franck-Condon simulations for the $\text{S}_1 \leftarrow \text{S}_0$ transition of $\text{H}^+\text{LF}(\text{N1})$ with planar structure (transition state) and slightly bent structure (minimum).

Figure S12. Comparison between Franck-Condon simulations for the $S_1 \leftarrow S_0$ transition of various H^+LF protomers shown in Figure 1 and S3.

Figure S13: Absolute distances of neutral lumiflavin in its electronic ground state S_0 . Geometry changes upon protonation (O2+/N1). Positive values indicate elongations, negative values indicate contractions. All values are given in pm.

Figure S14. Dependence of the intensity of the 0^0 transition of the $H^+LF(O2^+)$ protomer (top) and $H^+LF(N1)$ protomer (bottom) as a function of the laser power. According to a least-square error analysis, the experimental data is better fitted by linear than a quadratic curve.

Figure S15. Comparison of VISPD spectrum of cryogenic H^+LF ins in the gas phase with absorption spectrum of LF and H^+LF in solution.

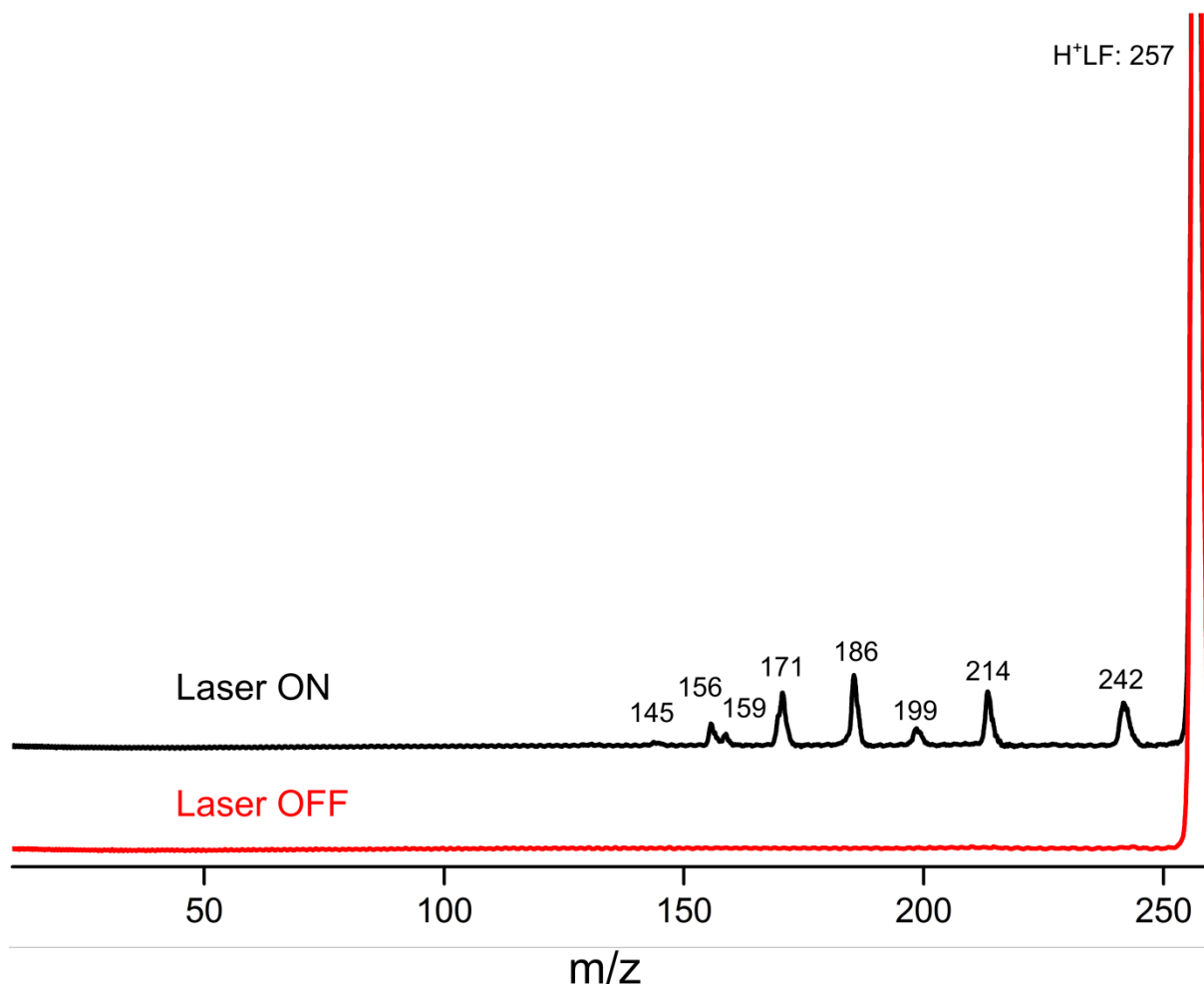


Figure S1

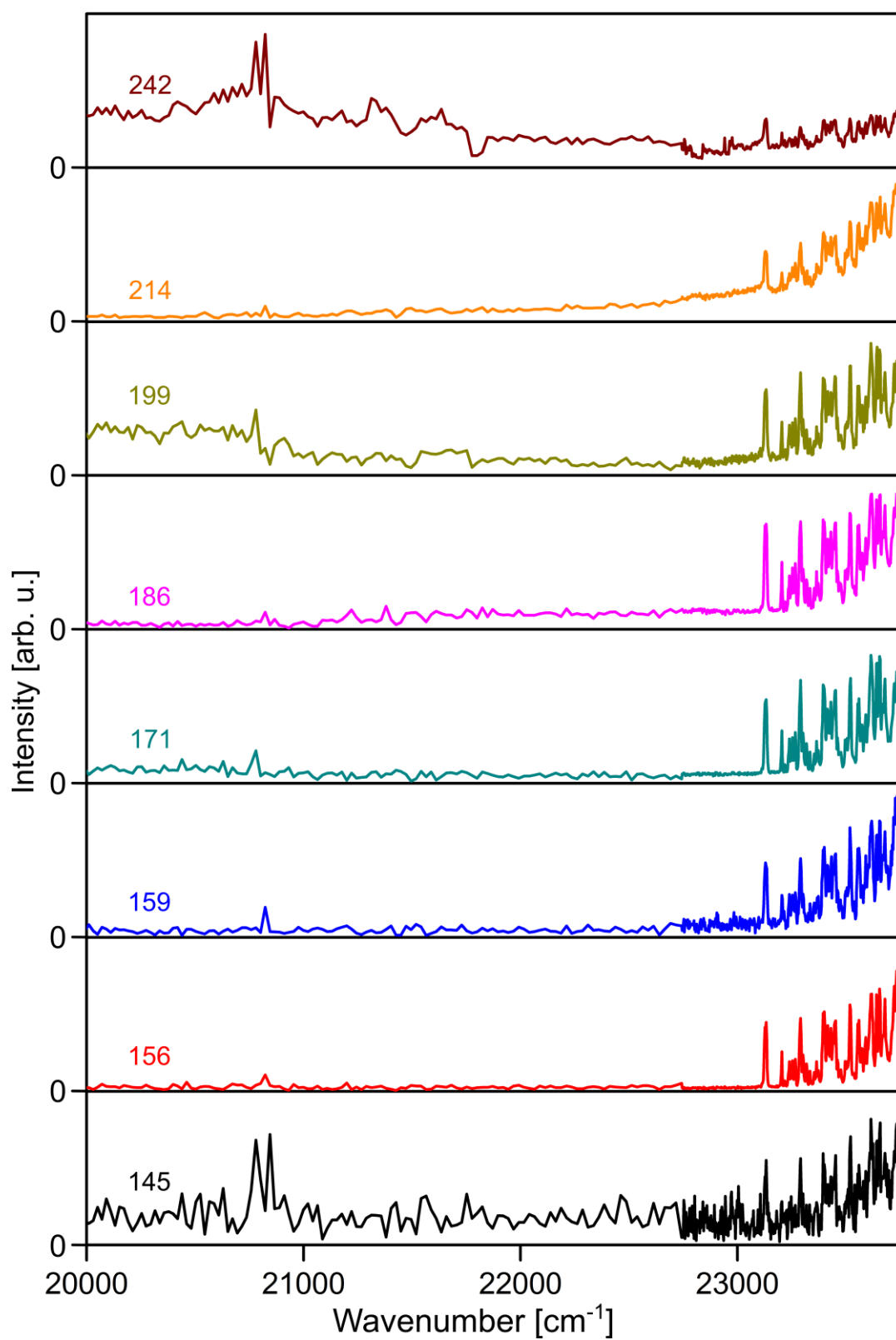
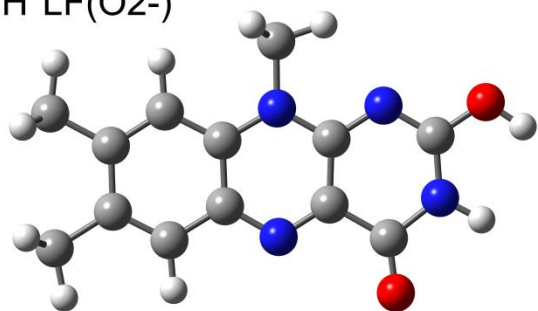
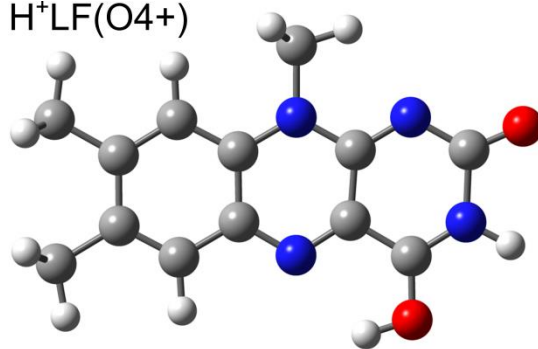


Figure S2

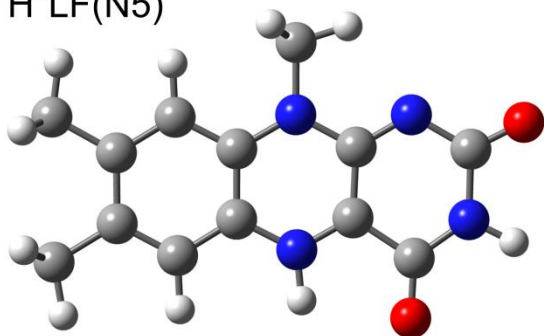
H⁺LF(O2-)



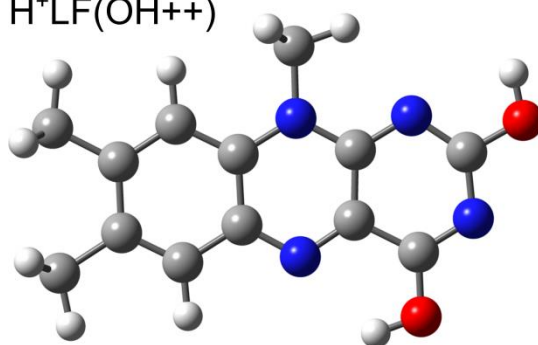
H⁺LF(O4+)



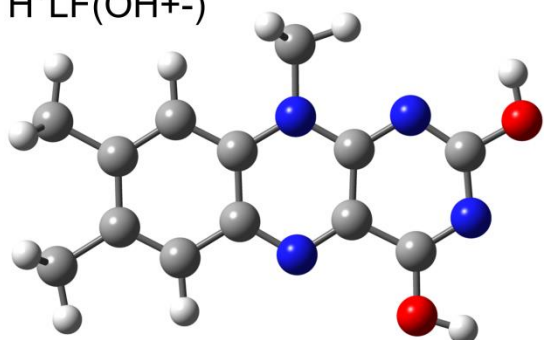
H⁺LF(N5)



H⁺LF(OH++)



H⁺LF(OH+-)



H⁺LF(O4-)

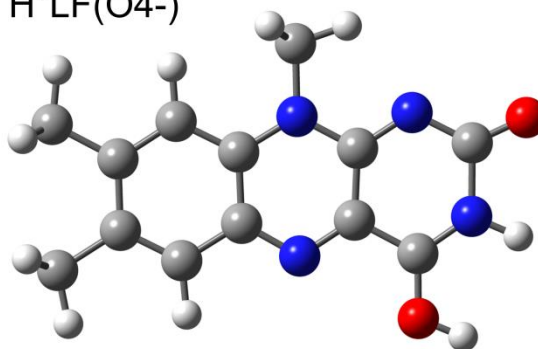


Figure S3

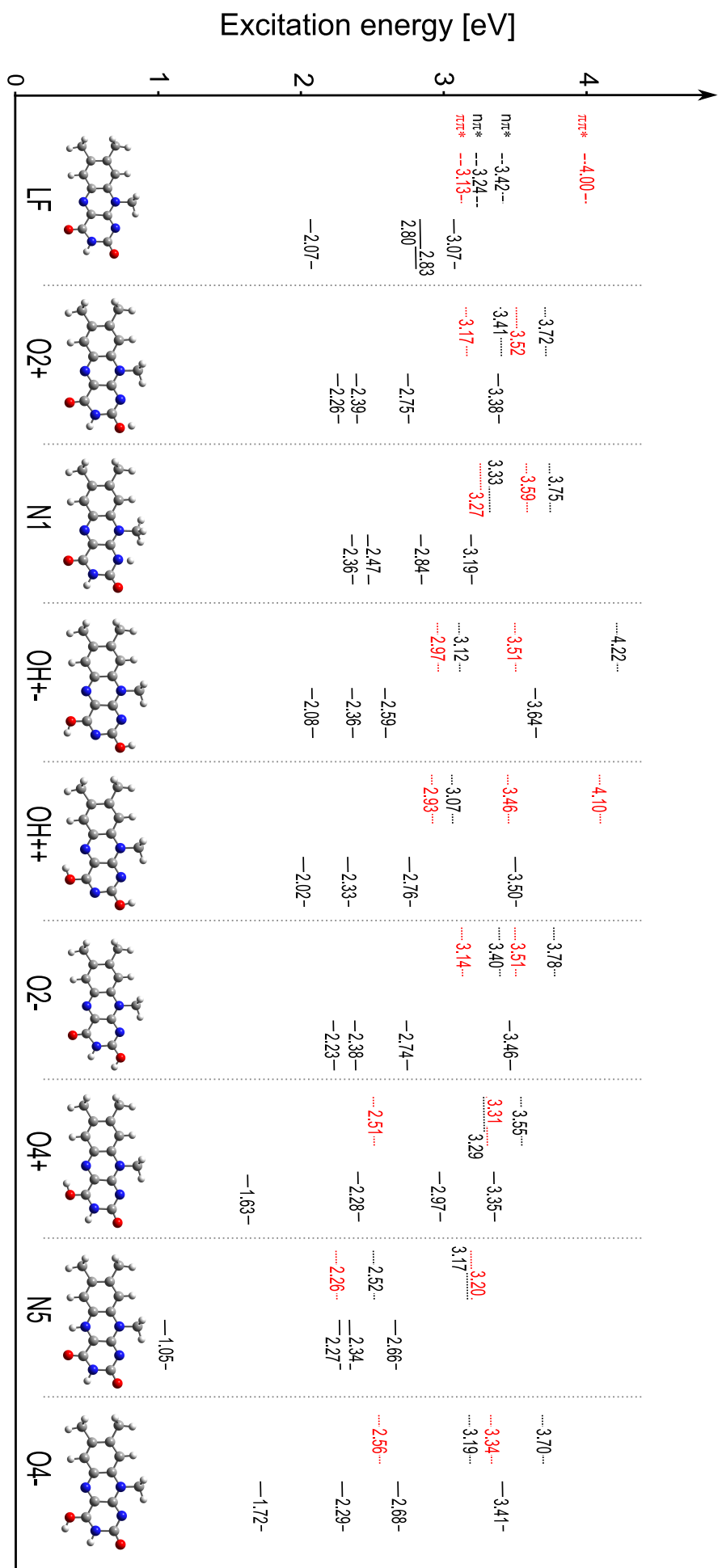


Figure S4

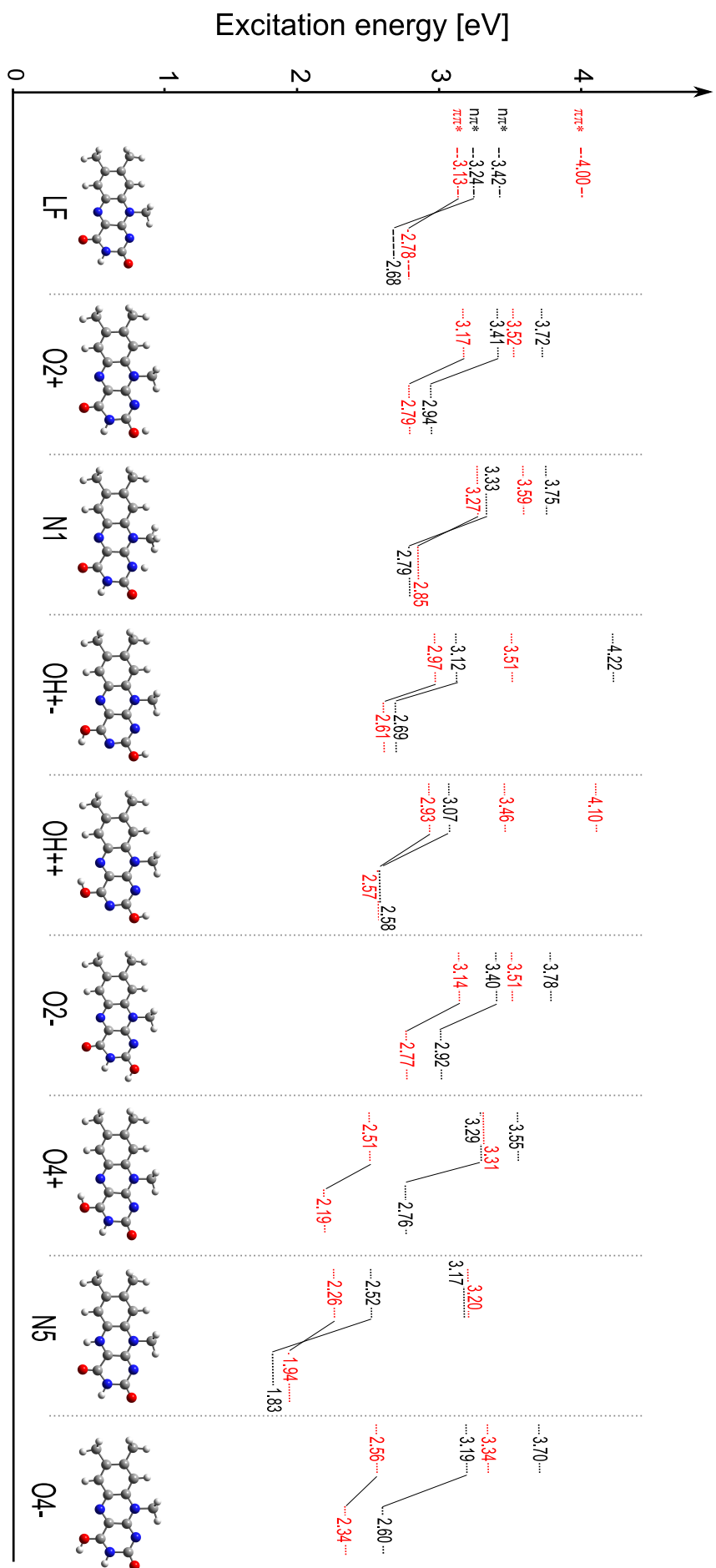


Figure S5

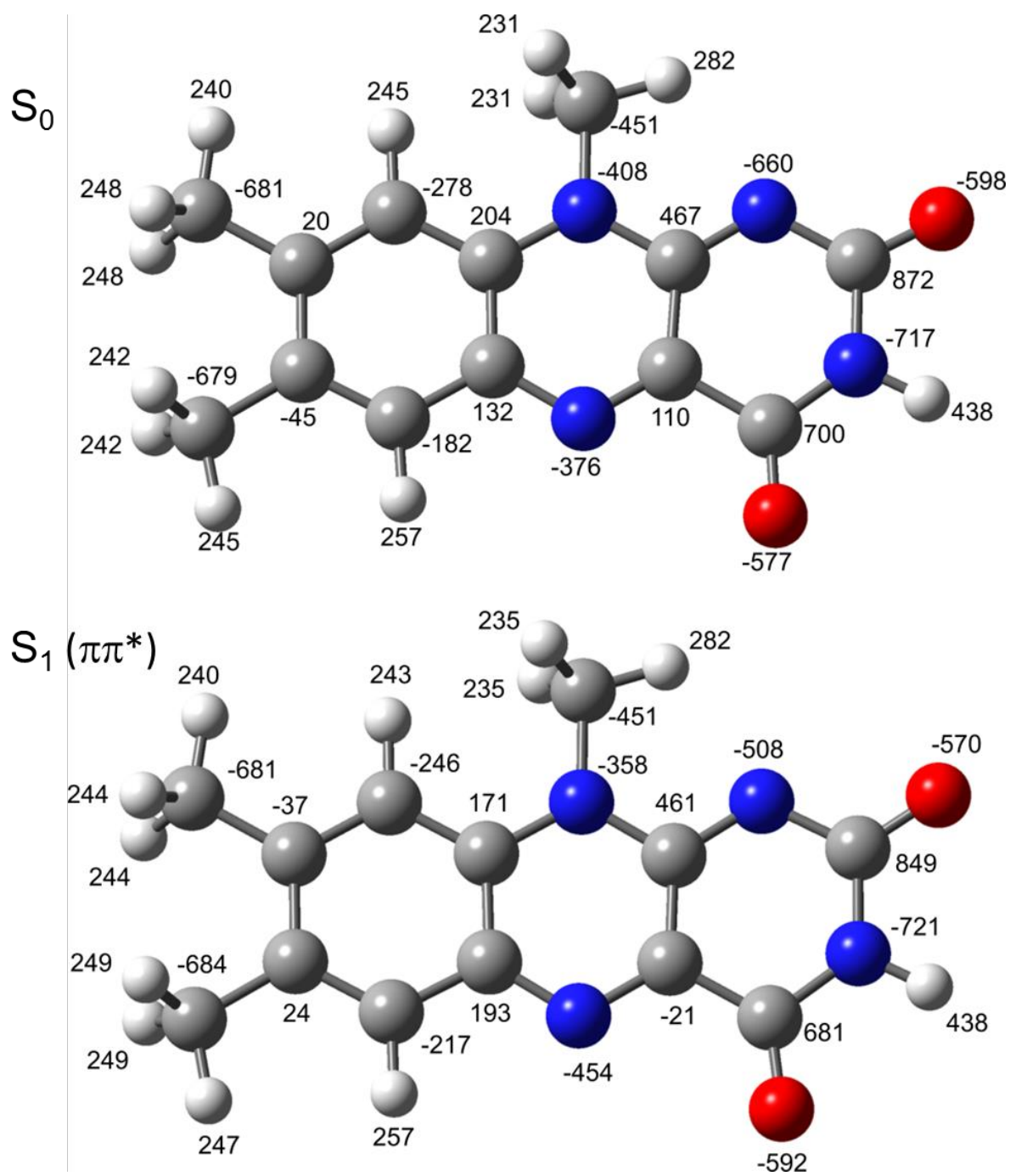


Figure S6

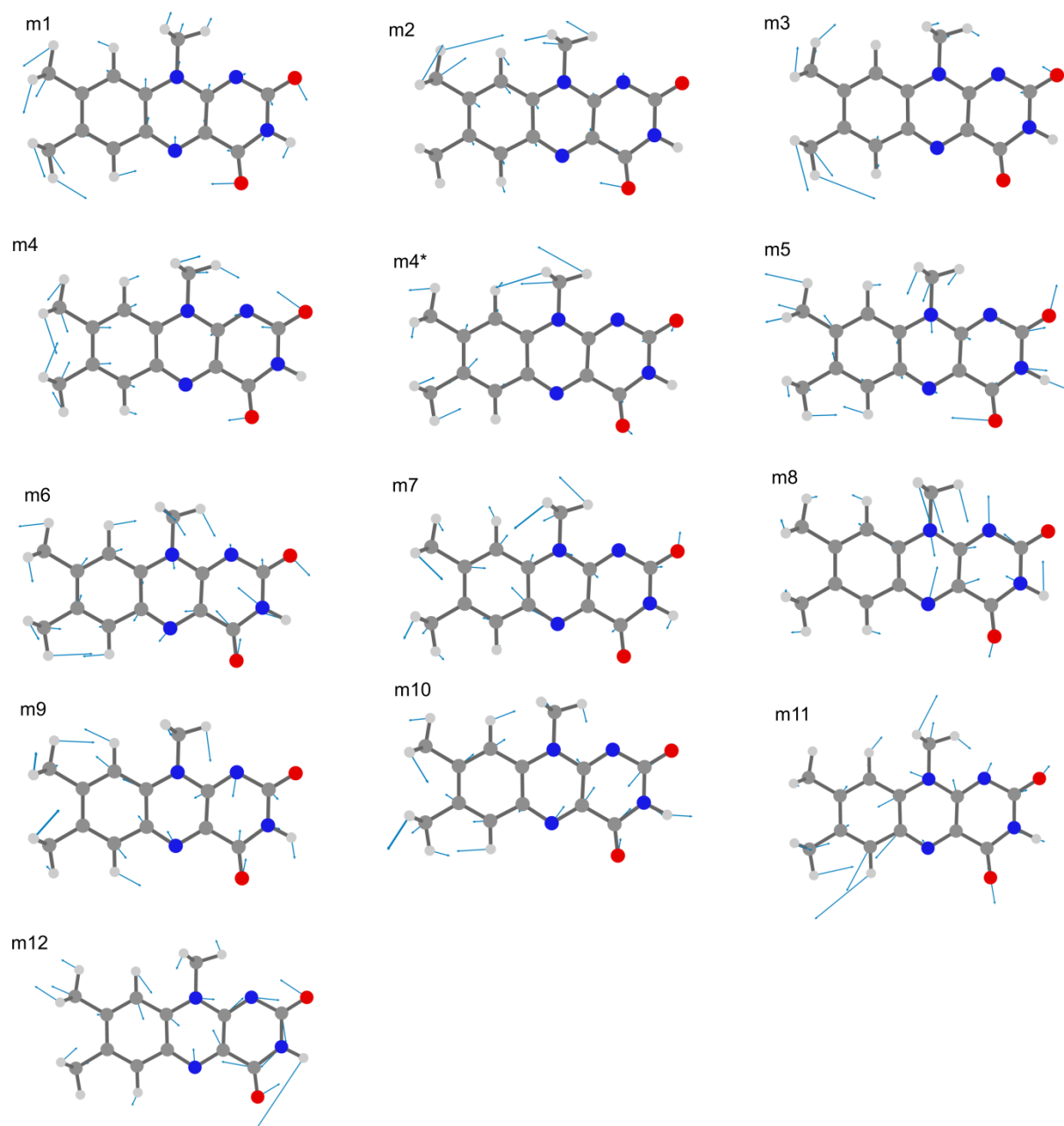


Figure S7

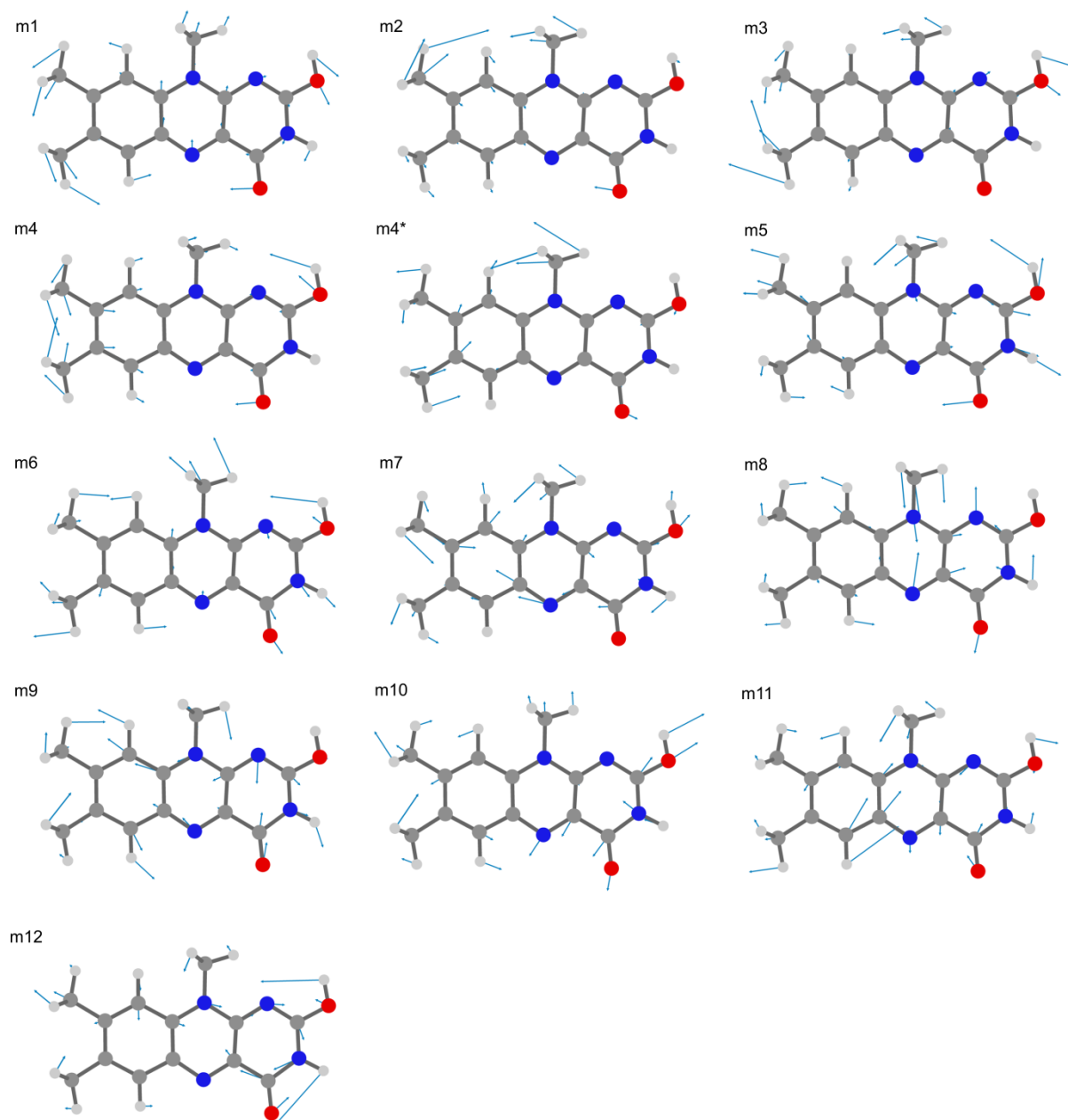


Figure S8

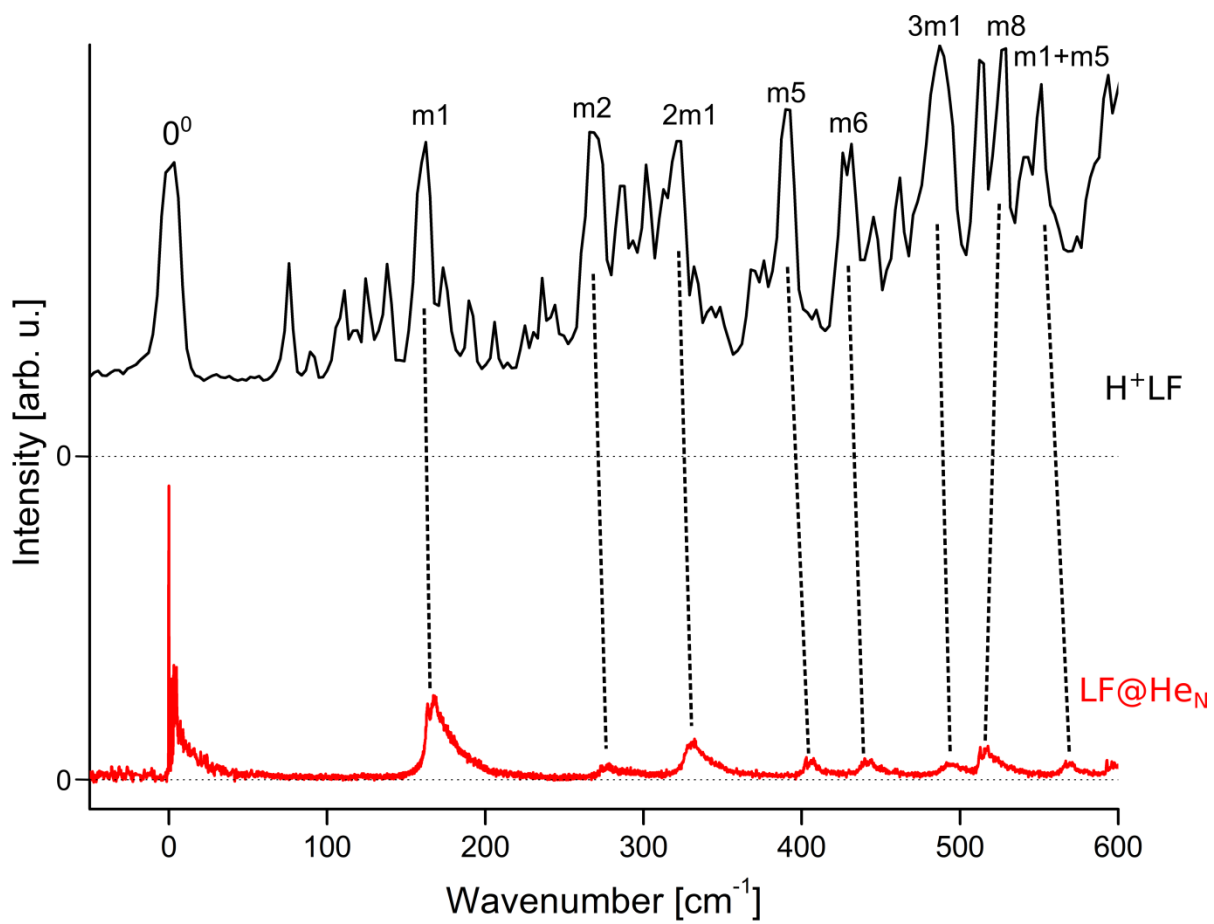


Figure S9

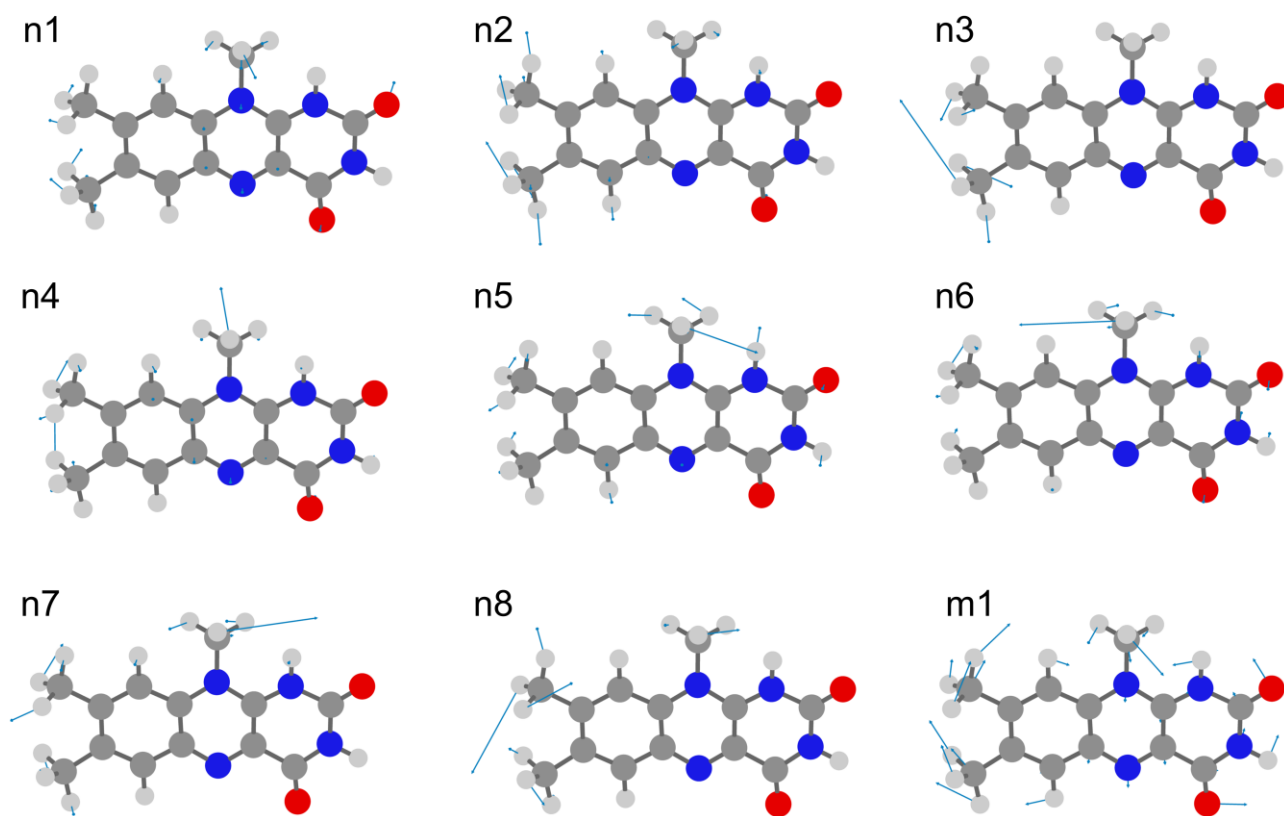


Figure S10

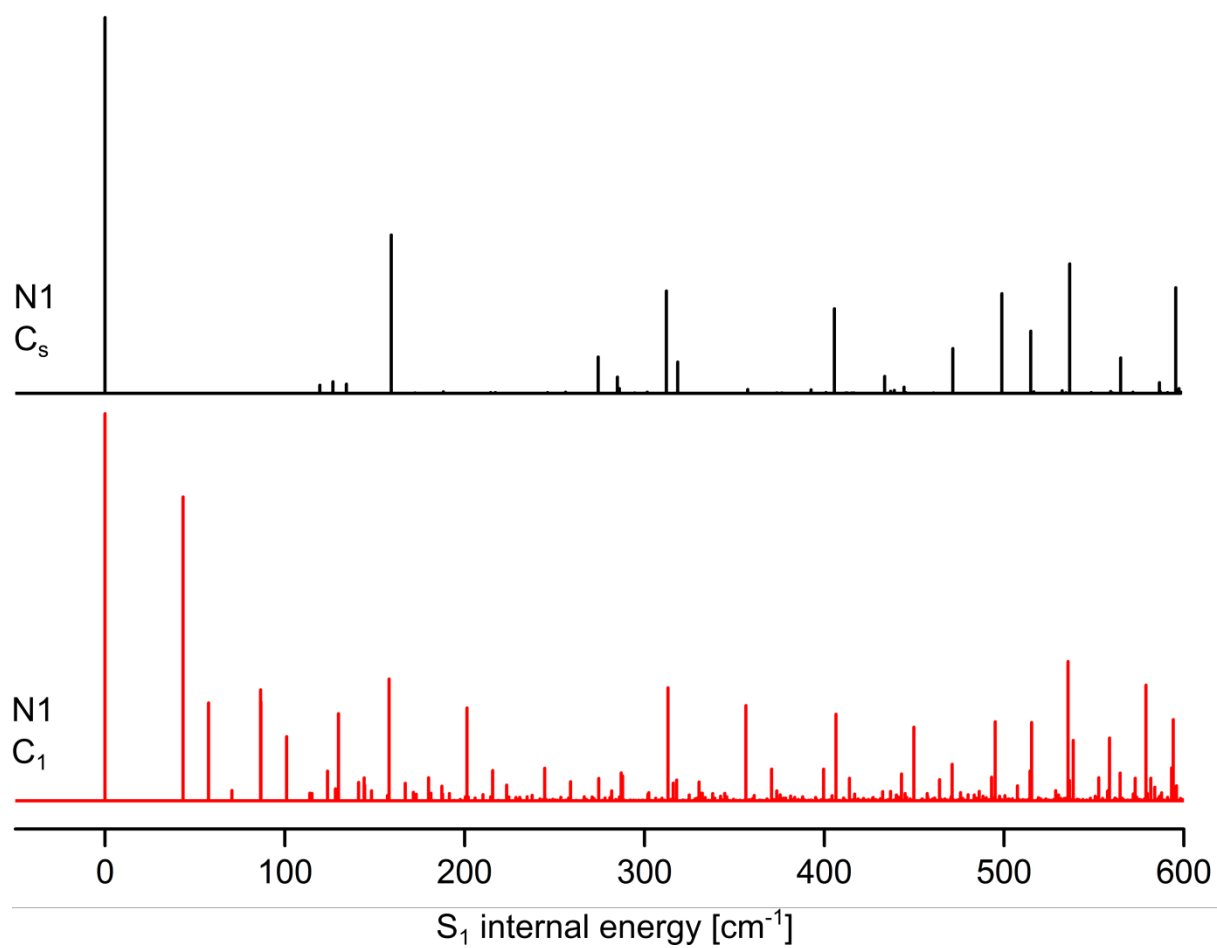


Figure S11

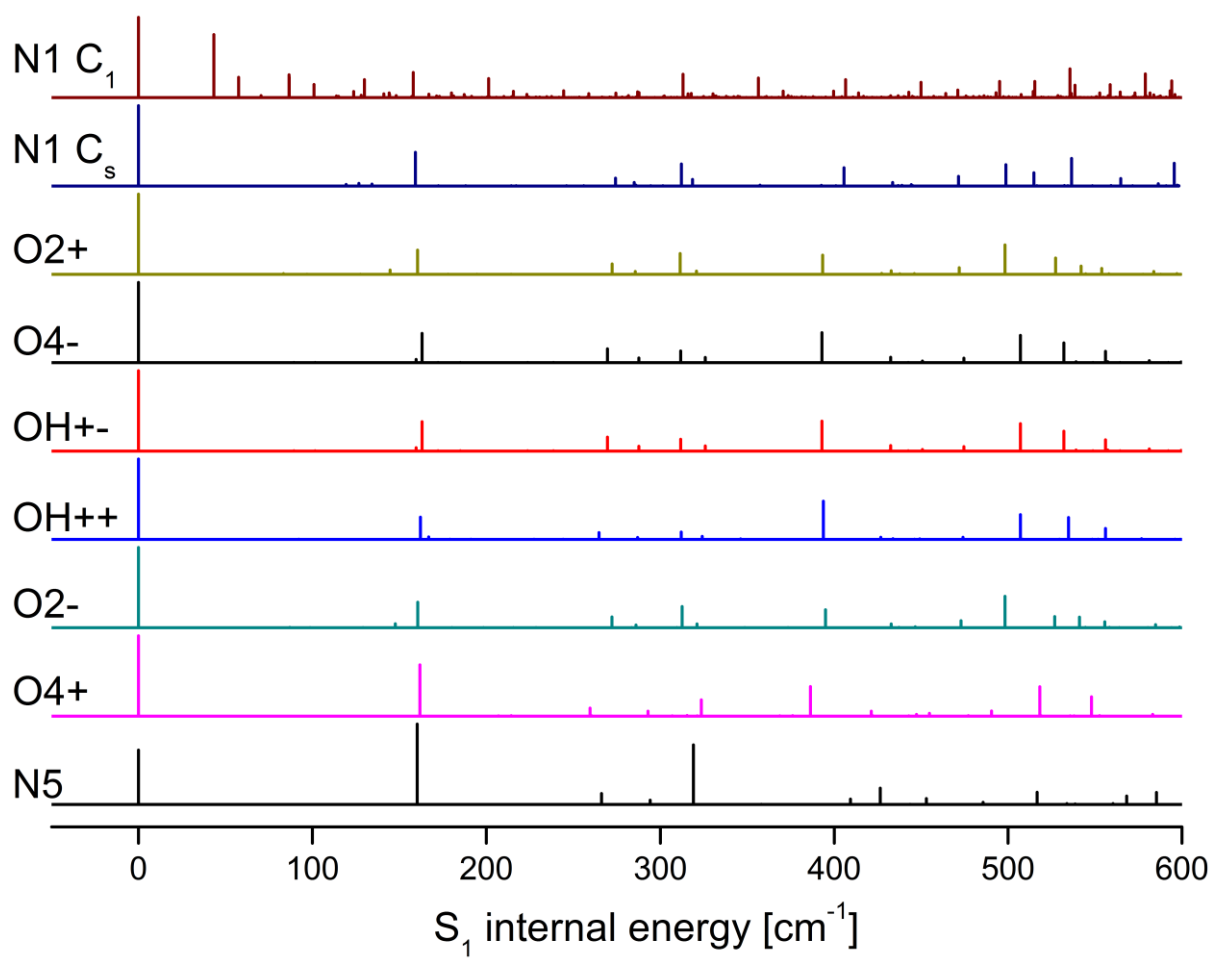
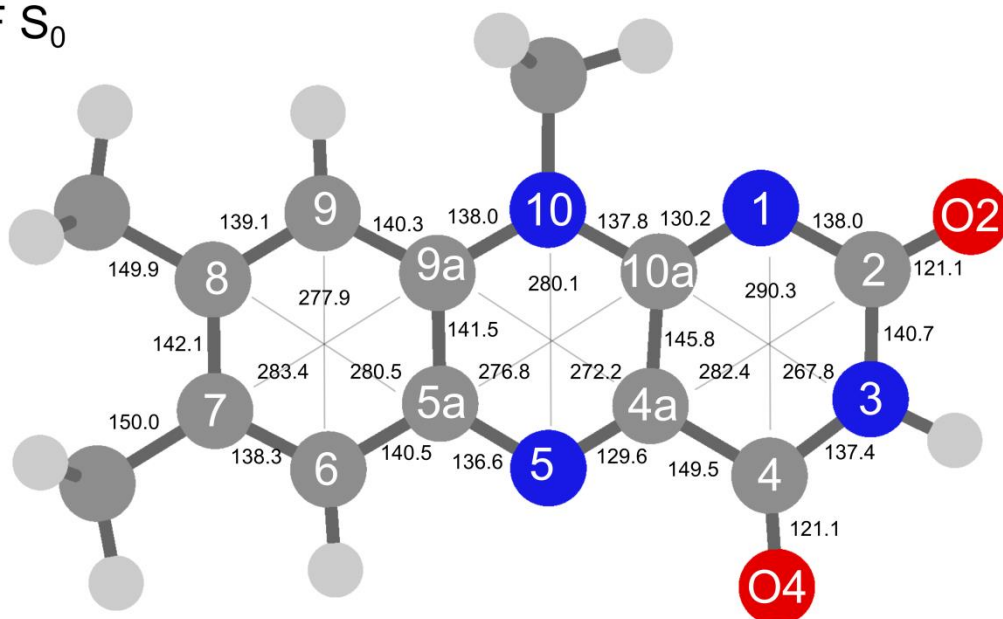


Figure S12

LF S₀



LF → H⁺LF(O2⁺/N1)

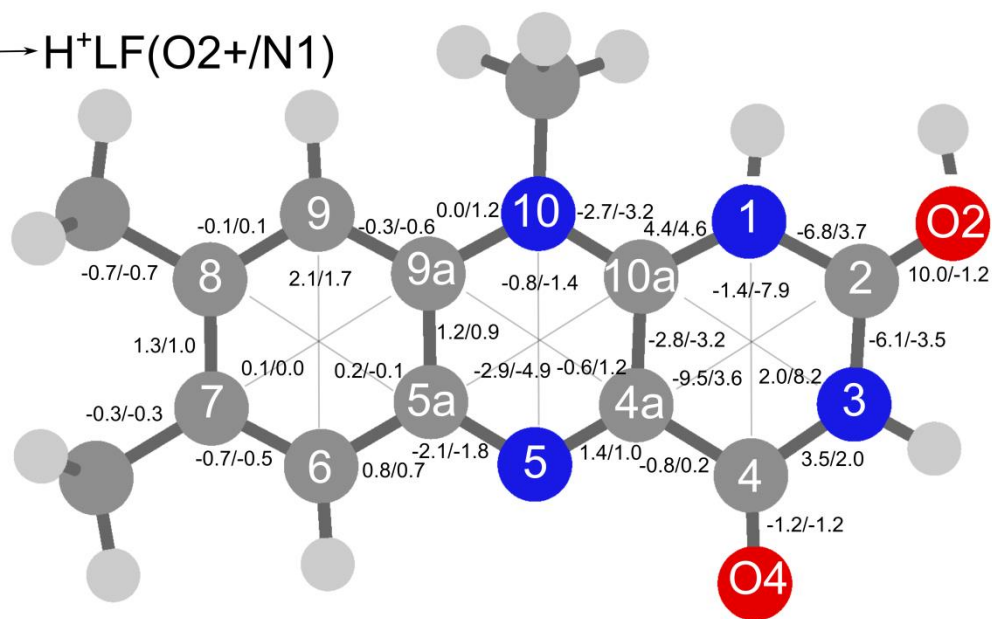


Figure S13

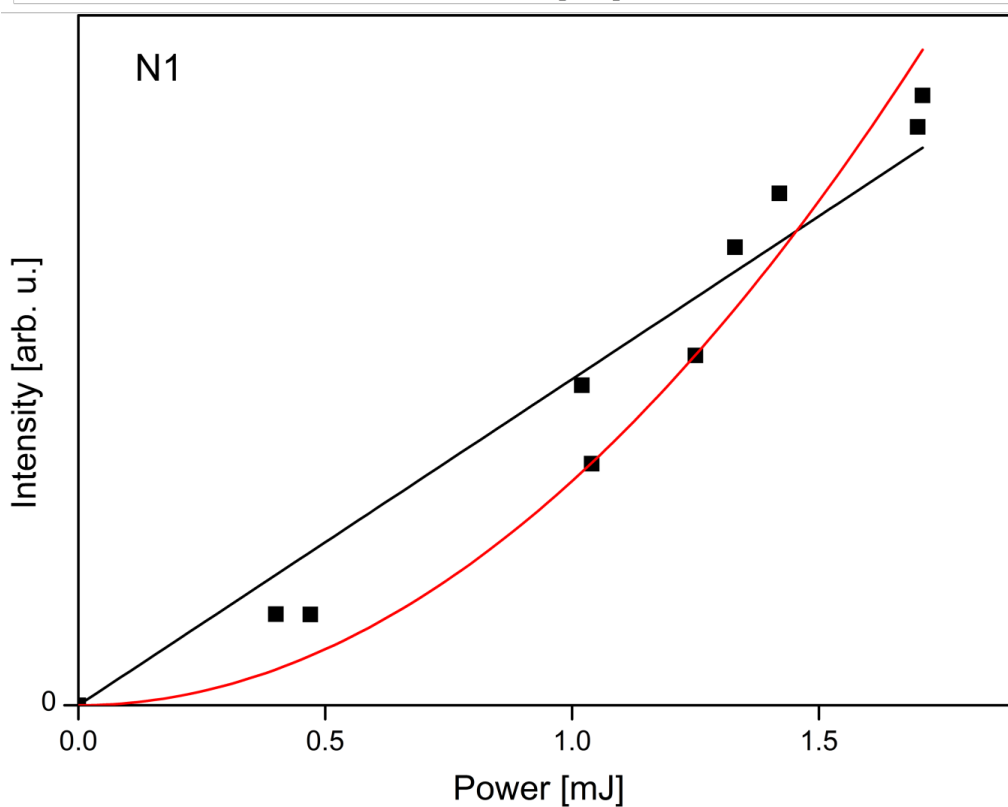
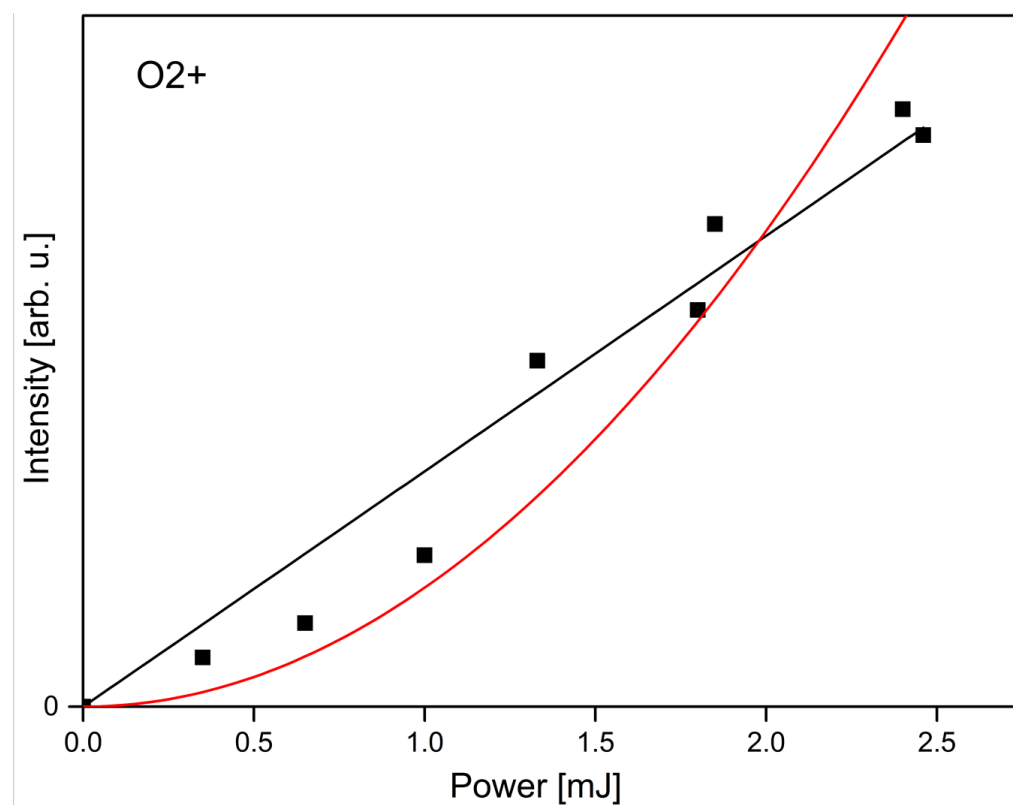


Figure S14

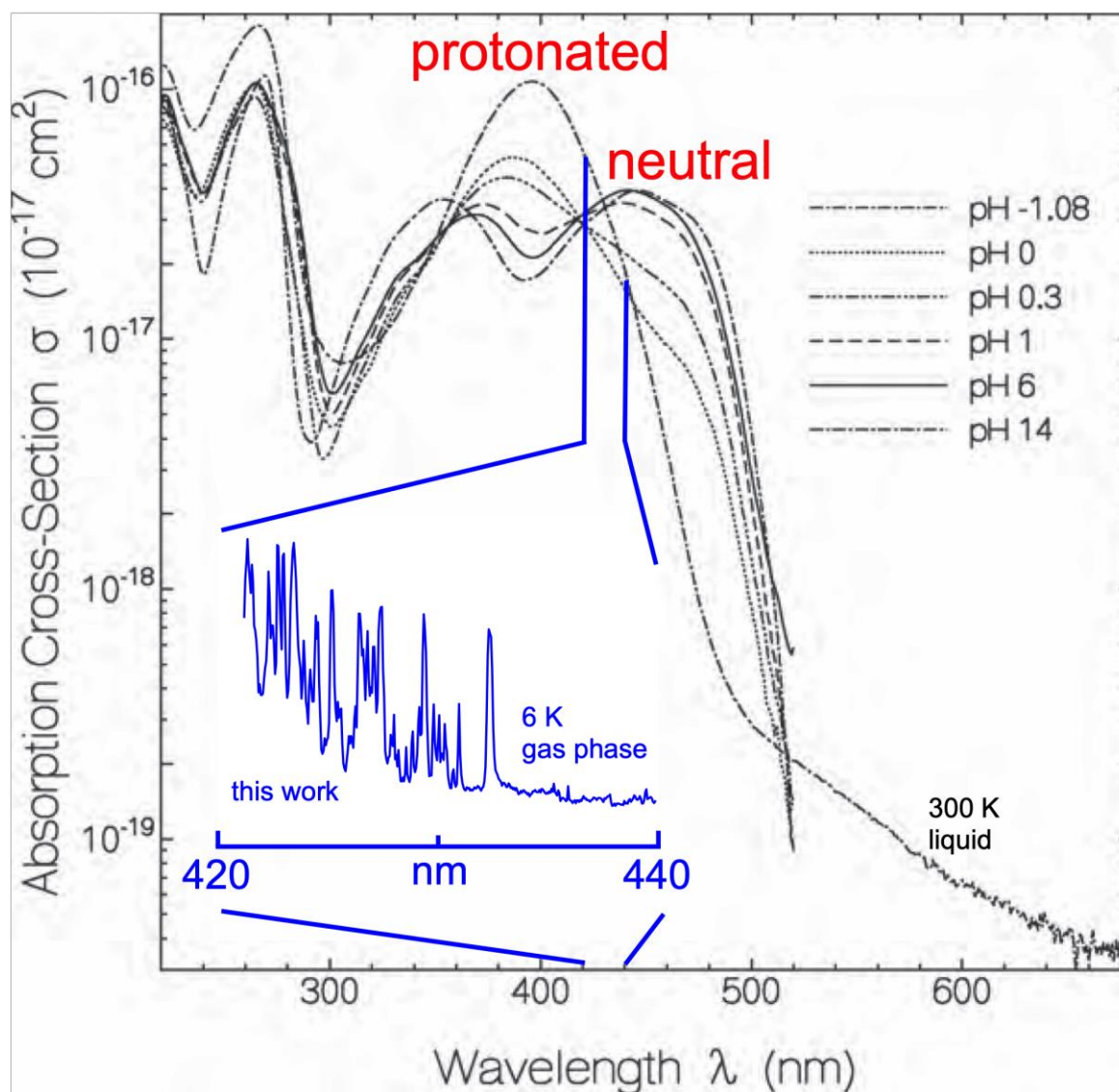


Figure S15

Table S1. Fragmentation channels of H^+LF (m/z 257) observed upon VISPD and possible assignment of neutral fragment molecules.

Fragment Ion (m/z)	Assignment	Loss from H^+LF (m/z)
145	$2\text{CO} + \text{CH}_3\text{CN} + \text{CH}_3$ $\text{CO} + \text{CH}_3\text{CN} + \text{OCNH}$	112
156	$\text{OCNH} + \text{CO} + 2\text{CH}_3$	101
159	$\text{OCNH} + \text{CO} + \text{HCN}$	98
171	$\text{OCNH} + \text{CO} + \text{CH}_3$	86
186	$\text{OCNH} + \text{CO}$	71
199	$\text{CH}_3 + \text{OCNH}$ $\text{CO} + 2\text{CH}_3$	58
214	$\text{CO} + \text{CH}_3$ OCNH	43
242	CH_3	15

Table S2. Selected atomic charges (in e) of $\text{H}^+\text{LF}(\text{O}_2^+/\text{N}_1)$ and LF for the S_0 and S_1 states using natural bond orbital analysis (PBE0/cc-pVDZ).

	q_{H}		q_{N5}		q_{O4}		q_{O2}		q_{N1}	
	S_0	S_1	S_0	S_1	S_0	S_1	S_0	S_1	S_0	S_1
O2+	0.521	0.517	-0.336	-0.457	-0.507	-0.533	-0.639	-0.645	-0.671	-0.655
N1	0.462	0.457	-0.327	-0.456	-0.508	-0.530	-0.555	-0.574	-0.671	-0.659
LF			-0.376	-0.454	-0.577	-0.592	-0.598	-0.570	-0.660	-0.508

Table S3. Calculated frequencies (in cm^{-1}) of $\text{H}^+\text{LF}(\text{O}_2^+)$ for the S_0 and S_1 states at the PBE0/cc-pVDZ level of theory. Frequencies are listed according to symmetry following the Mullikan notation.

S_0		S_1	
a''	a'	a''	a'
50.91	164.25	41.67	160.42
61.00	281.26	55.14	272.39
102.56	298.26	72.36	285.68
134.29	322.24	88.95	311.49
149.23	357.74	141.89	348.26
164.24	398.21	152.99	393.39
177.48	431	158.43	427.30
193.66	497.66	176.05	498.28
207.08	531.75	195.42	527.39
266.53	548.9	218.89	541.95
347.46	603.25	311.51	603.27
400.17	642.12	346.47	631.04
465.55	650.26	388.87	647.84
536.68	758.05	453.14	747.29
562.93	790.12	537.15	787.16
639.88	838.75	586.08	830.83
675.21	894.65	640.79	893.72
731.54	998.83	697.71	992.97
757.96	1023.89	737.35	1007.58
782.37	1030.1	743.71	1026.94
837.02	1090.02	793.81	1080.10
868.33	1112.68	871.33	1103.48
921.80	1176.55	900.03	1166.80
1029.66	1184.46	990.18	1177.52
1053.37	1214.26	1039.02	1208.38
1133.92	1248.13	1127.24	1229.47
1438.16	1261.77	1413.95	1255.73
1454.48	1309.35	1449.42	1272.21
1472.41	1329.83	1474.99	1319.26
3134.36	1354.52	3089.84	1342.48
3138.27	1372.71	3134.53	1351.39
3186.33	1384.95	3152.86	1361.99
	1395.14		1382.53
	1405.22		1392.81
	1426.54		1400.65
	1432.96		1414.90
	1452.65		1442.95
	1464.6		1450.31
	1482.7		1464.76
	1506.29		1470.27
	1545.15		1485.36
	1550.12		1526.85
	1620.26		1564.94
	1634.99		1595.28
	1650.21		1635.10
	1681.71		1664.09
	1700.67		1703.13
	1889.33		1855.31
	3062.16		3031.46
	3064.36		3060.97
	3092.97		3068.84
	3180.5		3177.19
	3181.28		3188.41
	3235.34		3227.03
	3246.62		3230.26
	3249.32		3240.20
	3586.67		3590.35
	3770.09		3779.48

Table S4. Calculated frequencies (in cm^{-1}) of $\text{H}^+\text{LF}(\text{N1})$ for the S_0 and S_1 state at the PBE0/cc-pVDZ level of theory.

S_0 a''	S_1 a''		
47.25	43.30	1437.69	1421.82
61.67	57.56	1438.94	1440.41
97.64	70.49	1454.55	1449.43
105.55	86.50	1458.87	1461.92
132.34	123.69	1469.58	1467.76
133.59	132.29	1493.96	1470.65
140.89	144.39	1496.71	1479.05
163.27	148.19	1519.79	1486.87
181.45	157.98	1563.24	1524.46
199.12	179.96	1573.27	1566.79
249.75	197.55	1630.79	1590.04
289.00	274.56	1675.56	1636.99
298.62	287.08	1701.75	1686.57
324.23	287.96	1882.05	1856.35
339.66	313.11	1909.16	1893.05
374.94	333.72	3062.37	3026.97
388.29	365.56	3065.09	3062.42
410.95	378.50	3088.26	3062.60
431.05	406.63	3134.91	3083.74
457.31	427.19	3139.56	3136.88
498.21	440.13	3180.47	3161.58
517.34	495.11	3182.29	3177.82
525.77	515.37	3188.52	3190.58
543.62	535.64	3223.75	3192.89
572.52	547.93	3235.85	3226.62
596.63	583.82	3246.27	3233.83
630.98	594.13	3596.50	3606.75
637.87	614.55	3630.52	3634.84
660.74	629.07		
666.82	659.90		
720.19	686.67		
756.04	714.76		
764.55	745.19		
774.40	761.75		
786.51	780.88		
820.71	786.29		
841.61	836.09		
862.58	871.07		
879.21	877.60		
923.12	895.66		
996.67	985.61		
1017.54	990.16		
1025.43	1005.42		
1028.87	1013.45		
1035.83	1035.68		
1053.19	1039.94		
1109.51	1101.67		
1121.85	1117.14		
1183.01	1175.21		
1196.61	1181.11		
1228.29	1213.63		
1266.79	1259.28		
1295.22	1271.74		
1306.95	1304.47		
1349.22	1331.30		
1366.03	1333.91		
1383.21	1343.32		
1392.52	1378.12		
1400.55	1379.92		
1424.64	1396.92		
1430.40	1408.50		
1435.61	1416.17		

Table S5. Possible peak assignment of the sharp peaks a-t in the VISPD spectrum of H⁺LF to low-frequency a" modes of the H⁺LF(O2+) isomer.

Peak	Exp	Calc O2+	a" modes
	75	83, 72	2x42, 72
a	90	97, 89	42+55, 89
b	104	97	42+55
c	110/111	110	2x55
d	117	114	42+72
e	124	131	42+89
f	127	131	42+89
g	132	131	42+89
h	138	144	55+89
i	165	161	72+89
j	174/176	178	2x89
k	180	178	2x89
l	190	195	153+42
m	206	200	158+42
n	214	214	158+55, 142+72
o	225	225	153+72
p	231	231	158+72, 89+142, 55+176
q	237	237	195+42
r	241	242	153+89
s	245	247	158+89
t	262	261	219+42

Table S6. Adiabatic S₁ energies of LC, LF, and various protonated tautomers computed at the PBE0/cc-pVDZ level compared to available experimental values (in cm⁻¹).

tautomer	H ⁺ LC (S ₁) calc ^a	H ⁺ LC (S ₁) exp ^a	H ⁺ LF (S ₁) calc	H ⁺ LF (S ₁) exp
neutral	24826		22448	21511 ^b
N1	-	-	23025	23202
O2+	22422		22535	23128
O2-			22341	
O4+	18451		17682	
O4-			18046	
N5	19153	19962	15622	
N10	22555		-	-

^a Sheldrick et al., Phys. Chem. Chem. Phys. **20**, 7407 (2018)

^b Vdovin et al., Chem. Phys. **422**, 195 (2013)

Table S7. Vertical and adiabatic triplet excitation energies computed at the PBE0/cc-pVDZ level with respect to the optimized electronic ground state S_0 (in cm^{-1}).

	T_1	T_2	T_3	T_4
	$E_v(E_a)$	E_v	E_v	E_v
LF	16699	22605	22791	24748
O2+	18250 (16522)	19301	22186	27250
N1	19009 (17413)	19957	22906	25715
O2-	17947 (16258)	19215	22135	27898
O4+	13175 (11803)	18361	23981	26980
N5	8469 (7745)	18280	18910	21491
OH++	16266 (14615)	18765	22281	28217
OH+-	16743 (15005)	19073	20896	29350
O4-	16743 (12372)	19073	20896	29350

Table S8. Optimized geometries of S₀-S₂ of LF and H⁺LF shown in Figure 1 and Figure S3**LF S₀**

C	3.38348600	0.85042200	-0.00001600
C	2.16039400	1.49512100	-0.00003800
C	0.94383400	0.78947700	-0.00002300
C	0.96364100	-0.62542700	0.00001400
C	2.20235500	-1.28386500	0.00003900
C	3.39646100	-0.57089900	0.00002400
C	-1.43638600	-0.62289000	0.00001000
C	-1.33517300	0.83160900	-0.00002800
C	-2.61876800	1.59714400	-0.00005000
C	-3.75101300	-0.63136900	0.00001400
H	2.09192200	2.58466300	-0.00006900
H	-4.62871600	1.22926700	-0.00003400
N	-0.23791700	-1.30367400	0.00002700
N	-2.54596300	-1.30467200	0.00003100
N	-3.71992900	0.77525500	-0.00002400
N	-0.22368300	1.49765300	-0.00004500
O	-2.68970000	2.80593600	-0.00007600
O	-4.82340100	-1.19474600	0.00003000
C	4.70096100	-1.30875100	0.00004800
H	5.30637400	-1.04711900	0.88291200
H	4.55111300	-2.39638200	0.00013700
H	5.30632200	-1.04725900	-0.88289400
C	4.66497100	1.62989100	-0.00002700
H	5.28059200	1.39850400	0.88434000
H	5.28067800	1.39834400	-0.88429000
H	4.46900600	2.71018700	-0.00013200
H	0.24896700	-3.14193000	0.89746000
C	-0.25734700	-2.75829400	0.00006200
H	-1.30700300	-3.06833300	0.00005100
H	0.24900100	-3.14197200	-0.89729800
H	2.24450900	-2.37242900	0.00007100

Sum of electronic and zero-point Energies= -870.962549
Sum of electronic and thermal Energies= -870.946653
Sum of electronic and thermal Enthalpies= -870.945708
Sum of electronic and thermal Free Energies= -871.005463

LF S₁

C	3.38995800	0.83517600	-0.00001600
C	2.17233200	1.50837000	-0.00003500
C	0.92872600	0.84540600	-0.00001800
C	0.96735000	-0.59631300	0.00002300
C	2.19824700	-1.27370000	0.00004300
C	3.40955600	-0.59124400	0.00002400
C	-1.41105700	-0.55920500	0.00001800
C	-1.35859600	0.86358800	-0.00001800
C	-2.62630000	1.57782700	-0.00002500
C	-3.75333900	-0.64568400	-0.00000300
H	2.13668200	2.59913700	-0.00006600
H	-4.65063100	1.18868000	-0.00006100
N	-0.23642300	-1.27166700	0.00004000
N	-2.51875800	-1.29827300	0.00002900
N	-3.74553000	0.72957900	-0.00003100
N	-0.20134400	1.56862600	-0.00003700
O	-2.77116600	2.78544800	-0.00009700
O	-4.78578300	-1.29253500	0.00000300
C	4.70573500	-1.34114300	0.00004600
H	5.31884800	-1.09640700	0.88355600
H	4.53863900	-2.42681500	0.00008600
H	5.31884000	-1.09647200	-0.88348700
C	4.67190500	1.60455700	-0.00003500
H	5.28542100	1.35750000	0.88238700
H	5.28543600	1.35743300	-0.88242900
H	4.49070500	2.68685500	-0.00007700
H	0.25653000	-3.10295000	0.89629100
C	-0.25808700	-2.72668700	0.00007900
H	-1.30302300	-3.04734700	0.00008500
H	0.25653500	-3.10299800	-0.89610900
H	2.21741800	-2.36347200	0.00007400

Sum of electronic and zero-point Energies= -870.860269
Sum of electronic and thermal Energies= -870.844696
Sum of electronic and thermal Enthalpies= -870.843752
Sum of electronic and thermal Free Energies= -870.902746

LF S₂

C	3.39693900	0.84006400	-0.00001200
C	2.18502300	1.50613400	-0.00003100
C	0.93926900	0.82991700	-0.00001500
C	0.96839600	-0.59818100	0.00002500
C	2.19064400	-1.26981900	0.00004200
C	3.40469800	-0.57832100	0.00002500
C	-1.42208400	-0.57612200	0.00002200
C	-1.34713700	0.83040500	-0.00002600
C	-2.59652900	1.56146600	-0.00005900
C	-3.68138900	-0.63452500	-0.00002000
H	2.14010700	2.59665400	-0.00006100
H	-4.64503300	1.19663900	-0.00005800
N	-0.25124800	-1.27864100	0.00004600
N	-2.56083400	-1.31203800	0.00002400
N	-3.74541700	0.72642000	-0.00005800
N	-0.19485300	1.54532800	-0.00003900
O	-2.77545800	2.76173300	-0.00007600
O	-4.83444700	-1.19476900	0.00001700
C	4.69802900	-1.33530400	0.00004500
H	5.31187100	-1.09064100	0.88301400
H	4.52828800	-2.42066200	0.00007100
H	5.31187300	-1.09068400	-0.88293400
C	4.68675800	1.60694400	-0.00003200
H	5.29980900	1.36669900	0.88394800
H	5.29980200	1.36666400	-0.88400700
H	4.50353300	2.68953800	-0.00005300
H	0.25468800	-3.10864300	0.89528000
C	-0.26087200	-2.72926600	0.00009400
H	-1.30190200	-3.06113900	0.00011800
H	0.25466200	-3.10870400	-0.89508200
H	2.21754100	-2.35925600	0.00007000

Sum of electronic and zero-point Energies= -870.864040
Sum of electronic and thermal Energies= -870.847986
Sum of electronic and thermal Enthalpies= -870.847042
Sum of electronic and thermal Free Energies= -870.906828

H*LF(O2+) S₀

C	-2.53002800	2.45026300	0.00000000
C	-2.44872100	1.07629800	0.00000000
C	-1.20394500	0.40467500	0.00000000
C	0.00000000	1.17105600	0.00000000
C	-0.07997400	2.56900100	0.00000000
C	-1.31324400	3.20929900	0.00000000
C	1.22491700	-0.86058100	0.00000000
C	-0.03132600	-1.54458600	0.00000000
C	-0.02418700	-3.03109800	0.00000000
C	2.39290000	-2.79758400	0.00000000
H	-3.34203400	0.44970600	0.00000000
H	0.82194000	3.17881900	0.00000000
H	1.37163900	-4.57308500	0.00000000
N	1.20259300	0.49378500	0.00000000
N	2.41685800	-1.48606700	0.00000000
N	1.28213300	-3.55821800	0.00000000
N	-1.19389000	-0.93979100	0.00000000
O	-0.98775500	-3.74381300	0.00000000
O	3.51106200	-3.48167200	0.00000000
C	-1.37105900	4.70150900	0.00000000
H	-1.91839300	5.07150000	0.88170100
H	-0.37091900	5.15190500	0.00000000
H	-1.91839300	5.07150000	-0.88170100
C	-3.85624500	3.14294900	0.00000000
H	-3.96819500	3.79003400	0.88414800
H	-3.96819500	3.79003400	-0.88414800
H	-4.68153200	2.42037600	0.00000000
H	2.50065800	1.87866500	0.89839300
C	2.45645700	1.24917900	0.00000000
H	3.28555700	0.53914300	0.00000000
H	2.50065800	1.87866500	-0.89839300
H	4.25361900	-2.85361400	0.00000000

Sum of electronic and zero-point Energies= -871.332633
Sum of electronic and thermal Energies= -871.316667
Sum of electronic and thermal Enthalpies= -871.315723
Sum of electronic and thermal Free Energies= -871.375306

H*LF(O2+) S₁

C	-2.44955800	2.57754500	0.00000000
C	-2.38814500	1.14606900	0.00000000
C	-1.18671000	0.40804300	0.00000000
C	0.00000000	1.13847000	0.00000000
C	-0.05160500	2.57736200	0.00000000
C	-1.24242800	3.30314000	0.00000000
C	1.17215600	-0.92537900	0.00000000
C	-0.08457300	-1.57454400	0.00000000
C	-0.09085900	-3.04570000	0.00000000
C	2.33199400	-2.86883400	0.00000000
H	-3.31439500	0.56584700	0.00000000
H	0.88606800	3.13413200	0.00000000
H	1.27558000	-4.61758100	0.00000000
N	1.20562800	0.46794600	0.00000000
N	2.35732100	-1.55119300	0.00000000
N	1.21399400	-3.60097400	0.00000000
N	-1.27062500	-0.95475500	0.00000000
O	-1.05853600	-3.76247400	0.00000000
O	3.45358000	-3.55505600	0.00000000
C	-1.23167500	4.79923800	0.00000000
H	-1.74980100	5.20198100	0.88489000
H	-0.20828200	5.19501800	0.00000000
H	-1.74980100	5.20198100	-0.88489000
C	-3.76836400	3.25193900	0.00000000
H	-3.86612900	3.91709000	0.87698600
H	-3.86612900	3.91709000	-0.87698600
H	-4.60388800	2.54257600	0.00000000
H	2.56174700	1.80880700	0.89990100
C	2.47313700	1.18250000	0.00000000
H	3.27634700	0.44175300	0.00000000
H	2.56174700	1.80880700	-0.89990100
H	4.19214100	-2.92352300	0.00000000

Sum of electronic and zero-point Energies= -871.229954
Sum of electronic and thermal Energies= -871.213184
Sum of electronic and thermal Enthalpies= -871.212239
Sum of electronic and thermal Free Energies= -871.274094

H*LF(O2+) S₂

C	-2.48994700	2.55460200	0.00000000
C	-2.46703400	1.16748100	0.00000000
C	-1.25104000	0.46792000	0.00000000
C	0.00000000	1.18076700	0.00000000
C	-0.05388100	2.56873800	0.00000000
C	-1.26514200	3.26999800	0.00000000
C	1.20141000	-0.91963800	0.00000000
C	-0.03746700	-1.60910100	0.00000000
C	-0.06840700	-3.07417100	0.00000000
C	2.35253700	-2.88139000	0.00000000
H	-3.38939100	0.58669700	0.00000000
H	0.87386500	3.14028900	0.00000000
H	1.29150400	-4.63274800	0.00000000
N	1.19328500	0.44992200	0.00000000
N	2.37433700	-1.57304500	0.00000000
N	1.22687800	-3.61637100	0.00000000
N	-1.11467800	-0.84914800	0.00000000
O	-1.05706400	-3.76372700	0.00000000
O	3.46383300	-3.58203300	0.00000000
C	-1.25855200	4.76502500	0.00000000
H	-1.78307900	5.16476300	0.88279400
H	-0.23791400	5.16792100	0.00000000
H	-1.78307900	5.16476300	-0.88279400
C	-3.79798300	3.28201300	0.00000000
H	-3.88815100	3.93286700	0.88392700
H	-3.88815100	3.93286700	-0.88392700
H	-4.64658700	2.58689400	0.00000000
H	2.51749900	1.81281700	0.89821500
C	2.45423200	1.18205600	0.00000000
H	3.27316900	0.45919000	0.00000000
H	2.51749900	1.81281700	-0.89821500
H	4.21755700	-2.96836900	0.00000000

Sum of electronic and zero-point Energies= -871.224636
Sum of electronic and thermal Energies= -871.208110
Sum of electronic and thermal Enthalpies= -871.207166
Sum of electronic and thermal Free Energies= -871.267987

H*LF(N1) S₀

C	-3.43333700	0.84615600	0.02885800
C	-2.21484200	1.48905400	0.05360100
C	-0.99654800	0.77430900	0.04377900
C	-1.02571200	-0.64960100	0.02432700
C	-2.25856400	-1.30602500	-0.01637800
C	-3.44898000	-0.58398000	-0.01650500
C	1.34026700	-0.61396000	-0.02035000
C	1.28513900	0.81096800	0.00409200
C	2.55965400	1.59517500	-0.00986400
C	3.79024000	-0.56277200	-0.12584200
H	-2.14166100	2.57756300	0.07588300
H	-2.32017100	-2.39167100	-0.07262800
H	4.59711700	1.29961600	-0.08085400
N	0.19538400	-1.31814200	0.04103500
N	2.53882100	-1.22753000	-0.09215400
N	3.70680300	0.80520700	-0.06407000
N	0.15832000	1.46902400	0.04792300
O	2.60375500	2.79331300	0.02438700
O	4.80377600	-1.19894400	-0.20349400
C	-4.75204900	-1.31121000	-0.06998900
H	-5.33454900	-1.00494100	-0.95354100
H	-4.61664000	-2.39913900	-0.10547400
H	-5.37093800	-1.06729400	0.80830200
C	-4.71312500	1.62092100	0.03875700
H	-5.31484400	1.40828400	-0.85879000
H	-5.33327300	1.35371400	0.90875600
H	-4.52370400	2.70071400	0.07410100
H	0.27366200	-3.22569300	-0.88230500
C	0.23978200	-2.77885100	0.12206900
H	1.11149800	-3.08892400	0.71096200
H	-0.64624200	-3.13506100	0.65419300
H	2.63338900	-2.23358200	-0.18440500

Sum of electronic and zero-point Energies= -871.326940
Sum of electronic and thermal Energies= -871.310683
Sum of electronic and thermal Enthalpies= -871.309738
Sum of electronic and thermal Free Energies= -871.370320

H*LF(N1) S₁

C	-3.45066500	0.82287700	-0.02051500
C	-2.18013800	1.48370800	0.06488600
C	-0.93835500	0.81152500	0.07993300
C	-0.98519900	-0.57649500	0.05761600
C	-2.25383200	-1.25052700	-0.06386900
C	-3.47602400	-0.58542200	-0.08983300
C	1.37323200	-0.54719400	0.03316700
C	1.33128300	0.85340200	0.06470000
C	2.61430300	1.59865800	0.01970300
C	3.81350500	-0.57734800	-0.14239900
H	-2.14256100	2.57401700	0.13399100
H	-2.26333300	-2.33678200	-0.16545400
H	4.64548500	1.27300400	-0.10720600
N	0.20551700	-1.28769300	0.13221300
N	2.54946600	-1.20330200	-0.07508300
N	3.75192400	0.78757100	-0.06866800
N	0.20099800	1.56684200	0.13166900
O	2.69726500	2.79888300	0.05914400
O	4.81326100	-1.23792700	-0.25118000
C	-4.76361600	-1.33820600	-0.20912800
H	-5.32102900	-1.03623300	-1.10989400
H	-4.59382800	-2.42078300	-0.26539500
H	-5.41961600	-1.14452600	0.65442300
C	-4.68979400	1.63039300	-0.04960000
H	-5.26380300	1.42952900	-0.97298800
H	-5.36586700	1.33450600	0.77335300
H	-4.49547500	2.70675900	0.01814900
H	0.26210400	-3.29182900	-0.58967000
C	0.24237900	-2.72492300	0.35523500
H	1.12311800	-2.98105300	0.95867100
H	-0.63075500	-3.02968300	0.94296700
H	2.60354300	-2.21117700	-0.17495100

Sum of electronic and zero-point Energies= -871.222032
Sum of electronic and thermal Energies= -871.204993
Sum of electronic and thermal Enthalpies= -871.204048
Sum of electronic and thermal Free Energies= -871.266664

H*LF(N1) S₂

C	3.42299800	0.83622000	0.00373800
C	2.21235400	1.50210100	-0.05771500
C	0.97145100	0.82558600	-0.06420900
C	0.99129100	-0.60576700	-0.03179700
C	2.20430500	-1.27621900	0.04880900
C	3.42099800	-0.58345400	0.06946900
C	-1.38088800	-0.57279500	-0.03173200
C	-1.30289800	0.81334000	-0.03699700
C	-2.54663300	1.52330400	0.00088100
C	-3.81185600	-0.56125900	0.08184500
H	2.17043800	2.59165800	-0.09423500
H	2.23817300	-2.36352300	0.11045000
H	-4.59468300	1.34929200	0.07439000
N	-0.24061800	-1.29855500	-0.09123500
N	-2.60091000	-1.20530200	0.03287400
N	-3.70692800	0.84894900	0.04255000
N	-0.16320900	1.54916000	-0.08864100
O	-2.60917200	2.78487400	-0.01158300
O	-4.88084600	-1.09522300	0.15426600
C	4.70610300	-1.34057800	0.16133200
H	5.27921500	-1.04274000	1.05428000
H	4.54060200	-2.42442800	0.20841900
H	5.35305800	-1.13058200	-0.70586400
C	4.71298100	1.59646300	0.01119400
H	5.29254900	1.39002800	0.92477800
H	5.34983700	1.30885000	-0.84018500
H	4.53905900	2.67823400	-0.04424700
H	-0.08926400	-3.24102000	0.75167500
C	-0.24662100	-2.74711700	-0.21940900
H	-1.18344500	-3.09459500	-0.66992400
H	0.55390100	-3.04344300	-0.90795400
H	-2.66914100	-2.21365400	0.11566400

Sum of electronic and zero-point Energies= -871.224478
Sum of electronic and thermal Energies= -871.208060
Sum of electronic and thermal Enthalpies= -871.207116
Sum of electronic and thermal Free Energies= -871.267734

H*LF(O2-) S₀

C	-2.52707400	2.45957700	0.00000000
C	-2.45018700	1.08569500	0.00000000
C	-1.20737900	0.40959200	0.00000000
C	0.00000000	1.17267300	0.00000000
C	-0.07643100	2.57108200	0.00000000
C	-1.30746200	3.21496000	0.00000000
C	1.21902600	-0.86208100	0.00000000
C	-0.03937600	-1.54025300	0.00000000
C	-0.02714200	-3.02222900	0.00000000
C	2.40722200	-2.78724100	0.00000000
H	-3.34562600	0.46215800	0.00000000
H	0.82800900	3.17710500	0.00000000
H	1.32851100	-4.56606600	0.00000000
N	1.20001600	0.49386400	0.00000000
N	2.40987200	-1.48013100	0.00000000
N	1.28625900	-3.54857000	0.00000000
N	-1.20225400	-0.93448200	0.00000000
O	-0.98090900	-3.74852700	0.00000000
O	3.58672600	-3.36693900	0.00000000
C	-1.36073200	4.70727600	0.00000000
H	-1.90692500	5.07892500	0.88172300
H	-0.35916000	5.15442000	0.00000000
H	-1.90692500	5.07892500	-0.88172300
C	-3.85095000	3.15675200	0.00000000
H	-3.96076300	3.80424100	0.88412400
H	-3.96076300	3.80424100	-0.88412400
H	-4.67867200	2.43694500	0.00000000
H	2.50642500	1.87074500	0.89865600
C	2.45935100	1.24185200	0.00000000
H	3.28300800	0.52432400	0.00000000
H	2.50642500	1.87074500	-0.89865600
H	3.52946900	-4.33368900	0.00000000

Sum of electronic and zero-point Energies= -871.322692
Sum of electronic and thermal Energies= -871.306578
Sum of electronic and thermal Enthalpies= -871.305634
Sum of electronic and thermal Free Energies= -871.365446

H*LF(O2-) S₁

C	-2.44468300	2.58742400	0.00000000
C	-2.38877300	1.15610500	0.00000000
C	-1.19076400	0.41416200	0.00000000
C	0.00000000	1.14081000	0.00000000
C	-0.04633300	2.57920200	0.00000000
C	-1.23501700	3.30878000	0.00000000
C	1.16611400	-0.92614800	0.00000000
C	-0.09429300	-1.57097200	0.00000000
C	-0.09547400	-3.03674100	0.00000000
C	2.34430400	-2.85931900	0.00000000
H	-3.31729500	0.57961900	0.00000000
H	0.89375100	3.13185500	0.00000000
H	1.23408900	-4.60936100	0.00000000
N	1.20235900	0.46695900	0.00000000
N	2.34940900	-1.54432800	0.00000000
N	1.21826500	-3.59120500	0.00000000
N	-1.27906700	-0.94832400	0.00000000
O	-1.05204200	-3.76936100	0.00000000
O	3.52700600	-3.44051600	0.00000000
C	-1.21909500	4.80482000	0.00000000
H	-1.73585000	5.20937400	0.88487800
H	-0.19430400	5.19694200	0.00000000
H	-1.73585000	5.20937400	-0.88487800
C	-3.76102700	3.26724700	0.00000000
H	-3.85644500	3.93243900	0.87712200
H	-3.85644500	3.93243900	-0.87712200
H	-4.59918000	2.56094300	0.00000000
H	2.56617600	1.79932400	0.90015900
C	2.47560100	1.17389800	0.00000000
H	3.27321600	0.42599200	0.00000000
H	2.56617600	1.79932400	-0.90015900
H	3.46212600	-4.40655800	0.00000000

Sum of electronic and zero-point Energies= -871.220900
Sum of electronic and thermal Energies= -871.204018
Sum of electronic and thermal Enthalpies= -871.203074
Sum of electronic and thermal Free Energies= -871.265043

H*LF(O2-) S₂

C	-2.48625500	2.56284500	0.00000000
C	-2.46671800	1.17592500	0.00000000
C	-1.25244900	0.47264700	0.00000000
C	0.00000000	1.18313000	0.00000000
C	-0.05010400	2.57151400	0.00000000
C	-1.25943600	3.27541700	0.00000000
C	1.19549700	-0.91828300	0.00000000
C	-0.04690800	-1.60675300	0.00000000
C	-0.07198700	-3.06457100	0.00000000
C	2.36560900	-2.87449700	0.00000000
H	-3.39065900	0.59765200	0.00000000
H	0.87946600	3.14000100	0.00000000
H	1.24926400	-4.62616900	0.00000000
N	1.19075900	0.45034200	0.00000000
N	2.36313300	-1.56835200	0.00000000
N	1.23196400	-3.60848300	0.00000000
N	-1.12413700	-0.84570100	0.00000000
O	-1.05079800	-3.76954300	0.00000000
O	3.54465500	-3.45987400	0.00000000
C	-1.24936700	4.77041700	0.00000000
H	-1.77296300	5.17137800	0.88279800
H	-0.22774600	5.17077500	0.00000000
H	-1.77296300	5.17137800	-0.88279800
C	-3.79241500	3.29367900	0.00000000
H	-3.88098700	3.94477800	0.88391300
H	-3.88098700	3.94477800	-0.88391300
H	-4.64278900	2.60069500	0.00000000
H	2.52363600	1.80468900	0.89847600
C	2.45744000	1.17479800	0.00000000
H	3.27082400	0.44445800	0.00000000
H	2.52363600	1.80468900	-0.89847600
H	3.48192500	-4.42601900	0.00000000

Sum of electronic and zero-point Energies= -871.215308
Sum of electronic and thermal Energies= -871.198607
Sum of electronic and thermal Enthalpies= -871.197663
Sum of electronic and thermal Free Energies= -871.258749

H*LF(O4+) S₀

C	-2.60737800	2.31395100	0.00000000
C	-2.45524500	0.94817700	0.00000000
C	-1.17657000	0.33949500	0.00000000
C	0.00000000	1.16085100	0.00000000
C	-0.16178900	2.55149800	0.00000000
C	-1.42624300	3.12987800	0.00000000
C	1.36491700	-0.80206200	0.00000000
C	0.11993700	-1.51993400	0.00000000
C	0.21527100	-2.95394500	0.00000000
C	2.66348700	-2.71468200	0.00000000
H	-3.32017500	0.28280500	0.00000000
H	0.70859500	3.20518300	0.00000000
H	1.52735500	-4.50243200	0.00000000
N	1.24090300	0.56718700	0.00000000
N	2.54686900	-1.35680600	0.00000000
N	1.41124200	-3.48823900	0.00000000
N	-1.08537000	-1.00096700	0.00000000
O	-0.84787700	-3.69684000	0.00000000
O	3.67587500	-3.35465400	0.00000000
C	-1.55561200	4.61626500	0.00000000
H	-2.12168200	4.95827300	0.88140600
H	-0.57893700	5.11496400	0.00000000
H	-2.12168200	4.95827300	-0.88140600
C	-3.96557100	2.94180400	0.00000000
H	-4.10955400	3.58239000	0.88416300
H	-4.10955400	3.58239000	-0.88416300
H	-4.75549900	2.18051600	0.00000000
H	2.47566600	2.01254100	0.89951100
C	2.45474200	1.38264000	0.00000000
H	3.31097700	0.70194600	0.00000000
H	2.47566600	2.01254100	-0.89951100
H	-1.62034300	-3.08926900	0.00000000

Sum of electronic and zero-point Energies= -871.319077
Sum of electronic and thermal Energies= -871.303116
Sum of electronic and thermal Enthalpies= -871.302172
Sum of electronic and thermal Free Energies= -871.361722

H*LF(O4+) S₁

C	-2.52086800	2.42697000	0.00000000
C	-2.40812600	1.01810800	0.00000000
C	-1.18196100	0.35099100	0.00000000
C	0.00000000	1.14497200	0.00000000
C	-0.10957900	2.55385100	0.00000000
C	-1.34095800	3.20936100	0.00000000
C	1.29735200	-0.84187300	0.00000000
C	0.05422300	-1.55904200	0.00000000
C	0.15460300	-2.96339600	0.00000000
C	2.56659000	-2.80359700	0.00000000
H	-3.30918100	0.40159600	0.00000000
H	0.79535100	3.16098900	0.00000000
H	1.44549500	-4.56142500	0.00000000
N	1.23716400	0.52410100	0.00000000
N	2.47905100	-1.42056400	0.00000000
N	1.36127000	-3.54754500	0.00000000
N	-1.16685100	-1.01203400	0.00000000
O	-0.90888700	-3.72204500	0.00000000
O	3.62152300	-3.38665300	0.00000000
C	-1.40693200	4.70335800	0.00000000
H	-1.94707500	5.07867200	0.88393900
H	-0.40579400	5.15248200	0.00000000
H	-1.94707500	5.07867200	-0.88393900
C	-3.86474700	3.06347300	0.00000000
H	-3.98905200	3.71830100	0.87956600
H	-3.98905200	3.71830100	-0.87956600
H	-4.67341700	2.32302600	0.00000000
H	2.51451500	1.93237800	0.89964000
C	2.47394400	1.30310800	0.00000000
H	3.31290200	0.60196600	0.00000000
H	2.51451500	1.93237800	-0.89964000
H	-1.67890800	-3.11317700	0.00000000

Sum of electronic and zero-point Energies= -871.238512
Sum of electronic and thermal Energies= -871.222084
Sum of electronic and thermal Enthalpies= -871.221140
Sum of electronic and thermal Free Energies= -871.281755

H*LF(O4+) S₂

C	-2.51916700	2.45275500	0.00000000
C	-2.43123400	1.07152400	0.00000000
C	-1.19058700	0.40031800	0.00000000
C	0.00000000	1.18549500	0.00000000
C	-0.08408800	2.56986700	0.00000000
C	-1.32333100	3.22068300	0.00000000
C	1.27918800	-0.81456800	0.00000000
C	0.04393900	-1.56314000	0.00000000
C	0.14429100	-2.95709000	0.00000000
C	2.58506300	-2.89952800	0.00000000
H	-3.33101400	0.45476100	0.00000000
H	0.81760400	3.18119700	0.00000000
H	1.40116400	-4.58678100	0.00000000
N	1.24528300	0.51313500	0.00000000
N	2.38002000	-1.53146400	0.00000000
N	1.34757900	-3.56983300	0.00000000
N	-1.14090200	-0.94476700	0.00000000
O	-0.91368700	-3.73008800	0.00000000
O	3.64103600	-3.45726100	0.00000000
C	-1.37988200	4.71402800	0.00000000
H	-1.92249100	5.09051500	0.88221900
H	-0.37786500	5.16127600	0.00000000
H	-1.92249100	5.09051500	-0.88221900
C	-3.85528000	3.12840400	0.00000000
H	-3.97384400	3.77477100	0.88382000
H	-3.97384400	3.77477100	-0.88382000
H	-4.67405700	2.39818200	0.00000000
H	2.54907800	1.89920200	0.89875500
C	2.49479900	1.27046000	0.00000000
H	3.33437400	0.56527600	0.00000000
H	2.54907800	1.89920200	-0.89875500
H	-1.70060700	-3.14884300	0.00000000

Sum of electronic and zero-point Energies= -871.217562
Sum of electronic and thermal Energies= -871.201359
Sum of electronic and thermal Enthalpies= -871.200415
Sum of electronic and thermal Free Energies= -871.260296

H*LF(N5) S₀

C	-2.60490600	2.32358600	0.00000000
C	-2.45868900	0.95216400	0.00000000
C	-1.18185800	0.36945300	0.00000000
C	0.00000000	1.15995500	0.00000000
C	-0.16280300	2.55180600	0.00000000
C	-1.42454100	3.13569400	0.00000000
C	1.37621600	-0.82347000	0.00000000
C	0.15080900	-1.56821600	0.00000000
C	0.16529200	-3.05077300	0.00000000
C	2.63559800	-2.77263200	0.00000000
H	-3.33596500	0.30117000	0.00000000
H	0.71170700	3.19969900	0.00000000
H	1.55737300	-4.54681300	0.00000000
N	1.23843800	0.55482000	0.00000000
N	2.54062300	-1.38731800	0.00000000
N	1.42839300	-3.53615800	0.00000000
N	-1.01657700	-0.98527300	0.00000000
O	-0.88154800	-3.66824600	0.00000000
O	3.68221500	-3.36020100	0.00000000
C	-1.54971200	4.62322500	0.00000000
H	-2.11258700	4.96824500	0.88208900
H	-0.57071400	5.11729100	0.00000000
H	-2.11258700	4.96824500	-0.88208900
C	-3.96241100	2.95021600	0.00000000
H	-4.10328700	3.59185800	0.88389500
H	-4.10328700	3.59185800	-0.88389500
H	-4.75547100	2.19220500	0.00000000
H	2.48134300	1.99414500	0.90011500
C	2.45520700	1.36459200	0.00000000
H	3.30719400	0.67773400	0.00000000
H	2.48134300	1.99414500	-0.90011500
H	-1.81574100	-1.63831400	0.00000000

Sum of electronic and zero-point Energies= -871.312878
Sum of electronic and thermal Energies= -871.296823
Sum of electronic and thermal Enthalpies= -871.295879
Sum of electronic and thermal Free Energies= -871.355815

H*LF(N5) S₁

C	-2.51077800	2.44762900	0.00000000
C	-2.42293000	1.04124100	0.00000000
C	-1.20171500	0.38290300	0.00000000
C	0.00000000	1.13727200	0.00000000
C	-0.09582000	2.54402100	0.00000000
C	-1.31866900	3.21142300	0.00000000
C	1.28480800	-0.87075900	0.00000000
C	0.06950000	-1.61882200	0.00000000
C	0.09011700	-3.06553400	0.00000000
C	2.55043000	-2.85313900	0.00000000
H	-3.34097800	0.44921000	0.00000000
H	0.81598900	3.13977300	0.00000000
H	1.46605900	-4.59938400	0.00000000
N	1.22977100	0.49418300	0.00000000
N	2.46785400	-1.44580300	0.00000000
N	1.36852100	-3.58686300	0.00000000
N	-1.12403400	-0.98840100	0.00000000
O	-0.93291800	-3.72704300	0.00000000
O	3.63233200	-3.38673900	0.00000000
C	-1.36629400	4.70655900	0.00000000
H	-1.90173500	5.08745400	0.88413500
H	-0.35978400	5.14323700	0.00000000
H	-1.90173500	5.08745400	-0.88413500
C	-3.84496100	3.10697000	0.00000000
H	-3.95773700	3.76188000	0.88038100
H	-3.95773700	3.76188000	-0.88038100
H	-4.66676200	2.38094600	0.00000000
H	2.51203100	1.89624100	0.90011100
C	2.47170000	1.26756000	0.00000000
H	3.30621600	0.56100000	0.00000000
H	2.51203100	1.89624100	-0.90011100
H	-1.94829900	-1.59141900	0.00000000

Sum of electronic and zero-point Energies= -871.241701
Sum of electronic and thermal Energies= -871.225913
Sum of electronic and thermal Enthalpies= -871.224968
Sum of electronic and thermal Free Energies= -871.284244

H*LF(N5) S₂

C	-2.52838300	2.42852000	0.00000000
C	-2.44759800	1.04742900	0.00000000
C	-1.20811700	0.39201000	0.00000000
C	0.00000000	1.14312200	0.00000000
C	-0.09226400	2.53808600	0.00000000
C	-1.32137800	3.19025500	0.00000000
C	1.29215600	-0.87914700	0.00000000
C	0.08155800	-1.60074800	0.00000000
C	0.10008100	-3.04164200	0.00000000
C	2.51126600	-2.78486500	0.00000000
H	-3.35823800	0.44450300	0.00000000
H	0.81339800	3.14162800	0.00000000
H	1.48257200	-4.58748400	0.00000000
N	1.22785100	0.48276900	0.00000000
N	2.49182900	-1.45798200	0.00000000
N	1.39694200	-3.57354800	0.00000000
N	-1.11822700	-0.96275800	0.00000000
O	-0.88347400	-3.75007100	0.00000000
O	3.61330800	-3.41248300	0.00000000
C	-1.37473900	4.68352800	0.00000000
H	-1.91624000	5.05997300	0.88264100
H	-0.37131800	5.12684600	0.00000000
H	-1.91624000	5.05997300	-0.88264100
C	-3.85815100	3.11130000	0.00000000
H	-3.96960700	3.75977500	0.88331600
H	-3.96960700	3.75977500	-0.88331600
H	-4.68388200	2.38909300	0.00000000
H	2.50068000	1.89201100	0.89879200
C	2.46369600	1.26099400	0.00000000
H	3.30246900	0.56068200	0.00000000
H	2.50068000	1.89201100	-0.89879200
H	-1.95087200	-1.55078000	0.00000000

Sum of electronic and zero-point Energies= -871.245759
Sum of electronic and thermal Energies= -871.229554
Sum of electronic and thermal Enthalpies= -871.228610
Sum of electronic and thermal Free Energies= -871.288633

H*LF(OH++) S₀

C	-2.58116400	2.34865400	0.00000000
C	-2.45213900	0.98027500	0.00000000
C	-1.18422500	0.35005800	0.00000000
C	0.00000000	1.15843800	0.00000000
C	-0.13532300	2.55324300	0.00000000
C	-1.38874800	3.15016400	0.00000000
C	1.30951000	-0.81976800	0.00000000
C	0.07767500	-1.53927500	0.00000000
C	0.20131600	-2.98687000	0.00000000
C	2.43717300	-2.76938400	0.00000000
H	-3.32706700	0.32831200	0.00000000
H	0.74548600	3.19305500	0.00000000
N	1.22889700	0.53859100	0.00000000
N	2.48778900	-1.43171500	0.00000000
N	1.36141200	-3.57998400	0.00000000
N	-1.11730900	-0.99187000	0.00000000
O	-0.88643200	-3.71072100	0.00000000
O	3.57893700	-3.40979600	0.00000000
C	-1.49847000	4.63858400	0.00000000
H	-2.05905200	4.98867100	0.88159800
H	-0.51489600	5.12373900	0.00000000
H	-2.05905200	4.98867100	-0.88159800
C	-3.92951700	2.99636300	0.00000000
H	-4.06265500	3.63942600	0.88408500
H	-4.06265500	3.63942600	-0.88408500
H	-4.73087700	2.24731300	0.00000000
H	2.48682200	1.96215700	0.89910100
C	2.45773500	1.33256000	0.00000000
H	3.30393500	0.64127500	0.00000000
H	2.48682200	1.96215700	-0.89910100
H	4.29473600	-2.75240300	0.00000000
H	-1.65006400	-3.10107100	0.00000000

Sum of electronic and zero-point Energies= -871.322326
Sum of electronic and thermal Energies= -871.306536
Sum of electronic and thermal Enthalpies= -871.305592
Sum of electronic and thermal Free Energies= -871.364672

H*LF(OH++) S₁

C	-2.50601100	2.47214600	0.00000000
C	-2.39489400	1.04728100	0.00000000
C	-1.17081200	0.35463400	0.00000000
C	0.00000000	1.12646300	0.00000000
C	-0.10652500	2.55778000	0.00000000
C	-1.32470600	3.23888400	0.00000000
C	1.26434900	-0.87710500	0.00000000
C	0.02607200	-1.57286300	0.00000000
C	0.13965900	-2.99995100	0.00000000
C	2.37213900	-2.85197300	0.00000000
H	-3.30341900	0.44028400	0.00000000
H	0.80970400	3.14899100	0.00000000
N	1.23211100	0.51103300	0.00000000
N	2.42844400	-1.49419200	0.00000000
N	1.30098900	-3.63061900	0.00000000
N	-1.19058200	-1.01178300	0.00000000
O	-0.95734300	-3.71852900	0.00000000
O	3.52870300	-3.47595500	0.00000000
C	-1.36698100	4.73400000	0.00000000
H	-1.90010400	5.11724100	0.88467800
H	-0.35876200	5.16676800	0.00000000
H	-1.90010400	5.11724100	-0.88467800
C	-3.84738800	3.10344700	0.00000000
H	-3.96823800	3.76345900	0.87758100
H	-3.96823800	3.76345900	-0.87758100
H	-4.65879800	2.36643500	0.00000000
H	2.54411400	1.89552800	0.90049300
C	2.47645600	1.26825900	0.00000000
H	3.29971200	0.54848100	0.00000000
H	2.54411400	1.89552800	-0.90049300
H	4.23039100	-2.80499800	0.00000000
H	-1.70614100	-3.08963300	0.00000000

Sum of electronic and zero-point Energies= -871.227728
Sum of electronic and thermal Energies= -871.211247
Sum of electronic and thermal Enthalpies= -871.210303
Sum of electronic and thermal Free Energies= -871.271218

H*LF(OH++) S₂

C	-2.51232300	2.45678400	0.00000000
C	-2.43809100	1.07438700	0.00000000
C	-1.20946300	0.38727500	0.00000000
C	0.00000000	1.15543500	0.00000000
C	-0.07566600	2.54454900	0.00000000
C	-1.30556600	3.20868300	0.00000000
C	1.24549400	-0.86715000	0.00000000
C	0.00926700	-1.53993700	0.00000000
C	0.10403800	-2.96507800	0.00000000
C	2.44543600	-2.87903400	0.00000000
H	-3.34415500	0.46666900	0.00000000
H	0.83208600	3.14651100	0.00000000
N	1.23716800	0.48711200	0.00000000
N	2.39485500	-1.56307800	0.00000000
N	1.29471700	-3.53506000	0.00000000
N	-1.19011100	-0.96748000	0.00000000
O	-0.96971200	-3.70158400	0.00000000
O	3.55619200	-3.56949600	0.00000000
C	-1.34460600	4.70280000	0.00000000
H	-1.88291000	5.08542500	0.88218300
H	-0.33726000	5.13794800	0.00000000
H	-1.88291000	5.08542500	-0.88218300
C	-3.83977500	3.14845700	0.00000000
H	-3.95137400	3.79648900	0.88367200
H	-3.95137400	3.79648900	-0.88367200
H	-4.66689000	2.42766600	0.00000000
H	2.53692900	1.87581400	0.89719300
C	2.48035700	1.24326100	0.00000000
H	3.32051400	0.54265700	0.00000000
H	2.53692900	1.87581400	-0.89719300
H	4.31509700	-2.96411300	0.00000000
H	-1.72753100	-3.07720300	0.00000000

Sum of electronic and zero-point Energies= -871.227425
Sum of electronic and thermal Energies= -871.211061
Sum of electronic and thermal Enthalpies= -871.210116
Sum of electronic and thermal Free Energies= -871.270326

H*LF(OH+-) S₀

C	-2.56819800	2.38408700	0.00000000
C	-2.45271000	1.01502100	0.00000000
C	-1.18986200	0.37078200	0.00000000
C	0.00000000	1.16901000	0.00000000
C	-0.11914000	2.56504600	0.00000000
C	-1.36746600	3.17330700	0.00000000
C	1.27796600	-0.82853300	0.00000000
C	0.03605600	-1.53933500	0.00000000
C	0.17565400	-2.98346800	0.00000000
C	2.42192200	-2.76906400	0.00000000
H	-3.33036700	0.36671700	0.00000000
H	0.76749800	3.19680000	0.00000000
N	1.21778000	0.53085900	0.00000000
N	2.46191100	-1.43815300	0.00000000
N	1.34078300	-3.57351000	0.00000000
N	-1.15068700	-0.96870100	0.00000000
O	-0.92308900	-3.69067100	0.00000000
O	3.56252500	-3.41437300	0.00000000
C	-1.46269000	4.66282900	0.00000000
H	-2.02011800	5.01816900	0.88150200
H	-0.47452200	5.13864800	0.00000000
H	-2.02011800	5.01816900	-0.88150200
C	-3.91014300	3.04570500	0.00000000
H	-4.03757900	3.68976000	0.88422000
H	-4.03757900	3.68976000	-0.88422000
H	-4.71809100	2.30377000	0.00000000
H	2.48989200	1.94101400	0.89879300
C	2.45531900	1.31129700	0.00000000
H	3.29524900	0.61308500	0.00000000
H	2.48989200	1.94101400	-0.89879300
H	4.27958000	-2.75848100	0.00000000
H	-0.66797900	-4.63164600	0.00000000

Sum of electronic and zero-point Energies= -871.324135
Sum of electronic and thermal Energies= -871.308301
Sum of electronic and thermal Enthalpies= -871.307357
Sum of electronic and thermal Free Energies= -871.366574

H*LF(OH+-) S₁

C	-2.48706900	2.51379400	0.00000000
C	-2.39224900	1.08689000	0.00000000
C	-1.17504000	0.37943800	0.00000000
C	0.00000000	1.13905000	0.00000000
C	-0.08678000	2.57317700	0.00000000
C	-1.29648300	3.26797800	0.00000000
C	1.22974900	-0.88912100	0.00000000
C	-0.02306300	-1.57412700	0.00000000
C	0.10701900	-2.99938100	0.00000000
C	2.35246700	-2.85279100	0.00000000
H	-3.30461500	0.48530800	0.00000000
H	0.83653100	3.15334100	0.00000000
N	1.21855200	0.50120500	0.00000000
N	2.39776100	-1.50262300	0.00000000
N	1.27565900	-3.62407700	0.00000000
N	-1.22512800	-0.98345800	0.00000000
O	-0.99427000	-3.71512100	0.00000000
O	3.50741200	-3.48267600	0.00000000
C	-1.32259800	4.76356700	0.00000000
H	-1.85122000	5.15297400	0.88470400
H	-0.30955200	5.18501900	0.00000000
H	-1.85122000	5.15297400	-0.88470400
C	-3.82107300	3.15952700	0.00000000
H	-3.93450600	3.82125500	0.87741200
H	-3.93450600	3.82125500	-0.87741200
H	-4.64012600	2.43110300	0.00000000
H	2.54811000	1.86826100	0.90029100
C	2.47309400	1.24152300	0.00000000
H	3.28770100	0.51263300	0.00000000
H	2.54811000	1.86826100	-0.90029100
H	4.21043200	-2.81326700	0.00000000
H	-0.72603600	-4.65121500	0.00000000

Sum of electronic and zero-point Energies= -871.228114
Sum of electronic and thermal Energies= -871.211546
Sum of electronic and thermal Enthalpies= -871.210602
Sum of electronic and thermal Free Energies= -871.271793

H*LF(OH+-) S₂

C	-2.51914700	2.49006200	0.00000000
C	-2.45782800	1.10628400	0.00000000
C	-1.22555300	0.43097300	0.00000000
C	0.00000000	1.18059500	0.00000000
C	-0.08134200	2.56915400	0.00000000
C	-1.30973100	3.23665500	0.00000000
C	1.25071800	-0.87401100	0.00000000
C	0.00886000	-1.58752400	0.00000000
C	0.11915900	-3.01099800	0.00000000
C	2.38891300	-2.88022000	0.00000000
H	-3.36564300	0.50245200	0.00000000
H	0.82982200	3.16625900	0.00000000
N	1.21510600	0.48796400	0.00000000
N	2.38836100	-1.54748700	0.00000000
N	1.28595500	-3.61838000	0.00000000
N	-1.10578300	-0.89682400	0.00000000
O	-1.00506000	-3.69789000	0.00000000
O	3.53033400	-3.53088500	0.00000000
C	-1.34287500	4.73104700	0.00000000
H	-1.87886400	5.11602800	0.88250700
H	-0.33360300	5.16156000	0.00000000
H	-1.87886400	5.11602800	-0.88250700
C	-3.84380000	3.18670200	0.00000000
H	-3.95085400	3.83515600	0.88383500
H	-3.95085400	3.83515600	-0.88383500
H	-4.67485500	2.47059700	0.00000000
H	2.51983900	1.87148200	0.89821000
C	2.46358300	1.24047500	0.00000000
H	3.29374400	0.52856800	0.00000000
H	2.51983900	1.87148200	-0.89821000
H	4.25990900	-2.89113500	0.00000000
H	-0.78300400	-4.64552100	0.00000000

Sum of electronic and zero-point Energies= -871.225108
Sum of electronic and thermal Energies= -871.208552
Sum of electronic and thermal Enthalpies= -871.207607
Sum of electronic and thermal Free Energies= -871.268219

H*LF(O4-) S₀

C	-2.59678500	2.34258500	0.00000000
C	-2.45480600	0.97626500	0.00000000
C	-1.17911900	0.35658600	0.00000000
C	0.00000000	1.17093800	0.00000000
C	-0.14816300	2.56280600	0.00000000
C	-1.40920400	3.14940900	0.00000000
C	1.33729000	-0.81034100	0.00000000
C	0.08342400	-1.52675400	0.00000000
C	0.19223600	-2.96198100	0.00000000
C	2.65805700	-2.70171600	0.00000000
H	-3.32057600	0.31205400	0.00000000
H	0.72655900	3.21066700	0.00000000
H	1.56059500	-4.48648000	0.00000000
N	1.23022900	0.55970900	0.00000000
N	2.52802500	-1.35376600	0.00000000
N	1.40230600	-3.47858100	0.00000000
N	-1.11309300	-0.98075900	0.00000000
O	-0.90342300	-3.66535400	0.00000000
O	3.66653100	-3.34966000	0.00000000
C	-1.52787300	4.63680400	0.00000000
H	-2.09173600	4.98269700	0.88130900
H	-0.54771000	5.12870100	0.00000000
H	-2.09173600	4.98269700	-0.88130900
C	-3.95033400	2.98116900	0.00000000
H	-4.09019500	3.62251100	0.88429800
H	-4.09019500	3.62251100	-0.88429800
H	-4.74509600	2.22493600	0.00000000
H	2.47529100	1.99521400	0.89922100
C	2.45126000	1.36510600	0.00000000
H	3.30330200	0.68002200	0.00000000
H	2.47529100	1.99521400	-0.89922100
H	-0.73681400	-4.62210200	0.00000000

Sum of electronic and zero-point Energies= -871.307077
Sum of electronic and thermal Energies= -871.290966
Sum of electronic and thermal Enthalpies= -871.290022
Sum of electronic and thermal Free Energies= -871.349883

H*LF(O4-) S₁

C	-2.50727900	2.46038900	0.00000000
C	-2.40241900	1.04684200	0.00000000
C	-1.18069600	0.37141200	0.00000000
C	0.00000000	1.15601900	0.00000000
C	-0.09693900	2.56918800	0.00000000
C	-1.32311900	3.23454400	0.00000000
C	1.27130500	-0.85376700	0.00000000
C	0.01314500	-1.56717400	0.00000000
C	0.12738300	-2.97631300	0.00000000
C	2.55922500	-2.79134700	0.00000000
H	-3.30499100	0.43221400	0.00000000
H	0.81324300	3.16860300	0.00000000
H	1.48223400	-4.54837500	0.00000000
N	1.22371700	0.51849500	0.00000000
N	2.45627400	-1.41810500	0.00000000
N	1.35320600	-3.53987600	0.00000000
N	-1.19021400	-0.99062900	0.00000000
O	-0.96794100	-3.70068200	0.00000000
O	3.61016100	-3.38219500	0.00000000
C	-1.37832100	4.72929400	0.00000000
H	-1.91520300	5.10884100	0.88409400
H	-0.37373500	5.17076200	0.00000000
H	-1.91520300	5.10884100	-0.88409400
C	-3.84745500	3.10254600	0.00000000
H	-3.96827700	3.75902800	0.87915700
H	-3.96827700	3.75902800	-0.87915700
H	-4.65967300	2.36609800	0.00000000
H	2.51578400	1.91348400	0.89961800
C	2.46869000	1.28459500	0.00000000
H	3.30089600	0.57603800	0.00000000
H	2.51578400	1.91348400	-0.89961800
H	-0.78234500	-4.65158500	0.00000000

Sum of electronic and zero-point Energies= -871.224855
Sum of electronic and thermal Energies= -871.208089
Sum of electronic and thermal Enthalpies= -871.207144
Sum of electronic and thermal Free Energies= -871.268480

H*LF(O4-) S₂

C	-2.53083800	2.46227500	0.00000000
C	-2.44808300	1.08165100	0.00000000
C	-1.20276900	0.42045300	0.00000000
C	0.00000000	1.19331800	0.00000000
C	-0.09330200	2.57941000	0.00000000
C	-1.33221800	3.22817700	0.00000000
C	1.28556400	-0.83345900	0.00000000
C	0.03160100	-1.59176000	0.00000000
C	0.13557200	-2.98733300	0.00000000
C	2.58602900	-2.85203300	0.00000000
H	-3.34640000	0.46357800	0.00000000
H	0.80864900	3.19012800	0.00000000
H	1.47304100	-4.57338000	0.00000000
N	1.22525800	0.51116500	0.00000000
N	2.40652500	-1.49178000	0.00000000
N	1.35838000	-3.56264300	0.00000000
N	-1.09832900	-0.90834600	0.00000000
O	-0.97642600	-3.69516600	0.00000000
O	3.63603600	-3.42906400	0.00000000
C	-1.38833600	4.72157500	0.00000000
H	-1.93064100	5.09815100	0.88235100
H	-0.38599200	5.16795800	0.00000000
H	-1.93064100	5.09815100	-0.88235100
C	-3.86589900	3.13997300	0.00000000
H	-3.98298100	3.78638900	0.88397000
H	-3.98298100	3.78638900	-0.88397000
H	-4.68600900	2.41127200	0.00000000
H	2.52342900	1.90176800	0.89901800
C	2.47292700	1.27264800	0.00000000
H	3.30767400	0.56334200	0.00000000
H	2.52342900	1.90176800	-0.89901800
H	-0.81178100	-4.64981700	0.00000000

Sum of electronic and zero-point Energies= -871.211420
Sum of electronic and thermal Energies= -871.194830
Sum of electronic and thermal Enthalpies= -871.193885
Sum of electronic and thermal Free Energies= -871.254532

Electronic Supporting Information

Interaction of Alkali Ions with Flavins: Infrared and Optical Spectra of Metal-Riboflavin Complexes

David Müller and Otto Dopfer*

Institut für Optik und Atomare Physik, Technische Universität Berlin, Hardenbergstr. 36, D-10623 Berlin, Germany

* corresponding author: dopfer@physik.tu-berlin.de; Fax: +49 30 314 23018

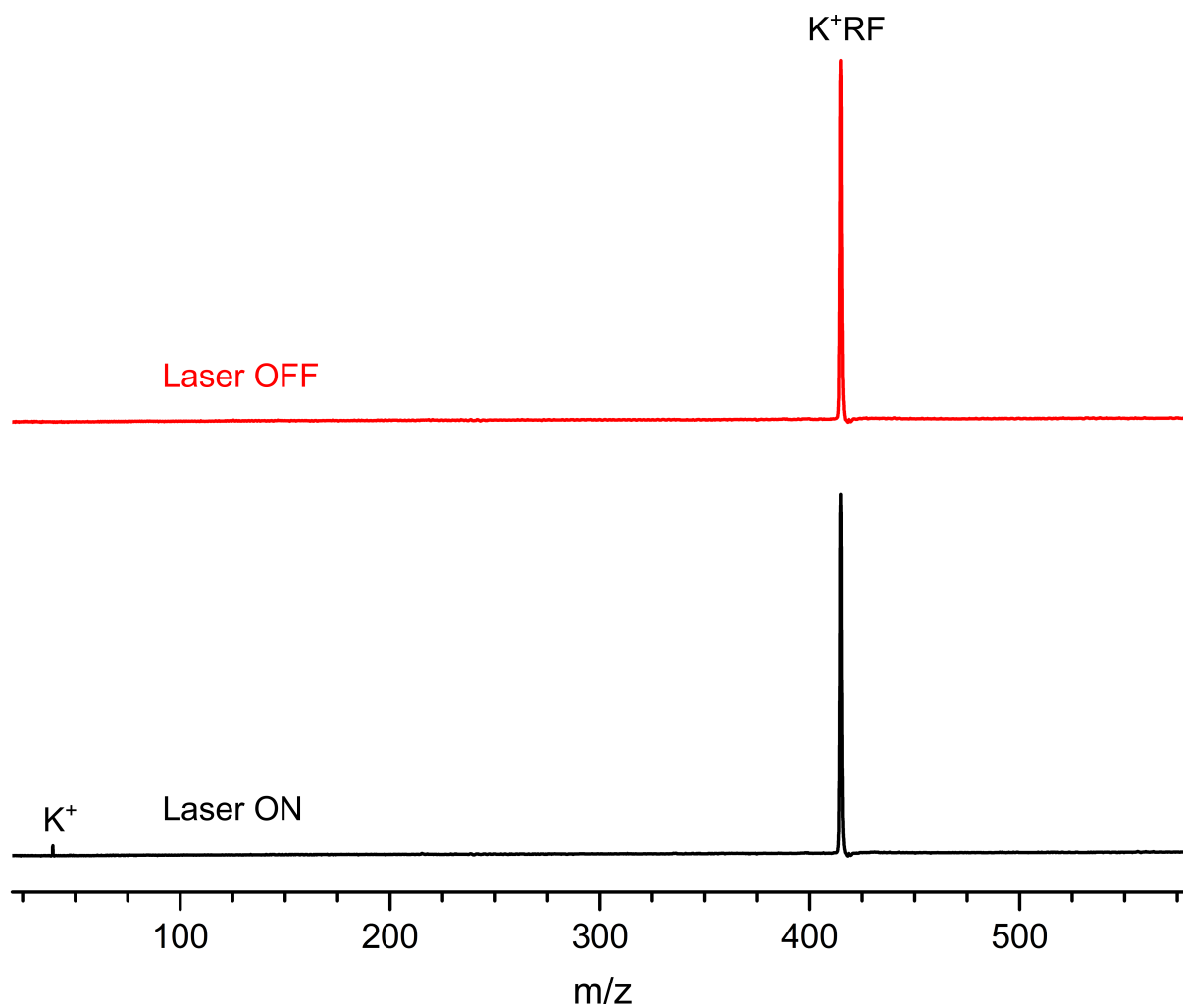


Figure S1. Mass spectra taken with the ReTOF-MS after mass-selecting K^+RF by the QMS and trapping in the cryogenic 22-pole trap ($T=6$ K). Laser off (red) and laser set resonantly to the S_10^0 origin transition at 22670 cm^{-1} (laser on, black). The only fragmentation channel observed is K^+ with an efficiency of around 1%.

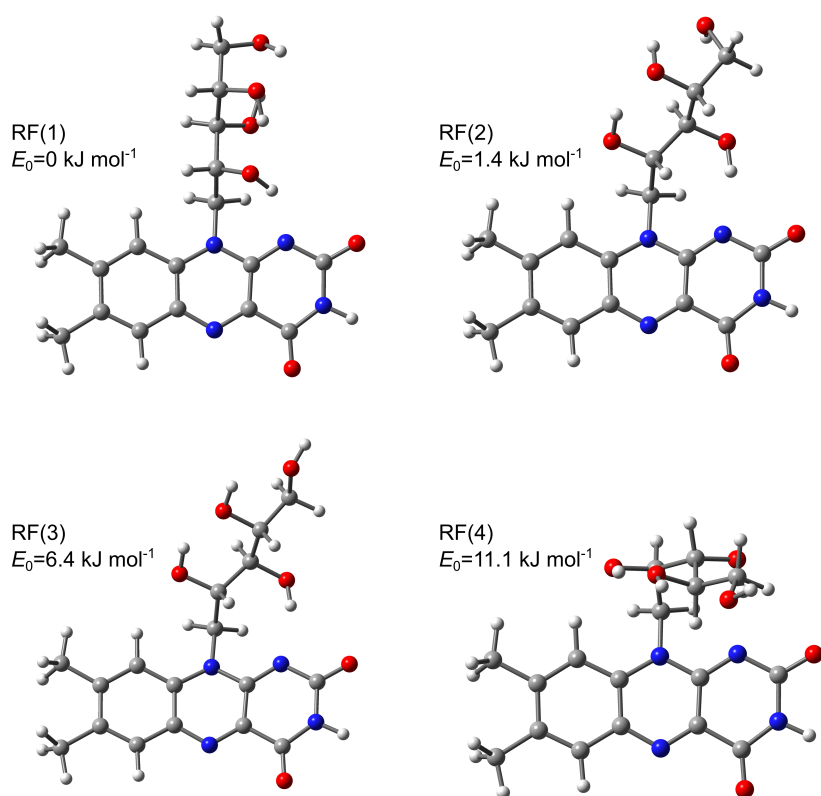


Figure S2. Most stable structures of RF in the S_0 state obtained at the PBE0/cc-pVDZ level, along with their relative energies.

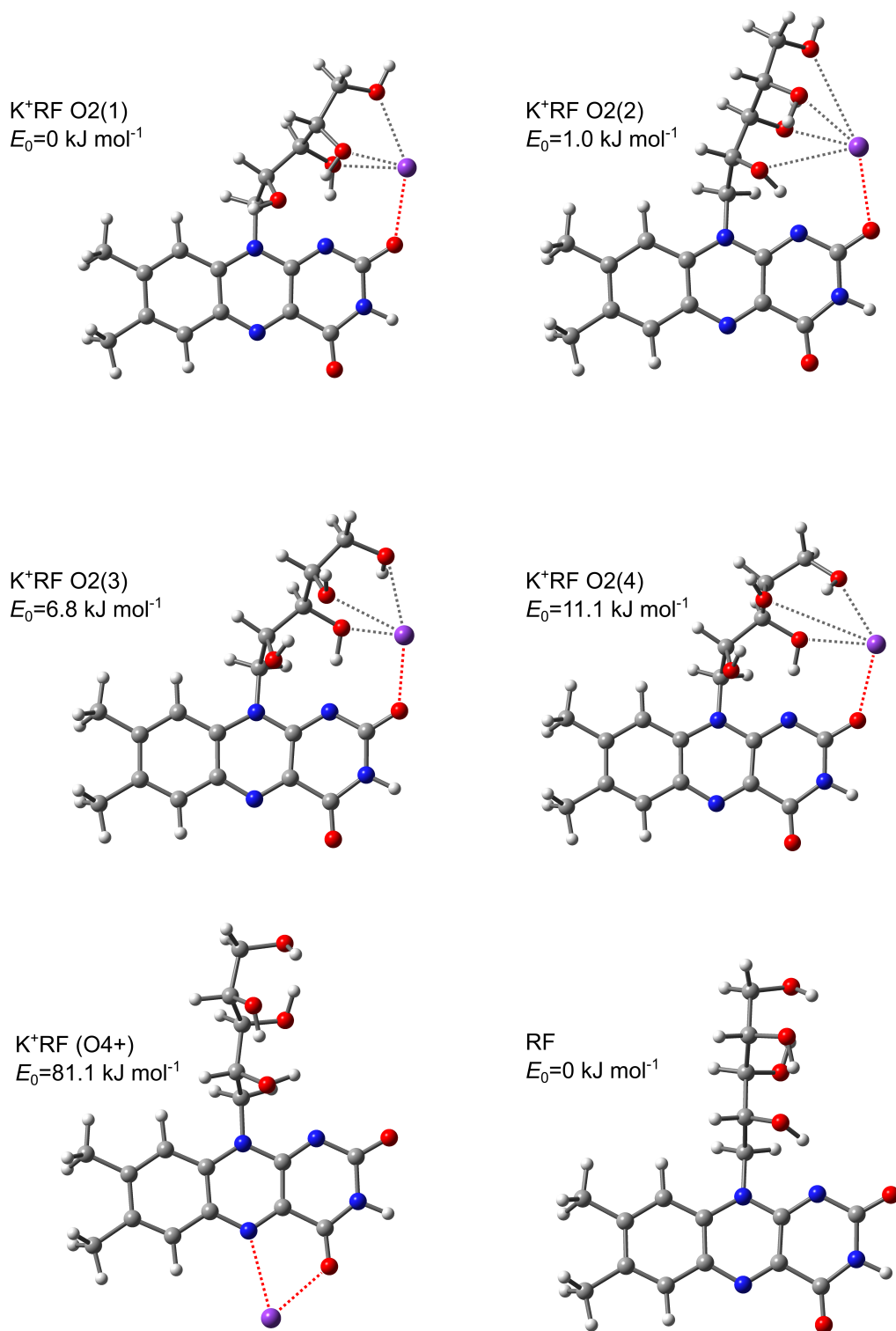


Figure. S3. Most stable structures of $K^+RF(O2/O4+)$ and RF in the S_0 ground electronic state computed at the PBE0/cc-pVDZ level, along with their relative energies.

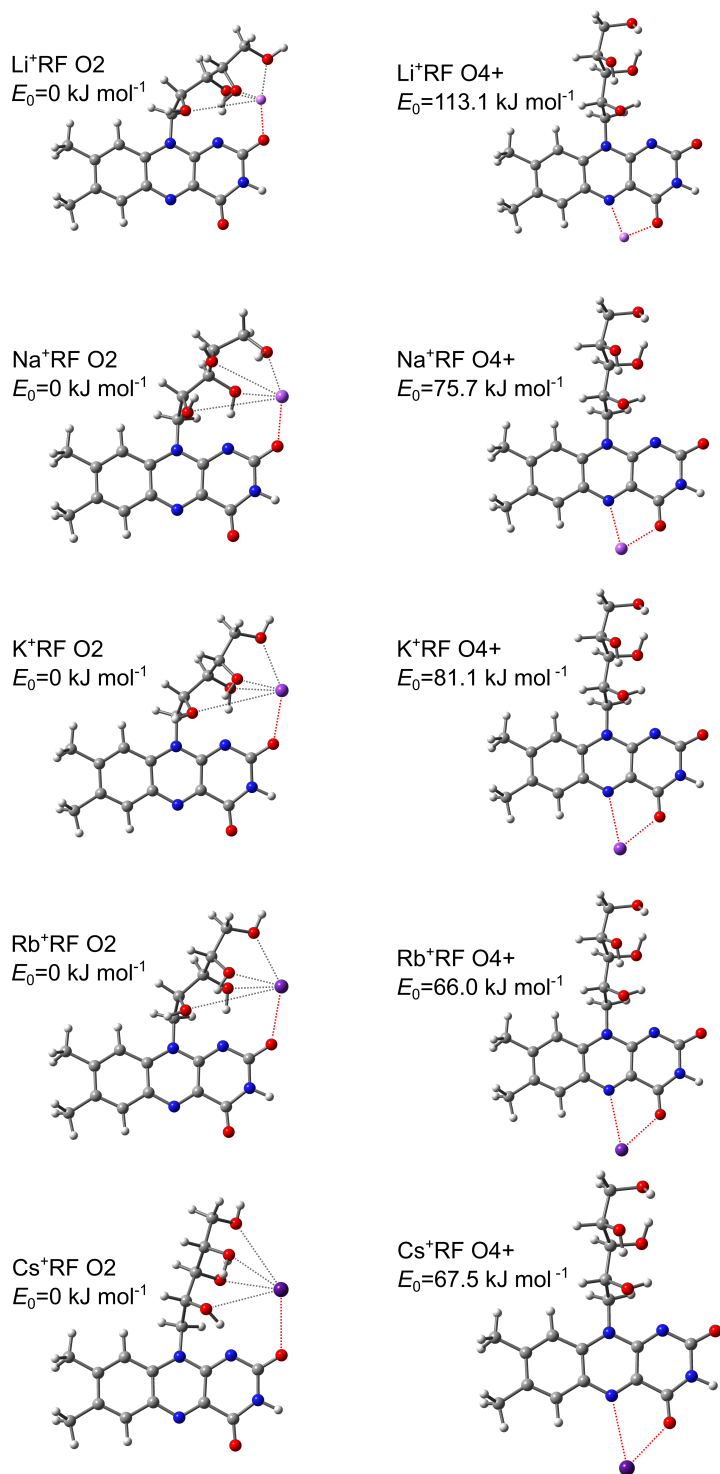


Figure. S4. Most stable structures of M⁺RF(O2) and the less stable M⁺RF(O4+) isomers with M=Li-Cs in the S₀ electronic ground state computed at the PBE0/cc-pVDZ level, along with their relative energies.

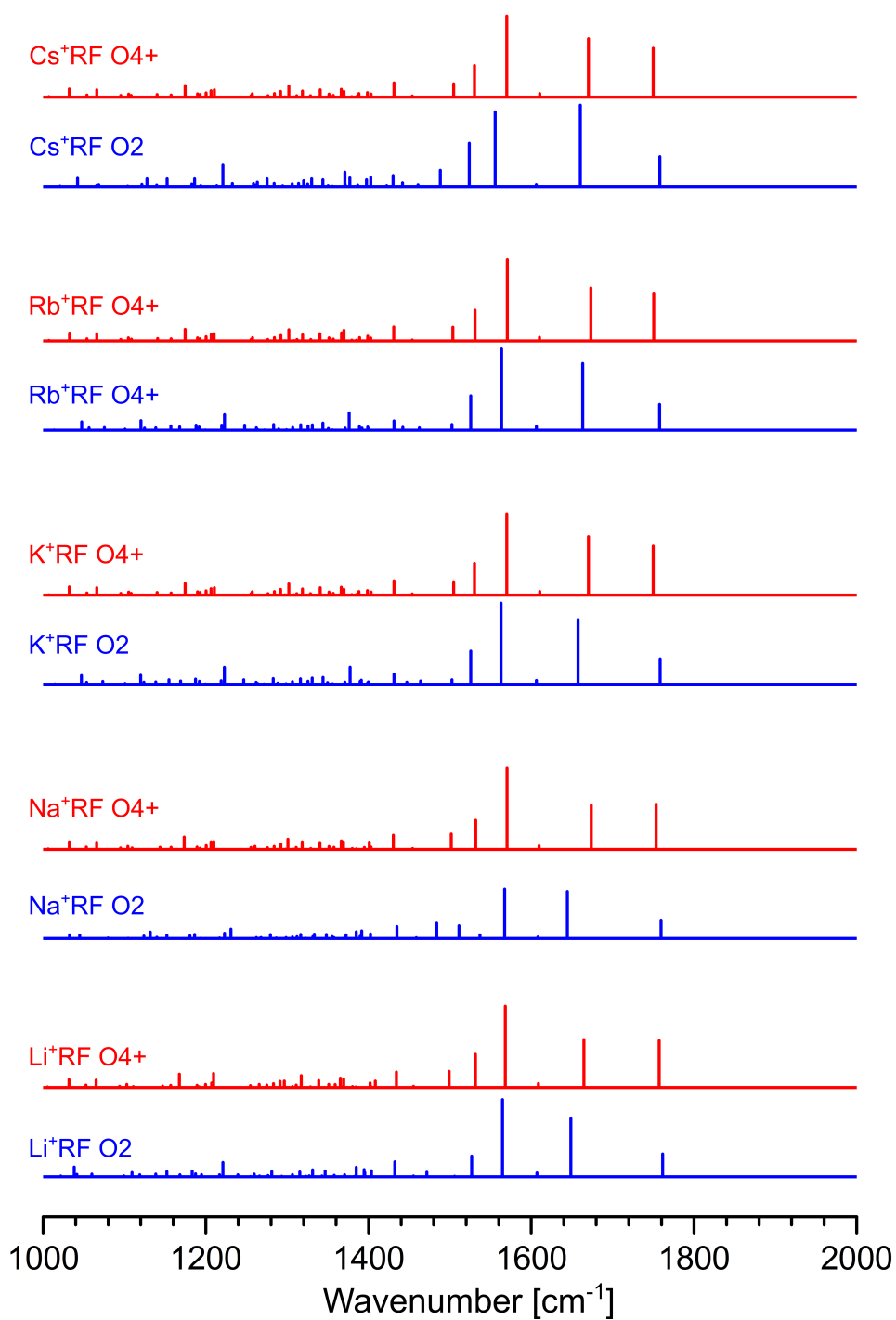


Figure S5. Linear IR absorption spectra of M^+RF with $M=Li-Cs$ computed for the most stable O_2 isomer (blue) and the less stable O_{4+} isomer (red) at the PBE0/cc-pVDZ level. Computed frequencies are scaled empirically by 0.941.

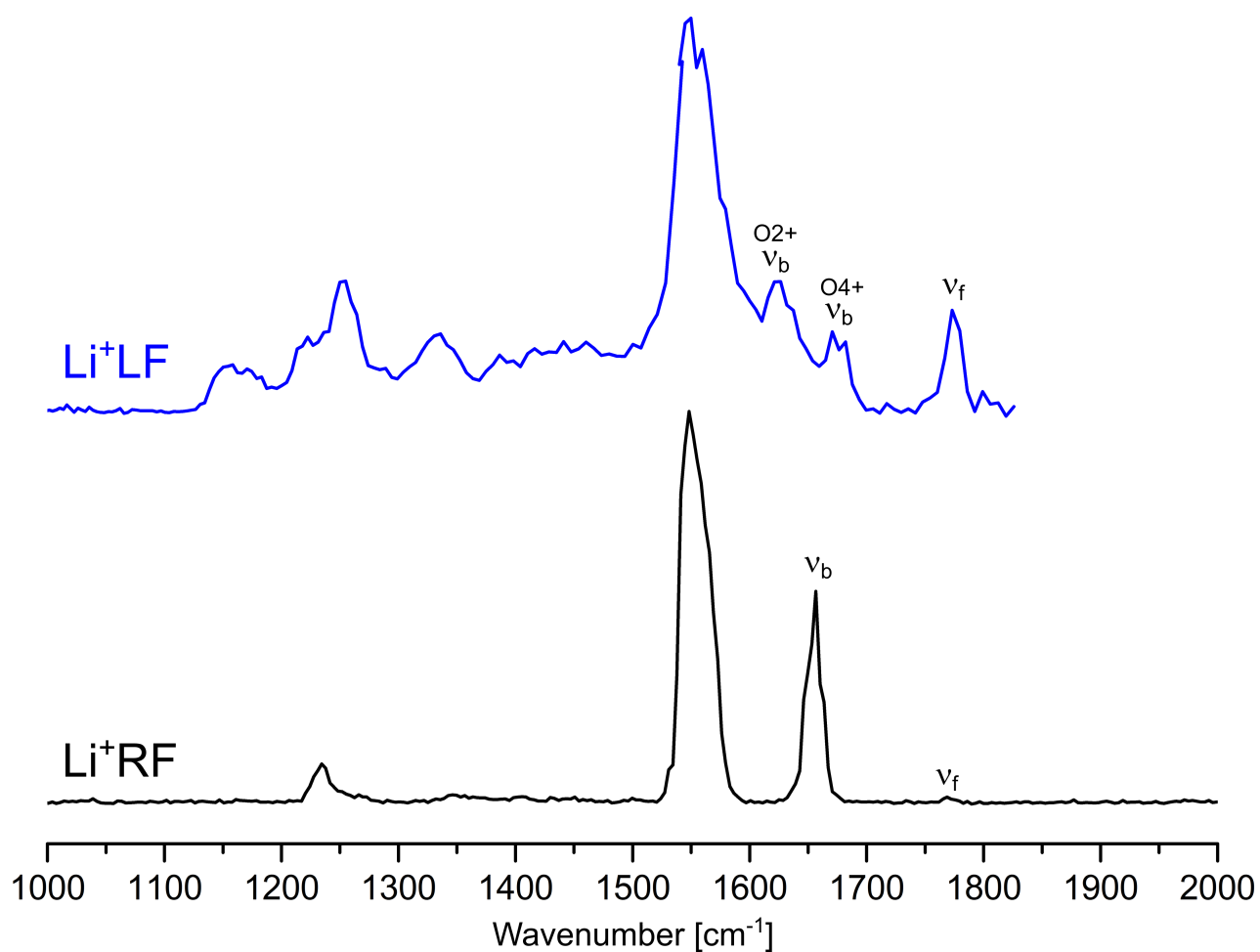


Figure S6. IRMPD spectra of Li^+LF (Nieto et al., *J. Phys. Chem. A*, **120**, 8297, 2016) and Li^+RF (this work). The bound and free CO_2 and CO_4 stretch vibrations are indicated.

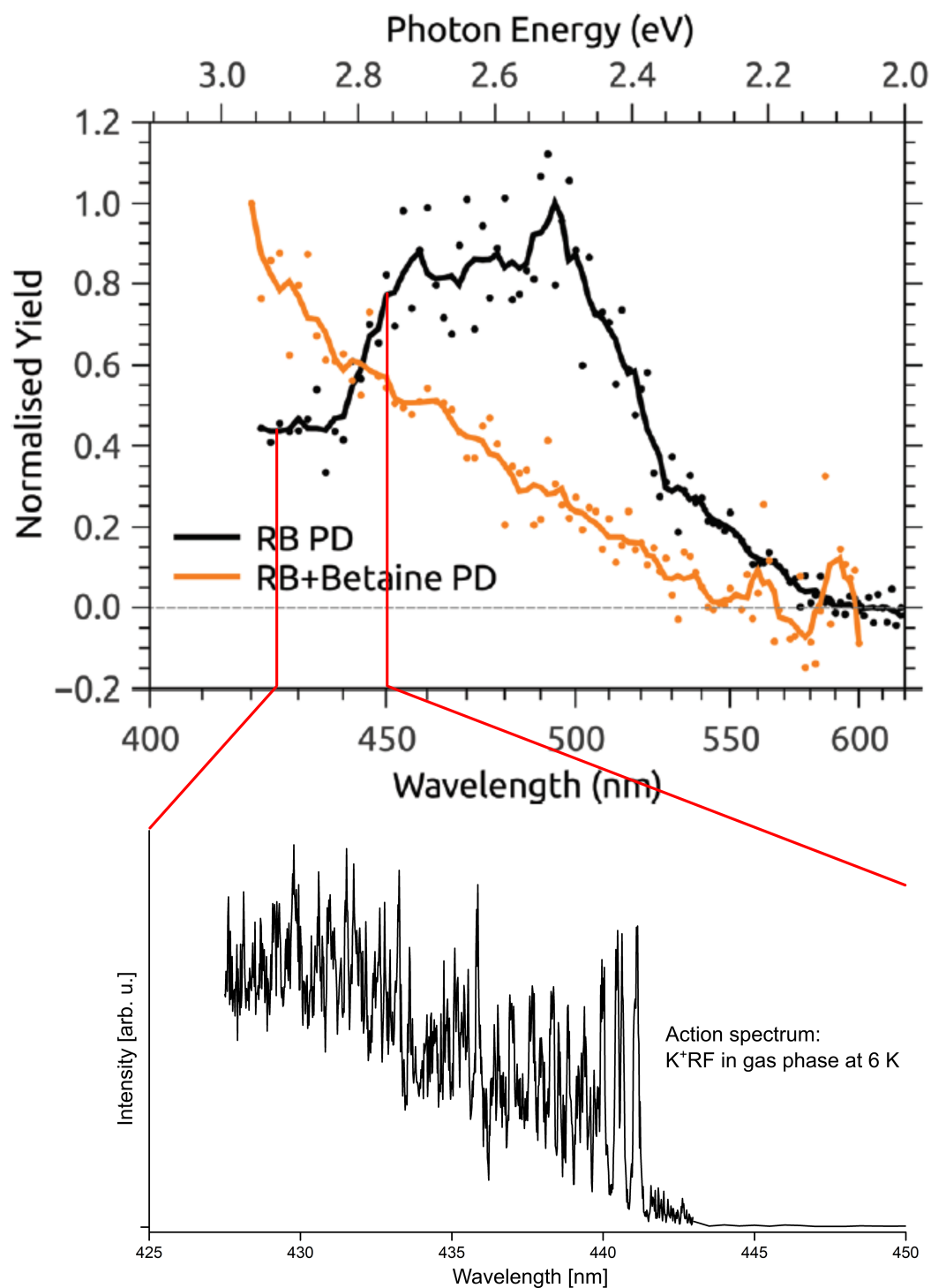


Figure S7. Comparison of VISPD spectrum of K⁺RF recorded at cryogenic temperatures (bottom, this work) to photodissociation action spectrum of deprotonated RF (top, RB=RF, black trace) recorded at 300 K (Bull et al., *Phys. Chem. Chem. Phys.*, **20**, 19672, 2018).

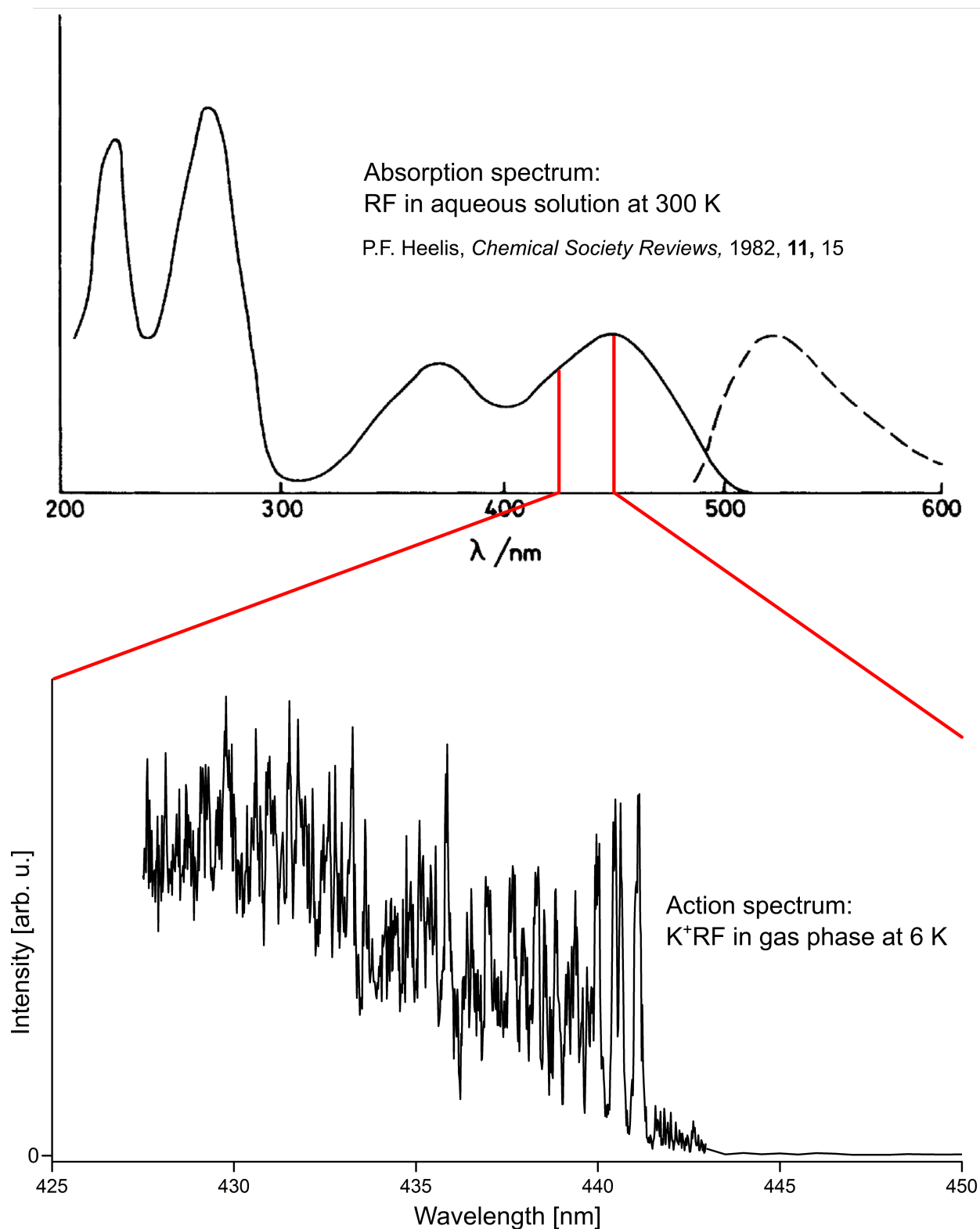


Figure S8. Comparison of VISPD spectrum of K^+RF recorded at cryogenic temperatures (bottom, this work) to absorption spectrum of bare RF (top, solid line) in aqueous solution at 300 K.

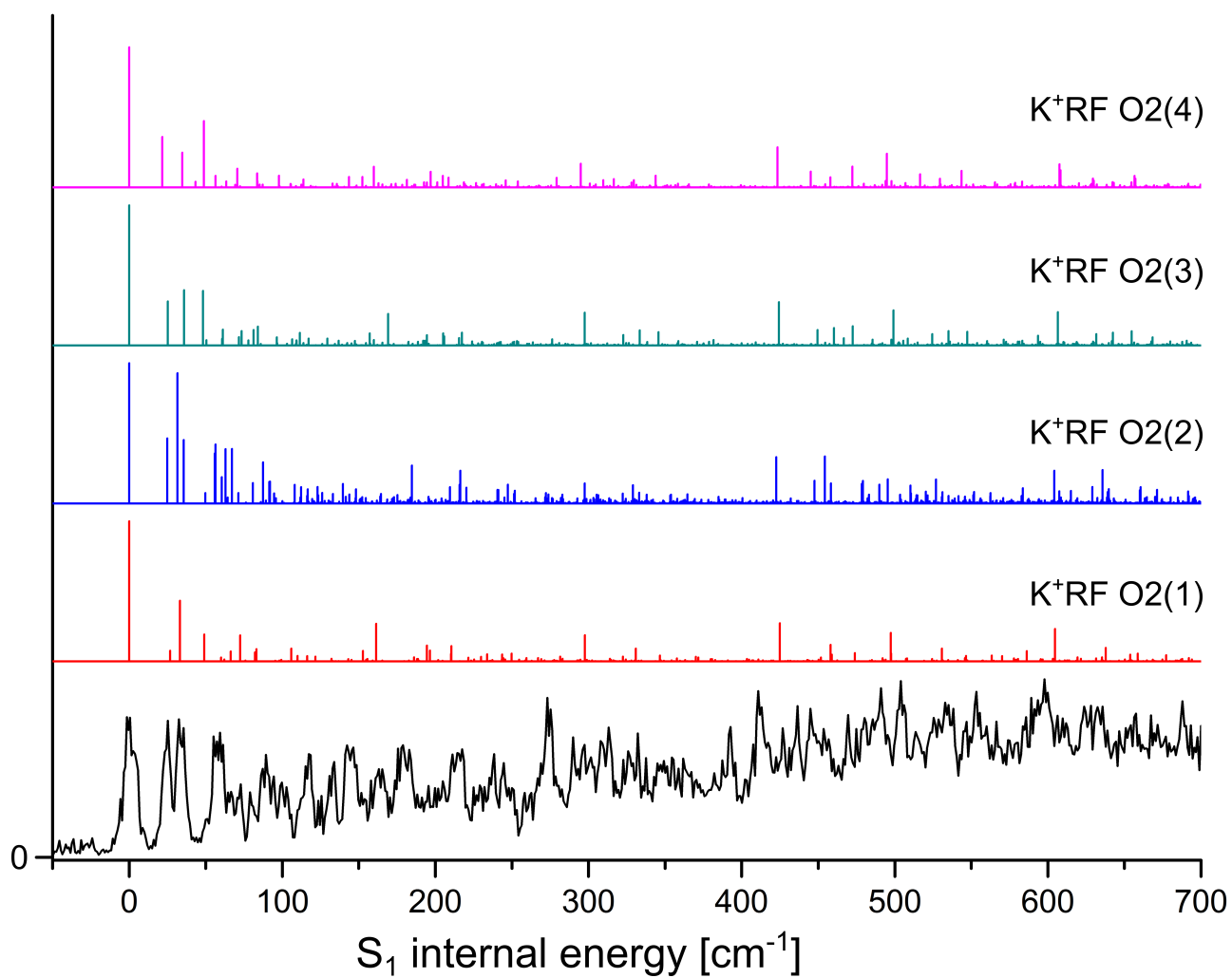


Figure S9. Comparison between VISPD spectrum of K⁺RF and Franck-Condon simulations for the O₂ isomers presented in Figure S3 as a function of S₁ internal energy.

Table S1. Binding energies (D_0) and relative energies (E_0) of several O2 isomers and the less stable O4+ isomer (in kJ mol^{-1}) of M^+RF computed at the PBE0/cc-pVDZ level. For the sake of completeness, related data of M^+LF are also presented.

K⁺RF			K⁺LF		
Isomer	D_0	E_0	Isomer	D_0	E_0
O2(1)	254.3	0	O2	175.9	0.1
(2)	253.2	1.0	O2+	175.5	0.5
(3)	247.4	6.8			
(4)	243.2	11.1			
(5)	232.8	21.5			
(6)	232.0	22.2			
(7)	227.4	26.9			
(8)	227.3	27.0			
(9)	225.6	28.7			
(10)	220.2	34.1			
(11)	220.2	34.1			
(12)	218.0	36.3			
(13)	214.2	40.0			
(14)	208.0	46.3			
(15)	207.3	47.0			
(16)	202.6	51.7			
O4+	173.2	81.1	O4+	176.0	0.0

Li⁺RF			Li⁺LF		
Isomer	D_0	E_0	Isomer	D_0	E_0
O2(1)	411.4	0.0	O2	279.7	20.4
(2)	379.9	31.5	O2+	289.5	10.6
(3)	378.4	33.1			
(4)	363.6	47.8			
(5)	355.2	56.2			
(6)	347.1	64.3			
(7)	325.6	85.9			
(8)	325.6	85.9			
O4+	298.3	113.1	O4+	300.1	0.0

Na ⁺ RF			Na ⁺ LF		
Isomer	D_0	E_0	Isomer	D_0	E_0
O2(1)	292.7	0.0	O2	209.5	10.2
(2)	279.6	13.1	O2+	214.2	5.5
(3)	276.1	16.7			
(4)	276.1	16.7			
(5)	269.5	23.2			
(6)	268.2	24.5			
(7)	259.4	33.3			
(8)	249.5	43.2			
(9)	244.8	47.9			
(10)	243.4	49.3			
O4+	217.0	75.7	O4+	219.7	0.0

Rb ⁺ RF			Rb ⁺ LF		
Isomer	D_0	E_0	Isomer	D_0	E_0
O2(1)	220.7	0.0	O2	158.9	0.0
(2)	217.6	3.2			
(3)	212.9	7.9			
(4)	203.8	17.0			
(5)	198.5	22.2			
(6)	198.2	22.6			
(7)	197.6	23.1			
(8)	193.4	27.3			
(9)	192.0	28.7			
O4+	154.7	66.0	O4+	157.9	1.0

Cs ⁺ RF			Cs ⁺ LF		
Isomer	D_0	E_0	Isomer	D_0	E_0
O2(1)	209.3	0.0	O2	148.2	0.0
(2)	197.5	11.9			
(3)	197.5	11.9			
(4)	197.4	11.9			
(5)	192.8	16.5			
(6)	184.1	25.3			
(7)	182.6	26.7			
(8)	178.7	30.7			
(9)	178.6	30.8			
(10)	176.3	33.0			
O4+	141.8	67.5	O4+	145.8	2.9

Table S2. Selected atomic charges (in e) of RF and $K^+RF(O2(1)/O4+)$ in the S_0 and S_1 state using natural bond orbital analysis (PBE0/cc-pVDZ).

	RF		K^+RF O2(1)		K^+RF O4+	
	S_0	S_1	S_0	S_1	S_0	S_1
q_M			0.932	0.930	0.963	0.953
q_{N5}	-0.371	-0.448	-0.348	-0.452	-0.475	-0.601
q_{O4}	-0.571	-0.592	-0.535	-0.553	-0.736	-0.756
q_{O2}	-0.594	-0.602	-0.714	-0.716	-0.554	-0.598
q_{N1}	-0.701	-0.496	-0.714	-0.627	-0.644	-0.570
q_{Oa}	-0.803	-0.731	-0.777	-0.775	-0.775	-0.502
q_{Ob}	-0.790	-0.795	-0.849	-0.842	-0.800	-0.793
q_{Oc}	-0.801	-0.788	-0.810	-0.809	-0.787	-0.752
q_{Od}	-0.757	-0.762	-0.798	-0.798	-0.759	-0.752

Table S3. Absolute distances (in pm) of the O2(1,2) and O4+ isomers of K⁺RF in the S₀ and S₁ states (PBE0/cc-pVDZ). Relative changes upon electronic excitation are tabulated as Δ (in pm).

Distance [Å]	K ⁺ RF O2(1) S ₀	K ⁺ RF O2(1) S ₁	Δ	K ⁺ RF O2(2) S ₀	K ⁺ RF O2(2) S ₁	Δ	K ⁺ RF O4+ S ₀	K ⁺ RF O4+ S ₁	Δ
O4, C4	120.4	121.0	0.6	120.3	120.9	0.6	123.5	124.3	0.8
C4, N3	139.0	141.2	2.1	139.4	141.1	1.7	134.5	137.8	3.3
C4, C4a	149.2	146.4	-2.8	149.2	146.9	-2.3	148.4	144.3	-4.1
C4a, N5	130.0	134.2	4.2	130.3	134.0	3.7	130.5	135.6	5.1
N5, C5a	135.8	136.0	0.2	135.6	136.4	0.9	136.3	136.3	0.1
N1/N5, M	379.9	385.0	5.1	326.5	333.9	7.4	289.7	273.7	-15.9
O2/O4, M	263.7	262.0	-1.6	263.8	261.7	-2.2	247.8	248.4	0.5
C5a, C6	141.0	139.4	-1.6	141.1	139.5	-1.7	141.1	141.0	-0.2
C6, C7	138.0	141.8	3.8	137.9	142.4	4.6	137.8	138.8	1.0
C7, M1	149.8	148.5	-1.3	149.8	148.4	-1.4	149.8	149.9	0.1
C7, C8	142.6	142.1	-0.5	142.8	141.6	-1.1	142.8	141.3	-1.4
C8, M2	149.6	149.7	0.1	149.6	149.7	0.1	149.6	149.8	0.2
C8, C9	139.1	138.9	-0.3	139.0	139.0	0.0	138.8	139.8	1.0
C9, C9a	140.2	142.1	2.0	140.0	142.5	2.4	140.5	139.2	-1.3
C9a, C5a	142.1	142.9	0.8	142.3	142.1	-0.2	142.2	142.4	0.3
N10, M3	146.0	145.3	-0.7	146.9	146.0	-0.9	146.4	144.7	-1.8
C9a, N10	138.7	138.0	-0.7	138.5	137.8	-0.7	137.7	141.2	3.5
N10, C10a	136.5	139.6	3.1	136.4	140.1	3.7	137.7	136.0	-1.7
C10a, C4a	144.2	141.9	-2.4	143.6	141.5	-2.1	145.1	141.8	-3.2
C10a, N1	131.9	132.2	0.3	132.6	132.5	-0.1	130.2	132.6	2.4
N1, C2	137.2	138.6	1.4	137.2	131.2	-6.1	137.2	138.2	1.1
C2, N3	138.0	136.1	-2.0	137.8	136.2	-1.6	143.1	139.5	-3.6
C2, O2	123.1	123.4	0.4	123.2	123.6	0.4	120.4	121.0	0.6
N1, C4	288.0	285.5	-2.5	287.9	285.3	-2.6	287.8	281.4	-6.5
C2, C4a	280.7	282.1	1.3	281.5	283.0	1.4	281.6	283.6	2.0
N3, C10a	269.3	267.1	-2.2	269.1	266.7	-2.4	268.2	267.0	-1.2
N10, N5	279.5	285.5	6.0	279.7	285.8	6.2	280.2	283.2	3.1
C10a, C5a	274.5	271.7	-2.8	273.5	270.6	-2.9	277.3	275.6	-1.7
C4a, C9a	273.0	274.6	1.6	273.0	274.2	1.1	271.7	274.1	2.4
C9, C6	278.4	276.3	-2.1	278.8	275.6	-3.1	277.5	275.6	-1.9
C9a, C7	284.1	282.3	-1.7	283.6	282.3	-1.4	280.8	282.3	1.5
C5a, C8	280.4	288.2	7.8	280.6	288.9	8.2	284.7	284.4	-0.3
N10, C1'	146.0	145.3	-0.7	146.9	146.0	-0.9	146.4	144.7	-1.8
C1', C2'	156.2	156.6	0.4	154.1	154.8	0.7	153.4	154.1	0.7
C2', C3'	154.3	154.0	-0.3	154.2	154.1	-0.1	153.3	153.9	0.6
C3', C4'	154.5	154.5	0.1	154.2	154.2	0.0	153.6	153.6	0.1
C4', C5'	151.7	151.7	0.0	151.7	151.8	0.0	152.5	152.8	0.3
Oa, M	449.6	444.8	-4.7	341.9	340.3	-1.6			0.0
Ob, M	263.8	264.5	0.7	271.6	272.4	0.8			0.0
Oc, M	274.2	273.9	-0.3	277.0	275.8	-1.2			0.0
Od, M	266.1	266.5	0.4	357.5	352.4	-5.1			0.0

Table S4. Comparison of geometry changes upon optical excitation between K⁺LF and K⁺RF. Δ indicates relative changes upon electronic excitation (in pm).

	Δ K ⁺ LF (O2)	Δ K ⁺ LF (O2+)	Δ K ⁺ LF (O2) - Δ K ⁺ RF O2(1)	Δ K ⁺ LF (O2+) - Δ K ⁺ RF O2(1)
O4, C4	0.6	0.6	0.0	0.0
C4, N3	2.3	1.9	-0.2	-0.2
C4, C4a	-2.8	-2.6	0.0	0.2
C4a, N5	3.9	3.9	0.3	-0.3
N5, C5a	0.5	0.7	-0.3	0.5
N1/N5, M	8.8	9.8	-3.7	4.7
O2/O4, M	-0.5	-1.5	-1.1	0.1
C5a, C6	-1.7	-1.7	0.1	-0.1
C6, C7	4.2	4.6	-0.4	0.8
C7, M1	-1.3	-1.5	0.0	-0.2
C7, C8	-1	-0.9	0.5	-0.4
C8, M2	0.1	0.1	0.0	0.0
C8, C9	0	-0.2	-0.3	0.1
C9, C9a	2.2	2.6	-0.2	0.6
C9a, C5a	0.3	0.1	0.5	-0.7
N10, M3	-0.5	-0.5	-0.2	0.2
C9a, N10	-0.7	-0.9	0.0	-0.2
N10, C10a	2.9	3.4	0.2	0.3
C10a, C4a	-2.1	-2.3	-0.3	0.1
C10a, N1	0.1	-0.1	0.2	-0.4
N1, C2	1.7	1.2	-0.3	-0.2
C2, N3	-2.2	-1.8	0.2	0.2
C2, O2	0.2	0.4	0.2	0.0
N1, C4	-2.6	-2.6	0.1	-0.1
C2, C4a	1.4	1.33	-0.1	0.0
N3, C10a	-2	-2.4	-0.2	-0.2
N10, N5	6.1	6.4	-0.1	0.4
C10a, C5a	-3	-3.2	0.2	-0.4
C4a, C9a	1.6	1.6	0.0	0.0
C9, C6	-2.7	-3	0.6	-0.9
C9a, C7	-1.3	-1.2	-0.4	0.5
C5a, C8	7.9	8.4	-0.1	0.6

Table S5. Optimized geometries and energies (in Å and hartree) of RF and M⁺RF (M=Li-Cs) shown in Figure 1 and Figure S2-S4.

RF(1) S₀

C	3.87629800	-2.45974300	0.14161200
C	4.00340200	-1.08681900	0.21958200
C	2.90610800	-0.22245800	0.04402300
C	1.62727300	-0.76860800	-0.22753700
C	1.49545100	-2.16385200	-0.30313200
C	2.58851500	-3.00301000	-0.12326600
C	0.73542100	1.45085600	-0.22224900
C	2.09536900	1.90652600	0.00086300
C	2.30983000	3.38195100	0.09524400
C	-0.16808100	3.59280600	-0.14927500
H	4.96668700	-0.61468900	0.42140200
H	0.52174200	-2.61625600	-0.48626800
H	1.20691800	5.10345200	0.06164300
N	0.56837700	0.10167300	-0.40943300
N	-0.32091900	2.22262500	-0.27046300
N	1.13612500	4.09254300	-0.01175500
N	3.11980400	1.12152200	0.12840800
O	3.39054800	3.90371800	0.24829100
O	-1.10449400	4.35948700	-0.15634200
C	2.40405800	-4.48786800	-0.20360700
H	2.70419200	-4.97750600	0.73681000
H	1.35966600	-4.75625900	-0.40965800
H	3.03174500	-4.92367700	-0.99757400
C	5.06254100	-3.35643100	0.33512100
H	4.91660700	-4.04334100	1.18441100
H	5.24529500	-3.98344600	-0.55246700
H	5.97143200	-2.77151500	0.52750300
C	-0.74362000	-0.37358900	-0.85528900
H	-1.17997800	0.41396800	-1.48230500
H	-0.59175000	-1.25995900	-1.48291400
C	-1.72032500	-0.67524200	0.27813100
C	-3.03401500	-1.18966100	-0.32355900
C	-4.10115900	-1.44805400	0.75146900
C	-5.40944500	-1.93121600	0.13208600
H	-1.30888800	-1.46699400	0.93163900
O	-1.92253300	0.46498200	1.09028500
H	-1.68974900	1.25885200	0.55568000
O	-3.44752600	-0.26458400	-1.29544300
O	-4.45360900	-0.28291800	1.46299600
O	-6.01048400	-0.86111500	-0.57849100
H	-4.41960500	-0.33893900	-1.35850700
H	-2.81205300	-2.18201300	-0.78209800
H	-3.63437500	0.24965700	1.52889700
H	-5.24068800	-2.75393400	-0.57914100
H	-6.08186700	-2.29598700	0.92969900
H	-5.96102500	-0.12291100	0.05639600
H	-3.70894700	-2.23715400	1.42787900
Sum of electronic and zero-point Energies=			-1328.500913
Sum of electronic and thermal Energies=			-1328.476878
Sum of electronic and thermal Enthalpies=			-1328.475934
Sum of electronic and thermal Free Energies=			-1328.555131

RF(1) S₁

C	4.09434200	-2.10783100	0.23302600
C	4.07313700	-0.72785000	0.35477600
C	2.92944300	0.05381700	0.06730000
C	1.75800100	-0.65316700	-0.37079100
C	1.77528700	-2.04811000	-0.46918700
C	2.91867700	-2.79155300	-0.18288100
C	0.65919700	1.45775700	-0.44684100
C	1.84898200	2.07803600	0.00507600
C	1.80437200	3.51454100	0.23446700
C	-0.63858600	3.40405600	-0.25682700
H	4.95646400	-0.17992300	0.68732100
H	0.88319700	-2.59036100	-0.78369300
H	0.42601400	5.04922300	0.32015600
N	0.62747500	0.11279600	-0.66653200
N	-0.47081200	2.11173100	-0.74077800
N	0.51930200	4.07251100	0.05853300
N	2.98554900	1.38148300	0.24590200
O	2.72921500	4.22018900	0.58507000
O	-1.75165700	3.88903700	-0.16473000
C	2.90300700	-4.28425400	-0.31137700
H	3.14095900	-4.77926600	0.64504300
H	1.91970200	-4.64804700	-0.64010000
H	3.65090400	-4.63871500	-1.04034900
C	5.34332400	-2.87450200	0.54422900
H	5.17548800	-3.60375400	1.35377600
H	5.68841700	-3.45063800	-0.32999800
H	6.15590500	-2.20416600	0.85271800
C	-0.63264200	-0.48283500	-1.05484700
H	-1.13965200	0.21497000	-1.73496000
H	-0.43550800	-1.42117800	-1.58393100
C	-1.58059700	-0.72732700	0.13543300
C	-2.89515400	-1.33271600	-0.36972600
C	-3.79817000	-1.79687400	0.78288400
C	-5.14603400	-2.28965500	0.26514900
H	-1.09686500	-1.39630100	0.86535900
O	-1.84498200	0.47929100	0.81476400
H	-2.32917700	1.04247200	0.17795200
O	-3.48222300	-0.33411100	-1.16792400
O	-4.11926900	-0.76551900	1.69116200
O	-5.88180800	-1.19405600	-0.25451500
H	-4.45107900	-0.47230900	-1.12960200
H	-2.65531000	-2.23835000	-0.96828300
H	-3.35225100	-0.16723400	1.74232100
H	-5.02128900	-3.02046600	-0.54757900
H	-5.69886700	-2.77781400	1.08720200
H	-5.86261700	-0.53977200	0.46558900
H	-3.27875300	-2.63587900	1.29139500
Sum of electronic and zero-point Energies=			-1328.399216
Sum of electronic and thermal Energies=			-1328.374542
Sum of electronic and thermal Enthalpies=			-1328.373597
Sum of electronic and thermal Free Energies=			-1328.454102

RF(2) S₀

N	-0.73591900	1.98463600	-0.33316900
C	-0.87226100	3.34002600	-0.09866200
O	-1.94864600	3.89770500	-0.11926000
N	0.28747400	4.07942100	0.17265100
H	0.14348400	5.07378800	0.32309000
C	1.57952200	3.61706100	0.29747100
O	2.51710100	4.33731400	0.55453700
C	1.68020700	2.14304500	0.08618000
N	2.84184200	1.57388300	0.20301500
C	2.90873700	0.22276800	0.04038200
C	4.14679100	-0.42192200	0.23175900
H	4.99700100	0.21628100	0.47954900
C	4.28059800	-1.79185000	0.12514800
C	5.60989400	-2.45369000	0.33487300
H	5.92024100	-3.02760200	-0.55321700
H	5.58032000	-3.16430300	1.17669800
H	6.39094800	-1.71188200	0.54720200
C	3.12061700	-2.56674000	-0.16431900
C	3.21491800	-4.06071500	-0.23052400
H	3.91935800	-4.38003400	-1.01575100
H	2.23865600	-4.51610100	-0.44052600
H	3.59183000	-4.47827600	0.71701500
C	1.89392600	-1.94913200	-0.37084100
H	1.00484100	-2.56237000	-0.51929500
C	1.77298900	-0.55350700	-0.29863100
N	0.58282900	0.10770400	-0.53251800
C	0.45654200	1.44166700	-0.25371000
C	-0.59632100	-0.57624500	-1.05680200
H	-0.26896200	-1.44931400	-1.63130800
H	-1.09301200	0.13067200	-1.73186600
C	-1.56964100	-1.02388100	0.03419900
H	-1.36080100	-0.41990300	0.94264400
O	-1.34639600	-2.39176300	0.27730800
H	-2.10227600	-2.67901500	0.82759900
C	-3.02484000	-0.74714200	-0.37290000
H	-3.27455200	-1.47445100	-1.17337200
O	-3.22349000	0.54494600	-0.88281900
H	-2.51697900	1.14403800	-0.55867700
C	-3.97550600	-0.99439700	0.80975800
H	-3.70137500	-0.29626300	1.61964600
O	-3.83218700	-2.31940400	1.31368900
H	-4.47387600	-2.83220800	0.78789600
C	-5.43384600	-0.78064200	0.42894100
H	-5.55017300	0.17916100	-0.09717800
H	-6.05348200	-0.77221900	1.33755100
O	-5.88625800	-1.88587300	-0.34381900
H	-5.61971100	-1.73110200	-1.25858500
Sum of electronic and zero-point Energies=			-1328.500367
Sum of electronic and thermal Energies=			-1328.475957
Sum of electronic and thermal Enthalpies=			-1328.475013
Sum of electronic and thermal Free Energies=			-1328.554756

RF(3) S₀

C	-1.41230700	3.63394100	-0.39197900
O	-2.29969500	4.38745700	-0.72237600
C	-1.59256200	2.17266200	-0.14758800
N	-0.10970700	4.04177900	-0.20486000
C	-0.42323300	1.42777400	0.28056800
N	-2.77094400	1.65295900	-0.31589300
C	0.99740200	3.25935200	0.15369500
N	-0.62601800	0.10867200	0.58508200
N	0.78611300	1.91935400	0.41517500
C	-2.90884800	0.31135200	-0.12170300
O	2.09513300	3.77009600	0.22273500
C	-4.16298500	-0.28263800	-0.36534400
C	-4.36576800	-1.64151400	-0.23025500
H	-4.96788800	0.38560100	-0.67708300
C	-3.26043100	-2.45878100	0.14396200
C	-3.42727600	-3.94456600	0.24457500
H	-3.77068600	-4.37253200	-0.71105100
H	-2.48603900	-4.43667600	0.52116300
H	-4.18755500	-4.20904700	0.99746600
C	-5.71098900	-2.24889500	-0.49610100
H	-6.09585600	-2.78173700	0.38844300
H	-6.44391000	-1.47926300	-0.77173200
H	-5.66876800	-2.98475200	-1.31543100
H	0.08829100	5.02393300	-0.37283200
C	0.48950300	-0.61254700	1.19310200
C	1.50163500	-1.12903600	0.17159900
H	0.09086100	-1.45476200	1.76848700
H	0.98013400	0.08864600	1.87830100
C	2.94352800	-0.90660100	0.66110400
H	1.37205300	-0.54259700	-0.76182500
H	3.13548700	-1.65412400	1.45472800
C	3.93666300	-1.14923900	-0.47314600
C	5.37818000	-1.04568800	-0.01908200
H	3.76328400	-0.37878200	-1.25294800
H	5.59776900	-0.01312100	0.29770200
H	5.53725500	-1.72453000	0.84085600
O	1.22768300	-2.49260800	-0.04960000
H	1.97033300	-2.82709800	-0.58538900
O	3.15809200	0.36701600	1.21136700
H	2.54325800	1.00868700	0.79822100
O	3.71583600	-2.44405900	-1.01371800
H	4.51860900	-2.64556000	-1.52094700
O	6.15038100	-1.44950900	-1.14023500
H	7.06273300	-1.56969500	-0.85577100
C	-2.01971800	-1.89103800	0.40241200
H	-1.16926400	-2.53858400	0.61671500
C	-1.83040300	-0.50462200	0.30101800
Sum of electronic and zero-point Energies=			-1328.498483
Sum of electronic and thermal Energies=			-1328.473779
Sum of electronic and thermal Enthalpies=			-1328.472835
Sum of electronic and thermal Free Energies=			-1328.553173

RF(4) S₀

C	4.28261900	0.39675600	0.46189700
C	3.36529300	1.41109900	0.64308700
C	2.03051800	1.29707900	0.20511900
C	1.61022900	0.10973800	-0.44534500
C	2.53525900	-0.93179000	-0.61203100
C	3.84607900	-0.80165000	-0.17183200
C	-0.57773700	1.05294000	-0.64028800
C	-0.04230500	2.22199400	0.03061700
C	-0.97331800	3.36551600	0.26339200
C	-2.73243800	1.92919500	-0.76389200
H	3.63784900	2.34724100	1.13385200
H	2.20066500	-1.88509900	-1.01748900
H	-2.94311500	3.83545900	-0.03141700
N	0.30368800	0.03582600	-0.90387200
N	-1.82809700	0.91537200	-1.01604000
N	-2.24992400	3.10900800	-0.18555900
N	1.19026800	2.34556800	0.41952900
O	-0.65593000	4.40752200	0.78993800
O	-3.91346400	1.82314300	-1.01987100
C	4.80009500	-1.94279300	-0.35451500
H	5.20746000	-2.27998500	0.61233800
H	4.31351400	-2.79957700	-0.83783400
H	5.66374600	-1.64434800	-0.97092400
C	5.69827100	0.54342000	0.93389600
H	5.95856600	-0.22696000	1.67773000
H	6.41435100	0.43583500	0.10322500
H	5.86098900	1.52643300	1.39506200
C	-0.11549600	-1.03117000	-1.82678600
H	-0.89341700	-0.59786300	-2.46801600
H	0.75946600	-1.25476600	-2.45164100
C	-0.63914700	-2.36082900	-1.26184000
C	-2.01234200	-2.31302600	-0.56048600
C	-1.96974900	-1.79880300	0.88024600
C	-3.35187300	-1.68348700	1.49155000
H	-0.81992000	-2.94475200	-2.18492300
O	0.34062200	-3.03441100	-0.51061600
H	0.05457900	-3.02863100	0.42325600
O	-2.96363600	-1.64993000	-1.34086500
O	-1.20542800	-2.72798100	1.64090800
O	-3.11700900	-1.40694800	2.86501900
H	-2.72973000	-0.69486700	-1.33079600
H	-2.33803700	-3.36562500	-0.48218400
H	-1.40179200	-2.51579800	2.56797000
H	-3.92602800	-0.88430000	0.99470900
H	-3.89121100	-2.64022500	1.35830600
H	-3.94939100	-1.49659900	3.34140600
H	-1.49509500	-0.80228500	0.93614100
Sum of electronic and zero-point Energies=			-1328.496718
Sum of electronic and thermal Energies=			-1328.472218
Sum of electronic and thermal Enthalpies=			-1328.471274
Sum of electronic and thermal Free Energies=			-1328.551077

K⁺RF O2(1) S₀

C	5.17241000	-0.73114700	0.22757200
C	4.57598700	0.50817800	0.33701100
C	3.20621500	0.70615100	0.06756200
C	2.40957200	-0.39693200	-0.34162900
C	3.01099500	-1.65905000	-0.44019400
C	4.36323000	-1.83731900	-0.16466700
C	0.52885700	1.07421600	-0.41388300
C	1.42514800	2.12651700	-0.00143900
C	0.84571100	3.48890900	0.18394300
C	-1.34438100	2.44885000	-0.32856600
H	5.14397100	1.38927400	0.64067800
H	2.43190700	-2.53479200	-0.73149700
H	-0.99275000	4.40877800	0.15186500
N	1.07182900	-0.16031500	-0.62270900
N	-0.76610300	1.23542300	-0.60297600
N	-0.53068700	3.51729500	-0.00986900
N	2.69514900	1.95494500	0.21669700
O	1.47785800	4.46807000	0.48590700
O	-2.56657900	2.59051200	-0.35187000
C	4.96978200	-3.19976600	-0.28438400
H	5.41807500	-3.51895300	0.66992400
H	4.23098100	-3.95288700	-0.58690200
H	5.78445900	-3.20229500	-1.02608500
C	6.63094600	-0.91376100	0.51597600
H	6.79285800	-1.63438200	1.33317800
H	7.16743400	-1.30393800	-0.36337500
H	7.09937100	0.03576200	0.80393000
C	0.18556700	-1.21159400	-1.11294400
H	-0.43469300	-0.76571900	-1.90052200
H	0.79902400	-1.98430900	-1.58402000
C	-0.72543600	-1.82180500	-0.00046100
C	-2.20142900	-1.84937700	-0.44967400
C	-3.12276600	-2.19662400	0.74049800
C	-4.49649300	-2.71378700	0.35712200
H	-0.42301600	-2.87001400	0.16793000
O	-0.61924600	-1.10866400	1.22494300
H	0.15243300	-1.42624900	1.71061800
O	-2.60880700	-0.66140200	-1.07665800
O	-3.29580700	-1.07433600	1.58808600
O	-5.25888500	-1.70240500	-0.28749200
H	-1.92829400	0.05059200	-0.90612700
H	-2.28092000	-2.67123300	-1.18714900
H	-2.39835300	-0.84039800	1.88152900
H	-4.36920500	-3.59127900	-0.30157200
H	-5.00324500	-3.04493000	1.28047600
H	-6.10906700	-2.08742100	-0.53072900
H	-2.64901200	-3.03031700	1.29748600
K	-4.49236900	0.82732200	0.01568300

Sum of electronic and zero-point Energies= -1356.736208
Sum of electronic and thermal Energies= -1356.710054
Sum of electronic and thermal Enthalpies= -1356.709110
Sum of electronic and thermal Free Energies= -1356.791554

K⁺RF O2(1) S₁

C	5.16358500	-0.79421800	0.18927100
C	4.58320300	0.49742500	0.25758700
C	3.23038000	0.74725800	0.03195400
C	2.41759300	-0.37528700	-0.31667300
C	2.99034700	-1.67534300	-0.35673700
C	4.33747000	-1.90977600	-0.11315800
C	0.57589100	1.13413700	-0.39979200
C	1.45687300	2.17965700	-0.02057800
C	0.86815300	3.50515200	0.17765500
C	-1.33701700	2.46949300	-0.27678000
H	5.20365900	1.36305700	0.49807200
H	2.35913000	-2.53537800	-0.58381900
H	-0.98525300	4.42034500	0.19928200
N	1.09010100	-0.14558100	-0.61489200
N	-0.72879000	1.25916000	-0.56913800
N	-0.53382300	3.52801000	0.01547900
N	2.77794600	2.02342000	0.15885900
O	1.46586100	4.51554400	0.46982300
O	-2.56832700	2.55614800	-0.28187500
C	4.90125000	-3.29512000	-0.17266200
H	5.36012200	-3.58737700	0.78562500
H	4.12576100	-4.03420000	-0.41315800
H	5.68938200	-3.37617400	-0.93865900
C	6.61748600	-0.96284400	0.43900000
H	6.79629600	-1.65967100	1.27677600
H	7.11560600	-1.41986300	-0.43435300
H	7.11170100	-0.01045000	0.66411900
C	0.19347500	-1.18172800	-1.09916300
H	-0.42940200	-0.73329900	-1.88279100
H	0.79456100	-1.95975000	-1.58029500
C	-0.72552300	-1.79917900	0.00802800
C	-2.19085700	-1.83715900	-0.46564600
C	-3.13237300	-2.22014000	0.69848900
C	-4.49558000	-2.73325600	0.27359100
H	-0.41386400	-2.84386100	0.18791000
O	-0.66028000	-1.07746300	1.22776300
H	0.16086400	-1.29316900	1.68763500
O	-2.59825000	-0.63584400	-1.07023400
O	-3.32972700	-1.12376600	1.57289400
O	-5.25032900	-1.70666000	-0.35524200
H	-1.91727500	0.06843900	-0.89151100
H	-2.25066700	-2.64180100	-1.22350700
H	-2.44015500	-0.88536900	1.88617900
H	-4.35115100	-3.59051200	-0.40784800
H	-5.01753200	-3.09378700	1.17726900
H	-6.09465000	-2.08726400	-0.62450500
H	-2.66316700	-3.06637600	1.24008400
K	-4.50472300	0.82070000	0.04284200

Sum of electronic and zero-point Energies= -1356.629620
Sum of electronic and thermal Energies= -1356.602808
Sum of electronic and thermal Enthalpies= -1356.601864
Sum of electronic and thermal Free Energies= -1356.686008

K⁺RF O2(2) S₀

C	4.98564700	-1.32837500	0.08582400
C	4.63200500	0.00376300	0.12258300
C	3.29159700	0.42554800	-0.00793200
C	2.27243600	-0.54978400	-0.19187000
C	2.62878800	-1.90367600	-0.22284800
C	3.95403700	-2.30023600	-0.08517000
C	0.68141100	1.22158000	-0.18806500
C	1.78261700	2.13223400	-0.04383400
C	1.46047500	3.58795200	0.01637300
C	-0.92328600	2.90910500	-0.07014100
H	5.37859200	0.78845100	0.25619600
H	1.86770900	-2.67595600	-0.33066600
H	-0.18937900	4.81776400	0.03949500
N	0.96927800	-0.10326200	-0.33466200
N	-0.59478000	1.58133900	-0.17935700
N	0.09042000	3.84175600	-0.02414900
N	3.02662900	1.75429800	0.03571300
O	2.27633300	4.46902500	0.09523700
O	-2.10237800	3.26029400	-0.00846100
C	4.29872200	-3.75556200	-0.11047600
H	4.79892200	-4.05851000	0.82312900
H	3.40966400	-4.38493100	-0.24386300
H	5.00361100	-3.97845200	-0.92729100
C	6.41579600	-1.75029500	0.22808100
H	6.55580500	-2.40700500	1.10127300
H	6.75703800	-2.31551100	-0.65359300
H	7.07460900	-0.88126400	0.34903900
C	-0.12181500	-0.98647800	-0.76919200
H	-0.70614400	-0.40933200	-1.49521700
H	0.31977800	-1.83933100	-1.29620100
C	-1.06644900	-1.47431900	0.34573800
C	-2.39019600	-1.94553700	-0.28820200
C	-3.48295700	-2.21385200	0.76631100
C	-4.74946400	-2.79368400	0.16435000
H	-0.62442200	-2.33944400	0.86832400
O	-1.26880200	-0.48170700	1.33459800
H	-1.19222400	0.39100000	0.86623900
O	-2.82853500	-0.96295200	-1.21722800
O	-3.83123700	-1.03022200	1.46365100
O	-5.22788200	-1.92014500	-0.85989100
H	-3.71363700	-1.26688600	-1.50539200
H	-2.18281900	-2.89849000	-0.81594700
H	-2.98267800	-0.72531400	1.84578100
H	-4.53007100	-3.79416400	-0.24808300
H	-5.49990900	-2.89677500	0.96527500
H	-6.01807100	-2.30764800	-1.25663900
H	-3.09861100	-2.97751900	1.47106300
K	-3.84340900	1.27872400	-0.06674500

Sum of electronic and zero-point Energies= -1356.735891

Sum of electronic and thermal Energies= -1356.710063

Sum of electronic and thermal Enthalpies= -1356.709119

Sum of electronic and thermal Free Energies= -1356.791683

K⁺RF O2(2) S₁

C	4.98080500	-1.36119500	0.04637700
C	4.62440000	0.01707800	-0.00302700
C	3.30871600	0.47422800	-0.07535100
C	2.29441800	-0.51771600	-0.14946600
C	2.64301900	-1.89721100	-0.08116300
C	3.95715300	-2.33930600	0.01286600
C	0.72231200	1.26256400	-0.17221800
C	1.79851700	2.17863000	-0.10835000
C	1.44480900	3.60164500	-0.02316700
C	-0.93417000	2.90013200	0.02963100
H	5.40569700	0.78013700	0.00601500
H	1.84624000	-2.64263100	-0.07434800
H	-0.22568200	4.81204300	0.09701700
N	0.98818200	-0.10662700	-0.29967300
N	-0.56232800	1.57501000	-0.09096600
N	0.05391700	3.83745500	0.01797200
N	3.08936700	1.82061100	-0.09689200
O	2.22367800	4.52569700	0.00736500
O	-2.12933700	3.19632500	0.13697500
C	4.27729300	-3.79978400	0.08918200
H	4.81571500	-4.04656200	1.01822100
H	3.36643900	-4.41169500	0.05732800
H	4.92286700	-4.11492900	-0.74629700
C	6.41097200	-1.74543500	0.14232300
H	6.59752100	-2.34001000	1.05438200
H	6.69925000	-2.40144300	-0.69810700
H	7.07577100	-0.87374100	0.15168500
C	-0.08514700	-0.97688900	-0.77211100
H	-0.66014700	-0.40170900	-1.50733100
H	0.36498100	-1.82669200	-1.30033200
C	-1.06364100	-1.48843500	0.31233000
C	-2.37697200	-1.92765000	-0.36271900
C	-3.48037300	-2.25988800	0.66260600
C	-4.74398800	-2.79431600	0.01402900
H	-0.63626000	-2.37361900	0.81522600
O	-1.28295500	-0.52762100	1.32346700
H	-1.16629500	0.36155800	0.88596600
O	-2.80467400	-0.89237000	-1.23729100
O	-3.83171000	-1.12520900	1.43412800
O	-5.21520500	-1.85086200	-0.95014000
H	-3.68540300	-1.17727100	-1.55512800
H	-2.16124200	-2.84847300	-0.94209000
H	-2.98036400	-0.82454700	1.81550600
H	-4.52399700	-3.76428100	-0.46556000
H	-5.49960100	-2.95110100	0.80131900
H	-6.00599100	-2.20731700	-1.37393400
H	-3.10352000	-3.07060400	1.31750500
K	-3.88300400	1.25638700	0.04437900
Sum of electronic and zero-point Energies=			-1356.631121
Sum of electronic and thermal Energies=			-1356.604621
Sum of electronic and thermal Enthalpies=			-1356.603677
Sum of electronic and thermal Free Energies=			-1356.688135

K⁺RF O2(3) S₀

C	5.13821000	-0.77435700	0.27014500
C	4.56646600	0.47860300	0.33075700
C	3.20061800	0.69126500	0.04817400
C	2.38584300	-0.41102900	-0.32621000
C	2.96211800	-1.68709200	-0.37225900
C	4.30776100	-1.87995700	-0.08161500
C	0.53416200	1.08613900	-0.46069000
C	1.44281000	2.13497300	-0.07458800
C	0.88756200	3.51044500	0.06966800
C	-1.31981200	2.48177500	-0.37480700
H	5.14922300	1.35934900	0.60582400
H	2.36281600	-2.56310500	-0.61664900
H	-0.94388500	4.44748500	0.05811400
N	1.05770400	-0.15909100	-0.62947000
N	-0.76102400	1.26657700	-0.66649400
N	-0.49270900	3.55049100	-0.10303000
N	2.71088900	1.95051000	0.15238500
O	1.53360600	4.49192000	0.33203100
O	-2.54494900	2.62680200	-0.33516600
C	4.88640700	-3.25860000	-0.13480000
H	5.31487300	-3.54455100	0.83898700
H	4.13438200	-4.00804100	-0.41267200
H	5.71001900	-3.31155600	-0.86461400
C	6.59101800	-0.97555500	0.57456400
H	6.73260400	-1.66389500	1.42281200
H	7.12387500	-1.41429100	-0.28387100
H	7.07807000	-0.02476900	0.82513600
C	0.16568600	-1.20846800	-1.11010400
H	-0.42624300	-0.76563600	-1.92180100
H	0.77834600	-1.99567300	-1.55710900
C	-0.76993600	-1.79046400	-0.00892100
C	-2.21162800	-1.82964800	-0.54322000
C	-3.21064700	-2.43211400	0.45086000
C	-4.60701300	-2.62694400	-0.13437400
H	-0.46786300	-2.84146000	0.17625800
O	-0.62172100	-1.02993100	1.15993200
H	-1.41776600	-1.18453100	1.69612100
O	-2.67006600	-0.56065600	-0.95139400
O	-3.25970800	-1.56088300	1.59664000
O	-5.21912000	-1.42876900	-0.56946700
H	-1.91883800	0.11578900	-0.89841400
H	-2.19780500	-2.51673700	-1.41532500
H	-3.70908200	-2.03147600	2.31220000
H	-4.55442200	-3.37180700	-0.94930900
H	-5.26779900	-3.04914000	0.63939000
H	-4.71300400	-1.12271900	-1.33769500
H	-2.83139600	-3.42621600	0.75434700
K	-4.26222100	0.91009900	0.58202300
Sum of electronic and zero-point Energies=			-1356.733610
Sum of electronic and thermal Energies=			-1356.707690
Sum of electronic and thermal Enthalpies=			-1356.706745
Sum of electronic and thermal Free Energies=			-1356.788751

K⁺RF O2(3) S₁

C	5.11742300	-0.84750800	0.24202700
C	4.56479000	0.46211700	0.24493000
C	3.21997800	0.73205500	-0.00290500
C	2.38857000	-0.38132400	-0.31095400
C	2.92872800	-1.69700600	-0.27743600
C	4.26827700	-1.95366100	-0.01172000
C	0.57610000	1.15165800	-0.45343500
C	1.47458700	2.19284700	-0.10425100
C	0.90897500	3.53268100	0.05977200
C	-1.31470300	2.50565300	-0.30194200
H	5.20417300	1.32276000	0.45200700
H	2.27136400	-2.54942500	-0.45165200
H	-0.93698400	4.46225300	0.12460900
N	1.07374100	-0.13648700	-0.64210900
N	-0.72897800	1.29565000	-0.62415500
N	-0.49725500	3.56579100	-0.06669500
N	2.79350200	2.02315900	0.07105300
O	1.52279100	4.54546400	0.30679000
O	-2.54696700	2.59605100	-0.22490500
C	4.79491600	-3.35494700	0.01060000
H	5.23343400	-3.60624100	0.98971000
H	4.00153200	-4.08444700	-0.19839600
H	5.58898800	-3.49935200	-0.73969500
C	6.56438600	-1.03549200	0.51619200
H	6.71646300	-1.68095600	1.39950600
H	7.05888000	-1.56090400	-0.31972300
H	7.08090700	-0.08353800	0.68660000
C	0.17545100	-1.16684000	-1.12834300
H	-0.41948400	-0.71393500	-1.93234900
H	0.77884900	-1.95240600	-1.59480800
C	-0.76818400	-1.77112900	-0.04198200
C	-2.20373300	-1.81080400	-0.59025200
C	-3.20810800	-2.45158100	0.37324500
C	-4.60259000	-2.62054900	-0.22500700
H	-0.45913800	-2.82233100	0.13488000
O	-0.64166400	-1.02036000	1.13383800
H	-1.42743100	-1.21333300	1.67309400
O	-2.66591000	-0.53007300	-0.95955400
O	-3.26134100	-1.63079800	1.55496400
O	-5.21535600	-1.40429800	-0.60464100
H	-1.91542500	0.13860700	-0.89658100
H	-2.17792700	-2.46795300	-1.48470700
H	-3.71618200	-2.12996900	2.24728000
H	-4.54664400	-3.32652900	-1.07364000
H	-5.26452800	-3.07958000	0.52651400
H	-4.71251700	-1.06490700	-1.36082500
H	-2.83044200	-3.45808100	0.63514200
K	-4.25560800	0.88255700	0.65122200
Sum of electronic and zero-point Energies=			-1356.627365
Sum of electronic and thermal Energies=			-1356.600789
Sum of electronic and thermal Enthalpies=			-1356.599844
Sum of electronic and thermal Free Energies=			-1356.683596

K⁺RF O2(4) S₀

C	5.12766200	-0.70186700	0.22146100
C	4.53795200	0.53297700	0.38855400
C	3.17195400	0.75231200	0.11147600
C	2.37701000	-0.32363400	-0.36758900
C	2.97122800	-1.58268200	-0.52271300
C	4.31670900	-1.78262400	-0.23749900
C	0.50576300	1.15067100	-0.38464500
C	1.39485200	2.17652600	0.09520800
C	0.81608900	3.52700100	0.34481800
C	-1.36427300	2.52847100	-0.27524800
H	5.10599300	1.39286700	0.74759500
H	2.38398400	-2.43960500	-0.85021300
H	-1.01715900	4.45869700	0.31418900
N	1.04970300	-0.06570500	-0.66264300
N	-0.79019600	1.32722400	-0.58573900
N	-0.55685600	3.57304500	0.12013600
N	2.66349600	1.99121600	0.31989500
O	1.44057800	4.48844700	0.71313200
O	-2.58788500	2.68609700	-0.33409200
C	4.91615700	-3.14272600	-0.40890100
H	5.33914400	-3.51008700	0.53965800
H	4.17774400	-3.87391600	-0.76182800
H	5.74753000	-3.11820300	-1.13139200
C	6.58032400	-0.91026200	0.52219500
H	6.72381800	-1.67075900	1.30607300
H	7.12792300	-1.26186300	-0.36656500
H	7.05103600	0.02037000	0.86336400
C	0.17837200	-1.08705400	-1.23487000
H	-0.47166000	-0.57060000	-1.95263200
H	0.80205600	-1.78128200	-1.80548500
C	-0.67353500	-1.84069800	-0.17062400
C	-2.15154200	-1.84296300	-0.60058700
C	-3.03123300	-2.73743500	0.27756100
C	-4.53313400	-2.57837900	0.01079300
H	-0.33344600	-2.89673100	-0.14257700
O	-0.47138100	-1.21501900	1.06536600
H	-1.15258900	-1.57725100	1.65838500
O	-2.67071200	-0.53960600	-0.65829700
O	-2.80298000	-2.44234600	1.66653400
O	-5.05118500	-1.43185100	0.66254000
H	-1.91792800	0.13153400	-0.65164300
H	-2.19003800	-2.30454900	-1.61115200
H	-2.93317200	-3.25121100	2.17968700
H	-4.73097400	-2.47807000	-1.06665600
H	-5.06552800	-3.48062800	0.36322000
H	-4.63233800	-1.44463000	1.53949800
H	-2.74065100	-3.78150700	0.06656800
K	-4.60686300	1.07712600	-0.26933900
Sum of electronic and zero-point Energies=			-1356.731991
Sum of electronic and thermal Energies=			-1356.705993
Sum of electronic and thermal Enthalpies=			-1356.705049
Sum of electronic and thermal Free Energies=			-1356.787685

K⁺RF O2(4) S₁

C	5.10289100	-0.76605000	0.19583600
C	4.52814900	0.53173100	0.30880800
C	3.18247800	0.80354000	0.06961100
C	2.37402700	-0.28859800	-0.34792800
C	2.93556600	-1.59474600	-0.42814600
C	4.27600200	-1.85597300	-0.16994900
C	0.53887400	1.21954900	-0.37558600
C	1.41880200	2.24398600	0.06278100
C	0.82935100	3.55793800	0.32577500
C	-1.36934900	2.55252600	-0.21374200
H	5.15282400	1.37959300	0.59773200
H	2.29023700	-2.43553000	-0.68449600
H	-1.02162600	4.47666500	0.36173400
N	1.06102800	-0.03847800	-0.67484500
N	-0.76604600	1.35495400	-0.54171400
N	-0.57043600	3.59158400	0.14639400
N	2.73635700	2.07894100	0.24655700
O	1.42316400	4.55294000	0.67471500
O	-2.60309700	2.65763000	-0.25032100
C	4.82401700	-3.24589000	-0.26794800
H	5.25423200	-3.57922400	0.69012100
H	4.04430900	-3.96424600	-0.55309500
H	5.62908900	-3.31025900	-1.01765000
C	6.54839300	-0.95522800	0.47510900
H	6.69830200	-1.67497600	1.29952000
H	7.06347200	-1.39670300	-0.39627000
H	7.04674600	-0.01471900	0.73800600
C	0.19058200	-1.04356600	-1.25925200
H	-0.46752600	-0.51845300	-1.96287100
H	0.81006500	-1.72331500	-1.85500200
C	-0.65880400	-1.83456100	-0.21589200
C	-2.13772800	-1.82748800	-0.63967000
C	-3.01279900	-2.75173900	0.21133100
C	-4.51606300	-2.59095300	-0.04655900
H	-0.31788400	-2.89168300	-0.22349100
O	-0.45316600	-1.24690500	1.03669200
H	-1.13175800	-1.62654200	1.62172400
O	-2.65894400	-0.52293900	-0.65290000
O	-2.78178600	-2.49985700	1.60804900
O	-5.03711000	-1.46847300	0.64291900
H	-1.90772700	0.14441800	-0.63569700
H	-2.17974200	-2.25501700	-1.66487700
H	-2.91171300	-3.32396600	2.09636600
H	-4.71726900	-2.45711300	-1.11976400
H	-5.04337400	-3.50660600	0.27800800
H	-4.61391500	-1.50579800	1.51712000
H	-2.71854400	-3.78736700	-0.03381000
K	-4.61175600	1.07135800	-0.20361800
Sum of electronic and zero-point Energies=			-1356.625428
Sum of electronic and thermal Energies=			-1356.598723
Sum of electronic and thermal Enthalpies=			-1356.597778
Sum of electronic and thermal Free Energies=			-1356.682447

K⁺RF O4⁺ S₀

C	-2.66363100	3.33677700	-0.00381600
C	-3.07137900	2.02876000	0.14345200
C	-2.21116200	0.93536800	-0.09277700
C	-0.87141200	1.18099800	-0.49955800
C	-0.45586300	2.51511400	-0.64554200
C	-1.31645900	3.57789800	-0.40990100
C	-0.48237900	-1.18135100	-0.56380300
C	-1.86700000	-1.32391300	-0.15502700
C	-2.37261300	-2.70783200	0.02120900
C	-0.09636900	-3.46087900	-0.63114700
H	-4.09667800	1.81092000	0.45226700
H	0.56523400	2.73945600	-0.94782000
H	-1.73912500	-4.63174800	-0.13542000
N	-0.04021800	0.11065200	-0.74171000
N	0.33920000	-2.16860200	-0.77843500
N	-1.45686700	-3.65864000	-0.23527700
N	-2.68395300	-0.33186100	0.07283100
O	-3.53024800	-2.95943100	0.37070800
O	0.58391600	-4.43937600	-0.80525400
C	-0.82893000	4.98152000	-0.58125700
H	-0.92514000	5.55028300	0.35734400
H	0.22194200	5.01289800	-0.89485400
H	-1.42788600	5.51775300	-1.33453800
C	-3.60001400	4.47698900	0.25347600
H	-3.22098400	5.13608700	1.05036800
H	-3.72513000	5.10416200	-0.64322000
H	-4.59306300	4.11948400	0.55584400
C	1.35733300	0.30423500	-1.13288000
H	1.67718400	-0.61543400	-1.63695400
H	1.41534900	1.13699200	-1.84497600
C	2.26431900	0.53401200	0.08318500
C	3.73272100	0.49684800	-0.35612200
C	4.68491300	0.95945400	0.75622400
C	6.14229800	0.79388700	0.33942200
H	2.03278700	1.49840400	0.56403300
O	2.03318700	-0.46327800	1.05773200
H	2.39056200	-1.27599300	0.65024300
O	3.95286600	-0.83462000	-0.75651400
O	4.55602300	0.20858900	1.94463400
O	6.44882700	-0.58643500	0.22039400
H	4.90590500	-1.01920100	-0.61082300
H	3.86825800	1.20074200	-1.20574600
H	3.62667000	-0.07004900	2.01756700
H	6.33575600	1.25861900	-0.63857400
H	6.79566100	1.27751500	1.08612500
H	6.21613400	-0.95919000	1.08737500
H	4.48406700	2.03700000	0.93554500
K	-5.28091800	-1.29370800	0.92157500
Sum of electronic and zero-point Energies=			-1356.705319
Sum of electronic and thermal Energies=			-1356.678933
Sum of electronic and thermal Enthalpies=			-1356.677988
Sum of electronic and thermal Free Energies=			-1356.763739

K⁺RF O4⁺ S₁

C	-3.38775500	2.98112100	0.10559700
C	-3.54718500	1.60285100	0.12538300
C	-2.48575200	0.69571800	-0.06822200
C	-1.19685200	1.25068800	-0.31161000
C	-1.02883900	2.63222900	-0.31318300
C	-2.09629000	3.51214000	-0.11113200
C	-0.34966100	-0.98542000	-0.42085000
C	-1.65591300	-1.46114600	-0.13937800
C	-1.80365200	-2.89000700	-0.00365000
C	0.64571400	-3.11100600	-0.28494100
H	-4.53992400	1.18191200	0.30431300
H	-0.04389700	3.06991100	-0.47567900
H	-0.70747200	-4.62121500	0.05939200
N	-0.13587200	0.35083900	-0.55331300
N	0.70558100	-1.76735900	-0.60382200
N	-0.64038200	-3.62131700	-0.10752000
N	-2.72964300	-0.64394300	-0.00056700
O	-2.88372600	-3.46638100	0.21323400
O	1.63085900	-3.80807100	-0.19237500
C	-1.86724000	4.99241300	-0.12820800
H	-2.16584000	5.45854700	0.82475900
H	-0.81153600	5.23686300	-0.30596600
H	-2.46204700	5.48254300	-0.91600300
C	-4.56119100	3.88959200	0.31673300
H	-4.41223300	4.54189400	1.19194500
H	-4.71445800	4.55387600	-0.54868900
H	-5.48743000	3.32107300	0.47344200
C	1.20309700	0.76874800	-0.90686300
H	1.56458400	0.12988400	-1.72447900
H	1.18122600	1.80687200	-1.24927100
C	2.22296000	0.64083500	0.24147500
C	3.63160900	0.97532200	-0.28124600
C	4.65543200	1.10646600	0.85684100
C	6.06428900	1.30856600	0.30093400
H	1.92084300	1.27183300	1.09070100
O	2.25664200	-0.68534200	0.71723000
H	2.85800600	-1.16155000	0.09165000
O	3.93373800	-0.09528700	-1.13983400
O	4.71102700	-0.08965200	1.61149400
O	6.48323000	0.15695500	-0.41177600
H	4.91324900	-0.19130800	-1.15515900
H	3.58456600	1.93831500	-0.82788000
H	4.10773500	-0.03945000	2.36216700
H	6.08835900	2.14961200	-0.40710200
H	6.75539500	1.53544700	1.12912500
H	6.58730700	-0.55241000	0.24086600
H	4.38953800	1.98114900	1.47819900
K	-4.98497500	-2.15125200	0.36686100
Sum of electronic and zero-point Energies=			-1356.627746
Sum of electronic and thermal Energies=			-1356.600805
Sum of electronic and thermal Enthalpies=			-1356.599861
Sum of electronic and thermal Free Energies=			-1356.686458

Li*RF O2(1) S₀

C	4.88198100	-0.50537300	0.23203500
C	4.19386100	0.68612100	0.32211700
C	2.81108000	0.77607500	0.05674400
C	2.09611800	-0.39487200	-0.32586700
C	2.79316100	-1.60765500	-0.40465900
C	4.15635200	-1.67704400	-0.13548800
C	0.13363400	0.94556000	-0.44669400
C	0.93581000	2.06493400	-0.03816500
C	0.24397200	3.37715800	0.13716700
C	-1.84840400	2.16556700	-0.37427100
H	4.69407500	1.61354100	0.60622200
H	2.28568000	-2.53134700	-0.67952000
H	-1.67140700	4.14216100	0.13381900
N	0.74277000	-0.26115200	-0.60314900
N	-1.16306900	1.02199100	-0.67108200
N	-1.13808600	3.29469900	-0.04705000
N	2.21427200	1.98675200	0.19127800
O	0.79133400	4.40598700	0.43387100
O	-3.08505200	2.17505500	-0.38626500
C	4.86431800	-2.99068600	-0.23695400
H	5.33910500	-3.25862600	0.72031100
H	4.18454900	-3.80300800	-0.52394200
H	5.67443500	-2.94227100	-0.98202400
C	6.35125200	-0.57184200	0.51428600
H	6.57110500	-1.26486400	1.34167300
H	6.91100200	-0.93470900	-0.36221500
H	6.74766200	0.41499300	0.78410400
C	-0.09527300	-1.38725900	-1.02323900
H	-0.66079600	-1.06674500	-1.90815300
H	0.56409200	-2.19553400	-1.34624600
C	-1.07399000	-1.88722600	0.09431000
C	-2.56235100	-1.87266000	-0.36604200
C	-3.52227900	-1.83104500	0.83820600
C	-4.98297500	-2.06890700	0.47858100
H	-0.83322000	-2.94194700	0.30676100
O	-0.91018800	-1.13861200	1.29357400
H	-0.25481100	-1.57261300	1.85350200
O	-2.88650400	-0.81598000	-1.23787600
O	-3.47943300	-0.53423100	1.42115700
O	-5.47324100	-0.92746700	-0.22248300
H	-2.17335400	-0.11198600	-1.12791600
H	-2.72645600	-2.81922700	-0.91239000
H	-2.56121100	-0.41855700	1.72476100
H	-5.08034500	-2.97979900	-0.13592900
H	-5.55002300	-2.20777900	1.41316300
H	-6.43693200	-0.93870500	-0.21086400
H	-3.23381800	-2.60623500	1.57181300
Li	-4.09782000	0.49471600	-0.23504800

Sum of electronic and zero-point Energies= -1335.919347

Sum of electronic and thermal Energies= -1335.894580

Sum of electronic and thermal Enthalpies= -1335.893636

Sum of electronic and thermal Free Energies= -1335.971628

Li*RF O4+ S₀

C	3.57390000	-2.67995100	0.15627200
C	3.75303500	-1.33121800	0.36740400
C	2.73620000	-0.38833000	0.10682100
C	1.47568800	-0.82877900	-0.39139300
C	1.29769100	-2.20584200	-0.60153700
C	2.30841000	-3.12100800	-0.34259800
C	0.70161700	1.43795900	-0.42008700
C	2.00969400	1.78274300	0.07942900
C	2.28963100	3.20833200	0.33254000
C	-0.02038000	3.63611500	-0.44963000
H	4.70808800	-0.96064000	0.74754700
H	0.34772800	-2.58257100	-0.97520000
H	1.39617400	5.02821600	0.20056300
N	0.49114800	0.09745500	-0.65493400
N	-0.24345600	2.29990700	-0.66312000
N	1.27331100	4.02747000	0.05292200
N	2.97151200	0.93188200	0.33466200
O	3.39484100	3.57839800	0.76959300
O	-0.82173500	4.51105700	-0.64357700
C	2.07172300	-4.57658500	-0.58597000
H	2.20736500	-5.15739100	0.34033000
H	1.06141400	-4.76862000	-0.96768500
H	2.79639800	-4.97616500	-1.31323700
C	4.66799100	-3.66152300	0.43918500
H	4.35515300	-4.40391200	1.19013200
H	4.94521300	-4.22373800	-0.46633500
H	5.56900200	-3.15987000	0.81477300
C	-0.83610700	-0.30832600	-1.12306800
H	-1.28183300	0.56729000	-1.61014500
H	-0.72321700	-1.10878500	-1.86486700
C	-1.74169300	-0.73230000	0.04261000
C	-3.17888700	-0.90824700	-0.46254100
C	-4.08491600	-1.57889600	0.58039700
C	-5.53219200	-1.62531700	0.10274100
H	-1.37595900	-1.66710600	0.49777200
O	-1.71507100	0.24901200	1.05772400
H	-2.23341500	0.98556200	0.67698900
O	-3.59516500	0.39334500	-0.80212700
O	-4.12613800	-0.88441700	1.80825400
O	-6.05213200	-0.30703600	0.02611200
H	-4.57146000	0.41391000	-0.69356800
H	-3.16726600	-1.57274600	-1.35309400
H	-3.25474300	-0.47739100	1.95005100
H	-5.60923300	-2.06621500	-0.90193100
H	-6.12859200	-2.24238400	0.79654000
H	-5.94165700	0.05081900	0.92263900
H	-3.71944000	-2.61897400	0.71550400
Li	4.51581800	2.13595300	1.03174500
Sum of electronic and zero-point Energies=			-1335.876262
Sum of electronic and thermal Energies=			-1335.850980
Sum of electronic and thermal Enthalpies=			-1335.850036
Sum of electronic and thermal Free Energies=			-1335.931507

Na⁺RF O2(1) S₀

C	4.94569900	-0.73156200	0.25149600
C	4.35784400	0.50687100	0.39420600
C	2.99353600	0.72490200	0.10624000
C	2.19787000	-0.35796100	-0.35988500
C	2.79075000	-1.62052200	-0.48894700
C	4.13417800	-1.81839800	-0.19274200
C	0.33903000	1.12562100	-0.41922100
C	1.22189200	2.15408200	0.05966000
C	0.63930300	3.50583900	0.29855000
C	-1.53729100	2.49867700	-0.30631300
H	4.92537400	1.37157800	0.74222600
H	2.20526600	-2.48252500	-0.80562600
H	-1.20277000	4.42742300	0.29361200
N	0.87270500	-0.10067500	-0.66743300
N	-0.95196500	1.31228000	-0.64157200
N	-0.73827200	3.54703300	0.08530700
N	2.48860400	1.96757700	0.29667500
O	1.26162000	4.47124500	0.65789600
O	-2.76746500	2.63384000	-0.33859200
C	4.73114700	-3.18245400	-0.33745300
H	5.14867700	-3.53384900	0.61952700
H	3.99308300	-3.91821600	-0.68132900
H	5.56629200	-3.17194700	-1.05591500
C	6.39614000	-0.93807200	0.56323700
H	6.53357800	-1.68553800	1.36057700
H	6.94715100	-1.30612800	-0.31667800
H	6.86740100	-0.00291100	0.89087800
C	-0.00759900	-1.13028900	-1.21808900
H	-0.61726800	-0.63894400	-1.98743200
H	0.61625200	-1.86898800	-1.72817100
C	-0.91900400	-1.80505400	-0.14624900
C	-2.38372900	-1.78059500	-0.62679200
C	-3.35567300	-2.52698900	0.29877600
C	-4.82485500	-2.18184500	0.02084700
H	-0.61663600	-2.86905700	-0.05681400
O	-0.72901900	-1.12513800	1.06226000
H	-1.43524400	-1.43850200	1.65379500
O	-2.82438300	-0.46681100	-0.85226900
O	-3.09936100	-2.20899200	1.67887200
O	-5.18316600	-0.95052200	0.63576100
H	-2.03823400	0.17588500	-0.80210400
H	-2.41369800	-2.34111300	-1.58553500
H	-3.27019500	-2.99526400	2.21437000
H	-5.01120800	-2.08653800	-1.05830500
H	-5.47615300	-2.98689600	0.40431500
H	-4.83516800	-1.02190800	1.54044600
H	-3.20110400	-3.60711100	0.13461900
Na	-4.36037800	1.03768900	-0.31115100
Sum of electronic and zero-point Energies=			-1490.593788
Sum of electronic and thermal Energies=			-1490.568264
Sum of electronic and thermal Enthalpies=			-1490.567320
Sum of electronic and thermal Free Energies=			-1490.648021

Na⁺RF O4⁺ S₀

C	-3.10493200	3.07909000	0.07554500
C	-3.41873300	1.74945000	0.25213600
C	-2.49175500	0.71447700	0.00636500
C	-1.18189200	1.04240800	-0.44101700
C	-0.86327300	2.39924400	-0.61694500
C	-1.78798100	3.40441500	-0.37192100
C	-0.63216100	-1.28902700	-0.48516300
C	-1.99007600	-1.51908100	-0.03644400
C	-2.39944400	-2.92945900	0.17293800
C	-0.09936600	-3.53980700	-0.53415000
H	-4.41866600	1.46940600	0.59328300
H	0.13138100	2.68765300	-0.95104900
H	-1.64873900	-4.81030200	0.02650000
N	-0.28566100	0.02815700	-0.69139200
N	0.24513800	-2.22360200	-0.71107000
N	-1.43362000	-3.82225800	-0.09437000
N	-2.86774600	-0.58037700	0.20065400
O	-3.53194100	-3.24473100	0.55815700
O	0.63772200	-4.47375400	-0.71604800
C	-1.40254200	4.83469000	-0.57633100
H	-1.51184400	5.40984400	0.35693200
H	-0.36549700	4.93286200	-0.92044300
H	-2.05799100	5.31690500	-1.31899800
C	-4.10917300	4.15689200	0.34360100
H	-3.75342300	4.85226600	1.12006300
H	-4.30067900	4.75983300	-0.55793700
H	-5.06685500	3.73814300	0.67905300
C	1.08485000	0.31068500	-1.12319200
H	1.45418300	-0.59386300	-1.62087400
H	1.06639700	1.13274600	-1.84966300
C	2.00448300	0.62314200	0.06522100
C	3.46003100	0.68008300	-0.41328500
C	4.40612900	1.22996900	0.66408800
C	5.85973700	1.15880800	0.20926400
H	1.71830000	1.57705400	0.53751500
O	1.86959900	-0.37214800	1.05885800
H	2.29142300	-1.15780400	0.65932900
O	3.76152100	-0.64148500	-0.79343800
O	4.36248200	0.49511100	1.86830600
O	6.25905500	-0.19858700	0.10126700
H	4.72923700	-0.75586100	-0.67235200
H	3.52436400	1.37330600	-1.27972500
H	3.45596500	0.15985500	1.97743800
H	5.99387500	1.61963000	-0.78040800
H	6.49744000	1.69888600	0.93023100
H	6.08619400	-0.57168000	0.98181400
H	4.13480000	2.29421300	0.82971000
Na	-4.94886900	-1.64524100	0.96106700
Sum of electronic and zero-point Energies=			-1490.564954
Sum of electronic and thermal Energies=			-1490.538903
Sum of electronic and thermal Enthalpies=			-1490.537959
Sum of electronic and thermal Free Energies=			-1490.621887

Rb⁺RF O2(1) S₀

C	5.55539900	-0.62189700	0.23281500
C	4.92491300	0.60058600	0.34235300
C	3.55097300	0.76112800	0.06998400
C	2.78609400	-0.36266000	-0.34193600
C	3.42202600	-1.60774200	-0.44118400
C	4.77803100	-1.74926000	-0.16287200
C	0.86291800	1.05424900	-0.41289800
C	1.73103300	2.13155800	-0.00190300
C	1.11520100	3.47835000	0.17892500
C	-1.04600600	2.37858700	-0.33938000
H	5.46795000	1.49655000	0.64815400
H	2.86716000	-2.49831800	-0.73482300
H	-0.74521200	4.34965500	0.13070200
N	1.44303700	-0.16313400	-0.62525100
N	-0.43637900	1.17636200	-0.59903100
N	-0.25947300	3.46927600	-0.02158200
N	3.00490800	1.99551800	0.21750800
O	1.72060900	4.47466700	0.48067400
O	-2.26928200	2.49367200	-0.37410800
C	5.42210500	-3.09443600	-0.28301100
H	5.87613600	-3.40299400	0.67208500
H	4.70497300	-3.86691200	-0.58889300
H	6.23864200	-3.07356100	-1.02236600
C	7.01779400	-0.76465100	0.52451600
H	7.19772600	-1.48194200	1.34088900
H	7.56711700	-1.13818800	-0.35415200
H	7.45903900	0.19697400	0.81527800
C	0.58931600	-1.23723800	-1.12122000
H	-0.05225200	-0.80208800	-1.89748400
H	1.22406700	-1.98406300	-1.60617800
C	-0.29154600	-1.88856900	-0.00926000
C	-1.76345200	-1.97908200	-0.45764700
C	-2.65957300	-2.39892700	0.72899200
C	-3.99213300	-3.00763200	0.33951100
H	0.05755300	-2.92219000	0.15978800
O	-0.22115000	-1.16945400	1.21532600
H	0.56271200	-1.45102200	1.70356000
O	-2.22735900	-0.79742300	-1.05727400
O	-2.90216400	-1.30102900	1.59014600
O	-4.80406600	-2.06636100	-0.34637700
H	-1.57651600	-0.06084700	-0.88371100
H	-1.80389700	-2.78735300	-1.21321700
H	-2.01814500	-1.00371900	1.86743600
H	-3.79658900	-3.89327400	-0.29159100
H	-4.49089000	-3.34830500	1.26446700
H	-5.61657300	-2.51788000	-0.60506300
H	-2.12970400	-3.20539200	1.27614900
Rb	-4.31484400	0.67086400	0.03717900

Sum of electronic and zero-point Energies= -1352.502496
 Sum of electronic and thermal Energies= -1352.476061
 Sum of electronic and thermal Enthalpies= -1352.475116
 Sum of electronic and thermal Free Energies= -1352.559135

Rb⁺RF O4+ S₀

C	-1.96203200	3.59897300	-0.10100100
C	-2.47333900	2.32402800	0.00969900
C	-1.69107900	1.17117000	-0.21387800
C	-0.32276900	1.31960000	-0.56849100
C	0.19846600	2.61972700	-0.67753700
C	-0.58673000	3.74199600	-0.45475900
C	-0.11249300	-1.06455700	-0.65615300
C	-1.51904300	-1.10609300	-0.30081700
C	-2.13424900	-2.45044600	-0.16728600
C	0.10350500	-3.36562300	-0.74495500
H	-3.52264400	2.18059100	0.27796000
H	1.24413400	2.76926500	-0.93947200
H	-1.63972700	-4.41446700	-0.33242800
N	0.43280700	0.19192200	-0.79840700
N	0.64058200	-2.10813400	-0.85542800
N	-1.28143300	-3.46443200	-0.40517700
N	-2.26563300	-0.05801200	-0.08665100
O	-3.31876800	-2.62168300	0.13298500
O	0.71571800	-4.39021000	-0.90827300
C	0.01253500	5.10639700	-0.58494800
H	-0.07356900	5.66750400	0.35923900
H	1.07343900	5.06105100	-0.86088300
H	-0.51563400	5.69803800	-1.34961400
C	-2.81789000	4.80392000	0.14200400
H	-2.41946600	5.42115400	0.96263600
H	-2.86267700	5.45133800	-0.74793200
H	-3.84554800	4.51900200	0.40322000
C	1.85338400	0.28338700	-1.14003900
H	2.11957100	-0.65097800	-1.64823700
H	1.99851500	1.11887400	-1.83638400
C	2.73431300	0.42728500	0.10764500
C	4.20968300	0.28997200	-0.28583700
C	5.15598300	0.66140900	0.86500000
C	6.61050100	0.39776500	0.49102900
H	2.55792000	1.39852800	0.59799700
O	2.39951600	-0.56476400	1.05739000
H	2.70163000	-1.39680100	0.64456100
O	4.34572700	-1.04648500	-0.70633200
O	4.93408900	-0.09952700	2.03307600
O	6.82063100	-0.99885400	0.35432800
H	5.27744500	-1.30283300	-0.53477900
H	4.42394500	0.99744800	-1.11614100
H	3.98508600	-0.31161000	2.06961500
H	6.86893100	0.86431900	-0.47096900
H	7.27215300	0.81948400	1.26742100
H	6.53136900	-1.36888100	1.20533900
H	5.02781900	1.74730900	1.06008800
Rb	-5.12472200	-0.83727100	0.70229700

Sum of electronic and zero-point Energies= -1352.477345
 Sum of electronic and thermal Energies= -1352.450785
 Sum of electronic and thermal Enthalpies= -1352.449841
 Sum of electronic and thermal Free Energies= -1352.537014

Cs⁺RF O2(1) S₀

C	5.70558700	-1.01203200	0.08316700
C	5.24853000	0.28821700	0.12824800
C	3.87990900	0.60480800	-0.00375800
C	2.94058100	-0.44476100	-0.19776800
C	3.40206000	-1.76653000	-0.23835100
C	4.75389200	-2.05965400	-0.09933900
C	1.21315500	1.19621800	-0.18398000
C	2.24239600	2.18885200	-0.03271200
C	1.80871500	3.61482800	0.03535400
C	-0.51759000	2.75261800	-0.06179800
H	5.93111600	1.12787000	0.26994900
H	2.70414700	-2.59502000	-0.35548900
H	0.06956200	4.71106700	0.06035900
N	1.60636400	-0.10099900	-0.33958200
N	-0.08581900	1.45422800	-0.17703000
N	0.42490400	3.76045200	-0.00740100
N	3.51136400	1.90899500	0.04813200
O	2.55479200	4.55578800	0.12138900
O	-1.71643000	3.01914700	-0.00298400
C	5.21116700	-3.48360900	-0.13524200
H	5.73073200	-3.75471300	0.79758400
H	4.37405600	-4.17904600	-0.27674800
H	5.93337700	-3.64447500	-0.95149800
C	7.16402100	-1.32175600	0.22813600
H	7.35221600	-1.97206600	1.09708800
H	7.55190800	-1.85164000	-0.65620900
H	7.75216500	-0.40464000	0.35827200
C	0.59069800	-1.06921700	-0.77437000
H	-0.05922300	-0.53606300	-1.47806700
H	1.09678300	-1.86975600	-1.32551800
C	-0.27972700	-1.65837600	0.34605800
C	-1.50463600	-2.34815700	-0.28123100
C	-2.52660100	-2.80366700	0.77986500
C	-3.69246400	-3.56851900	0.18102000
H	0.28527000	-2.42530900	0.90361900
O	-0.65234400	-0.67124500	1.29026400
H	-0.64726300	0.19850400	0.80652900
O	-2.09536200	-1.45373300	-1.21126200
O	-3.04885200	-1.71376600	1.51357300
O	-4.32560700	-2.76466000	-0.81725300
H	-2.93614900	-1.87977100	-1.47341100
H	-1.13905200	-3.25590500	-0.80438400
H	-2.25436500	-1.22737000	1.81851700
H	-3.32190900	-4.51194100	-0.25683900
H	-4.40270000	-3.80795800	0.98963100
H	-5.04335700	-3.27336900	-1.21476500
H	-2.01013600	-3.51495800	1.45612700
Cs	-3.72241100	0.85600000	-0.04042200

Sum of electronic and zero-point Energies= -1348.572019

Sum of electronic and thermal Energies= -1348.545890

Sum of electronic and thermal Enthalpies= -1348.544946

Sum of electronic and thermal Free Energies= -1348.629586

Cs⁺RF O4+ S₀

C	-1.39444100	3.73177300	-0.16650000
C	-1.95978600	2.47753400	-0.08467800
C	-1.21843600	1.29633200	-0.29929700
C	0.16411600	1.39303600	-0.61380900
C	0.74053000	2.67182300	-0.69287400
C	-0.00510900	3.82262600	-0.47935400
C	0.27936100	-0.99656900	-0.72303400
C	-1.13745400	-0.98378400	-0.40715400
C	-1.80934900	-2.30322600	-0.30594400
C	0.40546000	-3.30331900	-0.83143300
H	-3.02091300	2.37162500	0.15184500
H	1.79853900	2.78172000	-0.92314400
H	-1.38948200	-4.28400800	-0.47987000
N	0.87931400	0.23755400	-0.83583900
N	0.99572500	-2.06791400	-0.91282000
N	-0.99122500	-3.34878100	-0.53205700
N	-1.84637000	0.09112800	-0.20185300
O	-3.00737100	-2.43106600	-0.04027600
O	0.98028500	-4.35060700	-0.98845100
C	0.65216800	5.16298300	-0.57670200
H	0.56202400	5.71723200	0.37116300
H	1.71784100	5.07744900	-0.82327000
H	0.17042100	5.78367600	-1.34896400
C	-2.20792400	4.96797700	0.06565600
H	-1.80946100	5.56020500	0.90452600
H	-2.20085900	5.62595700	-0.81763300
H	-3.25335300	4.72186100	0.29379600
C	2.31103400	0.27438400	-1.13856100
H	2.55233200	-0.66279800	-1.65391700
H	2.50931200	1.11278000	-1.81805300
C	3.16398000	0.36382600	0.13322100
C	4.64232700	0.17356600	-0.22500500
C	5.57247300	0.48324200	0.95688500
C	7.02464200	0.16877900	0.61424300
H	3.01394500	1.33391000	0.63453000
O	2.76438900	-0.62755300	1.05856100
H	3.03058800	-1.46661900	0.63581800
O	4.73593800	-1.15840400	-0.67026900
O	5.29025800	-0.29155500	2.10263000
O	7.18273800	-1.23224600	0.45479300
H	5.65172000	-1.45556600	-0.48067300
H	4.90661900	0.88861600	-1.03427300
H	4.33281000	-0.46584100	2.10999600
H	7.32613500	0.64304000	-0.33133000
H	7.68216600	0.54866700	1.41539700
H	6.85379400	-1.60631200	1.28952500
H	5.48256000	1.56926900	1.17169400
Cs	-4.98346000	-0.61551300	0.57129000

Sum of electronic and zero-point Energies= -1348.545631

Sum of electronic and thermal Energies= -1348.518966

Sum of electronic and thermal Enthalpies= -1348.518022

Sum of electronic and thermal Free Energies= -1348.606309

Li⁺
Sum of electronic and zero-point Energies= -7.261731
Sum of electronic and thermal Energies= -7.260315
Sum of electronic and thermal Enthalpies= -7.259371
Sum of electronic and thermal Free Energies= -7.274479

Na⁺
Sum of electronic and zero-point Energies= -161.981387
Sum of electronic and thermal Energies= -161.979971
Sum of electronic and thermal Enthalpies= -161.979027
Sum of electronic and thermal Free Energies= -161.995816

K⁺
Sum of electronic and zero-point Energies= -28.138454
Sum of electronic and thermal Energies= -28.137037
Sum of electronic and thermal Enthalpies= -28.136093
Sum of electronic and thermal Free Energies= -28.153630

Rb⁺
Sum of electronic and zero-point Energies= -23.917509
Sum of electronic and thermal Energies= -23.916092
Sum of electronic and thermal Enthalpies= -23.915148
Sum of electronic and thermal Free Energies= -23.933788

Cs⁺
Sum of electronic and zero-point Energies= -19.991377
Sum of electronic and thermal Energies= -19.989960
Sum of electronic and thermal Enthalpies= -19.989016
Sum of electronic and thermal Free Energies= -20.008290

Electronic Supplementary Information

Optical spectroscopy of isolated flavins: photodissociation of protonated lumichrome

Alexander Sheldrick, David Müller, Alan Günther, Pablo Nieto, and Otto Dopfer*

*Technische Universität Berlin, Institut für Optik und Atomare Physik
Hardenbergstr. 36, D-10623 Berlin, Germany*

* corresponding author: dopfer@physik.tu-berlin.de; Fax: +49 30 314 23018

Figure S1. Structures of the H⁺iso-LC(N5) and H⁺iso-LC(O4) isomers calculated at the PBE0/cc-pVDZ level.

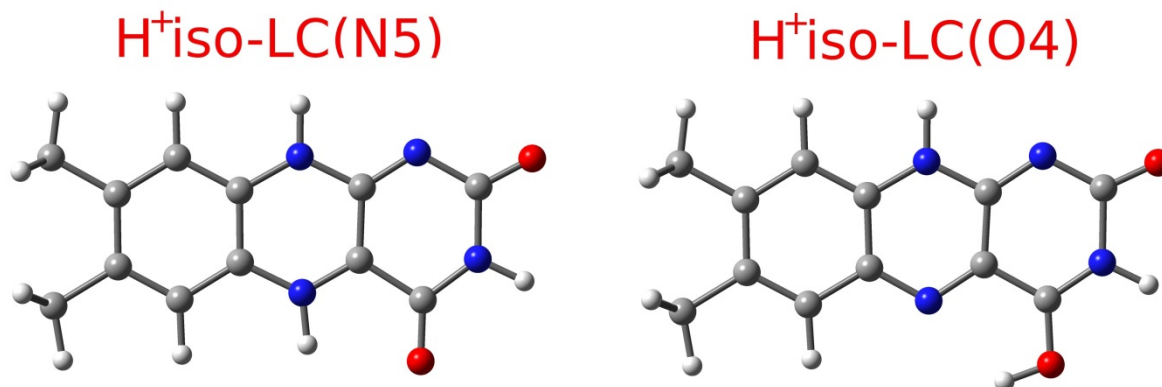


Figure S2. Photodissociation mass spectra of protonated lumichrome. Laser-on (solid line) and laser-off (dotted line) mass spectra of H^+LC (m/z 243) with the laser frequency tuned resonantly to the $\text{S}_1 \leftarrow \text{S}_0$ band origin at 19962 cm^{-1} . The difference between both spectra is given by the dashed line. Major photo-induced fragments are m/z 198 and m/z 172.

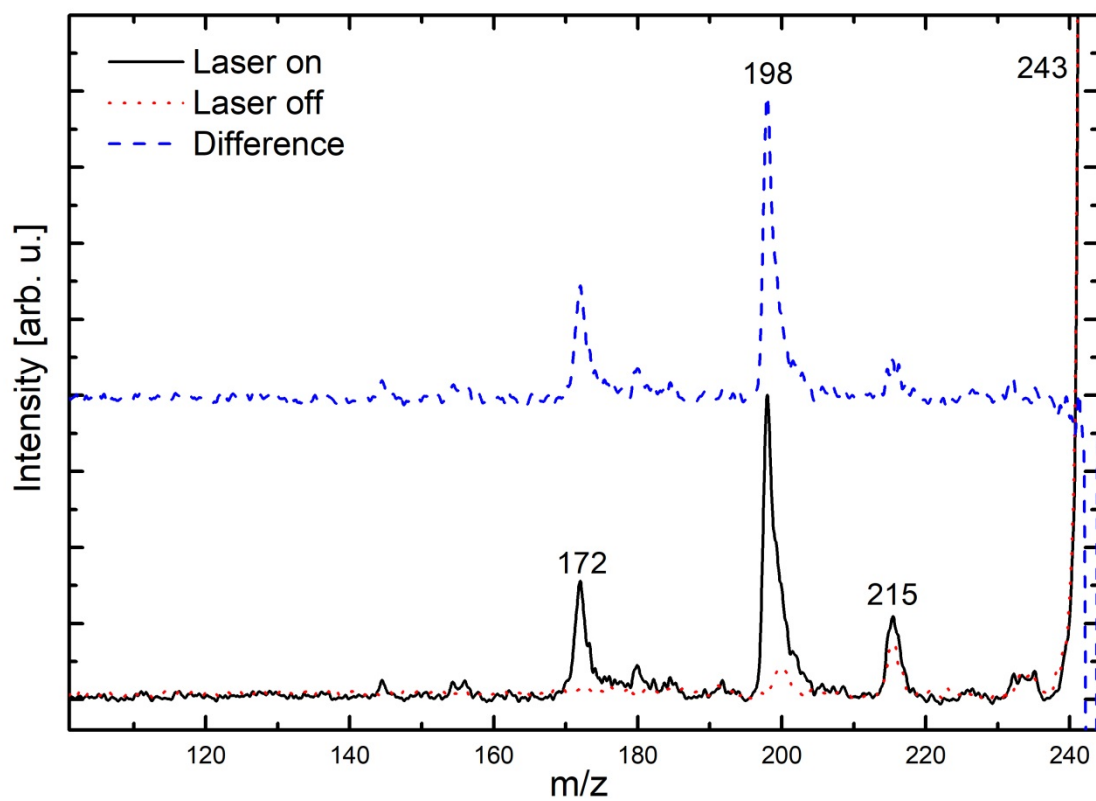


Figure S3. Overview of recorded VISPD spectrum of protonated lumichrome (H^+LC) obtained at an ion trap temperature of 25 K.

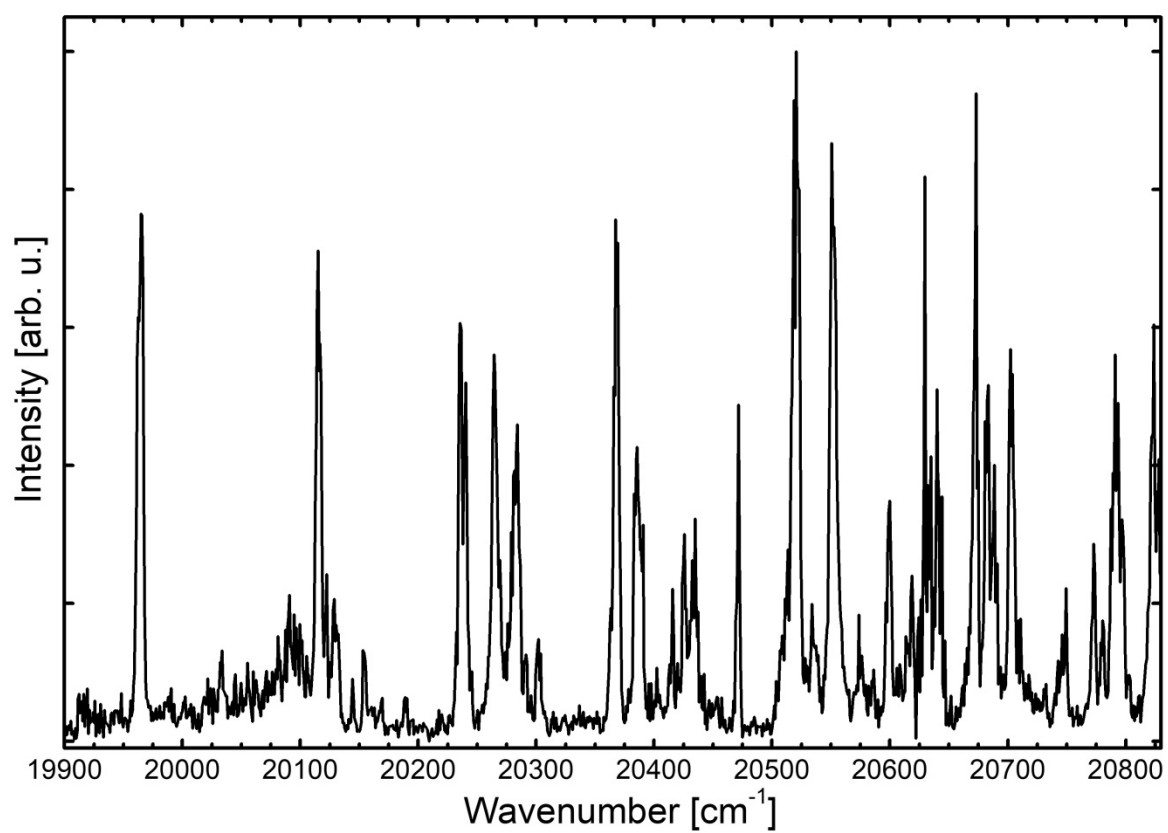


Figure S4. VISPD spectra of the $S_1 \leftarrow S_0$ electronic transition of H^+LC for a trap temperature of 25 K recorded in the m/z 172 and 198 fragment channels.

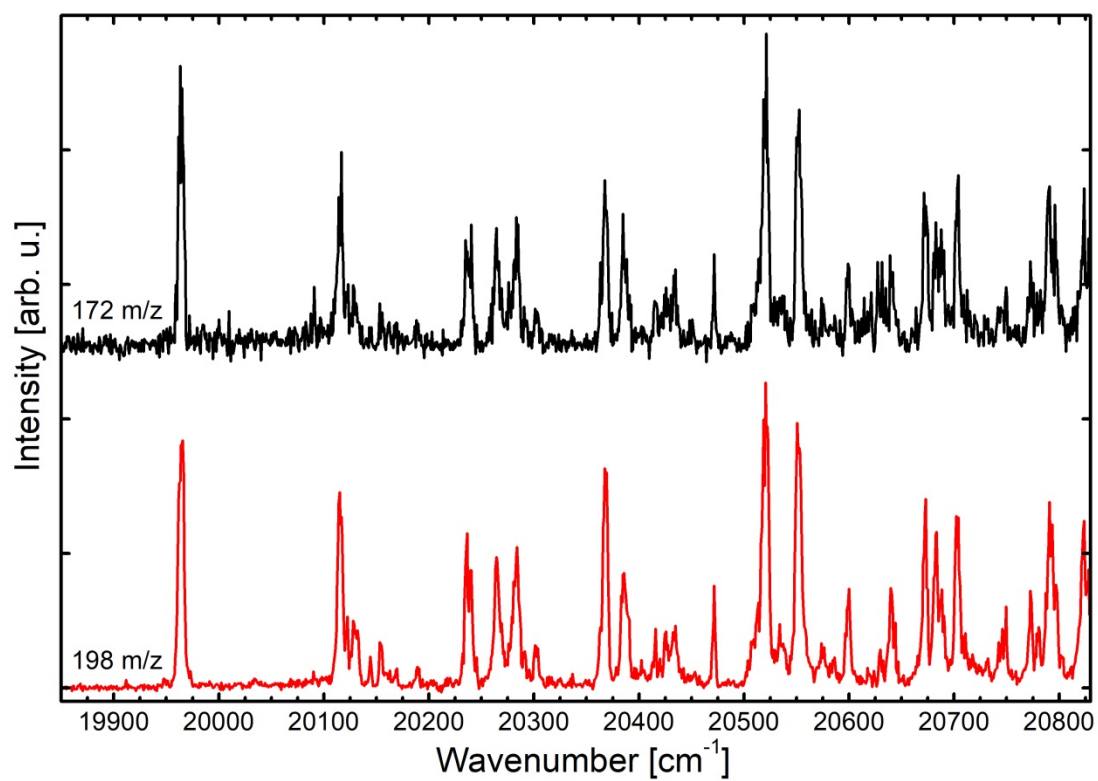


Figure S5. Comparison between experimental VISPD spectrum recorded for H⁺LC and Franck-Condon simulations for the protonated iso-LC isomers shown in Figure S1 calculated at the PBE0/cc-pVDZ level using a convolution width of 6 cm⁻¹. Isomers are ordered from top to bottom according to their relative energy (Table 1). The energy scale of the simulated spectra is shifted by $\Delta\nu$ to match the frequencies of calculated and observed S₁ origins at 19965 cm⁻¹.

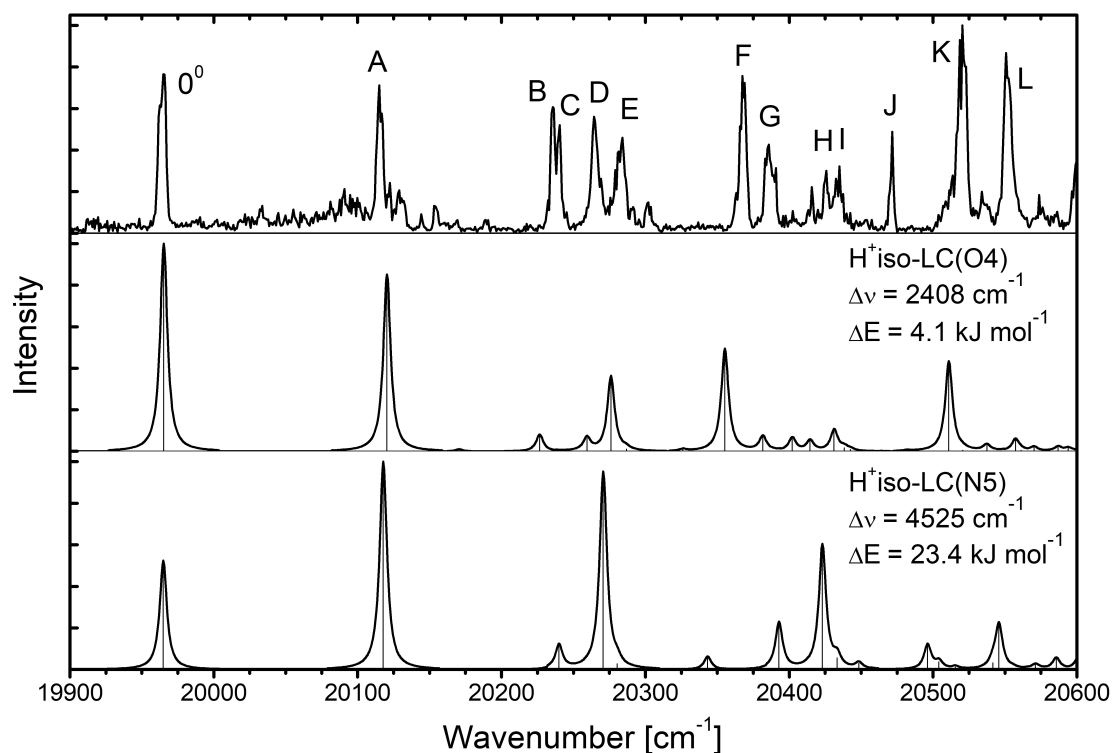
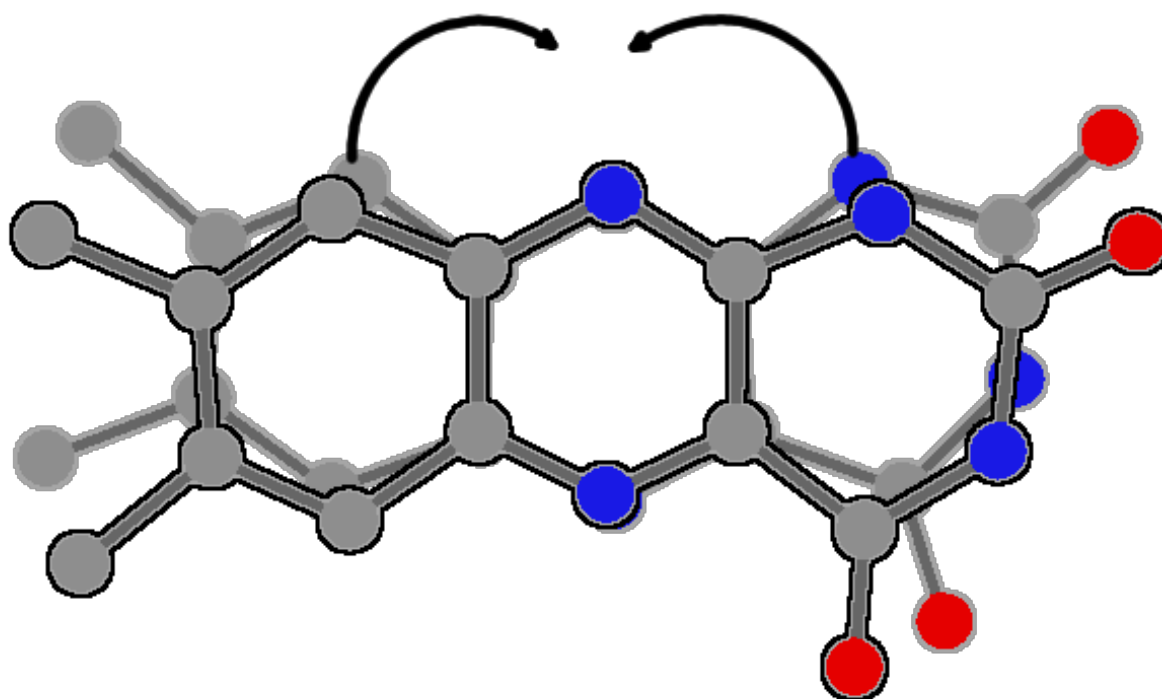
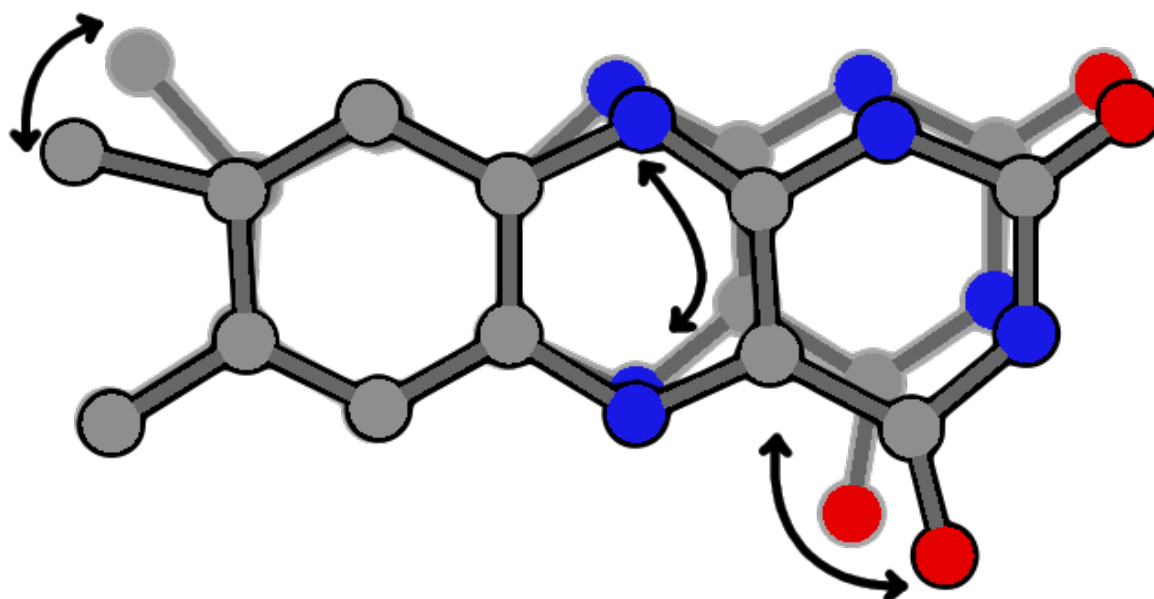


Figure S6. Schematic representation of various normal coordinates in the S_1 state of $H^+LC(N5)$ calculated at the PBE0/cc-pVDZ level. Hydrogen atoms are omitted for the sake of simplicity. Shown are the structures for maximum positive and maximum negative elongation. The arrows indicate major movements.

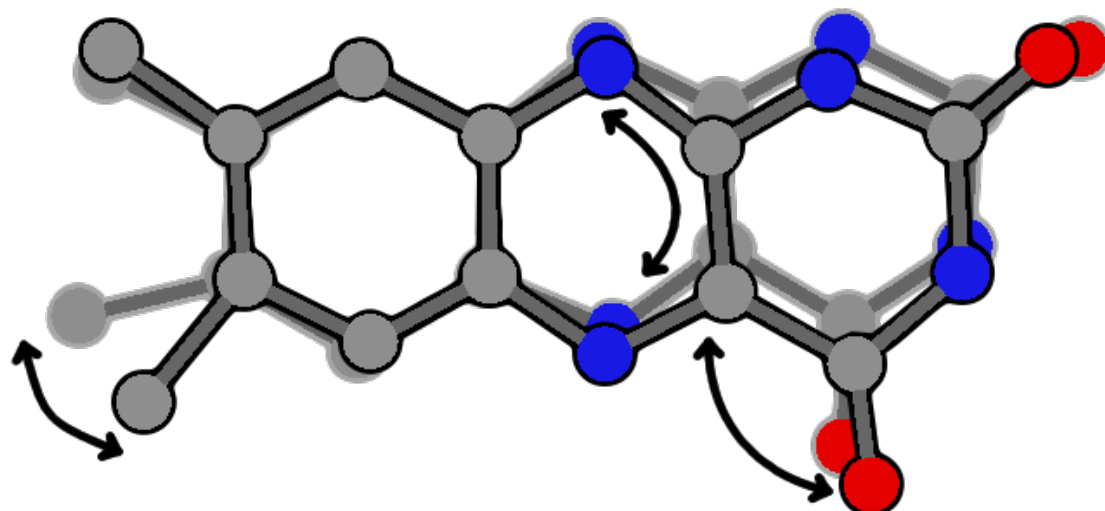
(a) mode 53



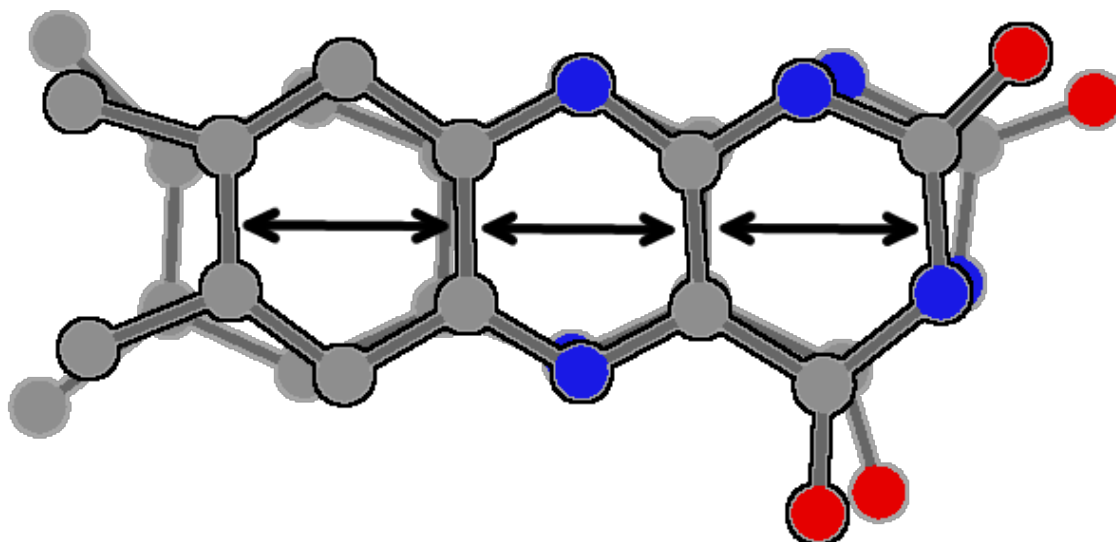
(b) mode 52



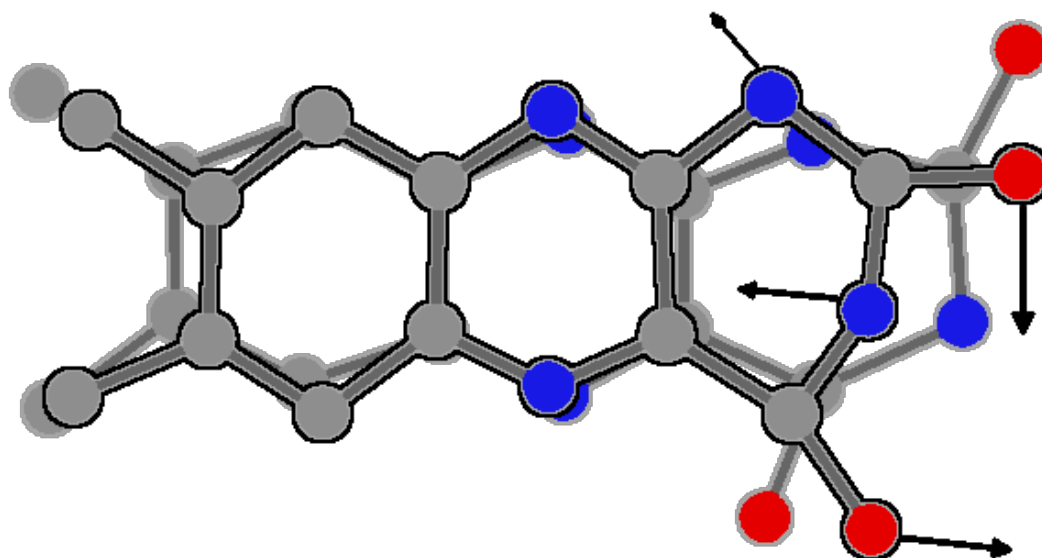
(c) mode 51



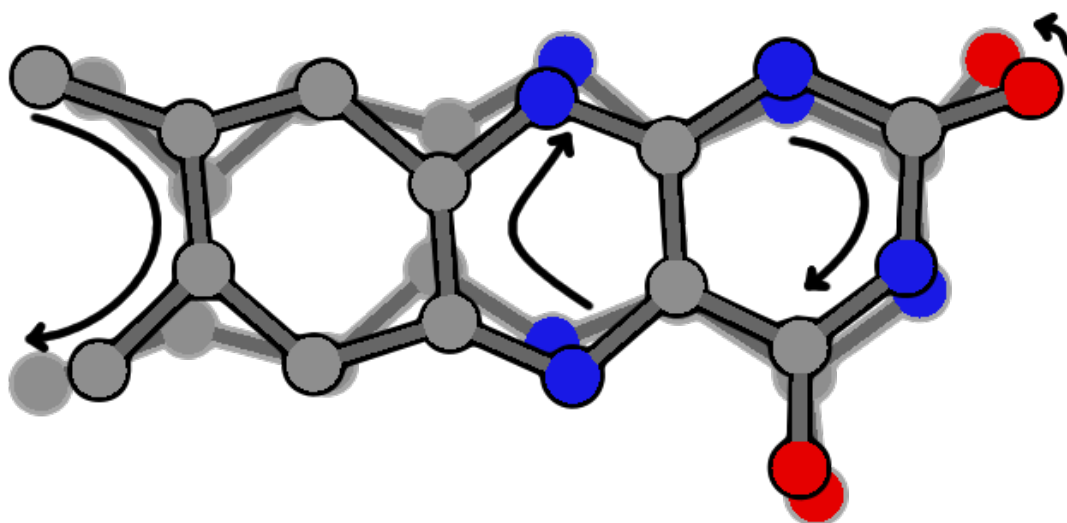
(d) mode 50



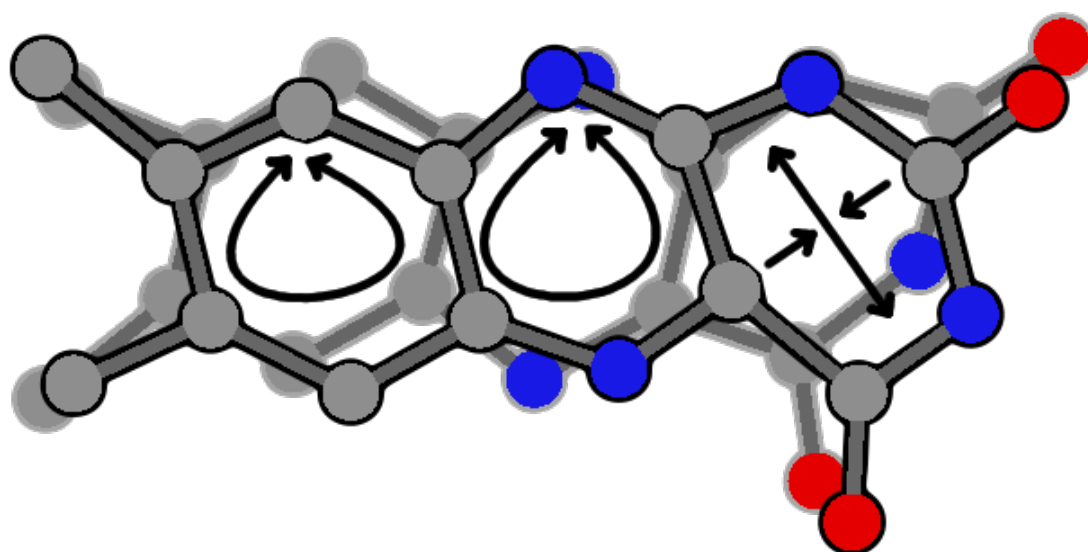
(e) mode 49



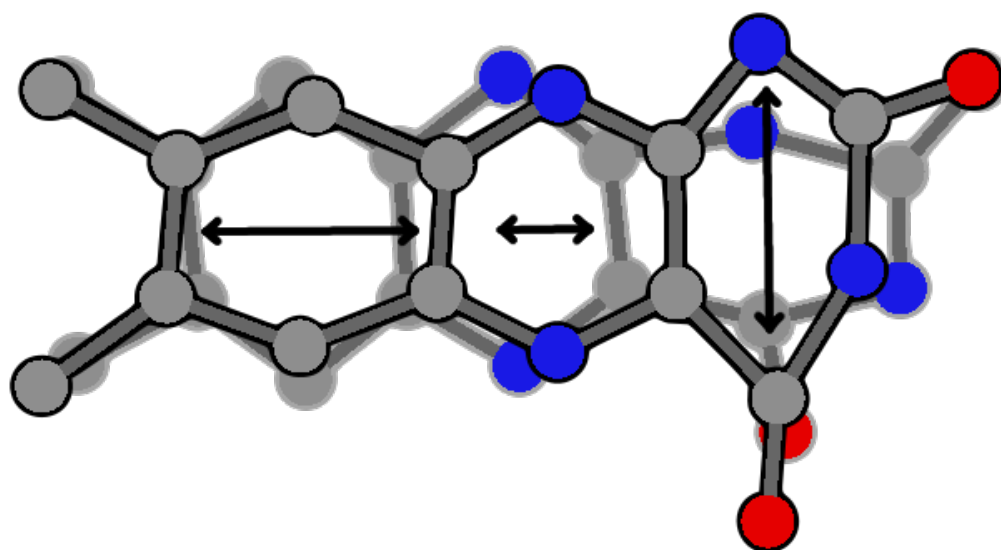
(f) mode 48



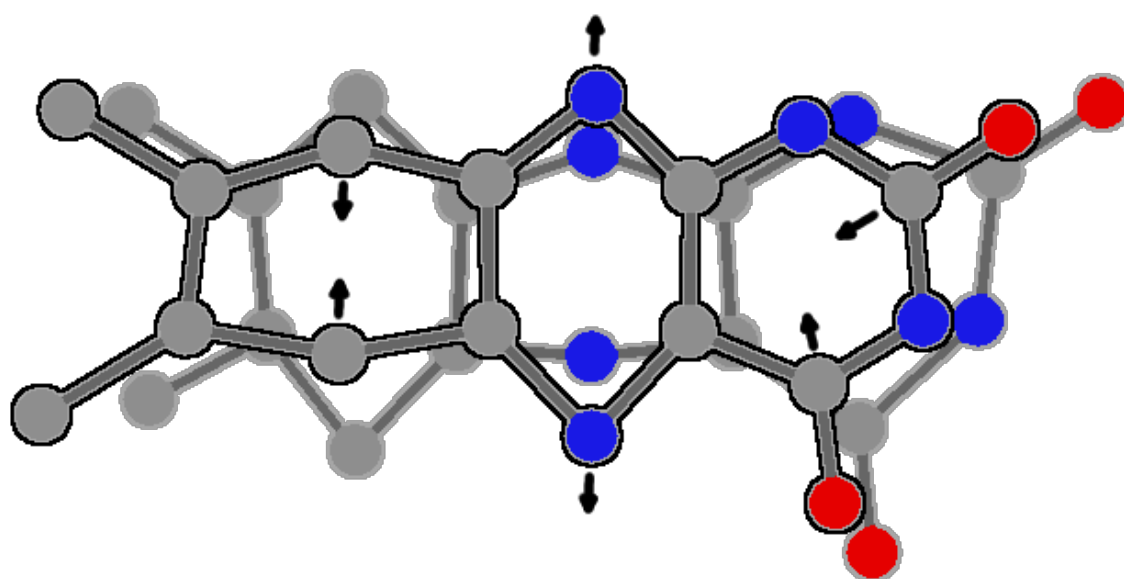
(g) mode 47



(h) mode 46



(i) mode 45



(k) mode 44

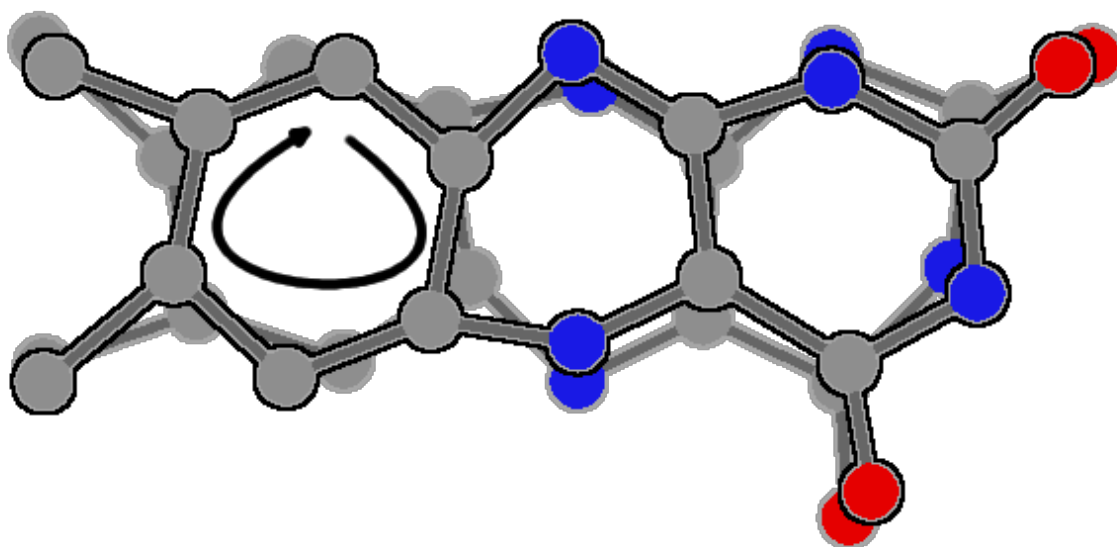


Figure S7. Ground state S_0 (top, absolute distances) and S_1 excited state geometry (bottom, relative distances relative to S_0) of neutral lumichrome calculated at the PBE0/cc-pVDZ level. All values are given in pm. Positive values correspond to elongations, negative values indicate contractions upon S_1 excitation.

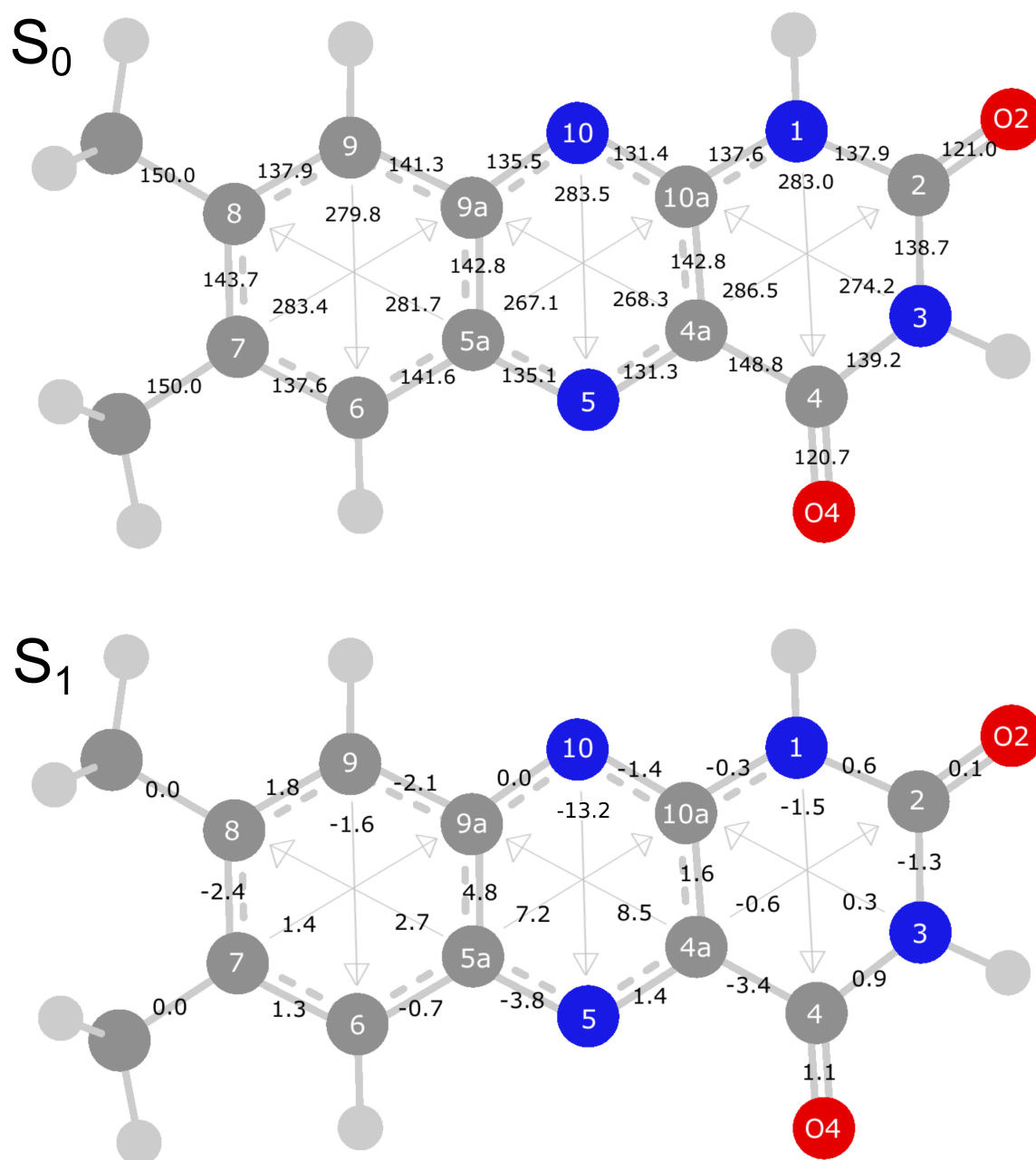


Figure S8. Geometry (in pm) of of $\text{H}^+\text{LC}(\text{N5})$ in the S_0 state calculated at the PBE0/cc-pVDZ level.

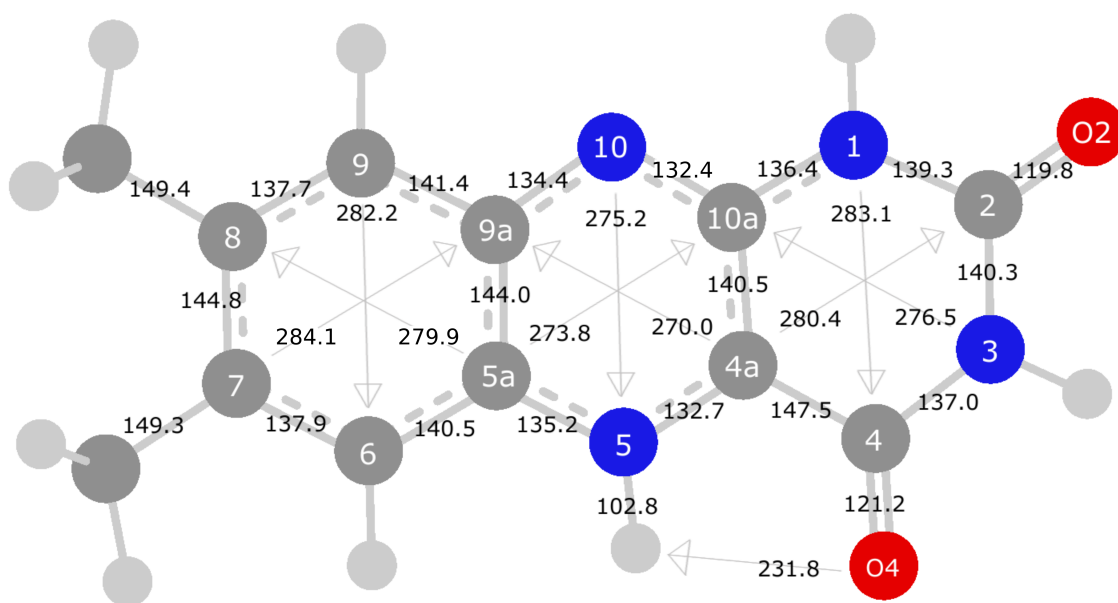


Table S1. Calculated vibrations (in cm^{-1}) for the S_0 and S_1 states of the $\text{H}^+\text{LC}(\text{N5})$ isomer.

S_0				S_1			
ν	sym(a')	ν	sym(a'')	ν	sym(a')	ν	sym(a'')
152.8	53	56.8	81	153.1	53	53.4	81
282.6	52	68.3	80	273.9	52	67.3	80
304.5	51	121.5	79	289.0	51	104.7	79
329.7	50	134.8	78	314.7	50	121.7	78
412.9	49	158.1	77	411.7	49	142.2	77
431.6	48	169.0	76	430.8	48	155.1	76
473.6	47	200.1	75	471.5	47	172.7	75
525.3	46	246.5	74	519.9	46	220.1	74
572.8	45	314.2	73	569.8	45	287.3	73
609.5	44	391.1	72	598.6	44	329.6	72
651.4	43	439.7	71	649.2	43	369.2	71
694.8	42	489.6	70	690.9	42	424.1	70
749.0	41	612.9	69	759.5	41	585.6	69
798.0	40	635.4	68	800.5	40	617.2	68
847.4	39	664.5	67	850.4	39	632.9	67
898.7	38	720.0	66	895.4	38	672.6	66
1003.8	37	768.0	65	999.7	37	687.4	65
1013.7	36	773.4	64	1010.0	36	719.5	64
1025.0	35	815.6	63	1013.2	35	762.8	63
1151.5	34	861.4	62	1142.9	34	767.3	62
1175.9	33	910.2	61	1165.9	33	877.5	61
1210.7	32	929.0	60	1212.7	32	903.9	60
1257.2	31	1029.6	59	1227.2	31	1006.1	59
1265.8	30	1049.0	58	1269.1	30	1035.4	58
1310.2	29	1436.3	57	1287.5	29	1429.6	57
1341.1	28	1452.1	56	1301.1	28	1444.1	56
1375.4	27	3137.6	55	1342.7	27	3116.6	55
1385.3	26	3137.8	54	1353.6	26	3127.9	54
1386.8	25			1377.6	25		
1398.6	24			1381.1	24		
1406.2	23			1387.9	23		
1428.4	22			1418.2	22		
1438.0	21			1426.7	21		
1448.1	20			1443.9	20		
1462.2	19			1463.7	19		
1492.9	18			1480.6	18		
1531.3	17			1492.2	17		
1557.6	16			1545.0	16		
1602.8	15			1576.6	15		
1639.3	14			1601.1	14		
1693.1	13			1649.8	13		
1712.8	12			1726.7	12		
1846.5	11			1806.1	11		
1905.1	10			1863.7	10		
3063.9	9			3050.1	9		
3064.5	8			3056.1	8		
3183.3	7			3182.4	7		
3185.9	6			3184.8	6		
3214.9	5			3210.0	5		
3239.5	4			3228.0	4		
3455.3	3			3554.6	3		
3593.6	2			3600.2	2		
3615.4	1			3612.6	1		

Electronic Supplementary Information (ESI)

Effect of alkali ions on optical properties of flavins: Vibronic spectra of cryogenic M^+ lumichrome ions ($M=Li-Cs$) in the gas phase

Pablo Nieto,^a David Müller,^a Alexander Sheldrick,^a Alan Günther,^a Mitsuhiro Miyazaki,^{a,b} and Otto Dopfer^{a*}

^a Institut für Optik und Atomare Physik, Technische Universität Berlin, Hardenbergstr. 36, D-10623 Berlin, Germany

^b Laboratory for Chemistry and Life Science, Institute of Innovative Research, Tokyo Institute of Technology, 4259, Nagatsuta-cho, Midori-ku, Yokohama, Japan

* corresponding author: dopfer@physik.tu-berlin.de; Fax: +49 30 314 23018

Figure S1. Experimental VISPD spectra of the $S_1 \leftarrow S_0$ transition of M^+LC ($M=H, Li-Cs$). The spectra of H^+LC and Li^+LC are recorded with the OPO laser, while the dye laser is used for the spectra of M^+LC with $M=Na-Cs$.

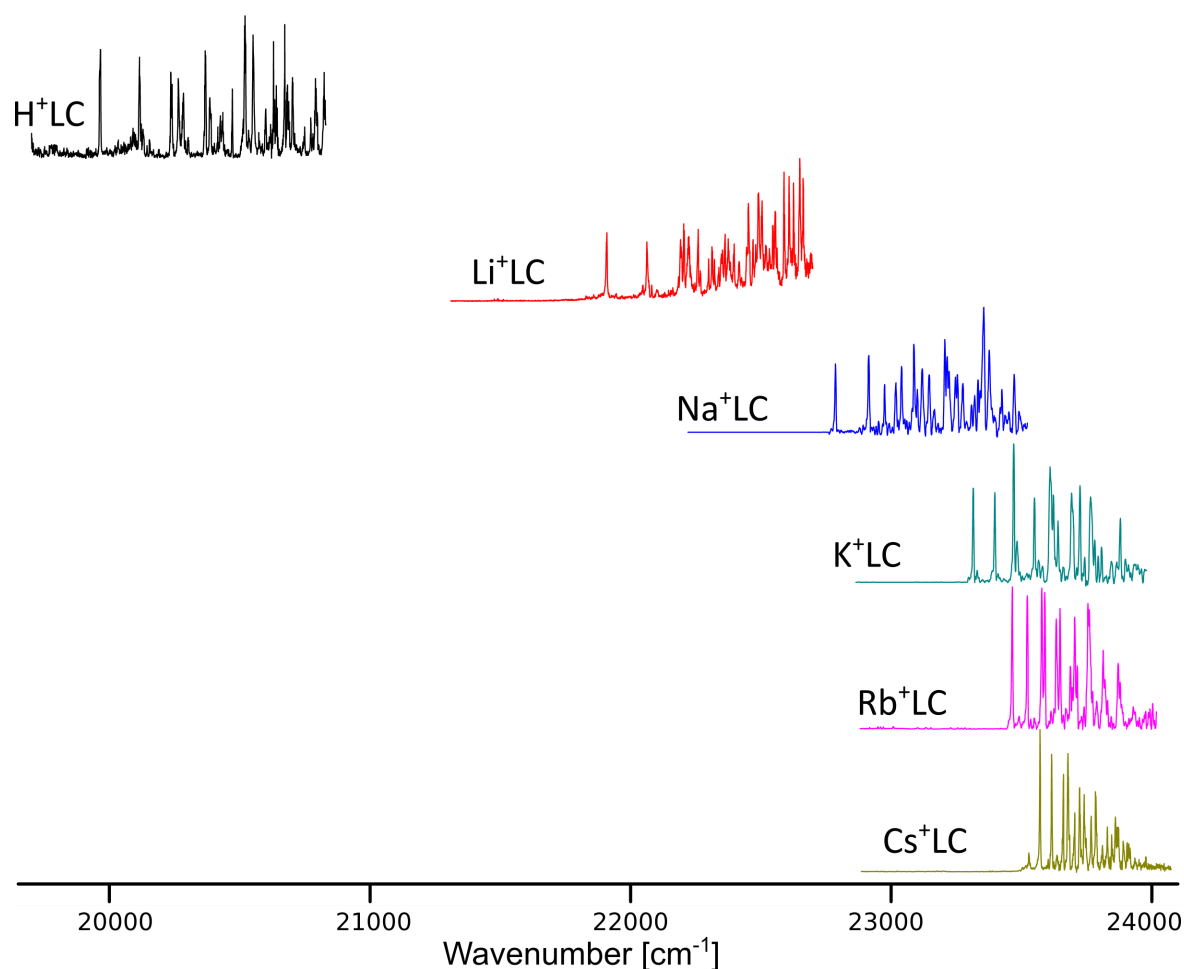


Figure S2. Experimental VISPD spectra of the $S_1 \leftarrow S_0$ transition of Cs^+LC recorded for ion trap temperatures of 25, 50, and 100 K. The Franck-Condon analysis of the intensities of the S_1 origin (0^0), the hot band and fundamental of the in-plane $\text{Cs}^+\dots\text{LC}$ bend (-42 and $+45$ cm^{-1}) yields a vibrational temperature of 29 ± 3 K for a nominal trap temperature measured as 25 ± 1 K.

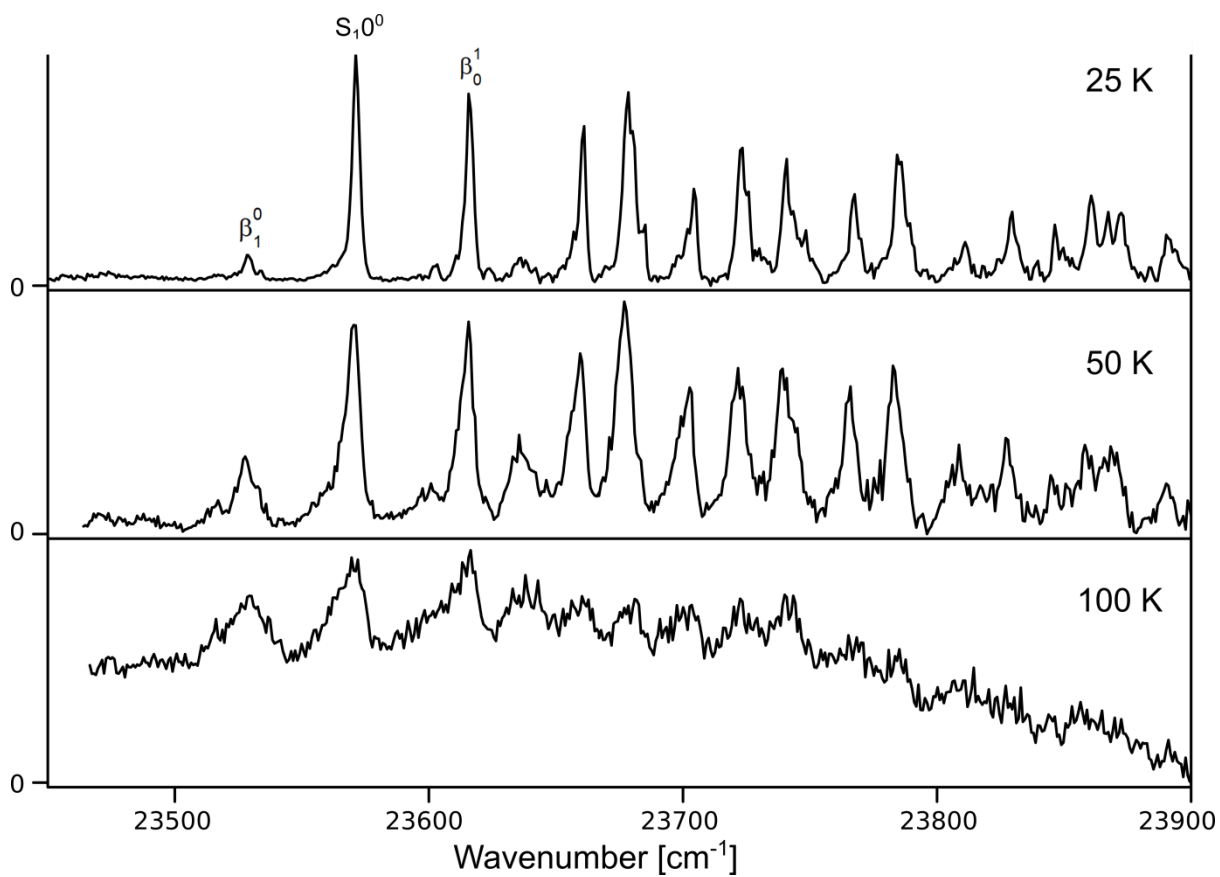
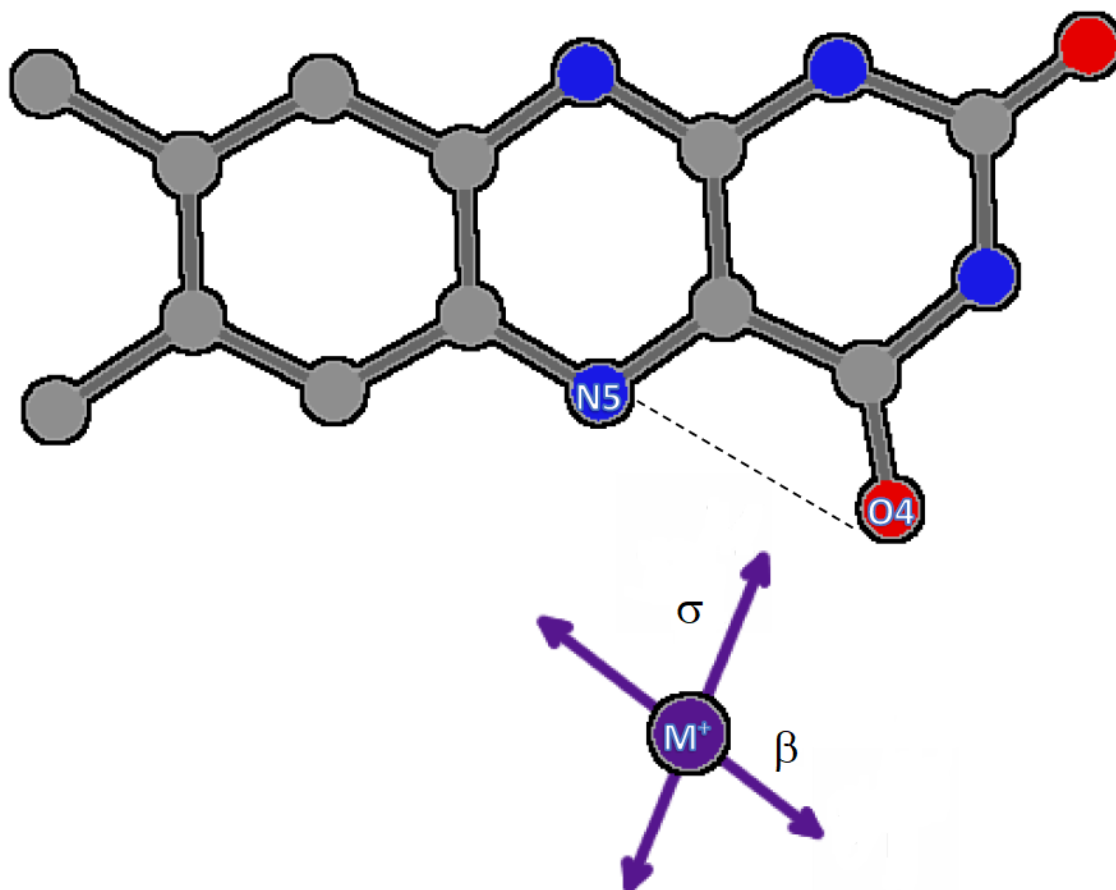
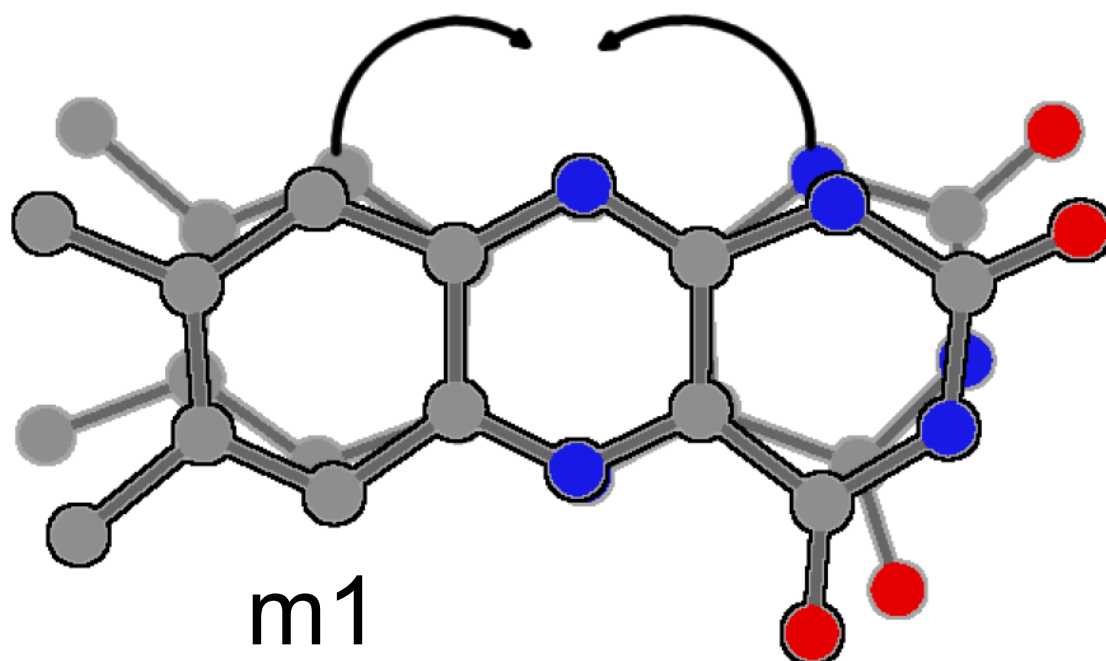


Figure S3. Schematic representation of relevant low-frequency in-plane normal coordinates in the S_1 state of $\text{Cs}^+\text{LC}(\text{O4})$ calculated at the PBE0/cc-pVDZ level. Hydrogen atoms are omitted for the sake of simplicity. Similarly, the metal ion is not shown for vibrations of the LC moiety. Shown are the structures for maximum positive and maximum negative elongation. The arrows indicate major movements. Labels used in Table 3 are indicated.

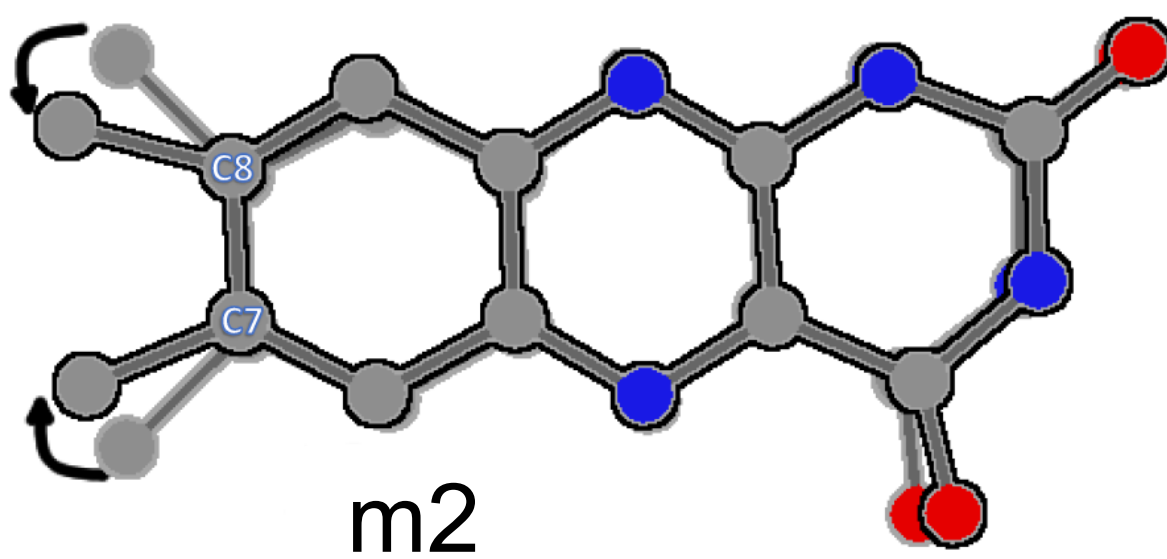
(a) modes 53 and 52



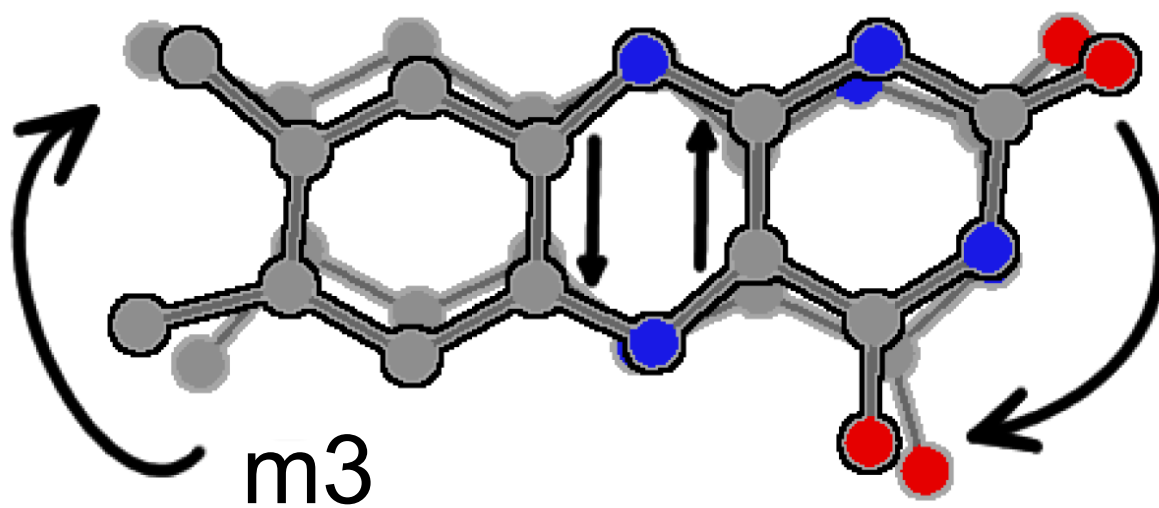
(b) mode 51



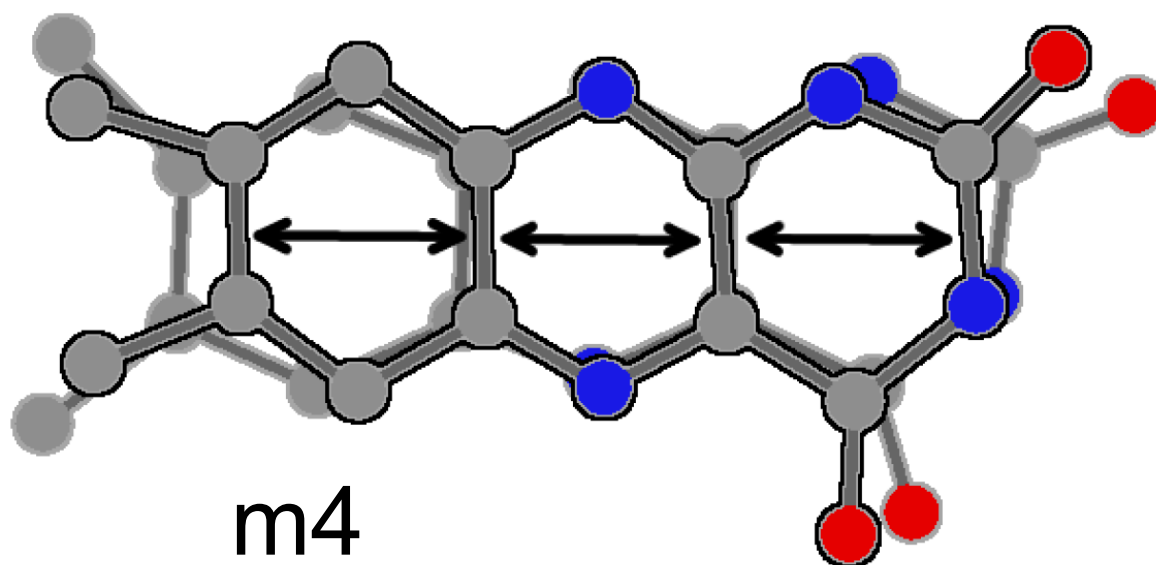
(c) mode 50



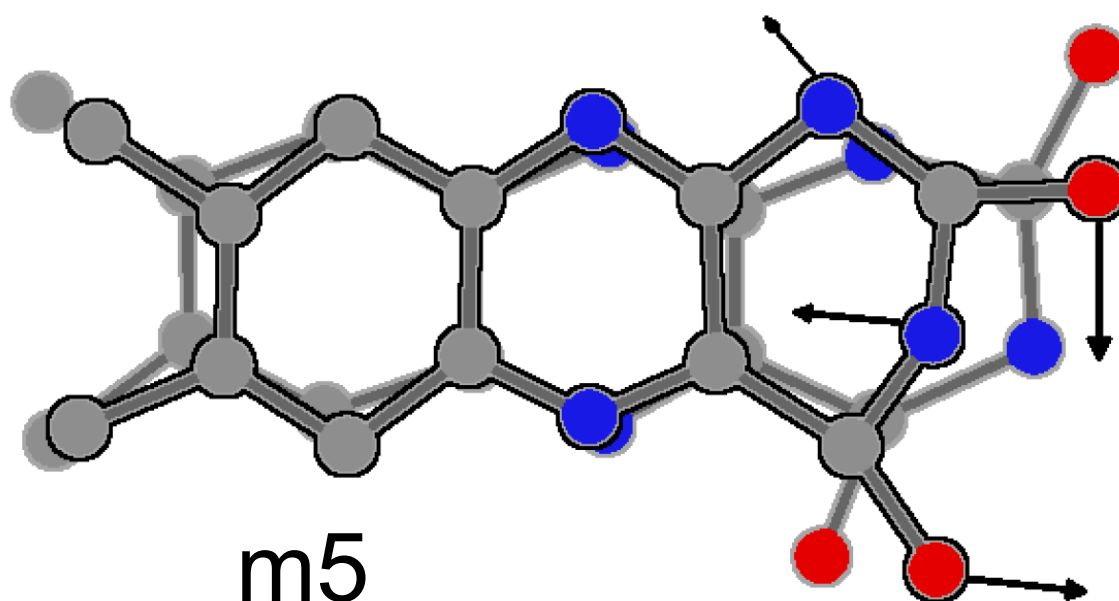
(d) mode 49



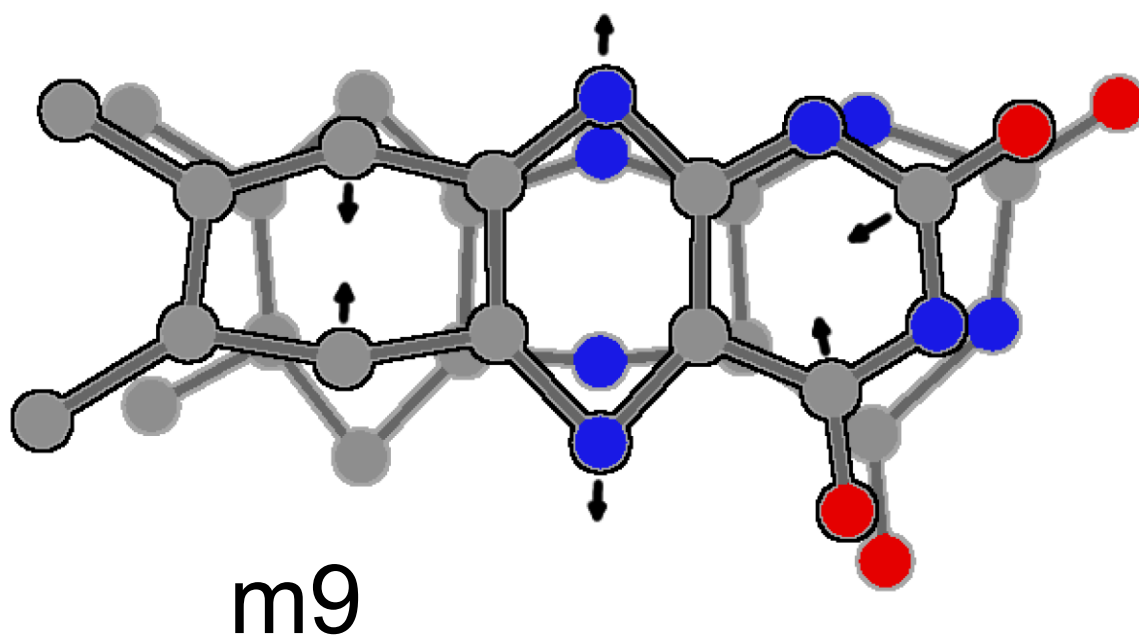
(e) mode 48



(f) mode 47



(g) mode 43



(h) mode 42

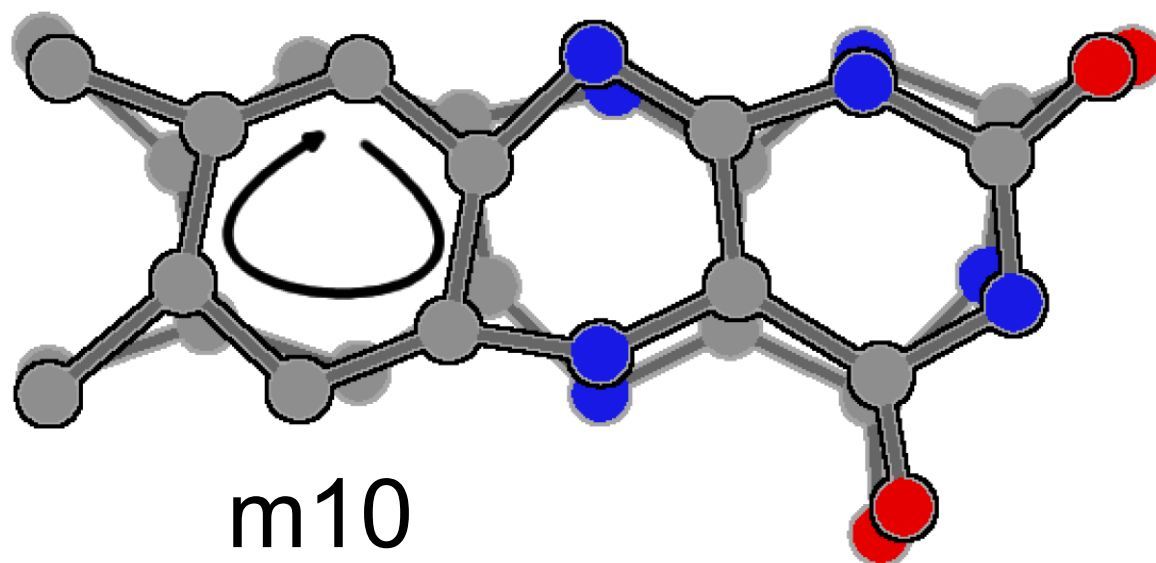
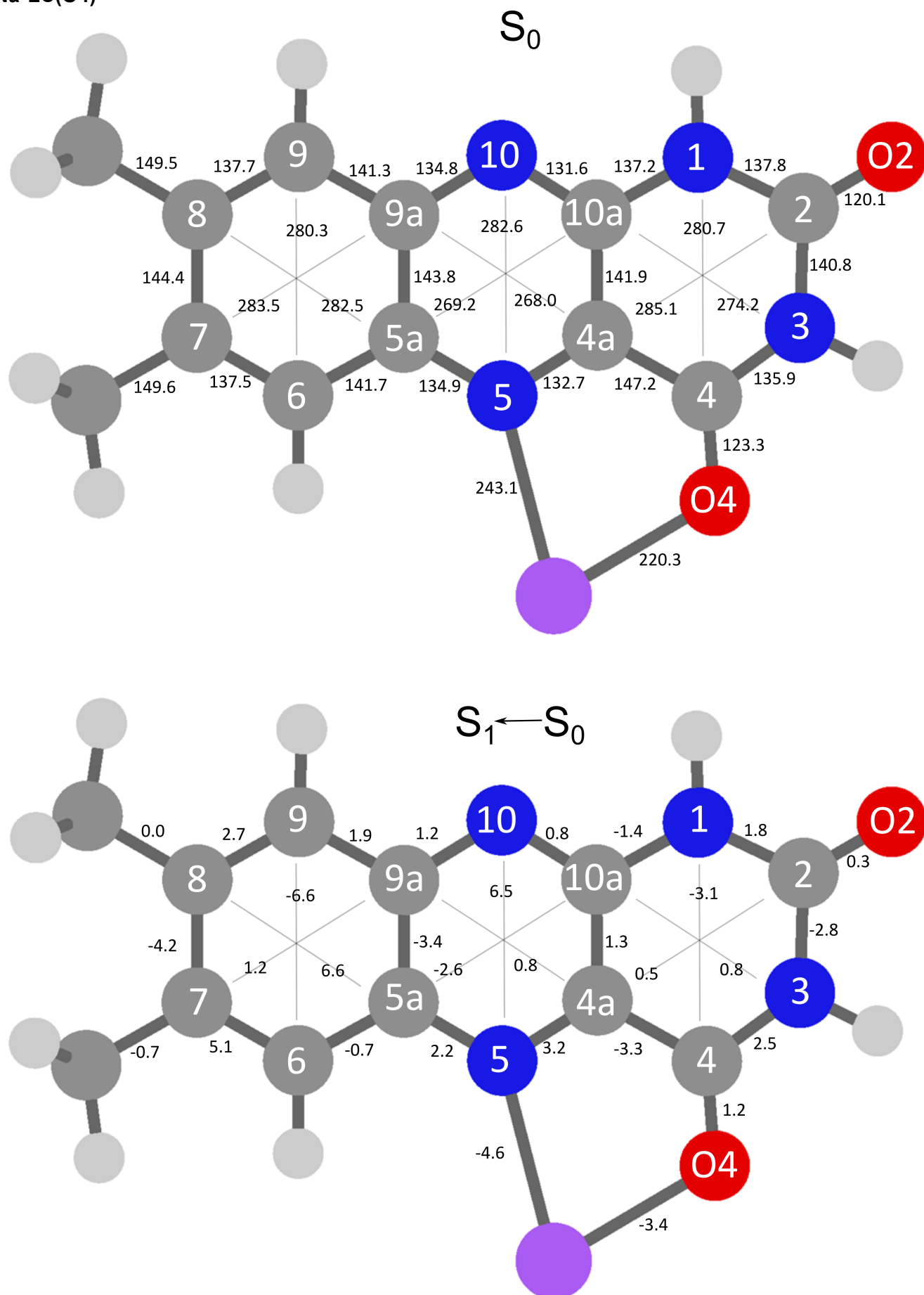
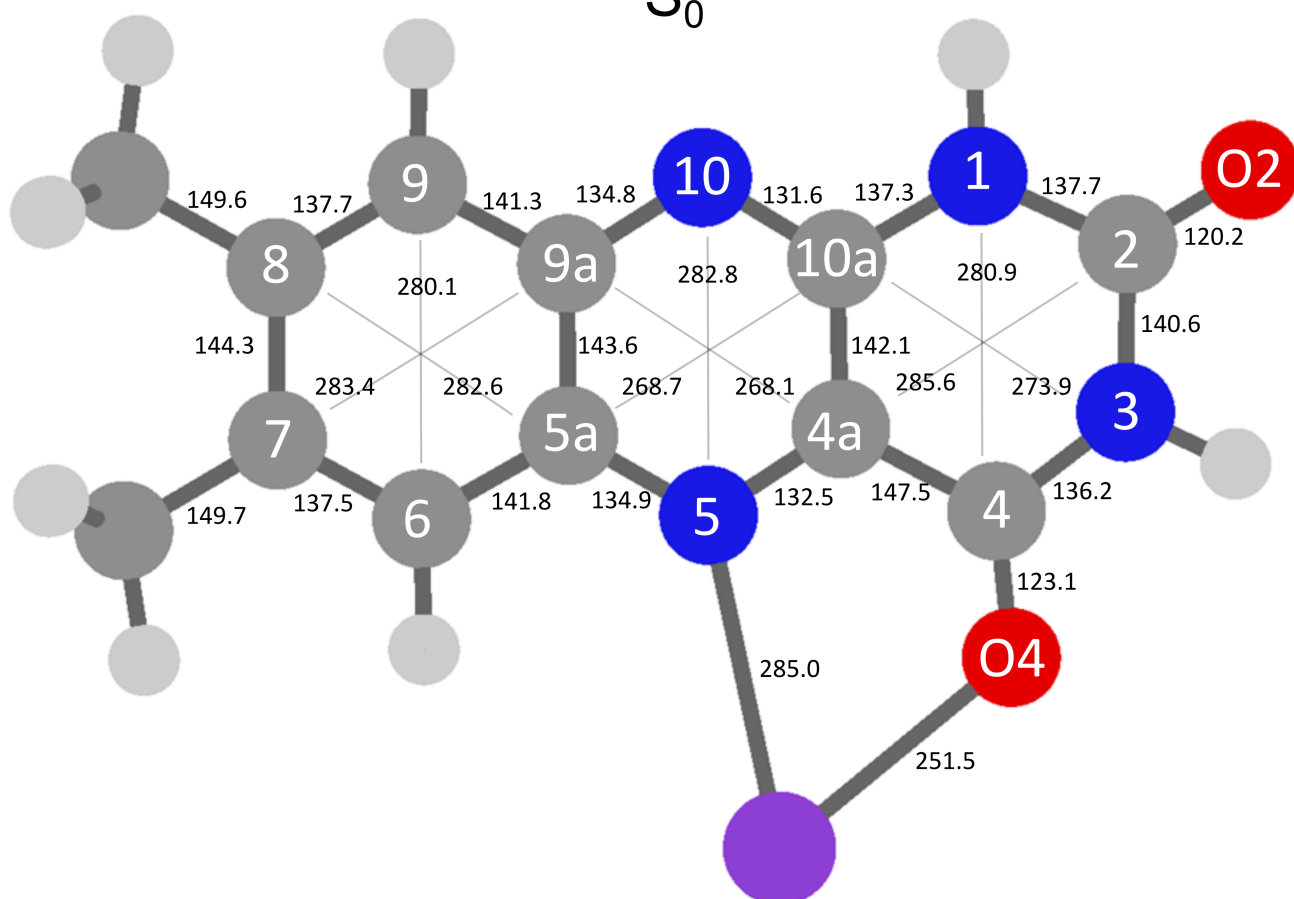
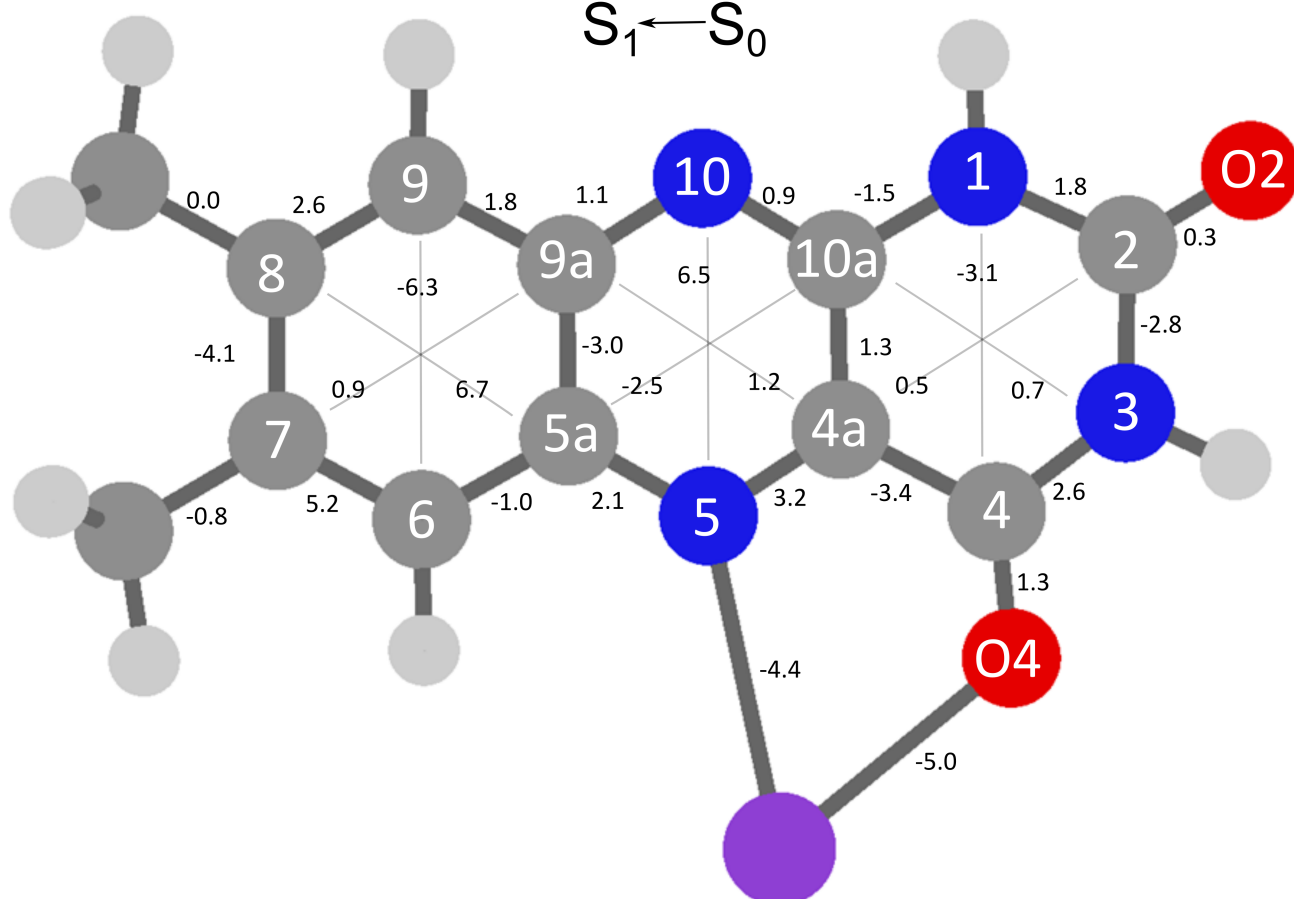
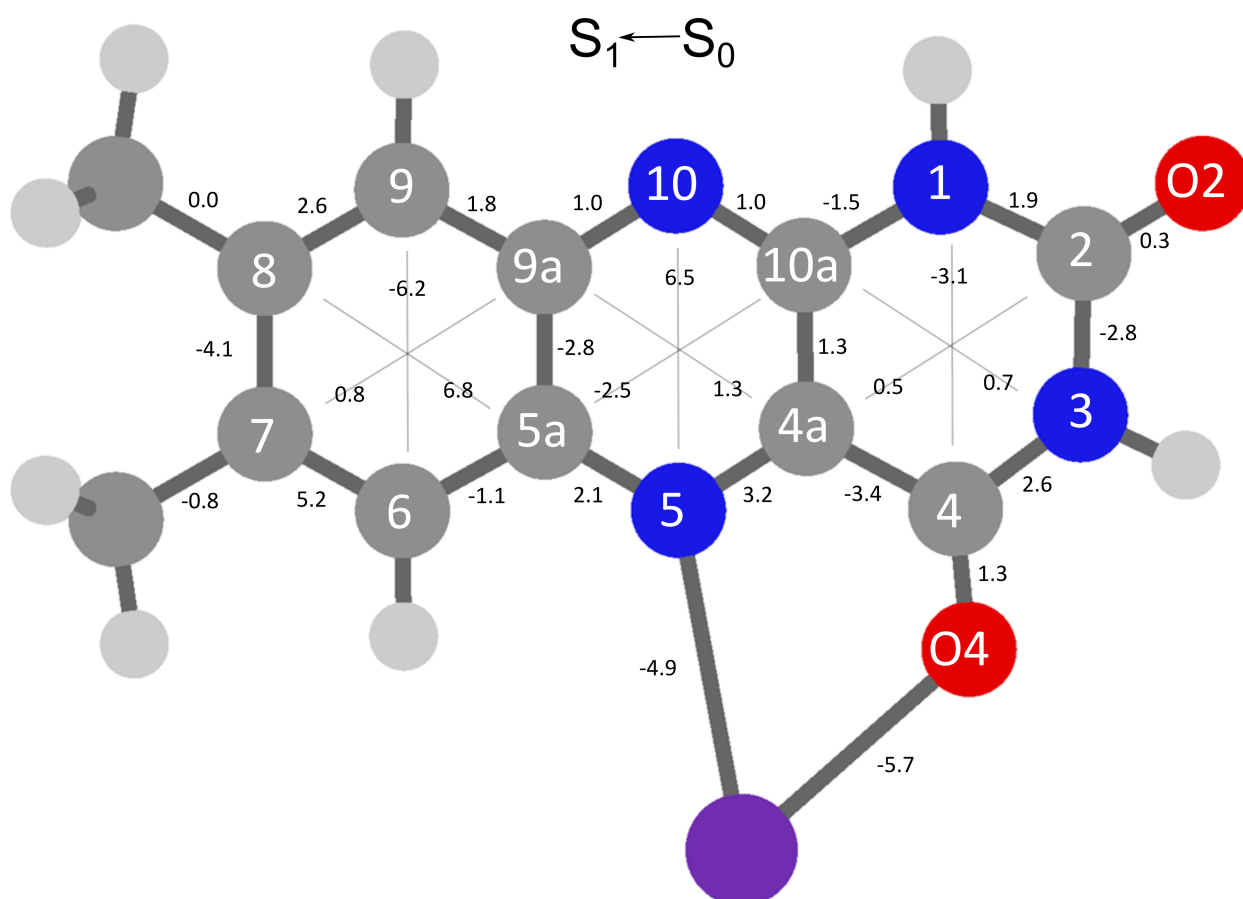
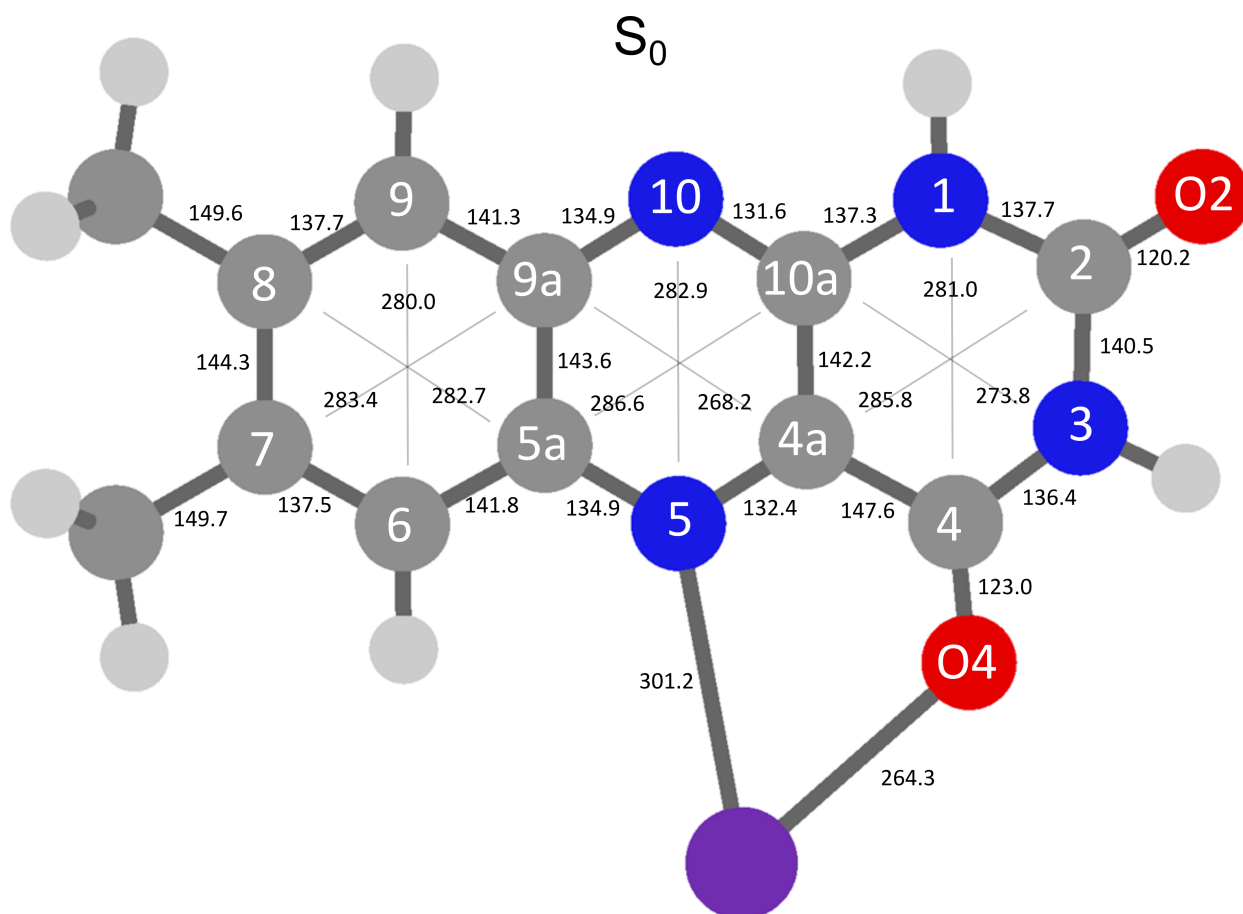


Figure S4. Ground state S_0 (top, absolute distances) and S_1 excited state geometries (bottom, distances relative to S_0) of $M^+LC(O4)$ calculated at the PBE0/cc-pVDZ level. All values are given in pm. Positive values correspond to elongations; negative values indicate contractions upon S_1 excitation.

Na⁺LC(O4)



S_0  $S_1 \leftarrow S_0$ 



Cs⁺LC(O4)

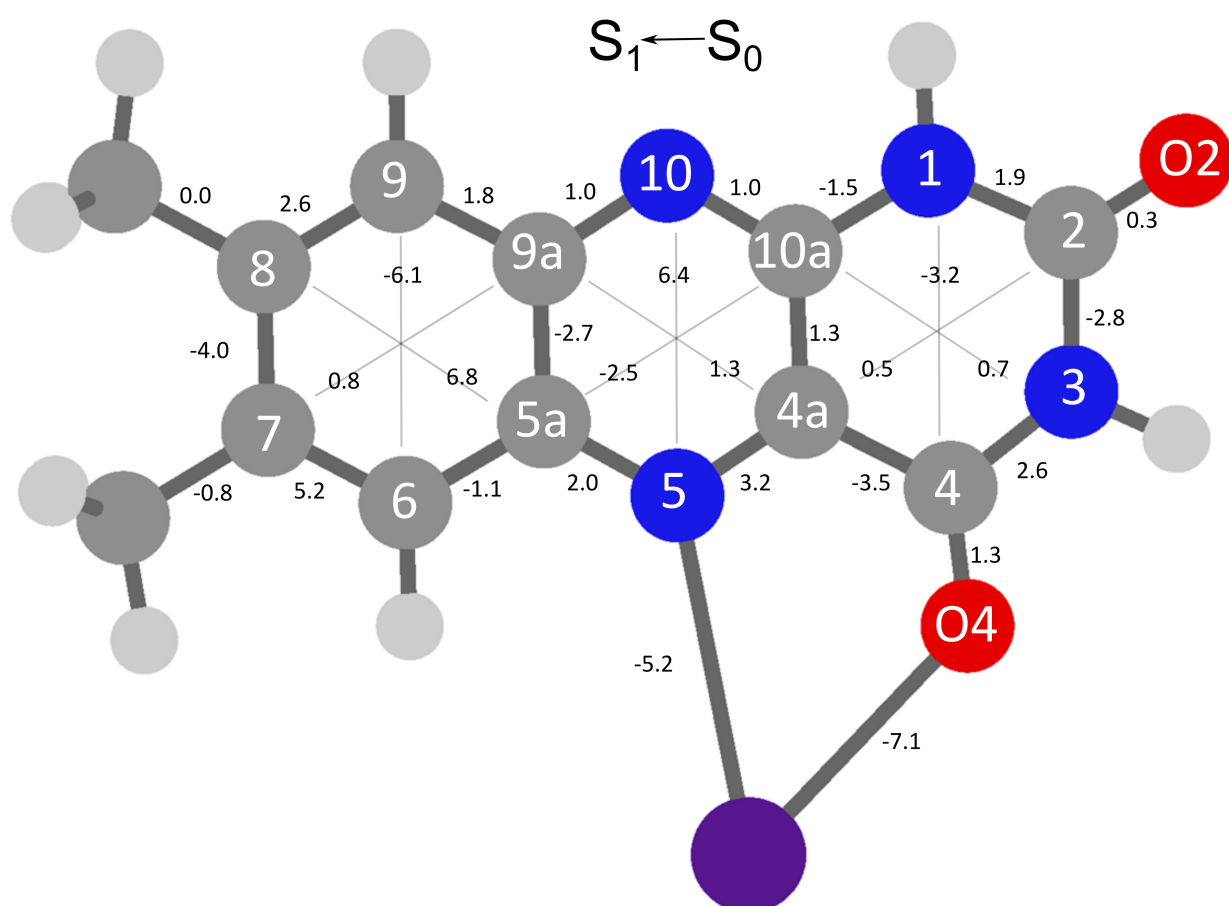
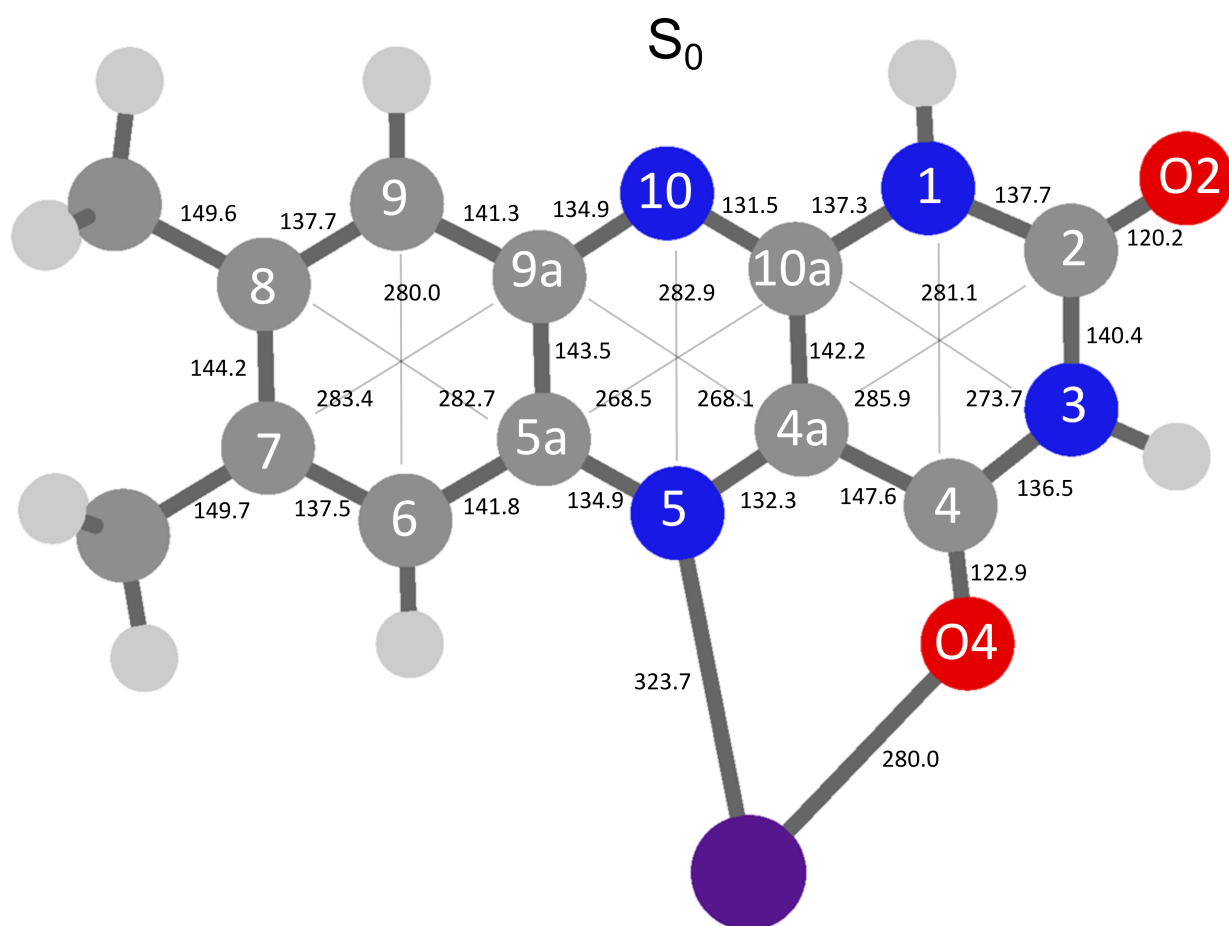


Table S1. Experimental frequencies for vibronic transitions (in cm^{-1}) observed in the VISPD spectrum of the S_1 state of M^+LC compared to harmonic frequencies of the $M^+LC(O4)$ isomer computed at the PBE0/cc-pVDZ level, along with the mode assignment.

(a) $Li^+LC(O4)$

Band	ν (exp)	ν (calc)	Assignment
	21911	20757	0^0
A	157	161	m1
B	288	307	m3
C	299	314	m4
D	319	322	2m1
E	350	373	β
F	403	418	m5
G	470	468	m1+m3
H	454	475	m1+m4
I	466	483	3m1
J	507	534	m1+ β
K	548	569	m10
L	561	579	m1+ m5
M	581	607	m9
N	595	615	σ

(b) Na⁺LC(O4)

Band	ν (exp)	ν (calc)	Assignment
	22786	21817	0^0
A	128	132	β
B	189	195	m1
C	232	240	σ
D	254	264	2β
E	301	307	m3
F	314	327	m1+ β
G	333	342	m4
H	360	372	$\sigma+\beta$
I	379	396	3β
J	420	428	m5
K	429	435	m1+ σ
		439	m3+ β
L	436	445	m6
	443	459	m1+ 2β
M	460	474	m4+ β
N	468	480	2σ
O	489	504	$\sigma+2\beta$
P	522	537	m1+m4
Q	534	538	m8
R	547	560	m5+ β
S	569	582	m9
T	590	601	m10

(c) K⁺LC(O4)

Band	ν (exp)	ν (calc)	assignment
	23315	22360	σ^0
A	83	86	β
B	155	161	σ
C	168	172	2β
D	235	247	$\sigma+\beta$
E	295	303	m3
F	308	322	2σ
G	325	328	m4
		333	$\sigma+2\beta$
H	377	389	$m3+\beta$
I	410	408	$2\sigma+\beta$
		419	$\sigma+3\beta$
		419	m5
J	450	464	$m3+\sigma$
K	466	476	m7
		475	$m3+2\beta$
L	480	489	$m4+\sigma$
M	492	505	$m5+\beta$
N	565	579	m9
		580	$m5+\sigma$

(d) Rb⁺LC(O4)

Band	v (exp)	v (calc)	assignment
	23465	22584	0 ⁰
A	57	60	β
B	113	120	2β
C	125	132	σ
D	169	180	3β
	Shoulder: 182	180	m1
E	183	192	σ+β
F	223	240	m1+β
	Shoulder:230	240	4β
G	239	252	σ+2β
H	249	264	2σ
I	293	301	m3
		312	m1+σ
		312	σ+3β
J	323	324	2σ+β
		325	m4

(e) Cs⁺LC(O4)

Band	ν (exp)	ν (calc)	assignment
	23571	22717	0^0
A	45	45	β
B	90	90	2β
C	108	114	σ
D	133	135	3β
E	152	159	$\sigma+\beta$
F	170	174	m1
G	196	204	$\sigma+2\beta$
H	214	228	2σ
I	240	249	$\sigma+3\beta$

Table S2. Calculated vibrations (in cm^{-1}) for the S_0 and S_1 states of the $M^+LC(O4)$ isomers, $H^+LC(N5)$, and LC.

(a) $Li^+LC(O4)$

S_0				S_1			
ν	sym(a')	ν	sym (a'')	ν	sym(a')	ν	sym (a'')
159.4	53	56.1	81	161.3	53	54.2	81
293.7	52	67.1	80	280.4	52	66.2	80
310.2	51	120.2	79	306.5	51	102.0	79
325.3	50	136.7	78	313.8	50	117.9	78
354.3	49	149.0	77	372.9	49	137.7	77
414.1	48	171.0	76	417.9	48	153.7	76
446.0	47	200.2	75	445.5	47	169.4	75
481.0	46	203.8	74	480.0	46	205.1	74
496.5	45	252.5	73	504.6	45	226.6	73
568.1	44	315.0	72	568.6	44	292.0	72
598.4	43	392.5	71	607.0	43	346.9	71
622.7	42	466.8	70	615.0	42	380.6	70
661.8	41	517.1	69	659.6	41	454.4	69
710.9	40	625.4	68	711.8	40	590.7	68
754.1	39	645.3	67	763.1	39	619.2	67
806.6	38	681.3	66	810.4	38	668.7	66
858.7	37	733.7	65	856.9	37	689.8	65
903.7	36	774.6	64	905.6	36	716.2	64
1005.7	35	791.4	63	1001.3	35	767.0	63
1017.9	34	835.2	62	1010.6	34	784.6	62
1026.7	33	872.6	61	1021.6	33	884.0	61
1170.3	32	914.2	60	1156.7	32	903.4	60
1185.7	31	1031.6	59	1178.4	31	1005.2	59
1220.7	30	1051.7	58	1222.6	30	1037.7	58
1257.2	29	1438.8	57	1236.8	29	1429.5	57
1286.0	28	1454.4	56	1274.0	28	1448.1	56
1315.9	27	3134.9	55	1296.4	27	3112.5	55
1340.2	26	3137.4	54	1330.6	26	3129.6	54
1380.2	25			1349.8	25		
1387.9	24			1353.5	24		
1392.1	23			1375.3	23		
1399.4	22			1389.2	22		
1427.7	21			1392.6	21		
1433.3	20			1429.5	20		
1457.1	19			1446.0	19		
1467.3	18			1460.0	18		
1488.5	17			1472.1	17		
1529.0	16			1496.8	16		
1547.5	15			1510.8	15		
1576.0	14			1576.9	14		
1641.4	13			1595.3	13		
1643.6	12			1625.1	12		
1709.3	11			1691.6	11		
1758.9	10			1710.6	10		
1906.5	9			1878.0	9		
3062.4	8			3047.2	8		
3063.5	7			3057.9	7		
3175.8	6			3179.8	6		
3182.5	5			3181.2	5		
3202.1	4			3208.0	4		
3233.8	3			3224.5	3		
3592.5	2			3602.7	2		
3613.6	1			3619.2	1		

(b) Na⁺LC(O4)

S ₀				S ₁			
v	sym(a')	v	sym (a'')	v	sym(a')	v	sym (a'')
123.2	53	50.1	81	132.1	53	48.1	81
186.8	52	64.8	80	194.8	52	63.6	80
232.8	51	78.9	79	239.5	51	73.4	79
303.1	50	126.8	78	288.7	50	102.1	78
314.2	49	138.7	77	306.5	49	126.4	77
343.9	48	166.6	76	341.8	48	146.0	76
428.1	47	176.6	75	427.8	47	162.0	75
444.8	46	200.5	74	445.4	46	175.4	74
478.9	45	253.9	73	476.9	45	223.4	73
541.3	44	316.0	72	538.2	44	290.8	72
585.7	43	391.9	71	582.1	43	343.1	71
615.7	42	466.0	70	601.0	42	380.8	70
656.6	41	512.6	69	653.7	41	448.0	69
703.4	40	625.0	68	699.7	40	592.9	68
754.8	39	646.3	67	759.0	39	617.9	67
804.6	38	681.3	66	780.6	38	671.0	66
854.6	37	733.0	65	848.7	37	691.5	65
901.4	36	773.7	64	903.5	36	715.8	64
1007.0	35	790.9	63	1001.9	35	767.5	63
1022.8	34	835.3	62	1010.3	34	806.7	62
1027.0	33	867.9	61	1027.0	33	880.9	61
1168.4	32	914.8	60	1156.1	32	902.5	60
1177.7	31	1031.8	59	1169.7	31	1004.7	59
1217.6	30	1052.6	58	1219.4	30	1038.4	58
1254.9	29	1439.5	57	1235.9	29	1430.1	57
1288.8	28	1455.2	56	1266.2	28	1449.5	56
1313.9	27	3134.3	55	1291.4	27	3111.8	55
1337.1	26	3136.8	54	1325.2	26	3129.2	54
1375.4	25			1352.4	25		
1388.3	24			1357.7	24		
1394.9	23			1375.4	23		
1403.0	22			1391.1	22		
1427.5	21			1395.7	21		
1434.4	20			1426.4	20		
1456.7	19			1446.0	19		
1465.8	18			1456.1	18		
1479.9	17			1467.5	17		
1527.6	16			1493.7	16		
1544.8	15			1500.1	15		
1572.5	14			1574.0	14		
1638.6	13			1582.7	13		
1646.4	12			1614.4	12		
1710.5	11			1679.4	11		
1773.6	10			1720.5	10		
1902.8	9			1871.3	9		
3062.0	8			3046.8	8		
3062.8	7			3057.7	7		
3172.6	6			3177.4	6		
3181.2	5			3179.6	5		
3193.5	4			3202.2	4		
3232.3	3			3223.2	3		
3600.0	2			3602.7	2		
3617.2	1			3625.3	1		

(c) K⁺LC(O4)

S ₀				S ₁			
v	sym(a')	v	sym (a'')	v	sym(a')	v	sym (a'')
78.9	53	38.9	81	86.0	53	37.0	81
156.1	52	60.0	80	160.7	52	59.5	80
189.5	51	67.4	79	198.7	51	62.5	79
298.6	50	125.0	78	285.0	50	101.9	78
309.4	49	138.4	77	302.5	49	124.7	77
336.0	48	161.1	76	328.4	48	144.8	76
418.8	47	172.6	75	418.6	47	155.7	75
440.3	46	199.1	74	436.6	46	170.6	74
478.0	45	253.4	73	475.7	45	221.8	73
539.0	44	315.8	72	535.0	44	287.4	72
584.7	43	391.1	71	578.5	43	337.6	71
613.0	42	464.9	70	598.3	42	380.1	70
654.6	41	509.0	69	651.1	41	441.5	69
701.3	40	624.1	68	696.9	40	593.4	68
754.7	39	646.1	67	756.3	39	615.2	67
804.2	38	680.9	66	805.6	38	668.4	66
852.2	37	731.4	65	844.3	37	691.0	65
900.0	36	772.7	64	902.1	36	713.5	64
1006.8	35	790.4	63	1001.6	35	767.1	63
1024.1	34	835.5	62	1009.9	34	779.3	62
1027.3	33	867.4	61	1028.3	33	878.6	61
1167.0	32	914.3	60	1155.4	32	900.8	60
1174.2	31	1031.9	59	1165.0	31	1004.4	59
1215.2	30	1052.9	58	1216.1	30	1038.8	58
1253.0	29	1439.8	57	1235.5	29	1430.5	57
1288.7	28	1455.4	56	1261.6	28	1450.2	56
1312.5	27	3133.5	55	1288.7	27	3111.1	55
1335.0	26	3135.8	54	1321.6	26	3128.7	54
1372.2	25			1352.0	25		
1388.3	24			1361.6	24		
1395.3	23			1375.4	23		
1404.0	22			1391.2	22		
1427.1	21			1395.8	21		
1434.3	20			1424.7	20		
1455.9	19			1446.1	19		
1464.2	18			1453.8	18		
1478.4	17			1466.1	17		
1526.7	16			1490.6	16		
1543.0	15			1500.5	15		
1570.7	14			1571.8	14		
1636.8	13			1575.5	13		
1648.4	12			1610.6	12		
1711.2	11			1671.8	11		
1771.5	10			1717.5	10		
1900.2	9			1867.9	9		
3061.4	8			3046.3	8		
3061.9	7			3057.3	7		
3170.2	6			3175.8	6		
3180.0	5			3178.3	5		
3193.7	4			3202.2	4		
3230.6	3			3222.1	3		
3603.1	2			3603.0	2		
3619.0	1			3628.2	1		

(d) Rb⁺LC(O4)

S ₀				S ₁			
v	sym(a')	v	sym (a'')	v	sym(a')	v	sym (a'')
54.9	53	33.1	81	59.8	53	31.5	81
122.4	52	58.1	80	131.5	52	57.6	80
175.9	51	66.8	79	179.6	51	62.4	79
296.8	50	124.8	78	283.4	50	100.3	78
308.3	49	138.3	77	301.4	49	124.8	77
334.0	48	158.8	76	324.6	48	144.6	76
416.4	47	172.0	75	415.8	47	153.8	75
439.8	46	199.1	74	435.1	46	170.1	74
477.8	45	253.6	73	475.3	45	221.0	73
538.2	44	316.0	72	533.9	44	286.1	72
584.4	43	391.1	71	577.2	43	336.5	71
612.4	42	464.6	70	597.7	42	379.8	70
654.3	41	508.7	69	650.8	41	440.6	69
700.7	40	623.8	68	696.0	40	593.5	68
754.9	39	646.1	67	755.4	39	614.3	67
804.0	38	680.5	66	805.2	38	668.3	66
851.9	37	730.8	65	843.5	37	691.1	65
899.8	36	772.3	64	901.7	36	712.9	64
1006.9	35	790.6	63	1001.5	35	767.1	63
1024.4	34	835.5	62	1009.8	34	778.3	62
1027.8	33	868.2	61	1028.7	33	878.2	61
1166.6	32	914.4	60	1155.1	32	900.3	60
1173.2	31	1032.1	59	1164.1	31	1004.1	59
1214.3	30	1053.1	58	1215.4	30	1038.9	58
1252.3	29	1440.0	57	1235.5	29	1430.4	57
1289.2	28	1455.7	56	1260.7	28	1450.7	56
1312.2	27	3133.3	55	1288.3	27	3110.8	55
1334.7	26	3135.5	54	1321.0	26	3128.5	54
1371.4	25			1352.3	25		
1388.4	24			1363.4	24		
1395.6	23			1375.0	23		
1404.7	22			1391.4	22		
1427.4	21			1396.1	21		
1434.4	20			1424.0	20		
1455.7	19			1446.0	19		
1463.6	18			1453.2	18		
1478.3	17			1465.7	17		
1526.6	16			1489.9	16		
1543.3	15			1500.8	15		
1570.3	14			1571.2	14		
1636.9	13			1573.2	13		
1649.5	12			1608.9	12		
1711.7	11			1670.0	11		
1776.5	10			1721.0	10		
1899.2	9			1866.8	9		
3061.3	8			3046.0	8		
3061.6	7			3057.3	7		
3169.4	6			3175.2	6		
3179.7	5			3178.0	5		
3195.6	4			3203.2	4		
3230.2	3			3221.6	3		
3605.5	2			3603.4	2		
3619.9	1			3629.8	1		

(e) Cs⁺LC(O4)

S ₀				S ₁			
v	sym(a')	v	sym (a'')	v	sym(a')	v	sym (a'')
42.0	53	29.4	81	45.2	53	28.8	81
103.7	52	57.5	80	113.5	52	56.9	80
171.4	51	66.6	79	173.5	51	62.0	79
295.6	50	124.7	78	282.7	50	101.6	78
307.6	49	138.6	77	300.7	49	124.3	77
332.9	48	157.9	76	322.4	48	144.8	76
414.3	47	171.7	75	413.2	47	153.1	75
439.3	46	199.2	74	434.3	46	169.5	74
477.7	45	253.7	73	475.2	45	221.0	73
537.5	44	316.0	72	532.9	44	285.0	72
584.1	43	391.2	71	576.1	43	335.5	71
611.8	42	464.5	70	597.2	42	380.2	70
653.8	41	508.1	69	650.3	41	440.3	69
700.1	40	623.6	68	695.4	40	593.5	68
754.9	39	646.1	67	754.7	39	613.2	67
804.0	38	680.7	66	805.3	38	667.4	66
851.2	37	730.8	65	842.5	37	690.8	65
899.5	36	772.2	64	901.9	36	712.5	64
1006.9	35	791.2	63	1001.4	35	767.0	63
1024.3	34	836.2	62	1009.6	34	778.8	62
1028.0	33	869.1	61	1028.8	33	878.8	61
1166.3	32	914.4	60	1155.1	32	899.9	60
1172.2	31	1032.1	59	1163.0	31	1004.1	59
1213.4	30	1053.3	58	1214.1	30	1039.1	58
1251.5	29	1440.2	57	1235.5	29	1430.7	57
1289.3	28	1455.9	56	1260.1	28	1450.9	56
1311.8	27	3133.1	55	1287.8	27	3110.5	55
1334.0	26	3135.1	54	1320.4	26	3128.4	54
1370.5	25			1352.2	25		
1388.4	24			1364.5	24		
1395.6	23			1374.9	23		
1404.7	22			1391.1	22		
1427.3	21			1395.9	21		
1434.3	20			1423.8	20		
1455.6	19			1446.3	19		
1463.3	18			1452.9	18		
1478.0	17			1465.7	17		
1526.3	16			1489.5	16		
1543.1	15			1501.1	15		
1569.9	14			1570.2	14		
1636.4	13			1571.9	13		
1650.0	12			1608.5	12		
1711.9	11			1668.2	11		
1774.7	10			1718.0	10		
1898.4	9			1866.3	9		
3061.0	8			3045.9	8		
3061.3	7			3057.2	7		
3168.7	6			3175.1	6		
3179.3	5			3177.6	5		
3197.8	4			3204.8	4		
3229.8	3			3221.6	3		
3607.1	2			3603.6	2		
3620.3	1			3631.2	1		

(f) LC

S ₀				S ₁			
v	sym(a')	v	sym (a'')	v	sym(a')	v	sym (a'')
158.7	51	53.3	78	158.5	51	52.6	78
289.1	50	65.4	77	278.1	50	58.7	77
302.7	49	120.9	76	295.7	49	89.6	76
327.9	48	136.9	75	314.3	48	114.9	75
406.4	47	142.3	74	404.0	47	130.9	74
436.2	46	170.5	73	430.1	46	135.9	73
474.8	45	196.9	72	471.2	45	159.3	72
528.6	44	252.9	71	522.0	44	202.0	71
580.7	43	319.1	70	563.7	43	212.4	70
607.3	42	392.9	69	592.3	42	308.3	69
653.1	41	462.2	68	646.9	41	383.6	68
691.9	40	507.7	67	683.3	40	437.1	67
758.0	39	605.9	66	741.6	39	592.1	66
803.8	38	642.2	65	799.8	38	614.4	65
848.2	37	675.2	64	837.3	37	672.6	64
899.0	36	722.6	63	896.5	36	677.7	63
1006.0	35	770.0	62	998.3	35	719.9	62
1021.7	34	798.8	61	1006.3	34	768.1	61
1035.1	33	843.9	60	1027.2	33	775.8	60
1150.0	32	902.3	59	1131.5	32	872.4	59
1163.5	31	920.2	58	1156.4	31	904.0	58
1208.0	30	1035.5	57	1204.5	30	1003.8	57
1244.1	29	1056.6	56	1234.3	29	1039.2	56
1294.2	28	1443.3	55	1242.6	28	1433.7	55
1307.4	27	1458.9	54	1286.3	27	1453.6	54
1320.6	26	3122.4	53	1309.0	26	3101.5	53
1356.5	25	3124.5	52	1352.1	25	3114.6	52
1387.1	24			1371.4	24		
1396.1	23			1381.0	23		
1406.7	22			1390.2	22		
1427.0	21			1397.9	21		
1434.1	20			1418.1	20		
1450.2	19			1431.4	19		
1461.8	18			1451.7	18		
1480.6	17			1461.4	17		
1522.4	16			1478.3	16		
1545.5	15			1499.5	15		
1561.6	14			1538.1	14		
1638.9	13			1566.4	13		
1661.8	12			1573.0	12		
1715.3	11			1655.7	11		
1854.0	10			1800.0	10		
1871.3	9			1844.1	9		
3053.2	8			3039.6	8		
3054.4	7			3047.5	7		
3165.6	6			3163.6	6		
3167.3	5			3172.9	5		
3218.2	4			3210.6	4		
3220.7	3			3216.4	3		
3629.4	2			3618.4	2		
3642.1	1			3643.5	1		

(g) H⁺LC (N5)

S ₀				S ₁			
v	sym(a')	v	sym(a'')	v	sym(a')	v	sym(a'')
152.8	53	56.8	81	153.1	53	53.4	81
282.6	52	68.3	80	273.9	52	67.3	80
304.5	51	121.5	79	289.0	51	104.7	79
329.7	50	134.8	78	314.7	50	121.7	78
412.9	49	158.1	77	411.7	49	142.2	77
431.6	48	169.0	76	430.8	48	155.1	76
473.6	47	200.1	75	471.5	47	172.7	75
525.3	46	246.5	74	519.9	46	220.1	74
572.8	45	314.2	73	569.8	45	287.3	73
609.5	44	391.1	72	598.6	44	329.6	72
651.4	43	439.7	71	649.2	43	369.2	71
694.8	42	489.6	70	690.9	42	424.1	70
749.0	41	612.9	69	759.5	41	585.6	69
798.0	40	635.4	68	800.5	40	617.2	68
847.4	39	664.5	67	850.4	39	632.9	67
898.7	38	720.0	66	895.4	38	672.6	66
1003.8	37	768.0	65	999.7	37	687.4	65
1013.7	36	773.4	64	1010.0	36	719.5	64
1025.0	35	815.6	63	1013.2	35	762.8	63
1151.5	34	861.4	62	1142.9	34	767.3	62
1175.9	33	910.2	61	1165.9	33	877.5	61
1210.7	32	929.0	60	1212.7	32	903.9	60
1257.2	31	1029.6	59	1227.2	31	1006.1	59
1265.8	30	1049.0	58	1269.1	30	1035.4	58
1310.2	29	1436.3	57	1287.5	29	1429.6	57
1341.1	28	1452.1	56	1301.1	28	1444.1	56
1375.4	27	3137.6	55	1342.7	27	3116.6	55
1385.3	26	3137.8	54	1353.6	26	3127.9	54
1386.8	25			1377.6	25		
1398.6	24			1381.1	24		
1406.2	23			1387.9	23		
1428.4	22			1418.2	22		
1438.0	21			1426.7	21		
1448.1	20			1443.9	20		
1462.2	19			1463.7	19		
1492.9	18			1480.6	18		
1531.3	17			1492.2	17		
1557.6	16			1545.0	16		
1602.8	15			1576.6	15		
1639.3	14			1601.1	14		
1693.1	13			1649.8	13		
1712.8	12			1726.7	12		
1846.5	11			1806.1	11		
1905.1	10			1863.7	10		
3063.9	9			3050.1	9		
3064.5	8			3056.1	8		
3183.3	7			3182.4	7		
3185.9	6			3184.8	6		
3214.9	5			3210.0	5		
3239.5	4			3228.0	4		
3455.3	3			3554.6	3		
3593.6	2			3600.2	2		
3615.4	1			3612.6	1		

Table S3. Optimized geometries for the S_0 and S_1 states of the $M^+LC(O4)$ isomers, $H^+LC(N5)$ and $H^+LC(O4)$, LC, and iso-LC.

(a) $Li^+LC(O4)$

S_0				S_1			
	x	y	z		x	y	z
C	-3.17	-0.46	0.00	C	-3.22	-0.44	0.00
C	-1.94	-1.08	0.00	C	-1.94	-1.06	0.00
C	-0.74	-0.34	0.00	C	-0.71	-0.36	0.00
C	-0.79	1.10	0.00	C	-0.77	1.04	0.00
C	-2.06	1.72	0.00	C	-2.06	1.67	0.00
C	-3.23	0.99	0.00	C	-3.28	0.97	0.00
C	1.47	1.22	0.00	C	1.47	1.19	0.00
C	1.54	-0.19	0.00	C	1.57	-0.23	0.00
C	2.85	-0.86	0.00	C	2.87	-0.85	0.00
C	3.91	1.38	0.00	C	3.92	1.37	0.00
H	-1.89	-2.17	0.00	H	-1.90	-2.16	0.00
H	-2.08	2.81	0.00	H	-2.07	2.76	0.00
H	4.85	-0.45	0.00	H	4.88	-0.43	0.00
H	2.59	2.94	0.00	H	2.57	2.92	0.00
N	0.32	1.86	0.00	N	0.32	1.85	0.00
N	2.64	1.93	0.00	N	2.62	1.90	0.00
N	3.92	-0.04	0.00	N	3.95	-0.01	0.00
N	0.46	-0.96	0.00	N	0.48	-1.04	0.00
O	2.95	-2.10	0.00	O	3.01	-2.10	0.00
O	4.92	2.01	0.00	O	4.90	2.07	0.00
C	-4.55	1.67	0.00	C	-4.58	1.69	0.00
H	-5.15	1.39	0.88	H	-5.19	1.43	0.88
H	-4.44	2.77	0.00	H	-4.44	2.78	0.00
H	-5.15	1.39	-0.88	H	-5.19	1.43	-0.88
C	-4.43	-1.25	0.00	C	-4.45	-1.27	0.00
H	-5.05	-1.02	0.88	H	-5.08	-1.04	0.88
H	-5.05	-1.02	-0.88	H	-5.08	-1.04	-0.88
H	-4.23	-2.33	0.00	H	-4.23	-2.34	0.00
Li	1.24	-2.87	0.00	Li	1.33	-2.86	0.00

(b) $Na^+LC(O4)$

S_0				S_1			
	x	y	z		x	y	z
C	-3.43	0.49	0.00	C	3.32	0.28	0.00
C	-2.21	1.13	0.00	C	2.02	0.86	0.00
C	-1.00	0.41	0.00	C	0.82	0.12	0.00
C	-1.04	-1.03	0.00	C	0.94	-1.28	0.00
C	-2.30	-1.67	0.00	C	2.25	-1.86	0.00
C	-3.47	-0.95	0.00	C	3.44	-1.12	0.00
C	1.22	-1.11	0.00	C	-1.30	-1.50	0.00
C	1.29	0.30	0.00	C	-1.46	-0.07	0.00
C	2.60	0.97	0.00	C	-2.80	0.48	0.00
C	3.66	-1.28	0.00	C	-3.73	-1.81	0.00
H	-2.17	2.22	0.00	H	1.95	1.95	0.00
H	-2.31	-2.76	0.00	H	2.29	-2.96	0.00
H	4.60	0.55	0.00	H	-4.78	-0.06	0.00
H	2.34	-2.84	0.00	H	-2.30	-3.28	0.00
N	0.08	-1.77	0.00	N	-0.13	-2.12	0.00
N	2.40	-1.83	0.00	N	-2.41	-2.27	0.00
N	3.67	0.13	0.00	N	-3.84	-0.44	0.00
N	0.19	1.05	0.00	N	-0.39	0.76	0.00
O	2.73	2.20	0.00	O	-3.05	1.70	0.00
O	4.68	-1.91	0.00	O	-4.67	-2.56	0.00
C	-4.79	-1.65	0.00	C	4.77	-1.79	0.00
H	-5.39	-1.38	-0.88	H	5.36	-1.51	0.88
H	-4.67	-2.74	0.00	H	4.66	-2.89	0.00
H	-5.39	-1.38	0.88	H	5.36	-1.51	-0.88
C	-4.71	1.28	0.00	C	4.52	1.16	0.00
H	-5.32	1.04	-0.88	H	5.16	0.96	0.88
H	-5.32	1.04	0.88	H	5.16	0.96	-0.88
H	-4.52	2.36	0.00	H	4.26	2.22	0.00
Na	0.88	3.38	0.00	Na	-1.29	2.97	0.00

(c) K⁺LC(O4)

S ₀				S ₁			
	x	y	z		x	y	z
C	-3.46	0.38	0.00	C	-3.42	0.15	0.00
C	-2.22	0.97	0.00	C	-2.09	0.67	0.00
C	-1.03	0.20	0.00	C	-0.93	-0.14	0.00
C	-1.13	-1.23	0.00	C	-1.12	-1.53	0.00
C	-2.42	-1.82	0.00	C	-2.46	-2.04	0.00
C	-3.56	-1.06	0.00	C	-3.61	-1.24	0.00
C	1.13	-1.40	0.00	C	1.10	-1.86	0.00
C	1.24	0.02	0.00	C	1.34	-0.44	0.00
C	2.58	0.63	0.00	C	2.70	0.03	0.00
C	3.55	-1.66	0.00	C	3.51	-2.31	0.00
H	-2.14	2.06	0.00	H	-1.96	1.75	0.00
H	-2.47	-2.91	0.00	H	-2.56	-3.13	0.00
H	4.56	0.12	0.00	H	4.65	-0.62	0.00
H	2.17	-3.17	0.00	H	1.99	-3.70	0.00
N	-0.04	-2.02	0.00	N	-0.10	-2.42	0.00
N	2.27	-2.16	0.00	N	2.17	-2.70	0.00
N	3.62	-0.26	0.00	N	3.69	-0.94	0.00
N	0.18	0.80	0.00	N	0.31	0.44	0.00
O	2.78	1.84	0.00	O	3.03	1.23	0.00
O	4.54	-2.34	0.00	O	4.41	-3.12	0.00
C	-4.91	-1.71	0.00	C	-4.97	-1.84	0.00
H	-5.49	-1.41	-0.88	H	-5.55	-1.53	-0.88
H	-4.82	-2.80	0.00	H	-4.93	-2.94	0.00
H	-5.49	-1.41	0.88	H	-5.55	-1.53	0.88
C	-4.71	1.21	0.00	C	-4.57	1.09	0.00
H	-5.33	1.00	-0.88	H	-5.22	0.92	-0.88
H	-5.33	1.00	0.88	H	-5.22	0.92	0.88
H	-4.47	2.29	0.00	H	-4.25	2.14	0.00
K	0.93	3.55	0.00	K	1.36	3.04	0.00

(d) Rb⁺LC(O4)

S ₀				S ₁			
	x	y	z		x	y	z
C	3.54	-0.03	0.00	C	-3.62	0.48	0.00
C	2.22	-0.41	0.00	C	-2.24	0.87	0.00
C	1.17	0.55	0.00	C	-1.16	-0.03	0.00
C	1.50	1.94	0.00	C	-1.48	-1.40	0.00
C	2.87	2.32	0.00	C	-2.86	-1.79	0.00
C	3.87	1.38	0.00	C	-3.93	-0.89	0.00
C	-0.70	2.48	0.00	C	0.70	-1.93	0.00
C	-1.04	1.10	0.00	C	1.07	-0.54	0.00
C	-2.47	0.71	0.00	C	2.47	-0.19	0.00
C	-3.05	3.14	0.00	C	3.06	-2.60	0.00
H	1.96	-1.47	0.00	H	-2.02	1.94	0.00
H	3.09	3.39	0.00	H	-3.05	-2.87	0.00
H	-4.33	1.54	0.00	H	4.35	-1.02	0.00
H	-1.44	4.40	0.00	H	1.42	-3.84	0.00
N	0.55	2.90	0.00	N	-0.54	-2.38	0.00
N	-1.70	3.42	0.00	N	1.69	-2.86	0.00
N	-3.34	1.76	0.00	N	3.36	-1.25	0.00
N	-0.12	0.15	0.00	N	0.12	0.43	0.00
O	-2.86	-0.45	0.00	O	2.91	0.97	0.00
O	-3.91	3.97	0.00	O	3.88	-3.48	0.00
C	5.31	1.80	0.00	C	-5.35	-1.37	0.00
H	5.84	1.41	-0.88	H	-5.89	-1.00	-0.88
H	5.40	2.90	0.00	H	-5.40	-2.46	0.00
H	5.84	1.41	0.88	H	-5.89	-1.00	0.88
C	4.63	-1.05	0.00	C	-4.68	1.52	0.00
H	5.28	-0.94	-0.88	H	-5.34	1.41	-0.88
H	5.28	-0.94	0.88	H	-5.34	1.41	0.88
H	4.23	-2.07	0.00	H	-4.27	2.54	0.00
Rb	-1.33	-2.61	0.00	Rb	1.43	3.09	0.00

(e) Cs⁺LC(O4)

S ₀				S ₁			
	x	y	z		x	y	z
C	-3.75	-0.21	0.00	C	-3.85	-0.30	0.00
C	-2.38	-0.37	0.00	C	-2.43	-0.43	0.00
C	-1.50	0.74	0.00	C	-1.54	0.66	0.00
C	-2.05	2.06	0.00	C	-2.12	1.95	0.00
C	-3.46	2.21	0.00	C	-3.54	2.07	0.00
C	-4.30	1.12	0.00	C	-4.42	0.98	0.00
C	0.03	2.94	0.00	C	-0.07	2.88	0.00
C	0.60	1.63	0.00	C	0.55	1.58	0.00
C	2.06	1.48	0.00	C	1.99	1.50	0.00
C	2.25	3.97	0.00	C	2.12	3.98	0.00
H	-1.95	-1.38	0.00	H	-2.01	-1.44	0.00
H	-3.85	3.23	0.00	H	-3.94	3.09	0.00
H	3.77	2.60	0.00	H	3.69	2.68	0.00
H	0.46	4.96	0.00	H	0.28	4.89	0.00
N	-1.26	3.16	0.00	N	-1.38	3.09	0.00
N	0.87	4.03	0.00	N	0.72	3.98	0.00
N	2.76	2.66	0.00	N	2.67	2.72	0.00
N	-0.16	0.55	0.00	N	-0.19	0.45	0.00
O	2.64	0.40	0.00	O	2.65	0.45	0.00
O	2.97	4.93	0.00	O	2.76	5.00	0.00
C	-5.78	1.31	0.00	C	-5.90	1.18	0.00
H	-6.24	0.84	0.88	H	-6.37	0.72	0.88
H	-6.05	2.38	0.00	H	-6.16	2.25	0.00
H	-6.24	0.84	-0.88	H	-6.37	0.72	-0.88
C	-4.66	-1.40	0.00	C	-4.70	-1.53	0.00
H	-5.32	-1.39	0.88	H	-5.37	-1.54	0.88
H	-5.32	-1.39	-0.88	H	-5.37	-1.54	-0.88
H	-4.10	-2.34	0.00	H	-4.11	-2.45	0.00
Cs	1.57	-2.19	0.00	Cs	1.70	-2.11	0.00

(f) LC

S ₀				S ₂			
	x	y	z		x	y	z
C	-3.38	0.66	0.00	C	-3.41	0.63	0.00
C	-2.18	1.34	0.00	C	-2.16	1.33	0.00
C	-0.94	0.65	0.00	C	-0.92	0.68	0.00
C	-0.94	-0.78	0.00	C	-0.93	-0.74	0.00
C	-2.18	-1.46	0.00	C	-2.18	-1.43	0.00
C	-3.37	-0.78	0.00	C	-3.42	-0.77	0.00
C	1.32	-0.76	0.00	C	1.32	-0.73	0.00
C	1.33	0.66	0.00	C	1.36	0.70	0.00
C	2.62	1.40	0.00	C	2.64	1.38	0.00
C	3.77	-0.84	0.00	C	3.77	-0.85	0.00
H	-2.14	2.43	0.00	H	-2.15	2.42	0.00
H	-2.15	-2.55	0.00	H	-2.14	-2.52	0.00
H	4.64	1.00	0.00	H	4.67	0.96	0.00
H	2.51	-2.45	0.00	H	2.44	-2.43	0.00
N	0.22	-1.48	0.00	N	0.21	-1.47	0.00
N	2.52	-1.43	0.00	N	2.49	-1.42	0.00
N	3.73	0.55	0.00	N	3.76	0.51	0.00
N	0.21	1.36	0.00	N	0.22	1.42	0.00
O	2.74	2.60	0.00	O	2.83	2.58	0.00
O	4.80	-1.46	0.00	O	4.76	-1.56	0.00
C	-4.67	-1.53	0.00	C	-4.71	-1.54	0.00
H	-5.28	-1.27	-0.88	H	-5.32	-1.31	-0.88
H	-4.50	-2.61	0.00	H	-4.52	-2.63	0.00
H	-5.28	-1.27	0.88	H	-5.32	-1.31	0.88
C	-4.68	1.41	0.00	C	-4.68	1.42	0.00
H	-5.29	1.16	-0.88	H	-5.30	1.17	-0.88
H	-5.29	1.16	0.88	H	-5.30	1.17	0.88
H	-4.51	2.49	0.00	H	-4.50	2.50	0.00

e) iso-LC

S ₀				S ₁			
	x	y	z		x	y	z
C	-3.37	0.68	0.00	C	-3.37	0.66	0.00
C	-2.15	1.33	0.00	C	-2.16	1.35	0.00
C	-0.93	0.63	0.00	C	-0.91	0.70	0.00
C	-0.96	-0.78	0.00	C	-0.96	-0.74	0.00
C	-2.19	-1.45	0.00	C	-2.18	-1.44	0.00
C	-3.38	-0.74	0.00	C	-3.39	-0.77	0.00
C	1.45	-0.80	0.00	C	1.42	-0.72	0.00
C	1.36	0.66	0.00	C	1.39	0.70	0.00
C	2.66	1.39	0.00	C	2.67	1.38	0.00
C	3.75	-0.87	0.00	C	3.74	-0.89	0.00
H	-2.09	2.42	0.00	H	-2.14	2.44	0.00
H	-2.20	-2.55	0.00	H	-2.16	-2.53	0.00
H	4.66	0.97	0.00	H	4.68	0.92	0.00
N	0.24	-1.44	0.00	N	0.24	-1.39	0.00
N	2.53	-1.53	0.00	N	2.49	-1.52	0.00
N	3.74	0.54	0.00	N	3.76	0.48	0.00
N	0.25	1.33	0.00	N	0.23	1.41	0.00
O	2.76	2.60	0.00	O	2.87	2.58	0.00
O	4.81	-1.45	0.00	O	4.76	-1.56	0.00
C	-4.69	-1.48	0.00	C	-4.68	-1.52	0.00
H	-5.29	-1.22	-0.88	H	-5.30	-1.28	-0.88
H	-4.54	-2.57	0.00	H	-4.51	-2.61	0.00
H	-5.29	-1.22	0.88	H	-5.30	-1.28	0.88
C	-4.65	1.45	0.00	C	-4.66	1.42	0.00
H	-5.27	1.22	-0.88	H	-5.27	1.17	-0.88
H	-5.27	1.22	0.88	H	-5.27	1.17	0.88
H	-4.46	2.54	0.00	H	-4.49	2.51	0.00
H	0.28	-2.45	0.00	H	0.31	-2.40	0.00

f) H⁺LC(N5)

S ₀				S ₁			
	x	y	z		x	y	z
C	-3.38	0.65	0.00	C	-3.44	0.62	0.00
C	-2.19	1.34	0.00	C	-2.20	1.31	0.00
C	-0.98	0.64	0.00	C	-0.96	0.64	0.00
C	-0.94	-0.80	0.00	C	-0.92	-0.76	0.00
C	-2.18	-1.48	0.00	C	-2.18	-1.44	0.00
C	-3.38	-0.80	0.00	C	-3.43	-0.78	0.00
C	1.34	-0.81	0.00	C	1.34	-0.79	0.00
C	1.37	0.59	0.00	C	1.40	0.62	0.00
C	2.63	1.37	0.00	C	2.65	1.36	0.00
C	3.79	-0.83	0.00	C	3.80	-0.83	0.00
H	-2.19	2.44	0.00	H	-2.21	2.40	0.00
H	-2.15	-2.57	0.00	H	-2.14	-2.53	0.00
H	4.65	1.03	0.00	H	4.68	1.01	0.00
H	2.56	-2.47	0.00	H	2.54	-2.46	0.00
N	0.21	-1.49	0.00	N	0.22	-1.50	0.00
N	2.55	-1.46	0.00	N	2.53	-1.44	0.00
N	3.74	0.57	0.00	N	3.77	0.55	0.00
N	0.23	1.26	0.00	N	0.24	1.31	0.00
O	2.62	2.58	0.00	O	2.68	2.58	0.00
O	4.82	-1.44	0.00	O	4.81	-1.49	0.00
C	-4.67	-1.54	0.00	C	-4.69	-1.57	0.00
H	-5.28	-1.28	-0.88	H	-5.31	-1.33	-0.88
H	-4.51	-2.63	0.00	H	-4.50	-2.65	0.00
H	-5.28	-1.28	0.88	H	-5.31	-1.33	0.88
C	-4.68	1.39	0.00	C	-4.72	1.39	0.00
H	-5.29	1.12	-0.88	H	-5.33	1.14	-0.88
H	-5.29	1.12	0.88	H	-5.33	1.14	0.88
H	-4.54	2.47	0.00	H	-4.55	2.48	0.00
H	0.32	2.28	0.00	H	0.32	2.33	0.00

g) H⁺LC(O4)

S ₀				S ₁			
	x	y	z		x	y	z
C	-3.38	0.66	0.00	C	-3.42	0.63	0.00
C	-2.18	1.34	0.00	C	-2.17	1.31	0.00
C	-0.94	0.64	0.00	C	-0.93	0.65	0.00
C	-0.94	-0.81	0.00	C	-0.94	-0.75	0.00
C	-2.18	-1.48	0.00	C	-2.21	-1.44	0.00
C	-3.37	-0.79	0.00	C	-3.44	-0.77	0.00
C	1.32	-0.83	0.00	C	1.31	-0.81	0.00
C	1.31	0.58	0.00	C	1.34	0.62	0.00
C	2.56	1.27	0.00	C	2.60	1.26	0.00
C	3.76	-0.86	0.00	C	3.77	-0.87	0.00
H	-2.15	2.43	0.00	H	-2.16	2.41	0.00
H	-2.16	-2.57	0.00	H	-2.17	-2.53	0.00
H	4.59	1.04	0.00	H	4.64	0.99	0.00
H	2.54	-2.49	0.00	H	2.50	-2.49	0.00
N	0.20	-1.53	0.00	N	0.19	-1.51	0.00
N	2.53	-1.48	0.00	N	2.50	-1.47	0.00
N	3.69	0.57	0.00	N	3.73	0.52	0.00
N	0.21	1.32	0.00	N	0.23	1.37	0.00
O	2.62	2.57	0.00	O	2.72	2.56	0.00
O	4.82	-1.41	0.00	O	4.79	-1.50	0.00
C	-4.67	-1.53	0.00	C	-4.72	-1.54	0.00
H	-5.27	-1.26	-0.88	H	-5.33	-1.29	-0.88
H	-4.52	-2.61	0.00	H	-4.54	-2.62	0.00
H	-5.27	-1.26	0.88	H	-5.33	-1.29	0.88
C	-4.67	1.40	0.00	C	-4.69	1.42	0.00
H	-5.28	1.14	-0.88	H	-5.30	1.17	-0.88
H	-5.28	1.14	0.88	H	-5.30	1.17	0.88
H	-4.52	2.49	0.00	H	-4.51	2.50	0.00
H	1.68	2.88	0.00	H	1.80	2.92	0.00

Acknowledgements

First, I would like to thank Prof. Dopfer, who gave me the opportunity to write my dissertation in his research group. I thank you for the great support in the last years.

Second, I thank Prof. Schmitt for reviewing this thesis and Prof. Knorr for the chair of the doctoral defense.

Third, I would also like to thank all past and current group members. Without their help this dissertation would not have been possible. Special thanks to Dr. Alan Günther and Dr. Pablo Nieto. Dr. Günther built the BerlinTrap setup and introduced me well to it. Dr. Nieto helped me with many calculations. I thank Prof. Miyazaki, who joined the group with a Humboldt fellowship. He always helped me with any scientific question. The students Alexander Sheldrick and Ronan Demarbaix helped me to conduct the experiments. I thank Dr. Marko Förstel and Parker Crandall for support in the laboratory. The last few years in the group have been great and I will miss that time.

I acknowledge financial support by the Deutsche Forschungsgemeinschaft.